THE JOURNAL OF PHYSICAL CHEMISTRY

Volume 69

JANUARY—APRIL 1965

PAGES 1—1436

EASTON, PA.
MACK PRINTING COMPANY
1965

THE JOURNAL OF
PHYSICAL CHEMISTRY

Published monthly by the American Chemical Society at 20th and Northampton Sts., Easton, Pa. 18043. Second-class postage paid at Easton, Pa.

The Journal of Physical Chemistry is devoted to the publication of selected symposia in the broad field of physical chemistry and to other contributed papers.

Manuscripts originating in the British Isles, Europe, and Africa should be sent to F. C. Tompkins, The Faraday Society, 6 Square, London W. C. 1, England.

Manuscripts originating elsewhere should be sent to Frederick Department of Chemistry, University of California, Santa Barbara, California.

Correspondence regarding accepted copy, proofs, and reprints should be directed to Research Journals Production Office, American Chemical Society, 20th and Northampton Sts., Easton, Pa. 18043. Senior Production Editor: Charles R. Bertsch. Assistant Senior Production Editor: Marianne C. Brogan. Assistant Editors: Edward A. Borger and Celia B. McFarland.

Advertising Office: Reinhold Publishing Corporation, 430 Park Avenue, New York, N. Y. 10022.

Articles must be submitted in duplicate, typed, and double spaced. They should have at the beginning a brief Abstract, in no case exceeding 300 words. Original drawings should accompany the manuscript. Lettering at the sides of graphs (black on white or blue) may be pencilled in and will be typeset. Figures and tables should be held to a minimum consistent with adequate presentation of information. All footnotes and references to the literature should be numbered consecutively and placed in the manuscript at the proper places. Initials of authors referred to in citations should be given. Nomenclature should conform to that used in *Chemical Abstracts*, mathematical characters be marked for italic, Greek letters carefully made or annotated, and subscripts and superscripts clearly shown. Articles should be written as briefly as possible consistent with clarity, avoiding historical background unnecessary for specialists.

Notes are similar to articles in every way except as to length and are subjected to the same editorial appraisal. In their preparation particular attention should be paid to brevity and conciseness. Material included in Notes must be definitive and may not be republished subsequently.

Symposium papers should be sent in all cases to Secretaries of Divisions sponsoring the symposium, who will be responsible for their transmittal to the Editor. The Secretary of the Division by agreement with the Editor will specify a time after which symposium papers cannot be accepted. The Editor reserves the right to refuse to publish symposium articles, for valid scientific reasons. Each symposium paper may not exceed four printed pages (about sixteen double spaced typewritten pages) in length except by prior arrangement with the Editor.

Alterations in an article after it has been set in type are made at the author's expense, and it is understood that by entering such alterations on proofs the author agrees to defray the cost thereof.

The American Chemical Society and the Editors of *The Journal of Physical Chemistry* assume no responsibility for the statements and opinions advanced by contributors.

Business and Subscription Information

Remittances and orders for subscriptions and for single copies, notices of changes of address and new professional connections, and claims for missing numbers should be sent to the Subscription Service Department, American Chemical Society, 1155 Sixteenth St., N.W., Washington, D. C. 20036. Allow four weeks for changes of address. Please include an old address label with the notification.

Claims for missing numbers will not be allowed (1) if received more than sixty days from date of issue, (2) if loss was due to failure of notice of change of address to be received before the date specified in the preceding paragraph, or (3) if the reason for the claim is "missing from files."

Subscription rates (1965): members of the American Chemical Society, $12.00 for 1 year; to nonmembers, $24.00 for 1 year. Postage to Canada and countries in the Pan-American Union, $2.00; all other countries, $3.00. Single copies for current year: $2.50. Postage, single copies: to Canada and countries in the Pan-American Union, $0.15; all other countries, $0.20. Rates for back issues are available from the Special Issues Sales Department, 1155 Sixteenth St., N.W., Washington, D. C. 20036.

A High Temperature Lab You Can Really Control

The Mettler Thermoanalyzer for thermogravimetric analysis (TGA) and simultaneous differential thermal analysis (DTA) is a new instrument with many degrees of flexibility and control. For example, it permits linear programming of temperatures to 1600° C. It allows work to be done in any gaseous atmosphere—including corrosive gases—and under pressures from 1000 to 8×10^{-4} mmHg. Pictured here is the sample chamber. For information about the complete system, write to Mettler Instrument Corporation, 20 Nassau Street, Princeton, New Jersey.

METTLER®

THE JOURNAL OF

PHYSICAL CHEMISTRY

Volume 69, Number 1 January 1965

NOTES

THE JOURNAL OF
PHYSICAL CHEMISTRY

VOLUME 69, NUMBER 1 JANUARY 15, 1965

Proton Resonance Spectra of Thiopyrones

by Jiří Jonáš, William Derbyshire, and H. S. Gutowsky

Noyes Chemical Laboratory, University of Illinois, Urbana, Illinois 61803 *(Received September 25, 1964)*

The proton magnetic resonance spectra of 4-pyrone, 4-thiapyrone, 4-thiopyrone, and 4-thiothiapyrone have been observed and analyzed. Comparisons of the experimental spectra with those calculated for all combinations of relative signs for the coupling constants indicate that in each molecule the coupling constants have the same sign, which presumably is positive. The average deviation between the observed line positions and those calculated for each of the various sign permutations is found to be a useful criterion in assigning the relative signs. The effect on the coupling constants of the introduction of sulfur into the molecule is discussed. The downfield shift of the midpoint of the spectra, found upon sulfur introduction, is interpreted in terms of an increased ring current.

Introduction

As an aid in developing an adequate theory of the proton–proton couplings in heterocyclic unsaturated molecules, more experimental data on the n.m.r. spectra of these systems are desirable. In this context, the thiopyrones studied in the present paper are interesting for several reasons. The spectra of these compounds are of the A_2B_2 type and amenable to a rigorous analysis. Furthermore, these compounds form a series of closely related molecules suitable for a study of the effect upon n.m.r. spectral parameters of the replacement of oxygen by sulfur. Another feature is the presence of oxygen or sulfur in the ring, which may provide information on the transmission of proton–proton coupling through a heteroatom. The polarographic behavior and chemical reactivity[1] of the thiopyrones have recently been studied, as have the physical properties,[2] and quantum chemical calculations have been made.[2] Hence, there is also interest in their n.m.r. parameters.

The general analysis of A_2B_2 type spectra has been discussed by a number of authors[3–6] who treated the effects of the magnitudes and relative signs of the n.m.r. parameters on the spectra in considerable detail. In the present paper, the n.m.r. spectra of 4-pyrone, 4-thiapyrone, 4-thiopyrone, and 4-thiothiapyrone have been analyzed and their chemical shifts and coupling constants are compared. Optimum values of the latter were calculated for all combinations of signs of coupling constants for each compound, and the calcu-

(1) C. Parkányi and R. Zahradník, *Collection Czech. Chem. Commun.*, **27**, 1355 (1962).

(2) R. Zahradník, C. Parkányi, and J. Koutecký, *ibid.*, **27**, 1242 (1962).

(3) J. A. Pople, W. G. Schneider, and H. J. Bernstein, "High Resolution Nuclear Magnetic Resonance," McGraw-Hill Book Co., Inc., New York, N. Y., 1959.

(4) B. Dischler and G. Englert, *Z. Naturforsch.*, **16b**, 1180 (1961).

(5) D. M. Grant, R. C. Hirst, and H. S. Gutowsky, *J. Chem. Phys.*, **38**, 470 (1963).

(6) H. M. Hutton and T. Schaefer, *Can. J. Chem.*, **41**, 2429 (1963).

lated spectra were compared with the experimental ones. In the case of the strongly coupled 4-thiothiapyrone, the comparison showed unambiguously that all four coupling constants have the same sign; in the less strongly coupled 4-thiapyrone and 4-thiopyrone cases this is the most probable assignment, but for the weakly coupled 4-pyrone, an assignment could not be made on this basis as the calculated spectra are almost independent of the combination of signs used, and the choice of all having the same sign is made by analogy with the other three compounds.

Experimental

Procedure and Results. The n.m.r. spectra were recorded with a Varian A60 spectrometer. The spectrum of each compound was run eight times and the arithmetic mean of each line position is used. The standard deviation in the mean line positions is ±0.08 c.p.s., except when several lines overlap. The spectrometer resolution was 0.4 c.p.s., but in the spectra of 4-thiothiapyrone the line widths were 0.8 c.p.s., possibly due to traces of decomposition products.

The compounds, all crystalline solids, were measured as 0.15 mole fraction solutions in $CDCl_3$, and tetramethylsilane was added as an internal reference. The chemical shift between the A_2 and B_2 protons is concentration-dependent. This dependence was studied in the neighborhood of 0.15 mole fraction. The change of chemical shift with dilution may be given as a quantity S defined as the change in magnitude of the chemical shift (in c.p.s.) per decrease in mole fraction of 0.01, calculated at 0.15 mole fraction. The values obtained for 4-pyrone, 4-thiapyrone, 4-thiopyrone, and 4-thiothiapyrone are S = 0.2, 0.3, 0.3, and −0.3, respectively. The relative positions of the lines observed in individual multiplets are practically independent of concentration in the 0.10 to 0.20 mole fraction range.

The samples of 4-pyrone, 4-thiapyrone, 4-thiopyrone, and 4-thiothiapyrone were provided by Dr. C. Parkányi of the Institute of Physical Chemistry of the Czechoslovak Academy of Science, Prague. The physical constants and synthesis of the thiopyrones are described in a recent paper by Parkányi and Zahradník.[1] The samples of 2,6- and 3,5-dimethyl-4-pyrones[7,8] were supplied by Dr. P. Beak of this laboratory. The sample of 2,6-dimethyl-4-thiopyrone[9] was obtained from Dr. M. A. F. Elkaschef of the National Research Centre, Cairo, U. A. R.

The analyses of the A_2B_2 spectra were carried out using the Swalen–Reilly[10] iterative programs for analysis of complex n.m.r. spectra (NMREN 1, NMRIT) and were run on the University of Illinois IBM 7094 computer. The results of the analyses are given in

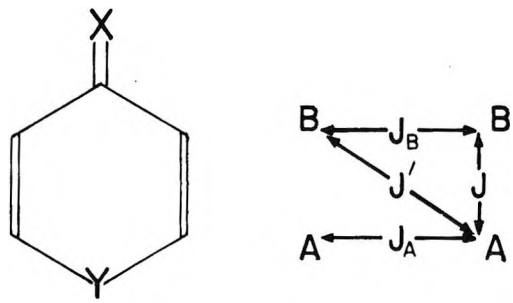

Figure 1. The structural formulas of the thiopyrones, with the designations used for the protons and coupling constants: X = O, Y = O, 4-pyrone; X = O, Y = S, 4-thiapyrone; X = S, Y = O, 4-thiopyrone; X = S, Y = S, 4-thiothiapyrone.

Table I. The structural formulas of the compounds and the definitions used in designating the protons and coupling constants are shown in Figure 1.

Discussion

A_2B_2 Spectra of Thiopyrones. The n.m.r. spectra of A_2X_2 and A_2B_2 spin systems have been discussed in detail in several papers.[3−6] Analysis of the spectra of the thiopyrones is straightforward so we will limit discussion of it to a minimum. An A_2B_2 spectrum, except in the case of very strong coupling, is composed of a high-field and a low-field multiplet, but it is not possible to assign these multiplets to the A_2 and B_2 nuclei in the molecule without further information. Fortunately, methylated 4-pyrones and a methylated 4-thiopyrone were available and the chemical shifts of the ring protons of these compounds permitted assignments to be made for the thiopyrones by comparison. The chemical shift of the ring protons in 3,5-dimethyl-4-pyrone is 456 c.p.s. downfield from TMS at 60 Mc.p.s.; in 2,6-dimethyl-4-pyrone it is 361 c.p.s., and in 2,6-dimethyl-4-thiopyrone it is 416 c.p.s. Upon comparing these values with those given in Table I for 4-pyrone (483 and 389 c.p.s.) and 4-thiopyrone (470 and 416 c.p.s.), we assign the low-field multiplet to the protons in the 2- and 6-positions (A protons) and the high-field multiplet to those in the 3- and 5-positions (B protons) for both compounds. In the absence of further experimental data, we assume the same assignments to be valid for 4-thiapyrone and 4-thiothiapyrone. Calculations of the electron density at the carbon atoms have been made using the MO–LCAO approximation[2] for all of the thiopyrones studied here. The electron density was

(7) P. Beak, *Tetrahedron*, 20, 831 (1964).

(8) P. Beak and G. A. Carls, *J. Org. Chem.*, 29, 2678 (1964).

(9) M. A. F. Elkaschef and M. H. Nosseir, *J. Chem. Soc.*, 4643 (1963).

(10) J. D. Swalen and C. A. Reilly, *J. Chem. Phys.*, 37, 21 (1962).

found to be higher at the 3- and 5-positions than at the 2- and 6-positions, which is consistent with the high-field assignments of the former.

Table I: Chemical Shifts and Coupling Constants of Thiopyrones[a]

Compound	ν_A	ν_B	$\Delta\nu$	J_A	J_B	J	J'
4-Pyrone	482.6	389.3	93.3	2.89	1.22	6.33	0.42
4-Thiapyrone	469.5	415.7	53.8	4.12	2.00	10.74	0.44
4-Thiopyrone	448.6	421.9	26.7	2.20	0.88	5.79	0.65
4-Thiothiapyrone	471.8	452.5	19.3	3.41	1.79	10.39	0.67

[a] All values are in c.p.s. The symbols used to designate the protons and coupling constants are defined in Figure 1. The chemical shifts are in c.p.s. downfield from TMS at 60 Mc.p.s.

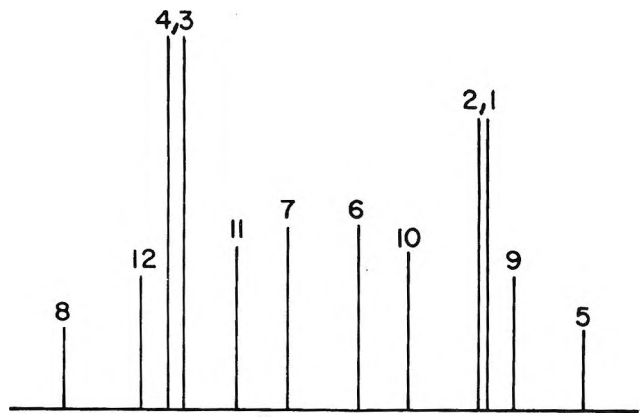

Figure 2. Schematic appearance of the high-field multiplet of the thiopyrone spectra. The frequency and intensity scales are arbitrary. For numbering of the transitions, see ref. 5.

The general appearance of the thiopyrone spectra studied by us is the same; the main difference is the decrease in the chemical shift between the A_2 and B_2 protons in going from 4-pyrone to 4-thiothiapyrone. A schematic high-field multiplet of a general thiopyrone spectrum is shown in Figure 2; the transitions are numbered as in previous work.[3,5] In all of the spectra, the lines due to transitions 3 and 4 overlap as do 1 and 2. This and similar overlap in the low-field multiplet reduce the number of resolved lines from 24 to 20. In the spectra of 4-pyrone and 4-thiapyrone, lines 9 and 12 are observed as shoulders on intense neighboring lines, but for 4-thiopyrone they were not resolved and the number of observed lines is reduced to 16.

Analyses of the spectra were performed for all combinations of relative signs for the coupling constants, by means of the Swalen–Reilly[10] energy level program MNREN 1 and the iterative program NMRIT. For each sign combination, the program converged to an optimum set of values for the parameters ν_a, ν_b, and the four coupling constants. The magnitudes obtained for a particular parameter depend upon the sign combination, but the main differences are the changes in the signs themselves. Therefore, we give only the final assigned sets of values, which are in Table I. A measure of relatively how well the different sets of parameters agree with experiment is the average deviation between the positions of the observed lines and those calculated with each set of parameters. These average deviations are listed in Table II for the eight relative sign combinations for each compound. For 4-thiothiapyrone, the best fit by a threefold factor is obtained when all the signs are the same. The results of the calculations for 4-thiopyrone favor sign assignments of $++++$ and $++--$ for J_A, J_B, J, and J', respectively. However, if the sign of J changes on going from 4-thiothiapyrone to 4-thiopyrone, then, as may be seen in Table I, its magnitude changes by about 16 c.p.s. This seems very unlikely, so the sign combination $++++$ is assigned to 4-thiopyrone. Similar reasoning in the case of 4-thiapyrone eliminates the sign combinations $+++-$, $++-+$, and $++--$ which give nearly the same low average deviation as does the combination $++++$.

The spectrum of 4-pyrone closely resembles an A_2X_2 spectrum, and it is almost insensitive to change in relative signs of the coupling constants, as can be seen from Table II. To illustrate how closely the spectrum of 4-pyrone resembles an A_2X_2 spectrum, the results of an A_2X_2 analysis for this compound are, in c.p.s.: $J_A = 2.88$, $J_B = 1.21$, $J = 6.36$, and $J' = 0.39$, all of which agree to within 0.03 c.p.s. of the values given in Table I for the A_2B_2 analysis. However, in view of the close similarities in the magnitudes of the coupling constants for 4-pyrone and the other three thiopyrones, we conclude that their relative signs are the same. Moreover, it seems most probable that these signs are positive. The finding that the coupling constants are of the same sign in the thiopyrones agrees with previous results on the signs of the coupling constants in aromatic and other heteroaromatic systems.[11–16]

(11) H. S. Gutowsky, C. H. Holm, A. Saika, and G. A. Williams, *J. Am. Chem. Soc.*, 79, 4596 (1957).

(12) R. E. Richards and T. Schaefer, *Mol. Phys.*, 1, 331 (1958).

(13) R. E. Richards and T. Schaefer, *Trans. Faraday Soc.*, 54, 1280 (1958).

(14) B. D. N. Rao and J. D. Baldeschwieler, *J. Chem. Phys.*, 37, 2473 (1962).

(15) W. G. Patterson and G. Bigam, *Can. J. Chem.*, 41, 1841 (1963).

(16) R. Freeman, N. S. Bhacca, and C. A. Reilly, *J. Chem. Phys.*, 38, 293 (1963).

Table II: Average Deviations in C.p.s. between the Transition Frequencies[a] for the Best Fit Calculated and the Observed Spectra of Thiopyrones Obtained by NMRIT for Each Combination of Relative Signs of the Coupling Constants[b]

Compound	Average deviation for given combination of signs							
	++++	−+++	+−++	++−+	+++−	++−−	+−−+	+−+−
4-Pyrone	0.023	0.025	0.025	0.020	0.023	0.020	0.025	0.025
4-Thiapyrone	0.047	0.073	0.069	0.054	0.047	0.054	0.073	0.069
4-Thiopyrone	0.077	0.096	0.092	0.389	0.374	0.058	0.394	0.394
4-Thiothiapyrone	0.113	0.311	0.269	0.540	0.396	0.322	0.530	0.530

[a] A similar analysis of the integrated intensities also can be used as an aid in establishing the correct combination of relative signs. [b] The signs given correspond to the following order of the coupling constants: J_A, J_B, J, and J'.

Effect of Replacement of Oxygen by Sulfur on N.m.r. Parameters. A comparison of the values for ν_A and ν_B in Table I shows that the chemical shift $\Delta\nu$ between the A_2 (2,6) and B_2 (3,5) protons is reduced as sulfur is introduced into the molecule. This reduction may be ascribed to the smaller electronegativity difference between C and S compared to that between C and O. In addition to the decrease in $\Delta\nu$, there is a concurrent downfield displacement of the average chemical shift $(\nu_A + \nu_B)/2$. One would expect the decreased electronegativity difference to produce upfield shifts,[3] so some other effect must be present. The average chemical shifts for the thiopyrones and some similar compounds[17] are listed in Table III, and in all heterocyclic "aromatic" compounds the shift of the sulfur derivative is downfield from that of the oxygen. It is apparent that this downfield shift is not the result of diamagnetic anisotropy of the sulfur because both cyclic and acyclic saturated compounds have an upfield shift, as expected from the electronegativity difference. The fact that only the unsaturated heterocyclic compounds have the downfield shift leads us to propose that it occurs as a result of an increased ring current in these compounds. Elvidge and Jackman[18] have based their definition of aromatic character on the ability of a compound to sustain an induced ring current. Therefore, in these terms the aromatic character and the delocalization of π-electrons increase when going from 4-pyrone to 4-thiothiapyrone. This observation may be regarded as evidence that due to its d-orbitals sulfur exhibits greater ability to enter into conjugation than oxygen.[19]

It is also interesting to compare the magnitudes of the coupling constants obtained by analyzing the spectra observed for the four thiopyrones. As is well known, the analysis of an A_2B_2 spin system does not distinguish between J_A and J_B, nor between J and J'. However, by means of other information, a tentative assignment can be made of the J_A coupling constant to coupling between the 2,6-protons (AA in Figure 1) and

Table III: Average Chemical Shifts of the A_2 and B_2 Protons in Thiopyrones and Related Compounds

Compound	Chemical shift,[a] c.p.s.	Compound	Chemical shift, c.p.s.
4-Pyrone	435	Thiophene[b]	432
4-Thiopyrone	435	Tetrahydrofuran[b]	168
4-Thiapyrone	443	Tetrahydrothiophene[b]	142
4-Thiothiapyrone	462	Anisole[b]	227
Furan[b]	414	Thioanisole[b]	148

[a] The shifts, at 60 Mc.p.s., are downfield from TMS and correspond to the midpoint of the A_2B_2 spectrum. [b] Data taken from ref. 17.

of J_B to coupling between 3,5-protons. This is based on the following facts. It has been found[20] for furan and thiophene that sulfur substitution increases J (our J_A) from 1.55 to 2.85 c.p.s. Similarly, recent data[21] on oxazole and thiazole derivatives have shown that J (J_A) in 4-methyloxazole is 1.0 c.p.s., whereas in 4-methylthiazole this coupling constant is 1.86 c.p.s. Thus, we would expect an increase in J_A of 0.9 to 1.3 c.p.s. to accompany the replacement of the *endo*-oxygen by sulfur in the thiopyrones.

Fortunately, the values found for J_A and J_B are such that there is only the one way, given in Table I, of arranging the coupling constants so that replacement of the *endo*-oxygen by sulfur causes an increase of $\sim$1 c.p.s., *i.e.*, upon going from 4-pyrone to 4-thiapyrone and from 4-thiopyrone to 4-thiothiapyrone. Moreover, this increase is 1.2 c.p.s. for what we list as J_A and appreciably less, 0.8 c.p.s., for J_B. Because of this dif-

(17) L. M. Jackman, "Applications of Nuclear Magnetic Resonance Spectroscopy in Organic Chemistry," Pergamon Press, New York, N. Y., 1959.

(18) J. A. Elvidge and L. M. Jackman, *J. Chem. Soc.*, 859 (1961).

(19) H. C. Longuet-Higgins, *Trans. Faraday Soc.*, 45, 173 (1949).

(20) R. J. Abraham and H. J. Bernstein, *Can. J. Chem.*, 39, 905 (1961).

(21) P. Haake and W. B. Miller, *J. Am. Chem. Soc.*, 85, 4044 (1963).

ference, we tentatively assign J_A as the coupling between the 2,6-protons which thus ranges from 2.2 to 4.1 c.p.s. and J_B as the 3,5-coupling from 0.9 to 2.0 c.p.s.

The assignment of the coupling constants J and J' can be made without ambiguity. For each of the four compounds, one of these constants is large (5.8 to 10.7 c.p.s.) and the other small (0.4 to 0.7 c.p.s.). The large constant is assigned as J, the coupling between the *ortho* protons 2 and 3 (5,6), and the small constant is assigned as J', the cross-coupling constant between *para* protons 2 and 5 (3,6). The assignment is made by comparison with *ortho* and *para* coupling constants in aromatic systems.[11]

A distinct change in the value of the J coupling constant accompanies the introduction of sulfur into the ring, as can be observed in Table I. This coupling constant changes from approximately 6 c.p.s. in 4-pyrone and 4-thiopyrone to 10 c.p.s. in 4-thiapyrone and 4-thiothiapyrone. A similar change of the corresponding constant is observed between furan and thiophene (the coupling constant increases from 1.8 to 4.7 c.p.s.). In the latter case, Abraham and Bernstein[20] ascribed the change to the decrease in the CCH bond angles produced by introducing a larger sulfur atom into the five-membered ring. Also, there is a large amount of evidence that the vinyl coupling constant increases with the ring size in cyclic olefins.[22] However, it has been argued[23] that the change of J in thiophene compared to furan is primarily an electronegativity effect upon the ionic character of the C–H bonds which are α to the *endo*-oxygen or sulfur. It seems reasonable to assume that both of these effects operate in the thiopyrones and tend to increase the J coupling constant upon substitution of sulfur for oxygen in the ring.

Acknowledgments. The authors wish to express their thanks to Dr. C. Parkányi for his gift of the compounds used in this study, and to Dr. J. D. Swalen for supplying the iterative programs. We are indebted to the staff of the Digital Computer Laboratory for their assistance. The research was supported by the U. S. Office of Naval Research and by the National Science Foundation.

(22) O. L. Chapman, *J. Am. Chem. Soc.* **85**, 2014 (1963).

(23) H. S. Gutowsky and A. L. Porte, *J. Chem. Phys.*, **35**, 839 (1961).

The Solution Thermochemistry of Polyvalent Electrolytes.

I. Calcium Hydroxide

by Harry P. Hopkins, Jr., and Claus A. Wulff

Department of Chemistry, Carnegie Institute of Technology, Pittsburgh, Pennsylvania
(Received September 5, 1964)

Values for the thermodynamic functions characterizing the solution of calcium hydroxide have been obtained by utilizing data from the literature and newly determined values for the enthalpy of solution both in water and in dilute hydrochloric acid. It has been shown that previous evaluations of these quantities are in error, partially because of nonconsideration of the "weak" second ionization step. For the change in state, $Ca(OH)_2(s) = Ca^{+2}(aq) + 2OH^-(aq)$, the following values have been determined for increments in the thermodynamic state functions at 25°: $\Delta G^\circ = 7100$ cal./mole, $\Delta H^\circ = -4290$ cal./mole, and $\Delta S^\circ = -38.2$ cal./(mole °K.). The standard entropy of the aqueous $Ca(OH)^+$ ion has been estimated as -4.4 cal./(mole °K.).

An analysis of the solution thermochemistry of calcium hydroxide, *i.e.*, values for the thermodynamic functions characterizing the change in state

$$Ca(OH)_2(s) = Ca^{+2}(aq) + 2OH^-(aq) \qquad (1)$$

is dependent upon the assumptions made concerning the second ionization step

$$Ca(OH)^+(aq) = Ca^{+2}(aq) + OH^-(aq) \qquad (2)$$

Values for the standard Gibbs free energy, ΔG_1°, the standard enthalpy, ΔH_1°, and the standard entropy, ΔS_1°, increments for eq. 1 have been reported by Latimer, Schutz, and Hicks[1] and by Greenberg and Copeland.[2] Their values, at 25°, have been summarized in Table I.

Table I: Literature Values for the Thermodynamics of Solution of $Ca(OH)_2(s)$

	ΔG_1°, cal./mole	ΔH_1°, cal./mole	ΔS_1°, cal./(mole °K.)
Reference 1	6810	−3290	−34.0
Reference 2	6960	−3385	−34.7

Although the accord shown by these data is excellent, the values cannot be accepted until the effects of several sources of errors are considered. The data used by Latimer, *et al.*, include a standard entropy for $Ca(OH)_2(s)$ of 18.24 cal./(mole °K.), which has since been superseded by a value of 19.93 cal./(mole °K.).[3] Their enthalpy of solution is derived from the determinations of Thomsen[4] and Berthelot[5] with estimated corrections for dilution and temperature changes. Latimer, *et al.*,[1] do not consider the effect of a possibly "weak" second ionization, and Thomsen and Berthelot's work was performed during the period when the existence of ions in solution was still questioned.

Greenberg and Copeland,[2] while cognizant of the "weak" second ionization step, made no use of it in their data reduction. Their value for the entropy increment, derived from the temperature dependence of the solubility, is markedly different from the value that can be computed from tabulations of standard entropy values.

A number of studies have been made to determine

(1) W. M. Latimer, P. W. Schutz, and J. F. G. Hicks, Jr., *J. Am. Chem. Soc.*, 55, 971 (1933).

(2) S. A. Greenberg and L. E. Copeland, *J. Phys. Chem.*, 64, 1057 (1960).

(3) W. E. Hatton, D. L. Hildenbrand, G. C. Sinke, and D. R. Stull, *J. Am. Chem. Soc.*, 81, 5028 (1959).

(4) J. Thomsen, "Thermochemische Untersuchungen," Vol. III, Johann Ambrosius Barth Verlag, Leipzig, 1883.

(5) M. Berthelot, *Ann. chim. phys.*, 4, 531 (1875).

the value of the ionization constant, K_2, for eq. 2.[6-12] The results range between $K_2 = 0.04$ and 0.07. Bates, *et al.*,[12] in the most exhaustive study, conclude that no unambiguous value can be derived for K_2. They present three equations for that quantity as a function of the ionic strength, each reflecting a different concentration dependence for an activity coefficient ratio. Their intermediate relationship has been adopted herein and appears as eq. 5 below.

The standard free energy increment for eq. 1 can be computed from

$$\Delta G_1^\circ = -RT \ln m_{Ca^{+2}} m_{OH^-}{}^2 \gamma_{Ca^{+2}} \gamma_{OH^-}{}^2 \qquad (3)$$

where the m and γ values are, respectively, the molal concentrations and molal activity coefficients in the saturated solution. The solubility of $Ca(OH)_2(s)$ is given as 0.0203 m.[13]

The activity coefficients and concentrations in eq. 3 are solutions to the following set of equations.

$$I = {}^1/_2[4m_{Ca^{+2}} + m_{OH^-} + m_{Ca(OH)^+}] \qquad (4)$$

$$-\log K_2 = 1.221 + 2.802I \qquad (5)$$

$$[m_{Ca^{+2}} m_{OH^-}/m_{Ca(OH)^+}][\gamma_{Ca^{+2}} \gamma_{OH^-}/\gamma_{Ca(OH)^+}] = K_2 \qquad (6)$$

$$-\log \gamma = [0.505z^2 I^{1/2}/(1 + I^{1/2})] - 0.3I \qquad (7)$$

Equation 7 is an extended Debye–Hückel relation at 25° for the activity coefficient of an ion with charge z in a solution of ionic strength I. The solutions to these equations are $m_{Ca^{+2}} = 0.0145$, $m_{OH^-} = 0.0345$, $\gamma_{Ca^{+2}} = 0.507$, $\gamma_{OH^-} = 0.838$, and $\Delta G_1^\circ = 7100$ cal./mole.

The standard entropy of the aqueous hydroxide ion is −2.5 cal./(mole °K.),[1,14] that of the aqueous calcium ion is −13.2 cal./(mole °K.),[15] and that of $Ca(OH)_2(s)$ is 19.93 cal./(mole °K.),[3] leading to $\Delta S_1^\circ = -38.2$ cal./(mole °K.). The enthalpy of solution can now be computed as $\Delta H_1^\circ = 7100 + 298.15(-38.2) = -4290$ cal./mole.

This value differs by almost 1 kcal./mole from those given in Table I. To resolve this discrepancy a direct determination of the enthalpy of solution of $Ca(OH)_2(s)$ was undertaken.

Experimental

Fisher certified reagent calcium hydroxide was used without further purification although efforts were made to minimize its exposure to moist air during weighing and loading. Satisfactory rates of dissolution were obtained for samples ranging between 0.25 and 1.45 g. All samples were dissolved into 950 ml. of freshly boiled, distilled water. The solution calorimeter, which has been described previously,[16] has as its temperature-sensing element a laboratory-wound resistance thermometer. The Mueller bridge circuitry and adjuvant electrical standards have also been described. Sixteen experimental determinations of the heat of solution in water, at 25.0 ± 0.1°, between $m = 0.004$ and 0.020 were fitted, by the method of least squares, to the straight line, $\Delta H_{obsd} = -4535 + 7160m^{1/2} \pm 30$ cal./mole, where the uncertainty is the r.m.s. deviation.

A second series of measurements were performed in which calcium hydroxide samples, ranging from 0.18 to 1.05 g., were dissolved into 950 ml. of 0.04 N hydrochloric acid. The observed heat effects approached the upper limit of the calorimeter's useful range, and are, therefore, less reliable. In addition, rates of dissolution were slower—as long as 6 min. being required for attainment of equilibrium. Ten determinations (corrected for dilution of the unreacted acid) at 25.0 ± 0.3° were fitted by least squares to the straight line, $\Delta H_{acid} = -31.09 + 8.76m^{1/2} \pm 0.18$ kcal./mole. Three additional data points, more than 300 cal./mole different from the straight line value, were observed but were not included in the least-squares analysis.

Data Analysis

The observed concentration dependence of the heats of solution in water has almost twice the slope reported for other electrolytes of the type MX_2.[17] The additional heat effect must be caused by the "weak" second ionization, the extent of which is a function of concentration. The observed heats of solution can be represented by

$$\Delta H_{obsd} - \Delta H_{dil} = \Delta H_1^\circ - (1 - \alpha)\Delta H_2^\circ \qquad (8)$$

where ΔH_{dil} is the concentration-dependent heat of dilution, ΔH_1° and ΔH_2° are the standard enthalpy

(6) C. W. Davies, *Endeavour*, **4**, 114 (1945).

(7) R. P. Bell and J. E. Prue, *J. Chem. Soc.*, 362 (1949).

(8) R. P. Bell and G. M. Wiand, *ibid.*, 1979 (1950).

(9) C. W. Davies and B. E. Hoyle, *ibid.*, 233 (1951).

(10) R. P. Bell and J. H. B. George, *Trans. Faraday Soc.*, **49**, 619 (1953).

(11) F. G. R. Gimblett and C. M. Monk, *ibid.*, **50**, 965 (1954).

(12) R. G. Bates, V. E. Bower, R. G. Canham, and J. E. Prue, *ibid.*, **55**, 2062 (1959).

(13) R. G. Bates, V. E. Bower, and E. R. Smith, *J. Res. Natl. Bur. Std.*, **56**, 305 (1956).

(14) W. M. Latimer, K. S. Pitzer, and W. V. Smith, *J. Am. Chem. Soc.*, **60**, 1829 (1938).

(15) C. C. Stephenson, personal communication.

(16) C. Wu, M. M. Birky, and L. G. Hepler, *J. Phys. Chem.*, **67**, 1202 (1963).

(17) H. S. Harned and B. B. Owen, "The Physical Chemistry of Electrolytic Solutions," Reinhold Publishing Corp., New York, N. Y., 1958.

increments for eq. 1 and 2, respectively, and $\alpha = m_{Ca^{+2}}/[m_{Ca^{+2}} + m_{Ca(OH)^+}]$ is the degree of second ionization. The quantity α can be determined, as was indicated previously for the saturated solution, and is given in Table II for selected concentrations. Also listed in Table II are ΔH_{obsd} and ΔH_{dil}—the latter estimated from data for alkaline earth halides[17] which are strong electrolytes in both steps.[6]

Table II: Heats of Solution and Dilution

m	ΔH_{obsd}, cal./mole	ΔH_{dil}, cal./mole	α
0.0064	−3962	165	0.878
0.0100	−3819	200	0.828
0.0144	−3681	230	0.775
0.0203	−3515	270	0.713

The values of $\Delta H_1°$ and $\Delta H_2°$, as determined from a least-squares analysis of eq. 8, are −4360 ± 50 cal./mole and −2.0 ± 0.4 kcal./mole, respectively. It should be remarked, at this point, that assumption of the alternate equations for log K_2 proposed by Bates, *et al.*,[12] leads to estimates of $\Delta H_1°$ within 50 cal./mole of the value derived above.

If twice the enthalpy of ionization of water, 13.36 kcal./mole[18] is subtracted from the limiting heat of solution of $Ca(OH)_2$(s) in dilute HCl, a value of 4.37 ± 0.20 kcal./mole is obtained for $\Delta H_1°$.

Discussion

The accord of the two experimentally determined values of the enthalpy of solution of calcium hydroxide (4.36 and 4.37 kcal./mole) with the value calculated (4.29 kcal./mole) from ionic entropies and the solubility substantiates the existence of a "weak" second ionization step. That these values are almost 1 kcal./mole different from that derived from a temperature derivative of a solubility relation indicates the care that must be exercised in the latter method. By combining literature data and our experimental determinations, the values for the thermodynamic functions characteristic of the solution of calcium hydroxide are $\Delta G_1° = 7100$ cal./mole, $\Delta H_1° = -4290$ cal./mole, and $\Delta S_1° = -38.2$ cal./(mole °K.).

The data for solution in HCl are in fair accord with previous determinations of this enthalpy of solution: 30.85,[19] 30.71,[20] 30.85,[21] and 31.23.[22]

The values of K_2 at infinite dilution [0.06 from eq. 5] and of $\Delta H_2°$ lead to an entropy increment for eq. 2 of −12.3 cal./(mole °K.). That value is in good accord with estimates of −10.4[10] and −11.3[11] from the temperature derivative of K_2. The standard entropy of the aqueous $Ca(OH)^+$ ion can be calculated as −4.4 cal./(mole °K.) from the previous datum and the standard entropies of the aqueous calcium and hydroxide ions.

Acknowledgment. The authors are grateful to Professor Loren G. Hepler for the use of his laboratory facilities and to Professor Clark C. Stephenson, of the Massachusetts Institute of Technology, for suggestion of the problem. The partial financial support of the National Science Foundation is also gratefully acknowledged.

(18) K. S. Pitzer, *J. Am. Chem. Soc.*, **59**, 2365 (1937).

(19) T. Thorvaldson and W. G. Brown, *ibid.*, **52**, 80 (1930).

(20) W. A. Roth and P. Chall, *Z. Elektrochem.*, **34**, 185 (1928).

(21) H. E. Schweite and E. Hey, *Z. anorg. allgem. Chem.*, **217**, 396 (1934).

(22) K. Taylor and L. S. Wells, *J. Res. Natl. Bur. Std.*, **21**, 133 (1938).

The Solution Thermochemistry of Polyvalent Electrolytes. II. Silver Sulfate

by Harry P. Hopkins, Jr., and Claus A. Wulff

Department of Chemistry, Carnegie Institute of Technology, Pittsburgh, Pennsylvania
(Received September 5, 1964)

Values for the thermodynamic functions characterizing the solution of silver sulfate have been obtained by utilizing data from the literature and newly determined values for the enthalpy of solution. It has been shown that previous evaluations of these quantities are in error, partially because of nonconsideration of the "weak" second ionization step. For the change in state, $Ag_2SO_4(s) = 2Ag^+(aq) + SO_4^{-2}(aq)$, the following values have been determined for increments in the thermodynamic state functions, at 25°: ΔG° = 6740 cal./mole, ΔH° = 4120 cal./mole, and ΔS° = −8.8 cal./(mole °K.). The standard entropy of the aqueous $AgSO_4^-$ ion has been estimated as 33 cal./(mole °K.).

The solution thermochemistry of salts whose aqueous solutions contain other than univalent ions is often complicated by secondary processes concomitant with solution and ionization, *i.e.*, "weak" ionization steps and hydrolysis. The failure to account for thermal effects arising from such sources (or, indeed, even to recognize them in the case of older work) has resulted in a thermochemical literature rich with inconsistent evaluations of the standard thermodynamic functions describing the solution and ionization of complex electrolytes. In favorable cases, such as calcium hydroxide,[1] it has been possible to unravel the thermodynamics of the primary and secondary processes by a careful analysis of the concentration dependence of the heats of solution. This work describes such an analysis for the solution of silver sulfate

$$Ag_2SO_4(s) = 2Ag^+(aq) + SO_4^{-2}(aq) \qquad (1)$$

Documentation of a "weak" second ionization step for silver sulfate

$$AgSO_4^-(aq) = Ag^+(aq) + SO_4^{-2}(aq) \qquad (2)$$

is sparse and consists of only the conductance measurements of Righellato and Davies[2] and the potentiometric studies of Leden[3] at high ionic strength.

The standard Gibbs free energy of solution, ΔG_1°, has been determined in several studies on the assumption (usually implicit) that silver sulfate is completely ionized. For example, the solubility quoted in Seidell,[4] 0.02676 m, and the mean activity coefficient in the saturated solution,[5] $\gamma_\pm$ = 0.588, lead to $\Delta G_1^\circ = -RT \ln 4\gamma_\pm^3 m^3$ = 6557 cal./mole. Determination of the activity product by Kenttamaa[6] and by Vosburgh and McClure[7] led to values of 6510 and 6550 cal./mole, respectively, for ΔG_1°. An extensive series of determination of the solubility of silver sulfate in solutions of various supporting electrolytes has been reported by Stoughton and Lietzke.[8] These authors average the extrapolated values of their measurements (to zero ionic strength) in H_2SO_4, HNO_3, and $MgSO_4$ as 6595 cal./mole. In all these studies the supporting electrolyte contributed hydrogen and/or sulfate ions to the solution, surpressing the second ionization step if it is "weak" or masking it with the formation of bisulfate ions. The accord shown by the four values cited permits their average, 6550 ± 30 cal./mole, to

(1) H. P. Hopkins, Jr., and C. A. Wulff, *J. Phys. Chem.*, **69**, 6 (1965).

(2) E. C. Righellato and C. W. Davies, *Trans. Faraday Soc.*, **26**, 592 (1930).

(3) I. Leden, *Acta Chem. Scand.*, **6**, 971 (1952).

(4) W. F. Linke, "Seidell's Solubilities of Inorganic and Metal Organic Compounds," 4th Ed., D. van Nostrand Co., Inc., Princeton, N. J., 1958.

(5) J. B. Chloupek and Vl. Z. Danes, *Collection Czech. Chem. Commun.*, **4**, 8 (1932).

(6) J. Kenttamaa, *Suomen Kemistilehti*, **30B**, 9 (1957); *Chem. Abstr.*; **51**, 10159 (1957).

(7) W. C. Vosburgh and R. S. McClure, *J. Am. Chem. Soc.*, **65**, 1060 (1943).

(8) R. W. Stoughton and M. R. Lietzke, *J. Phys. Chem.*, **64**, 133 (1960).

be adopted for $\Delta G_1°$ *if* the second ionization step is not "weak."

In their tabulation of the activity product of silver sulfate, Stoughton and Lietzke[8] did not include their results utilizing KNO_3 as the supporting medium. This latter value they report to be low by 0.103 pK unit—140 cal./mole. This is perhaps the only electrolyte in which the solubility of silver sulfate is uncomplicated by the medium. The value of $\Delta G_1°$, in KNO_3, is then 6595 + 140 = 6735 cal./mole. An independent evaluation of $\Delta G_1°$ is reported by Pan and Lin[9] from their thorough study of the electromotive force of the $Ag(s)/Ag_2SO_4(s)$ electrode. Their value for the standard free energy of solution is 6707 cal./mole and is independent of any assumption about the strength of the second ionization step.

Righellato and Davies[2] report the extent of the second ionization step at only two concentrations of silver sulfate. If the concentration dependence of this quantity (but not its numerical value) is assumed to be the same as that for Tl_2SO_4 and K_2SO_4, the degree of second ionization in the saturated solution is 0.77. This datum leads to a silver ion concentration of 0.047 m and a sulfate ion concentration of 0.021 m. The saturated solution is still sufficiently dilute to permit estimation of the activity coefficients by $-\log \gamma = 0.505z^2 \cdot \sqrt{I}/(1 + \sqrt{I})$, as $\gamma_{Ag^+} = 0.785$ and $\gamma_{SO_4^{-2}} = 0.382$. The standard free energy of solution corresponding to these data is $\Delta G_1° = -RT \ln (0.047)^2(0.785)^2(0.021) \cdot (0.382) = 6770$ cal./mole.

The average of the last three values cited for $\Delta G_1°$, 6740 ± 25 cal./mole, may tentatively be taken as representing the standard free energy of solution for silver sulfate on the assumption of a "weak" second ionization step.

The entropy of $Ag_2SO_4(s)$ has been determined by Latimer, Hicks, and Schutz[10] as 47.8 cal./(mole°K.). The sum $2S°_{Ag^+} + S°_{SO_4^{-2}}$ has been evaluated as 39.0 cal./mole °K.) from a consideration of the data for silver and alkali halides, nitrates, and sulfates.[11] The standard entropy increment for eq. 1 is then 39.0 − 47.8 = −8.8 cal./(mole °K.). The standard enthalpy of solution, $\Delta H_1°$, can now be computed as either 6550 − 298.15(8.8) = 3930 cal./mole or 6740 − 298.15(8.8) = 4120 cal./mole, representing the choices of "strong" and "weak" second ionization, respectively.

An indirect determination of the enthalpy of solution by Thomsen,[12] at 18°, as 4480 cal./mole for $Ag_2SO_4 \cdot 1400H_2O$ has been corrected by Latimer, *et al.*,[10] to give $\Delta H_1° = 4207$ cal./mole. This value is supported by the result of Pan and Lin,[9] 4215 cal./mole, derived from the temperature dependence of the e.m.f. of the $Ag(s)/Ag_2SO_4(s)$ electrode. In contrast, Stoughton and Lietzke[8] report 4.47 kcal./mole from the temperature dependence of the solubility. No attempt was made to account for the effect of the second ionization step in the derivations of these values.

To permit a choice between the inconsistent values available for the thermodynamic functions describing the solution of silver sulfate, a direct determination of the heat of solution was undertaken.

Experimental

Several commercial samples of silver sulfate were tested for suitability as experimental material and were rejected because of slow rates of dissolution. A fresh sample was prepared by treating a solution of Fisher certified reagent silver nitrate with a dilute solution of sulfuric acid. Only the initial precipitate was collected. After successive washing with cold absolute ethanol and cold ether, the sample was dried under vacuum for 1 week. Duplicate gravimetric determinations of the silver content (as silver chloride) indicated a purity of 99.8%; a value comparable to the purity of the initial silver nitrate.

Calorimetric determinations were made using the existing apparatus,[13] which includes a resistance thermometer to sense temperature increments. Samples of the silver sulfate, described above, ranging between 1.56 and 4.28 g. were dissolved into 950 ml. of distilled water at 25.0 ± 0.1°. The data were converted to enthalpies of solution on the basis of a gram formula mass of 311.83. Twelve determinations, covering the concentration range m = 0.005 to 0.014, were fitted, by least squares, to the straight line

$$\Delta H_{obsd} = 4175 + 3370m^{1/2} \pm 40 \text{ cal./mole} \quad (3)$$

where the uncertainty is the r.m.s. deviation.

Discussion

The existence of a "weak" second ionization step can be tested as follows. The observed heat of solution can be represented by

$$\Delta H_{obsd} - \Delta H_{dil} = \Delta H_1° - (1 - \alpha)\Delta H_2° \quad (4)$$

where ΔH_{dil} is the concentration-dependent heat of dilution (estimated from values for the alkali sulfates), $\Delta H_2°$ is the standard enthalpy increment for eq. 2, and α is the extent of the weak second ionization. If

(9) K. Pan and C-L. Lin, *J. Chinese Chem. Soc.* (Taiwan), 6, 1 (1959).

(10) W. M. Latimer, J. F. G. Hicks, and P. W. Schutz, *J. Chem. Phys.*, 1, 424 (1933).

(11) C. C. Stephenson, personal communication.

(12) J. Thomsen, "Thermochemische Untersuchungen," Vol. III, Johann Ambrosius Barth Verlag, Leipzig, 1883.

(13) C. Wu, M. M. Birky, and L. G. Hepler, *J. Phys. Chem.*, 67, 1202 (1963).

values of α are chosen (as described previously for the saturated solution) at selected concentrations in the range covered by our measurements and the quantity $(1 - \alpha)$ is plotted against the left-hand side of eq. 4, a straight line can be fitted through the points. The intercept, 4140 ± 50 cal./mole, and slope, −1.5 ± 0.3 kcal./mole, correspond to $\Delta H_1°$ and $\Delta H_2°$, respectively. The accord between the experimental value for $\Delta H_1°$ and that estimated previously on the assumption of a "weak" second ionization step is excellent and substantiates that assumption.

Additional evidence that a second process occurs concomitantly with solution and ionization of silver sulfate is the over-all concentration dependence of the heat of solution. When compared to "normal" electrolytes of the same valence type (alkali sulfates and alkaline earth halides) the slope of ΔH_{obsd} against $\sqrt{m}$ is nearly twice as steep for silver sulfate as for the others.

The estimated equilibrium constant for eq. 2 is 0.05, from the work of Righellato and Davies.[2] The standard free energy is then $\Delta G_2° = -RT \ln 0.05 = 1.8$ kcal./mole, and the standard entropy increment for eq. 2 is $(-1.5 - 1.8)/0.298 = -11$ cal./(mole °K.). This last datum combined with the ionic entropies for the aqueous silver and sulfate ions can be used to estimate the entropy of the aqueous $AgSO_4^-$ ion as 33 cal./(mole °K.). This value is consistent with those of other univalent oxy anions.

Acknowledgment.—The authors are grateful to Professor Loren G. Hepler for the use of his laboratory and its facilities and to Professor Clark C. Stephenson, of the Massachusetts Institute of Technology, for his helpful discussion. The partial financial support of the National Science Foundation is gratefully acknowledged.

Thermodynamic Considerations in Molten Metal–Metal Salt Solutions[1a]

by L. E. Topol[1b]

Atomics International, A Division of North American Aviation, Canoga Park, California
(Received September 16, 1963)

The standard free energies of solution of isolated metal atoms with the molten chloride of that metal were calculated from vapor pressure and solubility data for 34 systems. Based on the values of these standard free energies of dissolution, a useful correlation is obtained. This correlation allows one to classify systems in terms of the magnitude of the energies and to estimate solubilities in some systems where experimental data are not available.

Introduction

Solutions of various metals in their respective molten salts have been the subject of numerous investigations.[2] It is the purpose of this paper to calculate the standard free energies of dissolution involved in the equilibrium between isolated gaseous metal atoms and metal atoms dissolved in molten salts from solubility and vapor pressure data and to correlate these values. The results of this study suggest that the dissolution energy may be employed as a measure of the interaction energy of isolated metal atoms with the solvent. A classi-

(1) (a) This work was supported by the Research Division of the U. S. Atomic Energy Commission. It has been presented before the Division of Physical Chemistry at the 145th National Meeting of the American Chemical Society, New York, N. Y., Sept. 1963. (b) North American Aviation Science Center, Thousand Oaks, Calif.

(2) See, for example, M. Bredig in "Molten Salt Chemistry," M. Blander, Ed., Interscience Publishers, Inc., New York, N. Y., 1964, p. 367.

fication of these systems, based on the magnitude of these energies, appears to be more meaningful and useful (for the estimation of solubilities in unknown systems) than a correlation based on a nonquantitative property, *e.g.*, subhalide formation.

To calculate the solution energy of isolated metal atoms with a fused salt, one may consider the dissolution of a metal as the removal of metal atoms from the bulk metal to the gas phase followed by interaction of the atoms with the solvent to yield a solution of concentration C. (The process requires the formation of holes in the solvent to accommodate the metal atoms.) The work required to overcome the cohesive binding energy of the metal in the first step is equal to the standard free energy of sublimation or vaporization of the metal to a monatomic gas. This work (along with that involved in the formation of holes) is then compensated by the interaction energy arising in the second step. A similar approach was suggested by Blander[3] and used to calculate the interaction energy of a hypothetical alkali–alkali halide melt.[2]

Thermodynamic Considerations

To calculate the standard chemical potential or free energy of dissolution $\Delta\mu_D^*$ for a metal–salt system, consider a solution of a metal M in a molten salt MX_n in equilibrium with metal atoms in the gas phase above the solution at a temperature T. $\Delta\mu_D^*$ is then given by the relation

$$\Delta\mu_D^* = \mu_M^*(\text{soln.}) - \mu_M^*(g) = RT \ln \frac{f_M(g)}{a_M(\text{soln})} = RT \ln \frac{C_M(g)}{C_M(\text{soln})} \frac{\gamma_M(g)}{\gamma_M(\text{soln})} \quad (1)$$

where $\mu_M^*(g)$, $f_M(g)$, and $\gamma_M(g)$ are the standard state chemical potential, fugacity, and activity coefficient, respectively, of the metal in the vapor phase, and $\mu_M^*(\text{soln})$, $a_M(\text{soln})$, and $\gamma_M(\text{soln})$ are the standard chemical potential, activity, and activity coefficient of the metal in solution. The standard state for the components is taken as the hypothetical solution with a concentration of 1 mole/l. The equilibrium concentration C_M of metal in the two phases should be taken in similar units, such as moles/l., in order to eliminate a physically unimportant contribution to the free energy arising from the choice of two different standard states.

In the application of eq. 1 to calculate the change in the standard free energy of a mole of isolated metal atoms going from the gas phase into solution, the concentration or partial pressure of the metal as monomer atoms in the vapor phase above the solution must be known. Since these values are usually available only for solutions in equilibrium with a pure metal phase, one is restricted to the consideration of such saturated solutions. Then $C_M(g)$ can be calculated from the vapor pressure data[4] for the pure metal with the aid of the perfect gas relation. Even if an appreciable amount of the gas consists of metal polymers, no error is involved, as long as the concentration of monomer $C_M(g)$ is known. The $C_M(\text{soln})$ values used were calculated from the data (given in mole %) cited in the references in Table I and the densities of the solutions. When no density data for the solutions were available, the densities were estimated from those of the pure components. Even if these estimates were to be wrong by as much as a factor of two, the error in the resulting solution energy would be of the order of only 1 kcal. The activity coefficients also are not available for most of the systems. However, if $C_M(g)$ is taken as the concentration of metal monomer atoms, then, at the low metal vapor pressures that prevail at the temperatures under consideration, $\gamma_M(g)$ is unity.

For the metal dissolved in the molten salt the standard state has been chosen so that $\gamma_M(\text{soln})$ is unity at infinite dilution. Consequently, $\gamma_M(\text{soln})$ represents the deviation from Henry's law, and for the majority of the systems considered its contribution can be assumed to be small, relative to the magnitude of the energies calculated. (Estimates of $RT \ln \gamma_M(\text{soln})$ in some typical solutions can be shown to be about 2 to 3 kcal./mole for metal concentrations of as much as 20 mole %.) For those systems where the saturating phase is not the pure metal, *i.e.*, where there is either some salt solubility in the metal or where a solid subhalide is formed, additional corrections must be applied. The solubility of salts in metals is negligible in all but a few systems. In these systems, Raoult's law was applied to calculate the vapor pressure of the metal above the solution.

For systems in which a reaction occurs and a lower valent compound is the separating phase, a more detailed correction is necessary. For example, in the case of the reaction

$$Hg(l) + HgCl_2(l) = Hg_2Cl_2(s) \quad (2)$$

it can be shown (see Appendix) that

$$\Delta\mu_D^* = \mu_M^*(\text{soln}) - \mu_M^*(g) = RT \ln a_M(g)/a_M(\text{soln}) + RT \ln a_{MX_2}(l)/a_{MX_2}(\text{soln}) + \Delta\mu^\circ \quad (3)$$

where $a_{MX_2}(l)$ is the activity of the pure divalent salt and $\Delta\mu^\circ$ is the standard free energy of formation of the

(3) M. Blander, as quoted in ref. 2.

(4) D. Stull and G. Sinke, "Thermodynamic Properties of the Elements," American Chemical Society, Washington, D. C., 1956.

Table I: Dissolution Energies of Metal–Metal Salt Systems

System	T, °K.	Vapor pressure of metal,[a] atm.	Metal soly., mole %	ρ_{soln},[b] g./cc.	$-\Delta\mu_D^*$, kcal./mole
Li–LiCl[c]	913	1.64×10^{-4}	0.50	1.49	20
Na–NaCl[d]	1068	0.344	2.1	1.56	10
K–KCl[e]	1025	0.70	10.5	1.53	11
Rb–RbCl[f]	969	0.57	18	2.05	12
Ag–AgCl[g]	763	1.1×10^{-13}	0.03	4.80	44
Ag–AgCl[g]	973	1.81×10^{-9}	0.06	4.60	40
Tl–TlCl[g]	923	3.52×10^{-6}	0.009	5.23	15
Cu–$CuCl_2$[h]	1000	1.23×10^{-11}	50[h]	5.5	~65[h]
Mg–$MgCl_2$[i]	1073	0.034	0.30	1.66	6
Ca–$CaCl_2$[j,k]	1093	1.52×10^{-3}	2.70	2.06	12
Sr–$SrCl_2$[k,l]	1112	7.10×10^{-3}	5.5	2.75	11
Ba–$BaCl_2$[m]	1151	1.60×10^{-3}	15.0	3.23	17
Zn–$ZnCl_2$[n]	973	0.076	1.64	2.35	11
Cd–$CdCl_2$[o]	973	0.44	18.0	3.60	13
Hg–$HgCl_2$[p]	553	0.184	5.0	4.55	11
Hg–$HgCl_2$[p]	973	50[q]	55.0	7.0	7
Au–$AuCl_3$[h]	1000	2.0×10^{-12}	66.7[h]	13.0	~69[h]
Al–AlI_3[g]	696	6.8×10^{-18}	0.3	2.5	55
Ga–Ga_2Cl_4[g]	453	4.1×10^{-26}	1.92	2.41	55
Ga–$GaCl_3$[r]	453	4.1×10^{-26}	35.2[r]	2.41	57[r]
In–$InCl_3$[h]	900	6.9×10^{-9}	66.7[h]	5.5	~47[h]
Tl–$TlCl_3$[h]	923	3.52×10^{-6}	66.7[h]	5.23	32[h]
La–$LaCl_3$[s]	1193	1.5×10^{-12}	11.0	3.20	65
Ce–$CeCl_3$[t]	1050	2.5×10^{-11}	9.3	3.60	61
Nd–$NdCl_3$[u]	1128	7.1×10^{-10}	30.5	4.0	~60
U–UCl_3[v]	1093	1.2×10^{-16}	4.1	4.1	88
Ni–$NiCl_2$[w]	1250	1.0×10^{-10}	9.1	2.6	70
Fe–$FeCl_3$[r]	1000	1.2×10^{-14}	33.3[r]	5.0	~77[r]
Sn–$SnCl_2$[g]	773	2.1×10^{-15}	3.2×10^{-3}	3.09	46
Pb–$PbCl_2$[g]	973	1.5×10^{-5}	0.052	4.65	21
Pb–PbI_2[n]	973	1.5×10^{-5}	0.41	5.5	25
Cr–$CrCl_2$[x]	1191	1.7×10^{-10}	1.9	2.2	61
Cr–$CrCl_2$[r]	1191	1.7×10^{-10}	35.3[r]	2.2	68[r]
Mn–$MnCl_2$[x]	925	2.5×10^{-9}	0.8	2.3	41
Sb–$SbCl_3$[n]	546	4.8×10^{-19}	0.018	2.1	43
Bi–$BiCl_3$[y]	553	5.7×10^{-13}	35.0	4.65[z]	38
Bi–$BiCl_3$[y]	973	2.3×10^{-5}	35.0	3.75[z]	32

[a] See ref. 4. [b] See A. Klemm in "Molten Salt Chemistry," M. Blander, Ed., Interscience Publishers, Inc., New York, N. Y., 1964, p. 535. [c] A. S. Dworkin, H. R. Bronstein, and M. A. Bredig, *J. Phys. Chem.*, **66**, 572 (1962). [d] M. A. Bredig and H. R. Bronstein, *ibid.*, **64**, 64 (1960). [e] J. W. Johnson and M. A. Bredig, *ibid.*, **62**, 604 (1958). [f] M. A. Bredig and J. W. Johnson, *ibid.*, **64**, 1899 (1960). [g] J. D. Corbett and S. von Winbush, *J. Am. Chem. Soc.*, **77**, 3964 (1955). [h] Calculated for monovalent salt formation. [i] P. S. Rogers, J. W. Tomlinson, and F. D. Richardson, International Symposium on the Physical Chemistry of Process Metallurgy, Pittsburgh, Pa., 1959, Vol. 8, G. R. St. Pierre, Ed., Interscience Publishers, Inc., New York, N. Y., 1961, p. 909. [j] D. T. Peterson and J. A. Hinkebein, *J. Phys. Chem.*, **63**, 1360 (1959). [k] A. S. Dworkin, H. R. Bronstein, and M. A. Bredig, *Discussions Faraday Soc.*, **32**, 188 (1962). [l] L. E. Staffansson, Ph.D. Thesis, London, Dec. 1959. [m] H. Schafer and A. Niklas, *Angew. Chem.*, **64**, 611 (1952). [n] J. D. Corbett, S. von Winbush, and F. C. Albers, *J. Am. Chem. Soc.*, **79**, 3020 (1957). [o] L. E. Topol and A. L. Landis, *ibid.*, **82**, 6291 (1960). [p] S. J. Yosim and S. W. Mayer, *J. Phys. Chem.*, **64**, 909 (1960). [q] N. A. Lange, "Handbook of Chemistry," McGraw-Hill Book Co., Inc., New York, N. Y., 1961. [r] Calculated for divalent salt formation. [s] F. J. Keneshea, Jr., and D. Cubicciotti, *J. Chem. Eng. Data*, **6**, 507 (1961). [t] G. W. Mellors and S. Senderoff, *J. Phys. Chem.*, **63**, 1110 (1959). [u] L. F. Druding and J. D. Corbett, *J. Am. Chem. Soc.*, **83**, 2462 (1961). [v] D. Cubicciotti, "High Temperature Equilibria in Metal–Metal Halide Systems," MDDC-1058 (1946). [w] J. W. Johnson, D. Cubicciotti, and C. M. Kelley, *J. Phys. Chem.*, **62**, 1107 (1958). [x] J. D. Corbett, R. J. Clark, and T. F. Munday, *J. Inorg. Nucl. Chem.*, **25**, 1287 (1963). [y] S. J. Yosim, A. J. Darnell, W. G. Gehman, and S. W. Mayer, *J. Phys. Chem.*, **63**, 230 (1959). [z] F. J. Keneshea, Jr., and D. Cubicciotti, *ibid.*, **62**, 843 (1958).

solid subhalide from the metal and normal halide. For reactions of the type

$$2M(s,l) + MX_3(l) = 3MX(s) \quad (4)$$

e.g.

$$2Bi(s,l) + BiCl_3(l) = 3BiCl(s) \quad (5)$$

a similar treatment yields

$$\mu_M^*(soln) - \mu_M^*(g) = RT \ln a_M(g)/a_M(soln) + {}^1/_2RT \ln a_{MX_3}(l)/a_{MX_3}(soln) + {}^1/_2\Delta\mu^\circ \quad (6)$$

and for a reaction such as

$$M(s,l) + 2MX_3(l) = 3MX_2(s) \quad (7)$$

e.g., Nd–$NdCl_3$, one finds

$$\mu_M^*(soln) - \mu_M^*(g) = RT \ln a_M(g)/a_M(soln) + 2RT \ln a_{MX_3}(l)/a_{MX_3}(soln) + \Delta\mu^\circ \quad (8)$$

From the above relations (eq. 3, 6, and 8) involving subhalide formation and eq. 1, it can be seen that, for dilute solutions where a solid subhalide is the separating phase, the magnitude of the standard free energy of dissolution is essentially increased by a quantity proportional to $\Delta\mu^\circ$. For the calomel reaction (2), $\Delta\mu^\circ$ at 280° is −5.7 kcal.[5] For the Bi–$BiCl_3$ system reaction 5, with all three components in the solid state, has a $\Delta\mu^\circ$ of −2.1 kcal.[6] at 450°K. Correcting

(5) L. Brewer, "Chemistry and Metallurgy of Miscellaneous Materials: Thermodynamics," L. L. Quill, Ed., McGraw-Hill Book Co., Inc., New York, N. Y., 1950.

(6) A. J. Darnell and S. J. Yosim, *J. Phys. Chem.*, **63**, 1813 (1959).

to the hypothetical liquid for Bi and $BiCl_3$ using 5.68[7] and 2.60[4] kcal./mole for the heats of fusion of $BiCl_3$ and Bi, respectively, we obtain a $\Delta\mu^\circ$ of -2.7 kcal. for reaction 5 at 553°K. For the Au–$AuCl_3$, Cu–$CuCl_2$, Tl–$TlCl_3$, Ga–$GaCl_3$, In–$InCl_3$, Cr–$CrCl_3$, and Fe–$FeCl_3$ systems no solid subhalides exist at the temperatures considered in this study. For the Nd–$NdCl_3$ system, unfortunately, the value of $\Delta\mu^\circ$ for subhalide formation is unknown.

Results

In Table I are listed the pertinent data and $\Delta\mu_D^*$ values calculated from eq. 1, 3, 6, or 8 for various metal–metal halide systems with the assumption that the activities can be replaced by concentrations, *i.e.*, that Henry's law and ideal gas behavior hold. The results indicate that all the energies of dissolution are appreciable, and they illustrate, with a few exceptions, some interesting relations between the energies and the periodicity of the metals. For the alkali metal systems, with the exception of Li, the values of $\Delta\mu_D^*$ at $T \simeq 1000$°K. are all approximately equal and exhibit only a slight trend if any. The anomalous behavior of Li is probably related to its small size and its presence largely as atom dimers[2] Li_2 in the melt. The alkaline earths have dissolution energies of similar magnitude, but the energies become increasingly negative with increasing atomic number. Dissolution energies similar to those for groups I-A and II-A are observed for systems containing the group II-B metals, Zn, Cd, and Hg, and also for Tl (in TlCl) and Pb. Much larger energies are observed with the Ag, Sn, Tl (in $TlCl_3$), In (in $InCl_3$), Sb, Bi, and Mn solutions, and still larger values are evident with Cu (in $CuCl_2$), Au (in $AuCl_3$), Al, Ga, the lanthanides, Cr, Fe (in $FeCl_3$), Ni, and U. (Recent solubility measurements[8] of U in UBr_3 and in UI_3 yield virtually identical values of $\Delta\mu_D^*$ as in U–UCl_3.) The high energy value for the silver system and the large difference between the tin and lead systems cannot be explained. However, the chemical similarity of the lanthanides is again shown in the almost identical solution energy values. Further, since the actinides are also expected to show mutually similar dissolution energies (about -90 kcal./mole as for U–UCl_3), one would expect a large increase in $\Delta\mu_D^*$ as one goes from the lanthanides to the actinides. Thus, although the values of the dissolution energies in Table I may be somewhat in error, all the systems considered can be categorized arbitrarily in terms of weak (say, less negative than -25 kcal.) or strong (more negative than -35 kcal.) solution energies.

In a compilation of energy values, such as that presented here, the values should be correlated at a common reference temperature such as the temperature where the metal vapor pressures are equal. Unfortunately, such a tabulation is impossible because of the widely different temperature ranges at which the various solutions exist. This being the case, the energies were calculated at approximately 1000°K. wherever data were available. For most metals the free energy of sublimation or vaporization decreases about 2 to 4 kcal./g.-atom per 100° increase in temperature, whereas the change in the solution free energy for metal–salt systems for a ΔT of 100° is generally about 1 to 2 kcal./mole. Thus, a decrease in the negative partial molar free energy of dissolution of 1–2 kcal. for a 100° increase in temperature should occur. The typical effects of temperature on some of these systems are illustrated by Bi–$BiCl_3$ and Hg–$HgCl_2$ at 553 and 973°K. and by Ag–AgCl at 763 and 973°K.

The dependence upon the anion is shown by the increase in magnitude of the dissolution energy as one goes from chloride to iodide in the lead system and this behavior is typical of most of the cations listed in Table I (with the exception of the Cd system). This variation is due to the increase in solubility of the metal in its halide in the order I > Br > Cl. Since the solubility of Al in $AlCl_3$ is not known but appears to be about five orders of magnitude smaller[9] than in AlI_3, a less negative value of $\Delta\mu_D^*$ of about -40 to -45 kcal./mole appears likely for the chloride.

The Interaction Energy

In the calculation of $\Delta\mu_D^*$ values, Henry's law and ideal gas behavior were assumed. In those cases where departure from Henry's law occurs, the corrections should not be more and in most instances are much less than 3–4 kcal., and these corrections will usually make the dissolution energy less negative. (Again the reader is reminded that the standard state is not the pure metal but a hypothetical solution of the metal at 1 mole/l.)

In those systems where salt solubility in the metal occurs, the solubility is usually extremely small, and the extent of departure of the vapor pressure from that of the pure metal should also be correspondingly small. However, even in those systems where the salt solubility in the metal is appreciable, *e.g.*, K–KCl, Rb–RbCl, the errors involved in the use of Raoult's law should not be greater than 1–2 kcal., and the correction to

(7) L. E. Topol, S. W. Mayer, and L. D. Ransom, *J. Phys. Chem.*, 64, 862 (1960).

(8) See ref. *x*, Table I.

(9) See ref. *n*, Table I.

$\Delta\mu_D^*$ tends to cancel that due to the Henry's law correction. Thus, it should be stated that, although errors in the calculation are apparent, the magnitude of the errors is undoubtedly not large enough to mask the correlations we wish to illustrate.

The free energy of dissolution can be considered to consist of two parts: first, the free energy of formation of holes in the solvent large enough to accommodate the metal atoms and, second, the free energy of interaction of the atoms with the molten salt environment. An estimate of the free energy of hole formation leads to a value of +6 kcal./mole[10-12] and does not vary by more than ±3 kcal./mole for a wide range of possible hole sizes. This approximate constancy of the free energy of hole formation indicates that the relative values of $\Delta\mu_D^*$ are essentially in the same order as the relative values of the free energy of interaction of metal atoms with the salt.

A delineation of metal–salt systems in terms of solution or interaction energies as a measure of the strength of metal–salt interactions appears to be more meaningful than the use of a nonquantitative property such as subhalide or nonsubhalide formation. As is evident from Table I, there are many systems containing no known solid subhalide that have solution energies as large as or larger than systems, such as Hg and Bi, with a solid subhalide present. (If $\Delta\mu_D^*$ for Nd–$NdCl_3$ is about the same as that for the other lanthanide systems, it appears likely that the $\Delta\mu^\circ$ for subhalide formation here is of the order of −1 to −4 kcal.) It should be understood that the existence of a solid subhalide cannot be taken as confirmation that a stable subhalide species exists in the liquid; conversely, the nonoccurrence of a solid subhalide does not preclude the existence of a lower valent cation species in solution.

It is interesting to note that the transition metals and all the metals with three or more valence electrons exhibit large dissolution or interaction energies. In addition, many of these latter metals are known to exist *in their melts* as lower valent cations, *e.g.*, Sb^+, Bi^+, Ga^+,[13-15] Tl^+, In^+, Cr^{+2}, Fe^{+2}. (Although the data in Sb–SbI_3 are consistent with the species Sb^+, Corbett and Albers[13] assumed Sb_2I_4 entities because these melts are diamagnetic. However, in analogy with Bi–BiI_3 solutions Sb^+ would be expected to be diamagnetic[16] also.) It thus appears that lower oxidation states containing fully paired electrons are favored, and the large energies in the trivalent metal solutions are probably associated with the shift of electrons from a metal atom (or pair of atoms) to localized orbitals around the trivalent cation as depicted in reactions 4 and 7. For the normal divalent metals, the dimerization reaction (2) is consistent with the tendency for the s-electrons to remain paired. Although there is no evidence at present for the existence of monovalent monomeric cations of normal or transition divalent metals,[17] except for Ni,[18,19] no distinction can be made from existing evidence between entities of the type M_2^{+2} and metal atoms. Actually, the difference is a subtle one since metal atoms, being very polarizable, would presumably exist in these melts as strongly solvated species of the type $M–M^{+2}$. The difference between such a solvate and the entity M_2^{+2} is then mainly due to a difference in the degree of interaction between the metal atom and cation. With the monovalent metals, such as the alkali metals, silver, and thallium, the formation of fully paired electronic structures does not appear feasible except by dimerization of the atoms, and it is difficult to postulate a subhalide species although solvated species may exist.

(10) The expression for the work involved in the formation of an Avogadro's number N of holes derived by Reiss, *et al.*,[11] is given by

$$\Delta\mu_h^* = p(4/3)\pi r^3 + 4\pi r^2\sigma N(1 - 2\delta/r)$$

where p is the pressure of the fluid, σ is the interfacial tension between the fluid and the hole, δ is a distance of the order of the thickness of the inhomogeneous layer near the hole–fluid interface, and r equals the sum of the radius of the metal atom plus the average radius of the solvent ions. Since the p–V term is negligible (of the order of 1 cal.) for the systems under consideration, the above expression can be approximated by

$$\Delta\mu_h^* \cong 18.1r^2\sigma(1 - 2\delta/r)$$

where r is expressed in Å. and $\Delta\mu_h^*$ is given in cal. Taking average radii of 1.5 Å. for both metal atoms and salt ions and substituting typical values of r, $2\delta/r$, and σ of 3.0 Å., 0.64,[11] and 100 dynes/cm.,[12] respectively, into the above equation, we find a $\Delta\mu_h^*$ of approximately 6 kcal.

(11) H. Reiss, H. L. Frisch, E. Helfand, and J. L. Lebowitz, *J. Chem. Phys.*, **32**, 119 (1960).

(12) H. Bloom and J. O'M. Bockris, "Modern Aspects of Electrochemistry No. 2," J. O'M. Bockris, Ed., Academic Press Inc., New York, N. Y., 1959, Chapter 3.

(13) J. D. Corbett and F. C. Albers, *J. Am. Chem. Soc.*, **82**, 533 (1960).

(14) L. E. Topol, S. J. Yosim, and R. A. Osteryoung, *J. Phys. Chem.*, **65**, 1511 (1961).

(15) L. A. Woodward, G. Garton, and H. L. Roberts, *J. Chem. Soc.*, 3723 (1956).

(16) L. E. Topol and L. D. Ransom, *J. Chem. Phys.*, **38**, 1663 (1963).

(17) L. E. Topol, *J. Phys. Chem.*, **67**, 2222 (1963).

(18) See ref. *w*, Table I.

(19) The evidence for the apparent anomaly with Ni in $NiCl_2$ results from a cryoscopic study which favors the species Ni^+. These results are based on a heat of fusion[20] of 18.45 kcal./mole for $NiCl_2$, but this value, together with the melting point of the salt, 1282°K.,[18] yields an entropy of fusion of 14.4 e.u. or 4.8. e.u./g.-ion. Virtually all ionic salts have entropies of fusion of 2.5–3.5 e.u./g.-ion, and $FeCl_2$ and $CoCl_2$ have values[5] of 3.6 and 2.5 e.u./g.-ion, respectively. If the measured heat of fusion of $NiCl_2$ is in error and a more normal value of 10 kcal./mole is taken, *i.e.*, an entropy of fusion of 3.0 e.u./g.-ion is assumed, then the cryoscopy results are in accord with Ni atoms or Ni_2^{+2}. Although the removal of an electron to form Ni^+ is consistent with the high dissolution energy found in Ni–$NiCl_2$, it is difficult to see why Ni^+ should be more stable than Ni_2^{+2}, and a redetermination of the heat of fusion of $NiCl_2$ seems warranted.

(20) J. P. Coughlin, *J. Am. Chem. Soc.*, **73**, 5314 (1951).

Predictions

Since the dissolution or interaction energies of many of the systems discussed previously display a regularity which is not apparent from the solubility data alone, it appears that reasonable estimates of $\Delta\mu_D^*$ and, thus, the solubility of some unmeasured systems are feasible. Several systems for which solubility predictions can be made are Fe–$FeCl_2$, Co–$CoCl_2$, and the rare earth metals in their chlorides. It is interesting to note that the dissolution or interaction energies of the systems composed of the divalent metals (Ca, Cr, Mn, Ni, Cu, and Zn) of the fourth period, which comprises mainly the first transition series, closely parallel the lattice energies for the respective metal chlorides.[21,22] The Zn–$ZnCl_2$ dissolution energy appears to be an exception here since its value, −11 kcal., is much smaller than would be expected, −60 to −70 kcal., from the lattice energy or ligand field correlation. However, if an approximately parallel behavior between the lattice energies and dissolution or interaction energies is assumed for the other metals in this series, *i.e.*, if the shielding by the 4s-electrons does not alter the ligand field effect on the 3d-electrons appreciably, estimates of the solubilities of iron and cobalt in their molten chlorides can be made. The Fe–$FeCl_2$ system should be especially amenable to a solubility prediction since the number of d-electrons, as well as the ligand field effect, increases continuously as one goes from Mn to Co or Ni. (A maximum effect should be found for nickel or cobalt, respectively, depending on the environment, *i.e.*, whether octahedral- or tetrahedral-like coordination[22] is present.) In any case, the energy of dissolution for Fe in $FeCl_2$ at 1000°K. would be expected to be about −54 kcal., and a solubility of approximately 10^{-4} mole % is calculated. For Co in $CoCl_2$ at 1000°K. the $\Delta\mu_D^*$ could vary from about −62 kcal. for octahedral-like coordination to approximately −70 kcal. for tetrahedral-like coordination. These energies result in maximum solubilities of 10^{-2} and 1 mole %, respectively. Although the solubility of neither the iron nor cobalt system has been measured accurately, it is known that the values are very low[8] and thus are in accord with the probable estimates given above.

In the case of the rare earth metal systems all the measured data yield dissolution energies of −62 ± 3 kcal. (The Pr–$PrCl_3$ system, the solubility in which is 17.8 mole % metal at 1100°K.,[23] was not included in Table I since the vapor pressure of Pr is not known. However, if a reasonable value of about 10^{-10} atm. is assumed for Pr at 1100°K., *i.e.*, about the same as Nd since the boiling points are fairly similar, the $\Delta\mu_D^*$ would be in the above range also.) If a $\Delta\mu_D^*$ of about −62 kcal. is assumed for all the rare earth systems, then a solubility of the order of 1 mole % can be predicted for Gd–$GdCl_3$[24] at 1000°K., very much higher values (>10 mole %) for Tb, Dy, Ho, and Er, and exceedingly high solubilities (possibly complete solution) for Sm, Eu, Tm, Yb, and Lu in their respective chlorides near the melting point of the salt. In these systems of high solubility, large deviations from ideality would be expected to occur and complicate calculations based on the simple method used above. The agreement between the estimated and measured values for the Gd–$GdCl_3$ system and the apparent accord for Fe–$FeCl_2$ and Co–$CoCl_2$ illustrate the value of the compilation of dissolution energies. The Fe–$FeCl_2$ case is especially interesting since Fe and Ni, which have approximately equal free energies of vaporization, are shown to have widely different solubilities in their respective salts.

Conclusions

On the basis of the magnitude of the standard free energies of dissolution between individual atoms of metals and their molten chlorides, two chief classifications of metal–salt systems can be made. In the first category are systems which exhibit relatively weak solution energies (arbitrarily set as less negative than −25 kcal.), and these consist primarily of the mono- and divalent metals. The second category includes the transition metals and the trivalent metals, systems which are characterized by relatively strong solution energies (more negative than −35 kcal.). This classification of metal–salt systems in terms of dissolution energies appears to be a more reasonable and useful delineation than one based on a nonquantitative property such as solid subhalide formation since predictions of solubility from reasonable estimates of solution energies are feasible for many unmeasured systems.

Acknowledgment. The author expresses his gratitude to Dr. M. Blander for his many helpful comments and suggestions.

Appendix

Designate Hg_2Cl_2, $HgCl_2$, and the metal in reaction 2 by the subscripts 1, 2, and M, respectively. Then for the solid phase in equilibrium with the solution

(21) T. C. Waddington, "Advances in Inorganic Chemistry and Radiochemistry," H. J. Emeléus and A. G. Sharpe, Ed., Vol. 1, Academic Press Inc., New York, N. Y., 1959.

(22) L. E. Orgel, "An Introduction to Transition-Metal Chemistry: Ligand Field Theory," John Wiley and Sons Inc., New York, N. Y., 1960.

(23) A. S. Dworkin, H. R. Bronstein, and M. A. Bredig, *J. Phys. Chem.*, **66**, 1201 (1962).

(24) J. D. Corbett has recently measured the solubility to be 2.0 mole % at 943°K., private communication.

$$\mu_1^\circ = \mu_M(\text{soln}) + \mu_2(\text{soln}) \quad (1A)$$

and

$$\mu_1^\circ = \mu_M^\circ + \mu_2^\circ + \Delta\mu^\circ \quad (2A)$$

where μ° refers to the pure condensed phase, and $\Delta\mu^\circ$ is the standard free energy change of reaction 2. Equating eq. 1A and 2A and substituting for μ_M°

$$\mu_M^\circ = \mu_M^*(g) + RT \ln a_M(g) \quad (3A)$$

and for μ_2°

$$\mu_2^\circ = \mu_2^*(l) + RT \ln a_2(l) \quad (4A)$$

we obtain

$$\mu_M(\text{soln}) + \mu_2(\text{soln}) = \mu_M^*(g) + RT \ln a_M(g) + \mu_2^*(l) + RT \ln a_2(l) + \Delta\mu^\circ \quad (5A)$$

Now substituting

$$\mu_i(\text{soln}) = \mu_i^*(\text{soln}) + RT \ln a_i(\text{soln}) \quad (6A)$$

into (5a) for $\mu_M(\text{soln})$ and $\mu_2(\text{soln})$, recognizing that $\mu_2^*(l) = \mu_2^*(\text{soln})$, and rearranging terms, we find

$$\mu_M^*(\text{soln}) - \mu_M^*(g) = RT \ln a_M(g)/a_M(\text{soln}) + RT \ln a_{MX_2}(l)/a_{MX_2}(\text{soln}) + \Delta\mu^\circ \quad (7A)$$

Thermodynamics of Adsorption of Carbon Dioxide on Zinc Oxide

by R. J. Kokes and Rimantas Glemza

Department of Chemistry, The Johns Hopkins University, Baltimore, Maryland 21218
(Received December 23, 1963)

Chemisorption of carbon dioxide on zinc oxide has been studied between 473 and 588°K. for pressures ranging from 10^{-7} to 1 atm. Partial molal enthalpies and entropies of adsorption were computed by application of the Clausius–Clapeyron equation at fixed coverage; corresponding molar thermodynamic quantities were computed by application of the Clausius–Clapeyron equation at fixed spreading pressure. Experimental data show that the isosteric heat of adsorption at low coverage is about 25 kcal.; at coverages above half a monolayer, the isosteric heat is approximately equal to that for the formation of bulk zinc carbonate even though the bulk phase is thermodynamically unstable. Analysis of the data suggests that adsorption of carbon dioxide on zinc oxide results in the formation of surface carbonate groups.

Introduction

Although a large number of studies of adsorption on semiconductor oxides have been carried out, very few of these deal with equilibrium adsorption. In this paper we present such data for the ZnO–CO_2 system. This system was chosen for three reasons. (a) It yields reproducible data. (b) Bulk zinc carbonate (which is unstable under the conditions of our measurements) is a well-known compound, and it is possible to compare the properties of the bulk phase with those of the adsorbed phase. (c) Recent infrared studies[1] suggest the mode in which carbon dioxide is bound to the surface. Adsorption data for this system have been reported in the past,[2,3] but these data are in conflict.

(1) J. H. Taylor and C. H. Amberg, *Can. J. Chem.*, 39, 535 (1961).
(2) P. M. G. Hart and F. Sebba, *Trans. Faraday Soc.*, 56, 557 (1960).
(3) T. Kwan, T. Kinuyama, and Y. Fujita, *J. Res. Inst. Catalysis, Hokkaido Univ.*, 3, 31 (1953).

Experimental

The carbon dioxide was prepared by fractionating the thermal decomposition products of sodium bicarbonate. The zinc oxide used in this experiment is the zinc oxide SP500 pigment manufactured by the New Jersey Zinc Co. Prior to each set of runs, the catalyst was degassed at 515°, a procedure known to remove all but a trace of the residual carbon dioxide.[4] Two different vacuum systems were used in these experiments, one covering a pressure range from 10^{-5} to 10 mm. and the other covering a range from 1 to 800 mm. The results in the low-pressure region were obtained for a sample of zinc oxide weighing approximately 5 g.; the results in the high-pressure region were obtained for a different sample of zinc oxide weighing approximately 25 g. Surface areas were measured by nitrogen adsorption on both samples. Wherever necessary, connections for thermal transpiration were made with equations suggested by Bennett and Tompkins.[5] The temperatures for corresponding isotherms in the high- and low-pressure regions were the same to about ±1°, but the nominal variation in the high- or low-pressure region alone was ±0.2°. Normally, equilibrium was achieved within an hour, except at the lowest pressure and temperature for which data were obtained. Equilibrium was assured by the fact that data for adsorption and desorption agreed within experimental error. The raw data are presented in Figure 1 expressed in terms of the nominal θ, the ratio of the volume of carbon dioxide adsorbed to the B.E.T. v_m, and the measured pressure, *i.e.*, uncorrected for thermal transpiration. To avoid confusion, all of the experimental points are shown only for the data at 200°. Calculations of the thermodynamic quantities are based on these smoothed curves.

Calculations

Partial Molal Quantities. Isosteric heats of adsorption were computed by least-squares methods on the assumption that the data are represented by the following equation for a fixed θ

$$\ln P = -\left\{\frac{\bar{H}_g - \bar{H}_s}{R}\right\}\frac{1}{T} + \left\{\frac{\bar{S}_g - \bar{S}_s}{R}\right\}$$

In this equation P is the equilibrium pressure (corrected for thermal transpiration) for a given θ, R is the gas constant, T is the absolute temperature, $\bar{H}_g - \bar{H}_s$ ($\equiv q_{st}$) is the isosteric heat of adsorption, $\bar{H}_g$ and $\bar{S}_g$ are the molar enthalpies and entropies for CO_2 gas, and $\bar{H}_s$ and $\bar{S}_s$ are the partial molal enthalpies and entropies for the adsorbed phase. This equation is valid provided the quantities in braces are independent of temperature in the range covered. The validity

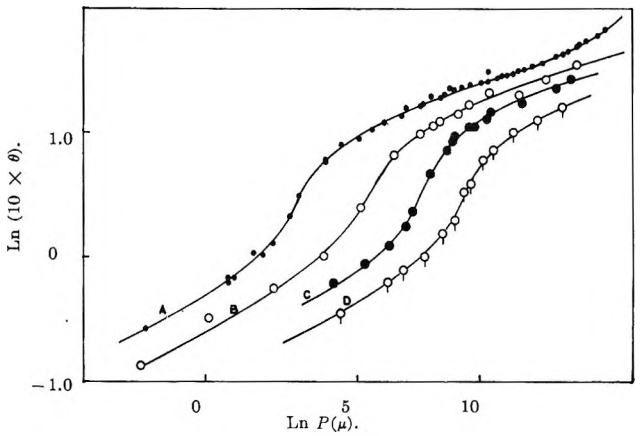

Figure 1. Isotherms for the adsorption of carbon dioxide on zinc oxide. The pressure, measured in μ, is not corrected for thermal transpiration. Temperatures are A, 473°K.; B, 510°K.; C, 548°K.; D, 588°K.

of this approximation is attested to by the fact that the average variance for both the entropy and enthalpy terms was about 1.5% of the values, *i.e.*, 0.4 kcal. in enthalpy and 0.8 e.u. in entropy.

Values of $\bar{H}_g - \bar{H}_s$ are plotted in Figure 2. The least-squares variance for each point is indicated by a perpendicular line if its value is greater than the diameter of the point symbol. Values of $\bar{S}_s$ were put on an absolute basis from $\bar{S}_g - \bar{S}_s$ with the help of the tabulated entropies for carbon dioxide in the "JANAF Tables."[6] In this computation it was assumed that the value of $\bar{S}_g - \bar{S}_s$ obtained from the least-squares computations was that corresponding to $\bar{T}$,[7] 528.8°K. A plot of $\bar{S}_s$ *vs.* θ is shown in Figure 3; the absolute variance for $\bar{S}_g - \bar{S}_s$ is indicated if its value is greater than the diameter of the point symbol.

Molar Quantities. The data were adequate to permit computation of molar enthalpies, entropies, and energies of adsorption by the procedures outlined by Hill.[8] For the sake of completeness, these calculations were carried out. The error inherent in such calculations is uncertain because extrapolation to zero coverage is required. Details of this extrapolation will not be given here, but analysis of the error thus introduced suggests the error is less than 0.5 kcal. for the energy terms and ranges from 2 e.u. at $\theta = 0.1$ to 0.4 e.u. at $\theta = 0.5$ for the entropy.

(4) R. J. Kokes, *J. Phys. Chem.*, **66**, 99 (1962).

(5) M. J. Bennett and F. C. Tompkins, *Trans. Faraday Soc.*, **53**, 185 (1957).

(6) D. R. Stull, *et al.*, "JANAF Interim Thermochemical Tables," Dow Chemical Co., Midland, Mich.

(7) T. L. Hill, P. H. Emmett, and L. G. Joyner, *J. Am. Chem. Soc.*, **73**, 5102 (1951).

(8) T. L. Hill, *J. Chem. Phys.*, **17**, 520 (1949); **18**, 246, 791 (1950).

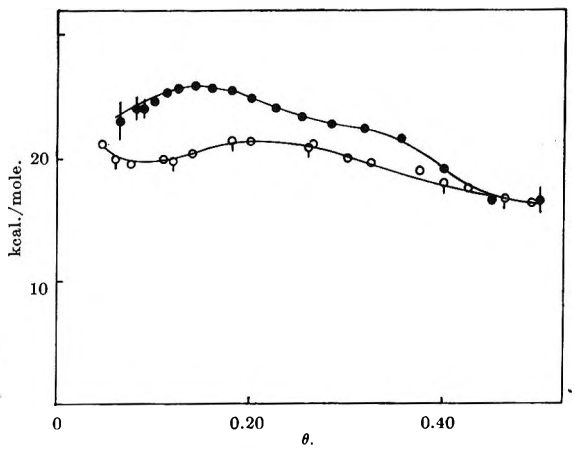

Figure 2. Heats of adsorption of carbon dioxide on zinc oxide. Solid points represent q_{st}. Plain open circles represent molar enthalpies of adsorption computed from the Clausius–Clapeyron equation at fixed spreading pressure.

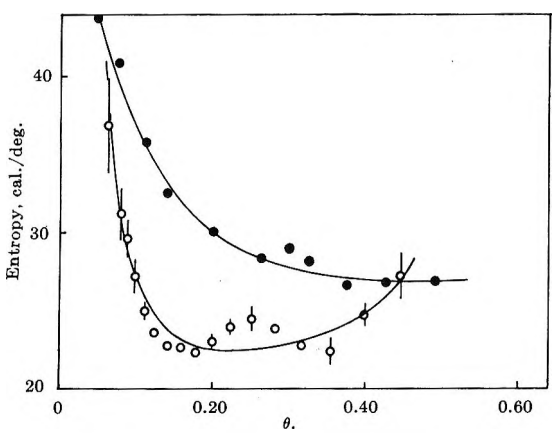

Figure 3. Entropies of adsorbed carbon dioxide on zinc oxide. Open circles represent $\bar{S}_2$; solid points represent $\tilde{S}_2$, molar entropies.

Discussion

Comparison of the isosteric heats in Figure 2 with those conflicting results[2,3] reported earlier in the literature show that these data are in essential agreement with those reported by Hart and Sebba.[2] The combined data suggest that the isosteric heat levels off at a value of about 16.5 kcal. The value of the enthalpy change for the reaction $ZnCO_3(s) \rightarrow ZnO(s) + CO_2(g)$ is +17.0 kcal. at 298°K.[9] If we make the crude approximation that the heat capacities do not vary with temperatures, we find the decrease in ΔH between 298 and 529°K. is less than 1 kcal. Thus, the ΔH for dissociation of $ZnCO_3$ at 529°K. is probably about 16–17 kcal., *i.e.*, essentially equal to the isosteric heat at higher coverages.

(It should be emphasized that the data reported, herein do not correspond to bulk reaction. Estimates based on data at 298°K.,[9] with the assumption that ΔH and ΔS do not vary appreciably with temperature, indicate that the dissociation pressure of zinc carbonate is 20 to 650 atm. in the temperature range studied. Since the highest pressures used were ~1 atm. we can exclude formation of bulk zinc carbonate. The formation of solid solutions of zinc carbonate in zinc oxide is regarded as unlikely.)

The over-all fall in isosteric heats of adsorption with increasing coverage is often associated with heterogeneity of sites.[10–12] Although in this present case there is a fall in q_{st} from about 25 kcal. at $\theta = 0.1$ to 16.5 kcal. at $\theta = 0.5$, this does not seem to be the result of a heterogeneity of sites *in the usual sense*. In the statistical, mechanical treatment of heterogeneity it is assumed that different sites have different *integral* energies of adsorption, $\Delta\tilde{E}$, at 0°K.[13] This results in a fall of $\Delta\tilde{E}$ with coverage at 0°K. Values of $\Delta\tilde{E}$ at 529°K. shown in Figure 4 are essentially constant at 23 ± 1 kcal. up to $\theta \sim 0.4$. Thus, by the usual standards, the zinc oxide surface is reasonably homogeneous in carbon dioxide chemisorption.

The absolute entropy values plotted in Figure 3 represent the value of the entropy of zinc oxide with adsorbed gas minus the entropy of zinc oxide in the absence of adsorbed gas. To compare this with the

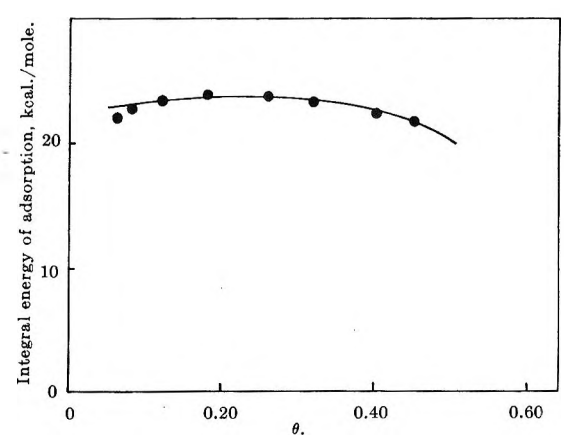

Figure 4. The integral energy of adsorption of carbon dioxide on zinc oxide.

(9) F. D. Rossini, D. D. Wagman, W. H. Evans, S. Levine, and J. Jaffe, National Bureau of Standards Circular 500, U. S. Government Printing Office, Washington, D. C., 1952.

(10) A. Clark and V. C. F. Holm, *J. Catalysis*, **2**, 21 (1963); A. Clark; V. C. F. Holm, and D. M. Blakburn, *ibid.*, **1**, 244 (1962).

(11) L. E. Drain and J. A. Morrison, *Trans. Faraday Soc.*, **48**, 316; 840 (1952); **49**, 654 (1953).

(12) D. H. Everett, *ibid.*, **46**, 453 (1950).

(13) T. L. Hill, *J. Chem. Phys.*, **17**, 762 (1949).

bulk phase, we must compare these entropy values to that of zinc carbonate minus that of zinc oxide. At 298°K. this value is 9.2 e.u.,[2] but the necessary thermodynamic data at 529°K. are not available. A crude estimate of entropies at 528.8°K. can be made if we assume the heat capacities are independent of temperature. This yields a value of 14.7 e.u. for $\bar{S}_{ZnCO_3} - \bar{S}_{ZnO}$ at 528°K. If this is subject to the same sort of error as in the similar $MgCO_3$–MgO system,[6] a better estimate for this quantity is 17.5 e.u. Comparison with Figure 3 shows that even near $\theta = 0.5$ (where the contributions of the configurational entropy should be the least) the entropy of the adsorbed phase is about 10 e.u. greater than that for the bulk phase.

Let us assume for simplicity that the fall in the heat of adsorption is due to interaction between adsorbed carbon dioxide molecules. Then $\bar{S}_a$ at $\theta \sim 0.5$ (27 e.u.) depends primarily on the mode of adsorption of carbon dioxide on a bare surface. The entropy of gaseous carbon dioxide at 529°K. is 56.7 e.u.[6] We can use the conventional approaches of statistical thermodynamics[14] and data given in ref. 6 to divide the entropy into rotational, vibrational, and translational entropy. The two degrees of rotational freedom contribute 14.2 e.u., the four degrees of vibrational freedom contribute 2.4 e.u., and the three degrees of translational freedom, 40.1 e.u. On adsorption without change in geometry the three translational degrees of freedom are replaced by three center-of-mass vibrational degrees of freedom; moreover, although the internal vibrational degrees of freedom will be little affected, on adsorption the rotational freedom will probably be curtailed. The center-of-mass vibrational entropy can be estimated by a variety of means, but for chemisorption it is probably small, *i.e.*, ~2 e.u. If this be so, we find an entropy for adsorbed carbon dioxide between 4.4 (no rotation) and 18.6 e.u. (free rotation), values far lower than that actually observed.

Infrared data[1] suggest that adsorbed carbon dioxide is not linear but bent with one of the structures

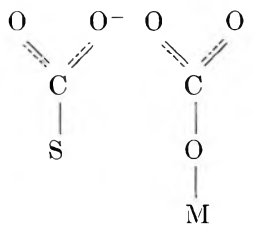

The first species is postulated because the spectrum of the strongly held carbon dioxide closely resembles that obtained for carboxylate ions; the nature of the surface atom is unspecified. The second species is regarded as possible, but not as likely, because the observed spectrum does not quite agree with that found for bicarbonate ions. The latter structure corresponds approximately to a surface carbonate ion. If such a species does form, there is the possibility of essentially free rotation around the M–O–C axis, a mode of motion that is unlikely for the bulk carbonate. The entropy contributed by this type of motion can be computed from the equation $S_{rot} = R/2 \ln (\pi Te/\sigma^2\theta_r)$[15,16] wherein all symbols have their conventional meaning. If this is the principal difference between the surface and bulk carbonate, we find that the entropy of the surface carbonate will be 7.5 e.u. higher than that of bulk carbonate, corresponding to an entropy for the adsorbed phase of 25 e.u., in fair agreement with the observed value of 27 e.u.

Although the above analysis is undoubtedly oversimplified, it does suggest an attractive picture for the adsorption of carbon dioxide on zinc oxide involving the formation of a surface carbonate. For convenience, let us compare adsorption and bulk carbonate formation. At low coverages, $\theta < 0.5$, adsorption is more favorable because of the higher isosteric heat and the higher entropy term. The higher heat term occurs in this region because an isolated carbonate group is more firmly bound than one interacting with its neighbors; the higher entropy term presumably results from the rotation of the carbonate group and configuration effects. At $\theta \backsim 0.5$ the slope of ln P *vs.* $1/T$ plots is the same as that for the bulk reaction (the isosteric heat of adsorption is the same as that for the bulk phase reaction); the more favorable entropy term is the only factor that makes adsorption occur under conditions that no bulk reaction occurs. Data are not available for higher coverages. In line with the above, it would appear that at $\theta \gtrsim 1$ the isosteric heat of adsorption is still that of the bulk reaction. At this point, moreover, the entropy approaches that for bulk reaction since the high surface coverage would curtail free rotation of the surface carbonate group. Accordingly, plots of ln P *vs.* $1/T$ would be the same for bulk phase reaction and adsorption because the partial molal properties are the same; this would occur even though the integral heats of reaction were different for the bulk and surface reaction.

(14) T. L. Hill, "Statistical Thermodynamics," Addison-Wesley Publishing Co., Inc., Reading, Mass., 1960, pp. 164-166.

(15) This yields a value different from that obtained using the general relation suggested by Kemball.[16] The difference in partition function is a factor of π, *i.e.*, a difference of 2 e.u.

(16) C. Kemball, *Advan. Catalysis*, **2**, 233 (1950).

Acknowledgment. Acknowledgment is made to the donors of the Petroleum Research Fund, administered by the American Chemical Society, for support of this research.

Reaction Kinetics of Monomolecular Films of Chlorophyll *a* on Aqueous Substrates

by Morton Rosoff and Carl Aron

IBM Watson Laboratory, Columbia University, New York, New York *(Received February 8, 1964)*

The kinetics at constant area of the monolayer reaction of chlorophyll *a* to pheophytin *a* on an acidic substrate were studied. The rate constants were found to depend upon pH, the initial surface pressure, the presence of O_2 at the interface, and divalent metal ions such as Ca^{+2} and Mg^{+2} in the subphase. The half-life of chlorophyll *a* at 23° on a pH 4 substrate and at an initial surface pressure of 6 dynes/cm. was about 6 min. Evidence was obtained for the participation of H_2O in the reaction and the probable existence of a charged intermediate.

Introduction

Film balance studies[1-3] of chlorophyll spread at an aqueous interface afford a unique way of approximating a molecular state of organization and environment which is closer to that present *in vivo* than the one which exists in simple solutions of photosynthetic substances in organic solvents.

In the course of investigating the stability, reproducibility, and physical properties of chlorophyll monolayers,[4] it was found that pheophytin was the primary product of chlorophyll decomposition at the surface. This work reports on the utilization of the techniques of monolayer reactions to study the kinetics of the conversion of chlorophyll *a* to pheophytin *a* in the presence of H^+ ion. Since the relationship between surface properties and time depends upon the interaction between reactant and product, the properties of mixed monolayers of these substances were also examined.

Experimental

The preparation of pigments, the apparatus, and spreading techniques used in these experiments have been described elsewhere.[4] Briefly, the chlorophyll *a* was prepared from fresh spinach leaves by the method of Jacobs, *et al.*[5] Pheophytin was formed from chlorophyll by the addition of HCl and rechromatographing. The surface balance was of a semiautomatic Wilhelmy type employing a Teflon trough and was sensitive to 0.1 dyne/cm. Surface potentials were measured by means of a Ra^{226} ionizing source and a Keithley 610H electrometer. Concentrations of solutions of pigments were obtained from measurements of optical density and previously determined extinction coefficients. Solute was delivered to the substrate surface by means of a Hamilton microliter syringe using benzene as the carrier solvent. Phosphate buffer, 10^{-3} *M*, was used

(1) A. E. Alexander, *J. Chem. Soc.*, 1813 (1937).

(2) H. J. Trurnit and G. Colmano, *Biochem. Biophys. Acta*, **36**, 447 (1958).

(3) W. O. Bellamy, J. L. Gaines, Jr., and A. G. Tweet, *J. Chem. Phys.*, **39**, 2528 (1963).

(4) M. Rosoff and C. Aron, *Nature*, to be published.

(5) E. E. Jacobs, A. E. Vatter, and A. S. Holt, *Arch. Biochem. Biophys.*, **53**, 278 (1954).

for measurements at pH 8. Conversion to pheophytin was carried out by the addition of about 1 ml. of HCl to the substrate to obtain a concentration of 10^{-4} M.

The initial effect of spreading chlorophyll at constant area on a pH 4 substrate was to elevate both the pressure (~3 dynes/cm.) and surface potential (~100 mv.) above that found at pH 8. The isotherms and surface potentials of pheophytin, however, were unaffected at pH 4. Since the voltages for pheophytin are almost the same as the initial values for chlorophyll at pH 4, the change in surface pressure was chosen as the more sensitive parameter to follow the conversion rate.

Results

Monomolecular Films of Mixture. An equimolar mixture of pheophytin and chlorophyll spread at the air–water interface at pH 8 gave π–σ isotherms which agree within experimental error with the calculated average curve, based on simple additivity of the two individual monolayers. The individual pressure–area relations as well as that for a mixture are given in Figure 1. If the molecules of the mixed film have no effect on each other, the applicable equation

$$\sigma_M{}^{\pi} = f_1\sigma_1{}^{\pi} + f_1\sigma_2{}^{\pi} \qquad (1)$$

where $\sigma_M{}^{\pi}$ = the molecular area of the mixture at surface pressure π, $\sigma_1{}^{\pi}$ and $\sigma_2{}^{\pi}$ = the molecular areas of species 1 and 2 at surface pressure π, and f_1 and f_2 are mole fractions of species 1 and 2 in the mixture, was found to hold over the composition range 5:1 to 1:5 for chlorophyll:pheophytin. Similarly, the surface potential, ΔV, of the mixed film assuming no interaction is given by

$$\sigma_M\Delta V = 12\pi(f_1\mu_1 + f_1\mu_2) \qquad (2)$$

where μ_1 and μ_2 are the apparent surface moments of species 1 and 2 at σ_M, and ΔV is in mv. Outside of experimental error, there were no systematic exceptions to eq. 1 and 2. However, near the collapse points the slopes of the ΔV–σ curves were similar to that of pheophytin alone and may be related to the mechanism of mixed film collapse.

From the mixture data it is evident that chlorophyll and pheophytin form a two-dimensional solution in which there is little interference or cooperation between the two molecules in the monolayer, *i.e.*, the excess free energy of mixing is zero.

π–σ plots for both chlorophyll and pheophytin are nearly linear and can be represented over most of the range by an equation of the form

$$\sigma = a - b\pi \qquad (3)$$

It follows from eq. 1 that the surface pressure for a mixture is a linear function of composition given by

$$\pi_M = \frac{\bar{a} - \bar{\sigma}}{\bar{b}} \qquad (4)$$

where the averages are taken with respect to mole fractions. If the variation of the slopes of the mixture isotherms is not too great, then π_M will be a linear fraction of composition. This will be particularly so at areas close to collapse, where the slopes of the pheophytin and chlorophyll isotherms are nearly identical. It was found empirically that the collapse pressure of the mixture was a linear function of the collapse pressures of the pure constituents weighted by their respective mole fractions. Using this relationship, 2 or 3% pheophytin was detectable from the experimental collapse pressure of mixed films, and this technique afforded a more sensitive method of estimating pheophytin than spectrometric determinations of films lifted off the subphase.

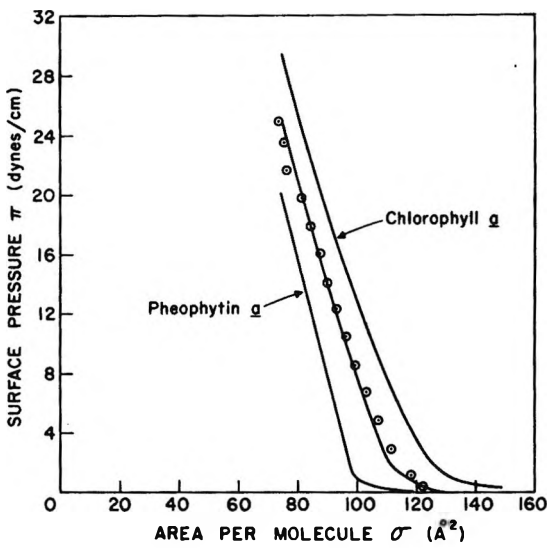

Figure 1. Surface isotherms of chlorophyll *a* and pheophytin *a*. Points are experimental data for a 1:1 mixture; solid line calculated from eq. 1 for a 1:1 mixture.

Kinetics of Pheophytinization. Measurements at constant area of the rate of change of surface pressure with time were carried out for a chlorophyll film spread on an acidic substrate. At pH 4, but not at higher pH values, the rate of pheophytinization was conveniently measurable. Since molecular areas of mixtures of starting material and reaction product were found to be additive, the data were treated using the expression for a pseudo-unimolecular reaction

$$\ln(\pi - \pi_\infty) = -k[H^+]t + \text{constant}$$

where π_∞ is the surface pressure when the reaction proceeds to completion, $[H^+]$ is the substrate hydrogen ion

concentration, and k is the specific rate constant in min.$^{-1}$ M^{-1}. Rate constants were calculated from the initial slopes of the linear plots. The reliability of the linear relationship found was tested by making up mixed films of 1:1 pheophytin–chlorophyll and showing that the slope so obtained agreed closely with that given by pure chlorophyll.

The rate constant at the air–water interface was found to be 1.36×10^3 min.$^{-1}$ M^{-1} at an initial pressure of about 6 dynes/cm.; *i.e.*, $\sigma = 120$ Å.^{2}/molecule. It was found that increasing the initial pressure to about 16 dynes/cm. produced a marked decrease in the rate constant to a value of 1.43×10^2 min.$^{-1}$ M^{-1} as shown in Figure 2. These results suggest that the change in orientation of the molecules in the interfacial film is responsible for these different rates and may be related to the availability of the ring magnesium for reaction.

The possibility that oxidation of the isocyclic ring (V) may accelerate the rate of removal of magnesium was checked by carrying out the kinetics in an N_2 environment after saturating the substrate and solution with purified N_2. A rate constant of 4.46×10^2 min.$^{-1}$ M^{-1} was found; this is about three times slower than that in air. Addition of 0.5% hydroquinone to the substrate in air produced no change in the initial rate, but the extent of the reaction was markedly reduced. When CO_2 was bubbled through the substrate and the pH adjusted to 4.0, the rate constant, 9.60×10^2, was close to the value found in air. The slightly slower rate may be due to O_2 having been displaced.

A series of experiments was carried out to determine the effect of various ions on the rate of pheophytinization. For the addition of Ca^{+2} at a concentration level in the substrate of 10^{-3} M, there was a 20% decrease in the velocity of the reaction; at 10^{-2} M, the rate decreased by about 35%. Mg^{+2} ion, however, at a concentration of 10^{-2} M, slowed down the reaction rate by somewhat more than one-half.

Discussion

The evident uniform mixing and distribution of pheophytin and chlorophyll molecules in the mixed films shed some light on the possible state of association in the surface phase of chlorophyll itself. If it is assumed that chlorophyll exists in the surface as aggregates as well as single molecules, then for eq. 1 to hold, each species must be considered to form a perfect solution. In going from pure chlorophyll to a pheophytin–chlorophyll mixture in the ratio 5:1, it would be expected that a one-sixth dilution of chlorophyll would affect the distribution of the various assumed single and multiplet species and result in an exception to eq. 1. Further, in

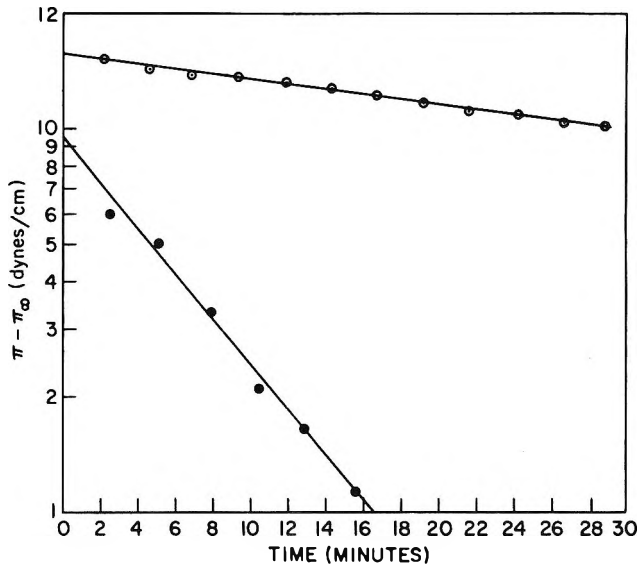

Figure 2. Rate of pheophytin formation on surface at constant film area: temp. 23°; substrate pH 4; ●, $\sigma = 120$ Å.^{2}, initial $\pi = 6$ dynes/cm.; O, $\sigma = 99$ Å.^{2}, initial $\pi = 16$ dynes/cm.

view of the random nature of the attack of H^+ during the conversion of chlorophyll to pheophytin on an acidic substrate, it is difficult to see why the assumed distribution should not be altered and consequently render the application of eq. 1 invalid. Since the mixture rule was found to apply even under the conditions of the kinetic experiments, it would seem that any appreciable association (to within the experimental uncertainty of about 5%) of chlorophyll molecules in the surface into discrete pairs or n-mers is unlikely.

It is of interest to compare the rate of pheophytinization found in the two-dimensional state with the values obtained in bulk.[6] At a comparable hydrogen ion concentration, 10^{-4} M, and at 25°, the specific rate constant in an acetone–water solution was 1.03×10^2 min.$^{-1}$ M^{-1}. The rate of conversion to pheophytin in the surface is approximately thirteen times faster. For most reactions carried out at constant surface area there is little deviation between the energies of activation and rate constants in the surface and the values of these for similar reactions in bulk phases.[7] The deviation that does occur in this case may be attributed to the high concentration of $[H^+]$ in the subphase resulting from the presence of a negative dipole end of the chlorophyll molecules oriented toward the substrate. The ion–dipole interaction can also be of importance in lowering the activation energy.

(6) S. H. Schanderl, C. O. Chichester, and G. L. Marsh, *J. Org. Chem.*, **27**, 3771 (1962).

(7) J. T. Davies, *Advan. Catalysis*, **6**, 1 (1954).

The observed variation of rate constant with surface pressure caused by the reduced accessibility of the reactive group supports the suggestions[8] that high pressures below the collapse point exert a protective action on the decomposition of chlorophyll. This contradicts the findings of Bellamy, *et al.*[3] The possibility of a primary oxidized intermediate is indicated by the results in an oxygen-free atmosphere and also by the results when hydroquinone, a known inhibitor of autoxidation, is added. On this view the rate constant for the unoxidized form at the lower compression is about one-third less than the corresponding value in air. The absence of an effect of CO_2 on the rate of pheophytin formation in an acidic substrate appears to rule out this variable except insofar as it contributes to the hydrogen ion concentration.

Some preliminary measurements have revealed that, even on a substrate buffered at pH 8, elevated temperatures, *i.e.*, 37°, led to rapid pheophytinization. The possibility that water participates in the reaction is suggested, and the kinetic scheme should then include a specific rate constant due to the reaction of the surface chlorophyll molecules with water. An estimate of the velocity of this simultaneous hydrolysis shows that it is slower by about one-third than the reaction with hydrogen ion. It is interesting to note in comparison the stability of chlorophyll in bulk solutions of organic solvents such as benzene and carbon tetrachloride, where heating for 25 min. at 55° produced no change in the visible spectra. These results indicate that care must be taken in preparative procedures to eliminate long exposures of chlorophyll solutions in contact with water, as in heterogeneous two-phase crystallizations.

The apparent protection against pheophytinization exhibited particularly by Mg^{+2} may indicate a specific ion effect, as well as competition with H^+ for sites in the surface. The actual mechanism of replacement of the Mg in the phorbin nucleus by H is still not quite clear. The evidence obtained from initial values that chlorophyll, when placed on a pH 4 substrate, gives an expanded film and more positive surface potentials suggests that the two hydrogen ions enter at different rates, and the first step may be the rapid substitution of one H^+ to give a singly charged intermediate.[9]

(8) G. Colmano, *Biochim. Biophys. Acta*, **47**, 454 (1961).

(9) E. Rabinowitch, "Photosynthesis," Vol. I, Interscience Publishers, New York, N. Y., 1945, pp. 493, 494.

Thermal Decomposition of Hexanitroethane[1a,b]

by Henry P. Marshall, Frank G. Borgardt, and Paul Noble, Jr.

Lockheed Missiles and Space Company, Palo Alto, California *(Received February 21, 1964)*

The rates of decomposition of hexanitroethane were determined in a number of solvents and as the pure solid in the temperature range of 60 to 100°. The products of reaction from the thermal decomposition of the solid are best represented by the equation: $(NO_2)_3C-C(NO_2)_3 \rightarrow 3NO_2 + NO + N_2O + 2CO_2$. Decomposition of hexanitroethane (HNE) for the pure solid and in CCl_4 proceeds by a first-order reaction; the specific first-order rate constants are, for solid HNE, $k = 10^{18.6} \exp(-38{,}900/RT)$ sec.$^{-1}$, and for HNE in CCl_4, $k = 10^{18.5} \exp(-37{,}800/RT)$ sec.$^{-1}$. The rate of decomposition of hexanitroethane in *n*-heptane is 11.5 times faster, and in cyclohexane it is 23 times faster, than that of the pure solid at 85°. Based on the kinetic data and products of reaction, a mechanism for the decomposition process is proposed.

I. Introduction

Hexanitroethane[2] was first prepared in 1914 by Will,[3] but its chemistry has been neglected until recent years. Preliminary data from these laboratories[4] have appeared in the literature describing some of the properties of HNE. We have undertaken an investigation of the kinetic behavior of HNE, because of our interest in this material as a potential oxidizer for propellants and because of our interest in the mechanism of decomposition of solids.

II. Experimental

Materials. Hexanitroethane was prepared by the method of Will[3] or was obtained from American Cyanamid.[5] Prior to use in kinetic studies, the HNE was recrystallized from methylene chloride and then sublimed; the m.p. was 140–150° with decomposition. A saturated solution of HNE in CCl_4 showed no proton spectra by n.m.r. although it exhibits a weak absorption band at 2060 cm.$^{-1}$. It has been observed that many polynitro-substituted compounds which contain no protons exhibit an absorption band in the 2860-cm.$^{-1}$ region.[6]

Solvents. Carbon tetrachloride and $CHCl_3$, ACS reagent grade, were used as received. The hydrocarbons, *n*-pentane and cyclohexane, were purified by the method described by Wiberg.[7] The perfluorokerosine (PFK, Halocarbon Co.)[8] was distilled prior to use; the fraction boiling between 70 and 90° was used in the kinetic studies.

Analytical Methods. Three methods of analysis were used for the rate measurements: (1) the infrared method, (2) the titrimetric method, and (3) the manometric method.

Infrared Method. HNE shows two intense absorption bands occurring at 6.10 and 6.17 μ. Comparison of the sample intensity, using the average of the two absorption bands, with that of a standard calibration curve permitted the determination of the amount of HNE at various stages of reaction.

For these studies, NaCl windowed cells were used, which readily become converted to $NaNO_3$ by the NO_2 formed in the samples. The $NaNO_3$ shows an intense absorption band at about 7.5 μ, and this may overlap with the absorption band used for analysis. Therefore, new cells were employed as required to obtain good kinetic data.

(1) (a) This paper was presented before the Division of Physical Chemistry at the 145th National Meeting of the American Chemical Society, New York, N. Y., Sept. 1963; (b) This work has been carried out as part of the Lockheed Independent Research Program.

(2) For the sake of brevity, hexanitroethane is abbreviated to HNE in the remainder of this paper.

(3) W. Will, *Ber.*, **47**, 961 (1914).

(4) F. G. Borgardt, J. A. Gallaghan, C. J. Hoffman, P. Noble, and W. Reed, *AIAA*, **1**, 395 (1963).

(5) American Cyanamid Co., Bound Brook, N. J.

(6) Unpublished results, this laboratory.

(7) K. Wiberg, "Laboratory Techniques in Organic Chemistry," McGraw-Hill Book Co., New York, N. Y., 1960.

(8) Halocarbon Co., Hackensack, N. J.

Titrimetric Method. The method of Johnson[9] was used to follow the amount of NO plus NO_2 produced during the course of reaction. This method was used only on the runs for the pure solid. Samples of HNE decomposed ten half-lives gave equivalent weights of 73.2, 74.5, 76.3, and 73.5, yielding an average value of 74.4 (theoretical value is 75.0; see eq. 1).

Manometric Method. For solid decomposition, the pressure developed due to the gases produced was measured continuously using a pressure transducer as the sensing device. The output of the transducer was read on a digital voltmeter after suitable amplification of the output signal of the transducer. The input voltage to the transducer was from a stabilized voltage supply.

The HNE was decomposed in a Pyrex glass container fitted with a Teflon stopcock with a Viton O-ring seat. Coupling of the transducer with the glass was accomplished through a stainless steel-to-glass seal. Decomposition of known weights of HNE for ten half-lives gave a final pressure reading, which showed that seven moles ($\pm 3\%$) of gases were produced in the decomposition.

Rate Procedures. Known weights of solid HNE or a standard solution of HNE in a solvent were transferred into glass ampoules, which were scaled *in vacuo*, using liquid nitrogen as the coolant. The rate studies were carried out in a constant temperature bath controlled to better than $\pm 0.3°$. For solution runs the samples after quenching were opened, and the solution was placed in the infrared cell. Then the intensity of the absorption band at 6.10 and 6.17 μ was determined and compared with the standard calibration curve. In the case of decomposition of solid HNE, after opening the ampoule, a known volume of the desired solvent was added followed by determination of the infrared spectra in the desired wave length region. For the rates determined by the titrimetric method, the ampoules after quenching were cooled to liquid nitrogen temperature to ensure complete condensation of the gaseous products. Then the ampoules were opened rapidly, immediately placed in 25 ml. of 3% hydrogen peroxide, and allowed to stand 1 hr. The nitric acid formed was titrated with standard base.

Rates determined by the manometric method were carried out using the equipment and procedure previously described. Pressures at various stages of reaction and a final infinity pressure value were obtained. From the data rate constants were calculated.

III. Results

The products of reaction from the thermal decomposition of HNE were established as follows. Gas phase chromatography, by the method of Szulozewski and Higuchi,[10] of the decomposition products showed peaks corresponding to the gases indicated in eq. 1; their relative amounts were estimated as being

$$NO_2 > CO_2 \gg N_2O \cong NO \qquad (1)$$

Infrared spectra of the gaseous products showed absorption bands for the same gases as given in eq. 1.

Although quantitative analysis of gas mixtures containing NO_2 has been performed with success mass spectrometrically, special conditioning of the system is required to obtain reproducible results.[11] Mass spectrometric analysis of the HNE decomposition products was carried out without preconditioning the system and, therefore, our analysis is considered only qualitative. The analysis does indicate that types of the gaseous products are represented by eq. 1. A particularly significant result of this analysis was that no other gaseous products were observed.

Tritrimetric analysis of the gaseous decomposition products showed the presence of 4 moles of NO_2 plus NO gases per mole of HNE decomposed. Also, it was demonstrated by manometric measurement that 7.0 moles ($\pm 3\%$) of gases are produced per mole of HNE decomposed.

The preceding observations are best represented for the gaseous products and their mole ratios as indicated by

$$HNE \longrightarrow 3NO_2 + NO + N_2O + 2CO_2 \qquad (2)$$

Rate Constants. The rate constants for the thermal decomposition of HNE were determined for the pure solid and also in a series of solvents at various temperature. The data are summarized in Table I.

Typical results in terms of the specific first-order rate constants for the thermal decomposition of HNE are given in Tables II, III, and IV. The manometric and titrimetric method of analysis, restricted to runs for decomposition of solid HNE, consistently gave rate constants with a smaller average deviation than the infrared method.

The studies in the hydrocarbon solvents were carried out by procedures similar to that described for CCl_4. In the latter stages of the reaction in the hydrocarbon runs, the solution became turbid. The turbidity for the runs in cyclohexane appears to be the result of adipic acid formation as indicated by the similarity

(9) C. L. Johnson, *Anal. Chem.*, **24**, 1572 (1952).

(10) D. H. Szulozewski and T. Higuchi, *ibid.*, **29**, 1541 (1957).

(11) I. M. Kolthoff, P. J. Elving, and E. B. Sandell, "Treatise on Analytic Chemistry," Part II, Vol. 5, Interscience Publishers, Inc., New York, N. Y., 1961, p. 253.

Table I: Specific First-Order Rate Constants for HNE Decomposition

T, °C.	Solvent	HNE concn. × 10^2, moles/l.	k, sec.$^{-1}$ [a]
60	None	[b]	$1.56 \pm 0.16 \times 10^{-7}$
70	None	[b]	$4.84 \pm 0.80 \times 10^{-7}$
85[c,d]	None	[b]	$6.41 \pm 0.55 \times 10^{-6}$
100	None	[b]	$6.79 \pm 0.48 \times 10^{-5}$
60	CCl_4	2.8	$4.70 \pm 0.30 \times 10^{-7}$
70	CCl_4	3.0	$2.41 \pm 0.10 \times 10^{-6}$
85[e]	CCl_4	3.0	$2.24 \pm 0.15 \times 10^{-5}$
100	CCl_4	2.2 to 3.2	$2.22 \pm 0.13 \times 10^{-4}$
85	$CHCl_3$	3.3	$2.43 \pm 0.18 \times 10^{-6}$
100	PFK[f]	2.7 to 4.1	$2.03 \pm 0.16 \times 10^{-4}$
85	*n*-Heptane	3.8 to 4.2	$7.35 \pm 0.45 \times 10^{-5}$
100	*n*-Heptane	3.0 to 4.1	$3.46 \pm 0.31 \times 10^{-4}$
85	Cyclohexane	3.1	$1.53 \pm 0.06 \times 10^{-4}$
100	Cyclohexane	3.7	$5.68 \pm 0.35 \times 10^{-4}$

[a] The k values are an average of at least two runs. The term following the ± sign represents the average deviation. [b] Sample size was about 7–15 mg. of HNE solid. [c] The specific rate constant for HNE in the presence of ground glass (surface) was found to be $5.82 \pm 0.78 \times 10^{-6}$ sec.$^{-1}$ at 85°. [d] The specific rate constant for a 100-mg. run was $5.90 \pm 0.30 \times 10^{-6}$ sec.$^{-1}$ at 85°. [e] Rate with added CF_3COOH (3.0×10^{-2} moles/l.) is unchanged; k is $2.17 \pm 0.05 \times 10^{-5}$ sec.$^{-1}$. [f] PFK = perfluorokerosene.

Table II: Decomposition of HNE at 100°[a]

t, min.	$x/a = 1 - e^{-kt}$ [b]	$k \times 10^3$, min.$^{-1}$
35	0.165	5.17
56	.212	4.24
95	.291	3.62
160	.459	3.85
265	.690	4.43
300	.674	3.74
		4.18 ± 0.44

[a] Analysis of HNE by infrared. [b] Fraction decomposed.

Table III: Decomposition of HNE at 100°[a]

t, min.	$x/a = 1 - e^{-kt}$ [b]	$k \times 10^3$, min.$^{-1}$
30.0	0.130	4.66
59.9	.229	4.34
90.0	.307	4.08
120.0	.405	4.32
150.0	.464	4.16
174.0	.506	4.05
268.0	.657	4.00
300.0	.712	4.15
		4.22 ± 0.16

[a] Titrimetric analysis of NO + NO_2. [b] Fraction decomposed.

Table IV: Decomposition of HNE[a] at 100°[b]

t, min.	Pressure, atm.[c]	$k \times 10^2$, min.$^{-1}$
40	0.148	4.71
63	.213	4.47
76	.250	4.47
95	.294	4.35
118	.350	4.38
157	.430	4.36
180	.472	4.36
217	.535	4.42
237	.565	4.44
256	.591	4.46
266	.606	4.50
287	.631	4.52
300	.648	4.58
324	.673	4.61
390	.701	4.23
421.6	.728	4.33
∞	.868[d]	...
		4.45 ± 0.09

[a] Least-square treatment of these data gives $k = 4.48 \times 10^{-3}$ min.$^{-1}$ with a standard deviation of 0.21×10^{-3} min.$^{-1}$ and an infinity pressure value of 0.876 atm. [b] Manometric method. [c] Pressures in atm. were computed from the output voltage of the transducer as read on the digital voltmeter after amplification. [d] Based on the volume of the system, weight of HNE used, the calculated final pressure is 0.849 atm., based on eq. 2 and ideal behavior of the gases.

of the infrared spectra of the precipitate to that of an authentic sample of adipic acid.

No enhancement of rate was observed for an increased sample size (10 to 100 mg.), increased surface (ground glass), or the presence of strong acids (trifluoroacetic acid).

Activation Parameters. The logarithms of the specific first-order rate constants were plotted against the reciprocal of the absolute temperature, giving straight lines as shown in Figure 1. From the slopes of the curves, which are equal to $-E^*/2.303R$, the energies of activation were determined.

In Table V, the specific first-order rate constants are given in terms of the Arrhenius equation. Included in this table are the entropies of activation at 85° and the relative rates of HNE decomposition at 85°.

IV. Discussion

From the kinetic parameters given in Table V; the thermal decomposition of HNE appears to fall into two classes, one being the decomposition in CCl_4 and that of the pure solid and the other being the decomposition of HNE in hydrocarbon solvents.

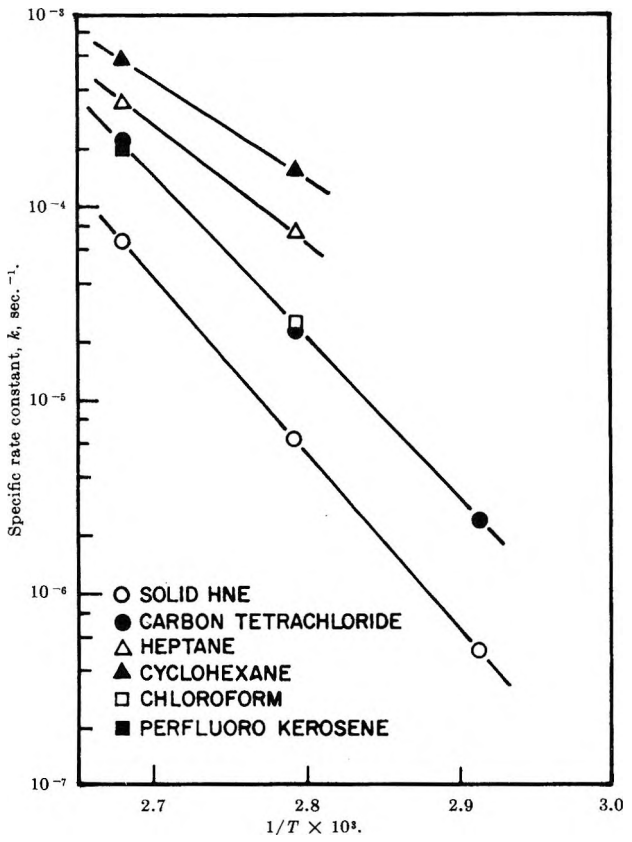

Figure 1. Kinetics of thermal decomposition of HNE; temperature dependence.

Table V: Thermodynamic Functions for the Thermal Decomposition of HNE

Solvent	k, sec.$^{-1}$	ΔS^* at 358°	Relative rates at 85°
None[a]	$10^{18.6}$ exp$(-38,900/RT)$[b]	24.2	1.0
CCl_4	$10^{18.5}$ exp$(-37,800/RT)$[b]	23.7	3.0
Heptane	10^{13} exp$(-28,000/RT)$	−3.1	11.5
Cyclohexane	$10^{9.1}$ exp$(-21,000/RT)$	−19	23.0

[a] J. M. Rosen gives $k = 10^{17.4}$ exp$(-39,000/RT)$ sec.$^{-1}$, private communication. [b] Calculated by least-squares method. Average deviation in E^* is about 10%.

A priori, the decomposition of HNE as the solid and in CCl_4 solutions might be considered as proceeding through the formation of trinitromethyl radicals as

$$(NO_2)_3C\text{–}C(NO_2)_3 \longrightarrow [(NO_2)_3C\ldots\ldots C(NO_2)_3] \longrightarrow 2(NO_2)_3C\cdot \longrightarrow \ldots \longrightarrow \text{products} \quad (3)$$

where the species in the brackets is the activated complex. This path for the decomposition would be proposed on the basis of the bulkiness of the groups and the electron-withdrawing effect of the nitro groups giving a C–C bond which is weaker than a normal C–C, much like in the system of hexaarylethanes. Also, intuitively, one would predict that the trinitromethyl radical should be fairly stable because of resonance stabilization of the radical species. However, the experimental facts are difficult to explain on the basis of a process as outlined in eq. 3. If the trinitromethyl radical is formed during the course of reaction, it should combine with some of the NO_2 to form tetranitromethane (TNM). It is realized that either CO of C–N bond formation can occur from the reaction of NO_2 with the trinitromethyl radical, but it would be expected that sufficient TNM would be formed to be identified. The rate of decomposition of TNM[6] is about one-hundredth as fast as that of the HNE and, therefore, would survive the course of reaction. No evidence for TNM has been observed although a great amount of effort was expended looking for it during the work on the identification of the reaction products.

A more plausible mechanism for the decomposition of HNE is given in eq. 4 or 4a

$$(NO_2)_3C\text{–}C(NO_2)_3 \longrightarrow \left[(NO_2)_2\text{–}C\text{—}C\text{–}(NO_2)_2 \;\; (NO_2\ NO_2)\right] \longrightarrow \quad (4)$$

$$(NO_2)_2\dot{C}\text{–}\dot{C}(NO_2)_2 + 2NO_2 \longrightarrow \ldots \longrightarrow \text{products}$$

$$(NO_2)_3C\text{–}C(NO_2)_3 \longrightarrow \left[(NO_2)\text{–}C\text{—}C\text{–}(NO_2)_3 \;\; (NO_2\ NO_2)\right] \longrightarrow \quad (4a)$$

$$\begin{matrix} NO_2 & & NO_2 \\ & \diagdown\ \diagup & \\ & C\text{–}C\text{–}NO_2 & \end{matrix} + 2NO_2 \text{——}\ldots\longrightarrow \text{products}$$

(with NO_2 below the C–C–NO_2 unit)

where the species in brackets is the activated complex. TNM would not be a product for a reaction proceeding as outlined in either (4) or (4a). The diradical written as an intermediate for the reaction (eq. 4) should give rise to tetranitroethylene. The existence of this ethylene drivative is doubtful since no reference to it is made in the literature, and our own efforts to prepare this compound have been unsuccessful. However, the behavior of dichlorotetranitroethane[6] seems to follow the same course of reaction (eq. 5) as outlined for HNE.

$$Cl(NO_2)_2C\text{–}C(NO_2)_2Cl \longrightarrow Cl(NO_2)C{=}C(NO_2)Cl + 2NO_2 \quad (5)$$

Although our analysis of the reaction products is incomplete for this reaction there is no doubt that the main course of the reaction proceeds as outlined above. For this reaction, a C–C bond cleavage would give

rise to the dinitrochloromethyl radical as an intermediate with a potentially high degree of resonance stabilization, but this is not the case, as indicated by the products of reaction. On the basis of the present data the reaction path giving rise to a carbene as indicated in eq. 4a cannot be excluded. Further work is under way in these laboratories to attempt to resolve this problem.

Looking at the data in Table VI, the entropy factors for activation of HNE decomposition in CCl_4 and for the pure solid are quite large, on the order of 25 e.u., and require further comment.

If we consider reaction 4 or 4a, the entropy for the unfreezing of two NO_2 groups is about 10–12 e.u.[12] This unfreezing process would be according to the reaction

$$N_2O_4 \longrightarrow 2NO_2 \qquad (6)$$

where the entropy of activation has been measured as 10 e.u. and ascribed to the vibrational and rotational entropy contributions of the free NO_2 groups, as compared to the NO_2 groups "frozen" in the N_2O_4 molecules. The additional 15 e.u. of activation observed for HNE decomposition must come about because of either additional unfreezing of the remainder of the carbon–nitro system or the leaving NO_2 groups being sufficiently removed from carbon in the transition state to have attained entropy of translation, in the transition state.

The thermal decomposition of HNE in the hydrocarbon solvents is probably proceeding by a path completely different from its decomposition in CCl_4 or as the solid. Recent findings indicate the formation of a complex from TNM and cyclohexane[13] or heptane.[14] Because of similarity of structure it would be anticipated that a complex also would be formed from HNE and cyclohexane. The thermal decomposition of the HNE–cyclohexane complex could very well proceed more rapidly and by a different mechanism than that for HNE in CCl_4. Solvolytic reactions of charge-transfer complexes[15] show rate enhancement and are associated with a decrease in the activation entropy, when compared to the solvolytic reaction of the uncomplexed material. Both these facts are in line with the finding for the decomposition of HNE in cyclohexane. Thus, possibly, the rate of product formation from HNE solutions in hydrocarbons (HC) with time may be given by

$$\frac{d(\text{product})}{dt} = k_1(\text{HNE}) + k_2(\text{HNE})(\text{HC}) + k_3(\text{HNE}\cdot\text{HC}) \qquad (7)$$

where k_1 is the first-order rate constant for HNE decomposition, k_2 is the bimolecular rate constant, and k_3 is the rate constant for the decomposition of the complex. Work is in progress in these laboratories to determine the nature of the decompositions of HNE in hydrocarbon systems.

V. Special Remarks

The decomposition of solid HNE appears to represent a unique case of thermal decomposition[16] of an organic solid. The decomposition of HNE proceeds without the formation of a liquid phase or the exhibition of an induction period. The reaction is one of a solid decomposing into all gaseous products. Also, the mode of formation of N_2O in the decomposition of HNE is not clear at present. We hope that future work on similar compounds will lead to a reasonable explanation for the formation of N_2O from the decomposition of HNE and other polynitro compounds.

(12) S. W. Benson, "The Foundations of Chemical Kinetics," McGraw-Hill Book Co., Inc., New York, N. Y., 1960, p. 260.

(13) D. F. Evans, *J. Chem. Soc.*, 4229 (1957).

(14) J. N. Chaudhuri and S. Basu, *ibid.*, 4232 (1957).

(15) A. K. Colter and S. S. Wang, *J. Am. Chem. Soc.*, **85**, 114 (1963).

(16) For a resumé of thermal decomposition of organic solids, see W. E. Garner, Ed., "The Chemistry of the Solid State," Butterworth and Co. Ltd., London, 1955. See, particularly, Chapter 10.

Investigation of First-Order Chemical Reactions Following Charge Transfer by a Step-Functional Controlled Potential Method. The Benzidine Rearrangement[1]

by W. M. Schwarz and Irving Shain

Department of Chemistry, University of Wisconsin, Madison, Wisconsin *(Received March 13, 1964)*

A method has been developed for the investigation of electrode processes in which the product of the electron-transfer step is involved in a further chemical reaction to produce an inactive species: $O + ne \rightleftarrows R \xrightarrow{k} Z$. The technique involves producing substance R at a stationary electrode under diffusion-controlled conditions by applying a constant potential for a timed interval. During this interval, substance R diffuses into the solution and simultaneously reacts. Then the potential is suddenly switched to a value where R is reoxidized to O. The anodic current is an indication of the amount of R which has not reacted and can be related to the rate constant k. The boundary value problem for this combined diffusion–electron transfer–kinetic system has been solved for the case of a plane electrode. The method was applied to the reduction of azobenzene to hydrazobenzene which, in turn, undergoes the benzidine rearrangement. The pseudo-first-order rate constants for the rearrangement in 50 wt. % ethanol–water were found to range from 0.58 sec.$^{-1}$ in 0.64 M perchloric acid to 87 sec.$^{-1}$ in 2.5 M acid. These values were shown to be compatible with conventional kinetic data.

Although there have been many studies of electrode processes which involve chemical reactions coupled to a charge-transfer step, several reaction sequences which are of particular interest in organic electrochemistry have received relatively little attention. One of the more important of these is the reaction scheme[2]

$$\begin{aligned} O + ne &\rightleftarrows R \\ R &\xrightarrow{k} Z \end{aligned} \qquad (I)$$

in which the product of the charge-transfer step, substance R, is subsequently involved in an irreversible first-order chemical reaction to produce the electroinactive species, Z.

Two basic electrochemical approaches have been used for generating R and measuring its rate of disappearance. In the *one-step* methods, R is generated under conditions where the electrochemical equilibrium can be shifted significantly by the removal of R from the vicinity of the electrode surface by the chemical reaction. Displacement of this equilibrium as indicated by the measured electrode potential can be related to the rate constant, k. Examples of such methods include the analysis of the shape and the half-wave potential shifts of polarographic waves[3] and the potential–time behavior of chronopotentiometric curves.[4] Unfortunately, the one-step methods are subject to several serious limitations: the charge-transfer step

(1) Presented in part before the Division of Physical Chemistry, 142nd National Meeting of the American Chemical Society, Atlantic City, N. J., Sept. 1962.

(2) Although the discussion emphasizes cases in which the initial charge transfer is a reduction, extension to oxidations is obvious.

(3) (a) D. M. H. Kern, *J. Am. Chem. Soc.*, **75**, 2473 (1953); **76**, 1011 (1954); (b) J. Koutecky, *Collection Czech. Chem. Commun.*, **20**, 116 (1955).

(4) (a) T. R. Rosebrugh and W. L. Miller, *J. Phys. Chem.*, **14**, 816 (1910); (b) P. Delahay, C. C. Mattax, and T. Berzins, *J. Am. Chem. Soc.*, **76**, 5319 (1954); (c) W. K. Snead and A. E. Remick, *ibid.*, **79**, 6121 (1957); (d) A. C. Testa and W. H. Reinmuth, *Anal. Chem.*, **32**, 1518 (1960).

must be reversible, the potential shifts are small and relatively insensitive to changes in the rate constant, and in most cases E° for the charge-transfer reaction in the absence of kinetic complications must be known.

The *two-step* methods, on the other hand, are more generally applicable. During the first step, R is electrochemically generated at a controlled rate for a short period of time. Then, in a second step, the electrolysis conditions are changed so that the unreacted R can be measured—usually by converting it back into O. Here the electrochemical reaction need be reversible only in the gross sense, *i.e.*, some conditions must be available where R can be converted back to O. Thus, these methods are not restricted to cases in which the electron-transfer step is reversible, nor does E° have to be known.

Chronopotentiometry with current reversal[5] is the only previous example of a two-step method which has been applied to this reaction scheme (eq. I). This method, however, has serious limitations when applied to systems involving rapid chemical reactions since an appreciable fraction of the current in both the generating step and the measuring step is required for charging the electrical double layer. In an attempt to minimize this source of error, Reinmuth[5a] has suggested the use of abnormally high depolarizer concentrations. Unfortunately, this introduces other problems, such as instrumental difficulties in rapidly switching high currents, the need for more concentrated buffer solutions of suitable speed and capacity, and the increased chance of streaming phenomena.

In this work, an alternate two-step method was developed in which the potential is controlled rather than the current. In the first step of the electrolysis, the potential is jumped to a value where the rate of generation of R (the cathodic current) is determined solely by the diffusion of substance O to the electrode surface. Then at some switching time, τ, the potential is suddenly returned to the initial value. The resulting anodic current, which is determined by the diffusion-controlled reoxidation of R, gives a measure of the unreacted R. This controlled potential method has the advantage that the faradaic current can be separated easily from the charging current and thus relatively fast chemical reactions following a charge-transfer step can be studied by a simple analysis of the cathodic and anodic current–time curves.

Theory

The theoretical relationship between the current, the time of electrolysis, and the rate constant, k, for a system following eq. I can be derived by solving Fick's laws of diffusion to a plane (modified by the appropriate kinetic terms)

$$(\partial C_O/\partial t) = D_O(\partial^2 C_O/\partial x^2) \quad (1)$$

$$(\partial C_R/\partial t) = D_R(\partial^2 C_R/\partial x^2) - kC_R \quad (2)$$

where C_O and C_R are concentrations of O and R, t is the time, x is the distance from the electrode, and D_O and D_R are the diffusion coefficients of O and R.

The electrolysis conditions resulting from the application of a single large amplitude square voltage pulse to the working electrode are expressed in the initial and boundary conditions

$$t = 0, x \geq 0: \quad C_O = C_O^*, C_R = 0 \quad (3)$$

$$t > 0, x \longrightarrow \infty: C_O \longrightarrow C_O^*, C_R \longrightarrow 0 \quad (4)$$

$$0 < t < \tau, x = 0: C_O = 0, D_O(\partial C_O/\partial x) = -D_R(\partial C_R/\partial x) \quad (5)$$

$$t > \tau, x = 0: C_R = 0, D_O(\partial C_O/\partial x) = -D_R(\partial C_R/\partial x) \quad (6)$$

$$i = nFAD_O(\partial C_O/\partial x)_{x=0} = -nFAD_R(\partial C_R/\partial x)_{x=0} \quad (7)$$

Here, C_O^* is the bulk concentration of substance O, τ is the switching time, n is the number of electrons involved in the charge transfer, F is the Faraday, and A is the area of the electrode.

The solution to this problem can be obtained by a relatively straightforward application of the Laplace transform. Transforming eq. 1 and 2, solving the resulting equations in the conventional manner, and applying boundary conditions (3) and (4), one obtains two general relationships which are valid for all values of time

$$(\partial \bar{C}_O/\partial x)_{x=0} = C_O^*/\sqrt{sD_O} - \sqrt{s/D_O}\,(\bar{C}_O)_{x=0} \quad (8)$$

$$(\partial \bar{C}_R/\partial x)_{x=0} = -\sqrt{(s+k)/D_R}\,(\bar{C}_R)_{x=0} \quad (9)$$

where s is the transform variable and the bar signifies the Laplace transform of the concentration variable. The problem is now reduced to evaluating $\bar{C}_{R(x=0)}$ for all times and untransforming eq. 9.

The time dependence of $C_{R(x=0)}$ for times less than τ can be obtained easily by combining eq. 8 and 9 and the boundary condition (5). The result is

$$C_{R(x=0)} = C_O^*\sqrt{D_O/D_R}\,\exp(-kt)\,{}_1F_1(1/2, 1, kt) \quad (10)$$

(5) (a) A. C. Testa and W. H. Reinmuth, *Anal. Chem.*, **32**, 1512 (1960); (b) O. Dracka, *Collection Czech. Chem. Commun.*, **25**, 338 (1960); (c) W. Jaenicke and H. Hoffmann, *Z. Elektrochem.*, **66**, 803, 814 (1962); (d) H. B. Herman and A. J. Bard, *Anal. Chem.*, **36**, 510 (1964).

where ${}_1F_1(1/2, 1, kt)$ is a confluent hypergeometric series[6] with the properties

$$\frac{d}{dx}\,[{}_1F_1(\alpha,\gamma,x)] = (\alpha/\gamma){}_1F_1(\alpha + 1, \gamma + 1, x) \quad (11)$$

and

$${}_1F_1(\alpha, \gamma, 0) = 1 \quad (12)$$

The evaluation of $C_{R(x=0)}$ can be extended to all times by combining eq. 10 and boundary condition (6), and noting the fundamental definition

$$\bar{C}_{R(x=0)} = \int_0^\tau C_{R(x=0)}\, e^{-st}dt + \int_\tau^\infty C_{R(x=0)}\, e^{-st}dt \quad (13)$$

The result is

$$\bar{C}_{R(x=0)} = C_O^*\sqrt{D_O/D_R}\int_0^\tau {}_1F_1(1/2, 1, kt)e^{-(s+k)t}dt \quad (14)$$

Substituting this into eq. 9

$$(\partial\bar{C}_R/\partial x)_{(x=0)} = -C_O^*(\sqrt{D_O(s + k)}/D_R) \times \int_0^\tau {}_1F_1(1/2, 1, kt)e^{-(s+k)t}dt \quad (15)$$

Integrating the right-hand side of eq. 15 by parts repeatedly

$$(\partial\bar{C}_R/\partial x)_{x=0} = C_O^*(\sqrt{D_O}/D_R) \times \left[\frac{{}_1F_1(1/2, 1, k\tau)e^{-(s+k)\tau}}{\sqrt{(s + k)}} + \sum_{n=1}^{\infty} \frac{1/2, 3/2, \ldots (n - 1/2)k^n}{n!(s + k)^{(n+1/2)}} \times {}_1F_1(n + 1/2, n + 1, k\tau)e^{-(s+k)\tau} - \frac{1}{\sqrt{(s + k)}} - \sum_{n=1}^{\infty} \frac{1/2, 3/2, \ldots (n - 1/2)k^n}{n!(s + k)^{(n+1/2)}}\right] \quad (16)$$

Equation 16 can be untransformed easily, and after recognizing the expression for the series expansion of e^{-kt}, one obtains for $t < \tau$

$$D_R(\partial C_R/\partial x)_{x=0} = -i_c/nFA = -C_O^*\sqrt{D_O/\pi t} \quad (17)$$

and for $t > \tau$

$$D_R(\partial C_R/\partial x)_{x=0} = i_a/nFA = C_O^*\sqrt{D_O/\pi(t - \tau)} \times \left[e^{-kt}{}_1F_1(1/2, 1, k\tau) + \sum_{n=1}^{\infty} \frac{e^{-kt}[(t - \tau)k]^n}{n!}\,{}_1F_1(n + 1/2, n + 1, k\tau)\right] - C_O^*\sqrt{D_O/\pi t} \quad (18)$$

where i_c and i_a refer to the cathodic and anodic currents, respectively. Equation 17 describes the cathodic current–time curve for the first potential jump. As expected, the cathodic current does not depend on the kinetics of the subsequent reaction.

Equation 18 represents the anodic current–time curve obtained when the potential suddenly reverts to its original value. The functional form of this expression can be seen more clearly by letting ϕ represent the terms in the brackets.

$$i_a/nFA = D_R(\partial C_R/\partial x)_{x=0} = C_O^*\sqrt{D_O} \times \left[\frac{\phi(k, t, \tau)}{\sqrt{\pi(t - \tau)}} - \frac{1}{\sqrt{\pi t}}\right] \quad (19)$$

For the case where $k = 0$, ϕ reduces to unity—a result expected in the absence of kinetic complications.[7] In the limit as $(t - \tau)$ approaches zero—a time infinitesimally greater than the switching time—the summation terms in ϕ become zero and the instantaneous current is directly proportional to the surface concentration of species R at the switching time τ (see eq. 10).

In considering the current–time curves for finite values of $t - \tau$ and k, the anodic current is still largely determined by the "surface concentration term." However, with the usual experimental values of $(t - \tau)$ and τ, it is necessary to retain several terms in the infinite series. For example, assuming that $k\tau = 1.2$ and $(t - \tau)/\tau = 0.5$, approximately 0.4% accuracy in the current is obtained using three terms of the series; 3% using two terms. More rapid convergence for the $k\tau$ and $(t - \tau)/\tau$ values of greatest interest, *i.e.*, $k\tau < 2$ and $(t - \tau)/\tau < 1$, can be obtained by algebraically manipulating ϕ into the form

$$\phi = e^{-k\tau/2}I_0(k\tau/2) + 2e^{-k\tau/2}e^{-k(t-\tau)} \times \sum_{n=1}^{\infty} I_n(k\tau/2)\,\frac{\int_0^{k(t-\tau)}\cdots\int_0^{\lambda_2}\lambda^n{}_1e^{\lambda_1}d\lambda_1\cdots d\lambda_n}{[k(t - \tau)]^n} \quad (20)$$

where $I_n(kt/2)$ represents the modified Bessel functions.[8] Using this expression with the above conditions, convergence to the 0.2% error level is obtained using only one term of the infinite series.

(6) (a) A. Erdelyi, "Higher Transcendental Functions," Vol. I, McGraw-Hill Book Co., Inc., New York, N. Y., 1953, Chapter VI; (b) L. J. Slater, "Confluent Hypergeometric Functions," Cambridge University Press, London, 1960; (c) I. N. Sneddon, "Special Functions of Mathematical Physics and Chemistry," Interscience Publishers, Inc., New York, N. Y., 1956, Chapter II.

(7) (a) T. Kambara, *Bull. Chem. Soc. Japan*, **27**, 527 (1954); (b) J. Weber, *Collection Czech. Chem. Commun.*, **24**, 1770 (1959).

(8) See ref. 6c, p. 113.

Although eq. 18 could be used to calculate the rate constant directly from the measured anodic current, in practice it is more convenient to eliminate the dependence on the initial depolarizer concentration, the electrode area, and the diffusion coefficient by simultaneously measuring the cathodic current, i_c, and working with the dimensionless ratio i_a/i_c. A further simplification results if the anodic current measured at a time t_1 is always coupled with the cathodic current measured at the time $t_1 - \tau$ as shown in Figure 1. The final working equation for i_a/i_c is obtained by dividing eq. 18 by eq. 17 and introducing the restrictions on the time of measurement

$$-i_a/i_c = \phi[k\tau, (t - \tau)/\tau] - \sqrt{\frac{(t - \tau)/\tau}{1 + (t - \tau)/\tau}} \quad (21)$$

In this case, the rate constants can be obtained directly from working curves constructed from eq. 21 in which the current ratios i_a/i_c are plotted against the dimensionless parameter $k\tau$ for various values of the time ratio, $(t - \tau)/\tau$. Several of these working curves are shown in Figure 2.

Kinetic and Electrochemical Characteristics of the Azobenzene System

In order to test the theoretical calculations, the reduction of azobenzene (eq. II) was investigated.

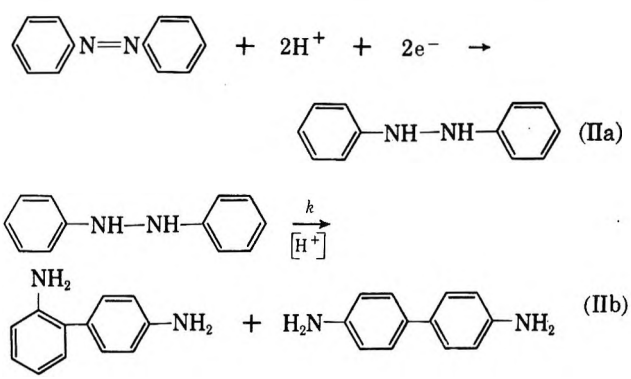

Here the initial compound, azobenzene, is reduced to hydrazobenzene which, in strong acid, undergoes the benzidine rearrangement.

The reduction of azobenzene has been studied polarographically[9] under conditions where the rate of the benzidine rearrangement is negligible. Although there are some inconsistencies among the various investigations, the results all indicate that in the pH range 1–13 both *cis*- and *trans*-azobenzene undergo a pH-dependent, two-electron reduction as shown in eq. IIa. In several cases,[9a,d,e] the reverse process, the oxidation of hydrazobenzene to azobenzene, was also reported and shown to occur at potentials close to those corresponding to the reductions.

The rearrangement of hydrazobenzene (eq. IIb)

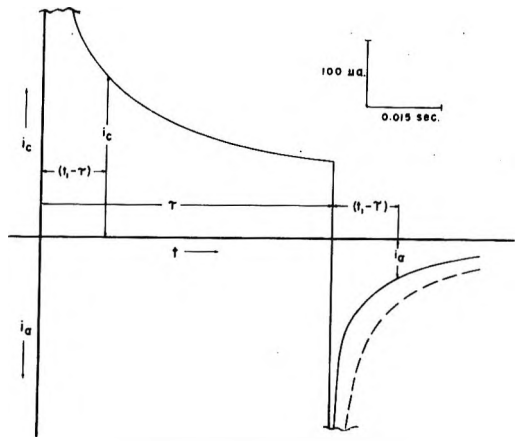

Figure 1. Typical cathodic–anodic current–time curves for the azobenzene–hydrazobenzene system, 2.0×10^{-3} *M* azobenzene–50 wt. % ethanol–water; $\tau = 0.060$ sec.: solid line 1.588 *M* $HClO_4$; half-life of the benzidine rearrangement $\approx \tau$; dashed line 0.40 *M* $HClO_4$; half-life of the benzidine rearrangement $\gg \tau$.

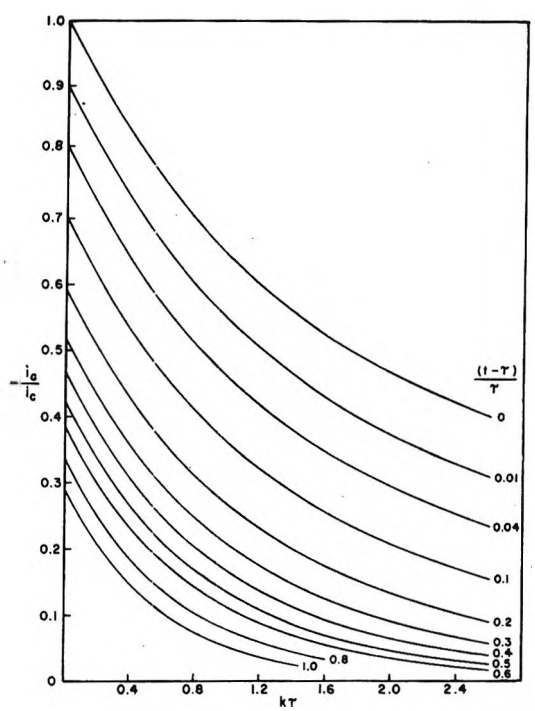

Figure 2. Theoretical working curves for the step-functional controlled potential method; charge transfer at a plane electrode followed by an irreversible first-order rate process.

(9) (a) A. Foffani and M. Fragiacomo, *Ric. Sci.*, **22**, 139 (1952); (b) P. J. Hillson and P. P. Birnbaum, *Trans. Faraday Soc.*, **48**, 478 (1952); (c) C. R. Castor and J. H. Saylor, *J. Am. Chem. Soc.*, **75**, 1427 (1953); (d) S. Wawzonek and J. D. Fredrickson, *ibid.*, **77**, 3985, 3988 (1955); (e) B. Nygard, *Arkiv Kemi*, **20**, 163 (1963).

has been the subject of numerous kinetic investigations[10] in which spectrophotometric,[11] potentiometric,[12] or titration[13] techniques were used to follow the rate of the reaction. These studies show that in dilute acid (<0.1 M), the rate law is first order in hydrazobenzene and second order in hydronium ion concentration. In stronger acids, the log of the pseudo-first-order rate constant follows the Hammett acidity function, H_0.[13g,h] At room temperature, the rearrangement proceeds irreversibly and intramolecularly to give two products, benzidine and diphenyline. These are formed in a ratio which is essentially invariant with changes in solvent or acid concentration.[11a] A disproportionation side reaction yielding 3–5% aniline and azobenzene also has been reported.[13f,i,14] Other aspects of the benzidine rearrangement have been discussed in two recent reviews.[14,15]

The azobenzene–hydrazobenzene system offers several advantages over the previously cited examples[3a,4c,d,5] of reaction scheme I. For example, in the solutions used here, the electrochemical step (reaction IIa) takes place at potentials where it is possible to use mercury electrodes, thereby minimizing difficulties such as surface contamination and oxide formation which are often encountered with solid electrodes. An important feature of this system from the kinetic standpoint is the second-order dependence of reaction IIb on the acidity which made possible the investigation of a wide range of reaction rates. Perhaps the greatest advantage, however, was the fact that the mechanism of the benzidine rearrangement had been established with great certainty by many previous workers. This made it possible to use the azobenzene–hydrazobenzene system for a critical evaluation of the step-functional controlled potential method and at the same time extend the rate data for the benzidine rearrangement to much higher acidities than previously reported.

Experimental

Instrumentation. Using a three-electrode cell, data were obtained with two different potentiostatic circuit configurations.

Potentiostat A consisted of a controller, a voltage follower, and a current follower arranged as shown previously.[16] Each unit contained a K2-X operational amplifier stabilized by a K2-P chopper amplifier (both manufactured by G. A. Philbrick Researches, Inc., Boston Mass.). In addition, the controller and current follower were used with K2-B1 booster amplifiers. The square pulse generator employed unstabilized K2-X operational amplifiers in a monostable multivibrator circuit similar to that shown previously.[17]

Potentiostat B consisted of a single controller unit arranged in an alternate configuration.[18] The operational amplifier was a single SK2-V plug-in unit (G. A. Philbrick Researches, Inc.) A Krohn-Hite (Cambridge, Mass.) Model DCA-10 10-w. d.c. power amplifier was used in the +10 gain position as a booster amplifier. The square pulse voltage was obtained from the gate output of a Tektronix Model 162 wave form generator. Although the controller unit was not chopper stabilized, it showed only an insignificant drift rate of ±3 mv./day when arranged as a simple 1–1 inverter.

For potentiostat A, adequate potential control could be obtained only for switching times greater than 20 msec. For shorter switching times and/or acid concentrations greater than 2 M, ringing became a serious problem. On the other hand, the response time of potentiostat B was considerably shorter than that of A. With 2 M perchloric acid solution, a load resistor of 200 ohms and a 0.6-v. applied square wave pulse, the voltage measured between the working and reference electrodes showed a rise time of 4 μsec. (to the 90% level) for arrangement B compared to 0.3 msec. for potentiostat A. In both circuits, the rise times are increased by increasing the load resistor and by increasing the acid concentration of the solution. (Normally, a small adjustable capacitor was used across the feedback loop of the controller unit in both potentiostats to damp out switching transients critically.)

Current–time curves were displayed on a Tektronix 536 oscilloscope equipped with a Type 53/54 D high gain differential preamplifier and a Type 53/54 T

(10) (a) E. S. Gould, "Mechanism and Structure in Organic Chemistry," Henry Holt and Co., New York, N. Y., 1959, p. 656; (b) H. Zollinger, "Azo and Diazo Chemistry," Interscience Publishers, Inc., New York, N. Y., 1961, Chapter 12.

(11) (a) R. B. Carlin, R. G. Nelb, and R. C. Odioso, *J. Am. Chem. Soc.*, **73**, 1002 (1951); (b) D. A. Blackadder and C. Hinshelwood, *J. Chem. Soc.*, 2898 (1957).

(12) E. Biilmann and J. H. Blom, *ibid.*, **125**, 1719 (1924).

(13) (a) M. J. S. Dewar, *ibid.*, 777 (1946); (b) G. S. Hammond and H. J. Shine, *J. Am. Chem. Soc.*, **72**, 220 (1950); (c) M. D. Cohen and G. S. Hammond, *ibid.*, **75**, 880 (1953); (d) G. S. Hammond and W. Grundemeier, *ibid.*, **77**, 2444 (1955); (e) L. J. Croce and J. D. Gettler, *ibid.*, **75**, 874 (1953); (f) C. K. Ingold and H. V. Kidd, *J. Chem. Soc.*, 984 (1933); (g) C. A. Bunton, C. K. Ingold, and M. M. Mhala, *ibid.*, 1906 (1957); (h) D. V. Banthorpe, E. D. Hughes, C. K. Ingold, and J. Roy, *ibid.*, 3294 (1962) (also see others in this series); (i) M. Vecera, L. Synek, and V. Sterba, *Collection Czech. Chem. Commun.*, **25**, 1992 (1960).

(14) M. Vecera, *Chem. Listy*, **52**, 1373 (1958).

(15) C. K. Ingold, *Boll. Sci. Fac. Chim. Ind. Bologna*, **21**, 34 (1963).

(16) See Figure 15b in W. M. Schwarz and I. Shain, *Anal. Chem.*, **35**, 1770 (1963).

(17) See Figure 8 in W. L. Underkofler and I. Shain, *ibid.*, **35**, 1778 (1963).

(18) See Figure 4b of ref. 16.

time base generator. The time base generator was calibrated to give less than 2% error on all time scales. Direct current triggering by the output of the square pulse generator allowed the trace to begin at either time zero or time τ. In this way, the full scale could be utilized for either the cathodic or anodic part of the current–time curve.

A DuMont Type 302 Polaroid camera was used to photograph the oscilloscopic traces.

Cell and Electrodes. The electrolytic cell consisted of a 100-ml. Pyrex weighing bottle with a 50/12 standard taper joint. It was equipped with a tight-fitting Teflon lid, in which holes were provided for the various electrodes, nitrogen inlet, and the mercury drop transfer scoop. The working electrode—the hanging mercury drop electrode (h.m.d.e.)—was constructed as described previously,[19] except that 6-mm. tubing was used. Normally, two drops of mercury from a d.m.e. capillary were collected and transferred to the working electrode. The radius of the hanging mercury drop ranged from 0.063 to 0.065 cm., depending on the acid concentration. The counter electrode, a 15-cm. length of 26 gauge platinum wire in the form of a spiral, was immersed directly in the solution under study.

The reference electrode (saturated calomel) was contained in a separate compartment, connected to the cell with a double junction salt bridge ending in a Luggin capillary. The section of the salt bridge next to the s.c.e. compartment contained aqueous 1 *M* sodium nitrate, while the Luggin capillary section contained 1 *M* perchloric acid in the ethanol–water solvent. The electrolytic cell was placed directly in a water bath maintained at 25.0 ± 0.1°. In order to isolate the cell from vibration, the cell assembly and water bath were mounted on a 60-lb. concrete slab supported by an inflated inner tube.

Chemicals. trans-Azobenzene (Eastman White Label) was recrystallized three times from hot 95% ethanol, m.p. 68.0° (uncor.).

Ethanol (95%) was purified by distillation through a 1-m. fractionating column of glass helices.

The 95% ethanol–water azeotropic mixture, 60% perchloric acid (Baker and Adamson reagent grade), and triply distilled water were used to prepare stock solutions of the following composition: 50 wt. % ethanol–water; 4.0 *M* perchloric acid–50 wt. % ethanol–water; and 4 or 8 m*M* azobenzene–50 wt. % ethanol–water. Acidic azobenzene solutions were prepared just prior to measurement by mixing appropriate volumes of the stock solutions. Under normal conditions, photooxidation of azobenzene[20] could not be detected after a day or so in 3 *M* perchloric acid–50 wt. % ethanol–water solutions. No special precautions were taken to prevent the photoisomerization of azobenzene[21] since this would have no effect on the kinetic measurements. The final acid concentration in all solutions was checked by titration with standard base.

High purity nitrogen (National Cylinder Gas Co.), which was used for deaeration, was purified and presaturated by passing it through a train consisting of a vanadous sulfate oxygen scrubber, a 1 *M* sodium hydroxide trap, a 95% ethanol gas saturator, and finally a saturator containing a sample of the solution under study.

Procedures. The potential applied to the working electrode was a single square pulse with an amplitude of −0.6 v. The initial d.c. level was set at 0.3 v. *vs.* s.c.e. Under these conditions, the cathodic polarization step was carried out at −0.3 v. *vs.* s.c.e.; the subsequent anodic step, at 0.3 v. Since the reduction potential of azobenzene ranged only from about −0.1 to 0.1 v. (*vs.* s.c.e.) in the solutions used here, the applied potential always fell in the diffusion-controlled limiting current region for each depolarizer species. In addition, by running suitable blanks in the absence of azobenzene, it was verified that the initial potential used was sufficiently cathodic at the foot of the mercury dissolution wave.

Immediately after switching the potential, both the anodic and cathodic current–time curves exhibited anomalous shoulders, *i.e.*, the current remained higher than would be expected for diffusion-controlled conditions. The currents involved were of the order of 20 to 30 ma., and lasted from 0.1 to 0.2 msec., depending on the experimental conditions. The quantity of electricity involved was perhaps three to four times larger than would be observed for the normal diffusion-controlled $1/\sqrt{t}$ decay of the current for the same time interval. This anomalous behavior was most probably caused by the respective reduction or oxidation of adsorbed depolarizer species and has been mentioned previously by Delahay and co-workers[22] in connection with other potentiostatic experiments with the azobenzene system.

The magnitude and duration of the extraneous currents were found to be affected by the uncompensated *IR* drop in the solution. For example, increasing the

(19) W. L. Underkofler and I. Shain, *Anal. Chem.*, 33, 1966 (1961).

(20) (a) G. E. Lewis, *J. Org. Chem.*, 25, 2193 (1960); (b) G. E. Lewis, *Tetrahedron Letters*, No. 9, 12 (1960); (c) F. Gerson, E. Heilbronner, A. vanVeen, and B. M. Wepster, *Helv. Chim. Acta*, 43, 1889 (1960).

(21) E. Fischer, *J. Am. Chem. Soc.*, 82, 3249 (1960), and references therein.

(22) P. Delahay, S. Oka, and H. Matsuda, *ibid.*, 82, 329 (1960).

solution electrolyte concentration or moving the Luggin capillary closer to the h.m.d.e. both resulted in an increase in the anomalous current, coupled with a simultaneous shortening of its duration. Thus, for experiments involving very rapid switching times, the tip of the Luggin capillary was placed within a fraction of a millimeter of the h.m.d.e. (compared to 1 mm. or so for less critical experiments). Under these conditions, the duration of the anomalously high currents was less than 0.1 msec., and they did not interfere seriously with measurements on the normal portions of the current–time curves.

For each azobenzene solution, a set of anodic current–time curves was obtained for each value of the switching time that was used. In addition, a single set of cathodic current–time curves was obtained. Each of these sets consisted of four replicate curves, and each curve was measured on a fresh h.m.d.e. A standardized procedure was used, in which the electrode potential was set at the initial value while transferring the mercury drop and then maintained at that value for an additional 15–30 sec. to allow the solution to come to rest. Reproducibility was excellent on every time scale, and only rarely could a deviation amounting to more than 1% of full scale be detected.

In all cases, a blank correction was made based on current–time curves measured in solutions containing no azobenzene. These corrections were generally small, except at the very fastest switching times, where they amounted to as much as 10% of the faradaic current.

Results and Discussion

Prior to making the kinetic measurements, a quantitative study was made of cathodic–anodic current–time curves obtained under experimental conditions where the rate of reaction IIb was negligible. That is, acid concentrations were selected such that for each experiment, the half-life of the rearrangement was very much longer than the switching time, τ. These control experiments were used to evaluate the general procedures of the step-functional method and simultaneously to test the electrochemical behavior of the azobenzene–hydrazobenzene system.

Then under identical experimental conditions, a second set of cathodic–anodic current–time curves was obtained using acid concentrations where the rate of the rearrangement reaction was important, *i.e.*, where the half-life of the reaction was the same order of magnitude as the selected values of τ. Since the cathodic portion of these curves should be unaffected by the subsequent chemical reaction, they could be used for further evaluation of the techniques and for investigation of possible side reactions. Then the anodic current–time curves were used along with the respective cathodic portions for the determination of the rate constants.

Nonreacting Systems. For the first set of experiments, 14 values of the switching time were used, ranging from 1.6 to 0.0025 sec. Over this range, three acid concentrations were used: 0.1 M (τ, 0.8 to 1.6 sec.), 0.4 M (τ, 0.03 to 0.6 sec.), and 1.0 M (τ, 0.0025 to 0.016 sec.). Thus, the most acid solutions were used only for the shortest switching times, and, for all practical purposes, the amount of rearrangement taking place during each experiment was negligible. This permitted running the control experiments at several acidities under conditions as similar as possible to the subsequent kinetic measurements. For each value of τ, three azobenzene concentrations (0.6, 1.0, and 2.0 mM) were used, except for the shortest switching times (less than 0.016 sec.) where only the most concentrated solution was investigated.

Cathodic Current–Time Curves. The cathodic current–time curves were analyzed according to eq. 17, and the results for the three azobenzene concentrations were essentially the same. Plots were made of i_c/C_O^* *vs.* $1/\sqrt{t}$ for each value of τ. Straight lines were obtained for all 14 of the time segments, and the individual slopes showed a deviation of less than 3% from the average. These results indicated that the initial reduction of azobenzene was a simple diffusion-controlled process over the entire time scale from 0.0005 to 1.6 sec. The diffusion coefficient calculated from the average slope was 0.34×10^{-5} cm.^{2}/sec., a value not inconsistent with the previously reported polarographic data.[9]

The cathodic current–time curves also were used to evaluate the errors introduced as a result of neglecting the spherical nature of the hanging mercury drop electrode. These errors were estimated from the magnitude of the positive intercept on the current axis on extrapolation of i_c/C_O^* *vs.* $1/\sqrt{t}$ plots to infinite time. Such deviations from eq. 17 were found only for the longest switching times ($\tau > 1$ sec.), and since they never amounted to more than a few per cent, they could be neglected without causing serious error.[23]

Anodic Current–Time Curves. The analysis of the anodic current–time curves involved measuring the ratio i_a/i_c for a series of time ratios $(t - \tau)/\tau$, as indicated in Figure 1. Some typical results for different values of τ are shown in Figure 3, where the points are the experimental values, and the solid lines represent

(23) The theory for the spherical case has been derived and will be presented elsewhere.

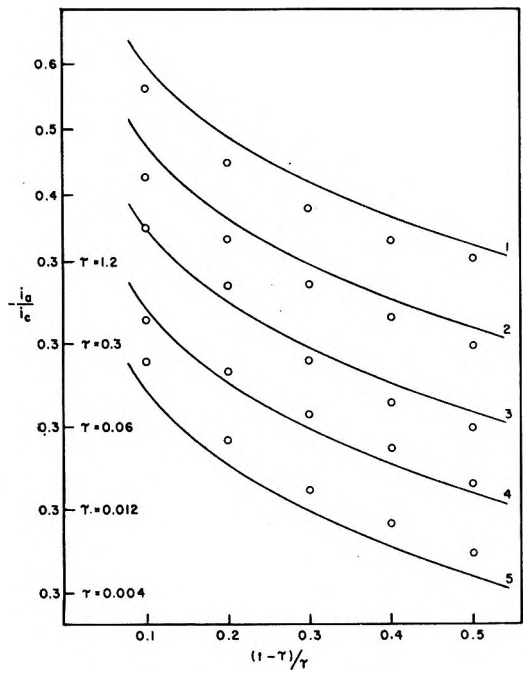

Figure 3. Comparison of experiment with theory when the half-life of the benzidine rearrangement $\gg \tau$: solid lines, theoretical; points, experimental for 2.0×10^{-3} *M* azobenzene in 50 wt. % ethanol–water; 1, 0.10 *M* $HClO_4$, $\tau = 1.2$ sec.; 2, 0.40 *M* $HClO_4$, $\tau = 0.30$ sec.; 3, 0.40 *M* $HClO_4$, $\tau = 0.060$ sec.; 4, 1.0 *M* $HClO_4$, $\tau = 0.012$ sec.; 5, 1.0 *M* $HClO_4$, $\tau = 0.0040$ sec.

the theoretical behavior for diffusion-controlled currents. The theoretical curves were calculated from eq. 21 assuming ϕ to be unity.

These results showed that for all values of τ, the anodic currents were essentially controlled by the diffusion of hydrazobenzene to the electrode surface. For each value of τ, the three azobenzene concentrations that were tested gave practically identical results. More important, the agreement between the experimental points and theory was reasonably good for all values of τ. In most cases, slight deviations of i_a/i_c from theory could be ascribed to deviations in i_a rather than i_c. The tendency for the experimental points to fall uniformly below the theoretical curves for the longer values of τ was probably the result of stirring in the hydrazobenzene diffusion layer initiated by momentary movement of the mercury drop at the switching time.[24] The tendency for the experimental values to be higher than theory at the shortest switching times probably is related to the adsorption phenomena involving hydrazobenzene discussed above.

Reacting Systems. In the second set of experiments, cathodic–anodic current–time curves were obtained in a series of 14 acid concentrations ranging from 0.65 to 2.6 *M*. For a number of these acid concentrations (see Table I), three different azobenzene concentrations (0.6, 1.0, and 2.0 m*M*) were investi-

Table I: Kinetic Data for the Perchloric Acid-Catalyzed Rearrangement of Hydrazobenzene in 50 Wt. % Ethanol–Water at 25°

Perchloric acid concn., moles/l.	H_0[a]	Azobenzene concn. × 10^3, moles/l.	Slope/concn., i_c *vs.* $1/\sqrt{t}$ curves	k, sec.$^{-1}$	Potentiostat circuit
0.641	1.10	0.60	11.7	0.570	B[b]
0.641		1.00	11.4	0.555	
0.641		2.00	11.2	0.616	
0.694	1.05	1.00	11.4	0.775	B[b]
0.793	0.95	0.60	11.2	1.02	A
0.793		1.00	10.6	1.04	
0.793		2.00	10.4	1.08	
0.886	0.86	1.00	11.4	1.61	B[b]
0.989	0.79	0.60	10.6	2.16	A
0.989		1.00	10.7	2.32	
0.989		2.00	10.5	2.40	
1.090	0.72	1.00	10.3	2.96	B[b]
1.185	0.66	0.60	11.0	4.57	A
1.185		1.00	10.9	4.45	
1.185		2.00	10.4	4.20	
1.385	0.56	1.00	11.2	6.60	B[b]
1.390		2.00	11.0	7.60	B
1.588	0.46	0.60	11.2	11.3	A
1.588		1.00	10.8	11.2	
1.588		2.00	10.1	10.9	
1.582		2.00	11.1	12.6	B
1.775	0.37	2.00	11.0	19.4	B
1.979	0.28	0.60	11.6	29.2	A
1.979		1.00	11.2	28.6	
1.979		2.00	10.5	27.8	
1.955		2.00	10.9	29.1	B
1.98		1.00	11.5	29.3	
1.98		2.00	10.8	29.9	
2.150	0.20	2.00	10.8	45.0	B
2.36	0.12	1.00	11.8	63.0	B
2.36		2.00	11.8	65.5	
2.345		2.00	10.7	61.2	
2.545		2.00	10.0	86.5	B

[a] The values of H_0 in this solvent were obtained by applying a small solvent correction, as indicated in the work of E. A. Braude and E. S. Stern, *J. Chem. Soc.*, 1976 (1948), to the H_0 values given by D. P. N. Satchell, *ibid.*, 2878 (1957), for perchloric acid in 67 wt. % ethanol–water. [b] In this case, the potentiostatic circuit contained no booster amplifier.

(24) I. Shain and K. J. Martin, *J. Phys. Chem.*, 65, 254 (1961). Note that in the present case the bulk concentration of hydrazobenzene is zero, so that stirring causes transport of material away from the electrode and results in low anodic currents.

gated; in others, only the most concentrated solution was used. As with the nonreacting systems, τ-values were in the range from 1.6 to 0.005 sec., depending on the acid concentration.

Cathodic Current–Time Curves. In addition to their use in the analysis of the rate data, the cathodic current–time curves also served as a method for detecting such side reactions as the disproportionation of hydrazobenzene mentioned previously.[13f,i,14] If such side reactions were present, the regeneration of depolarizer by the chemical step would result in an enhancement of the cathodic current.

As before, the cathodic current–time curves were analyzed according to eq. 17, which is still applicable. In general, the results were very similar to those obtained under conditions where the rate of the chemical reaction was negligible. The plots of i_c/C_O^* *vs.* $1/\sqrt{t}$ for each azobenzene concentration yielded straight lines for all 14 acid concentrations. The slope for each individual plot, as shown in Table I, deviated less than 5% from the average—a greater degree of scatter, however, than obtained previously. The magnitudes of the slopes tended to be 2 to 4% greater than those observed at the same time under comparable conditions in the less acidic nonreacting solutions. This difference in slope would result if 4 to 8% of the initially generated hydrazobenzene were involved in a disproportionation side reaction. On the other hand, a trend toward slightly greater deviations at lower azobenzene concentrations indicates that other factors are also present, and the estimate of the amount of side reaction based on a simple second-order disproportionation is probably too high.

In order to examine these side reactions further, several large-scale controlled potential coulometric electrolyses were carried out on 1 m*M* azobenzene solutions at acid concentrations ranging from 0.5 to 4.0 *M*. The observed current efficiencies ranged from 100% (0.5 *M*) to 95% (4.0 *M*), *i.e.*, in the more acid solutions, the quantity of electricity required for complete reduction was about 5% higher than expected for the stoichiometric reduction of the azobenzene present. Although these results cannot be compared directly with the potentiostatic current–time curves because of the differences in the mass-transfer processes, the magnitude of the side reaction is similar in the two cases and probably does not exceed the 3 to 5% previously reported.

Anodic Current–Time Curves. The shape of the curves in Figure 2 indicates that the maximum accuracy in the kinetic measurements is achieved for switching times, τ, which are the same order of magnitude as the half-life of the chemical reaction. Thus, the switching times used here were selected to be approximately $^2/_3$, 1, and $^3/_2$ times the half-life of the rearrangement reaction for each azobenzene solution at each acidity. This permitted a significant amount of reaction to take place, but at the same time enough hydrazobenzene remained so that the anodic currents could be measured with reasonable accuracy.

From any individual cathodic–anodic current–time curve, several estimates of the kinetic parameter were obtained. In principle, i_a and i_c could be measured at any arbitrarily selected value of t and $(t - \tau)$ as is shown in Figure 1. However, the analysis was greatly simplified by making measurements along the curves at values of t such that the ratio $(t - \tau)/\tau$ corresponded to values used in constructing the working curves, *i.e.*, $(t - \tau)/\tau$ equal to 0.1, 0.2, 0.3, 0.4, and 0.5. The measured current ratios, i_a/i_c, were then used with the working curves (Figure 2) to obtain the kinetic parameter, $k\tau$. Thus, for a given cathodic–anodic current–time curve (at a particular value of τ) five estimates of $k\tau$ were obtained. Similarly, five more measurements were made on the current–time curves obtained for each of the other two values of τ used.

For each azobenzene solution, all of these data were combined to obtain the best possible estimate of the rate constant. The values of $k\tau$ were converted to $k(t - \tau)$ so that data obtained with the three values of τ could be combined in a form which gives equal weight to each value. Then plots were made of $k(t - \tau)$ *vs.* $(t - \tau)$, and the rate constant was calculated directly from the slope.[25] In each case, the experimental data determined a straight line which passed through the origin, as required by theory. Several of these plots are shown in Figures 4 and 5.

A summary of the kinetic data is given in Table I. These results were obtained (in no particular order) over a period of several months, using two different potentiostats. For any given acidity, the rate constants calculated for the three different azobenzene concentrations are in good agreement. Generally, they fall within ±5% of an average value. The observed values of k show no systematic trend with azobenzene concentration, *i.e.*, for some acidities (0.8, 1.0 *M*), k increased slightly with concentration; for others (1.2, 1.6 *M*), k decreased. Thus, it was not possible to detect any effect due to the presence of second-order side reactions. This is not surprising, however, in view of the magnitude of the scatter in the experimental points (Figures 4 and 5), particularly for 0.6 m*M* solutions. Under these circumstances,

(25) Working curves calculated directly in terms of $k(t - \tau)$ could not be used conveniently because the plots for various values of the ratio $(t - \tau)/\tau$ intersect.

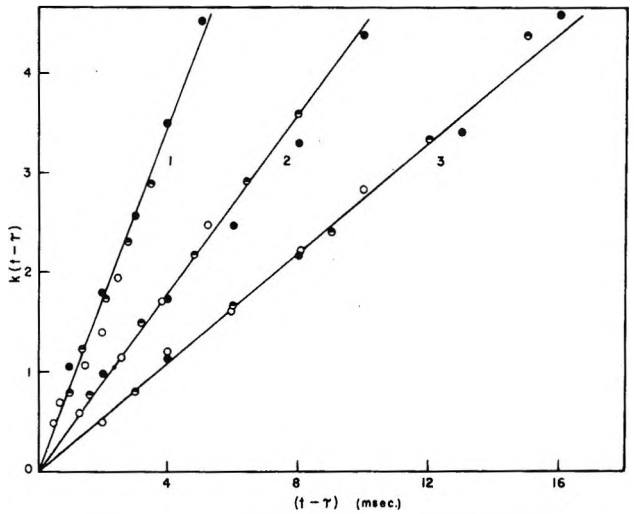

Figure 4. Rearrangement of hydrazobenzene in 50 wt. % ethanol–water; 1.0×10^{-3} M azobenene with: 1, 1.588 M $HClO_4$; 2, 1.185 M $HClO_4$; 3, 0.989 M $HClO_4$; ●, $\tau \approx {}^3/_2 t_{1/2}$; ◓, $\tau \approx t_{1/2}$; ○, $\tau \approx {}^2/_3 t_{1/2}$.

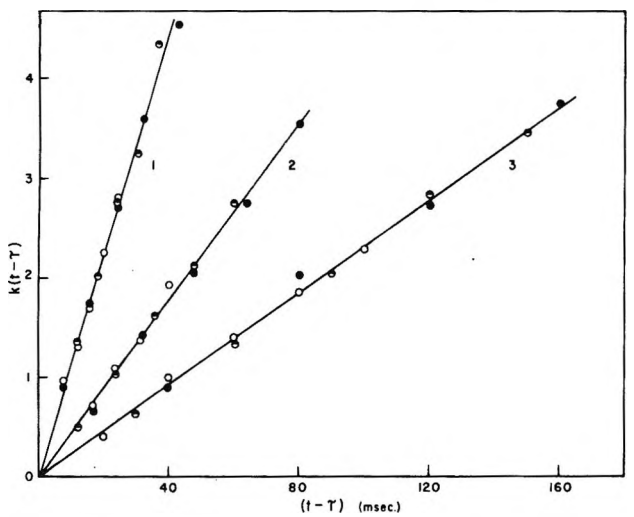

Figure 5. Rearrangement of hydrazobenzene in 50 wt. % ethanol–water; 2.0×10^{-3} M azobenzene with: 1, 2.545 M $HClO_4$; 2, 2.150 M $HClO_4$; 3, 1.979 M $HClO_4$; ●, $\tau \approx {}^3/_2 t_{1/2}$; ◓, $\tau \approx t_{1/2}$; ○, $\tau \approx {}^2/_3 t_{1/2}$.

the observed values of k accurately reflect the precision with which rate constants can be measured by this method.

An estimate of the accuracy of these kinetic measurements can be made easily. If it is assumed that the major errors are caused by phenomena which interfere with the mass-transfer processes, the ratio of the observed to the true value of i_a/i_c should be approximately the same for both the nonreacting and the reacting systems. Corrected values of i_a/i_c for the reacting system then can be calculated by dividing the observed values of i_a/i_c by the above ratio obtained from the

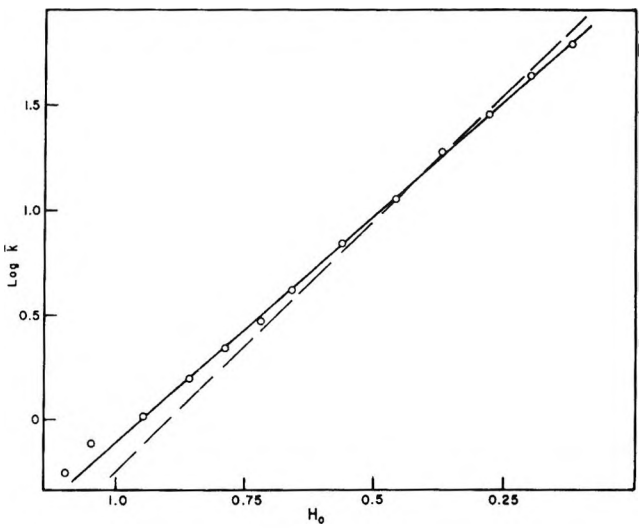

Figure 6. Dependence of the rate of hydrazobenzene rearrangement on the Hammett acidity function. $\bar{k}$ is the average value of k at each acidity.

analysis of the corresponding nonreacting system (Figure 3). The rate constants estimated in this way show that the measured values of k given in Table I could not be more than 25% too high for the slow reactions, nor more than 15% too low for the fast reactions. Another source of error, the presence of 3–5% second-order side reaction, would lead to small positive errors in the observed rate constants.

The dependence of the rate constants on acidity can be seen in Figure 6 where the log of the average rate constant, $\bar{k}$, is plotted against the Hammett acidity function, H_0. The dashed line indicates the magnitude and direction of the error limits discussed above. (The two low acidity points show a positive deviation which is due in part to the spherical nature of the hanging mercury drop electrode.) The experimental points define a reasonable straight line with a slope of 2.2, a slightly higher slope than the theoretical value of 2.0. These results are similar to those found by Bunton, Ingold, and Mhala[13g] for the perchloric acid catalyzed rearrangement of hydrazobenzene in 60 vol. % dioxane–water. These workers observed a slope of 2.6 for acidities in the range of 0.05 to 1.0 M. The deviation of these slopes from the theoretical value has been discussed at great length by Banthorpe and co-workers[13h] and has been shown to be caused primarily by a positive kinetic salt effect. The better agreement with theory observed in the present case is probably because of a smaller salt effect in the more polar ethanol–water solvent.

With the exception of the work in dioxane–water, classical kinetic measurements on the hydrazobenzene

system have been limited to acid concentrations less than 0.1 M. As a result, a direct comparison cannot be made between the electrochemical and the classical rate measurements. On the other hand, some checks are possible since the electrochemical measurements can be extrapolated to much lower acidities by using the linear relationship between log $\bar{k}$ and H_0. For instance, a rate constant of 1.4×10^{-3} sec.$^{-1}$ was estimated from the data of Croce and Gettler[13e] for the rearrangement reaction in 50 wt. % ethanol–water at 25° catalyzed by 0.093 M acid ($H_0 = 2.16$). Extrapolation of the data of Figure 6 to this acidity yields a rate constant of 2.4×10^{-3} sec.$^{-1}$. A second extrapolation following the dashed line (points of maximum error limit) gives a value of 1.0×10^{-3} sec.$^{-1}$. The rate constant determined by classical methods falls in between the two extrapolated values indicating general agreement between the step-functional controlled potential measurements and the classical results.

Conclusion

The rate constants listed in Table I indicate the range of applicability of the step-functional controlled potential method to the azobenzene system. Adsorption effects involving both azobenzene and hydrazobenzene limited measurements to acidities in which the half-life was greater than about 5 msec. Nevertheless, this represents a significant extension of the kinetic data for this system to a range in which the more classical methods cannot be used. The method was not extended to acidities where the half-life was more than about 1.5 sec., because the assumption of electrode planarity breaks down.

The general applicability of the method is much greater than illustrated here. Under favorable conditions, reactions with half-lives of the order of 20 μsec. could probably be measured although more elaborate potentiostats than those used here would be required. In addition, a number of problems concerning cell design, IR drop, and the effect of the electrical double layer on the kinetic process would have to be considered. Unfortunately, in most cases, measurement of these very fast rates is already prohibited by properties of the system such as adsorption.

At the other limit, slow reactions can be investigated as long as diffusion is the only means of mass transfer. Thus, a half-life of the order of 30 sec. probably represents the slowest reaction which could be studied conveniently, provided, of course, that a plane electrode is used, or that deviations from planarity could be accounted for.

Because of this wide range of applicability, it is expected that the step-functional controlled potential method will be extremely useful in the investigation of other systems in which a chemical reaction follows the initial charge-transfer step.

Acknowledgment. This work was supported by funds received from the National Science Foundation under Grant No. G 15741.

Relative Determination of Soret Coefficients of Electrolytes

by Toshio Ikeda and Hiroyuki Kimura

Department of Chemistry, Shizuoka University, Shizuoka, Japan (*Received March 30, 1964*)

From the thermoelectric power of an electrolytic thermocouple of a convenient type, the Soret coefficient was determined for six uni-univalent electrolytes at 25° and 0.01 *M* upon taking potassium chloride as a reference material. Our results were in fair agreement with the best values reported so far.

During the past ten years, the Soret coefficients of electrolytes have become measurable by a direct method[1-8] with considerable accuracy. Recently, Turner and his co-workers[5] have succeeded in the direct determination of the Soret coefficients for a number of electrolytes by the conductometric method with reasonable accuracy, and they also succeeded in compiling the conventional ionic heats of transfer for a number of ion species in good harmony with the Soret coefficients which they had determined. On the other hand, one of the present writers[9a] and Haase and his co-workers[9b] have indicated recently some indirect ways of determining the Soret coefficients from the initial thermoelectric powers of thermocells. Now, an alternative method may be possible along similar lines when an electrolytic thermocouple of a convenient type is used. An experiment by this method will be reported in the present paper. The principle[10] of this method was suggested by the Eastman school[11] and was used by Tyrrell and his co-workers.[12] However, they used merely the data on separate thermocells, without reference to the combined thermocells or such an "electrolytic thermocouple" as will be reported below. Our method of using the electrolytic thermocouple might be more advantageous in realizing the principle under identical experimental conditions than one using separate thermocells.

General

Let us consider an electrolytic thermocouple of the system

$$\underset{T}{\text{Hg–HgCl, KCl}(m)\text{, HgCl–Hg–HgCl, MCl}(m)\text{, HgCl–Hg}}\quad \underset{T+\Delta T}{\qquad\qquad}\quad \underset{T}{\qquad} \tag{1}$$

where MCl represents a univalent metal chloride having the same concentration as that of the potassium chloride, which was chosen as a reference substance in the present work.[13a] The initial thermoelectric powers, ${\epsilon_0}^{KCl}$ and ${\epsilon_0}^{MCl}$, for two thermocells consisting of the left and right halves of the cell system (1) can be expressed respectively as[13b]

$$F{\epsilon_0}^{KCl} = 2RTt_{K^+}{}^{KCl}B^{KCl}\sigma^{KCl} + \bar{S}_{Cl^-}{}^{KCl} + S_{Hg} - S_{HgCl} - \bar{S}_{el}$$

and

(1) K. F. Alexander, *Z. physik. Chem.*, **203**, 213 (1954).

(2) J. N. Agar and W. G. Breck, *Trans. Faraday Soc.*, **53**, 167, 179 (1957).

(3) J. N. Agar and J. C. R. Turner, *J. Phys. Chem.*, **64**, 1000 (1960).

(4) J. N. Agar and J. C. R. Turner, *Proc. Roy. Soc.* (London), **A255**, 307 (1960).

(5) P. N. Snowdon and J. C. R. Turner, *Trans. Faraday Soc.*, **56**, 1409 (1960).

(6) P. N. Snowdon and J. C. R. Turner, *ibid.*, **56**, 1 (1960).

(7) A. D. Payton and J. C. R. Turner, *ibid.*, **58**, 55 (1962).

(8) K. Sasaki, *Nippon Kagaku Zasshi*, **83**, 368 (1962).

(9) (a) T. Ikeda, *J. Chem. Phys.*, **30**, 345 (1959); *Rep. Lib. Arts Sci. Fac. Shizuoka Univ., Nat. Sci.*, **2**, 153 (1959); (b) R. Haase, K. Hoch, and H. Schönert, *Z. physik. Chem.* (Frankfurt), **27**, 421 (1961).

(10) The principle was outlined by J. N. Agar, *Rev. Pure Appl. Chem.*, **8**, 1 (1958).

(11) Especially, M. B. Young, Ph.D. Thesis, University of California, 1935.

(12) H. J. V. Tyrrell and G. L. Hollis, *Trans. Faraday Soc.*, **48**, 893 (1952); H. J. V. Tyrrell and R. Colledge, *ibid.*, **50**, 1056 (1954); H. J. V. Tyrrell, *ibid.*, **51** 383 (1955).

(13) (a) It might be better to use lithium chloride in place of potassium chloride, since the error introduced in the Soret coefficient values by the convection that occurs anyhow in the Soret cell in measuring the Soret coefficients would possibly be the smallest for lithium chloride which exhibits the slightest Soret effect; (b) *e.g.*, H. J. V. Tyrrell, "Diffusion and Heat Flow in Liquids," Butterworth and Co., Ltd., London, 1961.

$$F\epsilon_0^{MCl} = 2RTt_{M^+}^{MCl}B^{MCl}\sigma^{MCl} + \bar{S}_{Cl^-}^{MCl} + S_{Hg} - S_{HgCl} - \bar{S}_{el}$$

where F is the Faraday constant; R is the gas constant; T is the absolute temperature; t's are the ionic transport numbers for ions indicated by the subscripts regarding the solution phases indicated by the superscripts; $\bar{S}_{Cl^-}$'s are the transported entropies of the chloride ion in the solution phases indicated by the superscripts; S_{Hg} and S_{HgCl} are the molar entropies of mercury in the liquid phase and of mercurous chloride in the solid phase, respectively; $\bar{S}_{el}$ is the transported entropy of electrons in the metallic phase; and σ's represent the Soret coefficients and B's are defined by

$$B^{KCl} = 1 + \mathrm{d}\ln\gamma_{\pm}^{KCl}/\mathrm{d}\ln m$$

and

$$B^{MCl} = 1 + \mathrm{d}\ln\gamma_{\pm}^{MCl}/\mathrm{d}\ln m$$

$\gamma_{\pm}$ values are mean activity coefficients on the molality scale. Then, the resulting initial thermoelectric power, $(\mathrm{d}E/\mathrm{d}T)_0$, for the combined thermocell system (1) can be formulated as

$$F(\mathrm{d}E/\mathrm{d}T)_0 = 2RTt_{K^+}^{KCl}B^{KCl}\sigma^{KCl} - 2RTt_{M^+}^{MCl}B^{MCl}\sigma^{MCl} + \bar{S}_{Cl^-}^{KCl} - \bar{S}_{Cl^-}^{MCl} \quad (2)$$

If the Soret coefficient of the reference electrolyte, here the potassium chloride, is known accurately, we can calculate the Soret coefficient for all chlorides that are able to form cells of type 1, provided that the transported entropies of the chloride ions in two electrolytes, KCl and MCl, are known. If the solutions are so dilute that the ideal condition is satisfied to a sufficient extent for allowing to put $\bar{S}_{Cl^-}^{KCl} = \bar{S}_{Cl^-}^{MCl}$ in (2), we can calculate approximate values of the Soret coefficient by the equation

$$\sigma^{MCl} = \frac{t_{K^+}^{KCl}B^{KCl}}{t_{M^+}^{MCl}B^{MCl}}\sigma^{KCl} - \frac{F(\mathrm{d}E/\mathrm{d}T)_0}{2RTt_{M^+}^{MCl}B^{MCl}} \quad (3)$$

The arguments given above are, of course, applicable not only to chloride series but also to all the other electrolytes that are able to form electrolytic thermocouples with electrodes of a convenient type.

Experimental

All solutions were prepared by using G.R. chemicals and water distilled from a glass still in the presence of a trace of potassium permanganate acidified with sulfuric acid. The concentration was checked and adjusted by titration to 0.01 M. In the present work, its deviation from the designed value of 0.01 M was within 0.6%. Mercury used for electrodes was purified by the usual chemical refinements followed by distillation *in vacuo*.

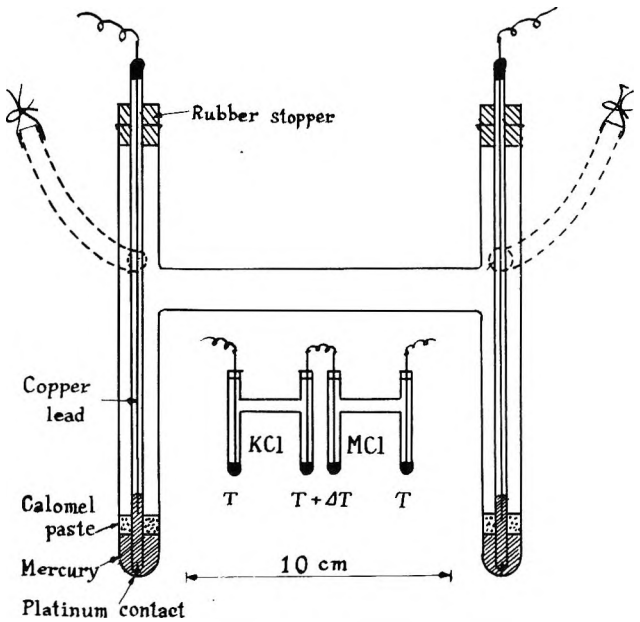

Figure 1. Cell system; the parts drawn with dotted lines represent the side tubes on the front of the paper.

An H-shaped cell, shown in Figure 1, was convenient for the present purpose. The copper lead for potentiometry was sheathed together with a little mercury in a glass tube, which was provided with a piece of fused platinum gauze at the bottom for the electric contact with electrode mercury. Of course, the platinum contact was set below the level of the electrode mercury to keep it dry. G.R. calomel, which was washed several times with the same electrolyte as that used for the measurements, was shaken together with a little pure mercury to yield a gray paste. This paste was carefully and slowly let flow into the cell from a side tube of the H-cell together with the electrolyte to form a layer of paste about 5 or 10 mm. thick on the surface of the electrode mercury. Then the solution was filled up to a level slightly above the horizontal bridge of the H-cell. The contact between paste and mercury preferably is to be clear-cut horizontal in appearance. Electrodes having such an appearance that the calomel paste penetrated between the mercury and cell wall often went unsteady with regard to the electrode potential. Such an electrode is unsuitable for our purpose of measuring the small change of e.m.f. and was therefore abandoned.

Two calomel thermocells that were filled with aqueous solutions of KCl and MCl of the same concentration, here 0.01 M, were doubled together by the legs of these two H-cells side by side and were placed in water thermostated in two respective dewar vessels. The

terminals of these two thermocells were joined electrically with each other on the warmer side, and the remaining terminals on the colder side were utilized for the measurement of e.m.f. The temperature was fixed constant at 17° on one side of the two dewar vessels, while it was changed on the other side from 17° up to about 32° so as to yield the mean 25°. Under moderate agitation with air bubbling, the system practically attained a thermal equilibrium in about 10 min. The temperature difference between the two dewar vessels was read with calibrated mercury thermometers with 0.1° divisions at the moment at which the e.m.f. of the cell system (1) was measured. The e.m.f. was measured by use of a precision potentiometer (Type P-7, Yokogawa Elec. Works, Ltd., for low voltage use, with an index of precision down to 0.1 μv.) by the aid of sensitive Yokogawa galvanometer as a zero indicator. Here, the sign convention for e.m.f. of system 1 was taken as positive if the sign of the electrode on the colder side of MCl was found to be positive against the sign of the electrode on the colder side of KCl.

In the practical measurements, every care was taken to get accurate and reproducible data. Even the best prepared thermocells must be allowed to stand for about 2 or 3 days after the preparation in order to bring them into stationary condition. The electric source, a battery, must be connected to the potentiometer for at least 3 hr. prior to performing the measurements so that the normalized state of the potentiometer may not drift during the potentiometry. In the present work, the drift was limited to within 0.1 μv./hr. Since the electromotive force of system 1 is substantially so small, further care must be taken not to introduce stray e.m.f. values such as those coming from the drift of the electrode potentials due to mechanical shocks imposed accidentally upon the calomel electrodes and those due to some extra thermoelectric effects of any sort which happen to occur in the system including the potentiometric device.

Each measurement was repeated by using three or four well-conditioned cell systems. Some of the typical results are represented in Figure 2. The plots of e.m.f., E, against the applied temperature difference, ΔT, fell on a straight line with a definite slope characteristic of the electrolyte, MCl, that was coupled with KCl. The cell system yielding nonlinear data was abandoned and the cell was renewed. The value of $(dE/dT)_0$ was determined on each experiment by the method of least squares, and the mean taken from more than ten such values is listed in Table I. Observed values were reproducible in most cases within a deviation of 1 to 3% from the mean, except for those in the

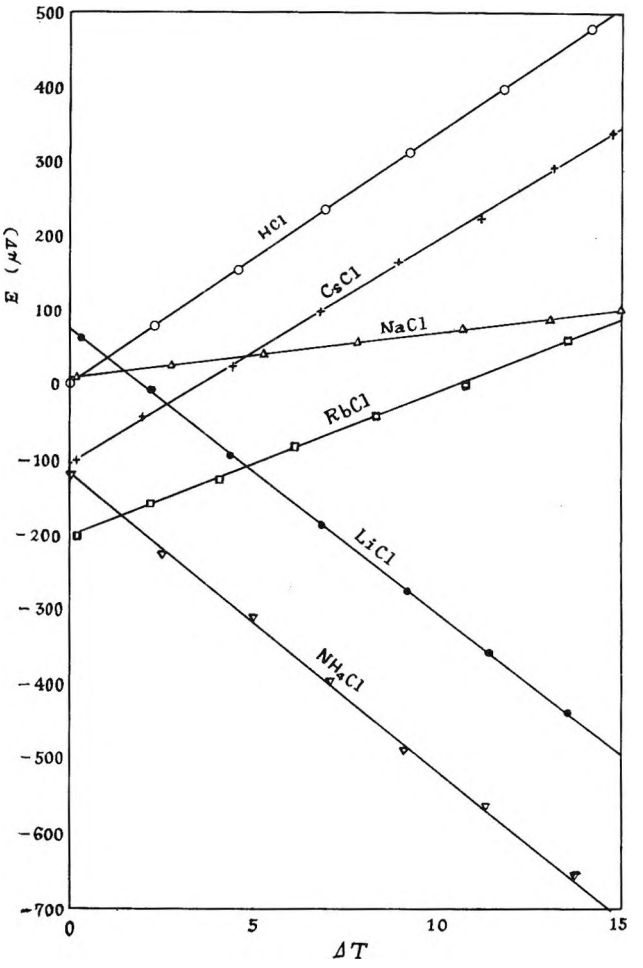

Figure 2. E.m.f. of electrolytic thermocouple of the system (1) in the case of concentration = 0.01 M, and the temperature difference ΔT applied upon it. E.m.f. scale for HCl should be read as ten times the indication.

Table I: Soret Coefficients of Some Electrolytes in Water at 25° and 0.01 M

Chloride	t_+,[a]	B[b]	$(dE/dT)_0$, μv./deg.	$\sigma \times 10^3$ deg.$^{-1}$ This work	$\sigma \times 10^3$ deg.$^{-1}$ Ref. 5[c]
HCl	0.8251	0.958	336.0	9.12	9.01
LiCl	0.3289	0.969	−37.58	−0.19	−0.01
NaCl	0.3918	0.958	6.19	2.10	2.02
KCl	0.4902	0.956	...	(1.43)	1.43
RbCl	0.497	0.945	19.28	2.22	2.33
CsCl	0.504	0.942	29.99	2.64	2.44
NH_4Cl	0.4907	0.967	−38.97	−0.18	...

[a] B. E. Conway, "Electrochemical Data," Elsevier Publishing Co., Amsterdam, The Netherlands, 1952. [b] Graphical determination, "Physikalischen Chemische Tabellen," Landolt-Börnstein, Erg. Bd. II, 1931, and III, 1936. [c] Values were corrected to 25°.

case of rubidium chloride, where the deviation was 5%. The sign of $(dE/dT)_0$, as based on the present sign convention, was found to be positive for HCl, NaCl, RbCl, and CsCl, while it was negative for LiCl and NH_4Cl.

Calculation and Discussion

The reference value adopted in the present work was $\sigma^{KCl} = -1.43 \times 10^{-3}$ deg.$^{-1}$ at 25° and 0.01 M, which was achieved by adjusting the Snowdon–Turner value[5] of -1.41×10^{-3} deg.$^{-1}$ for 0.01 M at 24.8° to the 25° value at a rate[4] of $d\sigma/dT = -0.1 \times 10^{-3}$ deg.$^{-2}$. Then, from our data on $(dE/dT)_0$ and by the aid of (3), we could get the approximate values of the Soret coefficients, σ^{MCl}, for 0.01 M MCl at 25°. The results are compared with Snowdon and Turner's values[5] in Table I. Fairly good agreement can be seen between Snowdon and Turner's values and ours.

The electrolytic thermocouple of type 1 can be used as a convenient means, though indirectly, for determining the relative values of the Soret coefficients. In spite of its simplicity in experimental sets, the present method could yield values agreeing well with those given by the other most sensitive method. In the present calculation, however, we have taken an approximation such as $\bar{S}_{Cl^-}{}^{KCl} = \bar{S}_{Cl^-}{}^{MCl}$. According to the molecular statistical theory of Helfand and Kirkwood,[14] the transported entropy of a single ion cannot be independent of the counterion. In the limiting law form, one may write

$$\bar{S}_{Cl^-}{}^{KCl} - \bar{S}_{Cl^-}{}^{MCl} = \kappa(A_{Cl^-}{}^{KCl} - A_{Cl^-}{}^{MCl})$$

where κ is the Debye–Hückel inverse length and A_{Cl^-}'s are constants characteristic of the concerning chloride ion, depending also on its counterion. According to their theory, the quantity A_{Cl^-} vanishes when two conjugate ions in a solution are equal in the valence type and size; otherwise, they may attain a considerable value. Consequently, the accuracy of our method is, in principle, limited by such a specificity of $\bar{S}_{Cl^-}$. On the other hand, the transported entropy of the chloride ion, $\bar{S}_{Cl^-}$, was calculated by Temkin and Khoroshin,[15] Haase and co-workers,[9b] and one of the present writers.[9a] Even in the best case of Haase, *et al.*, the calculated values involve some uncertainties, so that a slight difference of $\bar{S}_{Cl^-}$ values found between two chlorides, which they studied, is difficult to attribute to the difference due to such a specific dependence on the counterion as was demanded by the Helfand–Kirkwood theory.[14] At any rate, this contribution seems not large enough to have a significant effect in the dilute region we are studying now, but in the practical application of the present method, one must determine whether the approximation of $\bar{S}_{Cl^-}{}^{KCl} = \bar{S}_{Cl^-}{}^{MCl}$ can be allowed within the accuracy of the experimental system used.

(14) E. Helfand and J. G. Kirkwood, *J. Chem. Phys.*, **32**, 857 (1960)

(15) A. V. Khoroshin and M. I. Temkin, *Zh. Fiz. Khim.*, **26**, 773 (1952).

The Hydrogen-Deuterium Exchange Reaction. I. 6^3P_1 Mercury Photosensitized

by H. Niki,[1a] Yves Rousseau,[1b] and Gilbert J. Mains

Department of Chemistry, Carnegie Institute of Technology, Pittsburgh, Pennsylvania 15213
(Received April 13, 1964)

The kinetics of the $^3P_1$ Hg-photosensitized H_2–D_2 exchange is described by the differential rate law, $d(HD)/dt = A - k(HD)$. The photostationary constant, $Q_\infty = (HD)^2/(H_2)\cdot(D_2)$, at 25° is a function of initial H_2–D_2 ratio, the total pressure in the range 0.2–30 cm., and surface-to-volume ratio, and is larger than the equilibrium constant, K. Initial rate studies of the forward reaction at 25° as a function of H_2–D_2 pressure indicate the exchange reaction to occur *via* both a heterogeneous and a homogeneous mechanism. Initial rate data for HD formation are shown to be consistent with a heterogeneous combination of atomic hydrogens in competition with a reversible homogeneous chain mechanism. At 25° and 1 cm. of H_2–D_2 pressure, approximately 80% of the HD is formed on the walls; at 25° and 30 cm. of H_2–D_2 pressure, the wall reaction accounts for no more than 15% of the HD. Q_∞ is shown to approach K as both the temperature and pressure are raised. The mechanistic implications of these observations are discussed.

Introduction

The exchange reaction between hydrogen and deuterium, *i.e.*, $H_2 + D_2 \rightarrow 2HD$, is one of the simplest kinds of chemical reactions and, therefore, is frequently chosen as a test of the theories of chemical kinetics.[2] The homogeneous, thermally induced reaction occurs at a measurable rate only at temperatures in excess of 450°, and, in spite of the frequency and care of the investigations,[3–5] is still subject to some controversy.[2,6] The heterogeneous, thermally induced reaction occurs at lower temperatures in the presence of various catalysts (such as Ni, Cu, or Au) and these studies have been critically reviewed elsewhere.[7] The exchange reaction may also be induced by ionizing radiation[8–16] which, according to recent studies,[14–16] initiates an ionic chain reaction of 700 to 1100 cycles.

Because of the fundamental import to the field of radiation chemistry of the ionic chain reactions postulated by Schaeffer and Thompson,[14–16] this laboratory initiated a study of the H_2–D_2 exchange induced by ionizing radiation which would extend to temperatures as high as 250°. During the course of this investigation[17] it was found desirable to obtain data for comparable exchange studies which occurred *via* an atomic mechanism, such as might be expected in the $^3P_1$ mercury-photosensitized reaction. A careful search of the literature revealed that the mercury-photosensitized exchange of H_2 and D_2 has not been reported although the analogous ortho-para hydrogen conversion was studied to 20% conversion by this technique.[18]

(1) (a) Postdoctoral Fellow 1962–1963; (b) Postdoctoral Fellow 1963–1964.

(2) I. Shavitt, *J. Chem. Phys.*, **31**, 1359 (1959).

(3) A. Farkas and L. Farkas, *Proc. Roy. Soc.* (London), **A152**, 152 (1935).

(4) M. Van Meersche, *Bull. Soc. Chim. Belges*, **60**, 99 (1951).

(5) G. Boato, G. Careri, A. Cimino, E. Molinari, and G. G. Volpi, *J. Chem. Phys.*, **24**, 783 (1956).

(6) A. Cimino, E. Molinari, and G. G. Volpi, *ibid.*, **33**, 616 (1960).

(7) P. G. Ashmore, "Catalysis and Inhibition of Chemical Reactions," Butterworth and Co., Ltd., London, 1963, p. 196.

(8) P. C. Capron, *Ann. Soc. Sci. Bruxelles*, **55**, 222 (1935).

(9) J. Hirschfelder, H. Eyring, and B. Topley, *J. Chem. Phys.*, **4**, 170 (1936).

(10) W. Mund, T. DeHorne, and M. Van Meersche, *Bull. Soc. Chim. Belges*, **56**, 386 (1947).

(11) W. Mund and M. Van Meersche, *ibid.*, **57**, 88 (1948).

(12) L. M. Dorfman and F. J. Shipko, *J. Phys. Chem.*, **59**, 1110 (1955).

(13) L. M. Dorfman and H. C. Mattraw, *ibid.*, **57**, 723 (1953).

(14) S. O. Thompson and O. A. Schaeffer, *J. Chem. Phys.*, **23**, 759 (1955).

(15) S. O. Thompson and O. A. Schaeffer, *J. Am. Chem. Soc.*, **80**, 553 (1958).

(16) S. O. Thompson and O. A. Schaeffer, *Radiation Res.*, **10**, 671 (1959).

(17) H. Niki and G. J. Mains, part II of this study, to be published.

The only other related study was by Melville and Robb,[19] who attempted to use the ortho–para conversion reaction as a measure of the hydrogen atom concentration in the mercury-photosensitized dissociation of hydrogen. Since neither of these studies dealt directly with the H_2–D_2 system and were too fragmentary for comparison with the radiolysis studies,[17] this laboratory also studied the $^3P_1$ Hg-photosensitized exchange reaction of H_2 and D_2. The results of this investigation are reported here.

Experimental

Materials. Matheson Co. hydrogen and Stuart Co. deuterium were purified by passing them separately through a palladium thimble at about 500°. Mixtures of hydrogen and deuterium contained a small amount of HD as the only impurity detected by mass spectral analysis. HD, obtained from Merck Ltd., Canada, was found by mass spectrometry to contain 0.43% H_2 and 0.22% D_2 and was used without further purification. Airco reagent grade xenon, helium, and argon were used without further purification. They were mass spectrometrically pure, except for traces of other inert gases. Bethlehem Apparatus Co., triply distilled, instrument grade mercury was used in the mercury-sensitized experiments. International Nickel Co. nickel wool was used for the nickel-catalyzed exchange reaction of the mixture of hydrogen and deuterium.

Apparatus and Procedure. The light source was a Hanovia SC-2537 low-pressure mercury lamp coiled into a helix form. Three types of reaction vessels were used. All irradiations performed inside the coil of the lamp were carried out in a 100-cc. Vycor tube fitted with a three-way stopcock. The lamp intensity in this reaction vessel at 2537 Å. was estimated to be $1.08 \pm 0.05 \times 10^{16}$ photons cc.$^{-1}$ min.$^{-1}$ by propane actinometry as described by Bywater and Steacie.[20] For high-temperature experiments, the cylindrical vessel was inserted in an oven which was constructed by wrapping heating coils between two pieces of Vycor tubing of 3.5- and 5.2-cm. diameter. Steady temperature was controlled to within ±2° by a Variac and was monitored by an alumel–chromel thermocouple. An end-on-window type Vycor reaction vessel was used in the initial rate studies and was 15 cm. long and 3.3 cm. in diameter. For the latter experiments, a reflector mirror was placed inside the coil of the lamp to obtain the parallel light beam, and the reaction vessel was inserted into a black, paper cylinder to prevent scattered light from entering the system. A larger end-on-window type quartz reaction vessel (7 cm. in diameter and 12 cm. long) was used for comparing the rates at which H_2, HD, and D_2 quench Hg $6(^3P_1)$ atoms. The vessel was positioned as described for the initial rate studies except for the insertion of a neutral density filter before the window to reduce the intensity. The light flux, measured by butane–nitrous oxide actinometry,[21] was 6.8×10^{14} photons cm.$^{-2}$ min.$^{-1}$. Twenty μliters of mercury was placed in the reaction vessels for the photosensitization. The reaction vessels were preconditioned by irradiating a H_2–D_2 mixture at 30 cm. for about 2 hr.

All analyses of the isotopic hydrogens were performed using a Consolidated Electrodynamics Corp. Model 21-103C mass spectrometer. Standard mass spectra were based on the data by Friedel and Sharkey.[22] The validity of the mass spectral analyses in these experiments was confirmed by a determination of the equilibrium constant, 3.27 ± 0.02, for the nickel-catalyzed exchange reaction at 25°.

Results

The Rate Law. The extent of mercury-photosensitized exchange of a 1:1 mixture of H_2 and D_2 may be conveniently displayed graphically by plotting Q, defined as $(HD)^2/(H_2)(D_2)$, as a function of time. Typical curves (chosen from data for almost 100 experiments) are displayed in Figure 1. Sigmoidal curves of this type arise from a differential rate of the form $d(HD)/dt = A - k(HD)$, where A and k are constants. The integrated form of this rate law, $\ln [(HD)_\infty - (HD)]/(HD)_\infty = -kt$, where $(HD)_\infty$ is the final time-independent concentration of HD, *i.e.*, A/k, has been shown to describe accurately the progress of the thermally-induced, homogeneous exchange,[3] the thermally-induced, catalyzed exchange,[7] the radiation-induced exchange,[12,13,16] and the mercury-sensitized, radiation-induced exchange.[17] It is not altogether surprising that the kinetics of the mercury-photosensitized exchange reported here should also be accurately described by a rate law of identical form. The differential form of the rate law requires only a constant *initial* rate of HD formation, A, and a back-reaction which is first order in (HD). These mechanistic requirements are easily fulfilled so long as the concentrations of the kinetic intermediates are independent of the extent of conversion, regardless of

(18) L. Farkas and H. Sachsse, *Z. physik. Chem.*, **B27–28**, 111 (1934–1935).

(19) H. W. Melville and J. C. Robb, *Proc. Roy. Soc.* (London), **A196**, 445 (1949).

(20) S. Bywater and E. W. R. Steacie, *J. Chem. Phys.*, **19**, 319 (1951).

(21) Y. Rousseau and H. E. Gunning, *Can. J. Chem.*, **41**, 465 (1963).

(22) R. A. Friedel and A. G. Sharkey, Jr., *J. Chem. Phys.*, **17**, 584 (1949).

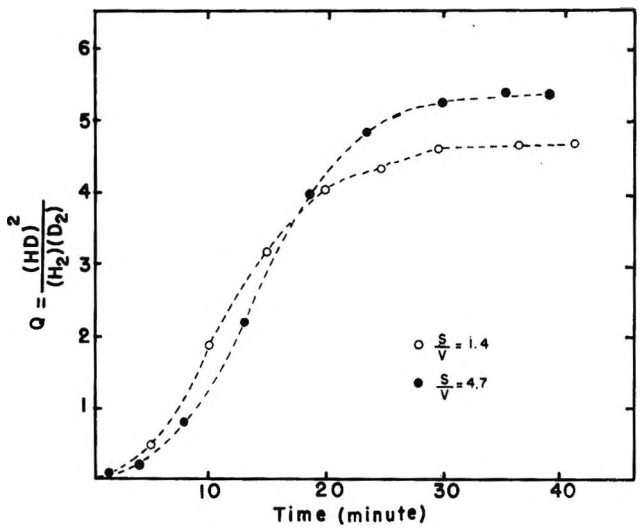

Figure 1. Effect of the surface-to-volume ratio on the isotopic quotient in the $^3P_1$ mercury-photosensitized reaction of an equimolar mixture of H_2 and D_2 at 30 cm. and at 25°.

whether these intermediates are hydrogen atoms, either in the gas phase or on a surface, or whether they are ionic. Under these circumstances the gross form of the rate law is of little help in choosing a mechanism and a detailed study of the effects of many variables is necessary.

Effect of Surface–Volume Ratio. The effect of varying the surface-to-volume ratio at 25° is depicted in Figure 1 where it may be observed that increasing the ratio from 1.4 to 4.7 cm.$^{-1}$ by the addition of sections of quartz tubing to the reaction vessel resulted in a decrease in the initial rate of the reaction and an increase in the photostationary isotopic quotient, Q_∞, from 4.55 ± 0.05 to 5.40 ± 0.05. Therefore, the exchange reaction must occur partially *via* a heterogeneous mechanism at 25° at a pressure of 30 cm.

Effect of Added He and Xe. Several experiments were conducted in order to ascertain whether the presence of an unreacting gas would alter either the rate of the reaction or the photostationary state, Q_∞, at 25°. In one experiment 13.0% Xe was added to 30 cm. of a 1:1 H_2–D_2 mixture. In another experiment, 36.2% He was added. The results of these experiments yielded data which fell precisely on the line drawn in Figure 1 for S/V = 1.4 cm.$^{-1}$, indicating these gases had no observable effect. Schaeffer and Thompson[16] also failed to find an inert gas effect in their experiments involving the mercury-photosensitized exchange. It is worthwhile mentioning that He would be expected to be an ideal inert gas to thermalize any translationally "hot" hydrogen atoms, and its failure to alter the rate of the reaction is especially significant.

Effect of Pressure. Reduction of the initial pressure of the 1:1 H_2–D_2 mixture from 30 to 15 cm. at 25° in the reaction vessel packed with quartz tubing (S/V = 4.7 cm.$^{-1}$) resulted in a shift of the photostationary state, Q_∞, from 5.40 ± 0.05 to 6.10 ± 0.05. The forms of the Q *vs.* t curves for these experiments were similar to those given in Figure 1 and, therefore, are not of particular interest. However, the observation that the photostationary state, Q_∞, is pressure dependent as well as surface dependent was of considerable interest, and it was decided to investigate the effect of pressure and composition on Q_∞ at 25°. The results of this study (S/V = 1.4 cm.$^{-1}$) are displayed in Figure 2. Each point on the curves represents a separate experiment. It should also be noted that each of the curves was extended into the low-pressure region, but, for clarity, these points are not included in Figure 2. The remarkable increase in Q_∞ for the 1:1 mixture from 4.55 ± 0.05 at 30 cm. to a maximum 6.75 ± 0.05 at about 2 cm., followed by a sharp decrease at lower pressures, is especially noteworthy. For comparison, the equilibrium composition, K = 3.25, is also depicted in Figure 2, where it will be observed that Q_∞ is greater than K for all the experiments below 30 cm. at 25°.

Effect of Temperatures. While extensive kinetic studies have not been carried out at elevated temperatures, a few experiments were performed to determine the effect of temperature on the photostationary state, Q_∞. The data, displayed in a graph of Q_∞/K *vs.* T

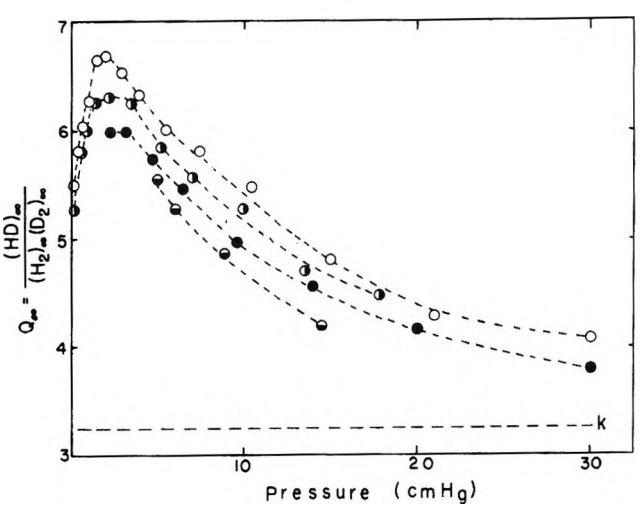

Figure 2. Effect of pressure on the photostationary state constant Q_∞ in the $^3P_1$ mercury-photosensitized exchange of H_2 and D_2 mixtures at 25°. $(H_2)/(D_2)$ ratio values: ○, 1.0; ◑, 1.6; ●, 6.9; ◒, 8.9. K is the thermodynamic equilibrium.

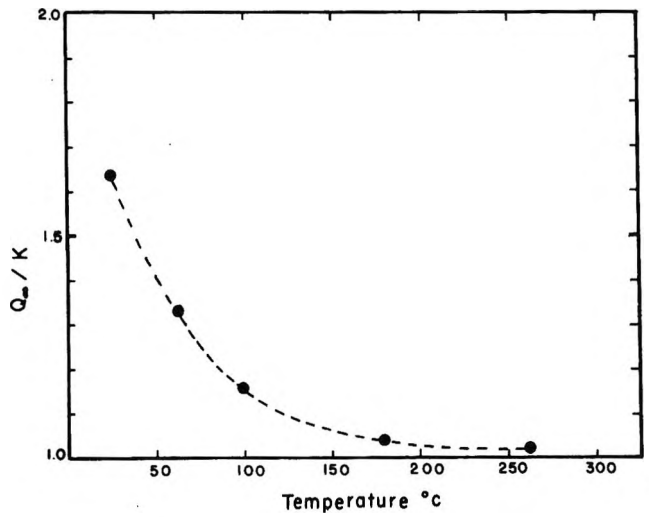

Figure 3. Effect of temperature on Q/K in the equimolar mixture of H_2 and D_2 at 5 cm.

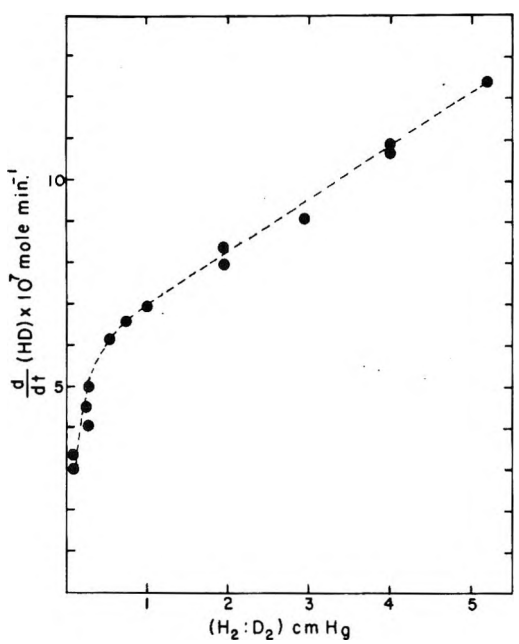

Figure 4. Effect of pressure on the rate of HD formation in the $^3P_1$ mercury-photosensitized exchange of an equimolar mixture of H_2 and D_2 at 25°.

in Figure 3, indicate that the photostationary state and the equilibrium state become virtually indistinguishable at temperatures above 250°. It should be noted that the thermally-induced exchange is negligible at 250° and, therefore, is not responsible for the approach of Q_∞ to K in this temperature region.

Initial Rate Studies. In order of ascertain the pressure and surface dependence of the forward and backward reactions, it was necessary to study them separately by the technique of initial rates. For these studies the end-on reaction vessels were used to ensure reproducibility of the lamp–reaction vessel geometry. The forward reaction was studied by filling the reaction vessel with the desired pressure of the 1:1 H_2–D_2 mixture and exposing the system to the actinic radiation, for a sufficient time to achieve a maximum of 1% conversion to HD. The effect of initial H_2–D_2 pressure on the rate of HD formation is depicted in Figure 4. The marked decrease in the initial rate of HD formation below 1 cm. is especially significant. The linear region of the curve, between 1 and 5 cm. in Figure 4, has been experimentally confirmed to 30 cm., but the data above 5 cm. are not included in order to depict clearly the curve below 1 cm.

The effect of surface on the forward reaction was studied by inserting a quartz disk into one of the end-on reaction vessels. This disk, which had twelve 0.16-cm. diameter holes bored in it to permit free diffusion of gas, could be moved forward until it touched the window through which the actinic light entered the vessel (x = 0 cm.) or back until it touched the rear window (x = 9 cm.) The disk was supported by quartz rods so that it remained approximately parallel to the front window at all locations. The effect of window location on the initial rate of HD formation is given in Figure 5 for initial H_2–D_2 mixture pressures of 6 cm., 1 cm., and 1 cm. with 5 cm. of argon. It should be noted in the 6-cm. experiments that the disk location did not alter the initial rate until it was within 2 cm. of the front window where it decreased the rate considerably. At 1 cm. of H_2–D_2 pressure, the disk decreased

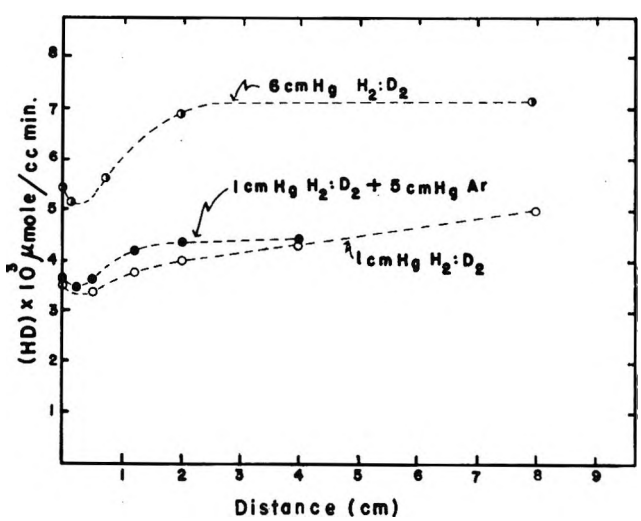

Figure 5. Effect of the location of a diffusion-free quartz disk in the $^3P_1$ mercury-photosensitized exchange of an equimolar mixture of H_2 and D_2 at 25°.

the initial rate over the entire range of locations. It is especially significant that the addition of 5 cm. of argon alters the shape of the low-pressure curve to approach that of the curve at 6 cm. These observations indicate that the exchange reaction is occurring in a reaction zone near the front window, the depth of which decreases as the total gas pressure in the system is increased. Furthermore, these experiments confirm the observations (*vide supra* and Figure 1) made using the cylindrical vessels located in the center of the lamp to the effect that an increase in surface to volume *decreased* the initial rate of HD formation.

The initial rate of the mercury-photosensitized back reaction, *i.e.*, $2HD \rightarrow H_2 + D_2$, was also studied at 25° as a function of HD pressure. The results of this study are displayed in Figure 6. It should be noted that the data in Figure 6 are reported in terms of the rate of D_2 production because less uncertainty is attached to D_2 analysis in excess HD than to H_2 analysis. However, the rate of H_2 production was found to equal the rate of D_2 production within experimental error. A comparison of Figures 4 and 6 reveals that, while the initial rate of the forward reaction diminishes very rapidly below 1 cm. of H_2–D_2 mixture, the back reaction showed signs of becoming constant in this low-pressure region. A similar "leveling-off" trend is observed in a graph (not reproduced here) of the initial rate of H_2 production as a function of HD pressure.

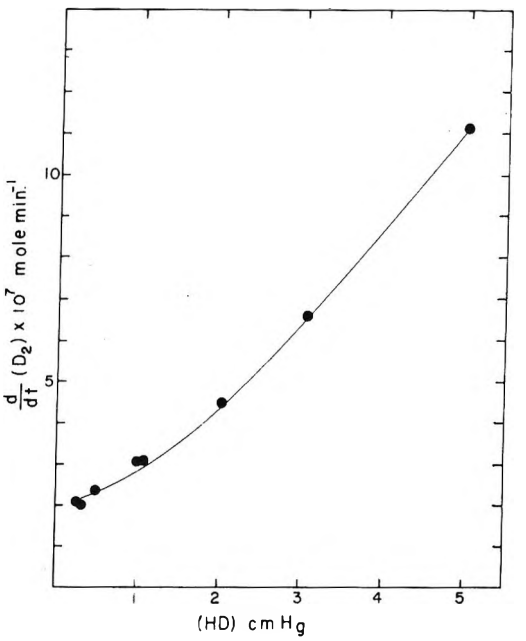

Figure 6. Effect of pressure on the rate of D_2 formation in the $^3P_1$ mercury-photosensitized decomposition of HD at 25°.

Discussion

In any experiment involving mercury photosensitization it is necessary to consider first the primary photophysical act, *viz.*

$$Hg + h\nu \longrightarrow Hg^* (^3P_1) \qquad (1)$$

The very large extinction coefficient[23] of Hg vapor at 25°, *i.e.*, 6 cm.$^{-1}$, results in a very inhomogeneous distribution of $^3P_1$ Hg atoms which, in the absence of a large concentration of quenching molecules, is not given by an exponential decrease from the incident window but is complicated by radiation diffusion.[24] In the presence of a large concentration of quenching molecules, say H_2, the competition between radiation and quenching, *viz.*

$$Hg^* (^3P_1) \longrightarrow Hg (^1S_0) + h\nu \qquad (2)$$

$$Hg^* (^3P_1) + H_2 \longrightarrow Hg + 2H \qquad (3)$$

greatly favors the latter, reaction 3, and over 99% of the incident radiation is absorbed within 1 cm. of the incident window. The hydrogen pressure at which 95% of the Hg^* ($^3P_1$) atoms are quenched may be readily estimated to be about 0.8 cm. from the Stern–Volmer equation and the corrected radiative lifetime[24] of the $^3P_1$ state. Thus, at hydrogen pressures above 0.8 cm. the rate of reaction 3 is approximately equal to Ia, below this pressure the rate of reaction 3 will fall, and reaction 2 will become more important. Similarly, any reaction initiated by the hydrogen quenching reaction should also fall below 0.8 cm. It is interesting to note that a marked decrease in the initial rate of HD formation is observed below 1 cm. of H_2–D_2 pressure (see Figure 4). In view of the uncertainties in the corrected radiative lifetime, the agreement between the predicted and experimental pressure for complete quenching is good. On the other hand, the initial rate of D_2 formation from HD (Figure 6) does not fall off below 1 cm. Based upon the quenching cross sections for H_2 and D_2, 6.0 and 8.4 Å.^{2}, respectively,[25] the rate constants for H_2 and D_2 quenching are almost identical.

The quenching cross section of HD for Hg 6($^3P_1$) atoms has not been measured, and one may suppose that the difference observed between the H_2–D_2 system and the HD system at low pressure could possibly be ascribed to a difference in the quenching rate constants

(23) R. G. W. Norrish and A. B. Callear, *Proc. Roy. Soc.* (London), A266, 299 (1962).

(24) T. Holstein, *Phys. Rev.*, 72, 1212 (1947).

(25) K. J. Laidler, "The Chemical Kinetics of Excited States," Oxford University Press, London, 1955, p. 107.

for H_2, HD, and D_2. A measurement of the relative quenching rates of H_2, HD, and D_2 for Hg $6(^3P_1)$ atoms was then undertaken.

Cvetanović[26] has shown that when a hydrocarbon is subjected to mercury photosensitization in the presence of different relative concentrations of N_2O, the following relationship is obeyed

$$\frac{1}{\phi_{N_2}} = 1 + \frac{k_a(RH)}{k_b(N_2O)} \qquad (4)$$

Where ϕ_{N_2} is the quantum yield of nitrogen formation, (RH) and (N_2O) are the concentrations of the hydrocarbon and nitrous oxide, respectively, k_a is the rate constant for the reaction of RH with Hg $6(^3P_1)$ atoms, and k_b represents the rate constant for the reaction of N_2O with Hg ($^3P_1$) atoms. The mechanism of reaction of Hg $6(^3P_1)$ atoms with hydrogen is similar to that observed for hydrocarbons, and relation 4 should also be obeyed.

Mixtures of H_2, HD, and D_2 with N_2O were irradiated in the presence of mercury, and the resulting graph of $1/\phi_{N_2}$ as a function of $(H_2)/(N_2O)$, $(HD)/(N_2O)$, and $(D_2)/(N_2O)$ is shown in Figure 7. Although there is some scattering in the experimental points, the graph clearly shows that the rate constants for the reaction of Hg $6(^3P_1)$ atoms with H_2, HD, and D_2 are all approximately equal. Therefore, the source of the difference in the low-pressure behavior of the H_2–D_2 mixture and HD is not readily ascribed to differences in quenching cross sections and will have to be investigated further. In any case, it seems reasonable to assume complete quenching of Hg* ($^3P_1$) in all experiments at pressures greater than 1 cm., and the overall primary processes in H_2, HD, and D_2 mixtures may be written as

$$Hg^*(^3P_1) + H_2 \longrightarrow Hg(^1S_0) + 2H \qquad (3)$$

$$Hg^*(^3P_1) + HD \longrightarrow Hg(^1S_0) + H + D \qquad (5)$$

$$Hg^*(^3P_1) + D_2 \longrightarrow Hg(^1S_0) + 2D \qquad (6)$$

It should be noted that while HgH has been spectroscopically observed[27] when mixtures of hydrogen and mercury vapor are irradiated at 2537 Å., this hydride is presumably formed by secondary reactions and not in the quenching act.[25,27] Since the HgH concentration must be quite low, it is not considered in the exchange mechanism.

The hydrogen and deuterium atoms produced by quenching reactions 3, 5, and 6 undergo collisions with the H_2, HD, and D_2 molecules present, some of which lead to chemical reactions. These homogeneous processes may be described in terms of two reversible homogeneous reactions, *viz.*

$$H + D_2 \rightleftharpoons HD + D \qquad (7f \text{ and } 7r)$$

$$D + H_2 \rightleftharpoons HD + H \qquad (8f \text{ and } 8r)$$

At the relatively low gas pressures used in these experiments, the removal of H and D atoms from the system by homogeneous three-body combination is negligible, a point somewhat substantiated by the failure of large amounts of Xe and He to influence the rate of the reaction. The ultimate fate of these atoms must be combination reactions at the walls. Linnett[28] has shown that hydrogen atoms rapidly adsorb on glass walls and saturate the available surface. Thus, the following equilibria may be assumed to be rapidly established

$$H + W \rightleftharpoons HW \qquad (9)$$

$$D + W \rightleftharpoons DW \qquad (10)$$

where W denotes the wall. Subsequent collisions of H and D atoms with the wall may be expected[28,29] to result in combination reactions 11, 12, 13, and 14

$$H + HW \longrightarrow H_2 + W \qquad (11)$$

$$D + HW \longrightarrow HD + W \qquad (12)$$

$$H + DW \longrightarrow HD + W \qquad (13)$$

$$D + DW \longrightarrow D_2 + W \qquad (14)$$

It is possible to rule out any large contribution to the exchange by heterogeneous reactions analogous to

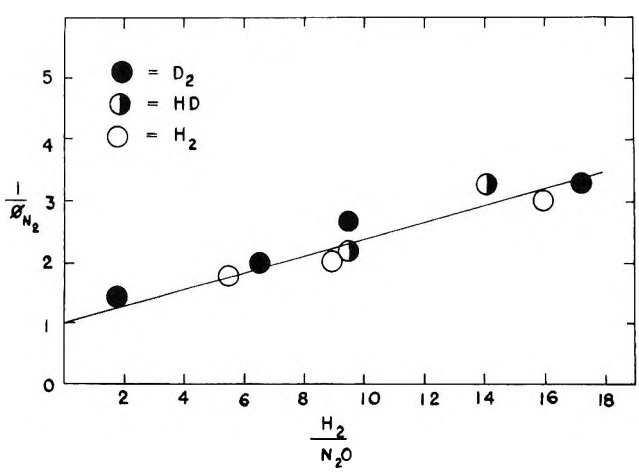

Figure 7. Comparison of the Hg $6(^3P_1)$ quenching rate constants for H_2, HD, and D_2 relative to N_2O.

(26) R. J. Cvetanović, *J. Chem. Phys.*, **23**, 1208 (1955).

(27) C. R. Masson and E. W. R. Steacie, *ibid.*, **18**, 210 (1950).

(28) M. Green, K. R. Jennings, J. W. Linnett, and D. Schufield, *Trans. Faraday Soc.*, **55**, 2152 (1959).

(29) P. Kebarle and M. Avrahami, *Can. J. Chem.*, **40**, 2409 (1962).

reactions 7f, 7r, 8f, and 8r involving H–W and D–W, even though these types of reactions are postulated in the presence of catalysts where H atoms are chemisorbed. It is difficult to reconcile the observed decrease in the initial rate of HD production (Figure 5) when fresh surface is brought into the reaction zone with a mechanism which includes significant contributions from heterogeneous analogs of reactions 7f, 7r, 8f, and 8r.

If equilibria 9 and 10 are assumed rapid and the hydrogen pressure assumed to be over 1 cm., it is possible to deduce an explicit equation for the sum of the photostationary state concentrations of H and D atoms. On this basis, one would expect the sum of these atomic concentrations to be directly proportional to the incident intensity, inversely proportional to the surface-to-volume ratio. It can also be shown that the concentration ratio, (H)/(D), depends primarily on the initial ratio of hydrogen and deuterium in the system and shifts only slightly during the course of the exchange reaction. It would uselessly lengthen this paper to write such equations explicitly, and, in view of the complications introduced by including diffusion considerations,[30,31] their inclusion would serve no purpose. It is sufficient to conclude that the concentrations of H and D are constant and inversely dependent on the surface to volume ratio in order to understand Figures 4 and 5.

We may write the following differential equation for the *initial* rate of HD production in the experiments involving H_2–D_2 mixtures

$$\frac{d(HD)}{dt} = k_{12}\left(\frac{S}{V}\right)(H) + k_{13}\left(\frac{S}{V}\right)(D) + k_{7f}(H)(D_2) + k_{8f}(D)(H_2) \quad (15)$$

The linear region of Figure 4 may be attributed to the last two terms in eq. 15; the intercept of the extrapolation of the linear region to zero pressure may be attributed to the first two terms in eq. 15. If these assumptions are correct, it is possible to estimate the magnitudes of the initial rate of the heterogeneous reaction and the initial rate of the homogeneous reaction by comparing the extrapolated intercept of Figure 4, *i.e.*, 0.59 μmole min.$^{-1}$, with the difference between the total observed rate and the extrapolated intercept. Thus, at 1 cm. of H_2–D_2 pressure the ratio of the heterogeneous reaction to the homogeneous reaction is 4.8, indicating that about 80% of the reaction occurs on the walls; at 30 cm. of H_2–D_2 pressure, the ratio is 0.16, indicating that about 15% of the reaction occurs on the walls. The ratio of the rates of the heterogeneous reactions to the homogeneous reactions may be written explicitly from eq. 15 as

$$\frac{R(\text{hetero})}{R(\text{homo})} = \frac{k_{12}\left(\frac{S}{V}\right)(H) + k_{13}\left(\frac{S}{V}\right)(D)}{k_{7f}(H)(D_2) + k_{8f}(D)(H_2)} \quad (16)$$

If we assume as a first approximation that (H) = (D), eq. 16 may be reduced to eq. 17.

$$\frac{R(\text{hetero})}{R(\text{homo})} = \frac{k_{12}\left(\frac{S}{V}\right) + k_{13}\left(\frac{S}{V}\right)}{k_{7f}(D_2) + k_{8f}(H_2)} \quad (17)$$

Since the relative ratio of heterogeneous to homogeneous reaction may be estimated from Figure 4, it is possible to estimate $k_{12}(S/V) + k_{13}(S/V)$ if k_{7f} and k_{8f} are known. Using the calculated data of Shavitt[2] for k_{8f} and k_{7f} at 300°K., we estimate $k_{12}(S/V) + k_{13}(S/V)$ to be 865 sec.$^{-1}$. Since the surface-to-volume ratio varies with the depth of the reaction zone from about 3.7 cm.$^{-1}$ at low pressures to perhaps as high as 6 or 7 cm.$^{-1}$ at high pressures, considerable uncertainty must be attached to any calculation based upon it. Nonetheless, assuming $(S/V) = 3.7$, we obtain a value of 234 cm. sec.$^{-1}$ for $k_{12} + k_{13}$, a value consistent with the value reported by Kebarle[29] for k_{11}, *i.e.*, 98 cm. sec.$^{-1}$, when the nature of the assumptions is borne in mind.

The effect on the initial rate of HD formation of bringing fresh surface into the reaction zone (*vide* Figure 5) is also readily accounted for in terms of eq. 15. When the quartz disk is moved sufficiently forward to enter the reaction zone, it adds surface for reactions 11 to 14 and thereby reduces the H and D atom concentrations. The net effect is to increase the rate of the heterogeneous reaction and to decrease the rate of the homogeneous reaction. At an H_2–D_2 pressure of 1 cm. the reaction occurs mainly on the walls, and the effect of additional surface is small; at an H_2–D_2 pressure of 6 cm., the wall reaction accounts for about half of the reaction, and the effect of fresh surface is more pronounced. The shapes of the curves in Figure 5 probably reflect the variation of the H and D atom concentration as a function of distance from the window. This interpretation is substantiated by the effect of 5 cm. of argon on the shape of the curve for an H_2–D_2 pressure of 1 cm. as argon would be expected to hinder the rate of diffusion of the H and D atoms from their zone of formation near the window.

The effect of HD pressure on the initial rate of the reverse reaction, shown in Figure 6, should be given by an equation analogous to eq. 15, *viz.*

(30) H. Wise and C. M. Ablow, *J. Chem. Phys.*, **29**, 634 (1958).

(31) W. R. Schultz and D. J. LeRoy, *Can. J. Chem.*, **40**, 2413 (1962).

$$\frac{d(D_2)}{dt} = k_{14}\left(\frac{S}{V}\right)(D) + [k_{7r}(D) + k_{8r}(H)](HD) \quad (18)$$

and, while a linear region apparently exists above 2 cm. of HD pressure, the low-pressure region does not fall off as expected. Furthermore, the extrapolation of the linear region to zero HD pressure passes through the origin, implying the heterogeneous production of D_2 (and H_2) is negligible. This conclusion, while in accord with the large photostationary yields of HD obtained at low pressures (Figure 2), can scarcely be correct in view of the experimental magnitude of k_{11}.[29] In view of this apparent inconsistency, it seems prudent to await the results of further study rather than speculate about the low-pressure behavior depicted in Figure 6. The results reported here would indicate that the heterogeneous reactions 11 to 14 favor HD production. The reason for this effect is not clear and shall be investigated further.

In view of the previously discussed effects of surface-to-volume and hydrogen pressure on the initial rates of the forward and reverse reactions, the observed effect of these variables on the photostationary composition, *i.e.*, Q_∞, is readily understood. Addition of surface or the reduction in pressure results in a shift in the mechanism of the reaction in favor of the heterogeneous contribution. Since the heterogeneous reaction favors HD formation, Q_∞ increases.

It should be observed that the homogeneous reactions, 7f, 7r, 8f, and 8r, constitute a potential chain mechanism which would be expected to become more important at high pressures and/or high temperatures. Under these high-temperature–high-pressure conditions the rate of HD consumption and formation occurs predominantly *via* these homogeneous processes, and, at the photostationary state, these reactions must occur at essentially *equal* rates in the forward and reverse directions. This equality of the rates of reaction of (7f) and (7r) and (8f) and (8r) requires[6] that Q_∞ equals $k_{7f}k_{8f}/k_{7r}k_{8r}$. Furthermore, if each reaction involves species in thermal equilibrium, the principle of microscopic reversibility[32] requires that the ratio of rate constants, $k_{7f}k_{8f}/k_{7r}k_{8r}$, equals the equilibrium constant, K. It is significant that Q_∞ does indeed approach K as the temperature is increased (Figure 3) and also appears to approach K as the pressure is increased (Figure 2). These observations are especially significant and rule out the participation of "hot" hydrogen atoms in the H_2–D_2 mercury-photosensitized exchange reaction at high temperature or high pressure, an observation also suggested by the failure of added helium to affect the kinetics of the exchange at 30 cm. and 25°. It should be emphasized that the equality of Q_∞ and K under high-temperature–high-pressure conditions is a consequence of the predominance of a reversible chain mechanism under these conditions and is not to be expected generally for photochemical reactions. Also, it should be noted that the temperature–pressure conditions at which the reversible, homogeneous chain reactions predominate will be dependent upon experimental variables, such as incident intensity and surface-to-volume ratio. Nonetheless, these observations support the proposed mechanism and indicate the feasibility of a photochemical study of reactions 7f, 7r, 8f, and 8r under conditions where heterogeneous contributions to product formation are negligible. Such a study, planned in this laboratory in the near future, might hopefully result in reliable experimental rate constants for reactions 7f, 7r, 8f, and 8r which, contrary to popular belief, are not readily available.[2]

Finally, it is necessary to mention the possible significance of these observations with respect to other studies. If, as the data reported here suggest, HD formation is favored in atomic combination processes at the walls, considerable care should be exercised in estimating the extent of molecular detachment processes based upon the H_2, HD, and D_2 product distribution from the photolysis or radiolysis of a mixture of deuterated and undeuterated compounds. Such calculations, based on deviations of Q from K, should actually be based upon the deviation of Q from Q_∞ and will, in general, underestimate the extent of molecular detachment. Furthermore, this research suggests that hydrogen formation in the mercury-photosensitized decomposition of hydrocarbons may occur partially on the walls, and mechanistic interpretations based upon exclusively homogeneous reactions should be reviewed.

Acknowledgments. This research was supported by Contract No. AT(30-1)-2007 from the U. S. Atomic Energy Commission and grateful acknowledgment is made thereto. We also wish to express our gratitude to Mr. Wrbican for careful determination of the mass spectra of the product gases. Special thanks are due Dr. Leon Dorfman, Argonne National Laboratory, and Dr. A. O. Allen, Brookhaven National Laboratory, for helpful and stimulating discussions of the results of this study.

(32) N. Davidson, "Statistical Mechanics," McGraw-Hill Book Co., Inc., New York, N. Y., pp. 230–235.

The Pulse Radiolysis of Aqueous Tetranitromethane.[1]

I. Rate Constants and the Extinction Coefficient of e_{aq}^-.

II. Oxygenated Solutions

by Joseph Rabani,[2] William A. Mulac, and Max S. Matheson

Department of Chemistry, Argonne National Laboratory, Argonne, Illinois (*Received April 30, 1964*)

Aqueous solutions of tetranitromethane (TNM), both deaerated and oxygenated, have been investigated by the technique of pulsed radiolysis. This system enabled the direct determination of ϵ_e^{5780}, the extinction coefficient of the hydrated electron, at 5780 Å. as 10,600 ($\pm 10\%$) M^{-1} cm.$^{-1}$. ϵ_e^{5780} is essential for evaluating rate constants previously determined as k/ϵ_e^{5780}. Also from ϵ_e^{5780} we calculate $G_e = 2.6$ from values of $G_e \times \epsilon_e^{5780}$ in the literature. A number of rate constants were determined, including $k(e_{aq}^- + \text{TNM}) = 4.6 \times 10^{10}\ M^{-1}$ sec.$^{-1}$, $k(\text{H} + \text{TNM}) = 5.5 \times 10^{9}\ M^{-1}$ sec.$^{-1}$, and $k(e_{aq}^- + \text{NF}^-) = 3.0 \times 10^{10}\ M^{-1}$ sec.$^{-1}$, where NF^- is the nitroform ion. Rate constants have also been measured for reaction of several organic radicals with TNM. In the presence of O_2, $k(O_2^- + \text{TNM})$ was measured as $1.9 \times 10^{9}\ M^{-1}$ sec.$^{-1}$. $k(HO_2 + \text{TNM})$ is less than 10^{-5} as large. Measurement of the effective k as a function of pH gave $pK = 4.45 \pm 0.25$ for the dissociation, $HO_2 \rightleftharpoons H^+ + O_2^-$.

Introduction

A direct determination of the extinction coefficient, ϵ_e^{λ}, of the hydrated electron is important for two reasons: (1) the rate constants, k_i, of e_{aq}^- in reactions with other transients in pulse radiolysis are determined as k_i/ϵ_e^{λ}, so that ϵ_e^{λ} must be known before absolute rate constants can be calculated; (2) the product $G_e \times \epsilon_e^{\lambda}$ has been determined[3,4] and previously ϵ_e^{λ} has been estimated from this product assuming G_e from steady radiolysis scavenger work. On the other hand, G_e can also be estimated from this product if ϵ_e^{λ} is directly determined in pulse radiolysis experiments.

Previous investigations of the steady radiolysis of tetranitromethane (TNM) by Henglein and Jaspert[5] and by Bielski and Allen[6] suggested that this system could be used to determine ϵ_e^{λ}. Their work showed that the reducing species in γ-irradiated water will convert tetranitromethane to nitroform. Nitroform is a moderately strong acid and ionizes in water to give $C(NO_2)_3^-$ (hereafter referred to as NF^-), which has a broad strong absorption peak at 3500 Å. The extinction coefficient at the peak has been measured.[5,6] From these facts it appeared probable that, if the hydrated electron reacted rapidly and completely with tetranitromethane to give nitroform, the extinction coefficient of the hydrated electron could be rather directly determined by pulse irradiating aqueous TNM and then comparing the initial absorption of e_{aq}^- at 5780 Å. with the final absorption of NF^- at 3660 Å.

In this paper the measurement of ϵ_e^{5780} by the above-mentioned method is described. The reactivity of e_{aq}^- and other species with TNM has also been measured, both because the rate constants are of interest in themselves and because they are necessary to the

(1) Based on work performed under the auspices of the U. S. Atomic Energy Commission.

(2) Postdoctoral Fellow from the Hebrew University, Jerusalem, Israel.

(3) (a) S. Gordon, E. J. Hart, M. S. Matheson, J. Rabani, and J. K. Thomas, *J. Am. Chem. Soc.*, **85**, 1375 (1963); (b) L. M. Dorfman and I. A. Taub, *ibid.*, **85**, 2370 (1963).

(4) J. P. Keene, *Discussions Faraday Soc.*, **36**, 304 (1963).

(5) A. Henglein and J. Jaspert, *Z. physik. Chem.* (Frankfurt), 12, 324 (1957).

(6) B. H. J. Bielski and A. O. Allen, unpublished work.

determination of ϵ_e^{5780}, the experimental situation not being as simple as implied above.

Work in oxygenated solutions of aqueous TNM is also described. The radical-ion O_2^- reacts much more rapidly with TNM than does HO_2, so the pH dependence of reactivity yields the dissociation constant for $HO_2 \rightleftarrows H^+ + O_2^-$.

Experimental

The pulse radiolysis apparatus developed by Matheson and Dorfman[7] has been described elsewhere.[8] In this work we used a modified apparatus and procedure[9] further modified by incorporating a multiple reflection cell based on the principle described by White.[10] This cell enabled the use of long optical paths of up to 80 cm. with an actual cell length of only 4 cm. In the present work this was important since low concentrations of transients could be used, thus minimizing the fraction of e_{aq}^- which reacted with itself and with other transients rather than with TNM. This minimizing of second-order reactions increased the precision of determination of both ϵ_e^{5780} and of the pseudo-first-order rate constants measured.

The multiple reflection arrangement is shown in Fig. 1. The reaction cell C, which has a 2-cm. internal diameter and a 4-cm. internal length, sits in thin V supports of Lucite in a Lucite box as indicated. The cell is fitted with two capillary 5/20 ground joints for use in the usual syringe technique of filling and draining. Not shown is a vertical rod and support for the syringe. The spherical mirrors M_1, M_2, and M_2' of the multiple reflection system are made of high purity silica (to minimize radiation discoloration and luminescence) 2 mm. thick, with both front and rear surfaces ground to the same center of curvature. The mirrors (silver is best for wave lengths longer than 4000 Å. and aluminum for general use) are deposited on the back surfaces and can be renewed as necessary. The analyzing light beam enters the unsilvered upper left-hand corner of the front mirror M_1 and exits through the unsilvered upper right-hand corner. M_2 and M_2', the halves of a single spherical mirror, pivot about pins P (only one shown) to vary the number of light traversals of the cell in the manner described by White.[10] A separate screw assembly S (only one shown) for each half controls the rotation of M_2 and M_2'.

To minimize the reflection losses at the windows of the cell C, the Lucite box was filled with distilled water. The cell C essentially touches the front (silica) surfaces of the mirrors so as to reduce the amount of irradiated water in the light path exterior to the cell. This water is aerated so that the strong e_{aq}^- absorption in the visible region is converted to weak O_2^- absorption

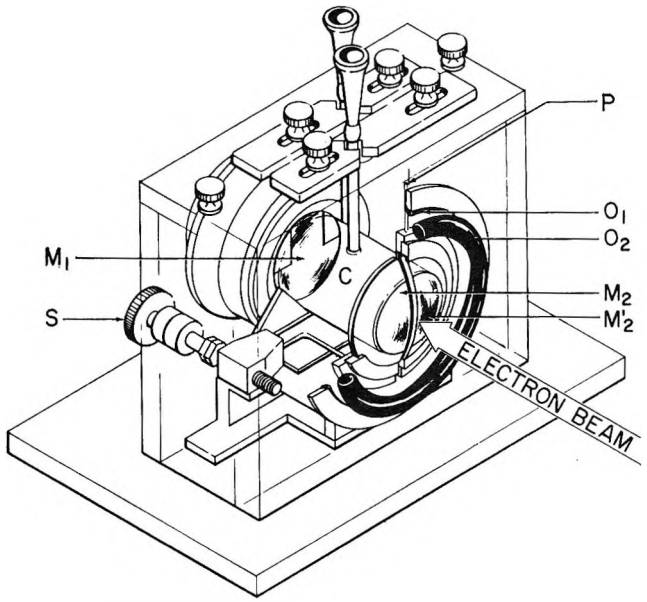

Figure 1. Multiple reflection cell assembly.

in the ultraviolet region. Pulse radiolysis experiments with deaerated 0.0001 *M* sulfuric acid in C showed that no absorption exterior to the cell was produced in our experiments. In this design M_1 must be drawn back in an O-ring sealed sleeve in order to insert the cell with a twisting motion. To seal the cell at the split mirror end, a plastic film (Saran wrap) was passed over O-ring O_2 and under O-ring O_1. The Saran wrap is close to (0.5 mm.) but does not touch the mirror, since silver in particular adheres poorly to silica. M_2 and M_2' were protected from the water by a thin spray coat of clear acrylic paint (Krylon). Although not exposed to water, the front mirror M_1 was also sprayed with Krylon except in the unsilvered corners. It was the susceptibility of the mirrors to corrosion that necessitated that the mirrors be deposited on the rear silica surfaces. The electron beam entered axially into the cell C as shown and was uniform across the entering face of the cell as checked by the discoloration produced in microscope slides.

Tetranitromethane (a toxic and explosive compound)[11] from K and K Laboratories, Jamaica, N. Y., was shaken 10 or 11 times with fresh volumes of distilled water, using a water to TNM volume ratio of

(7) M. S. Matheson and L. M. Dorfman, *J. Chem. Phys.*, **32**, 1870 (1960).

(8) L. M. Dorfman, I. A. Taub, and R. E. Bühler, *ibid.*, **36**, 3051 (1962).

(9) S. Gordon, E. J. Hart, M. S. Matheson, J. Rabani, and J. K. Thomas, *Discussions Faraday Soc.*, **36**, 193 (1963).

(10) J. U. White, *J. Opt. Soc. Am.*, **32**, 285 (1942).

(11) N. I. Sax, "Dangerous Properties of Industrial Materials," 2nd Ed., Reinhold Publishing Corp., New York, N. Y., 1963, p. 1236.

about 50 each time. Then the TNM was added to a dilute aqueous bicarbonate solution (volume ratio about 1:20). In a closed Pyrex system the TNM was fractionally distilled by bubbling a stream of nitrogen through the mixture, the gas stream then passing through a drying tube containing calcium chloride and finally through a trap surrounded by liquid nitrogen where the TNM was condensed. A stock solution was prepared, usually at a concentration of about 0.2 ml. of TNM in 1 l. of water. Triply distilled water was used to prepare all solutions. Generally, freshly distilled TNM was used for each day's experiments, except in a few cases where the distilled TNM was stored for up to 2 weeks in the dark at −20°. Stock solutions were prepared only a few hours before use (maximum 7 hr.) and were maintained at ice temperature. Suitable volumes of stock solution were diluted with room temperature water less than 1 hr. before the resulting dilute solution was irradiated. In experiments where relatively high concentrations of TNM were used, the amounts of cold stock solution used gave diluted solutions significantly below room (or irradiation) temperature (23° unless otherwise stated). For these experiments the stock solution was stored at room temperature before use. Solutions could be kept at 0° for periods up to 1 week with little decomposition, as indicated by the following data. Optical density changes measured with a Beckman DU spectrophotometer showed that in a 2.8×10^{-5} M TNM solution, 2.5×10^{-7} M NF^- was found after 36 hr. room temperature storage, and in a 1.6×10^{-3} M TNM solution, 4×10^{-7} M NF^- was found after 19 hr.

For experiments on the reaction of e_{aq}^- with TNM and on the determination of ϵ_e^λ, care was taken that the initial concentrations of NF^- and NO_3^- were so low that these species did not react appreciably with e_{aq}^- in the presence of TNM. Since the reaction of e_{aq}^- with TNM is very fast, this experimental requirement was easily met. However, when radicals less reactive toward TNM were studied, such as the HO_2–O_2^- combination in equilibrium in acid solution, it was not obvious *a priori* that the TNM hydrolysis products, NF^- and NO_3^-, would not compete with the TNM for the radicals, even though [TNM] >> [NF^-] + [NO_3^-]. However, our results, as will be seen later, indicate that such a competition could be of only minor importance.

In early experiments using the optical arrangement previously described,[9] the diluted TNM solutions were deaerated by shaking with argon gas in a syringe (see Fig. 1 of ref. 9 for the type of syringe) and then expelling the gas. This procedure was repeated four times for air-free solutions. For oxygenated solutions, a similar procedure of shaking with oxygen was repeated twice. Unfortunately, TNM is volatile and subsequent analysis showed that ~6% of the TNM was lost with each shaking for 10^{-3} M TNM and somewhat smaller percentages were lost for more dilute solutions. Controlled procedures were adopted and 6 to 4%, depending on TNM concentration, was subtracted for each shaking with gas, either oxygen or argon. Analysis indicated ±5% error in TNM concentration was introduced by this procedure and correction. In later experiments using the multiple reflection cell in which ϵ_e^{5780} was determined and the rate constants for e_{aq}^- + TNM and H + TNM were measured, this correction was avoided. In this latter case the stock solution was deaerated in a syringe and a portion of the contents subsequently analyzed. Dilutions were made with deaerated water or dilute acid by direct transfer from syringe to syringe, using microsyringes where necessary for accuracy.[12] Analyses for TNM were made by using hydrazine sulfate to reduce it to nitroform, the nitroform being estimated spectrophotometrically. Exposure of the solutions to air was minimized as much as possible before and during the reduction to avoid losses by evaporation.

The potassium salt of nitroform, $KC(NO_2)_3$ (also explosive),[13] was prepared by mixing about 3 ml. of TNM with 70 ml. of concentrated cold KOH and then shaking the mixture until the TNM had reacted (~30 min.). Yellow crystals of $KC(NO_2)_3$ precipitated during the reaction and were separated from the solution by decantation. The crystals were washed twice with cold distilled water and then washed with absolute ethyl alcohol and finally with diethyl ether. A sample of the crystals was weighed to make a solution of known concentration. From this solution the $\epsilon_{NF^-}^{3500}$ was measured as 14,600 M^{-1} cm.$^{-1}$ (log $(I_0/I) = \epsilon cl$) at 25°, using either a Beckman DU or Cary Model 14 spectrophotometer. This agrees satisfactorily with the value obtained by Allen and Bielski[6] of 14,800.

Because a mercury arc was used in our experiments, it was desirable to follow NF^- concentrations by the absorption at 3660 Å. Further, since a high-pressure mercury arc with broadened emission lines was used, since the aperture in front of the monitoring photomultiplier in the spectrograph passed a 44-Å. band, and since the extinction coefficient of NF^- decreases ~19% from 3638 to 3682 Å., the effective $\epsilon_{NF^-}^{3660}$ was determined

(12) E. J. Hart, S. Gordon, and J. K. Thomas, *J. Phys. Chem.*, 68, 1271 (1964).

(13) I. Heilbron and H. M. Bunbury, Ed., "Dictionary of Organic Compounds," Vol. III, Oxford University Press, New York, N. Y., 1946, p. 878.

directly with the experimental setup used in the pulse radiolysis experiments, that is the same lamp, optical train, and spectrograph. This was done by preparing six known concentrations (1.4 to 12 μM) of NF^- (from the potassium salt) and comparing the optical densities of a reaction cell containing these solutions with the optical density of the same reaction cell containing pure water. The optical densities were obtained by photographing photomultiplier signals on the oscilloscope with and without the reaction cell in the light beam path. The optical density was linear with concentration and the results yielded an effective $\epsilon_{NF^-}{}^{3660}$ of 10,200 ± 250 at 24°.

To make sure that the photomultipliers were always set on the same wave lengths before each experiment the apertures in front of the photomultipliers were reduced to pass a band of 15 Å., a medium-pressure mercury lamp (Hanovia AH-4) was set in front of the spectrograph, and the photomultiplier signals were maximized at 3660 and 5780 Å. (halfway between the maxima at 5770 and 5790 Å.). A Corning 0–52 filter giving 55% transmission at 3600 Å. was placed between the lamp and the reaction cell in all experiments to protect TNM and NF^- solutions from photolysis by the analyzing light beam.

Results and Discussion

I. Rate Constants and Extinction Coefficient of e_{aq}^-

The Reactivity of e_{aq}^- with TNM. When TNM alone is present in water, one can follow simultaneously both the decay of e_{eq}^- at 5780 Å. and the formation of NF^- at 3660 Å. The NF^- formation results from reaction 1.

$$e_{aq}^- + C(NO_2)_4 \longrightarrow C(NO_2)_3^- + NO_2 \quad (1)$$

It was observed that the absorption at 3660 Å. reaches a maximum and then decays to a somewhat lower (11 ± 4% lower) plateau. A similar decay occurs with TNM in 0.01 M $HClO_4$. Under our conditions, the slight decay at 3660 Å. was much slower than the increase due to reaction 1, so that we used the maximum optical density at 3660 Å. as D_∞ for rate constant calculations at this wave length. For solutions containing only water and TNM, eq. 2 and 3 may be written for our conditions

$$\frac{d(NF^-)}{dt} = k_1[TNM][e_{aq}^-] \quad (2)$$

$$\frac{-d(e_{aq}^-)}{dt} = k_1[TNM][e_{aq}^-] + k[e_{aq}^-] \quad (3)$$

where k is the total rate constant for the additional pseudo-first-order reactions consuming e_{aq}^-. If one integrates eq. 3 and then uses the result to substitute for $[e_{aq}^-]$ in eq. 2, one can then integrate eq. 2 and by substituting appropriate optical densities and extinction coefficients in the integrated equations obtain eq. 4 and 5.

$$\ln D_t^{5780} = -(k_1[TNM] + k)t + \ln D_0^{5780} \quad (4)$$

$$\ln [(D_\infty^{3660} - D_t^{3660})/D_\infty^{3660}] = -(k_1[TNM] + k)t + \ln \frac{\epsilon_{NF^-}{}^{3660} - \epsilon_e{}^{3660}}{\epsilon_{NF^-}{}^{3660}} \quad (5)$$

where the D's are optical densities with superscripts for wave length and subscripts for time.

Equations 4 and 5 show that the optical densities at both 5780 and 3660 Å. suitably plotted as a function of time should yield straight lines with the *same* slope although e_{aq}^- also has a small absorption at 3660 Å. and although NF^- is formed only by reaction 1 whereas e_{aq}^- disappears to a small extent by additional pseudo-first-order reactions also. Our experimental results have been plotted according to eq. 4 and 5 in Fig. 2. The rate constants k_1, obtained from the slopes of these plots, are given in Table I, and have been corrected for the reactions of the hydrated electron with other species in water (line A in Fig. 2). Corrections were also made for reactions of e_{aq}^- with the NF^-, H^+, and NO_3^- initially present and for TNM depletion (up to 6% TNM reacted) during the reaction. All [TNM] given in the tables and text are initial concentrations, while *average* [TNM] were always used to calculate all rate constants in this paper. It is true that k is not

Table I: The Rate Constant for the Reaction of e_{aq}^- with TNM[a] Measured at 5780 and 3660 Å.

TNM $M \times 10^5$	D_∞	k[b] at 5780 Å.	k[b] at 3660 Å.	Light path, cm.
1.30	0.145	4.4	4.6	48
1.48	0.260	3.9	4.2	32
1.59	0.300	4.7[c]	4.9	32
1.96	0.380	4.9[c]	4.9	48
2.28	0.360	4.9[c]	4.9	48
2.8	0.150	4.2	3.7	48
2.8	0.330	4.1	4.8	48
Average with appropriate weighting		4.6	4.7	

[a] Solutions contain TNM only. [b] In units of 10^{10} M^{-1} sec.$^{-1}$ (corrected for other reactions). Each value is the average of two or more experiments. [c] These are the most recent and reliable since: (1) there was no volatility loss of TNM during solution preparation, and (2) the correction for reactions in pure water was measured instead of calculated.

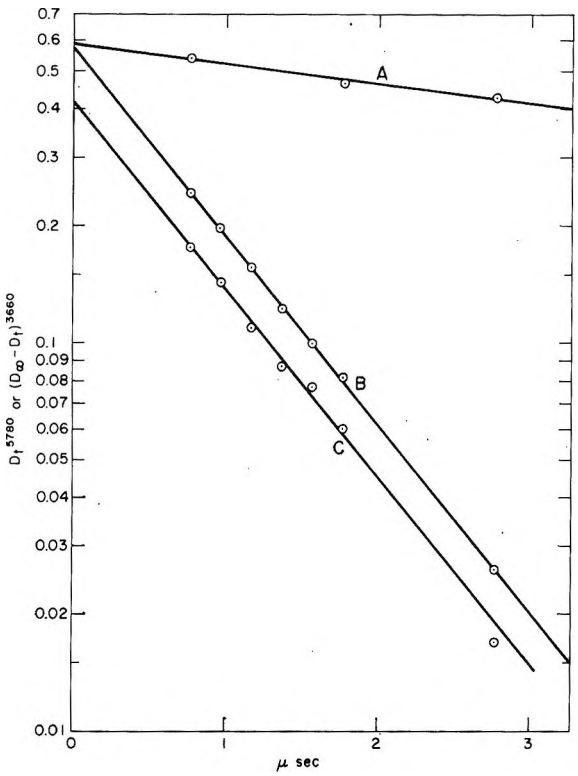

Figure 2. Pseudo-first-order disappearance of e_{aq}^- and simultaneous formation of NF^- using a 48-cm. light path: A, water alone, 5780 Å.; B, 1.96×10^{-5} *M* TNM, 5780 Å.; C, 1.96×10^{-5} *M* TNM, 3660 Å. The points at 5780 Å. usually showed less scatter about a straight line than those at 3660 Å.; time zero at middle of pulse.

accurately first order, but the deviation from first order is small (Fig. 2) and the correction due to k is 8 to 18%. The reaction of e_{aq}^- with NF^- will affect the kinetics at 3660 Å. more than at 5780 Å., but this is only a minor effect. This difference was neglected here, but corrected for in the calculation of the extinction coefficient. The corrections are discussed in more detail in the sections on ϵ_e^{5780}.

Experiments were also carried out measuring k_1 in solutions containing organic solutes as well as TNM. Again, measurements were made at 5780 and 3660 Å. and eq. 4 and 5 applied. At 3660 Å., D_∞ was chosen as the optical density measured at 3660 Å. just at the time when all e_{aq}^- had disappeared, this time being determined by examination of the decay curve at 5780 Å. In the experiments with sucrose, corrections were also made for the reaction of sucrose radicals with TNM which occurred before the complete decay of the e_{aq}^- absorption (cor. <15%). Corrections were made as before for other reactions of e_{aq}^-. The data are tabulated in Table II where the value of k_1 is in good

Table II: Rate Constant for the Reaction of e_{aq}^- with TNM in Aqueous Organic Solutions[a]

Solute	[TNM], $M \times 10^5$	Final D at 3660 Å.	k^b at 5780 Å.	k^b at 3660 Å.
0.0107 *M* sucrose	2.02	0.930	4.6[c]	4.6[c]
0.1 *M* sucrose	3.0	0.280	4.4	3.7
0.2 *M* ethanol	2.4	0.250	4.8	...
0.1 *M* CH_3COONa + 0.0002 *M* CH_3COOH	3.0	0.210	4.9	4.1
0.25 *M* glucose	3.0	0.500	4.5	4.8
0.0012 *M* phenol	4.0	0.230	5.0	...
Weighted average			4.6	4.4

[a] Light path was 16 cm. except for experiment of footnote *c*. [b] In units of 10^{10} M^{-1} sec.$^{-1}$. [c] Light path was 48 cm. Most reliable experiments for reasons listed under Table I.

agreement with the results in Table I. Since the organic radicals in ethanol or phenol solutions react with TNM about one-tenth as fast as e_{aq}^- does, no k was calculated at 3660 Å. because of this interference. For the other systems also, k_1 is measured more accurately at 5780 Å. than at 3660 Å. The organic solutes eliminated OH radicals and acetate suppressed H^+ as well. In acetate solutions a weakly absorbing transient was found at 3660 Å. with a half-life under our conditions of about 200 μsec. The "final D" in the table is a measure of the pulse intensity and includes the NF^- from the organic radical reaction (except for acetate where the radical did not react with TNM).

The Reactivity of H Atoms with TNM. Since H atoms also react with TNM to produce NF^-, it was essential to measure the rate constant for this reaction before proceeding to an evaluation of ϵ_e^λ. H atoms were produced by pulse irradiating 0.01 *M* $HClO_4$, the acid converting all e_{aq}^- to H. The subsequent reaction of H with TNM, eq. 6, was followed by observing

$$H + C(NO_2)_4 \longrightarrow H^+ + C(NO_2)_3^- + NO_2 \quad (6)$$

the change in optical density at 3660 Å. The rate constant, k_6, was calculated as before using eq. 5 for the psudo-first-order reaction plot. Two concentrations of TNM were employed. For 6.1×10^{-4} *M* TNM in 0.013 *M* $HClO_4$, k_6 was evaluated from the plot as 6.1×10^8 M^{-1} sec.$^{-1}$, while 1.36×10^{-3} *M* TNM in 0.01 *M* $HClO_4$ gave 5.6×10^8 M^{-1} sec.$^{-1}$. At 3660 Å., the increase in optical density, presumed due to NF^- formation, was followed by a slight decrease to a plateau just as was found for solutions without acid. In one example, D increased to 0.310 in 1 to 2 μsec., then decreased to 0.275 after 100 μsec., and finally remained constant to 200 μsec. or more. For our calcu-

lations of k_6 we used the maximum optical density as D_∞. The possible significance of the optical density decay is discussed later.

The reactions H + H and H + OH occur in parallel with reaction 6. Under our conditions these two reactions contribute about 17% to the initial rate of H atom disappearance in 6.1×10^{-4} M TNM and about 8% in 1.36×10^{-3} M TNM. This contribution decreases by about a factor of three, as the H atoms are used up since H + H depends upon $[H]^2$ while for H + OH the [OH] can be regarded as nearly constant, and since $k_{H+H} \simeq k_{H+OH}$[14] and $[H]_0 \simeq [OH]_0$. Correcting for the average contribution of these reactions, we get $k_6 = 5.6 \times 10^8$ M^{-1} sec.$^{-1}$ and 5.4×10^8 M^{-1} sec.$^{-1}$ for the low and high TNM concentrations, respectively. We see that $k_1 \simeq 100k_6$ and therefore, although H atoms form about 20% of the reducing species[15] in neutral solution, reaction 6 did not affect the measurement of k_1.[15c]

The Reactivity of e_{aq}^- with NF^-. It was also necessary in this work to investigate a possible reaction of e_{aq}^- with the product NF^-. To do this, a 4.0×10^{-5} M solution was prepared from a sample of $KC(NO_2)_3$. This sample was at least 99% pure as determined by its absorption at 3500 Å. using $\epsilon_{NF^-}^{3500} = 14{,}800$.[6] The pseudo-first-order reaction plots for decay of e_{aq}^- in this solution gave a rate constant $k_7 = 3.3 \times 10^{10}$ M^{-1} sec.$^{-1}$. This value (ref. 5 indicates the stable product of reduction of NF^- is nitroacetaldoxime (methazonic acid)) should be corrected for other reactions of e_{aq}^- occurring simultaneously, namely those with itself and with H^+, H, OH, H_2O_2, and H_2O. These other contributions are nearly first order since $e_{aq}^- + e_{aq}^-$ makes only a minor contribution and since the lifetimes of the other species are much greater than that of e_{aq}^- in the presence of this concentration of TNM. The intensity of the pulse was measured from the initial optical density observed in deaerated water irradiated under the same conditions and gave $D_0^{5780} = 0.60$. The decay in deaerated water plotted nearly first order with a half-life of 6 ± 1 μsec. Correcting for the decay observed in pure water gave $k_7 = 3.0 \times 10^{10}$ M^- sec.$^{-1}$. This value was used in later calculations.

$$e_{aq}^- + C(NO_2)_3^- \longrightarrow \text{nonabsorbing product} \quad (7)$$

Two earlier experiments with less pure samples of $KC(NO_2)_3$ (>95% purity) gave, respectively, k_7 values of 3.3×10^{10} and 3.1×10^{10}, uncorrected, and 2.8×10^{10} and $2.9_5 \times 10^{10}$ M^{-1} sec.$^{-1}$, corrected.

The Decay of Absorption at 3660 Å. If TNM is irradiated either in neutral water or in 0.01 M perchloric acid, the increase in absorption at 3660 Å. due to nitroform formation is followed by a small decay of this absorption. Because of the small changes in optical density, plots of log D or $1/D$ *vs.* time did not show whether the decay was first or second order. In four experiments (similar to the first experiment in Table III) the average decrease from the maximum D to the plateau was 11 ± 2% standard deviation (decreases ranging from 7 to 13%). Addition of 0.01 M $HClO_4$ did not measurably change the results. At neutral pH (no buffer) diluting TNM 100-fold from 2.3×10^{-3} M changed the half-life only to ~30 μsec., with a measured decay in D of 7%. Increases in electron pulse intensity shortened the half-life in 2.3×10^{-3} M TNM. See Table III. Because the changes in half-life are small, the results are not conclusive, but seem to be intermediate between those expected for a first-order reaction or for a second-order reaction of the type A + B, where $[A]_0 = [B]_0$.

Table III: Half-Life of Decay at 3660 Å. as a Function of Pulse Intensity: 2.3×10^{-3} M TNM (No Acid)

$(D_{max}/l.)^a$	Half-life, μsec.	Decay, %
0.380/32 = 0.012	18	12
0.430/16 = 0.027	16	12
0.302/4 = 0.076	8	14
0.840/4 = 0.210	4	10.5

[a] Pulse intensity ∝ $(D_{max}/l.)$.

The first possibility considered was that NO_2 absorbs at 3660 Å. and disappears by the reaction $NO_2 + NO_2$ or $NO_2 + OH$. This explanation of the decay would require that $\epsilon_{NO_2}^{3660} \simeq 0.1\epsilon_{NF^-}^{3660} \simeq 1000$. However, the gas phase extinction coefficient is much lower than this.[16] Further, we pulse-irradiated 2×10^{-4} M $NaNO_2$ in deaerated water saturated with N_2O (to convert e_{aq}^- to OH) in order to produce the NO_2 transient in water through the reaction of $OH + NO_2^-$. A pulse intensity about fourfold greater than that

(14) (a) J. K. Thomas, *J. Phys. Chem.*, **67**, 2593 (1963); (b) see also M. S. Matheson, *Radiation Res. Suppl.*, **4**, 1 (1964), for rate constants used to estimate corrections; (c) H. A. Schwarz, *J. Phys. Chem.*, **67**, 2827 (1963) ($2k_{H+H}$ is the rate constant for H atom disappearance).

(15) (a) J. T. Allan and G. Scholes, *Nature*, **187**, 218 (1960). (b) J. Rabani and G. Stein, *J. Chem. Phys.*, **37**, 1865 (1962). (c) NOTE ADDED IN PROOF. After this paper was submitted, we received a preprint of a paper by K. D. Asmus A. Henglein, M. Ebert, and J. P. Keene, *Ber. Bunsenges. physik. Chem.*, in press, on the pulse radiolysis of TNM. Their value for k(H + TNM) determined for the H atoms formed in radiolyzed neutral solution is $(2.6 \pm 0.3) \times 10^9$ M^{-1} sec.$^{-1}$, whereas our value determined for the larger yield of H atoms in acid solution is 5.5×10^8 M^{-1} sec.$^{-1}$. Two new experiments at pH ~2 yielded k(H + TNM) = 5.0×10^8 M^{-1} sec.$^{-1}$, in reasonable agreement with our earlier value.

(16) T. C. Hall and F. E. Blacet, *J. Chem. Phys.*, **20**, 1745 (1952).

which yielded $D_\infty = 0.350$ with TNM gave $D_0 = 0.025$ in the N_2O–NO_2^- system. The $\epsilon_{NO_2}^{3660}$ of $\sim$100 in water estimated from this result agrees with the gas phase value.[16] The half-life of this decay, probably due to the NO_2 reaction alone, was about 100 μsec. From this result the decay of NO_2 absorption cannot account for the decay at 3660 Å.

Another possible explanation of the decay is that e_{aq}^- reacts with TNM to give an intermediate with about 10% greater absorption than NF^- at 3660 Å.

$$e_{aq}^- + C(NO_2)_4 \longrightarrow C(NO_2)_4^- \quad (8)$$

$$C(NO_2)_4^- \longrightarrow C(NO_2)_3^- + NO_2 \quad (9)$$

However, we would expect reaction 9 to be first order with a half-life independent of intensity. Further, to check this possibility, 2.3×10^{-3} M TNM + 0.2 M ethanol or + 0.104 M sucrose was pulse-irradiated ($D_\infty = 0.31$, $l = 32$ cm.). No decay was observed at least up to 500 μsec. These two experiments suggest that NF^- may react with other products formed by the radiation but is protected by ethanol or sucrose. These other products should be among those listed on the right-hand side of eq. 10 and should be reactive toward ethanol and sucrose. Only H and OH qualify as

$$H_2O \rightsquigarrow H_2, H_2O_2, H, OH, e_{aq}^-, H_3O_{aq}^+, OH_{aq}^- \quad (10)$$

sufficiently reactive toward ethanol and sucrose. H can be eliminated since in 2.3×10^{-3} M TNM its half-life is less than 1 μsec. and therefore it cannot account for a decay of 10 to 20 μsec. The transients e_{aq}^-, $H_3O_{aq}^+$, and OH_{aq}^- can also be eliminated by other arguments: e_{aq}^- also has a half-life less than 1 μsec. in 2.3×10^{-3} M TNM, added $H_3O_{aq}^+$ does not affect the decay, and NF^- is relatively stable in high concentrations of OH_{aq}^-. Thus the possibility that OH reacts with NF^- to form nonabsorbing products must be examined more closely.

$$OH + C(NO_2)_3^- \longrightarrow \text{nonabsorbing products} \quad (11)$$

An attempt was made to measure k_{11}. An NF^- solution (1.8×10^{-6} M) was saturated with N_2O and irradiated with a pulse such that the absorption decreased about 25% with a half-life of $\sim$20 μsec. ($l = 16$ cm.). (A pulse of the same intensity gave $D_{max} = 0.400$ in 2.3×10^{-3} M TNM in water also using a light path of 16 cm.) From this experiment, assuming $[NF^-]$ essentially constant and [OH] governed by the recombination reaction, we calculate crudely $k_{11} \sim 3 \times 10^9$ M^{-1} sec.$^{-1}$.

It is possible to make another estimate of k_{11} using certain assumptions, which would disagree with the crudely measured value. Before proceeding with the estimate, it may be noted that most or all of the species designated as OH radicals really may be accepted as being such.[17] In the steady radiolysis of TNM in water, $G(NF^-) \simeq 3$ was found.[5,6] Since the reducing species are presumed to account for the NF^- formation, and since the yield of $G_e + G_H \simeq 3$, it appears that OH does not react appreciably with NF^- in the relatively low-intensity steady radiolysis. The NF^- may be protected from OH attack by NO_2^- or NO_2. If NO_2 hydrolyzes rapidly then NO_2^- would be the protective

$$NO_2 + NO_2 \xrightarrow{H_2O} 2H^+ + NO_2^- + NO_3^- \quad (12)$$

agent. From Schwarz[18] and Schwarz and Allen,[19] we can calculate $k_{13} = (55 \pm 20) \times k_{14} = 55 \times 4.5 \times 10^7$

$$OH + NO_2^- \longrightarrow OH^- + NO_2 \quad (13)$$

$$OH + H_2O_2 \longrightarrow H_2O + HO_2 \quad (14)$$

$= 2.5 \times 10^9$ M^{-1} sec.$^{-1}$. From eq. 12 each NO_2 gives $^1/_2NO_2^-$ so that $G(NO_2^-) = {}^1/_2 (G_e + G_H) \simeq 1.5$, while from eq. 13 one OH consumes $^1/_2NO_2^-$ or $\simeq 1.2$ so that the steady-state excess nitrite yield is $\sim$0.3 or $[NO_2^-] \simeq 0.1[NF^-]$. Assuming that 20% of the NF^- formed is destroyed by OH (an unreasonably high fraction in view of the measured $G(NF^-)$), then $k_{13}[NO_2^-] = 4k_{11}[NF^-]$ and $k_{13} = 40k_{11}$. Thus $k_{11} \leq 6 \times 10^7$ M^{-1} sec.$^{-1}$, and since in the pulsed radiolysis experiments $[NF^-]_\infty = 1$ to 2×10^{-6} $M \simeq [OH]_0$ and $2k_{15} = 1 \times 10^{10}$ M^{-1} sec.$^{-1}$, then about 4% or less of the OH would

$$OH + OH \longrightarrow H_2O_2 \quad (15)$$

react with NF^-. Whether or not NO_2^- reacts with OH to protect NF in low-intensity steady-state radiolysis, it is probable that the hydrolysis of NO_2 is too slow to form NO_2^- as a protective agent in these pulsed radiolysis experiments. In any case, we prefer the higher experimental value of k_{11}.

A possible alternative protective mechanism for NO_2^- in steady radiolysis, and one which could reconcile the experimental facts known to us, is the following. Reaction 11 is rewritten

$$OH + C(NO_2)_3^- \longrightarrow OH^- + C(NO_2)_3 \quad (11a)$$

and is followed by

$$C(NO_2)_3 + NO_2^- \longrightarrow C(NO_2)_3^- + NO_2 \quad (16)$$

Reaction 16 should proceed to the right, since the reac-

(17) A. Hummel and A. O. Allen, *Radiation Res.*, **17**, 302 (1962).

(18) H. A. Schwarz, *J. Phys. Chem.*, **66**, 255 (1962).

(19) H. A. Schwarz and A. O. Allen, *J. Am. Chem. Soc.*, **77**, 1324 (1955).

tion of e_{aq}^- + TNM gives as products the entities on the right-hand side of reaction 16 and not those on the left. The higher value of k_{11} (>10^9) could then be consistent with the steady radiolysis results. However, NO_2^- probably does not form rapidly enough in the pulsed radiolysis experiments to play a protective role. In this case (11a) could well be followed by reaction 17 and/or 18, so that some nitroform is destroyed in the pulse radiolysis experiments if an OH scavenger is not present.

$$C(NO_2)_3 + NO_2 \longrightarrow C(NO_2)_4 \quad (17)$$

$$2C(NO_2)_3 \longrightarrow \text{nonabsorbing products} \quad (18)$$

Other species such as H_2O^+, O^- (unlikely in acid solution), or O atoms[20] could be invoked to explain the absorption decay at 3660 Å., but such speculations are not warranted with our present knowledge of this system. Our present conclusion is that reaction 11, OH + NF^-, with a value of $k_{11} \sim 10^9$ may explain the observed decay. In any case, regardless of the detailed explanation, the measured rate of decay or the experiment on OH + NF^- (N_2O + NF^-) above both indicate that the decay can be corrected for in the estimations of ϵ_e^λ. This is particularly true if the optical density changes during a short time interval are compared at 3660 and 5780 Å., since the correction for the decay may then be less than 2% of ϵ_e^λ.

The Reactivity of Several Organic Radicals with TNM. A suitable organic solute may be added to an aqueous TNM solution in sufficient concentration to react with all H and OH radicals with the resultant formation of an equivalent number of organic radicals (reactions 19 and 20). The organic compounds used in this work are not reactive toward e_{aq}^-,[12,21] so that e_{aq}^- still disappears by reaction 1.

When a TNM–organic scavenger solution is pulse-irradiated, both the e_{aq}^- and organic radicals formed react with TNM to form NF^- and thereby increase the optical density at 3660 Å. Reactions 1 and 21 can be separated by three different experimental procedures.

$$OH + RH_2 \longrightarrow H_2O + RH \quad (19)$$

$$H + RH_2 \longrightarrow H_2 + RH \quad (20)$$

$$RH + C(NO_2)_4 \longrightarrow C(NO_2)_3^- + NO_2 + H^+ + R \quad (21)$$

(a) The decay of light absorptions at 5780 and 3660 Å. were followed simultaneously, the absorption at 5780 Å. being due solely to e_{aq}^- while that at 3660 Å. is mainly due to NF^- with a smaller contribution from the hydrated electron. For the organic radicals examined $k_1 \geq 10k_{21}$, and, therefore, k_{21} could be determined at 3660 Å. after all e_{aq}^- had disappeared, while k_1 was deduced from the decay at 5780 Å.

(b) By the use of an appropriate concentration of H_2O_2 or N_2O all e_{aq}^- were converted according to eq. 22 or 23. In the case of H_2O_2, the ratio of RH_2 to

$$e_{aq}^- + H_2O_2 \longrightarrow OH_{aq}^- + OH \quad k_{22} = 1.2 \times 10^{10}\ M^{-1}\ \text{sec.}^{-1} \quad (22)$$

$$e_{aq}^- + N_2O \xrightarrow{H_2O} N_2 + OH_{aq}^- + OH \quad (23)$$

H_2O_2 was made sufficiently high so that all OH radicals were converted to RH. The OH radicals probably do not react rapidly with N_2O. In this system about 90% of the RH radicals result from reaction 19 and about 10% from reaction 20. With this ratio, even if the products of the two reactions differ, the complication should be minor. Of course, reaction 19 itself might involve parallel reactions, giving different forms of the RH radical. However, in the case of ethanol the α-ethanol radical seems to be the only important radical formed,[22] and, in any case in the systems studied, no complications were observed which could be attributed to the simultaneous production of two forms of RH. Thus, it appears that reaction 19 in these systems gives essentially only one radical or that the different radicals formed have similar reactivities toward TNM. The rate constants for e_{aq}^- + H_2O_2, eq. 22, and OH + H_2O_2, eq. 14, are known,[3,18] and that for reaction 1 has been determined in this work as $4.6 \times 10^{10}\ M^{-1}$ sec.$^{-1}$, so that the adjustment of the H_2O_2 concentration to ensure that e_{aq}^- reacts only with H_2O_2 and not with TNM is rather easy. Of the compounds used to form RH, only for ethanol was it known in advance that k_{19} was sufficiently high.[23]

(c) An acid solution can be used for pulsed radiolysis, so that all e_{aq}^- are converted to H atoms by eq. 24, and then (19) and (20) will occur to approximately the same extent to produce RH. In procedure (b), H atoms were of minor significance, but here they somewhat exceed the OH radicals in number. Further, the concentration of RH_2 required here is less than in (b), since H reacts but slowly with the electron scavenger H^+,[24] and H + TNM we have found to be about

$$e_{aq}^- + H_3O_{aq}^+ \longrightarrow H + H_2O \quad 2.3 \times 10^{10}\ M^{-1}\ \text{sec.}^{-1}\ \text{(ref. 3)} \quad (24)$$

(20) A. O. Allen, *Radiation Res. Suppl.*, **4**, 54 (1964).

(21) E. J. Hart, J. K. Thomas, and S. Gordon, *ibid.*, **4**, 74 (1964).

(22) I. A. Taub and L. M. Dorfman, *J. Am. Chem. Soc.*, **84**, 4053 (1962).

(23) J. Rabani and G. Stein, *Trans. Faraday Soc.*, **58**, 2150 (1962).

100-fold slower than e_{aq}^- + TNM. However, procedure (c) cannot be used when RH_2 reacts with H^+ as is the case for sucrose.

Ethanol has been used as a source of RH using all three procedures. The concordance of results for k_{21} among the three methods supports the discussion and mechanism above (Table IV). The rate constant is also independent of TNM or ethanol concentration. The formation of NF^- in a solution of 0.2 M ethanol and 2.4 × 10^{-5} M TNM (procedure (a)) was plotted as a first-order reaction according to eq. 25, with quantities similarly defined as for eq. 5. The oscilloscope

$$\ln [(D_\infty^{3660} - D_t^{3660})/D_\infty^{3660}] = -k_{21}[\text{TNM}]t \quad (25)$$

trace at 5780 Å. showed that the electron disappeared in 4 μsec. Equation 25 is then valid for times greater than 4 μsec.

Table IV: Rate Constant for Reaction of Ethanol Radicals with TNM

Concn. of ethanol, M	Other additive	TNM concn. × 10^5, M	D_∞[a]	k[b]
0.1	...	12.3	0.47	6.3
0.1	...	3.1	0.38	6.3
0.2	...	2.4	0.25	5.0
0.5	0.1 N H_2SO_4	2.9	0.54	5.4
0.5	0.03 N H_2SO_4	2.9	0.54	5.8
0.1	0.02 M H_2O_2	1.7	0.37	5.4
0.1	0.02 M H_2O_2	3.1	0.36	4.5
0.1	0.02 M H_2O_2	4.4	0.45	6.0
0.45	0.09 M H_2O_2	12.3	0.46	5.1

[a] Light path was 16 cm. [b] In units of 10^9 M^{-1} sec.$^{-1}$ Each value is an average of 2–5 experiments.

In experiments similar to those for ethanol discussed above (procedure (a)), rate constants were measured for the reaction with TNM of radicals derived from sucrose, glucose, and phenol (Table V). For these solutes the reaction of RH + TNM was more easily separated from the reaction of e_{aq}^- + TNM than was the case for ethanol and no additives such as H_3O^+ or H_2O_2 were used. In the case of sucrose, experiments were also done with added N_2O. The final optical density is not changed by the presence of N_2O.

In Fig. 3, the absorption changes in pulse-irradiated TNM–sucrose solutions with and without added N_2O are plotted according to eq. 25. In the presence of N_2O the extrapolated D_∞ ($D_\infty - D_t$ at zero time) agrees with the measured value, but in the absence of N_2O (line b) the extrapolated D_∞ is less than the measured one. This difference is due to the rapid reaction of e_{aq}^- with TNM which is practically instantaneous on the time scale of Fig. 3.

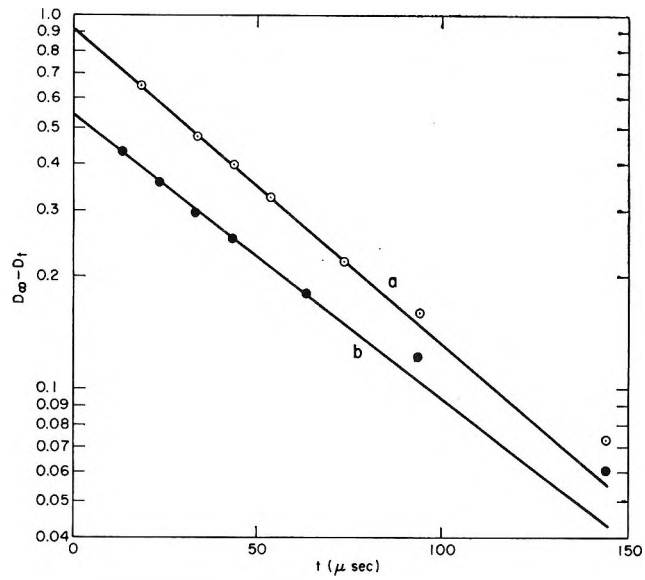

Figure 3. Pseudo-first-order formation of NF^- in solutions of 2.02 × 10^{-5} M TNM in 0.0107 M sucrose: ●, argon saturated; ○, N_2O saturated; time zero is middle of pulse.

Table V: Rate Constants for Reaction of Organic Radicals with TNM

Source of radical	Concn., M	TNM concn. × 10^5, M	D_∞	Time[a] to D_∞, μsec.	k[b]
Sucrose	0.1	3.0	0.270[c]	250–500	0.83
Sucrose	0.1	12	0.300[c]	60–100	0.71
Sucrose	0.0107	2.02	0.920[d]	250–1000	0.90
Sucrose	0.0107	2.02	0.930[d]	250–1000	1.0[e]
Glucose	0.25	3.0	0.490[c]	120–200	2.6
Phenol	0.0012	3.0	0.225[c]	120–200	1.2
Phenol	0.0012	9.0	0.260[c]	50–100	1.2

[a] Change in D less than 3% in indicated time interval. [b] Each number is average of 2–5 experiments, in units of 10^9 M^{-1} sec.$^{-1}$. [c] Light path was 16 cm. [d] Light path was 48 cm. Most reliable because there was no TNM volatility loss. [e] Saturated N_2O.

If the reactions in the presence of organic solute are as proposed in this section, then the ratio of the final optical density to the optical density at the end of the e_{aq}^- + TNM reaction should be $(G_{OH} + G_e + G_H)/G_e \simeq 2.1$. This expected result was confirmed in two ways.

(1) In Fig. 3 both lines are experiments of equal pulse intensity, and the ratio of the extrapolated D_∞ in

(24) M. S. Matheson, *Ann. Rev. Phys. Chem.*, 13, 77 (1962).

the presence of N_2O to the difference in the extrapolated values in the presence and absence of N_2O should be equal to the ratio of G values cited above. The observed D_∞ ratio of 2.4 is slightly greater, perhaps because a few per cent of e_{aq}^- reacted otherwise than with TNM.

(2) The final optical density at 3660 Å. in the ethanol experiments divided by the optical density at 3660 Å. found at the time of e_{aq}^- disappearance in sucrose experiments (this time determined at 5780 Å.) should again be $\simeq$2.1, since the e_{aq}^- + TNM and RH + TNM reactions are nearly separate in sucrose solutions. Comparison of several experiments done with equal electron pulse intensities showed that the optical density due to the total reaction of CH_3CHOH and e_{aq}^- was about twice that due to the reaction of e_{aq}^- alone, in agreement with $(G_H + G_e + G_{OH})/G_e \simeq 2.1$. This shows that the α-ethanol radicals reacted essentially only with TNM. In support of this, comparison of the rate constant for recombination of α-ethanol radicals[22] with the rate constant for α-ethanol radical + TNM shows that under our conditions radical recombination was negligible. The value of k_1 is so high that almost all e_{aq}^- must be scavenged by TNM.

The Evaluation of ϵ_e^{5780} in Aqueous TNM. In this evaluation it is assumed that NF^- is the immediate product of reaction 1. Then, if all e_{aq}^- react in (1), and if the absorption at 3660 Å. is due only to NF^- and e_{aq}^- and that at 5780 only to e_{aq}^-, eq. 26 is valid, where ϵ_x^λ is the extinction coefficient of the species

$$\frac{\epsilon_e^{5780}}{\epsilon_{NF^-}^{3660}} = \frac{(D_1^{5780} - D_2^{5780})}{(D_2^{3660} - D_1^{3660}) + A(D_1^{5780} - D_2^{5780})} \quad (26)$$

x at wave length λ, where A is defined as $\epsilon_e^{3660}/\epsilon_e^{5780}$, and where D_i^λ is the optical density at wave length λ at time t_i after the pulse. The decay of D^{5780} and the increase of D^{3660} were observed simultaneously after an electron pulse, so that the possibility of variations in pulse intensity from one pulse to another cannot affect the result. However, it appears to be impossible with the present equipment to use a concentration of TNM high enough to ensure that all the e_{aq}^- react with TNM and yet have a reaction slow enough that it can be followed accurately as a function of time. (It may be noted that the situation would be appreciably worse without the multiple reflection cell.) Therefore, it is necessary to correct the calculation of ϵ_e^{5780} for electrons disappearing in reactions other than (1). Equation 26 corrected for the various side reactions to be discussed below becomes eq. 27.

$$\Delta D^{5780} = \Delta D^{3660} \times \epsilon_r/(U - \epsilon_r A) \quad (27)$$

where

$$\Delta D^{5780} = D_1^{5780} - D_2^{5780}$$

$$\Delta D^{3660} = (D_2^{3660} - D_1^{3660}) \quad \text{(cor., see below)}$$

$$\epsilon_r = \epsilon_e^{5780}/\epsilon_{NF^-}^{3660}$$

$$U = k_1[TNM]/(k_1[TNM] + k_7[NF^-] + k_{24}[H_3O_{aq}^+]_0 + k_{28}[NO_3^-]_0 + k_{29}[NO_2] + k_w)$$

$$e_{aq}^- + NO_3^- \longrightarrow NO_3^{-2} \quad (28)$$

$$e_{aq}^- + NO_2 \longrightarrow NO_2^- \quad (29)$$

$[H_3O_{aq}^+]_0$ and $[NO_3^-]_0$ are the concentrations just before the pulse while $[NF^-]$ is the average concentration during the time interval used and includes the initial concentration, $[NF^-]_0$, as well as the radiolytic NF^-. The NO_2 is wholly radiolytic. U is that fraction of all electrons which disappear by reaction 1 to form NF^-. The calculation of U is discussed later.

The data to be used in eq. 27 to evaluate ϵ_r were taken from Tektronix 555 oscilloscope traces similar in appearance to those in Fig. 4. All such photographs

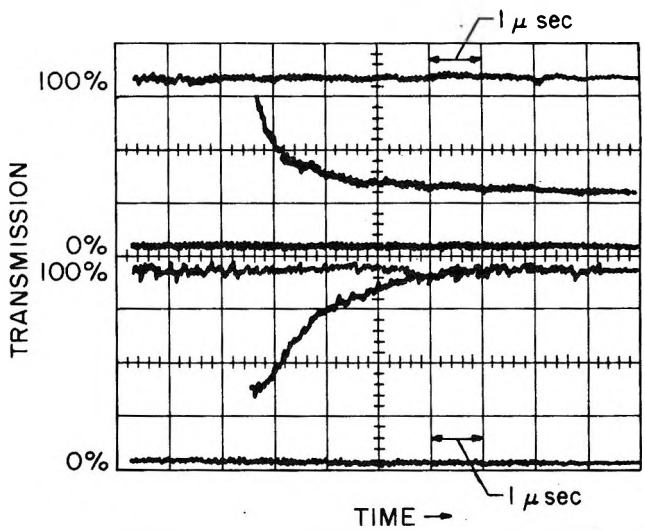

Figure 4. Simultaneous rate curves of NF^- (upper, 3660 Å.) and e_{aq}^- (lower, 5780 Å.); argon-saturated solution of 2.02×10^{-5} M TNM in 0.0107 M sucrose; 48-cm. light path. The "noise" (light emission) caused by the electron pulse begins at 2 μsec. and terminates at 3 μsec. in this figure.

were enlarged to a graticule size of 10 × 18 cm. for easier reading. The two independent beams of this scope were used to record the changes in D, and since in eq. 27 the ΔD's at 3660 and 5780 Å. are for identical time intervals, it was necessary to locate a point on each trace corresponding to the same instant. This was done by recording the same signal on both traces simultaneously. Such a signal was recorded for 3660 Å. with a shutter closed between the lamp and the re-

action cell. This signal showed effectively an increase in light transmission and is believed to represent Čerenkov radiation plus the decay of a small amount of fused silica luminescence. Total duration of this light emission signal at 3660 Å. was 1.1 μsec. for a 0.4-μsec. electron pulse. At 5780 Å., the signal is smaller and narrower and is probably due only to Čerenkov radiation during the pulse. Such traces with a closed shutter between lamp and cell also showed the point in time at which this "noise" ended. Therefore, only those parts of the oscilloscope traces later in time than this point were used for rate constant or ϵ_r evaluation.

In evaluating U, the corrections for reactions occurring in pure water are first considered. Figure 2 showed the decay at 5780 and 3660 Å. in the presence of 1.96×10^{-5} M TNM for an experiment similar to those used in the ϵ_r evaluations. Line A shows that for pure water irradiated with a similar electron pulse, the 5780-Å. decay is very close to first order, at least during the time required for complete e_{aq}^- decay in the 1.96×10^{-5} M TNM. We shall define k_w as the apparent pseudo-first-order rate constant for e_{aq}^- disappearance, which is derived from the slope of the pure water plot and which is valid for the specific conditions of our experiments. The value of k_w obtained is 1.3×10^5 sec.$^{-1}$, and it includes contributions of reactions 22, 24, 30, 31, 32, and 33, *i.e.*, of e + H_2O_2, e + H^+,

$$e_{aq}^- + OH \longrightarrow OH_{aq}^- \qquad (30)$$

$$e_{aq}^- + H \xrightarrow{H_2O} H_2 + OH_{aq}^- \qquad (31)$$

$$e_{aq}^- + e_{aq}^- \xrightarrow{H_2O} H_2 + 2OH_{aq}^- \qquad (32)$$

$$e_{aq}^- + H_2O \longrightarrow H + OH_{aq}^- \qquad (33)$$

e + OH, e + H, e + e, and e + H_2O. k_w should depend on the time and pulse intensity since of these reactants only [H_2O] is constant. However, in all experiments using eq. 26 (or its corrected form eq. 27) for determining $\epsilon_e^{5780}/\epsilon_{NF^-}^{3660}$, the same pulse intensity was used, and further, since the correction introduced by k_w in the value of ϵ_e is not large, small variations in k_w change ϵ_e only by a quite small amount.

In the presence of TNM the electrons may have other side reactions in addition to those grouped in k_w. Corrections for these must also be applied. NO_2 and NF^- are products of reaction 1. In reaction 7, whose rate constant k_7 was measured as 3.0×10^{10} M^{-1} sec.$^{-1}$, not only is an electron used in a side reaction not forming NF^-, but the effect of an electron which had previously reacted in (1) is cancelled. Half of the correction for reaction 7 appears in U; the other half is applied as discussed below. For reaction 29 we have no measurement, but 3×10^{10} M^{-1} sec.$^{-1}$ might be a reasonable value for k_{29}. Correction for (7) and (29) also requires a knowledge of the effective concentrations of NF^- and NO_2 in the time interval used. From experiments described elsewhere (or even from an estimate with a bimolecular decay constant of 5×10^{10} M^{-1} sec.$^{-1}$), the decay of NO_2 is much slower than the formation of NF^- in these experiments, so that [NO_2] will closely parallel the [NF^-] resulting from reaction 1. A small amount of thermal hydrolysis of TNM in the solution before the experiment produces NF^-, H^+, and NO_3^-. For these three products the concentrations produced by hydrolysis should be $[H^+]_0 = 2[NF^-]_0 = 2[NO_3^-]_0$ and they were determined from the absorption of NF^- at 3500 Å. using a 5-cm. cell in a Beckman spectrophotometer. The rate constants are known for (28) and (24) to be 1.1×10^{10} and 2.3×10^{10} M^{-1} sec.$^{-1}$, respectively.[3,9] The rate constant for reaction of H with NF^- is unknown, but, even if it were as high as 3×10^{10} M^{-1} sec.$^{-1}$, the correction would be only 1 to 2%, so, in the absence of definite data, this correction was neglected. The value of A in eq. 27 was obtained by measuring simultaneously, in pure water which was pulse-irradiated, the absorption at 3660 and 5780 Å. A was determined as 0.145 with a standard deviation of 0.001, using ten different pictures.

In eq. 27, ΔD^{5780} was used as experimentally measured; however, the experimental ΔD^{3660} was corrected for: (1) the loss of NF^- *via* reaction 7; (2) the formation of small amounts of NF^- *via* reaction 6; and (3) the decay at 3660 Å. which has previously been discussed. For correction (1), an average concentration of NF^- was used in combination with $k_7 = 3.0 \times 10^{10}$ M^{-1} sec.$^{-1}$ to calculate the decrease in NF^- due to the reaction of $e_{aq}^- + NF^-$ during the appropriate time interval. Since this correction of ϵ_r is small (0.5–2%), the error introduced by use of a constant [NF^-] is negligible. Actually, [NF^-] changed during any time interval used by a factor of two or less. To make correction (2), it was assumed that $G_H/G_e \simeq 0.2$ and that $G_e \simeq G_{OH}$. Rate constants for reactions involving H atom disappearance were taken[14] as $k_{34} = 1.0 \times 10^{10}$ and $k_{35} = 1.2 \times 10^{10}$ M^{-1} sec.$^{-1}$. Our value for the rate constant of H + TNM (reaction 6) is 5.5×10^8 M^{-1} sec.$^{-1}$. It can be shown that initially under our conditions the rate of formation of H atoms by $e_{aq}^- + H_3O_{aq}^+$, reaction 24, and $e_{aq}^- + H_2O$, reaction 33, is slightly greater than the rate of H atom disappearance. On the other hand, only about

$$H + H \longrightarrow H_2 \qquad (34)$$

$$H + OH \longrightarrow H_2O \qquad (35)$$

5% of the e_{aq}^- will eventually form H atoms since most e_{aq}^- will decay by reaction with TNM and other species not forming H atoms. Considering these facts, it is a sufficiently good approximation to assume [H] constant during the short time intervals used in evaluating ϵ_r or k_1. With these data and assumptions, the NF^- formed by the reaction H + TNM was calculated and the appropriate amount subtracted from ΔD^{3660} in each of the time intervals used in eq. 27. Correction (3) is for the decay at 3660 Å. and was estimated from plots of the decay measured in 2×10^{-3} *M* TNM with a pulse intensity equal to that used in the ϵ_r experiments. This correction of ΔD^{3660} varied from 0 to +3.5% and opposed the effect of correction (2).

Values of ΔD^{5780} as measured are plotted in Fig. 5 against the corresponding corrected values of ΔD^{3660}. These points were compiled from four different experiments. The ΔD values plotted in Fig. 5 were obtained by the following procedure: the oscilloscope traces from an experiment, such as shown in Fig. 4, were divided into approximately equal time intervals in the region of changing *D* by selecting the same six points in time on each trace. D^{5780} and D^{3660} were measured at each point. Then each pair $D_i^{5780} - D_j^{5780}$, $D_j^{3660} - D_i^{3660}$ (cor.) were plotted in Fig. 5 where $i = 1, 2, 3, 4$, and $j = 2, 3, 4, 5, 6$ and all pairs of i and j ($i < j$) were taken for which ΔD^{3660} was greater than 0.03. All experiments corresponded to the conditions of Fig. 2 (1.96×10^{-5} *M* TNM, 48-cm. light path) for which *U* was calculated to be 0.85. The conditions determining *U* were: $[NF^-]_0 = [NO_3^-]_0 = 1.85 \times 10^{-7}$ *M*, $[H^+]_0 = 3.0 \times 10^{-7}$ *M* (corrected for dissociation of water), $[NF^-]_{av}$ including $[NF^-]_0 = 7.8 \times 10^{-7}$ *M*, $[NO_2] = [NF^-]_{av} - [NF^-]_0$, and *k*'s as previously quoted.

The slope in Fig. 5 should correspond to $\epsilon_r/(U - \epsilon_r A)$ from which $\epsilon_r = 0.975$ was determined. Adding together the errors (for the slope of Fig. 5, 2%; for *U*, 5%; and all others, 2%), and correcting ϵ_r for the fact that k_w includes a small contribution of $e_{aq}^- + e_{aq}^-$ which is second order and considerably diminished in the presence of TNM, one obtains $\epsilon_r = 0.98 \pm 0.09$. Thus $\epsilon_e^{5780} = 10{,}000$. Two earlier experiments plotted as in Fig. 5 gave $\epsilon_e^{5780} = 11{,}200$ and 12,000, respectively. The average ϵ_e^{5780} is 11,100. The differences between experiments are unexpectedly large.

Evaluation of ϵ_e^{5780} in TNM–Sucrose Solution. Since the reactions of the H and OH radicals complicate the determination of ϵ_e^{5780} in water–TNM solutions, sucrose was added to react with and eliminate these radicals. Thus the measured D^{3660} values no longer are corrected for the H + TNM correction, or for the decay at 3660

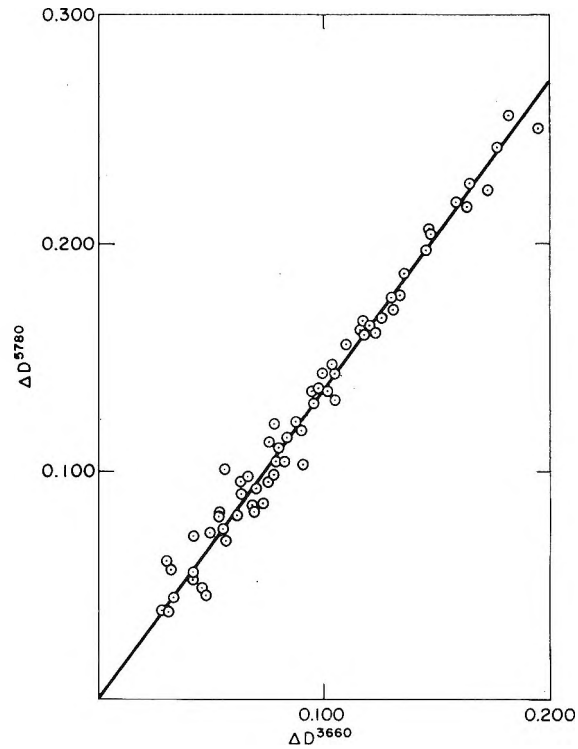

Figure 5. Evaluation of ϵ_e^{5780} in aqueous TNM. Points were obtained from four separate experiments.

Å., which was shown not to occur in sucrose solutions. (In an N_2O saturated solution 0.0104 *M* in sucrose and 3.87×10^{-5} *M* in NF^-, no decay at 3660 Å. (16-cm. optical path length) was observed after irradiation by a pulse which gave 5×10^{-6} *M* sucrose radicals.) The correction for $e_{aq}^- + NF^-$ (<2%) was still made as for TNM–water solutions. The D^{3660} was also corrected for the reaction of sucrose radicals with TNM, but these radicals react with TNM only one-fiftieth as rapidly as does e_{aq}^-. This small correction can be made rather precisely, since the rate constants for RH + TNM, k_{21}, and for $e_{aq}^- + TNM$, k_1, were measured in the same experiment used for evaluating ϵ_r. For this purpose, two scopes were used to follow the 5780 Å. absorption at 1 μsec./div. and simultaneously the 3660 Å. absorption at both 1 and 50 μsec./div. The solution used was 0.0107 *M* sucrose in 2.02×10^{-5} *M* TNM as in Fig. 4. This correction of D^{3660} amounted to ~15% after 6 μsec., where D^{5780} had just become zero, and of course decreased for shorter times.

In eq. 27, *U* is modified by using a different value of k_w, which now does not include the reactions of e_{aq}^- with H or OH. The value of $k_w = 5.6 \times 10^4$ sec.$^{-1}$ was obtained by plotting the decay of optical density at 5780 Å. in 0.0107 *M* sucrose, assuming the decay

to be first order. The pulse intensity was the same as that used in the sucrose–TNM solutions. The $D_{\infty}^{3660} = 0.930$ obtained with a light path of 48 cm. corresponds to $G_e + G_H + G_{OH}$ minus a correction due to electrons which reacted with other species than TNM as well as a correction for a possible reaction between some of the sucrose radicals. A (eq. 26 and 27) was directly determined in 0.0107 M sucrose solutions as an average from three pictures to be 0.140 ± 0.003. A very small long-lived absorption at 3660 Å. was observed, perhaps due to sucrose radicals. If a correction is made for this absorption, $A = 0.116$ would result. However, the uncorrected $A = 0.140$ agrees with the value found in pure water, and we shall make no correction, that is, we shall assume that the long-lived absorption at 3660 Å. is not formed initially, but is formed more slowly. This assumption could introduce an error into ϵ_r of ~2.5%. Further data used to compute U are: the gross first-order rate constant for e_{aq}^- decay in a solution of 0.0107 M sucrose and 2.02×10^{-5} M TNM (assumed equal to the denominator in the expression for U) = 1.02×10^6 sec.$^{-1}$, $[NF^-]_{av} = 9.8 \times 10^{-7}$ M, $[H^+]_0 = 4 \times 10^{-7}$ M, $[NO_3^-]_0 = 2.5 \times 10^{-7}$ M, and $[NO_2] = 7.3 \times 10^{-7}$ M. From these data, $U = 0.885$ was calculated and ϵ_r was estimated. Finally, the small (<1%) correction for the $e_{aq}^- + e_{aq}^-$ reaction was applied to ϵ_r, just as done for ϵ_r measured in aqueous TNM system. The final result gave $\epsilon_r = 1.03 \pm 0.11$ from the slope in Fig. 6, where ΔD^{5780} measured is plotted against ΔD^{3660} corrected as in this section. The error includes ±0.02 error in the slope in Fig. 6, ±0.05 error in U, ±0.02 in k_{21}, and ±0.01 error in the $e_{aq}^- + NF^-$ correction. In another identical set of experiments plotted as in Fig. 6, $\epsilon_r = 0.98$ was obtained, while from similar experiments in 1.91×10^{-5} M TNM in 0.104 M sucrose using a 32-cm. light path, $\epsilon_r = 0.99 \pm 0.11$. In the latter solution, $A = 0.136$ was measured neglecting the long-lived absorption at 3660 Å. Also, $(G_H + G_{OH})/G_e = 1.19 \pm 0.13$ was obtained in comparison with 1.10 ± 0.10 in the 0.0107 M sucrose solutions. The average $\epsilon_r = 1.00$ yields $\epsilon_e^{5780} = 10{,}200 \pm 1100$.

The ϵ_e^{5780} results in TNM–sucrose–water and in TNM–water solutions agree within the total estimated error, but better agreement was hoped for, since uncertainties in some corrections which are applied to both solutions increase the total estimated error, but should not affect the agreement between results in the two solutions. The authors prefer the sucrose results because we believe we can make the corrections more certainly in this system. The over-all average for the two systems is $\epsilon_e^{5780} = 10{,}600$ at pH ~7 and corresponds to[3,4] $G_e = 2.6$.

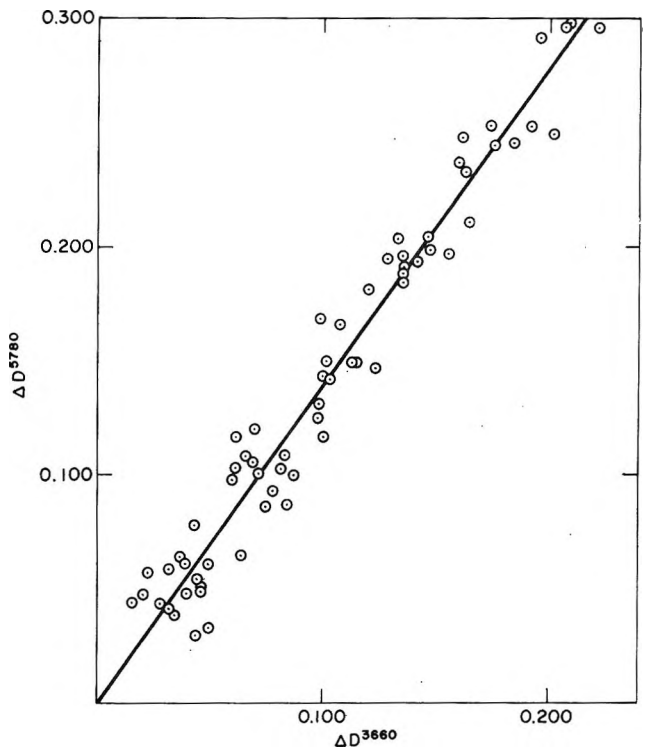

Figure 6. Evaluation of ϵ_e^{5780} in TNM–sucrose solutions. Points were obtained from four separate experiments.

The precision of this measurement can be improved by: (1) elimination of "noise" during and following the pulse (an arrangement which it is hoped will minimize the effect of Čerenkov and luminescence radiation is being constructed); and (2) by the use of shorter electron pulses than are now available to us. With such improvements a 10-fold higher concentration of TNM could be used, ensuring that more than 97% of e_{aq}^- would react with TNM and thereby reduce the corrections to be made.

Conclusion. It has been found that $k_1 = 4.6 \times 10^{10}$, $k_{21} = 5.5 \times 10^9$ for ethanol radicals, and $k_6 = 5.5 \times 10^8$ M^{-1} sec.$^{-1}$, giving ratios of 84:10:1 for the reactivity of e_{aq}^-, ethanol radicals, and H atoms toward TNM. The slower rate of reaction of TNM with H atoms as compared to e_{aq}^- is probably related to the necessity for solvation of the proton resulting from H, including O–H bond formation in H_3O^+, whereas capture of e_{aq}^- should require less reorganization of the solvent. In many reduction reactions it has been found that the rate constant for H atoms is much less than the diffusion-controlled limit (exception O_2), whereas a number of e_{aq}^- reactions are extremely fast. The temperature dependence of these rate constants, so that entropy and energy factors could be separated, would be helpful in interpreting these differences.

ϵ_e^{5780} has been directly determined. This enables evaluation of second-order rate constants previously determined as k/ϵ_e^{5780} for such reactions as $e_{aq}^- + e_{aq}^-$, $e_{aq}^- + 0^-$, $e_{aq}^- + OH$, and $e_{aq}^- + H$. ϵ_e^{5780} can also be combined with reported values of $G_e \times \epsilon_e^{5780} = 27{,}600$[4] in near neutral solution, or 28,500[3a] or 26,200[3b] in alkaline solutions, to give $G_e = 2.6$. G_e so obtained corresponds to the yield of electrons which escape the spurs by diffusion in the *absence* of scavengers. [The estimated error of 10% limits the significance of this yield of 2.6 in deciding which of the G_e scavenger measured values is correct. Actually in our opinion the 10% error estimate is a generous one.]

An experiment with an N_2O–TNM solution indicated that OH radicals do not react with TNM under our conditions to give a species absorbing at 3660 Å.

II. Oxygenated Solutions

Reduction of Tetranitromethane in the Presence of Oxygen. It is generally assumed that H atoms and electrons react with oxygen forming HO_2 and O_2^-, respectively.[25] The fate of these radicals then depends upon the radiation intensity. At low intensities they

$$H + O_2 \longrightarrow HO_2 \qquad (36)$$

$$e_{aq}^- + O_2 \longrightarrow O_2^- \qquad (37)$$

disproportionate to form H_2O_2 and O_2. The H_2O_2 formed scavenges the OH radicals so that the net result of radiolysis is a buildup of H_2O_2 with a net yield of[26]

$$G(H_2O_2) = G_{H_2O_2} + {}^1/_2(G_e + G_H - G_{OH})$$

The rate constants for the disappearance of HO_2 and O_2^- in the disproportionation reactions 38, 39, and 40

$$HO_2 + HO_2 \longrightarrow H_2O_2 + O_2 \qquad (38)$$

$$O_2^- + O_2^- \xrightarrow{H_2O} H_2O_2 + O_2 \qquad (39)$$

$$HO_2 + O_2^- \xrightarrow{H_2O} H_2O_2 + O_2 \qquad (40)$$

have been measured by several different techniques. Pulsed radiolysis,[27] flash photolysis,[28] and flow techniques[29,30] all gave $2k_{38} \simeq 2.5 \times 10^6\ M^{-1}$ sec.$^{-1}$, while pulsed radiolysis,[27] pulsed conductivity,[31] and a flow technique[30] yielded a consistent value of $2k_{39} = 2 \times 10^7\ M^{-1}$ sec.$^{-1}$. A different value for $2k_{39}$ was obtained in neutral solution with flash photolysis.[28] An upper limit of $7 \times 10^7\ M^{-1}$ sec.$^{-1}$ has been estimated[30] for k_{40}. Unless very efficiently scavenged, the HO_2 and O_2^- radicals will be maintained in equilibrium by reactions 41 and 42 with a pK of 4.4.[27,30]

$$HO_2 \longrightarrow H^+ + O_2^- \qquad (41)$$

$$H^+ + O_2^- \longrightarrow HO_2 \qquad (42)$$

Initially in neutral solutions O_2^- and HO_2 are formed with a concentration ratio of about 5, since $G_e/G_H \simeq 5$. At high radiation intensities such as are used in pulsed radiolysis experiments, the HO_2 and O_2^- radicals react to a large extent with OH radicals.[30] For reaction 43, 70% probably proceeds through the intermediate H_2O_3,[30] and an analogous intermediate may be involved in reaction 44.

$$HO_2 + OH \longrightarrow H_2O + O_2 \qquad (43)$$

$$O_2^- + OH \longrightarrow OH^- + O_2 \qquad (44)$$

If TNM is added to oxygenated water, the following reactions should be considered

$$O_2^- + C(NO_2)_4 \longrightarrow C(NO_2)_3^- + NO_2 + O_2 \qquad (45)$$

$$HO_2 + C(NO_2)_4 \longrightarrow C(NO_2)_3^- + NO_2 + H^+ + O_2 \qquad (46)$$

In our experiments we tried to establish conditions such that: (a) the e_{aq}^- and H atoms would react mostly with O_2 and not with TNM; (b) reactions 43 and 44 would be separated in time from (45) and (46), our experiments showing that TNM concentrations could be adjusted so that (43) plus (44) was faster in acid solution and (45) plus (46) was faster in neutral solution (the relatively slow reactions 38, 39, and 40 would, of course, be negligible); and (c) the dissociation of HO_2 to $H^+ + O_2^-$ would be faster than the reaction of O_2^- with TNM. With such conditions the evaluation of an accurate rate constant for $O_2^- + C(NO_2)_4$ would be fairly simple, since, as will be shown later, $k_{45} \gg k_{46}$. The desired conditions were in fact closely approached, although complications due to reactions 43, 44, and 41 do introduce a small error.

If H_2O_2 is added to an oxygenated TNM solution so that $[H_2O_2] \gg [TNM]$, then e_{aq}^- will react with it forming OH. Reaction 22 will be followed by reaction 14 to form HO_2. The H atoms will eventually yield HO_2 radicals whether they react with O_2 or H_2O_2. Above its pK the HO_2 will dissociate to H^+ and O_2^-. In this system the reactions of $HO_2 + OH$ (43) and $O_2^- + OH$ (44) are eliminated. If [TNM] is chosen low enough so that k_{45}[TNM] is much smaller than

(25) A. O. Allen and H. A. Schwarz, *Proc. 2nd Intern. Conf. Peaceful Uses At. Energy*, **29**, 30 (1958).

(26) A. O. Allen, "The Radiation Chemistry of Water and Aqueous Solutions," D. Van Nostrand, Inc., New York, N. Y., 1961, p. 40.

(27) G. Czapski and L. M. Dorfman, *J. Phys. Chem.*, **68**, 1169 (1964).

(28) J. H. Baxendale, *Radiation Res.*, **17**, 312 (1962).

(29) B. H. J. Bielski and E. Saito, *J. Phys. Chem.*, **66**, 2266 (1962).

(30) G. Czapski and B. H. J. Bielski, *ibid.*, **67**, 2180 (1963).

(31) K. Schmidt, *Z. Naturforsch.*, **16b**, 206 (1961).

both $k_{14}[H_2O_2]$ and k_{41}, then the rate of formation of NF^- can be used to measure k_{45}. Since[18] $k_{14} = 4.5 \times 10^7\ M^{-1}$ sec.$^{-1}$, the half-life for the reaction of OH + H_2O_2 is[18] about 1 μsec., using 0.02 M H_2O_2. We estimate the half-life for $HO_2 \rightarrow H^+ + O_2^-$ to be of the same order. Defining $K = k_{41}/k_{42}$, the limits of K are 1.6×10^{-5} (pK = 4.8) and 10^{-4} (pK = 4.0). By analogy with similar neutralization reactions, it seemed reasonable to assume $k_{42} = (2 \text{ to } 10) \times 10^{10}\ M^{-1}$ sec.$^{-1}$, and therefore the limits of k_{41} may be 3×10^5 to 10^7 sec.$^{-1}$, and the corresponding half-life limits 0.06 to 2 μsec. These considerations suggest that the results in Table VI represent k_{45} with only minor errors introduced by other reactions. The agreement found in the presence of H_2O_2 with only HO_2 formed initially, and in the absence of H_2O_2 with mostly O_2^- formed initially, supports the idea that the measured reaction is not limited by the dissociation of HO_2. Further, the fact that the same rate constant is obtained over a 50-fold variation of [TNM] also indicates that complications due to competing reactions were not significant. H_2O_2 absorbs enough light at 3660 Å. to make it difficult to work with more than 0.02 M H_2O_2 with a light path of 16 cm. Therefore, in the experiments with H_2O_2, in order to avoid photolysis, a filter eliminating light below 3400 Å. was used and the solutions were not exposed to the analyzing light beam for more than 1 min. while making the necessary oscilloscope adjustments. Indeed, these precautions were followed also where no H_2O_2 was present.

Table VI: The Reactivity of O_2^- with TNM[a]

[TNM], $M \times 10^5$	$[H_2O_2]$, M	Final optical density	pH[b]	k_{45}, M^{-1} sec.$^{-1}$ $\times 10^{-9}$
1.5[c]	0.02	0.18	6.2	2.65
2.9	0.02	0.65	6.2	2.0
3.7[c]	0.02	0.18	6.1	1.9
7.5[c]	0.01	0.19	6.1	1.5
17.2	...	0.64	6.0	1.9
18.5	...	0.40	6.0	2.0
30.8	...	0.62	5.7	2.3
35.8	...	0.71	5.8	1.6
58.6	...	0.71	5.8	1.45
69.0	...	0.68	5.6	1.65

[a] Solutions O_2 saturated except where otherwise stated; 16-cm. light path used. [b] Measured before pulse. [c] Air saturated.

Each value for k_{45} in Table VI is the average of two to four experiments. For each experiment, the variation of optical density, D, with time, t, was plotted according to eq. 47, and k_{45} was calculated from the slope

$$\ln [(D_\infty^{3660} - D_t^{3660})/D_\infty^{3660}] = -k_{45}[\text{TNM}]t \quad (47)$$

of the resulting line. In experiments without added H_2O_2 there was a fast initial rise in D, due to the direct reaction of e_{aq}^- with TNM, and this was followed by a slower rise due to the reaction of O_2^- with TNM. The ratio of the optical density at the end of the rapid rise to the increase in optical density during the slower reaction agreed with the ratio deduced from the known rate constants for $e_{aq}^- + \text{TNM}$ and $e_{aq}^- + O_2$.[3a,4,9] However, in oxygenated solutions some loss of oxygen occurred during transfer of solution to the cell (usually 10–20%) (see ref. 9 for transfer technique) as this transfer was not carried out under an oxygen atmosphere. Further, there was not a sharp limit ("noise" immediately following the pulse tended to obscure this limit) between the first rapid rise and the subsequent slow increase in D. Therefore, our directly measured k_1 is considered to be more accurate than the value deduced from the competition with O_2, as determined from the ratio of optical density changes discussed above. From this ratio of optical density changes $k_1/k_{37} = 2.3 \pm 0.7$ was obtained assuming $[O_2] = 8 \times 10^{-4}\ M$ in the oxygenated solutions.

The pH values in Table VI were measured with evacuated solutions subsequently exposed to air during the pH measurement so that CO_2 absorption probably occurred. Therefore, as the solutions were evacuated before oxygenation, these pH values are lower limits since no buffer was added. If the actual acidities of the evacuated solutions before irradiation were due to hydrolysis of TNM, then the measured absorptions due to NF^- definitely would indicate higher pH values than those in Table VI. On the other hand, hydrogen ions are formed by the pulse of electrons in concentrations of ~1 to $4 \times 10^{-6}\ M$ (see optical densities, Table VI), so that in some experiments the effective pH was only about 1 pH unit above the pK of HO_2. However, this would still mean 90% O_2^- to 10% HO_2 at equilibrium, while G values indicate[15b] that with only O_2 present the originally formed yields would be ~85% O_2^- and ~15% HO_2. Our conclusion is that k_{45} in Table VI is not lowered by more than 10% by the presence of some of the radical in the HO_2 form. The effect in low intensity experiments would be much less than 10%. No correction has been made for this effect. Each value of k_{45} in Table VI, being the average of a number of experiments, n, was given a weight n, and the over-all least-squares average was calculated as $(1.9 \pm 0.4) \times 10^9\ M^{-1}$ sec.$^{-1}$.

The Effect of pH in Oxygenated Solutions. For the pseudo-first-order reaction of O_2^- with TNM where

the absorbing species NF^- is formed, eq. 47 was used to calculate k_{45} under conditions such that little if any HO_2 was present. If both O_2^- and HO_2 react with TNM, then the rate of formation of NF^- is given by

$$\frac{d[NF^-]}{dt} = k_{45}[TNM][O_2^-] + k_{46}[TNM][HO_2] \quad (48)$$

If reactions 45 and 46 are slow compared to reactions 41 and 42 so that O_2^- and HO_2 are always in equilibrium, then one can substitute $[O_2^-][H^+]/K$ for HO_2 in eq. 48.

$$\frac{d[NF^-]}{dt} = \{k_{45} + k_{46}[H^+]/K\}[TNM][O_2^-] \quad (49)$$

One can manipulate the equilibrium equation for O_2^- and HO_2 to obtain (50), where the subscript, ∞, refers

$$[O_2^-] = ([HO_2] + [O_2^-])/(1 + [H^+]/K)$$
$$= ([NF^-]_\infty - [NF^-])/(1 + [H^+]/K) \quad (50)$$

to final concentration and the other concentrations are at time t. Substitution of (50) into (49) yields

$$\frac{d[NF^-]}{dt} = \frac{k_{45} + k_{46}[H^+]/K}{1 + [H^+]/K}[TNM]([NF^-]_\infty - [NF^-]) \quad (51)$$

which integrates, if [TNM], the pH, and the ionic strength are constant, to

$$\ln \frac{[NF^-]_\infty}{[NF^-]_\infty - [NF^-]} = \frac{Kk_{45} + k_{46}[H^+]}{K + [H^+]}[TNM]t \quad (52)$$

or

$$\ln \frac{D_\infty}{D_\infty - D} = Q[TNM]t \quad (53)$$

where Q is defined as $Q = (Kk_{45} + k_{46}[H^+])/(K + [H^+])$. In a given experiment, a plot of ln $(D_\infty - D)$ *vs.* t yields a straight line from whose slope the effective rate constant, Q, may be determined. At higher pH values above the pK of HO_2, $K \gg [H^+]$ and $Q = k_{45}$ since experiments showed $k_{45} > k_{46}$. Under these conditions Q should be independent of $[H^+]$. However, as can be seen from the previous discussion, it is difficult to maintain a constant pH near neutrality without the use of a buffer and we preferred not to use buffers in order to avoid possible complications in the mechanism.

If $[H^+] \gg K$ and if $[H^+]k_{46}$ were much greater than Kk_{45}, then again Q would be independent of pH and equal to k_{46}. However, even at a pH as low as 0, Q was found to be pH dependent showing that $k_{46} \ll k_{45}$ and that the term $k_{46}[H^+]$ may be neglected when the pH is greater than 0. This term may be significant at pH 0, even though our results can reasonably well be fitted by neglecting it, since corrections made for ionic strength are not accurate in this region. We conclude that the term $k_{46}[H^+]$ may be neglected for pH 0.5 and greater and perhaps also at 0.

Table VII: The Reactivity of the O_2^-–HO_2 Equilibrium Mixture with TNM

[TNM], $M \times 10^5$	D_∞[a]	Acid added	pH	Q, M^{-1} sec.$^{-1}$
34.3[b]	0.70	H_2SO_4	5.0	1.1×10^9
34.5[b]	0.61	H_2SO_4	4.9	1.2×10^9
37.2[b]	0.65	H_2SO_4	4.57	6.9×10^8
34.5[b]	0.57	H_2SO_4	4.51	1.0×10^9
35.7[b]	0.67	H_2SO_4	4.22	4.5×10^8
1.46[c]	0.26	2×10^{-4} N H_2SO_4	3.70	2.8×10^8
3.61[c]	0.41	1.9×10^{-3} N H_2SO_4	2.75	4.4×10^7
3.61[c]	0.10	1.8×10^{-2} N H_2SO_4	1.85	7.3×10^6
7.3[c]	0.11	1.9×10^{-2} N H_2SO_4	1.83	6.5×10^6
7.4[b]	0.15	2.0×10^{-2} N H_2SO_4	1.81	7.2×10^6
15.0[c]	0.36	2.0×10^{-2} N H_2SO_4	1.81	5.7×10^6
4.1[d]	0.15	2.0×10^{-2} N $HClO_4$	1.70	4.8×10^6
11.2	0.25	0.1 N H_2SO_4	1.17	1.9×10^6
37.2	0.24	0.1 N H_2SO_4	1.17	2.3×10^6
50.5	0.33	0.08 N $HClO_4$	1.10	1.6×10^6
43.4	0.31	0.2 N $HClO_4$	0.70	7.5×10^5
14.5	0.16	0.8 N H_2SO_4	0.32	5.5×10^5
15.2	0.18	0.8 N H_2SO_4	0.32	5.6×10^5
58.0	0.21	0.8 N H_2SO_4	0.32	4.8×10^5
43.4	0.26	0.5 N $HClO_4$	0.30	3.8×10^5
14.4	0.14	1.0 N $HClO_4$	0.00	2.0×10^5
43.4	0.17	1.0 N $HClO_4$	0.00	1.9×10^5

[a] A 16-cm. light path was used unless otherwise stated. [b] O_2-saturated, all other experiments air-saturated. [c] $[H_2O_2]$, 0.02 M, added. [d] Light path was 48 cm.

Table VII presents values of Q at different pH values, each value being the average of two to four experiments. Other experimental parameters varied were radiation intensity (measured by D_∞), TNM concentration, and the presence and absence of H_2O_2. Q decreases with decreasing pH. In the sulfuric acid experiments the pH was calculated from the first hydrogen to be completely ionized and the second ionized according to the relationship[32] $[H^+][SO_4^{-2}]/[HSO_4^-] = 0.0102 \times 10^{2.036\sqrt{\mu}/(1+0.4\sqrt{\mu})}$, where μ is the ionic strength.

(32) C. F. Baes, *J. Am. Chem. Soc.*, **79**, 5611 (1957).

D_∞ in Table VII is the optical density due to NF^- after all O_2^- and HO_2 have reacted. In the more acid region (definitely at pH 2 but not in neutral) the reaction due to O_2^- plus HO_2 was followed by a further slow formation of NF^- with a reaction lifetime of minutes. This very slow reaction was easily separated, and with fast oscilloscope sweep rates a plateau was readily observed at the end of the O_2^-–HO_2 reaction. The values of D_∞ in Table VII were obtained from this first plateau and do not include the absorption resulting from the slow reaction. Bielski and Allen[6] found a higher $G(NF^-)$ in acid as compared to neutral solution and pointed out that another reaction in addition to (45) and (46) occurs at low pH. We did not investigate the details of the slow reaction, which we presumed might be the reaction referred to by Allen and Bielski.

D_∞ is a measure of the electron beam intensity with two reservations: (a) At pH values below 3, the apparent ϵ_{NF^-} decreases, probably because of the formation of undissociated nitroform, $HC(NO_2)_3$ (see Allen and Bielski, ref. 6). (b) If H_2O_2 is absent but $Q \times [TNM]$ is high (and this is true for all experiments above pH 4.2) then D_∞ is a measure of all $O_2^- + HO_2$ radicals. However, for experiments in the absence of H_2O_2 at lower pH, a part of the HO_2 reacts with OH radicals and does not yield NF^-.

Neglecting the term $k_{46}[H^+]$, as seems justified by our results, one can rearrange the definition of Q.

$$\frac{1}{Q} = \frac{1}{k_{45}} + \frac{[H^+]}{Kk_{45}} \qquad (54)$$

Since reaction 42 should depend on the ionic strength, μ, while reaction 41 does not, we set $K = K_0 \times 10^{\sqrt{\mu}/(1+\sqrt{\mu})}$, where K_0 is the equilibrium constant at zero ionic strength.[33] Then (54) becomes

$$\frac{1}{Q} = \frac{1}{k_{45}} + \frac{[H^+] \times 10^{-\sqrt{\mu}/(1+\sqrt{\mu})}}{k_{45}K_0} \qquad (55)$$

A least-squares fit of $1/Q$ against $[H^+] \times 10^{-\sqrt{\mu}/(1+\sqrt{\mu})}$ was calculated for experiments in the pH region 1.8 to 4.6 (Table VII). Data at higher pH were not included, since the pH values are less certain and the O_2^-–HO_2 equilibrium may not be rapidly and fully established. Values of Q at lower pH were excluded because the correction for ionic strength is large, and worse, the theory is not expected to be valid at such high values of μ. Then from the slope and the intercept (eq. 55), $k_{45} = 1.3 \times 10^9\ M^{-1}$ sec.$^{-1}$ and $pK_0 = 4.25$. Excluding the two experiments at pH 4.57, $k_{45} = 1.5 \times 10^9\ M^{-1}$ sec.$^{-1}$ and $pK_0 = 4.31$. This result is in fair agreement with the averaged result from Table VI, $k_{45} = 1.9 \times 10^9\ M^{-1}$ sec.$^{-1}$. However, this latter value is considered more reliable than the extrapolated one, since the corrections discussed would raise the values in Table VI and not lower them. Fixing the intercept by using $k_{45} = 1.9 \times 10^9\ M^{-1}$ sec.$^{-1}$, the new least-squares calculation gave $K_0 = (3.43 \pm 1.12) \times 10^{-5}\ M$. Assuming that the error in k_{45} is $\pm 30\%$ (this includes 21% standard deviation plus a possible 10% consistent error), $pK_0 = 4.45 \pm 0.25$, in excellent agreement with other values.[27,30]

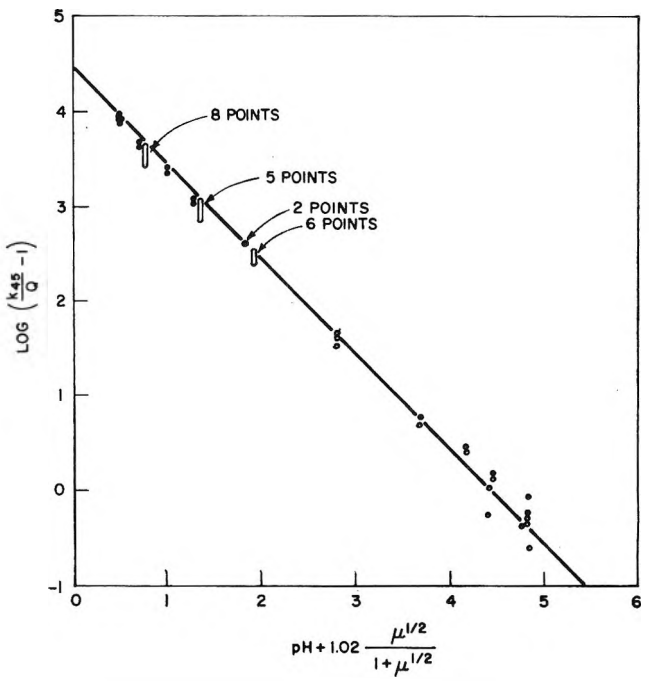

Figure 7. The effect of pH on Q (the effective rate constant for reaction of ($HO_2 + O_2^-$) with TNM): O, pH adjusted with H_2SO_4; ●, pH adjusted with $HClO_4$.

Equation 55 can be rearranged to

$$\log\left(\frac{k_{45}}{Q} - 1\right) = pK_0 - pH - \sqrt{\mu}/(1 + \sqrt{\mu}) \qquad (56)$$

The experimental points in Table VII have been used in Fig. 7 plotting the left-hand side of eq. 56 *vs.* [pH + $\sqrt{\mu}/(1 + \sqrt{\mu})$]. Only the points between pH 1.8 to 4.6 were used to determine the line in Fig. 7, but all the points fit the straight line rather well, even in the low pH range where the ionic strength correction for K was not expected to be valid. The intercept on either axis gives pK_0. From Fig. 7 we also conclude that

(33) This expression follows from Brønsted, Bjerrum, and Scatchard theories of ionic solutions: S. W. Benson, "The Foundations of Chemical Kinetics," McGraw-Hill Book Co., New York, N. Y., 1960, p. 525.

$k_{45} > 10^4 k_{46}$, so that the reaction of HO_2 + TNM is apparently negligible in all our experiments.

Acknowledgment. We wish to thank Ed. Backstrom, whose careful Linac operation was essential for the precision attained in these results, Steve Petrek for construction and maintenance of electronic equipment, and Miss Lynn Bogur of Rockford College, who as a summer student aide gave valuable help in carrying out experiments and calculations. We also are greatly indebted to Dr. B. H. J. Bielski of Brookhaven National Laboratory for information on procedures for handling and purifying TNM and for unpublished data on the steady-state radiolysis of TNM.

Volumetric Studies of Ion-Exchange Resin Particles Using Microscopy

by David H. Freeman

Department of Chemistry, Washington State University, Pullman, Washington

and George Scatchard

Department of Chemistry and Laboratory of Nuclear Science, Massachusetts Institute of Technology, Cambridge, Massachusetts *(Received May 4, 1964)*

Volume measurements of ion-exchange resin particles are obtained from diameter measurements after establishing equilibrium in varied concentrations of aqueous HCl, LiCl, NaCl, and KCl. The volume of cation-exchange resins, equilibrated in water and then immersed in concentrated LiCl, passes through a minimum and slowly increases to reach equilibrium.

The volume swelling of ion-exchange resin is a property of fundamental importance to the understanding and application of ion-exchange processes. Classical methods of measuring resin volume give discordant results; this is described in the work of Gregor, Held, and Bellin[1] and is further discussed by Scatchard and Anderson.[2] The latter workers investigated the errors of weighing centrifuged resin particles. Later, it was found[3] that low cross-linked resin may lose internal water during centrifugation. Such considerations led to the present efforts to refine the precision and accuracy of microscopic measurements of ion-exchange resin particle size.[4] The obvious advantage is that the measured particle is immersed in a given medium with no disturbance of the state of the system by measurement. We have investigated the accuracy of microscope measurements at low magnification (300×, or less) and find it possible to measure particle diameters rapidly, and with 0.1% relative error, or slightly less. In addition to the study of resin volume at equilibrium, the measuring microscope can be effectively applied to the study of resin swelling rates.

The feasibility of precise particle size measurements depends upon the particle geometry and the quality of

(1) H. P. Gregor, K. M. Held, and J. Bellin, *Anal. Chem.*, **23**, 620 (1951).

(2) G. Scatchard and N. E. Anderson, *J. Phys. Chem.*, **65**, 1536 (1961).

(3) A. T. Schwartz, Ph.D. Thesis, Department of Chemistry, Massachusetts Institute of Technology, 1963. We have confirmed this.

(4) Others have used this method. See, for example, C. Calmon, *Anal. Chem.*, **24**, 1456 (1952).

the optical and mechanical components used in the measurements. Ion-exchange resin particles that are derived from suspension copolymerized styrene–divinylbenzene are almost, but not quite, perfect spheres. The accuracy of diameter measurements is asphericity limited, so that less than 0.1% errors in the average diameter would only be obtained with access to higher than the usual degree of particle sphericity. The measuring components meet available standards of high quality as furnished by a good apochromatic objective, achromatic substage condenser, and a microscope free from focusing backlash. The measurements further depend upon conditions of illumination, alignment, and mechanical precision that have been described elsewhere[5] in connection with the accurate determination of microscope magnification and its variation with object size.

The systematic errors are handled by an equation of measurement[5] which relates the image size D to the particle size d

$$d = \frac{D + \delta}{M} + \epsilon$$

where the magnification M is independently corrected for distortion and periodic screw errors, δ. The edge error ϵ can be estimated from other work[6–8] which gives $\epsilon = -0.2\ \lambda/(\text{N.A.})$, with a calculated value of $-0.4\ \mu$ in the present work.[9] Instead of using this value, we determined ϵ as an assumed constant for each observer–microscope combination to within 0.3 μ on the basis of measured test particles furnished to us by the Bureau of Standards.[10] The study of resin particles was confined to particle diameters of 300 μ, or larger, so that the accuracy was within a maximum tolerance of 0.1% in the measured diameters. In the next section are described the experimental aspects of working with single resin particles, methods of establishing equilibrium, and studies of swelling in various aqueous electrolyte solutions.

Experimental

Materials. Samples of anion-exchange and cation-exchange resins of the styrene–divinylbenzene copolymer type, Dowex 1 and Dowex 50W, respectively, of various degrees of cross linking were obtained from the Dow Chemical Co. and thoroughly conditioned by washing with alternating base and acid, followed by ethanol and conductivity water. The ethanol wash was followed by vapor-phase transfer of water to the resin in a desiccator in order to prevent possible resin damage due to shock swelling. Reagent grade electrolyte solutions were prepared using conductivity water and were analyzed by potentiometric titration.

Sample Preparation. Particles that were free from apparent asphericity and internal flaws were selected under a survey microscope. A probe was used to isolate a selected particle, and transfer into a desired solution was accomplished by withdrawing the particle into a dropper pipet containing the same solution. When necessary, particles were drained and washed on a fine porous glass frit using suction. Temperature was controlled by air thermostating at 23 ± 0.5°.

Individual particles were transferred to a cell made by cementing a glass annulus (A. H. Thomas Catalog No. 7050) to a standard microscope slide using epoxy cement ("Crystal Clear," Epoxy Coatings Co., South San Francisco, Calif.). The cell was filled with solution, covered with a No. $1^1/_2$ cover slip, and then sealed around the edge of the cover slip with vinyl cement (Carter's Ink Co.). For kinetic studies, a small air bubble was sealed into the cell and caused agitation during rotation of the cell at 20 r.p.m.

Microscope Measurements. Most of the visual measurements of particle size were made with a Cooke, Troughton, and Simms image splitting ocular attached to an E. Leitz Ortholux microscope equipped with a Berek condenser and a 12.5× apochromat objective. The light was passed through a heat filter followed by a 550-mμ interference filter before entering the condenser. Each particle image was carefully centered and focused to determine the average focus level. Köhler illumination at constant aperture was precisely achieved. In most cases, the fullest aperture of the condenser was used. For 1% cross-linked resin, however, it was necessary to increase the image relief by stopping to six-tenths of the maximum aperture. The setting was determined by measuring the relative light intensity in the ocular position with a photometer. Then, four sets of four diameter measurements each were obtained every 45° by rotating the ocular.

A statistical analysis was made of several hundred particle measurements obtained with the image splitting ocular. This confirmed the expectation that the

(5) D. H. Freeman, *Appl. Opt.*, 3, 1005 (1964).

(6) A. A. Michelson, *J. Opt. Soc. Am.*, 8, 321 (1924).

(7) R. P. Loveland, *ASTM Bull.*, 143, 94 (1952).

(8) H. Schedling, *Acta Phys. Austriaca*, 2, 13 (1948); *ibid.*, 3, 293 (1949).

(9) There may be a small additional error upon varying the relative refractive indices of particle and medium, as reported by Bishop, *J. Res. Natl. Bur. Std.*, 12, 173 (1934). However, Loveland (ref. 7) points out the dependence of observer judgment upon image relief, or contrast, so that refractive indices *per se* become of secondary significance.

(10) The standard particles were four polystyrene balls, 0.4 to 0.7 mm. in size, that were measured by the National Bureau of Standards. Sizes were measured interferometrically at varying deformations of 0.2%, or less, under 2.7- to 0.7-g. loads; the measurements were then extrapolated to zero load.

consistency of volume measurements of the same particle in varied swelling states deteriorated with increasing particle asphericity. Those particles with an oriented diameter that deviated by 0.5% or more from the average were found likely to show volume deviations in excess of 0.3%; these were rejected from the study. It was also evident that the slightest internal crack or visible flaw would preclude precise measurements. When an occasional particle did inexplicably develop such a flaw, the entire set of measurements on that particle was rejected.

A portion of the measurements to be reported was obtained by photoelectric comparator measurements of photographic plates that were exposed to the magnified particle images. The conditions of exposure, and particularly of plate development, had to be controlled precisely in order to attain precise measuring criteria. This approach is discussed elsewhere.[5,7] The precision of photomicrographic plate measurements, at least for a given diameter orientation, was tenfold better than that obtainable by visual measurements. However, its achievement required considerably more time, and some experience with precise photographic methods. These techniques were especially useful in the study of particle asphericity. After determining that the magnification did not vary detectably upon rotation of the axis of measurement, it was found that the particle images were not circular, but showed characteristic deviations of 0.1% from the average diameter. The deviations were irregular and apparently random, implying the absence of ellipsoidal and of oblate spheroidal geometry. During kinetic swelling measurements, however, distorted geometry usually developed and caused a loss of precision which improved upon approaching swelling equilibrium.

Results

Kinetic Measurements. Swelling equilibrium was established upon attainment of constant particle diameter. Most of the equilibria studied with anion-exchange resins were reached within a few hours, although agitation times were extended up to 2 days. A similar situation was found with cation-exchange resins, but the swelling rates in concentrated LiCl solutions were found to be exceptionally slow.

When lithium form cation-exchange resin was transferred from water or dilute LiCl solution to 10 *m* (or higher) LiCl, the volume decreased very rapidly and then increased slowly until equilibrium was reached. An example of this behavior is shown as the upper curve in Figure 1. Similar but more rapid behavior was observed when water-swollen sodium form resin was immersed in concentrated NaCl solution. The volume

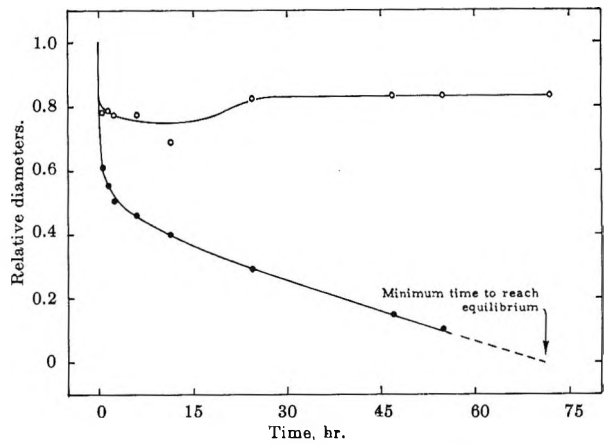

Figure 1. External diameter and apparent diffusion boundary dimensions shown as upper and lower curve, respectively. Initial conditions: 500-μ particle of lithium resinate, 8% divinylbenzene, in water. Zero time corresponds to immersion in 20 *m* LiCl. Compare this to Figure 5 of ref. 11.

minimum is explained by an initially rapid osmotic dehydration of the cation-exchange resin, followed by a slower inward diffusion of electrolyte and water. The first process impedes the second. After the first several minutes of the deswelling shown in Figure 1, an interference pattern was observed to be similar to that discussed by Gurney.[11] Later, an infusion gradient became visible with ordinary illumination. The measurements of the apparent dimension of this shell are shown by the lower curve in Figure 1. These are not the actual dimensions because the resin behaves as a lens. However, the contraction and disappearance of the shell or the disappearance of the optical anisotropy of the particle provides sensitive criteria for the minimum time required to reach the state of equilibrium.

The minimum agitation periods necessary for the achievement of swelling equilibrium with 1% cross-linked cation-exchange resin were approximately 20 and 40 hr. for a 500-μ diameter particle in 15 and 20 *m* LiCl, respectively; for 16% divinylbenzene the corresponding times were approximately 50-fold larger.

Swelling equilibrium was rapidly reached in water or dilute solution although an irreproducible size increase was usually observed as early as 30 min. after immersion. In one instance, this artifact was found to have been caused by an accumulation of a *penicillium* fungus[12] on the bead exterior.

Equilibrium Measurements. The equilibrium swelling of various resins was studied in aqueous solutions of

(11) E. Gurney, *J. Polymer Sci.*, **138**, 119 (1959).

(12) We are grateful to Dr. H. M. Kakata, Department of Bacteriology, Washington State University, for the identification of the fungus.

Table I: Swelling Properties of Ion-Exchange Resins in Aqueous Solution

Resin	C	q	Electrolyte	Volume relative to that in pure water (R) 0.2 m	0.5 m	1.0 m	1.5 m	2.0 m	4.0 m	6.0 m	10.0 m	15.0 m	20.0 m
Dowex 1-X1	5.00	5.23	HCl	0.89	0.77	0.73	0.75	0.75	0.76	0.78			
			LiCl	0.875	0.760	0.712	0.702	0.700	0.719	0.719			
			NaCl	0.878	0.755	0.698	0.681	0.672	0.655	0.637			
Dowex 1-X2	4.95	4.13	HCl	0.916	0.817	0.788	0.780	0.782	0.834	0.854	0.87	0.91	
			LiCl	0.864	0.780	0.743	0.732	0.726	0.735	0.750	0.747		
			NaCl	0.870	0.777	0.722	0.697	0.686	0.677	0.680			
Dowex 1-X7.5	4.38	1.65	HCl	0.991	0.980	0.964	0.962	0.964	0.981	0.993	1.005	1.006	
			LiCl	0.991	0.981	0.966	0.955	0.947	0.928	0.919	0.909	0.906	
			NaCl	0.990	0.978	0.960	0.946	0.933	0.902				
				0.995	0.985	0.972	0.959	0.949	0.924				
Dowex 50W-X1	6.89	6.68	LiCl					0.587			0.253	0.260	0.257
Dowex 50W-X4	7.26	2.95	LiCl					0.755			0.481	0.434	0.434
Dowex 50W-X8	5.71	1.97	HCl	0.991	0.977	0.952	0.928	0.906	0.832	0.788	0.733	0.692	
			LiCl	0.991	0.977	0.955	0.933	0.912	0.834	0.775	0.682	0.605	
			NaCl	0.987	0.971	0.949	0.931	0.915	0.872				
			KCl	0.990	0.976	0.955	0.935	0.916	0.855				
Dowex 50W-X12	5.91	1.48	LiCl					0.940			0.765	0.732	0.711
Dowex 50W-X16	5.40	1.26	LiCl					0.958			0.855	0.819	0.797

HCl, LiCl, NaCl, and KCl. Alternately high and low electrolyte concentrations were measured in succession in order to detect inconsistencies and demonstrate reproducibility. Single particles of ion-exchange resin were thus found to undergo cyclic variations of swollen volume with no evident irreproducibility, except for the rare instances noted earlier. Good agreement was also found in the swelling properties of different particles selected from the same resin sample. Such comparisons led to the initial conclusion that these materials were essentially homogeneous and apparent confirmation of this was reported.[13] In later work, small but real differences in the swelling properties of different particles were identified and a separate study of this is to be reported.

The results of the swelling measurements were treated by finding the swelling ratio R for each particle: volume in electrolyte solution divided by the corresponding particle volume in water. The swelling ratios were then averaged at each concentration among the three or more particles taken from each resin sample. The interpolated results are presented in Table I with the sodium or chloride dry exchange capacity, C (mequiv./ml.), and wet to dry volume ratio, q. The consistency and accuracy is that of the experimental precision or 0.3% tolerance in the measured volume. The extent to which the averages reflect the bulk swelling properties depends upon the control of sampling and homogeneity factors. The maximum error is estimated at approximately 0.5% for all but the 16% divinylbenzene resins.

The results are consistent with those of Scatchard and Anderson[2] on the weight of Dowex 50W-X8 and Dowex 1-X8 in HCl and NaCl, but they are more extended in the range of electrolyte concentration, electrolyte type, and resin cross linking. The results also agree with the measurements of Gregor and co-workers[1] although the present work is considerably more precise. This is especially evident in the study of swelling in LiCl solution with Dowex 50W-X8 where the method of centrifugal filtration appears to become fairly erratic as the viscosity increases.

The most notable characteristic of the swelling measurements is the marked difference between anion-exchange and cation-exchange resins. The volumes of the cation-exchange resins decrease steadily with increasing electrolyte concentration, though less rapidly at high concentrations. The volumes of the anion-exchange resins start to decrease at the same or higher rate and then tend to pass through minima. This behavior becomes less marked in the series HCl, LiCl, NaCl, and KCl. The anion exchangers show substantially larger differences with different cations although they are all in the chloride form. In contrast, the cation exchangers are resinates of different cations in the different electrolyte solutions but exhibit substantially smaller differences among their relative volumes in the different solutions.

Acknowledgments. This study was started at the

(13) W. D. Moseley, Jr., and D. H. Freeman, *J. Phys. Chem.*, 67, 2225 (1963).

Massachusetts Institute of Technology where it received the financial support of the U. S. Atomic Energy Commission under Contract AT(30-1)-905. The work was completed at Washington State University under Contract AT(45-1)-1544. Several stimulating discussions of the measurement problems were held with Dr. Roger P. Loveland of the Eastman Kodak Research Laboratory and with Professor Arthur C. Hardy of the Massachusetts Institute of Technology. We are grateful to Miss Mary Hood, Miss Cathy Butts, and Mr. John Marvin, who helped with visual measurements of particle swelling.

Infrared Spectra of Solid 1:1 Pyridine–Benzoic Acid Complexes; the Nature of the Hydrogen Bond as a Function of the Acid–Base Levels in the Complex[1]

by S. L. Johnson and K. A. Rumon

Mellon Institute, Pittsburgh, Pennsylvania 15213 *(Received May 6, 1964)*

The spectroscopic properties of 18 strongly hydrogen-bonded pyridine–benzoic acid adducts have been correlated with the ΔpK value of the complex. As the critical ΔpK for proton transfer is approached from either side of the critical region, increased broadening of the ν-NH or ν-OH and ν-C=O bands is observed. Also, strong background absorption below 1200 cm.$^{-1}$ occurs. At the critical ΔpK value, discontinuous changes take place in the ν-C=O and ν-C—O regions of the spectrum, indicating that the adducts are either predominantly ionized or are predominantly un-ionized. In all of the complexes, either no band above 1700 cm.$^{-1}$ could be ascribed to ν-OH or ν-NH, or two bands near 1900–2000 and 2500–2600 cm.$^{-1}$ could be attributed to these modes. These two situations have been interpreted as corresponding to single-minimum- or near single-minimum-type and double-minimum-type hydrogen bonds, respectively. The single-minimum-type, hydrogen-bonded complex occurs only when its ΔpK is close to the critical ΔpK for proton transfer as determined from the ν-C—O and ν-C=O bands.

Introduction

A study of the benzoic acid–pyridine system in the liquid state led Hadzi[2] to conclude that the strong hydrogen bond formed between the acid and the base was of the double-minimum type with a low potential barrier, giving rise to two OH stretching frequencies. The solid state spectra of nicotinic and isonicotinic acids gave similar results. In nonhydroxylic solvents, on the other hand, infrared[3a] and ultraviolet[3b] studies indicate that pyridine and carboxylic acids exist in two tautomeric forms, that is, a double-minimum potential prevails, but the central barrier is high. The infrared study, however, dealt only with C=O stretching and ring vibrations, and not with ν-OH or ν-NH.

(1) This investigation was supported in part by Public Health Service Grant GM 11834-01 from the National Institutes of Health.

(2) (a) D. Hadzi, *Vestn. Sloven. Kem. Drustva*, **1**, 21 (1958); (b) *Z. Elektrochem.*, **62**, 1157 (1958).

(3) (a) G. M. Barrow, *J. Am. Chem. Soc.*, **78**, 5803 (1956); (b) J. Nasielski and E. Vander Donckt, *Spectrochim. Acta*, **19**, 1989 (1963).

The present study deals with the infrared spectra of solid state complexes, benzoic acid and substituted benzoic acids with pyridine and substituted pyridines. A gradual variation between the acid–base levels of the reactants may be achieved, and the type of hydrogen-bonding interaction may be studied as a function of ΔpK, where ΔpK refers to the difference in pK_a of the pyridinium ion and the benzoic acid in water. Two extremes in interaction may be envisaged: B--HA and BH^+--A^-, where B represents the pyridine base and HA represents the carboxylic acid. In the current work we are trying to determine the nature of the intermediate state, B--H--A, and the value of the critical ΔpK associated with this state. In this intermediate state, A may not have a full negative charge, and B may not have a full positive charge. In the crystalline state a tautomeric equilibrium between AH--B and A^---HB^+ species is not likely; therefore, the intermediate state would be expected to have only one structure. Our cooling experiments have borne this out.

In order to assess fully the nature of the hydrogen bond in the series of pyridine–carboxylic acid adducts, the spectra of the parent acid, its sodium salt, the adduct, the pyridine, and the protonated pyridine have been recorded. Additional information is derived from the spectra of the deuterated acid, the deuterated adduct, and the adduct dissolved in a solvent.

Spectral Areas of Interest. The frequency of the stretching mode of NH or OH is an index[4] to the hydrogen-bond strength and dimensions. However, in the case of very short hydrogen bonds of the "symmetrical type" $[A–H–A]^-$ or $[B–H–B]^+$ either a single band under 1700 cm.$^{-1}$ or two bands in the 1700–2800-cm.$^{-1}$ region have been encountered.[5–12] The exact spectral location of these bands has little correlation with the actual dimensions, and, presumably, strength of the hydrogen bond in the case of short, strong bonds. By comparison[13–15] of the infrared data with crystallographic, n.m.r., and far-infrared data, it is generally accepted that the appearance of two widely separated ν-NH or ν-OH bands coincides with a double-minimum potential function for the proton-stretching motion with a low barrier separating the two minima; a single ν-NH or ν-OH below 1700 cm.$^{-1}$ corresponds to a single-minimum potential function for the hydrogen bond.

In the current work we are dealing with the unsymmetrical system A–H–B. Such systems have been theoretically discussed.[6,16] A variety of spectroscopic results is possible in the fundamental region: one to four hydrogen stretching modes may be infrared active, depending upon such factors as the energy relationships between the transitions (*i.e.*, the shape of the potential function) and the relative intensities of the possible bands. It is interesting to note that ferroelectric compounds with short hydrogen bonds exhibit nearly the same spectra in their antiferroelectric, symmetric double-minimum state as in their ferroelectric, unsymmetrical state.

When two ν-OH or ν-NH frequencies are found in double-minimum H-bonds, it is usually difficult to locate the lower frequency vibration in the deuterated analog.[2,5,7,8] Possibly this is because the lower frequency broad ν-ND or ν-OD band shifts into the ring vibration region where it remains unknown because strong, sharp ring modes are superimposed upon it. Other possibilities include a greatly diminished splitting of the energy levels or a change in the relative intensities of the two bands upon deuteration.

Bands in the 1200–1750-cm.$^{-1}$ region characteristic of RCO_2H or RCO_2^- are of importance in establishing the state of ionization of the RCO_2H moiety of the complex. In the 1200–1350-cm.$^{-1}$ region are found bands characteristic of RCO_2H which are completely absent from the spectrum of the sodium salt of the acid. In a number of carboxylic acids Hadzi and Sheppard[17] ascribed characteristic bands at 1300 ± 15 and at 1420 cm.$^{-1}$ to δ-OH + ν-C–O. Upon deuteration the 1300-cm.$^{-1}$ band moves to 1350 ± 50 cm.$^{-1}$, and the 1420 cm.$^{-1}$ band moves to 935 ± 15 cm.$^{-1}$, indicating that the 1350 cm.$^{-1}$ band is the uncoupled ν-C–O band. In some of the acid spectra observed here a strong band near 1300 cm.$^{-1}$, as well as lower frequency bands, was found in the ν-C–O region. It is our belief that the lower frequency bands are characteristic of the RCO_2H

(4) G. C. Pimentel and A. L. McClellan, "The Hydrogen Bond," Reinhold Publishing Corp., New York, N. Y., 1960.

(5) D. Hadzi and A. Novak, "Infrared Spectra of, and Hydrogen Bonding in, Some Acid Salts of Carboxylic Acids," University of Ljubljana, Ljubljana, Yugoslavia, 1960.

(6) R. Blinc and D. Hadzi, *Mol. Phys.*, **1**, 391 (1958).

(7) D. Hadzi, A. Novak, and J. E. Gordon, *J. Phys. Chem.*, **67**, 1118 (1963).

(8) D. Hadzi, *J. Chem. Soc.*, 5128 (1962).

(9) (a) D. Cook, *Can. J. Chem.*, **41**, 2575 (1963); (b) *Chem. Ind.* (London), 607 (1963).

(10) D. Hadzi, *Proc. Chem. Soc.*, 241 (1960).

(11) (a) N. Albert and R. M. Badger, *J. Chem. Phys.*, **29**, 1193 (1958); (b) E. H. White, *J. Am. Chem. Soc.*, **77**, 6215 (1955).

(12) D. Hadzi, *Bull. Sci. Fac. Chem. Ind.* (Bologna), **21**, 23 (1963).

(13) R. Blinc, D. Hadzi, and A. Novak, *Z. Elektrochem.*, **64**, 567 (1960).

(14) R. Blinc and D. Hadzi, *Spectrochim. Acta*, **16**, 853 (1960).

(15) D. Hadzi, *J. Chem. Phys.*, **34**, 1445 (1962).

(16) (a) R. L. Somorajai and D. F. Hornig, *ibid.*, **36**, 1980 (1962); (b) E. A. Pshenichnov and N. D. Sokolov, *Opt. Spectry.* (USSR), **11**, 8 (1961).

(17) D. Hadzi and N. Sheppard, *Proc. Roy. Soc.* (London), **A216**, 247 (1953).

group and that they probably arise from the coupling of the C–O stretching motion with other modes such as C–C stretching. These lower frequency bands characteristic of the carboxylic acid group have been described by a number of workers[18–20]; they are especially intense in α-branched acids. In the data describing the spectral assignments of the acids and their adducts, the notation of Hadzi is used for the strongest band present in the 1250–1320-cm.$^{-1}$ region, whereas the subsidiary bands will be referred to simply as ν-RCO_2H, as they are characteristic of the un-ionized CO_2H group. A carbonyl band near 1700 cm.$^{-1}$ is characteristic of an un-ionized CO_2H group; a band near 1600 cm.$^{-1}$ is characteristic of the CO_2^- group. However, the 1600-cm.$^{-1}$ antisymmetric stretching mode is subject to considerable variation[3,21–25] because of intermolecular interactions such as hydrogen bonding and partial covalent interactions with less electropositive metals. The 1400-cm.$^{-1}$ symmetrical carboxylate stretching frequency is sometimes weak and easily confused with other vibrations.

The bands due to the benzoic acid part of the adduct are much more intense that those due to the pyridine part; therefore, the pyridine *vs.* pyridinium vibrations are not very useful in the present study. The trifluoroacetic acid and trichloroacetic acid adducts did, however, show the characteristic pyridinium bands. Ring vibrations in the region 1400–1630 cm.$^{-1}$ are distinguished by their sharpness and by their near invariance in the series: acid, deuterated acid, adduct, deuterated adduct, and sodium salt of the acid.

Experimental

The crystalline adducts were prepared by dissolving the appropriate benzoic acid in acetonitrile and adding an equivalent amount of the pyridine. The pyridine bases used were redistilled Eastman White Label pyridine, redistilled Reilly 3,5-lutidine, Eastman White Label 2,6-lutidine, and Eastman White Label 2,4,6-collidine. All of the acids used for the preparation of the adducts were recrystallized and gave the correct melting point. Trichloroacetic acid was sublimed before use. K and K trifluoroacetic acid was used without further purification. All of the adducts, except those of *p*-toluic acid and 2,4-dimethylbenzoic acid, were recrystallized after their initial preparation. In many cases well-formed crystals slowly grew out of solution. Elemental analyses of a number of complexes indicate that 1:1 complexes were formed. The stoichiometry of the complexes was also determined by integration of the n.m.r. signals from the acid *vs.* the pyridine parts of the complex. Not all of the adducts could be tested in this way because of the extremely broadened nature of the pyridine signals in some cases.

In Table I are listed the melting points, chemical stability, and analysis of the adducts. The stability of an adduct increases with the ΔpK between the two parts of the adduct. For example, the *p*-toluic acid–pyridine adduct immediately effloresces upon ordinary handling, even when exposure to the atmosphere is as short as 1 min., while the 2,4-dinitrobenzoic acid–pyridine adduct is stable to 10^{-3} mm. for at least 1 day. However, sublimation at 90° (10^{-3} mm.) of this material results only in the parent acid.

All spectral measurments were made on Nujol or halocarbon mulled samples, except for the very volatile samples whose spectra were taken in a closed 0.015-mm. cell. A Beckman IR-9 instrument was used for all the spectral analyses, except for the analyses or the deuterated acids, the cooled samples, and some of the solution spectra which were performed on a Perkin-Elmer 21 spectrometer equipped with a sodium chloride prism.

Results

Pyridine–Carboxylic Acid Spectra: General Considerations. Before exploring, in detail, the spectral characteristics of each of the sets of adducts listed according to the parent acid, the general trends will first be indicated. The pyridine adducts with substituted benzoic acids will be discussed in order of increasing acidity as follows: *p*-toluic (I), 2,4-dimethylbenzoic (II), benzoic (III), *p*-chlorobenzoic (IV), 3,4-dichlorobenzoic (V), *p*-nitrobenzoic (VI), 2,4-dichlorobenzoic (VII), 3,5-dinitrobenzoic (VIII), and 2,4-dinitrobenzoic (IX) acids.

Three types of adduct spectra are observed. Class A is exemplified by I–IV, the spectra of which resemble that of the parent dimer acid, except for a slight increase in ν-C=O in some cases. The band width and intensity of the adduct bands are nearly identical with that of the original acid dimer, except for the broad background absorption below 1200 cm.$^{-1}$ which has replaced the γ-OH band of the dimer acid. Strong hydrogen bonding is present between pyridine and acid, as

(18) M. St. C. Flett, *J. Chem. Soc.*, 962 (1951).

(19) N. K. Freeman, *J. Am. Chem. Soc.*, **74**, 2523 (1952).

(20) (a) O. D. Shreve, M. R. Heether, H. B. Knight, and D. Swern, *Anal. Chem.*, **22**, 1498 (1950); (b) D. L. Guertin, S. E. Wiberly, W. H. Bauer, and J. Goldenstein, *ibid.*, **28**, 1194 (1956).

(21) (a) G. M. Barrow and E. A. Yerger, *J. Am. Chem. Soc.*, **76**, 5211 (1954); *ibid.*, **77**, 4474 (1955); (b) W. Klemperer and G. C. Pimentel, *J. Chem. Phys.*, **22**, 1399 (1954).

(22) B. Ellis and H. Pyszora, *Nature*, **181**, 181 (1958).

(23) R. E. Kagarise, *J. Phys. Chem.*, **59**, 271 (1955).

(24) M. M. Stimson, *J. Chem. Phys.*, **22**, 1942 (1954).

(25) R. Theimer and O. Theimer, *Monatsh. Chem.*, **81**, 313 (1950).

Table I: Properties of Pyridine–Carboxylic Acid Adducts

Compound	M.p., °C.	Stability[a]	Analysis
p-Toluic acid–pyridine	Eff.[b]	u	
Benzoic acid–pyridine	Eff.	u	N.m.r.
Benzoic acid–2,6-lutidine	42.5–44.5	m	N.m.r.
2,4-Dimethylbenzoic acid–pyridine	58.5–59.5	u	
p-Chlorobenzoic acid–pyridine	Eff.	u	
3,4-Dichlorobenzoic acid–pyridine	103–115, dec.	m	*Anal.* Calcd. for $C_{12}H_9Cl_2NO_2$: Cl, 26.25. Found: Cl, 25.44, 24.97
3,4-Dichlorobenzoic acid–2,4,6-collidine	100–101	s	*Anal.* Calcd. for $C_{12}H_{15}Cl_2NO_2$: Cl, 22.71. Found: Cl, 23.93
p-Nitrobenzoic acid–pyridine	134, dec.	m	*Anal.* Calcd. for $C_{12}H_{10}N_2O_4$: N, 11.38. Found: N, 11.19
3,5-Dinitrobenzoic acid–pyridine	170–171.5	s	*Anal.* Calcd. for $C_{12}H_9N_3O_6$: C, 49.49; H, 3.12; O, 32.96. Found: C, 46.19; H, 3.13; O, 29.58
3,5-Dinitrobenzoic acid–2,6-lutidine	125–126	s	N.m.r.
3,5-Dinitrobenzoic acid–3,5-lutidine	125–126	s	N.m.r. *Anal.* Calcd. for $C_{14}H_{13}N_3O_6$: N, 13.16. Found: N, 12.54
3,5-Dinitrobenzoic acid–2,4,6-collidine	152–153	s	N.m.r.
2,4-Dichlorobenzoic acid–pyridine	55.0–57.5	s	*Anal.* Calcd. for $C_{12}H_9Cl_2NO_2$: Cl, 26.25. Found: Cl, 26.15
2,4-Dichlorobenzoic acid–2,4,6-collidine	60–61	s	*Anal.* Calcd. for $C_{15}H_{15}Cl_2NO_2$: Cl, 22.71. Found: Cl, 21.87
2,4-Dinitrobenzoic acid–2,6-lutidine	156–159	s	N.m.r.
2,4-Dinitrobenzoic acid–pyridine	140.5–141.5	s	*Anal.* Calcd. for $C_{12}H_9N_3O_6$: C, 49.49; H, 3.11; N, 14.43. Found: C, 49.84; H, 2.73; N, 14.39
2,4-Dinitrobenzoic acid–3,5-lutidine	169–171	s	*Anal.* Calcd. for $C_{14}H_{13}N_3O_6$: C, 52.67; H, 4.10; O, 30.09. Found: C, 53.38; H, 4.33; O, 28.81
2,4-Dinitrobenzoic acid–2,4,6-collidine	137.5–138.0	s	N.m.r.
Trichloroacetic acid–pyridine	102.5, dec.	s	*Anal.* Calcd. for $C_7H_6Cl_3NO_2$: Cl, 44.33. Found: Cl, 44.05
Trifluoroacetic acid–pyridine	78.5–79.5	s	*Anal.* Calcd. for $C_7H_6F_3NO_2$: F, 29.51. Found: F, 28.40

[a] When exposed to the atmosphere: u, efflorescence in less than 5 min.; m, efflorescence between 1 and 24 hr.; s, no efflorescence even after 24 hr. [b] Eff. refers to such rapid efflorescence of the material that melting points by conventional techniques could not be determined.

judged from the two broad, well-defined ν-OH bands of medium intensity at 1900 and 2450 cm.$^{-1}$ which have replaced the broad ν-OH at 2600–3000 cm.$^{-1}$ in the parent acid dimer. However, this hydrogen bonding has not perturbed the structure of the CO_2H group much from its dimer state.

Class B is exemplified by V, VI, and VII, the spectra of which are characterized by a considerable broadening of ν-C=O and the two ν-OH bands. The half-width of the former band attains a value of 120 cm.$^{-1}$. These complexes are still in the form of AH--B since bands characteristic of RCO_2H are found in the ν-C–O region. In addition, the background below 1200 cm.$^{-1}$ becomes quite intense, making it impossible to find γ-OH.

Class C is exemplified by VIII and IX. There is no longer a distinct band above 1700 cm.$^{-1}$ attributable to ν-NH or ν-OH; no bands due to ν-C–O characteristic of the CO_2H group can be detected; and the ν-C=O band becomes broadened and complex. The proton deformation region below 1200 cm.$^{-1}$ is intense and very broad.

Class D is exemplified by the collidine–dinitrobenzoic acid complex. These ionic adducts of the type BH^+--A^-, which are formed after a certain critical ΔpK has been reached, possess distinct ν-NH and ν-CO_2^- bands.

There is, of course, a gradual merging between the first two classes, *i.e.*, between the amount of perturbation the acid experiences upon hydrogen bonding. The same is true of class D complexes which have varying amounts of spectral broadness.

2,4-Dimethylbenzoic, p-Toluic, Benzoic, p-Chlorobenzoic, and p-Nitrobenzoic Acid Adducts with Pyridine. These efflorescent adducts display similar spectral characteristics in that the ν-C=O and ν-C–O regions of the spectra are similar to that of the parent acid dimer. From this it may be concluded that the state of the adduct is AH--B. In these materials the ν-C=O frequency is equal to or higher than that of the parent acid dimer. All adducts in this section are class A or B.

Figure 1 is a reproduction of the spectra of 2,4-dimethylbenzoic acid, benzoic acid, and their pyridine adducts. In the adduct spectra there are two equally intense broad bands near 1930 and 2450 cm.$^{-1}$. Hadzi[2] has interpreted these two bands in the case of the benzoic acid adduct as arising from a double-minimum potential function for the OH stretching motion with a low central barrier, on the basis that deuteration of the OH group moves the 2450-cm.$^{-1}$ band to 1900 cm.$^{-1}$, indicating that at least the 2450-cm.$^{-1}$ band arises from an OH motion, and on the basis that the spectrum of the cooled sample does not show much variation in the 1900–2450-cm.$^{-1}$ region, as it would if an equilibrium were present between $BH^+--A^- \rightleftarrows B--HA$ or if the lower band were a difference or "hot" band. Also the spectra of all of the adducts considered here contain only one band in the 1550–1700-cm.$^{-1}$ region, indicating that the RCO_2H group is present in only one state of ionization. Since all of these adducts are in the crystalline state, it would not be expected that an equilibrium situation prevails since this will give rise to much disorder. The lutidine–benzoic acid adduct has what appears to be three broad bands at 1550, 2000, and 2440 cm.$^{-1}$.

The γ-OH of the dimer parent acid which falls in the 920–960-cm.$^{-1}$ region is replaced by a background absorption below 1300 cm.$^{-1}$ upon adduct formation. This background becomes increasingly intense as the ΔpK increases in class A or B complexes. Compare the pyridine complexes of 2,4-dimethylbenzoic acid and benzoic acid in Fig. 1. In Table II are listed the absorption areas of interest. The ring and substituent modes which are invariant through the derivative series are not included. Also not included are the assignments for the deformation modes for the adducts, as in no case could such assignment easily be made because of the diffuseness of the spectrum in this area.

Each of the adducts contain one ν-C–O + δ-OH band near 1300 cm.$^{-1}$ similar to the parent acid dimer, but the ν-CO + δ-OH band near 1400 cm.$^{-1}$ is of questionable existence. Upon deuteration the 1300 cm.$^{-1}$ band shifts to higher frequencies as it does in the dimer acids, indicating that an uncoupling of the C–O stretching motion with the O–H bending motion takes place.

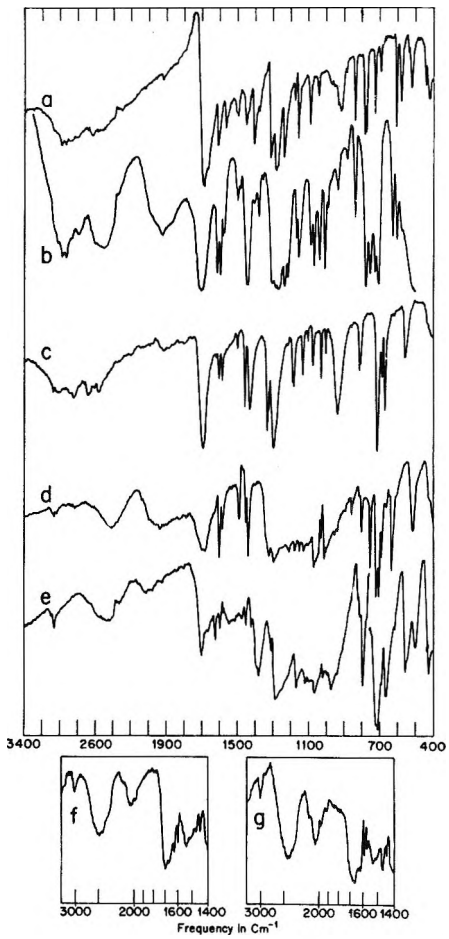

Figure 1. Infrared spectra of: a, 2,4-dimethylbenzoic acid; b, 2,4-dimethylbenzoic acid–pyridine; c, benzoic acid; d, benzoic acid-pyridine; e, benzoic acid–2,6-lutidine; f, benzoic acid–2,6-lutidine at room temperature; g, same as f, but cooled with liquid nitrogen. Ordinate, per cent transmission; abscissa, frequency in cm.$^{-1}$.

This means that the predominantly O–H bending mode must lie above 1300 cm.$^{-1}$. This band has not been found for any of the adducts with the possible exception of 2,6-lutidine–benzoic acid. The assignment of the strong 1442 cm.$^{-1}$ bands in 2,4-dimethylbenzoic acid and *p*-toluic acid adducts with pyridine is uncertain since a strong pyridine ring mode occurs here. No consistent set of other strong pyridine frequencies could be found. Advantageous amounts of pyridine could easily be present in these adducts because they could not be vacuum dried. In the case of benzoic acid–pyridine this band occurs at 1438 cm.$^{-1}$, and the same uncertainty is present. In the case of 2,6-lutidine–benzoic acid, a strong broadened band at 1380 cm.$^{-1}$ appears, and this is assigned to ν-C–O + δ-OH. Hadzi and Pintar could not locate the band near 1400 cm.$^{-1}$ for pyridine complexes with benzoic and other acids.[26]

Table II: Frequency Assignments of Carboxylic Acid–Pyridine Adducts[a]

R	Frequency, cm.$^{-1}$				
	RCO_2Na	RCO_2H	RCO_2H·pyridine[a]	RCO_2H·lutidine	Assignment
2,4-Dimethylphenyl		2400–3000	1922, 2450		ν-OH
		1690	1703		ν-C=O
	1545				ν-CO_2^-
		1450	1442 ?		ν-C–O + δ-OH
	1418				ν-CO_2^-
		1310, 1280	1305, 1282, 1268		ν-C–O + δ-OH
		1232	1232, 1212		ν-RCO_2H
p-Methylphenyl		2500–3050	1930, 2455		ν-OH
		1678	1708		ν-C=O
	1552				ν-CO_2^-
	1421				ν-CO_2^-
		1420	1442 ?		ν-C–O – δ-OH
		1321, 1289	1311, 1283, 1220		ν-C–O + δ-OH
Phenyl		2500–3000	1940, 2410	2500, 2000	ν-OH
		1692	1692	1702	ν-C=O
	1553				ν-CO_2^-
				1550	ν-OH ?
	1414				ν-CO_2^-
		1428	1438	1380	ν-C–O + δ-OH
		1329, 1293	1321, 1296	1290	ν-C–O + δ-OH
p-Chlorophenyl		2500–3100	1920, 2450		ν-OH
		1684	1695		ν-C=O
	1542				ν-CO_2^-
		1413	1390		ν-C–O + δ-OH
	1409				ν-CO_2^-
		1321, 1307	1273		ν-C–O + δ-OH
		1292, 1281	1233		ν-RCO_2H
p-Nitrophenyl		2450–3100	1950, 2420 (1870, 1940)		ν-OH or ν-OD
		1700	1720 (1710)		ν-C=O
	1594				ν-CO_2^-
	1410				ν-CO_2^-
		1432	1442 ?		ν-C–O + δ-OH
		1325, 1312	1320		ν-C–O + δ-OH
		1295, 1283			ν-RCO_2H
Cl_3C			2010, 2460		ν-NH
		1750			ν-C=O
	1674		1660		ν-CO_2^-
			1632, 1602, 1541, 1481		BH^+ ring
		1419, 1402			ν-C–O + δ-OH
	1358, 1382		1350		ν-CO_2^-
			1310		δ-NH
		1260			ν-C–O + δ-OH
			982		γ-NH
		832, 850			γ-OH
F_3C			2020, 2080, 2470		ν-NH
		1780			ν-C=O
	1680		1662		ν-CO_2^-
			1600, 1545, 1489		BH^+ ring
		1460			ν-C–O + δ-OH
	1450		1421		ν-CO_2^-
			1121 ?		δ-NH
			990		γ-NH

[a] Frequencies in parentheses are for deuterated derivatives.

The spectrum of the *p*-nitrobenzoic acid adduct compared to its parent acid shows more perturbations than the other adducts in this section. The carbonyl band is considerably broader than the dimer acid ν-C=O; the ν-OH region contains two broad bands in the 1900- and 2450-cm.$^{-1}$ regions; however, these bands are very poorly defined. Deuteration decreases the intensity of the 2500-cm.$^{-1}$ band. Only one of the parent acid ν-CO bands near 1300 cm.$^{-1}$ remains; deuteration removes this band.

2,4-Dichlorobenzoic Acid Adducts with Pyridine and Collidine. The pyridine adduct spectrum shown in Fig. 2 is that of a class B complex because of the existence of bands due to RCO_2H in the ν-C–O region and because of the extremely broadened nature of the ν-C=O and ν-OH bands. The broadened ν-C–O band of the adduct which has peaks at 1265, 1250, 1213, and 1300 cm.$^{-1}$ is replaced by a single strong ν-C–O band at 1322 cm.$^{-1}$ upon deuteration. A spike appears at 1735 cm.$^{-1}$ on the ν-C=O band; it is probably due to a combination band whose intensity is greatly increased by Fermi resonance. Such superpositioning of sharp peaks on the broad carbonyl band occurs widely throughont the series of compounds studied here. Assignments are in Table III.

The collidine complex has no band in the ν-C–O region; therefore, it must be largely ionized. The spectrum is rather complex, consisting of very broad bands and background absorption (Fig. 2). The two very diffuse bands near 1900 and 2500 cm.$^{-1}$ could possibly be ν-NH. The two ν-CO_2^- bands are broad and very complex. To be consistent throughout this paper, we will call the bands arising from the hydrogen-bonded CO_2 moiety "ν-CO_2^-" whenever the spectrum of the adduct differs greatly from that of the parent acid in the

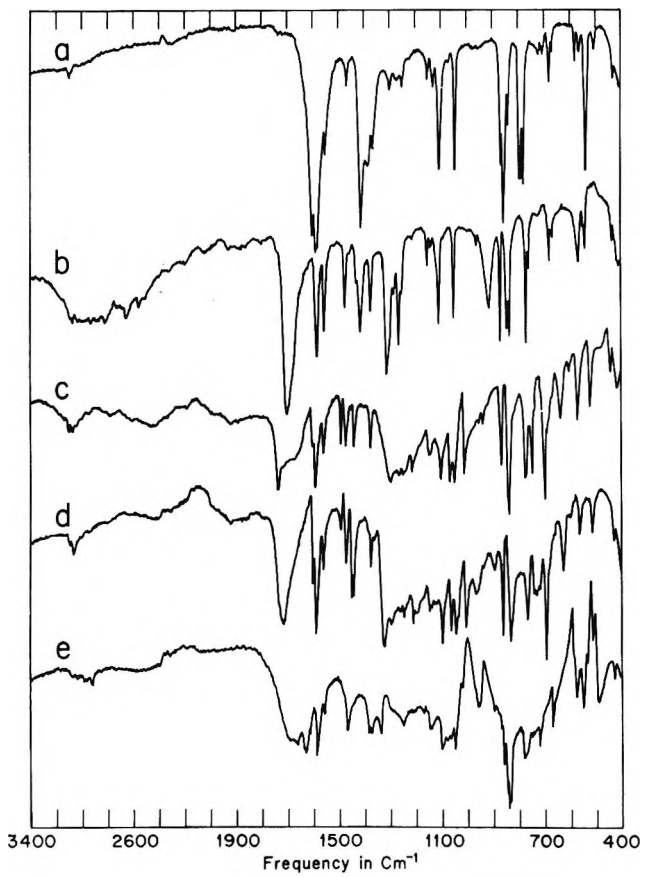

Figure 2. Infrared spectra of: a, sodium 2,4-dichlorobenzoate; b, 2,4-dichlorobenzoic acid; c, 2,4-dichlorobenzoic acid–pyridine; d, deuterio-2,4-dichlorobenzoic acid–pyridine; e, 2,4-dichlorobenzoic acid–2,4,6-collidine. Ordinate, per cent transmission; abscissa, frequency in cm.$^{-1}$.

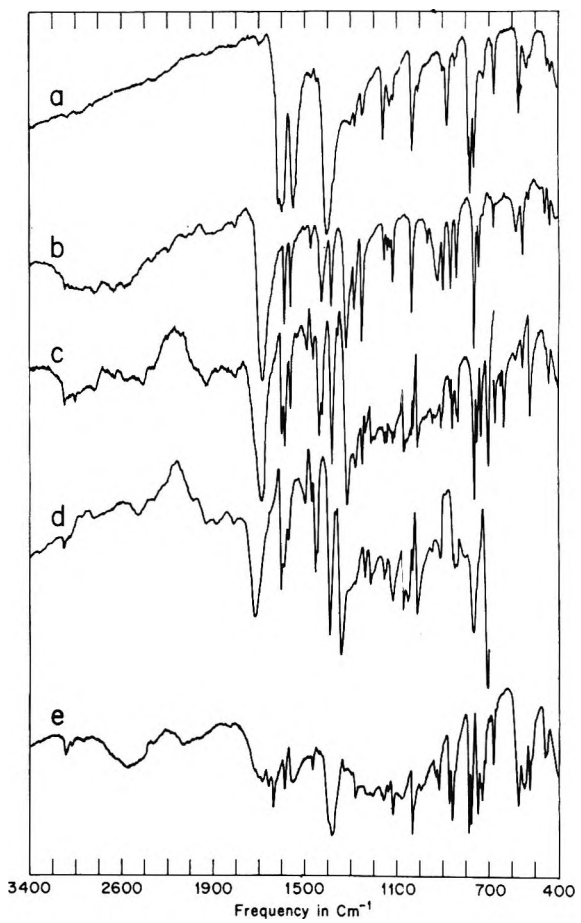

Figure 3. Infrared spectra of: a, sodium 3,4-dichlorobenzoate; b, 3,4-dichlorobenzoic acid; c, 3,4-dichlorobenzoic acid–pyridine; d, deuterio-3,4-dichlorobenzoic acid–pyridine; e, 3,4-dichlorobenzoic acid–2,4,6-collidine. Ordinate, per cent transmission; abscissa, frequency in cm.$^{-1}$.

(26) D. Hadzi and M. Pintar, *Spectrochim. Acta*, 12, 162 (1958).

Table III: Frequency Assignments of Dichlorobenzoic Acid Derivatives

R	Frequency, cm.$^{-1}$ RCO_2Na	RCO_2H	RCO_2H·pyridine	RCO_2D·pyridine	RCO_2H·collidine	Assignment
2,4-Dichlorobenzoic acid		2420–3100	1920, 2430			ν-OH
		1705	1690	1720		ν-C=O
	1589				1660	ν-CO_2^-
	1409				1350 broad	ν-CO_2^-
		1416	1440 ?			ν-CO + δ-OH
		1312	1300			ν-C–O + δ-OH
		1269	1265, 1250, 1213			ν-RCO_2H
				1322		ν-C–O
3,4-Dichlorobenzoic acid		2400–3050	1930, 2400	1885 ? Very broad		ν-OH or ν-OD
					2000, 2570	ν-NH
		1683	1710	1714		ν-C=O
	1547				1520–1720 Broad band	ν-CO_2^-
		1426	1440 ?			ν-C–O + δ-OH
	1407				1370–1395	ν-CO_2^-
		1318, 1282	1314, 1295, 1280			ν-C–O + δ-OH
		1250				ν-RCO_2H
				1338		ν-C–O

Table IV: Frequency Assignments for Dinitrobenzoic Acid Derivatives[a]

	Frequency, cm.$^{-1}$ RCO_2Na	RCO_2H	RCO_2H· pyridine	RCO_2H·3,5-lutidine	RCO_2H· 2,6-lutidine	RCO_2H· 2,4,6-collidine	Assignment
3,5-Dinitrobenzoic acid			2000 ?		2045, 2430	2010, 2420	ν-NH
		1708					ν-C=O
	1623		1722 (1718)	1710	1667	1670	ν-CO_2^-
		1416					ν-C–O + δ-OH
	1395			1382	1382	1378	ν-CO_2^-
		1289					ν-C–O + δ-OH
			1250, 1060 ?				δ-NH
			940 (700)				γ-NH
2,4-Dinitrobenzoic acid					2020, 2410	2025, 2426	ν-NH
		1722					ν-C=O
	1636						ν-CO_2^-
			(1300)	1645	2020, 2410	2025, 2426	ν-NH
			1670 (1682)	1680	1662	1664	ν-CO_2^- + ?
			1635 (1632)	1640	1625	1637	ν-CO_2^- + ?
	1400						ν-CO_2^-
		1417					ν-C–O + δ-OH
		1292					ν-C–O + δ-OH
			1150 ?				δ-NH
			850 (710)				γ-NH

[a] Frequencies for deuterated compounds in parentheses

ν-C–O region, even though the carboxylate group may not have achieved a full negative charge.

The sharp 1630-cm.$^{-1}$ band superimposed on the broad ν-CO_2^- band is due to a collidinium ring vibration: collidine and collidine hydrochloride have their most intense bands at 1609 and 1635 cm.$^{-1}$, respectively. This assignment supplements the ν-CO_2^- assignment and strengthens the proton transfer A^---HB^+ postulation for the 2,4-dichlorobenzoic acid–collidine adduct, placing it in class C or D.

3,4-Dichlorobenzoic Acid Adducts with Pyridine and Collidine. In Fig. 3 it may be seen that the pyridine

adduct of 3,4-dichlorobenzoic acid can be assigned as a class B adduct because of the presence of ν-C–O frequencies and because of the extremely broadened nature of the ν-C=O and ν-OH bands; the latter bands are barely discernible. Deuteration increases the 1900-cm.$^{-1}$ band relative to the 2500-cm.$^{-1}$ (after the background has been accounted for) and causes the three ν-C–O bands at 1314, 1295, and 1280 cm.$^{-1}$ to be replaced by a single peak at 1338 cm.$^{-1}$. The background absorption below 1200 cm.$^{-1}$ changes its pattern and a new peak appears at 800 cm.$^{-1}$.

The collidine adduct of 3,4-dichlorobenzoic acid is an ionized (class D) complex because of the complete absence of any bands in the 1250–1350-cm.$^{-1}$ ν-C–O region. The entire complex band from 1520 to 1720 cm.$^{-1}$ is probably due to ν-CO_2^-. The transmission windows at 1570 and 1600 cm.$^{-1}$ are most likely due to a Christiansen[27] effect commonly found in strongly H-bonded compounds. Table III contains a summary of the frequency assignments.

3,5-Dinitrobenzoic Acid Adducts. Four adducts with 3,5-dinitrobenzoic acid were studied: pyridine, 3,5-lutidine, 2,6-lutidine, and 2,4,6-collidine. Figures 4 and 5 are reproductions of the spectra of the adducts as well as the parent acid and its sodium salt. The frequency assignments are in Table IV. All four adducts have no bands due to RCO_2H in the ν-C–O region, therefore, it may be concluded that the state of ionization of the 3,5-dinitrobenzoic acid moiety in these complexes is close to anionic. The pyridine and 3,5-lutidine complexes have no absorption above 1700 cm.$^{-1}$ attributable to an H stretching motion; the 2,6-lutidine complex has two weak, broad bands at 2045 and 2430 cm.$^{-1}$; and the collidine complex has two unequally sized bands at 2010 and 2420 cm.$^{-1}$, the former band being more intense. The pyridine adduct does, however, have a band near 1900 cm.$^{-1}$ of questionable origin (see the section on the cooling experiments). Deuteration of the pyridine adduct causes a new band to appear at 1300 cm.$^{-1}$ and causes broad background absorption between 900 and 1200 cm.$^{-1}$. These two new features are undoubtedly due to stretching and deformation modes of the deuteron.

2,4-Dinitrobenzoic Acid Adducts. In Fig. 6 are illustrated the spectra of 2,4-dinitrobenzoic acid adducts with pyridine, 3,5-lutidine, 2,6-lutidine, and 2,4,6-collidine, as well as the spectra of the parent acid and its sodium salt for comparison. In Table IV are the frequency assignments. The most striking feature in the adduct spectra is the complete or nearly complete absence of vibrational bands above 1700 cm.$^{-1}$ attributable to NH or OH stretching in the pyridine and 3,5-lutidine derivatives, and the presence of the two ν-NH

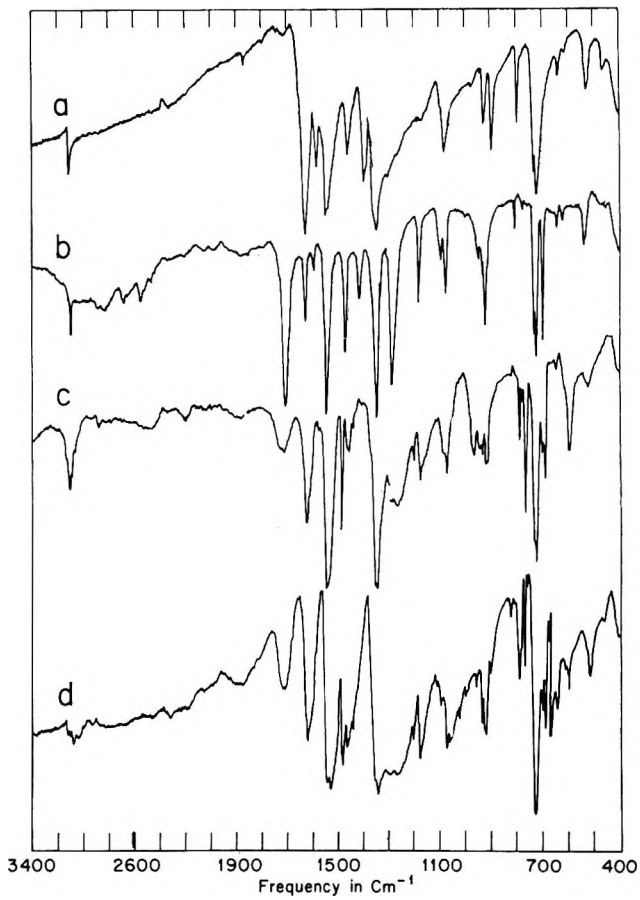

Figure 4. Infrared spectra of: a, sodium 3,5-dinitrobenzoate; b, 3,5-dinitrobenzoic acid; c, 3,5-dinitrobenzoic acid–pyridine; d, deuterio-3,5-dinitrobenzoic acid–pyridine. Ordinate, per cent transmission; abscissa, frequency in cm.$^{-1}$.

or ν-OH bands near 1900 and 2450 cm.$^{-1}$ for the 2,6-lutidine and 2,4,6-collidine adduct spectra. The characteristic frequencies of the RCO_2H group at 1252 and 1292 cm.$^{-1}$ have completely disappeared, and two broad bands near 1630 and 1660 cm.$^{-1}$ are present in the ν-C=O region. The absence of the ν-C—O bands in the 1250–1330-cm.$^{-1}$ region indicates the state of ionization of all four adducts is BH^+--A^-. The two bands in the ν-C=O region become more sharply defined but, nevertheless, retain the same over-all nature, along the adduct series: pyridine; 3,5-lutidine, 2,6-lutidine, and 2,4,6-collidine. It is difficult to say just where the NH stretching frequencies are in the pyridine and 3,5-lutidine adducts. One possibility for the pyridine adduct is the ill-defined broad band near 2000 cm.$^{-1}$. It is significant that the very broad ν-CO_2^-

(27) (a) C. Christiansen, *Ann. Physik.*, **23**, 298 (1884); (b) W. C. Price and K. S. Tetlow, *J. Chem. Phys.*, **16**, 1157 (1948).

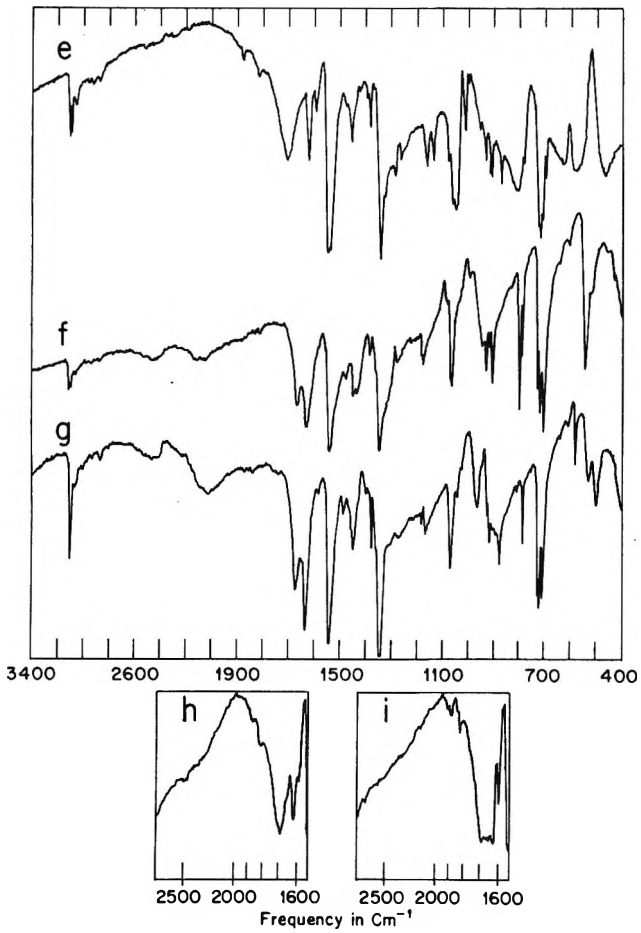

Figure 5. Infrared spectra of: e, 3,5-dinitrobenzoic acid–3,5-lutidine; f, 3,5-dinitrobenzoic acid–2,6-lutidine; g, 3,5-dinitrobenzoic acid–2,4,6-collidine; h, same as e, at room temperature; i, same as e, cooled with liquid nitrogen. Ordinate, per cent transmission; abscissa, frequency in cm.$^{-1}$.

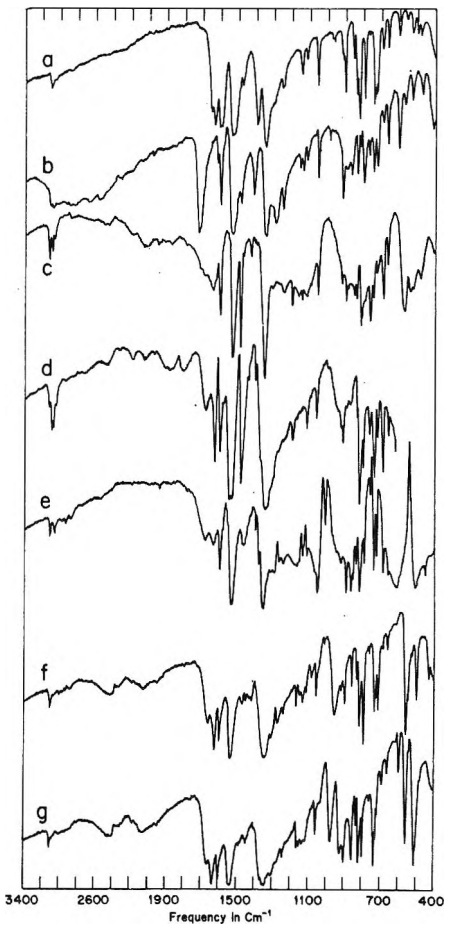

Figure 6. Infrared spectra of: a, sodium 2,4-dinitrobenzoate; b, 2,4-dinitrobenzoic acid; c, 2,4-dinitrobenzoic acid–pyridine; d, deuterio-2,4-dinitrobenzoic acid–pyridine; e, 2,4-dinitrobenzoic acid–3,5-lutidine; f, 2,4-dinitrobenzoic acid–2,6-lutidine; g, 3,5-dinitrobenzoic acid–2,4,6-collidine. Ordinate, per cent transmission; abscissa, frequency in cm.$^{-1}$.

band of the pyridine adduct becomes considerably sharpened upon deuteration, indicating that ν-NH possibly is in the ν-CO_2^- region. The 3,5-lutidine adduct has *no* band above 1700 cm.$^{-1}$ attributable to ν-NH. This adduct along with the 3,5-lutidine–3,5-dinitrobenzoic acid complex described in the last section are the two clearest-cut cases of adducts with *no* ν-NH above 1700 cm.$^{-1}$.

Trihaloacetic Acid Adducts with Pyridine. Trifluoro- and trichloroacetic acid form 1:1 solid complexes with pyridine in which the proton is transferred to pyridine, as judged from the typical pyridinium ring vibrations in the adduct spectra (Table II). In the spectra of the pyridinium trihaloacetates, no broad background absorption below 1200 cm.$^{-1}$ is observed, nor are extraordinarily broadened ν-C=O and ν-NH bands found as have been found in the case of the substituted benzoic acid–pyridine complexes. There are, however, two main ν-NH bands for both complexes near 2050 and 2460 cm.$^{-1}$.

The ν-CO_2^- bands for both the pyridinium trihaloacetates occur at lower frequencies by 12–18 cm.$^{-1}$ than in the corresponding sodium trihaloacetate. This is a somewhat unexpected result as hydrogen bonding on only one of the two oxygens should distort the CO_2^- group so as to cause an *upward* shift in the antisymmetric ν-CO_2^- frequency.[21]

Solvent Effects. The following adducts were dissolved in acetonitrile and their spectra determined: 2,4-dichlorobenzoic acid–collidine, 2,4-dinitrobenzoic acid–pyridine, 3,5-dinitrobenzoic acid–pyridine, benzoic acid–pyridine, benzoic acid–2,6-lutidine, 3,4-dichlorobenzoic acid–pyridine, and the pyridinium trihaloace-

tates. In the ν-OH or ν-NH region, no difference is seen between the solid state spectra and the solution spectra; all of those adducts with no absorption above 1700 cm.$^{-1}$ in the solid state do not have absorption above 1700 cm.$^{-1}$ in the liquid state either. Likewise, all of those adducts with two ν-NH or ν-OH bands in the solid state retain these bands in the liquid state. The strong diffuse absorption below 1200 cm.$^{-1}$ does not decrease in going from crystal state to solution state.

Cooling Experiments. Cooling the sample (thirteen complexes were measured) to liquid nitrogen temperature caused little change or a slight sharpening in the ν-NH or ν-OH region for the most part. An example is the 2,6-lutidine–benzoic acid complex (Fig. 1). The 3,5-lutidine–3,5-dinitrobenzoic acid complex gave the interesting result that a new band appeared at 1645 cm.$^{-1}$ (Fig. 5). This band undoubtedly is ν-NH, because there is absolutely no band above 1700 cm.$^{-1}$ attributable to ν-NH. The pyridine complexes of 3,5-dinitrobenzoic acid and 2,4-dinitrobenzoic acid show a slight intensification of a broad band near 1900 and 2000 cm.$^{-1}$, respectively. These could be ν-NH bands, or, alternatively, they could be overtone on combination bands. However, ν-NH for the pyridine–3,5-dinitrobenzoic acid complex is believed to occur in the ν-C=O region, since deuteration causes a *new* band to appear at 1300 cm.$^{-1}$. Assuming a deuteration shift of 1.3, the corresponding ν-NH would occur at 1690 cm.$^{-1}$, which is very close to the 1670-cm.$^{-1}$ ν-C=O band observed.

Another interesting result of the cooling experiments is the splitting up of the broad ν-CO_2^- bands belonging to the 2,4-dinitrobenzoic acid–pyridine, its deuterated derivative, trifluoroacetic acid–pyridine, trichloroacetic acid–pyridine, and 3,4-dichlorobenzoic acid–2,4,6-collidine. The latter band splits into five parts.

Interpretation

Because of the correlation of the infrared properties of strongly hydrogen-bonded materials with other physical methods,[13,15] the interpretation we have given to our data is that those adducts having no (or indeterminate) ν-NH or ν-OH absorption above 1700 cm.$^{-1}$ contain a single-minimum or nearly single-minimum hydrogen bond, and those adducts which have two widely separated ν-NH or ν-OH bands contain a double-minimum hydrogen bond (with a low central barrier). The observation of two ν-NH or two ν-OH bands could also arise from difference bands, combination bands, lattice effects, "hot bands," or the presence of tautomeric equilibrium. The observation that only sharpening of the bands occurs upon cooling rules out the possibility that the lower frequency band is a difference band or that tautomeric equilibrium is present. Lattice effects can be ruled out on the basis of the lack of solvent effect on the spectrum in the ν-OH or ν-NH region. The possibility of combination bands seems to be unlikely because of the improbability that the proper combination of fundamentals could occur in fifteen different adducts with widely varying acidic and basic moieties. One possibility for the doubling of the ν-OH and ν-NH is a Fermi resonance between the fundamental stretching mode and overtones of the deformation modes, as the deformation frequencies would not be expected to be too variable in these complexes. In most cases we could not isolate these deformation modes, but in certain favorable instances cooling and deuteration experiments indicated that ν-OH must be in the 1000-cm.$^{-1}$ region and ν-ND must be in the 800–1000-cm.$^{-1}$ region.

Correlation of Spectral Changes with ΔpK. Upon increasing the ΔpK for a benzoic acid–pyridine complex, the infrared spectrum of the complex undergoes gradual, but profound changes. At low ΔpK values (1 or 2) the carbonyl frequency of the acid part is intense and narrow, and shifted somewhat to higher frequencies; the two ν-OH bands are distinct. Higher ΔpK values (2 or 3) bring on a broadening of the ν-C—O, ν-C=O, and ν-OH bands, and a large increase in absorption intensity below 1200 cm.$^{-1}$. These interrelated effects must be due to a strong perturbation of the electronic structure of the carboxylic acids. Hydroxylic groups, upon hydrogen bonding,[3] normally show an increase in intensity in the OH stretching band. Strong hydrogen bonds, however, frequently show less "intense" OH stretching bands[28] undoubtedly due to extensive broadening and coupling with other modes because of increased anharmonicity. With increasing ΔpK values ($\sim$3.7), proton transfer takes place, and further increases in ΔpK result in the sharpening of the ν-CO_2^-, ν-NH, and deformation bands.

Only one ν-C=O is observed in all of these examples with ΔpK values ranging from 0.86–6.18, meaning that we are dealing with one and only one state of the hydrogen bond. A plot of the function $\Delta\nu/\Delta\nu_0$ *vs.* ΔpK is shown in Fig. 7, where

$$\Delta\nu/\Delta\nu_0 = \left[\nu\text{-C=O}^{\text{dimer acid}} - \nu\text{-C=O}^{\text{adduct}}\right] \Big/ \left[\nu\text{-C=O}^{\text{dimer acid}} - \nu\text{-COO}^{-\,\text{acid salt}}\right]$$

resembles a titration curve in that two slightly inclined plateaus are observed representing the fully ionized A^---HB^+ and the un-ionized AH--B states of the substrate. The analogy cannot be drawn too far, however,

(28) K. Nakamoto, M. Margoshes, and R. E. Rundle, *J. Am. Chem. Soc.*, 77, 6480 (1955).

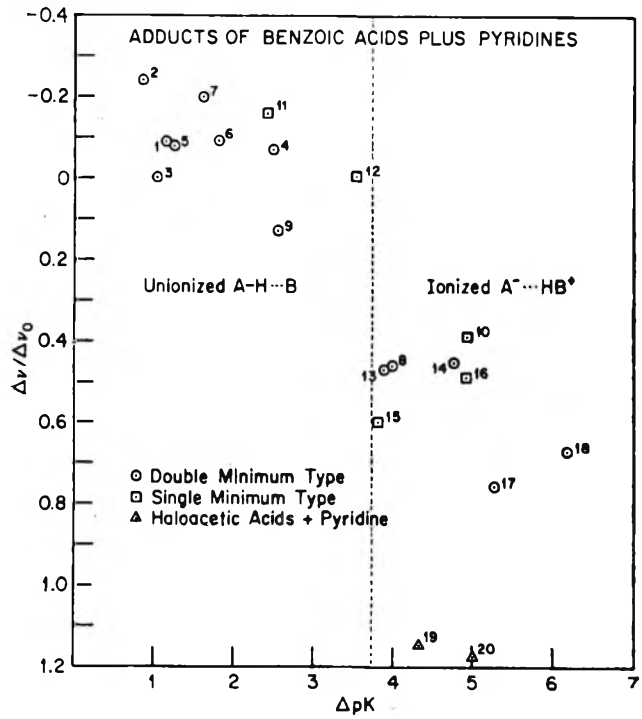

Figure 7. $\Delta\nu/\Delta\nu_0$ *vs.* ΔpK: O, double-minimum type benzoic acid–pyridine complexes; □, single-minimum type benzoic acid–pyridine complexes; Δ, pyridinium trihaloacetates. The numbers correspond to those in Table V.

since the "degree of proton transfer" is a function of ΔpK in the "plateau" areas, while as in a titration curve the degree of proton transfer is nearly 0 or 100% in the two plateau regions. The important thing is that an abrupt change in the spectral properties of the adducts occurs at *ca.* $\Delta pK = 3.75$. The vertical dotted line is drawn on the plot to emphasize that all those complexes to the right of this line are ionized. The single-minimum or near single-minimum type of hydrogen bonds all occur within 1 ΔpK unit of the dividing line. A summary of the data is given in Table V. The "titration curve" in Fig. 7 strengthens the postulation that the two NH or OH bands in the 1900–2500-cm.$^{-1}$ area are due to tunneling, as this doubling of the H-bond stretching frequency is seen on *both* sides of the critical ΔpK as would be expected.

The monomer acid C=O frequencies would give the true "per cent of proton transfer," but in the absence of these values the dimer acid ν-C=O frequencies were used. In carbon tetrachloride the dimer acid ν-C=O values are linearly[29] related to the monomer acid ν-C=O frequencies in a series of substituted benzoic acids. Assuming that this relation holds between the dimer acid in the solid state and the hypothetical monomer acid in this state, then the correlation in the form of the curve

Table V: Per Cent Proton Transfer, $\Delta\nu/\Delta\nu_0$, as a Function of ΔpK

No.	Acid	Base	ΔpK[a,b]	$\Delta\nu/\Delta\nu_0$[c]	Type of[d] adduct
1	2,4-Dimethyl-benzoic	Pyridine	1.15	−0.09	d, u
2	*p*-Toluic	Pyridine	0.86	−0.24	d, u
3	Benzoic	Pyridine	1.03	0.00	d, u
4	Benzoic	2,6-Lutidine	2.50	−0.07	d, u
5	*p*-Chloro-benzoic	Pyridine	1.25	−0.08	d, u
6	*p*-Nitro-benzoic	Pyridine	1.81	−0.09	d, u
7	3,4-Dichloro-benzoic	Pyridine	1.62	−0.20	d, u
8	3,4-Dichloro-benzoic	Collidine	3.99	40.46	d, i
9	2,4-Dichloro-benzoic	Pyridine	2.55	+0.13	d, u
10	2,4-Dichloro-benzoic	Collidine	4.92	+0.39	s
11	3,5-Dinitro-benzoic	Pyridine	2.41	−0.16	s
12	3,5-Dinitro-benzoic	3,5-Lutidine	3.52	−0.02	s
13	3,5-Dinitro-benzoic	2,6-Lutidine	3.88	+0.47	d, i
14	3,5-Dinitro-benzoic	Collidine	4.78	+0.45	d, i
15	2,4-Dinitro-benzoic	Pyridine	3.81	+0.60	s
16	2,4-Dinitro-benzoic	3,5-Lutidine	4.92	+0.49	s
17	2,4-Dinitro-benzoic	2,6-Lutidine	5.28	+0.76	d, i
18	2,4-Dinitro-benzoic	Collidine	6.18	+0.67	d, i
19	Trichloro-acetic	Pyridine	4.34	+1.15	d, i
20	Trifluoro-acetic	Pyridine	5.00	+1.18	d, i

[a] Carboxylic acid pK values as follows: 2,4-dimethylbenzoic acid, 4.182; *p*-toluic acid, 4.373; benzoic acid, 4.203; *p*-chlorobenzoic acid, 3.979; *p*-nitrobenzoic acid, 3.425; 2,4-dichlorobenzoic acid, 2.680; 3,5-dinitrobenzoic acid, 0.23; trichloroacetic acid, 0.89. ["Handbook of Chemistry," N. A. Lange, Ed., Handbook Publishers, Inc., Sandusky, Ohio, 1946; J. F. Dippy and S. R. C. Hughes, *Tetrahedron*, **19**, 1527 (1963); J. F. Dippy, *Chem. Rev.*, **25**, 151 (1939).] The pK of 3,4-dichlorobenzoic acid was estimated to be 3.61 from the Hammett $\sigma\rho$ relationship. [b] Pyridinium pK values as follows: pyridine, 5.23; 3,5-lutidine, 6.34; 2,6-lutidine, 6.70; 2,4,6-collidine, 7.60. ["Pyridine and its Derivatives," E. Klingsberg, Ed., Interscience Publishers, Inc., New York, N. Y., Part 2, p. 177.]

[c] $\Delta\nu/\Delta\nu_0 = \left(\nu\text{-C=O}_{\text{dimer acid}} - \nu\text{-C=O}_{\text{adduct}}\right) / \left(\nu\text{-C=O}_{\text{dimer acid}} - \nu\text{-COO}^-_{\text{RCO}_2\text{Na}}\right)$

[d] d, double-minimum potential; s, single-minimum potential; u, un-ionized A-H--B; i, ionized, A^---HB^+.

in Fig. 7 is valid. Evidence to support this validity is that the ν-C–O bands due to RCO_2H abruptly disappear above ΔpK values of *ca.* 3.7. The correlation shown in Fig. 7 is quite remarkable in view of the fact that many of the ν-C=O bands of the adducts are broadened; therefore, the center of gravity of these bands was taken to represent ν-C=O adduct. Also, for the class C adducts, ν-NH probably contributes to the absorption in the ν-C=O region, therefore distorting the true ν-C=O. The only adducts which deviate strongly from the correlation are the pyridinium trihaloacetates, which is not surprising since these adducts are in a different structural family of complexes.

The increase in ν-C=O in the complex compared to the corresponding parent acid dimer (denoted by a negative $\Delta\nu/\Delta\nu_0$ quantity in Table V) for nonproton-transferred adducts is the result of the removal of the H-bonding interaction of the carbonyl group upon adduct formation. This result is expected. Upon increasing the anionic character of the CO_2H group due to the increasing ΔpK this frequency becomes suddenly lowered. The range of values found here for $\Delta\nu/\Delta\nu_0$ in the case of the single-minimum hydrogen-bonded systems compares well with those values of $\Delta\nu/\Delta\nu_0$ calculated from the data of Hadzi and Novak[5] on the symmetrical biscarboxylate salts.

Solvent Effects. The preliminary work carried out to determine if crystal forces are the deciding factor in determining the shape of the potential function for the strong hydrogen bonds in the pyridine–benzoic acid adducts indicates that such is not the case. In some previous examples of single-minimum hydrogen bonds, the potential function for the hydrogen-bond asymmetric stretching motion becomes either a double-minimum potential function with a low barrier, the same with a high barrier, or an asymmetric potential function with a high barrier, upon destroying the crystalline nature of melting[4,5] or by dissolution[6,30] in dimethyl sulfoxide. However, the complex amide salts of hydrohalic acids do not exhibit this behavior upon dissolution.

None of the single-minimum hydrogen-bonded materials studied showed a departure from its solid state behavior in the ν-NH or ν-OH region upon dissolution in acetonitrile; no absorption above 1700 cm.$^{-1}$ attributable to ν-NH or ν-OH could be detected. In the complexes studied (2,4-dichlorobenzoic acid–collidine, 2,4-dinitrobenzoic acid–pyridine, and 3,5-dinitrobenzoic acid–pyridine) the broad band in the 1600–1700-cm.$^{-1}$ region shifts to somewhat higher frequencies, and the strong background absorption below 1200 cm.$^{-1}$ remains. This latter observation indicates that the absorption below 1200 cm.$^{-1}$ is a true absorption and is not due to solid state or two-phase effects. Only the sharp transmission windows believed to be due to Christiansen effects disappeared.

Similarly, none of the double-minimum hydrogen bonds changes its spectral behavior upon dissolution in acetonitrile. Very little difference is observable between the solid state and solution spectra in the ν-OH or ν-NH region although ν-C=O is somewhat sensitive to its medium. Those complexes having intense absorption below 1200 cm.$^{-1}$ retained this absorption in solution, indicating that lattice or Christiansen effects do not completely explain the spectra under 1200 cm.$^{-1}$. A better explanation for this behavior is that the proton moves in a very anharmonic force field which allows for the proton motion to be coupled with numerous other motions.

(29) C. J. W. Brooks, G. Eglinton, and J. F. Morman, *J. Chem. Soc.*, 106 (1961).

(30) D. Hadzi and A. Novak, *Spectrochim. Acta*, **18**, 1059 (1962).

Dissociation Constant and Degree of Dissociation for Tetraethylammonium Chloride in Ethylene Dichloride at 0, −15, and −30°

by David L. Lydy,[1a,b] V. Alan Mode,[1c] and Jack G. Kay

The William Albert Noyes Laboratory, University of Illinois, Urbana, Illinois *(Received May 15, 1964)*

The conductivities of millimolar solutions of $(C_2H_5)_4NCl$ in 1,2-dichloroethane have been measured and the degree of dissociation of the solute has been calculated. The results indicate that for 6×10^{-3} *M* solutions, the solute is approximately 27% dissociated at 0°, 30% at −15°, and 43% at −30°.

I. Introduction

In a series of papers, Kraus and co-workers have reported the conductance of a number of electrolytes in ethylene dichloride at 25°.[2]

In conjunction with some isotopic exchange studies, we have needed to determine the free halide ion concentration for solutions of tetraethylammonium chloride in ethylene dichloride over a range of temperatures. We have obtained new conductivity data from which the degree of dissociation of $(C_2H_5)_4NCl$ in ethylene dichloride at 0, −15, and −30° has been calculated. These data and calculations are reported herein.

II. Experimental

Materials. Fisher Certified reagent grade ethylene dichloride (1,2-dichloroethane) (Karl Fischer water analysis $< 0.01\%$) was treated by repeated mixing with activated alumina, mixing with calcium hydride, and distilling from calcium hydride through a 1.2-m. column packed with glass helices. Samples were stored in stoppered Pyrex flasks in a desiccator containing anhydrous calcium chloride. Gas chromatographic analysis indicated that the water concentration was less than 10^{-4} mole/l.

Eastman White Label tetraethylammonium chloride was dried under vacuum with P_2O_5. A typical analysis follows. *Anal.* Calcd.: C, 57.97; H, 12.16. Found: C, 57.63; H, 12.14.

Apparatus and Procedure. A Sargent conductivity cell designed for low specific conductivity work and a Model RC-16B-2 Industrial Instruments Inc. conductivity bridge were used for the measurements. The cell was prepared by standard methods and cell constants were determined at 0 and 25° during the course of the study. Cell constants at −15 and −30° were obtained by a linear extrapolation of the specific conductance for a standard KCl solution with a correction for water conductance. The resulting cell constants were nearly unchanged over the temperature range from 25 to −30°, confirming the conclusions of Robinson and Stokes[3] for the type of cell used.

The samples of tetraethylammonium chloride in ethylene dichloride were prepared by dilution of a stock solution, taking care to exclude moisture. Measurements at each concentration were repeated until constant values were obtained for the resistance. Temperature control was ±0.1°.

III. Results

The method of Fuoss and Shedlovsky[4] was employed to obtain the limiting conductance (Λ_0) and dissociation constant (K). Following substitution of the expression for α, the degree of dissociation, into the mass action equation, it was possible to obtain

(1) (a) This report is based on a portion of a thesis submitted by D. L. Lydy in partial fulfillment of the requirements for the degree of Doctor of Philosophy in the Department of Chemistry and Chemical Engineering at the University of Illinois, June 1963; (b) Procter and Gamble Predoctoral Fellow, 1961–1962; University of Illinois Fellow, 1962–1963; (c) University of Illinois Fellow, 1962–1964.

(2) W. E. Thompson and C. A. Kraus, *J. Am. Chem. Soc.*, 69, 1016 (1947), and associated references.

(3) R. A. Robinson and R. H. Stokes, "Electrolyte Solutions," 2nd Ed., Butterworth and Co., Ltd., London, 1959, pp. 97–99.

(4) R. M. Fuoss and T. Shedlovsky, *J. Am. Chem. Soc.*, 71, 1496 (1949).

$$\frac{1}{\Lambda S(z)} = \frac{1}{\Lambda_0} + \frac{C\Lambda S(z) f_{\pm}^2}{K\Lambda_0^2} \quad (1)$$

where Λ is the equivalent conductance, C is the total amount of tetraethylammonium chloride per liter of solvent, and $f_{\pm}$ is the mean activity coefficient determined with the Debye–Hückel limiting law.

In order to use tabulated values for the complex function $S(z)$,[5] it was necessary to determine the viscosity (η) and dielectric constant (ϵ) of the pure solvent at the temperatures of interest.

Viscosity values at 0, −15, and −30° were calculated using the equation

$$\log \eta = \left(\frac{532}{T}\right) - 3.891 \quad (2)$$

The dielectric constants, determined graphically,[6-8] were 11.86, 13.13, and 14.39 for 0, −15, and −30°, respectively.

Table I contains the values of Λ_0 and K for the temperatures of interest.

Table I: Limiting Conductance and Dissociation Constant for $(C_2H_5)_4NCl$ in Ethylene Dichloride over the Temperature Range 25 to −30°

Temp., °C.	Limiting conductance, ohms^{-1} cm.^{2}	Dissociation constant, $K \times 10^4$
25[a]	77.4	0.510
0	49.3 ± 1.5	0.958 ± 0.043
−15	38.0 ± 1.1	1.32 ± 0.05
−30	27.8 ± 0.5	2.59 ± 0.07

[a] See ref. 2.

By substitution of the mean activity coefficient in terms of α into the mass action equation, a function was obtained which was solved for α by successive approximations

$$\frac{K(1-\alpha)}{\alpha^2} = Ce^{A(C\alpha)^{1/2}} \quad (3)$$

where

$$A = \frac{-8.395 \times 10^6}{(\epsilon T)^{3/2}}$$

Values for α are shown in Figure 1.

IV. Discussion

The appearance of a minimum in the dissociation curve is not unexpected for ionic salts in nonaqueous solvents of small dielectric strength. Davies[9] has discussed the factors which produce a minimum and has

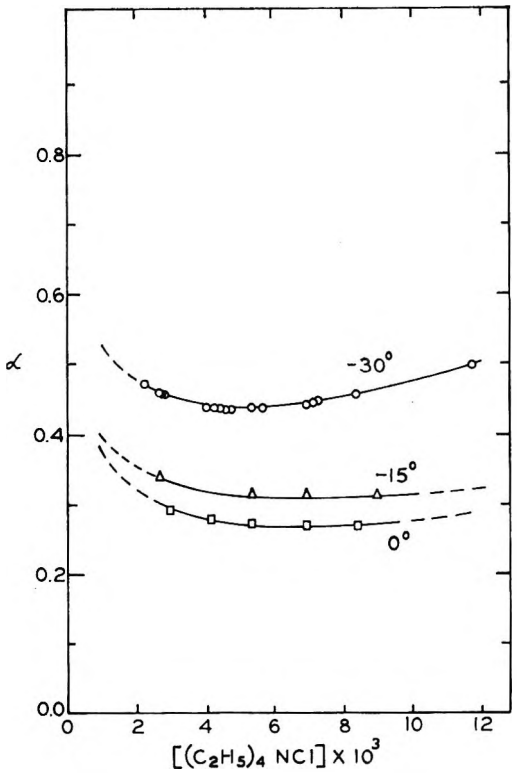

Figure 1. Degree of dissociation of $(C_2H_5)_4NCl$ in ethylene dichloride over a range of solute concentrations.

developed an equation from which it is possible to calculate the value of αC at which this minimum occurs.

As shown in Table II, our observed minima differ from the calculated minima by a factor of approximately 5.3. When compared with other work in this field, our results are in remarkably good agreement with the calculated values.

Table II: Calculated and Observed Minima in the Degree of Dissociation of $(C_2H_5)_4NCl$ in Ethylene Dichloride

Temp., °C.	$\alpha C \times 10^3$ M Obsd.	$\alpha C \times 10^3$ M Calcd.
0	1.92	10.21
−15	2.19	11.70
−30	2.44	12.87

It has been necessary in all calculations to use a

(5) H. M. Daggett, Jr., *J. Am. Chem. Soc.*, **73**, 4977 (1951).

(6) C. P. Smyth, R. W. Dornte, and E. B. Wilson, Jr., *ibid.*, **53**, 4242 (1931).

(7) M. Yasumi and M. Shirai, *J. Chem. Phys.*, **20**, 1325 (1950).

(8) A. H. White and S. O. Morgan, *ibid.*, **5**, 655 (1937).

(9) C. W. Davies, "Ion Association," Butterworth, Inc., Washington, D. C., 1962, pp. 105–116.

macroscopic dielectric constant. In a solvent such as ethylene dichloride, there appears to be a significant difference between the macroscopic dielectric constant and the effective "microscopic" dielectric constant which exists near the ionic and molecular species in solution. Inami, Bodenseh, and Ramsey[10] have indicated that the effective dielectric constant of ethylene dichloride may be as large as 12.4 in solutions of n-$(C_4H_9)_4NClO_4$ at 25° ($\epsilon_{macro} = 10.23^2$).

Glueckauf's[11] corrections of the conventional Debye–Hückel expression to include short-range changes in the dielectric strength are insignificant at the temperatures and concentrations used in this study.

As both A and K in eq. 3 are functions of the dielectric constant, our reported degree of dissociation may be slightly in error. This could account for the variation between the calculated and observed minima in the degree of dissociation. Further work will be necessary to clarify this point.

(10) Y. H. Inami, H. K. Bodenseh, and J. B. Ramsey, *J. Am. Chem. Soc.*, **83**, 4745 (1961).

(11) E. Glueckauf, *Trans. Faraday Soc.*, **60**, 776 (1964).

A Nuclear Magnetic Resonance Investigation of Ether–Boron Halide Molecular Addition Compounds in Dichloromethane

by Ernest Gore and Steven S. Danyluk

Department of Chemistry, University of Toronto, Toronto 5, Ontario, Canada *(Received May 27, 1964)*

A study has been made of the stabilities of a number of ether–boron halide addition compounds in dichloromethane at 23°. Equilibrium constants were determined for the reaction, $R_2O + BX_3 \rightleftharpoons R_2O \cdot BX_3$, by a least-squares analysis of the chemical shift–concentration curves for these systems. A shift to low field was observed for all of the ether protons on complexing with boron halide. The most marked deshielding (−1.25 p.p.m.) was noted for the 1:1 diethyl ether–boron trichloride compound and has been attributed to the formation of ethyl ethoxychloroborate, $C_2H_5{}^+C_2H_5OBCl_3{}^-$. Boron trichloride was found to be a stronger acceptor than boron trifluoride while the relative donor strengths of the ethers studied decreased in the order: $(C_2H_5)_2O \geq [(CH_3)_2CH]_2O > (CH_3)_2O$. The disagreement between the present n.m.r. results and earlier infrared and gas-phase dissociation studies has been attributed to the influence of the solvent on the mean chemical shift of ether–boron halide solutions in dichloromethane.

Introduction

Molecular addition compounds formed with group III-A acceptors such as boron and aluminum halides (MX_3) have been widely investigated and recent reviews emphasize the scope and importance of these compounds as intermediates in many organic reactions.[1–5] A variety of techniques including gas-phase dissociation,[6] cryoscopy,[7,8] electrical conductivity,[7,9,10] and infrared spectroscopy[11] have been used to establish the structure and stabilities of group III addition compounds. Re-

(1) W. Gerrard, "The Organic Chemistry of Boron," Academic Press, New York, N. Y., 1961.

(2) A. V. Topchiev, S. V. Zavgorodnii, and Ya. M. Pauskin, "Boron Fluoride," Pergamon Press, London, 1959.

(3) F. G. A. Stone, *Chem. Rev.*, **58**, 101 (1958).

(4) R. S. Mulliken, *J. Phys. Chem.*, **56**, 801 (1952).

cently, n.m.r. measurements have provided additional information about relative stabilities[12,13] and exchange rates[14] of boron addition compounds.

As part of a general study of solvent effects on the stabilities of addition compounds, we have determined the equilibrium constants for boron halide–ether complexes in dichloromethane. Chemical shifts were measured at 23° for the ether protons at varying boron halide concentrations and equilibrium constants were obtained by fitting the resultant chemical shift–concentration curves by a least-squares procedure. The relative stabilities for the complexes, determined by this method, are in disagreement with the results of earlier work.[11,13] This discrepancy can be attributed to the effect of the solvent molecules on the stability of the 1:1 complex.

Experimental

Reagent grade gases, BF_3, BCl_3, and $(CH_3)_2O$ (Matheson Co.), were further purified by the freeze–thaw technique in the vacuum system prior to passage into the reaction tube. Ethyl ether (Baker, analyzed) was used without further purification. The isopropyl ether (Fisher, certified reagent) was treated with ferrous sulfate to remove peroxides, dried over fresh Drierite, and then distilled in a 40-cm. vacuum-jacketed column packed with glass helices. The center portion boiling at 67.3° (uncor.) was collected for use.

Dichloromethane (Fisher, certified reagent) was dried over Drierite and distilled in the 40-cm. column; the fraction boiling at 38.9° (uncor.) was retained.

Solutions were prepared in a vacuum system and standard vacuum techniques were used to transfer the gases into calibrated volumes and then into the reaction tube. Diethyl ether and diisopropyl ether solutions in dichloromethane were prepared gravimetrically and were degassed before addition of the boron halide. Dimethyl ether was introduced by vacuum transfer into the reaction cell. The final ether concentrations were approximately 3 mole %. The shifts observed at this concentration differed by less than 0.1 c.p.s. from the shifts at infinite dilution.

The reaction tube was equipped with a magnetic stirrer and was attached to the vacuum system *via* a number of flexible joints. These permitted the tube to be tipped on its side in order to transfer a portion of the solution to an attached 5-mm. spinning tube. The solution in the side arm was cooled to liquid nitrogen temperature and sealed off prior to measurement. A slow irreversible reaction was noted in diethyl ether–boron trichloride solutions at room temperature. In order to minimize the effects of such reactions, the solutions were stored in Dry Ice until their measurement.

The n.m.r. spectra were recorded with a Varian DP-60 spectrometer at 23 ± 1°. All of the chemical shifts were measured relative to internal dichloromethane by the usual side-band technique. A minimum of four spectra were recorded for each concentration and the mean value was taken as the chemical shift. Chemical shifts for the methylene protons in ethyl ether complexes and the tertiary proton in diisopropyl ether addition compounds were taken as the midpoints of their respective multiplets. The measured chemical shifts are accurate to ±0.2 c.p.s.

Calculations

The relative stabilities of ether–boron fluoride addition compounds were determined by Craig and Richards[13] from an analysis of the mixing ratio, *i.e.*, n_{BX_3}/n_{R_2O}, chemical shift plots obtained for binary mixtures of the parent compounds. Satisfactory straight-line plots were obtained for each of the two component systems studied. In dichloromethane solutions, however, a linear relationship was only obtained for the diethyl ether–boron trichloride system and an alternative procedure was therefore adopted for evaluating the equilibrium constants.

The equilibrium constant for formation of the 1:1 addition compound

$$R_2O + BX_3 \rightleftharpoons R_2O{\cdot}BX_3$$

is given by

$$K = \frac{x(a + b - x)}{(a - x)(b - x)} \qquad (1)$$

where the initial moles of boron halide and ether are given by a and b, respectively, and x is the moles of 1:1 compound at equilibrium. Since the chemical shifts of the ether protons were independent of concentration at low concentrations in dichloromethane (3 mole %) the

(5) H. H. Prekampus and Th. Kranz, *Z. physik. Chem.* (Frankfurt), **34**, 213 (1963).

(6) D. E. McLaughlin and M. Tamres, *J. Am. Chem. Soc.*, **82**, 5618 (1960).

(7) N. N. Greenwood and R. L. Martin, *Quart. Rev.* (London), **8**, 1 (1954).

(8) H. E. Wirth, M. J. Jackson, and H. W. Griffiths, *J. Phys. Chem.*, **62**, 871 (1958).

(9) A. V. Topchiev, Ya. M. Pauskin, T. P. Vishny, and M. V. Hur, *Dokl. Akad. Nauk SSR*, **80**, 381 (1951).

(10) E. Gore and S. S. Danyluk, unpublished results.

(11) H. E. Wirth and P. I. Slick, *J. Phys. Chem.*, **66**, 2277 (1962).

(12) T. D. Coyle and F. G. A. Stone, *J. Am. Chem. Soc.*, **83**, 4138 (1961).

(13) R. A. Craig and R. E. Richards, *Trans. Faraday Soc.*, **59**, 1972 (1963).

(14) S. Brownstein, A. M. Eastham, and G. A. Latermouille, *J. Phys. Chem.*, **67**, 1028 (1963).

solvent concentration was not included in the calculations. If the initial mole fraction of boron halide is c then $c = a/(a + b)$; setting a equal to 1 mole, the equilibrium constant can be rewritten in the form

$$K = \frac{x\left(\frac{1}{c} - x\right)}{(1 - x)\left(\frac{1 - c}{c} - x\right)} \qquad (2)$$

In the present work only one set of signals was observed for the ether, indicating a rapid exchange of the ether molecule between free and complexed states. The observed chemical shift, δ_{obsd}, therefore corresponds to the weighted average of the chemical shifts for the addition compound, δ_{comp}, and the free ether, and is given by

$$\delta_{obsd} = \frac{x}{b}\delta_{comp} + \frac{b - x}{b}\delta_{R_2O} \qquad (3)$$

Solving (2) for x and substituting in (3), the observed chemical shift is then given by

$$\delta_{obsd} = \delta_{R_2O} + (\delta_{comp} - \delta_{R_2O})\left\{\frac{1 - \sqrt{1 - \frac{4K}{K + 1}c(1 - c)}}{2(1 - c)}\right\} \qquad (4)$$

The experimental and calculated shifts were analyzed by a least-squares procedure to obtain K and δ_{comp} values which gave the best fit of the experimental data. Calculations were carried out with an IBM 7090 computer using a program written for this purpose.

The limits of errors for the calculated equilibrium constants and chemical shifts could not be evaluated satisfactorily by Gutowsky's method.[15] An alternative procedure was therefore adopted and consisted basically of an analysis of the effect of random errors on K and δ_{comp}. A Fortran program was written to apply a random error to each chemical shift δ_{obsd} in turn. The random numbers were chosen to lie in the interval -1 to $+1$. For example, if the number lay within the interval ($^1/_3$, 1) an "error" of 0.5 c.p.s. was added to the shift; for a number in the interval ($-^1/_3$, $^1/_3$) the "error" added was zero, and for the interval ($-^1/_3$, -1) an "error" of -0.5 c.p.s was added. In this manner a series of random errors was generated and a new set of data was calculated in which a random error of ± 0.5 c.p.s. had been introduced. With this set of data a new K and δ_{comp} were calculated. The procedure was repeated a minimum of 25 times and from the 25 different values of K and δ_{comp} an estimate of the standard deviation in these two parameters was obtained.

The effect on the chemical shift δ_{obsd} of an additional reaction involving 2 moles of BX_3

$$R_2O + 2BX_3 \rightleftharpoons R_2O \cdot 2BX_3$$

to form the 1:2 addition compound was also investigated. However, the chemical shift–concentration curves could not be fitted satisfactorily when this reaction was included in the calculation and the chemical shift measurements therefore indicate that this reaction does not occur to any appreciable extent in the present systems over the concentration ranges studied.

Results

1. Dimethyl Ether Addition Compounds. A single signal was observed for the methyl protons in both the BF_3 and BCl_3 systems at the concentrations studied. The boron halide is therefore undergoing a rapid exchange between ether molecules at 23°. A slight broadening of the line widths was noted for $(CH_3)_2O$–BCl_3 solutions with increasing BCl_3 concentration; no change in line width was noted in BF_3 solutions. No new bands were observed to form in both systems over a period of several days. The variation of chemical shifts with boron halide concentration is illustrated in Figure 1. Concentrations are given in terms of the mole ratio of boron halide to ether in dichloromethane as solvent and the chemical shifts are relative to the solvent as reference. The solid curve represents the calculated chemical shifts obtained with the best values for K and δ_{comp}. A summary of chemical shifts, δ_{comp}, and equilibrium constants for the dimethyl ether compounds is given in Table I. The standard deviations between calculated and observed curves are also given in Table I.

A slight but measurable low-field shift of the pure ether signal was noted in dichloromethane at concentrations greater than 5 mole %.

Table I: Equilibrium Constants and Chemical Shifts for 1:1 Complexes

Complex	K	δ_{comp},[a] c.p.s.	Standard deviation between calculated and experimental curves, c.p.s.
$BF_3 \cdot Me_2O$	3.36 ± 1.06	61.2 ± 6.5	2.17
$BCl_3 \cdot Me_2O$	90.9 ± 6.3	61.9 ± 0.8	2.09
$BF_3 \cdot Et_2O$	171.4 ± 73.3	65.1 ± 0.5	1.20
$BCl_3 \cdot Et_2O$	472.6 ± 77.8	36.6 ± 0.2	1.50
$BF_3 \cdot i\text{-}Pr_2O$	106.8 ± 19.1	30.1 ± 0.5	1.31

[a] δ_{comp} is given relative to internal CH_2Cl_2.

(15) H. S. Gutowsky and C. H. Holm, *J. Chem. Phys.*, 25, 1228 (1956).

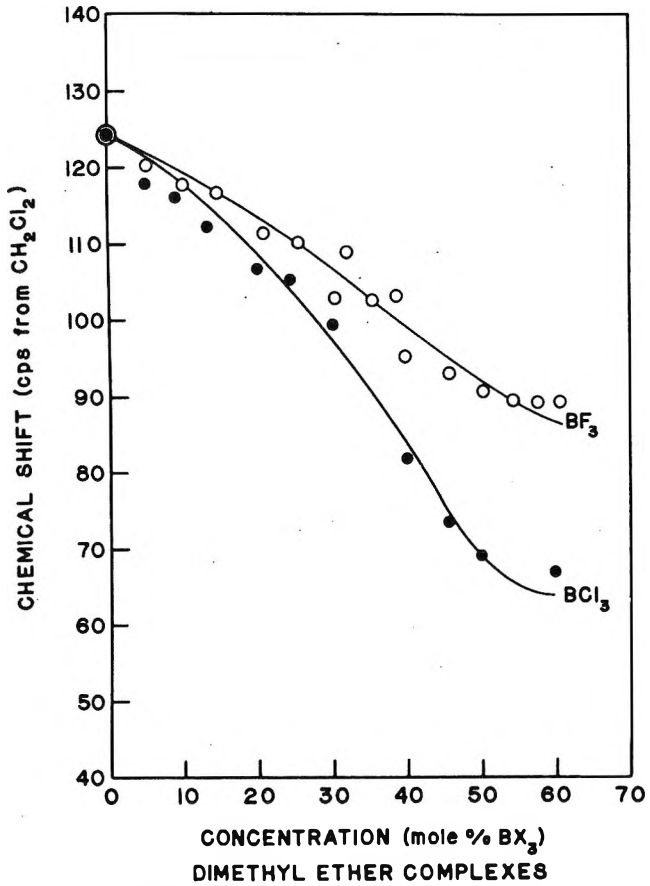

Figure 1. Variation of the chemical shift for dimethyl ether–boron halide solutions in dichloromethane at 23°: O, ●, measured shifts; ———, calculated shifts.

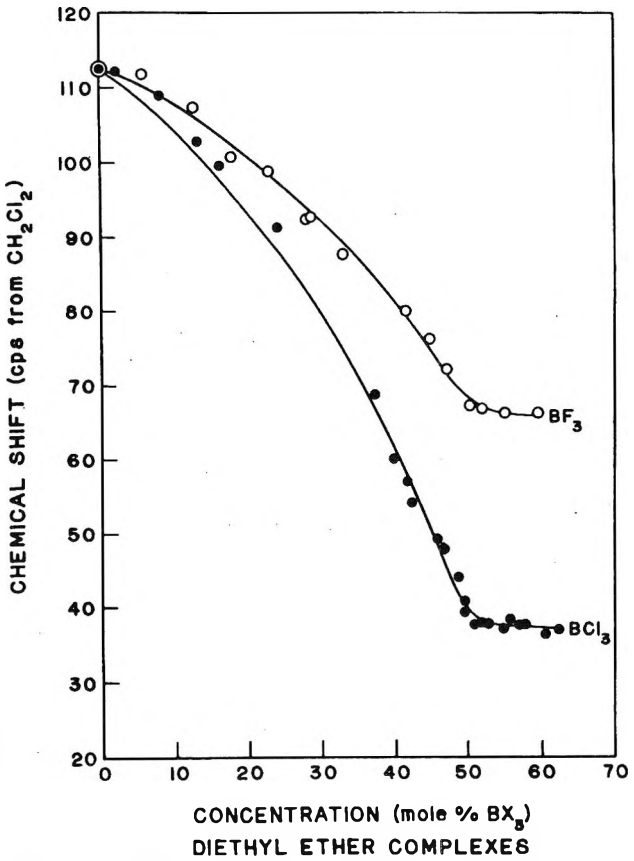

Figure 2. Variation of the chemical shift for diethyl ether–boron halide solutions in dichloromethane at 23°: O, ●, measured shifts; ———, calculated shifts.

2. Diethyl Ether Addition Compounds. A single triplet and quartet, characteristic of the methyl and methylene protons in an ethyl group with $J = 6.9 \pm 0.10$ c.p.s., was observed for all of the diethyl ether–BF_3 solutions. No change of the coupling constant was noted with increasing concentration of BF_3. Chemical shifts for the methylene protons are shown in Figure 2. Corresponding changes in the methyl group shifts were considerably less and have not been included. Analysis of the chemical shift data yields the δ_{comp} and K values listed in Table I. At high BF_3 concentrations a discernible broadening of the multiplets was observed, indicating a change in the exchange rate for the BF_3. All of the diethyl ether–BF_3 solutions were stable over a period of several days.

Freshly prepared solutions of BCl_3 and diethyl ether in dichloromethane also showed a characteristic ethyl group pattern. The chemical shift changes are shown in Figure 2 and the resultant K and δ_{comp} values are listed in Table I. Several differences in behavior from other ether–boron halide solutions were noted, however. A pronounced broadening of the multiplet signals was observed with increasing BCl_3 concentration. For example, line widths for the methylene protons increased steadily from 0.70 c.p.s. for pure diethyl ether to 3.5 c.p.s. for 27 mole % BCl_3 and then decreased again to 1.0 c.p.s. for a 1:1 mixture. The spectra for solutions with mixing ratios greater than 1 undergo a pronounced change with time when allowed to stand at room temperature. A similar time dependence has been noted previously[16] for the B^{11} spectrum of $(C_2H_5)_2O \cdot BCl_3$. A decrease of intensity was observed for the broad signals corresponding to $(C_2H_5)_2O \cdot BCl_3$ and two new sets of quartets and triplets appeared with the quartets centered at 63 ± 1 c.p.s. and 106 ± 1 c.p.s. relative to dichloromethane. After a period of several weeks, no signals were observable for the addition compound while intensities for the other signals had increased proportionately. A check of the chemical shift and coupling constant for the quartet at 106 c.p.s. showed that it was identical with that obtained for dilute solu-

(16) T. P. Onak, H. Landesman, R. E. Williams, and I. Shapiro, *J. Phys. Chem.*, **63**, 1533 (1959).

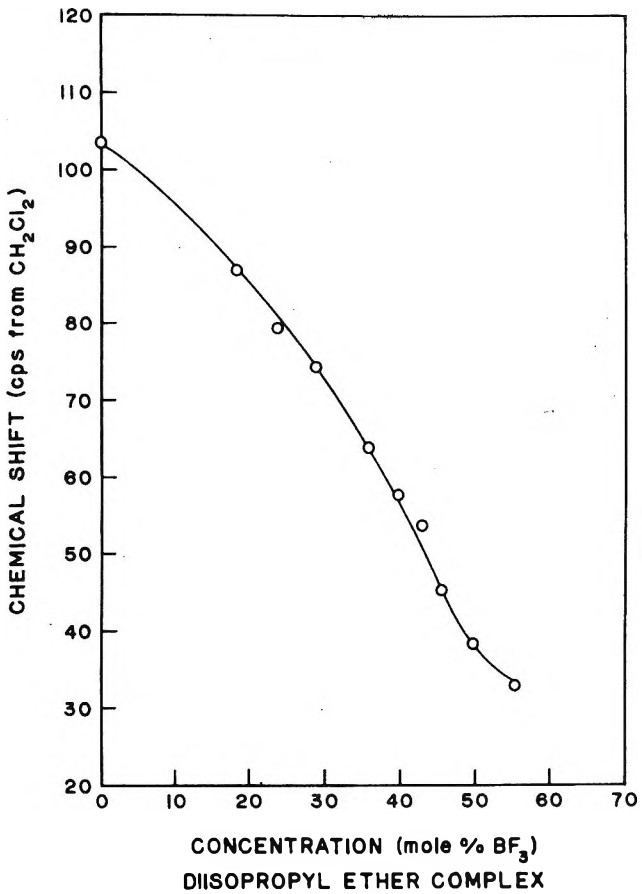

Figure 3. Variation of the chemical shift for diisopropyl ether–boron trifluoride solutions in dichloromethane at 23°: O, measured shifts; ———, calculated shifts.

tions of C_2H_5Cl in dichloromethane. This multiplet is accordingly attributed to C_2H_5Cl formed in the irreversible reaction of BCl_3 with diethyl ether. The second set of signals with considerably broader line widths ~2.0 c.p.s. is assigned to $C_2H_5OBCl_2$. This compound has been postulated as an intermediate in the over-all reaction of diethyl ether and BCl_3 (*cf.* Discussion). The CH_3–CH_2 coupling constants for the two new quartets were different from the $(C_2H_5)_2O \cdot BCl_3$ quartet. For the quartet at 63 c.p.s., $J = 7.2 \pm 0.2$ c.p.s., and for the quartet at 106 c.p.s., $J = 6.3 \pm 0.2$ c.p.s.

3. Diisopropyl Ether Addition Compound. The proton spectra for diisopropyl ether–boron fluoride solutions showed a septet and doublet characteristic of the isopropyl group. The variation of chemical shift for the tertiary proton (midpoint of the septet) with BF_3 concentration is shown in Figure 3. A summary of parameters derived from Figure 3 is given in Table I. Solutions of diisopropyl ether–BF_3 were stable over a period of several days with no evidence of other signals apparent. The coupling constant J_{CH_3-H} increases from 6.2 to 6.6 c.p.s. with increasing BF_3 concentration; no change in line width was observed over the concentration ranges studied.

Discussion

1. Proton Chemical Shifts. The proton resonances for all of the ethers are shifted to low field on complexing with boron halide; protons α to the oxygen are shifted by amounts approximately five times as large as β-protons. This deshielding results because of a decrease of electron density on the donor molecule (largely at the donor site) upon coordination with the acceptor. The decrease in shielding for α-protons in a given ether is significantly greater for the more stable BCl_3 compounds than for BF_3 compounds, in agreement with the trends observed for other addition compounds.[12] However, no correlation is noted between $(\delta_{R_2O} - \delta_{comp})$ for different ethers and the equilibrium constants of the corresponding addition compounds, indicating that factors such as steric hindrance and bond anisotropies are influencing the shifts in addition to electron density changes.

A comparison of the chemical shifts for $(CH_3)_2O \cdot BF_3$ and $(C_2H_5)_2O \cdot BF_3$ reported by Craig and Richards[13] with shifts for equimolar solutions of the components in dichloromethane shows that the latter are at higher field in each case. In addition, a linear plot of mixing ratio *vs.* δ was only obtained for $(C_2H_5)_2O$–BCl_3 solutions in dichloromethane; S-shaped curves resulted for all of the other systems with the largest deviation noted for $(CH_3)_2O$–BF_3 solutions. Both of these differences can be attributed to a partial dissociation of the addition compounds in dichloromethane at 23°. A significant difference (not explainable by susceptibility changes) is also noted between the calculated shift, δ_{comp}, for $(CH_3)_2O \cdot BF_3$ in dichloromethane and the shift for the pure compound.[13] In this instance it is likely that the discrepancy is due to hydrogen-bond interaction between $(CH_3)_2O$ and dichloromethane (section 3).

Of the ethers studied, the largest shift to low field on coordination with boron halide was observed in the diethyl ether–boron trichloride solutions. The methylene proton quartet of the addition compound, τ 5.32 p.p.m., lies outside the range normally observed for ethyl derivatives, *i.e.*, τ 5.64 to 6.80 p.p.m., and is in fact 0.32 p.p.m. to low field from ethyl fluoride.[17] This rather surprising deshielding cannot be interpreted in terms of any reasonable combination of electronegativity and diamagnetic anisotropy changes associated

(17) "NMR Spectra Catalogue," Vol. 1, Varian Associates Limited, Palo Alto, Calif., 1962.

with formation of the B–O coordinate bond. A more likely possibility is the presence of the addition compound as an ethyl ethoxychloroborate salt, $[C_2H_5]^+[C_2H_5OBCl_3]^-$, in solution with the positive charge localized on the methylene carbon of the $C_2H_5^+$ ion and the negative charge delocalized along the O–B–Cl bonds. The existence of such an ionic compound is supported by other experimental data. A study of the electrical conductivities of diethyl ether–BCl_3 solutions[10] has shown that the addition compound is in fact ionized to a significant extent in the molten state and in dichloromethane. For example, the equivalent conductance of a 1:1 mixture of $(C_2H_5)_2O$ and BCl_3 is 0.277 ohm^{-1} $cm.^2$ in dichloromethane at 25°. This is somewhat higher than the value reported for the molten $(C_2H_5)_2O \cdot BF_3$ addition compound where the existence of ethyl ethoxyfluoroborate, $[C_2H_5]^+[C_2H_5OBF_3]^-$, has been confirmed by electrolysis measurements.[9,18] In addition, conductivity changes with time observed for freshly prepared diethyl ether–BCl_3 solutions in dichloromethane can be correlated with changes observed in the proton resonance spectra for these solutions. It is likely that the ethyl ethoxychloroborate is formed as an intermediate in the irreversible reaction occurring at room temperature to form ethyl chloride and ethylchloroborinate.[19]

2. Relative Acceptor Strengths of the Boron Halides. The stabilities of the addition compounds in dichloromethane vary in the order $R_2O \cdot BCl_3 > R_2O \cdot BF_3$ for a given ether. Boron trichloride is therefore a stronger electron acceptor than boron trifluoride. This is in agreement with the relative acceptor strengths established in studies of dipole moments and heats of reaction for pyridine,[20–22] piperidine,[21] and acetonitrile[23] addition compounds. The order of acceptor strengths is consistent with a higher π-bond character in the B–F bond as compared with the B–Cl bond.[3,24] Thus, although it might be expected on the basis of electronegativities and steric requirements that BF_3 should be a stronger acceptor than BCl_3, the reorganization energy for the change in hybridization of the B atom from sp^2 to sp^3 is much higher for BF_3 and accounts for its weaker acceptor properties.

3. Relative Donor Strengths of Alkyl Ethers. It has been shown in earlier n.m.r.,[13] gas phase dissociation,[6] and distribution studies[11] that dimethyl ether is a stronger donor toward BF_3 than diethyl ether, while diisopropyl ether is a somewhat weaker donor than diethyl ether. Although the opposite order of base strengths would be expected on the basis of simple inductive effects, it is generally assumed that a strong steric effect predominates in the case of the diethyl and diisopropyl ethers. However, a recent study of infrared association shifts for hydroxy compounds[25] has shown that a larger shift, $\Delta\nu_{OH}$, occurs for methanol and phenol solutions containing diethyl ether as donor than for solutions containing dimethyl ether. Since the steric requirements for hydrogen-bond formation are undoubtedly less stringent than for addition compound formation with boron halides, the order of base strengths for the ethers is as expected on inductive grounds.

In the present investigation, the relative donor strengths decrease in the order diethyl ether > diisopropyl ether > dimethyl ether for a given boron halide in dichloromethane at 23°. The dimethyl ether addition compounds are clearly less stable than the other compounds with $(CH_3)_2O \cdot BF_3$ having the lowest equilibrium constant of the five compounds studied. The relatively low stabilities of the dimethyl ether compounds in dichloromethane are also indicated by electrical conductivity and vapor pressure measurements on these systems.[10]

A quantitative comparison of the present equilibrium constants with earlier results is not feasible because of wide differences in experimental conditions. However, the disagreement in the order of donor strengths and, in particular, the low stability observed for $(CH_3)_2O \cdot BF_3$ is surprising. It seems unlikely that the dichloromethane exerts any influence on the steric requirements of the higher ethers and the observed differences must be due to other complicating factors. Although dichloromethane has been regarded as an inert solvent in this work, the possibility of a weak hydrogen-bond interaction with ether molecules cannot be ruled out completely and would in fact be favored for dimethyl ether. A small concentration-dependent shift (3–5 c.p.s.) of dimethyl and diethyl ether protons was noted over the range 50 mole % ether to 1 mole % ether in CH_2Cl_2. A competing interaction of this type would alter the relative amounts of free and complexed ether calculated in (3) and would affect the calculated chemical shift–concentration curves in Figures 1–3. The

(18) N. N. Greenwood, R. L. Martin, and H. J. Emeléus, *J. Chem. Soc.*, 3030 (1950).

(19) H. Ramser and E. Wiberg, *Ber.*, **63**, 1136 (1930).

(20) C. M. Box, A. R. Katritzky, and L. E. Sutton, *J. Chem. Soc.*, 1248 (1958).

(21) N. N. Greenwood and K. Wade, *ibid.*, 1141 (1960).

(22) H. C. Brown and R. R. Holmes, *J. Am. Chem. Soc.*, **78**, 2173 (1956).

(23) A. W. Laubengayer and D. S. Sears, *ibid.*, **67**, 146 (1945).

(24) F. A. Cotton and J. R. Leto, *J. Chem. Phys.*, **30**, 993 (1959).

(25) C. H. Van Dyke and A. G. MacDiarmid, *J. Phys. Chem.*, **67**, 1930 (1963).

rather poor fit of the calculated and experimental chemical shift–concentration curves for the $(CH_3)_2O$–BCl_3 and $(CH_3)_2$-O–BF_3 systems could also be explained on this basis. An additional experimental difficulty arising from the high volatility of $(CH_3)_2O \cdot BF_3$ in dichloromethane would also affect the accuracy of the δ-concentration plot.

Acknowledgments. The financial assistance of the National Research Council and the National Cancer Institute of Canada are gratefully acknowledged.

Catalysis over Supported Metals. III. Comparison of Metals of Known Surface Area for Ethane Hydrogenolysis

by J. H. Sinfelt, W. F. Taylor, and D. J. C. Yates

Process Research Division, Esso Research and Engineering Co., Linden, New Jersey *(Received June 3, 1964)*

The kinetics of hydrogenolysis of ethane to methane have been investigated over a series of silica-supported metal catalysts containing 10 wt. % metal. The metals studied were nickel, cobalt, platinum, and copper, the surface areas of the metals being determined by hydrogen chemisorption. Over the range of temperatures studied (175–385°), the specific catalytic activities of the nickel, cobalt, and platinum for ethane hydrogenolysis vary in the order: Ni > Co > Pt. The position of copper in this sequence is far below that of nickel or cobalt, but its position relative to platinum changes over the range 175–385°. The rate of hydrogenolysis was found to be essentially first order in ethane pressure and to decrease with increasing hydrogen pressure over all the metals. However, the magnitude of the hydrogen pressure effect varied markedly for the different metals, the effect being greatest for nickel and platinum and least for copper. Apparent activation energies ranged from a maximum of 54 kcal./mole for platinum to a minimum of 21 kcal./mole for copper.

I. Introduction

Much of the fundamental work on catalysis over metals has been done using evaporated metal films as catalysts. In the classical work of Beeck and co-workers,[1] the catalytic activities of various metal films were determined for ethylene hydrogenation, and it was shown how the activities could be related to the lattice spacings. Boudart,[2] and subsequently also Beeck,[1] showed how the activities could be equally well explained in terms of an electronic picture. In any case, the activities of various metal films for ethylene hydrogenation were clearly established by the work of Beeck and co-workers.

The activities of supported metals for ethylene hydrogenation were studied by Schuit and van Reijen[3] in an effort to determine whether the earlier findings of Beeck and co-workers with metal films applied to supported metals. These workers reported data on a series of silica-supported metals and concluded that the results were generally in agreement with the results obtained over metal films. In this work the authors used hydrogen chemisorption measurements to enable them to account for differences in the surface areas of the various metals. This type of study is extremely

(1) O. Beeck, *Discussions Faraday Soc.*, **8**, 118 (1950).

(2) M. Boudart, *J. Am. Chem. Soc.*, **72**, 1040 (1950).

(3) G. C. A. Schuit and L. L. van Reijen, *Advan. Catalysis*, **10**, 242 (1950).

important to progress in understanding the catalytic properties of supported metals. In general, however, data on specific catalytic activity (rate per unit metal surface area) are nonexistent for supported metal catalysts. Consequently, comparisons of the catalytic activities of supported metals are very likely to be confused by differences in the metal surface areas. Investigations in which kinetic studies are combined with measurements of metal surface area are therefore highly desirable in elucidating the factors involved in catalysis over supported metals.

Recently, we have been interested in the catalytic hydrogenolysis of ethane over supported metals of known surface area. The kinetics of the reaction have been studied previously by Taylor and co-workers[4-6] over commercial iron and nickel catalysts. These studies established the main features of the kinetics, but were not intended to give a quantitative comparison of the specific activities of the metals. The nickel and iron catalysts used were different in form (supported *vs.* unsupported), and data on metal surface areas were not available. More recently, studies on the hydrogenolysis of saturated hydrocarbons over evaporated metal films have been reported by Anderson and Baker.[7] These investigators compared the specific activities of several different metal films (nickel, rhodium, tungsten, and platinum) and suggested that the rate-controlling step in the hydrogenolysis varied with the metal. However, the kinetics were not investigated in detail; *e.g.*, data on reaction orders with respect to hydrogen and hydrocarbon were not reported. Furthermiore, evaporated metal films are far less typical of real catalyst systems than a series of carefully prepared supported metals. Consequently, we have carried out an investigation of the kinetics of ethane hydrogenolysis over a series of supported metals, including nickel, cobalt, platinum, and copper. The catalysts were all prepared in the same way and contained 10 wt. % metal. Surface areas of the metals were determined by hydrogen chemisorption. Extensive kinetic data, including orders of reaction with respect to ethane and hydrogen as well as apparent activation energies, were obtained over all the metals.

II. Experimental

Apparatus and Procedure. The apparatus used for the hydrogen chemisorption work was a conventional glass vacuum system with an 80 l./sec. oil diffusion pump. Using a trap cooled in liquid nitrogen, ultimate dynamic vacua of about 10^{-7} torr were obtained. The sample cells were made of Pyrex glass and had two stopcocks to permit hydrogen to flow through the bed of material.

Samples of each of the catalysts, weighing about 2 g., were put in a vacuum apparatus. After evacuation at 100° for a short time, hydrogen was passed through the bed of the sample at a flow rate of 500 cm.^{3}/min. The temperature of the sample was then increased, in the flowing hydrogen, to 370°. This temperature was maintained overnight, and then the sample was evacuated for 1 hr. at the same temperature. After cooling to 18°, a hydrogen isotherm was measured; usually three points up to a pressure of about 30 cm. were obtained. The amount adsorbed at a pressure of 10 cm. was taken as the monolayer point, and the metal surface areas were calculated on the basis that each nickel atom in the surface adsorbs one hydrogen atom and that each hydrogen atom occupies 6.5 Å.^{2} of the surface.[8]

In the measurement of the hydrogen adsorption isotherms, the procedure adopted was to admit a known quantity of hydrogen to the adsorption cell and then wait for a period of about 1 hr. before reading the equilibrium pressure. The hydrogen adsorption isotherms for the various catalysts studied are plotted in Figure 1. The isotherms indicate that saturation is approached at hydrogen pressures above about 3 cm. and hence that the arbitrary choice of 10 cm. as the monolayer point is not unreasonable. Metal surface areas calculated from the isotherms are listed in Table I.

Table I: Summary of Metal Surface Areas of Catalysts as Determined by H_2 Chemisorption

Catalyst	Metal area, m.^{2}/g.[a]
Ni-SiO_2	13.6
Co-SiO_2	5.6
Pt-SiO_2	4.4
Cu-SiO_2	3.3

[a] Metal surface area per gram of catalyst after reduction with H_2 overnight at 370°.

An idea of the rate of adsorption of hydrogen on the nickel catalyst can be obtained from Figure 2, which shows the decline in hydrogen pressure in the adsorption cell as a function of time. The data are plotted

(4) K. Morikawa, W. S. Benedict, and H. S. Taylor, *J. Am. Chem. Soc.*, **58**, 1795 (1936).

(5) C. Kemball and H. S. Taylor, *ibid.*, **70**, 345 (1948).

(6) A. Cimino, M. Boudart, and H. S. Taylor, *J. Phys. Chem.*, **58**, 796 (1954).

(7) J. R. Anderson and B. G. Baker, *Proc. Roy. Soc.* (London), **A271**, 402 (1963).

(8) D. F. Klemperer and F. S. Stone, *ibid.*, **A243**, 375 (1958).

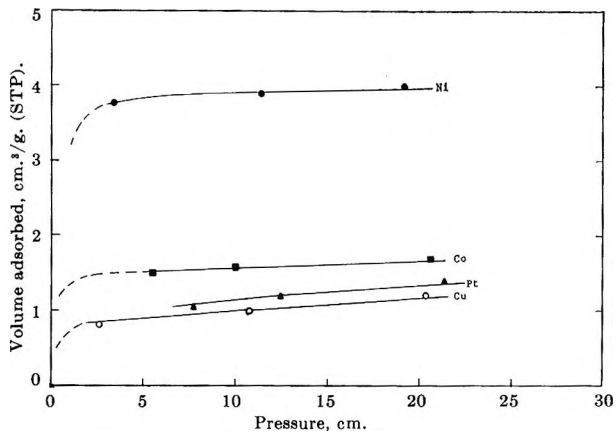

Figure 1. Adsorption isotherms for H_2 on the various silica-supported metals at 18°: ●, Ni; ■, Co; ▲, Pt; O, Cu.

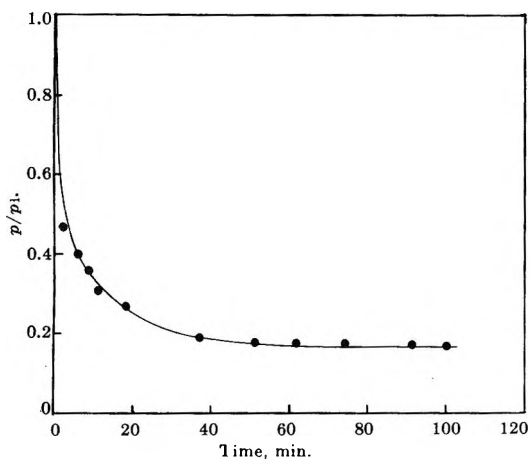

Figure 2. Pressure–time curve illustrating the rate of H_2 adsorption on the Ni on SiO_2 catalyst at room temperature: p = pressure at any given time; p_i = initial pressure.

as the ratio of the pressure, p, at any given time to the initial pressure, p_i. The rate of decline is negligible after about 1 hr., indicating attainment of equilibrium. Complete pressure–time curves were not obtained for the other catalysts, but in the case of the cobalt and platinum catalysts, at least, it was observed that the amount of adsorption after 1 hr. was negligible. Hence for nickel, cobalt, and platinum, the method of obtaining the hydrogen adsorption isotherms and the estimation of metal areas from the isotherms is reasonable.

In the case of the copper catalyst, however, the use of hydrogen chemisorption to determine the metal surface area may be less reliable. A considerable amount of work on copper catalysts reported in the literature indicates that the adsorption of hydrogen is slow and not completed in times comparable to the 1 hr. used in obtaining the isotherms in the present work.[9] Our experiments on the copper catalyst also gave an indication of this. Because of this complication, data obtained on the room temperature chemisorption of carbon monoxide over the copper catalyst are of interest. The adsorption in this case was found to be fast and essentially complete in about 15 min., and approached saturation at pressures below 10 cm. The ratio of the amount of carbon monoxide adsorbed at 10 cm. to the amount of hydrogen adsorbed was found to be 1.4. However, determination of metal surface area from carbon monoxide adsorption involves the complication that carbon monoxide may be chemisorbed in two forms, the bridge form occupying two sites and the linear form occupying one site. If the carbon monoxide is assumed to be adsorbed entirely in the linear form, with a cross-sectional area of 9.3 Å.^{2} per molecule of carbon monoxide,[10] the copper surface area agrees with that determined from the hydrogen adsorption data. If some of the carbon monoxide were adsorbed in the bridge form, the true copper surface area would be somewhat higher. In view of the fact that the hydrogen chemisorption method for estimating the surface area of the copper is not entirely free from objection, it could simply be fortuitous that the area obtained in this manner agrees even roughly with the carbon monoxide data. Nevertheless, the carbon monoxide adsorption data suggest that the surface area value reported in Table I is reasonable, although it is considered to be less reliable than the surface area values reported for the other supported metals in Table I. This is not a critical point, however, as the differences in the catalytic activities of the various metals are such that the uncertainty in the copper area has little bearing on the comparison of the catalysts.

The ethane hydrogenolysis data were obtained in a flow reactor system at atmospheric pressure, using a vertically mounted stainless steel reactor tube 1.0 cm. in diameter and 8.0 cm. in length. Details of the reactor assembly, flow rate measurements, and the gas chromatographic analysis of the reaction products have been reported previously.[11] The ethane and hydrogen were mixed with helium and passed downflow through a bed containing 0.20 g. of catalyst diluted uniformly with 0.50 g. of ground Vycor glass. By appropriate adjustment of the helium flow rate, it was possible to vary the partial pressures of ethane and hydrogen individually. The total gas flow was main-

(9) T. Kwan, *Advan. Catalysis*, 6, 67 (1954).

(10) B. M. W. Trapnell, "Chemisorption," Butterworth and Co., Ltd., London, 1955, p. 183.

(11) J. H. Sinfelt, *J. Phys. Chem.*, 68, 344 (1964).

tained at 1 l./min. throughout. In a typical run the reactant gases were passed over the catalyst for 3 min. prior to sampling products for analysis. The ethane was then cut out and the hydrogen flow continued for 10 min. prior to another reaction period. As an insurance against possible complications due to changing catalyst activity, most of the reaction periods were bracketed by periods at a standard set of conditions, so that the kinetic data could be expressed as rates relative to the rate at the standard conditions. Detailed data illustrating the utility of this technique have been published previously.[12] Prior to any reaction rate measurements, the catalysts were reduced overnight in flowing hydrogen (50 cc./min.) at 370° in the reactor.

Materials. The supported metal catalysts investigated in this work all contained 10% by weight of metal based on the combined weight of metal and support. The catalysts were prepared by impregnating silica with solutions of salts of the metals in deionized water. Aqueous solutions of $Ni(NO_3)_2 \cdot 6H_2O$, $Co(NO_3)_2 \cdot 6H_2O$, and $Cu(NO_3)_2 \cdot 6H_2O$ were used for impregnating the nickel, cobalt, and copper catalysts, respectively. The platinum catalyst was prepared by impregnating the silica with $Pt(NH_3)_2(NO_2)_2$, obtained from the Baker Division of Englehard Industries, Newark, N. J. The silica used as a support was Cabosil HS 5 (300 $m.^2/g.$ surface area), obtained from the Cabot Corp., Boston, Mass. After impregnation, the catalysts were all dried overnight at 105°. The dried catalysts were pressed at 8000 p.s.i. into wafers which were subsequently crushed and screened to a size between 45 and 50 mesh.

The ethane used in this work was obtained from the Matheson Co. A chromatographic analysis showed no detectable impurities. It is estimated that an impurity, *e.g.*, methane, would have been detected by the chromatographic analysis if it were present at a concentration above 0.01 wt. %. High purity hydrogen was obtained from the Linde Co., Linden, N. J. It was further purified in a Deoxo unit containing palladium catalyst to remove trace amounts of oxygen. The water formed was then removed by a trap cooled in Dry Ice or by a molecular sieve drier, the latter having been employed for the hydrogen used in the kinetic measurements.

III. Results

The metal surface areas of the various catalysts, as determined from the hydrogen chemisorption measurements, are listed in Table I. There was approximately a fourfold variation in the surface areas of the different metals.

The rate measurements on the hydrogenolysis of ethane to methane were made at low conversion levels (0.04 to 7.0%). Rates were calculated from the relation

$$r = \frac{F}{W} x \qquad (1)$$

where F represents the feed rate of ethane to the reactor in moles per hour, W represents the weight in grams of the catalyst, and x represents the fraction of ethane converted to methane. The reaction rate r is thus expressed as moles of ethane converted to methane per hour per gram of catalyst.

In a run to measure reaction rates the catalyst was first prereduced with hydrogen using the identical schedule of temperatures used in the hydrogen chemisorption measurements. This was done to ensure that the metal surface area of the freshly reduced catalysts would correspond exactly to that determined in the hydrogen chemisorption measurements. Then the temperature was lowered and at a standard set of hydrogen and ethane partial pressures (p_H = 0.20 atm., p_E = 0.030 atm.), the rates were measured at a series of temperatures in a rising temperature sequence. The data for the four catalysts are shown in the Arrhenius plots in Figure 3.

After determining the effect of temperature on rates, the temperature was lowered to an intermediate value in the range studied, and a series of measurements was made to determine the effects of the partial pressures of hydrogen, p_H, and ethane, p_E, on rates. As preliminary experiments had indicated that some variation of catalyst activity could occur in an extended set of rate measurements of this type, each reaction period was bracketed by periods at a standard set of conditions. The rate r at any given set of conditions, relative to the rate r_0 at the standard conditions (p_H = 0.20 atm., p_E = 0.030 atm.), is then given by the ratio r/r_0. This procedure serves to minimize the effects of variations in catalyst activity. Data on the effects of hydrogen and ethane partial pressures on r/r_0 are given in Table II.

For all four catalysts the data in Table II show that the rate of ethane hydrogenolysis increases with increasing ethane partial pressure, but decreases with increasing hydrogen partial pressure. The dependence of the rate on the partial pressures of ethane and hydrogen can be expressed in the form of a simple power law, $r = kp_E^n p_H^m$. Approximate values of the exponents n and m as derived from the experimental data are

(12) D. J. C. Yates, W. F. Taylor, and J. H. Sinfelt, *J. Am. Chem. Soc.*, 86, 2996 (1964).

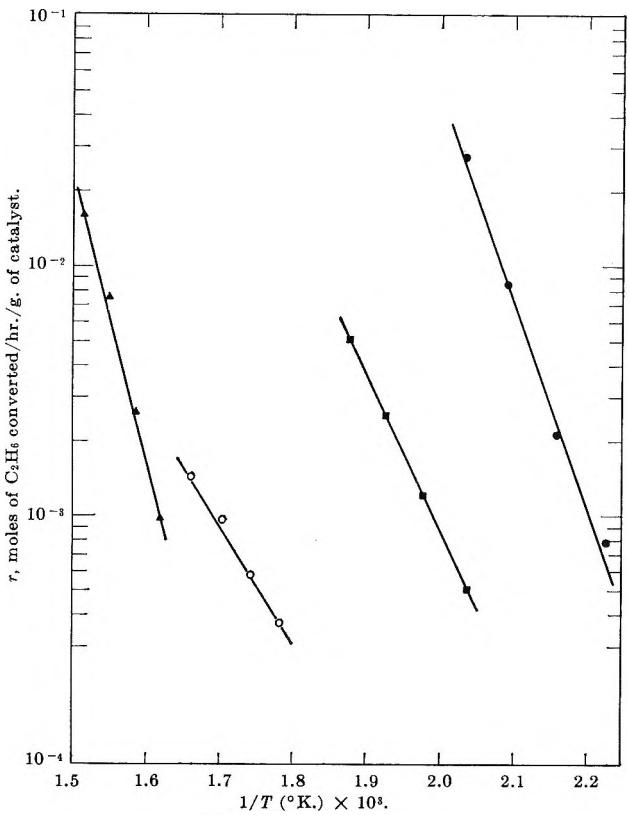

Figure 3. Effect of temperature on the rate of ethane hydrogenolysis over silica-supported metal catalysts at p_E = 0.030 atm. and p_H = 0.20 atm.: ●, Ni; ■, Co; ▲, Pt; O, Cu.

summarized in Table III. Values of the apparent activation energy E and the pre-exponential factor r' in the equation, $r = r' \exp(-E/RT)$, expressing the temperature dependence of the rate r at the standard conditions (p_H = 0.20 atm., p_E = 0.03 atm.) are also given in Table III. The pre-exponential factors were calculated per cm.^{2} of the supported metal, using the measured values of the metal surface areas given in Table I.

The general features of the kinetics of ethane hydrogenolysis over the catalysts employed in this study are in accord with the earlier studies of Taylor and coworkers,[4-6] in which the kinetics were investigated over nickel and iron catalysts of unknown metal surface area. These workers showed that the kinetics could be explained satisfactorily in terms of a mechanism involving a preliminary dehydrogenation of the ethane to an unsaturated radical C_2H_x on the surface, followed by attack of the surface radical by hydrogen

$$C_2H_6 \rightleftharpoons C_2H_x + aH_2 \qquad (2)$$

$$H_2 + C_2H_x \longrightarrow CH_y + CH_z \xrightarrow{H_2} CH_4 \qquad (3)$$

Table II: Effect of C_2H_6 and H_2 Pressures on Rates of C_2H_6 Hydrogenolysis

Catalyst	p_H, atm.	p_E, atm.	r/r_0[a]
Ni–SiO_2 (177°)	0.10	0.030	4.03
	0.20	0.030	1.00
	0.40	0.030	0.14
	0.20	0.010	0.37
	0.20	0.030	1.00
	0.20	0.100	3.91
Co–SiO_2 (219°)	0.10	0.030	1.69
	0.20	0.030	1.00
	0.40	0.030	0.52
	0.20	0.010	0.35
	0.20	0.030	1.00
	0.20	0.100	3.51
Pt–SiO_2 (357°)	0.10	0.030	4.25
	0.20	0.030	1.00
	0.40	0.030	0.13
	0.20	0.010	0.31
	0.20	0.030	1.00
	0.20	0.100	2.39
Cu–SiO_2 (330°)	0.10	0.030	1.46
	0.20	0.030	1.00
	0.40	0.030	0.79
	0.20	0.010	0.38
	0.20	0.030	1.00
	0.20	0.100	3.42

[a] Rate relative to the rate at standard conditions (p_H = 0.20 atm., p_E = 0.030 atm.) for the particular catalyst and temperature in question.

where a is equal to $(6 - x)/2$. On the assumption that the first step was an equilibrated one, and that the rate was limited by the rate of rupture of carbon–carbon bonds by reaction of the surface species C_2H_z with H_2, a rate law was derived which could be put in the form

$$r = k p_E^{\,n} p_H^{\,(1 - na)} \qquad (4)$$

From the experimental value of the exponent on ethane

Table III: Summary of Kinetic Parameters for Ethane Hydrogenolysis over the Various Supported Metals

Catalyst	Temp range, °C.	n[a]	m[b]	E[c]	r'[d]
Ni	177–219	1.0	−2.4	40.6	4.9×10^{31}
Co	219–259	1.0	−0.8	29.9	3.0×10^{25}
Pt	344–385	0.9	−2.5	54.1	5.9×10^{31}
Cu	288–330	1.0	−0.4	21.4	4.5×10^{20}

[a] Exponent on ethane pressure. [b] Exponent on hydrogen pressure. [c] Apparent activation energy, kcal./mole. [d] Pre-exponential factor, molecules/sec./cm.^{2}, in the equation, $r = r' \exp(-E/RT)$, expressing the temperature dependence of the rate r at the standard conditions (p_H = 0.20 atm., p_E = 0.030 atm.).

partial pressure n, the exponent $(1 - na)$ on hydrogen pressure can be calculated for a given value of a and compared with the experimental value m. A simple and reasonable assumption is that a can have values of 1, 2, or 3, corresponding to ethylene, acetylene, or acetylenic residues on the surface.[6] A comparison of observed and calculated values of the exponent on hydrogen pressure, in which a values are chosen to give the best fit to the data, is given in Table IV.

Table IV: Comparison of Observed and Calculated Values of the Exponent on Hydrogen Pressure

		Exponent on p_H	
Catalyst	a	Calcd.	Obsd.
$Ni–SiO_2$	3	−2.0	−2.4
$Co–SiO_2$	2	−1.0	−0.8
$Pt–SiO_2$	3	−1.7	−2.5
$Cu–SiO_2$	1	0	−0.4

It is clear that the value of a which gives best agreement between observed and calculated values of the exponent on hydrogen pressure varies when the ethane hydrogenolysis reaction is carried out over the different metals. Part of this could be an effect of temperature, since the catalysts were studied over different temperature ranges due to their wide variations in activity. In considering the results over platinum and nickel, the value of 3 for a indicates that the initial dehydrogenation step proceeds all the way to a completely hydrogen deficient dicarbon surface residue. Cimino, Boudart, and Taylor[6] arrived at a similar conclusion from a study of the kinetics over a nickel catalyst. In the case of the cobalt catalyst, a value of $a = 2$ accounts best for the observed kinetics, indicating that the surface residue is less hydrogen deficient. Finally, the data on the copper catalyst appear to be described best when a is taken equal to 1, indicating that the initial ethane chemisorption step involved in the hydrogenolysis over copper involves the least extensive rupture of carbon–hydrogen bonds in the molecule.

IV. Discussion

The results of this work show substantial differences in the catalytic activities per unit area of metal of various silica-supported metals for ethane hydrogenolysis. The order of activities of the three group VIII metals studied is: Ni > Co > Pt. The other metal studied (copper) is much less active than nickel or cobalt, but more active than platinum. However, a slight extrapolation of the data in Figure 1 on the copper catalyst indicates that at temperatures above 365° the position of copper relative to platinum would reverse, the platinum becoming more active. It should be noted that any comparison of the catalytic activities of these metals for ethane hydrogenolysis depends markedly on the hydrogen pressure, since the dependence of the rate on hydrogen pressure varies for the different metals.

In the analysis of the catalytic activities of the various metals, it is clear that the rate equations for ethane hydrogenolysis show considerable variation with respect to their dependence on hydrogen pressure. However, for the platinum and nickel, the rate equations are essentially the same with respect to the dependence on hydrogen as well as ethane pressure, suggesting that the intermediate surface residues formed in the initial ethane chemisorption step are similar. For these metals it is of interest to consider the difference in catalytic activities in terms of apparent activation energies and pre-exponential factors. From the data in Table II, it is clear that the large difference in catalytic activity between the nickel and platinum (about 10^5 to 10^6-fold in the temperature range studied) arises primarily from the difference in apparent activation energies, since the pre-exponential factors are the same within about 20%.

From the data on the effect of hydrogen pressure on the rate of ethane hydrogenolysis, we have concluded that the degree of unsaturation of the surface intermediate C_2H_x formed in the initial ethane chemisorption step increases in the order Cu < Co < Ni = Pt. It is interesting that the apparent activation energy also increases in a similar manner, except that the apparent activation energy for platinum is higher than that for nickel although the inferred degree of unsaturation of C_2H_x is the same for the latter two. If the degree of coverage of the surface by the intermediate C_2H_x is low, the apparent activation energy E is given by the equation $E = E_t + \Delta H$, where E_t is the true activation energy and ΔH is the heat of reaction associated with the over-all reaction indicated in eq. 2. The observation that the apparent activation energy increases as the degree of unsaturation of C_2H_x increases suggests that reaction 2 is endothermic, despite the fact that C_2H_x is an adsorbed species. The endothermic heat of dehydrogenation then more than counterbalances the exothermic energy of binding of C_2H_x to the surface. For two metals such as platinum and nickel, where the degree of unsaturation of the species C_2H_x is thought to be the same, the difference in apparent activation energies could be due to a difference in the binding energy of C_2H_x to the surface. Note that ΔH is given by the equation $\Delta H = \Delta H' -$

q, where $\Delta H'$ is the endothermic heat of dehydrogenation of the gas phase reaction, $C_2H_6 = C_2H_x + aH_2$, and q is the binding energy of C_2H_x to the surface. The higher apparent activation energy over platinum may then be due to a lower value of q for platinum.

It is interesting that the supported copper catalyst shows hydrogenolysis activity comparable to or higher than that of platinum. It is generally accepted that the chemisorption of saturated hydrocarbons takes place readily only on transition metals,[13] and hence hydrogenolysis activity might be expected to be limited to the transition metals. The activity of the transition metals is attributed to the existence of partly filled d-bands which are available for bonding. In the case of copper, which has no partly filled d-band but which immediately follows a transition metal series in the periodic table, it may be that electrons can be promoted from 3d to 4s states readily, since the energy required for d–s promotion is small.[14] It is possible that such a promotion could occur during the chemisorption process and hence create d-band vacancies which lead to formation of covalent bonds with the hydrocarbon.

Although it appears necessary for a metal to have an unfilled d-band to possess activity for chemisorption, it is clear that the activities of the various metals for ethane hydrogenolysis do not correlate with a parameter such as the % d-band character of the metal. Thus, platinum, with a significantly higher % d-band character than nickel, has a much lower activity. This is not unreasonable, however, if the chemisorption step is not the limiting factor in the reaction. As already discussed, it appears that the rupture of carbon–carbon bonds is probably rate limiting.

To summarize, the present work has combined hydrogen chemisorption measurements of the surface areas of supported metals with kinetic data to compare the specific catalytic activities of the metals for the hydrogenolysis of ethane. The use of such a procedure has made it possible to compare activities on a more fundamental basis than is usual for supported catalyst systems, since differences in the degree of dispersion of the metals are taken into account.

(13) G. C. Bond, "Catalysis by Metals," Academic Press, Inc., New York, N. Y., and London, 1962, p. 68.

(14) B. M. W. Trapnell, "Chemisorption," Butterworth and Co., Ltd., London, 1955, p. 174.

Oxygen Chemisorption on Ruthenium Dioxide

by J. T. Sommerfeld[1a] and G. Parravano

Department of Chemical and Metallurgical Engineering, University of Michigan, Ann Arbor, Michigan
(Received June 8, 1964)

The chemisorption of O_2 on RuO_2 was studied in a constant-volume system in the temperature range 100–385° and for starting pressures of 20–500 μ. Desorption was investigated at a pressure of 10^{-5} mm. and at temperatures in the range 200–385°. The rate of adsorption was found to decrease slightly with increasing temperature and was rapid at all temperatures investigated. The desorption-rate data could be correlated by an exponential equation, while the adsorption isotherms, covering the pressure range 0.01–500 μ, satisfied the Freundlich equation. The nature of the RuO_2 surface toward O_2 adsorption has been characterized by an exponential distribution of adsorption equilibrium functions. The isosteric heats of adsorption in the temperature range of 300 to 385° were found to decrease linearly with the logarithm of the surface coverage, and a value greater than 120 kcal. mole^{-1} was indicated for the heat effect at zero coverage. Isosteric activation energies of desorption in the same temperature range were also determined, and were observed to decrease linearly with the surface coverage. The activation energy of desorption at zero coverage was found to be 50.1 kcal. mole^{-1}. At temperatures below 300° both the isosteric heats of adsorption and the activation energies of desorption increased with decreasing temperature. The application of the absolute rate theory to the desorption results showed that the adsorbed species in the temperature range investigated are both mobile and dissociated.

Ruthenium dioxide is known to catalyze several types of reactions[1b] including inorganic and organic oxidations,[2] but there is no information on the chemisorption of gases, O_2 in particular, on this oxide. In order to obtain some insight into the nature of the surface interaction with molecular O_2, we have performed experiments on the thermodynamics and kinetics of the adsorption of O_2 on RuO_2 at temperatures of 100 to 385° and pressures of 0.01 to 500 μ. The results of these investigations are summarized in the present communication, together with calculations of the isosteric heats from adsorption isotherms and of activation energies from desorption rates.

Experimental

The RuO_2 (J. Bishop and Co.) was pretreated in a water–methanol solution at 80° for 2 hr., dried in nitrogen at 150° for 4 hr., and outgassed at a pressure of 10^{-5} mm. prior to each adsorption run. This treatment did not produce appreciable changes in surface area of the oxide. Three such measurements, with a number of adsorption–outgassing cycles between each one, were made, using the standard B.E.T. technique, and values of 3.81, 3.71, and 3.82 m.^{2} g.$^{-1}$ were obtained. Bulk reduction of the material at this outgassing temperature was considered unlikely. An extrapolation to 385° of the high-temperature equilibrium between O_2 and RuO_2[3] yielded a value for the equilibrium pressure of O_2 of 3.6×10^{-7} mm. This value is approximately one order of magnitude smaller than the lowest pressures ever achieved in the pretreatment of

(1) (a) National Science Foundation Fellow, 1959–1960; (b) J. E. Carnahan, T. A. Ford, W. F. Gresham, W. E. Grigsby, and G. F. Hager, *J. Am. Chem. Soc.*, 77, 3766 (1955); M. Freifelder and G. R. Stone, *ibid.*, 80, 5270 (1958); B. W. Howk, U. S. Patent 2,487,054 (Nov. 8, 1949); B. W. Howk and G. F. Hager, U. S. Patent 2,549,470 (April 17, 1951); E. Breitner, E. Roginski, and P. N. Rylander, *J. Chem. Soc.*, 2918 (1959); P. N. Rylander and J. Kaplan, *Englehard Ind. Tech. Bull.*, 2, 48 (1961).

(2) R. J. Mikovsky and R. F. Waters, *J. Phys. Chem.*, 59, 985 (1955); F. G. Oberender and J. A. Dixon, *J. Org. Chem.*, 24, 1226 (1959); A. E. Rea and M. Bebbington, "Annotated Bibliography on Ruthenium, Rhodium and Iridium as Catalysts," The International Nickel Company, New York, N. Y., 1959.

(3) H. Remy and M. Kohn, *Z. anorg. allgem. Chem.*, 137, 365 (1924).

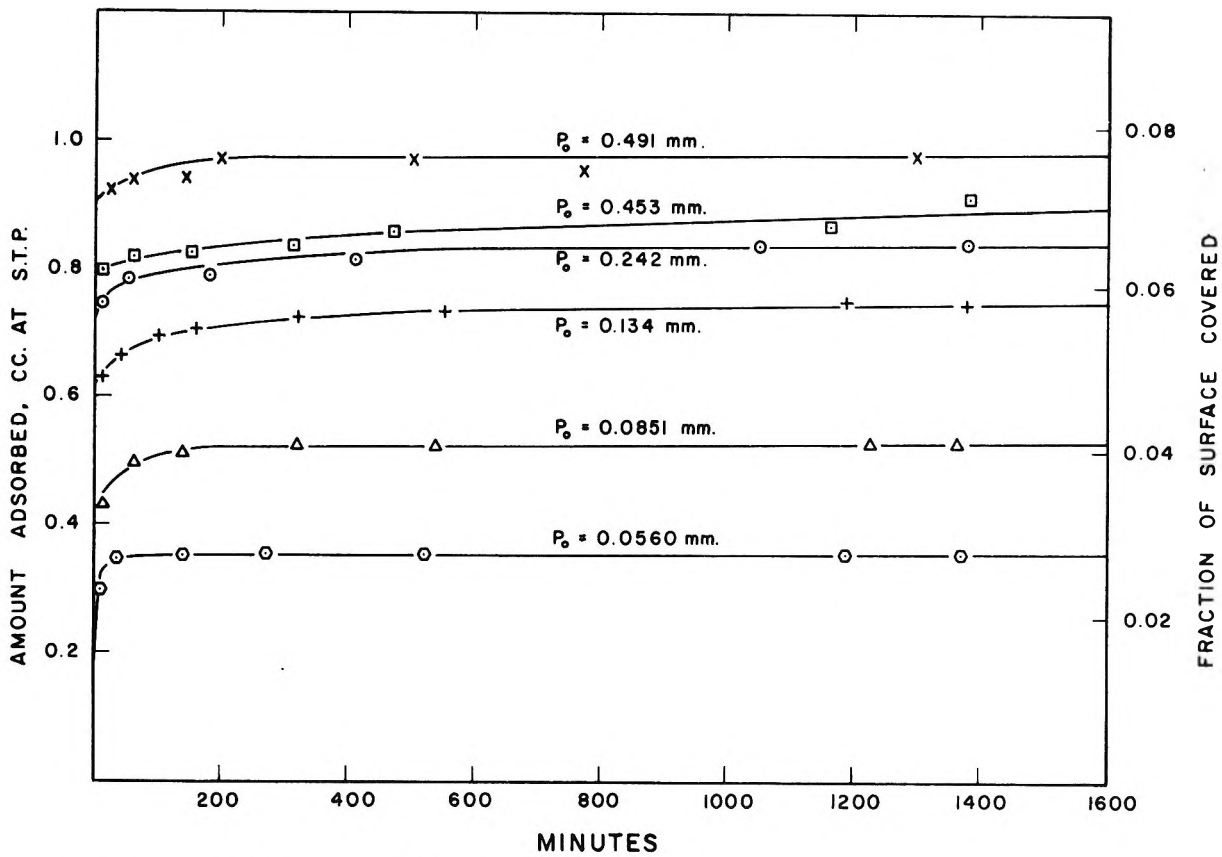

Figure 1. Adsorption of O_2 on 13.34 g. of RuO_2 at 350° and various pressures.

RuO_2. The validity of this conclusion was substantiated in desorption studies to be discussed below. The O_2 gas was prepared by thermal decomposition of potassium permanganate.

The high-vacuum adsorption apparatus was of standard design.[4] Pressures in the interval of 10–500 μ were measured *via* a Televac Model 2-A thermocouple gauge, and pressures in the range of 0.01–10 μ with a McLeod gauge. Adsorption was followed at constant volume by recording the pressure decrease as adsorption proceeded. The adsorption was essentially completed after 1 day and hence the amount adsorbed after this period of time was taken as the equilibrium uptake at the final resulting pressure in the system.

Desorption was followed by evacuating the sample with the diffusion pump only, collecting the desorbed gas in a previously evacuated 5-l. bulb on the low-vacuum side of the diffusion pump, and measuring the pressure increase with time in this bulb with the thermocouple gauge. Calculations showed that the desorption rate was not influenced by the gas flow through the connecting tubings and/or Knudsen diffusion through the voids of the adsorbent (see Appendix). Additional information on the calibration of the equipment and details of the experimental procedure used are summarized elsewhere.[5]

All of the results are presented on the basis of 13.34 g. of RuO_2, which corresponds to a total surface area of 50.7 m.^{2}. Using a value of 14.6 Å.^{2} for the cross-sectional area of an adsorbed O_2 molecule, a total uptake of 12.91 cc. (STP) of O_2 would be required to complete a B.E.T. monolayer on the surface.

Results

Adsorption and Desorption Rates. The observed initial rates of adsorption were extremely rapid for all of the temperatures and starting pressures investigated, and were essentially independent of the temperature. In most cases almost 50% of the final equilibrium amount adsorbed was taken up within the first minute of contact. Some typical results are presented in Figure 1, in which the amount adsorbed, q, at 350° is plotted *vs.* time for various starting pressures, p_0. The flat nature of these curves after 1 day of contact is

(4) G. C. A. Schuit and N. H. de Boer, *Rec. trav. chim.*, 70, 1067 (1951).

(5) J. T. Sommerfeld, Ph.D. Thesis, University of Michigan, 1963.

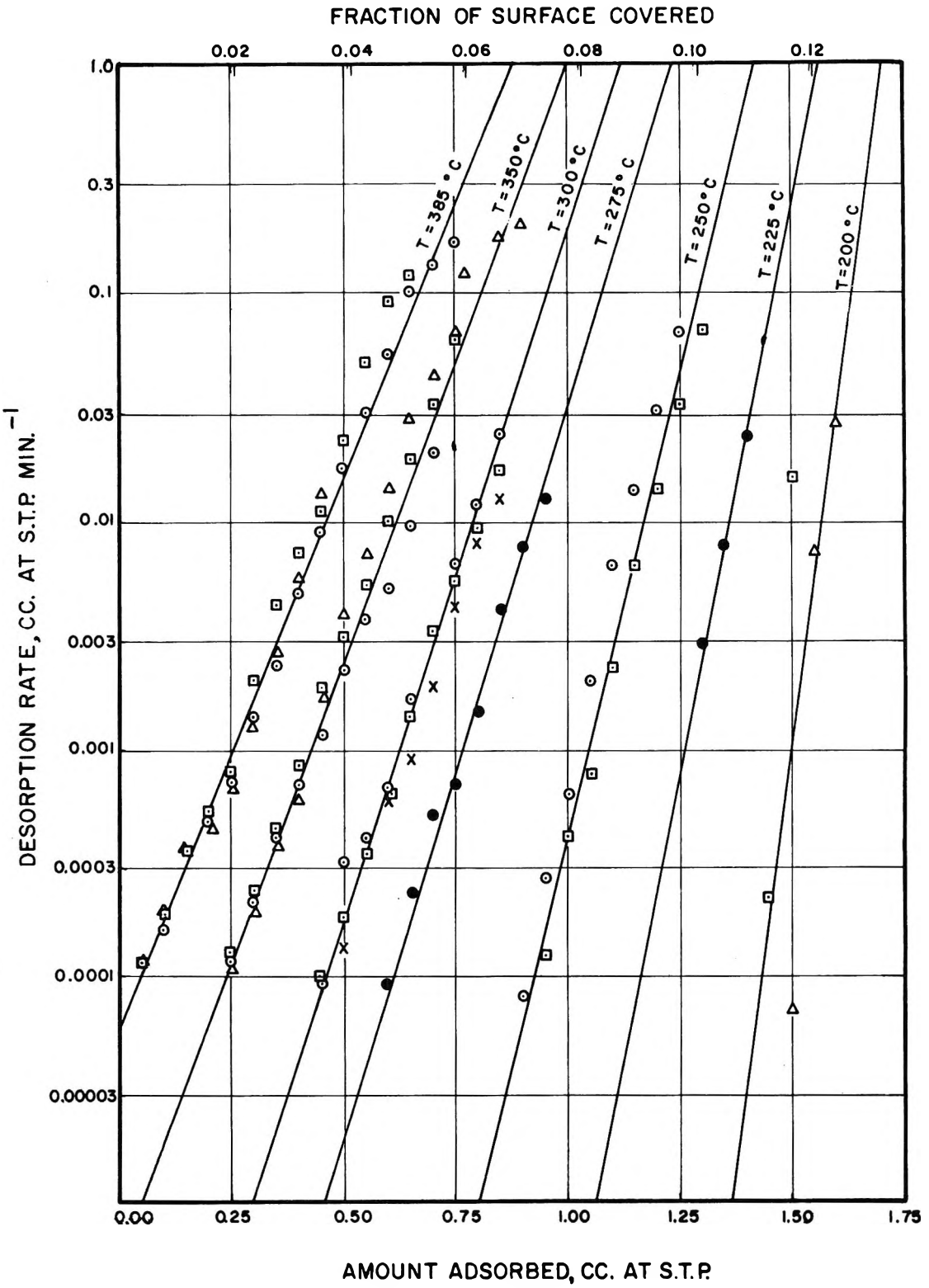

Figure 2. Rates of desorption of O_2 from 13.34 g. of RuO_2 at various temperatures. The various symbols employed for a given temperature correspond to different runs.

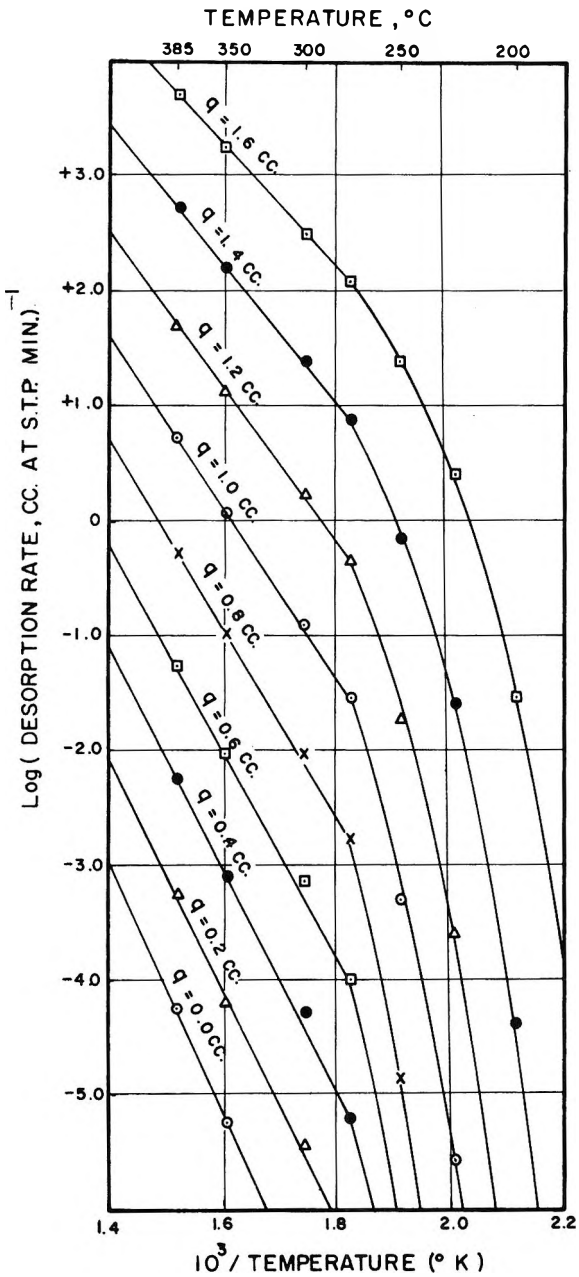

Figure 3. Isosteric Arrhenius plots for the rate of desorption of O_2 from 13.34 g. of RuO_2.

readily apparent. These high adsorption velocities in the regime where most of the adsorption is completed does not permit an accurate kinetic analysis of the results, since under these circumstances the diffusion through the RuO_2 bed and the response time of the thermocouple gauge may become limiting factors.

It is interesting to note that despite the uncertain kinetic nature of these adsorption rates, it is easy to fit the results of the early stages of adsorption with an equation of the type

$$q = 1/\alpha \ln t - 1/\alpha \ln t_0 \quad (1)$$

where α and t_0 are constants. Under the conditions in which this equation applies, O_2 adsorption could hardly be conceived as the limiting step. This fact throws some doubt, at least in the present instance, on the usefulness of eq. 1 for mechanistic studies in gas adsorption.

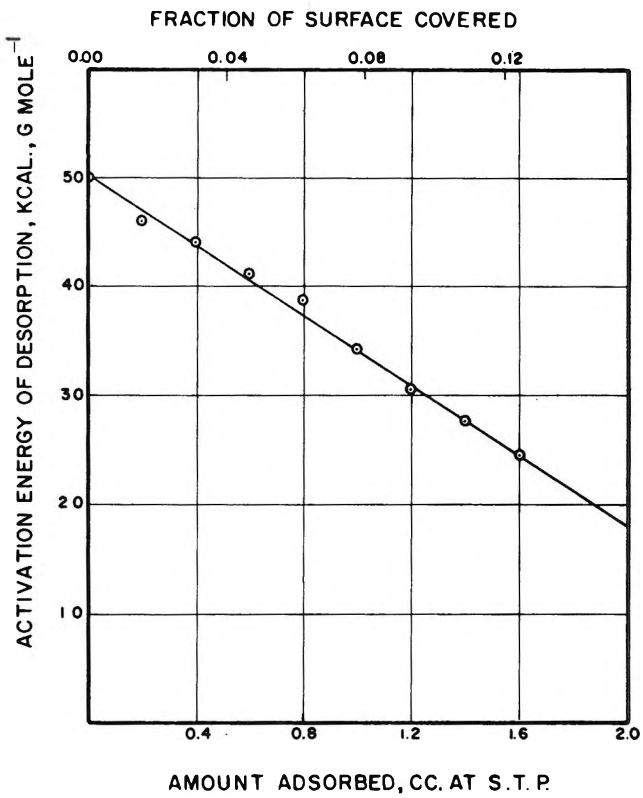

Figure 4. Activation energy of desorption of O_2 from RuO_2 as a function of surface coverage in the temperature range 275 to 385°.

The rate of desorption, as a function of the amount of gas remaining on the sample, was computed by numerical differentiation of the integral data. These results are shown in Figure 2, in which the logarithm of the rate is plotted *vs.* the surface coverage for temperatures of 200 to 385°. The rate of desorption can be represented by an expression of the type

$$-\frac{dq}{dt} = be^{\beta q} \quad (2)$$

where b and β are constants, dependent only upon the temperature.

Isosteric activation energies for desorption were obtained from the data of Figure 2 by means of an Arrhenius plot, using values of desorption rates at con-

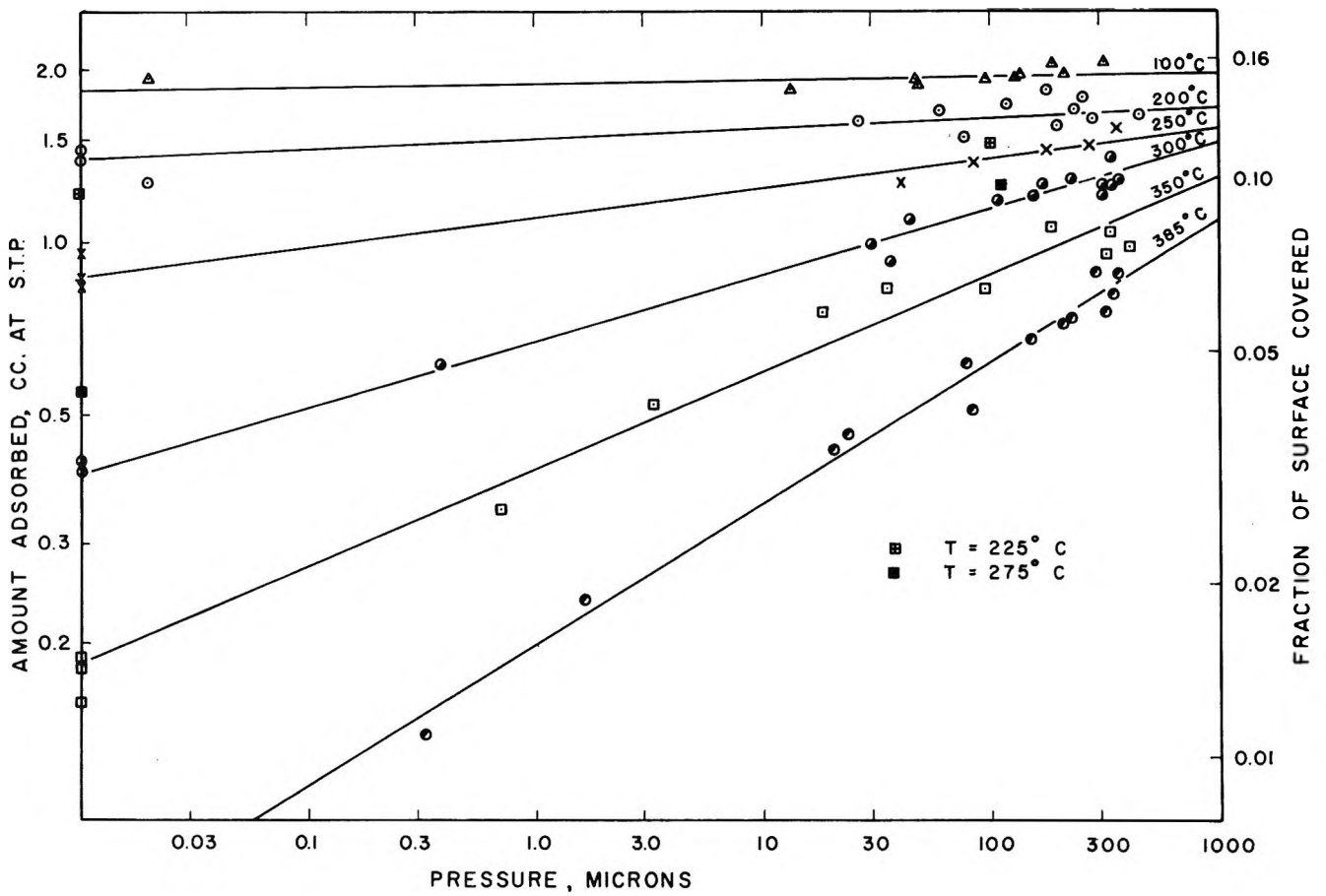

Figure 5. Isotherms for the adsorption of O_2 on 13.34 g. of RuO_2.

stant coverage. The computations are summarized in Figure 3, from which an increase of the isosteric activation energies with decreasing temperature, after exhibiting constancy in the temperature interval 275–385°, is observed. The activation energies, valid for this latter temperature region, are plotted in Figure 4 as a function of the surface coverage. The linear relationship may be expressed by the equation

$$E_{des}(q) = 50.1 - 15.94q \qquad (3)$$

where q is expressed in cc. (STP), and the value of 50.1 kcal. mole^{-1} is the activation energy for desorption at zero coverage. An expression of the form of eq. 3 is, of course, a necessary consequence if the constant β in eq. 2 in a linear function of $1/T$.

The pumping speed of the diffusion pump was not found to be a limiting factor in any of the desorption studies. In no case did the pressure in the collection reservoir exceed 200 μ and this value was approached only near the end of some runs where the desorption rate had become extremely small. On the other hand, leveling off of the desorption rates was occasionally observed in the initial stages of desorption for runs at sufficiently high temperatures and surface coverages, where the initial rates of desorption were rapid. However, under these conditions, such other factors as Knudsen diffusion of gas through the adsorbent bed and through the tubing connecting the sample container and diffusion pump must be considered (see Appendix).

Adsorption Thermodynamics. The adsorption isotherms are shown in Figure 5. They indicate that a relationship of the Freudlich type

$$q = Ap^{1/n} \quad (0 \leqslant 1/n < 1) \qquad (4)$$

can be satisfactorily used to describe the adsorption isotherms. The equilibrium values for $p = 10^{-5}$ mm. were assumed to be those which resulted after 1 day of adsorption at the temperature in question. This criterion was established after it was found that approaching the final pressure from the adsorption or desorption side produced a similar value of the amount adsorbed. (See Table I.)

Table I: Amount of O_2 Adsorbed at Equilibrium Pressure of 0.01 μ by 13.34 g. of RuO_2

Run	Temp., °C.	Amount adsorbed, cc. (STP)
Adsorption	200	1.38
Desorption		1.39
Desorption		1.42
Adsorption	250	0.85
Desorption		0.88
Adsorption		0.87
Adsorption	300	0.40
Desorption		0.40
Adsorption		0.42
Adsorption	350	0.18
Adsorption		0.19
Desorption		0.18
Adsorption		0.16

The problem of the reversibility of the adsorption as a function of the direction of temperature change was also investigated by reaching the equilibrium from the heating or cooling side. Some typical results obtained in this manner are summarized in Table II, together with representative runs corresponding to simple adsorption at a single temperature followed by desorption at the same temperature. Although it is difficult in the former type of experiments to set the experimental conditions in such a manner as to achieve a final equilibrium pressure similar to the values of the latter experiments, it is clear from Table II that there is good agreement between the two sets of experiments. It should be noted also that at the higher temperatures investigated it was possible to recover by desorption during an unduly long period of time 100% of the amount adsorbed at the same temperature.

Several values which resulted from adsorption–desorption studies at temperatures of 225 and 275° are also included in Figure 5. The experimentally determined values of A and n of (4), obtained *via* a least-squares technique, are given in Table III for the various temperatures investigated.

Adsorption isosteres are presented in Figure 6, where the logarithm of the equilibrium pressure is plotted *vs.* the reciprocal of the absolute temperature for various constant amounts of O_2 adsorbed. The slopes of these curves are directly related to the isosteric heats of adsorption

$$\ln p = \frac{\Delta H(q)}{RT} + I \qquad (5)$$

where $\Delta H(q)$ is the isosteric heat of adsorption and I is an integration constant. Figure 6 shows some typical adsorption isosteres.

Table II: Influence of the Direction Followed in the Temperature Change on the Adsorption of O_2 on 13.34 g. of RuO_2

Temp., °C.	Amount adsorbed, cc. (STP)	Equilibrium pressure, μ
300[a]	1.00	29
300[a]	1.24	303
350[a]	1.04	333
385[a]	0.89	356
250[a]	1.48	263
200[a]	1.69	232
300[b]	0.98	36
350[b]	0.91	318
385[b]	0.89	356
200[b]	1.78	253

[a] Experiments performed by adsorbing and reaching equilibrium at a given temperature and, subsequently, increasing or decreasing the temperature to a new value for equilibration; runs were carried out in the sequence reported from top. [b] Experiments of adsorption at a single temperature followed by desorption.

Table III: Freundlich Constants for the Adsorption of O_2 on 13.34 g. of Ruthenium Dioxide at Various Temperatures[a]

Temp., °C.	A, cc. (STP)	n
100	1.890	210
200	1.510	46.7
250	1.116	20.2
300	0.679	9.06
350	0.397	5.85
385	0.200	4.08

[a] Units: q, cc. (STP); p, μ.

Isosteric heats of adsorption were determined from the slopes of these isosteres in the temperature region 300–385°. The results are given in Figure 7 in which the heat, $-\Delta H$, is plotted *vs.* the logarithm of the surface coverage, θ. The rapid fall of the heat with the amount adsorbed, at least during the early stages of adsorption in this temperature range, is quite apparent, and may be described by the relationship

$$-\Delta H(q) = 27.0(1 - 3.641 \log q) \qquad (6)$$

wherein q is expressed in cc. (STP) and the factor of 27.0 kcal. mole^{-1} of O_2 is the heat at $q = 1.0$.

In a recent communication on the chemisorption of H_2 on ZnO,[6] it has been reported that the equilibrium amount adsorbed was a function of the manner in which the gas pressure was applied. A larger amount

(6) A. Cimino, E. Molinari, C. Borgianni, and E. Pepe, *J. Phys. Chem.*, **67**, 2238 (1963).

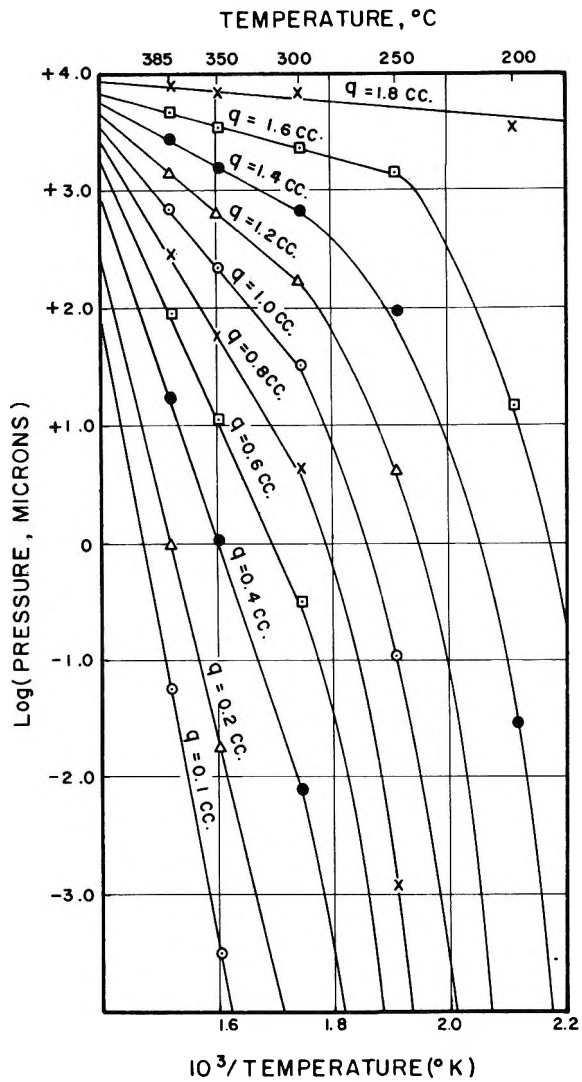

Figure 6. Isosteres for the adsorption of O_2 on 13.34 g. of RuO_2.

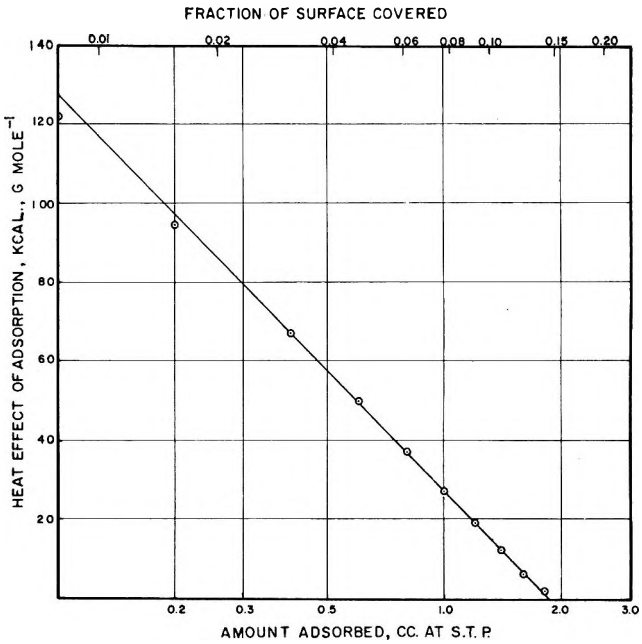

Figure 7. Heat of adsorption of O_2 on RuO_2 as a function of surface coverage in the temperature range 300 to 385°.

of gas adsorbed resulted when the final pressure was reached by means of different pressure incrementals instead of the more conventional method of introducing the gas over the sample in only one step. In order to verify this effect with RuO_2, O_2 was admitted at 300° at a starting pressure of 161 μ. After 1 day of contact, 1.000 cc. (STP) of O_2 was adsorbed; the pressure in the constant-volume adsorption system was increased to 344 μ by introducing additional O_2. The additional gas uptake was followed for 1 day until the resulting pressure in equilibrium with the sample was 303 μ and did not vary in 1 more day. The additional amount adsorbed was 0.239 for a total of 1.239 cc. (STP) of O_2. In a second experiment performed under similar conditions except that O_2 was introduced in one step only, the amount adsorbed was 1.240 cc. (STP). Thus the amount adsorbed was found to be independent of the method of O_2 addition to the sample.

Discussion

Adsorption Thermodynamics. Adsorption equilibria at solid surfaces may be formally described by a free energy function

$$\Delta F^\circ = \Delta F^\circ_{\text{intrinsic}} + RTf(\theta) \qquad (7)$$

where the superscript refers to a suitable standard state and $f(\theta) = 0$ for adsorption occurring without adatom interactions and/or surface heterogeneity effects. As a consequence of eq. 7, it is possible to define an adsorption equilibrium function

$$K(T,\theta) = \frac{\text{activity of occupied sites}}{\text{activity of free sites} \times \text{activity of gas molecules}} = K(T)_{\text{intrinsic}} \exp\{-f(\theta)\}$$

Since no restrictions are imposed on the function of $f(\theta)$, the latter can be used to characterize any conceivable deviation of the adsorption process from ideal behavior, for which $K = f(T)$ only. Assuming that the activity of occupied and nonoccupied surface sites and free gas molecules is given by θ, $1 - \theta$, and the pressure, p, respectively, the adsorption equilibrium function becomes for a diatomic molecule and dissociative adsorption

$$K(T,\theta) = \frac{\theta}{(1-\theta)p^{1/2}} \qquad (8)$$

The problem of deriving the function $f(\theta)$ from fundamental properties of the adsorbent–adsorbate system has been discussed at length in the past,[7,8] but no satisfactory solution is available due to a lack of detailed knowledge of the structure of the surface. Adatom interaction effects could probably be neglected in the present case in comparison to surface heterogeneity effects[9]; the only justification for the latter is the result that the experimental findings can be satisfactorily represented by eq. 4.[10] This situation, admittedly, cannot be taken as compelling since the Freundlich isotherm has been previously derived for a uniform surface.[11] Assuming that surface heterogeneity effects are preponderant, a distribution function, $\rho(K)$, of $K(T,\theta)$ can be introduced and defined in such manner that $\rho(K)\mathrm{d}K$ is the fraction of adsorption sites, $\mathrm{d}\theta$, having an equilibrium constant between K and $K + \mathrm{d}K$. Equation 8 may then be applied to an incremental portion of the surface in which all sites possess the same value of K. The fraction of these sites is given by

$$\mathrm{d}\theta = \frac{p^{1/2}K\rho(K)\mathrm{d}K}{1 + p^{1/2}K}$$

and the total fraction of surface sites involved

$$\theta = \int_{K_{min}}^{K_{max}} \theta(K)\rho(K)\mathrm{d}K = \int_{K_{min}}^{K_{max}} \frac{Kp^{1/2}}{1 + Kp^{1/2}}\rho(K)\mathrm{d}K \quad (9)$$

The integration limits K_{min} and K_{max} can be replaced with negligible error by 0 and ∞, respectively. Since in this work the equilibrium function can be calculated from the experimental results, one should solve eq. 9 for the distribution function $\rho(K)$. In general, this is not possible in a straightforward fashion, and the only practical approach to the problem is to calculate $\rho(K)$ directly from the experimental results.

It is possible to fit the experimental results reported in the previous section to an equation of the type

$$\ln K = a(T) - b(T)\theta \quad (10)$$

where $a(T)$, $b(T)$ are functions of temperature only, and $K(T,\theta)$ is given by eq. 8. A typical plot of the adsorption equilibrium function *vs.* the surface coverage at 385° is shown in Figure 8. Differentiation of eq. 10 with respect to θ and rearranging gives

$$\rho(K) = \frac{\mathrm{d}\theta}{\mathrm{d}K} = \frac{1}{bK} = \frac{\exp\{b\theta\}}{b\exp\{a\}} \quad (11)$$

Values of $\rho(K)$ for various values of K and T were computed and the results were plotted in Figure 9. The plots show that $\rho(K)$ decreases sharply as K in-

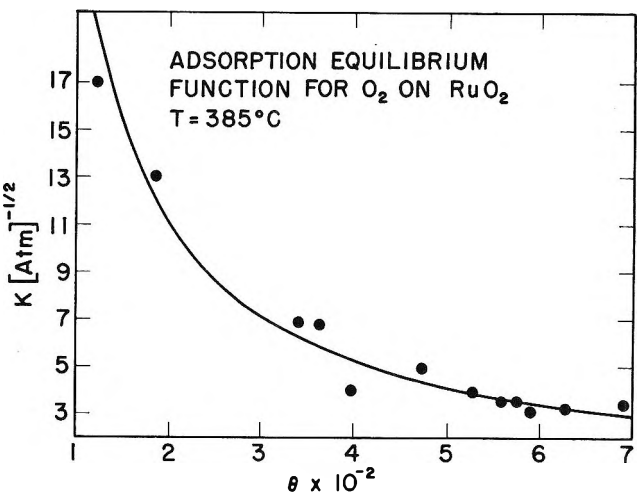

Figure 8. Adsorption equilibrium function, K, for O_2 on RuO_2 *vs.* surface coverage, θ, at 385°.

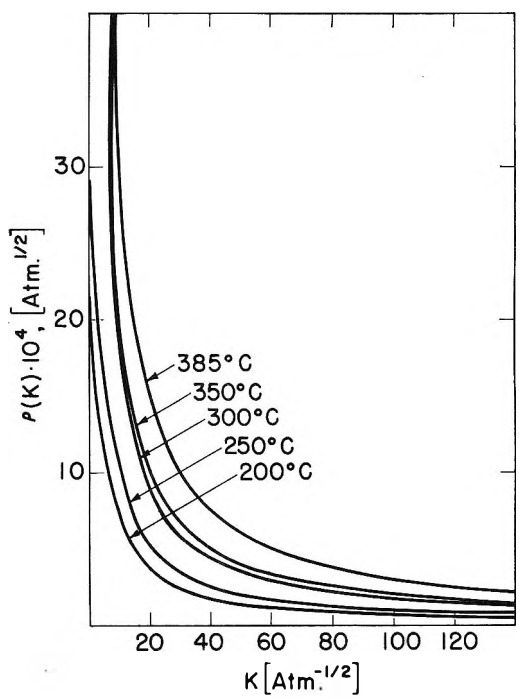

Figure 9. Distribution function $\rho(K)$ for the adsorption equilibrium function as a function of K at various temperatures for the adsorption of O_2 on RuO_2.

(7) S. Z. Roginskii, "Adsorption und Katalyse an Inhomogenen Oberflachen," Akademie-Verlag, Berlin, 1958.

(8) P. M. Nassonov, *Zh. Fiz. Khim.*, **35**, 118 (1961).

(9) J. Horiuti and T. Toya, *Kinetika i Kataliz*, **4**, 3 (1963).

(10) B. M. W. Trapnell, "Chemisorption," Butterworth and Co., Ltd., London, 1955.

(11) B. Tamamushi, *Bull. Chem. Soc. Japan*, **8**, 120 (1933).

creases, a steeper decrease resulting if the temperature is lowered. Under the assumptions previously mentioned, the distributions represented in Figure 9 can be taken as formally typifying the adsorption system RuO_2–O_2 and its deviation from ideal behavior. The graphs in Figure 9 show that adsorption sites with a low value of K make up the RuO_2 surface; 88% of the sites have $K \leq 20$ atm.$^{-1/2}$ at 200°.

Despite the lack of a well-defined physical basis, an attempt can be made to suggest possible surface configurations which may induce the type of distributions observed.

Let us consider surface adsorption zones with circular symmetry in such a fashion that a uniform radial energy distribution results.[7] In this instance it is possible to set

$$\frac{K}{K_1} = \left(\frac{r}{r_1}\right)^g \tag{12}$$

where K_1, K are the adsorption equilibrium functions for surface sites at distances r_1 and r, respectively, from the zone center and g is a constant. Setting

$$\rho(K)\mathrm{d}K = \rho(r)\mathrm{d}r \tag{13}$$

and $\rho(r) = 2\pi rm$, where m is the number of adsorption sites within a distance r from the zone center,[7] one gets from eq. 12 and 13

$$\rho(K) = \rho(r)\frac{\mathrm{d}r}{\mathrm{d}K} = AK^{(2/g)-1} \tag{14}$$

with $A = 2\pi m r_1^2/gK_1^{2/g}$. For large values of g, eq. 14 gives $\rho(K) \cong A/K$, which is similar to eq. 11.

Generally, the relation between the extent of surface covered with adatoms and the adsorption heat has been derived by comparing the equilibrium pressures at different temperatures for the same amount of surface coverage. This procedure implies that molecules adsorbed on surface regions corresponding to a value of the adsorption heat lower than a fixed quantity will not be adsorbed, while the opposite will apply to molecules adsorbed on surface sites possessing a higher value of the heat of adsorption. This, of course, is not strictly valid, since all surface regions contribute to the heat effect. The adsorption energy cannot be shown as a function of the fraction adsorbed, but can be represented as a function of the fraction of surface sites having an energy less than or equal to a certain value. An analysis similar to the previous one can be applied to the adsorption heats by defining a distribution function of the adsorption enthalpy, $\rho(\Delta H) = \mathrm{d}\theta/\mathrm{d}\Delta H$.

From the experimental results (Figure 7), one has

$$\Delta H(\theta) = 27.0[1 - 3.64 \log q]$$

where ΔH is in kcal. mole^{-1} and q in cc. (STP). Substitution of $\theta = q/12.91$ and differentiating with respect to θ gives

$$\frac{\mathrm{d}\Delta H}{\mathrm{d}\theta} = -\frac{42.66}{\theta} \tag{15}$$

or $\rho(\Delta H) = \theta/42.66 = 3.42 \times 10^{-3} \exp\{-\Delta H/42.66\}$. Thus $\rho(\Delta H)$ is a linear function of θ, as demanded by eq. 4, but varies exponentially with ΔH (Figure 10).

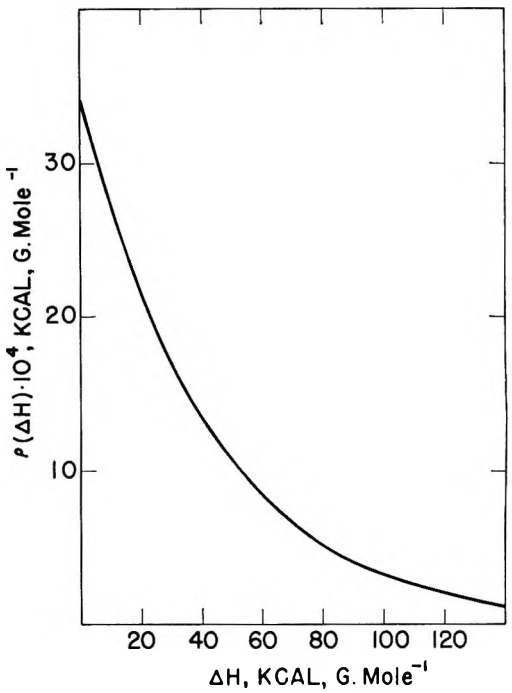

Figure 10. Distribution function $\rho(\Delta H)$ *vs.* ΔH for the adsorption of O_2 on RuO_2.

In terms of the simple model discussed above, a crude atomistic picture of the surface may be visualized by assuming the presence of surface centers (atoms, group of atoms, vacancies, and so on) capable of binding more than one adatom per center. Physically, this situation is equivalent to the presence of surface centers accommodating several electron trapping levels within each center. The various levels may result from rearrangements of the adsorption complex into more stable bonding configurations as the saturation of the center proceeds.

The computation of the energy distribution associated with this surface model can be easily done. Assuming that variations in the force field with distance, r, from the center of the surface complex and the saturation, z,

of the complex are the only contributions to the integral adsorption heat, ΔH, one has

$$\Delta H = -\int_{+\infty}^{r_0}\int_{0}^{z} F(r,z)\, dr dz \qquad (16)$$

where r_0 is a fixed distance, characteristic of the geometry of the site concerned. Taking $F(r,z) = c/r^f(1 + \alpha z)$, with c, f, and α constant, eq. 16 gives[12]

$$\Delta H = \frac{\Delta H_0}{a} \ln (1 + \alpha z) = \frac{\Delta H_0}{a} \ln (1 + \alpha S\theta)$$

where a, ΔH_0, and S are a constant, the adsorption heat for $z = 0$, and the total surface area, respectively. Then

$$\frac{d\theta}{d\Delta H} = \frac{(1 + \alpha S\theta)a}{\Delta H_0 \alpha S}$$

which is similar to eq. 15.

If metal cations are considered the primary sites for O_2 adsorption, the preceding analysis requires that surface cations show the possibility of different bonding arrangements with O_2. This is clearly related to thermodynamic, electronic, and geometric surface factors, the details of which are largely unknown. RuO_2 crystallizes in the rutile structure with close-packed O^{-2} ions arranged in hexagonal symmetry, with one half of the octahedral interstices filled. The cations lie at the corner and center of the tetragonal unit cell, and electrostatic repulsion among them produces distortion in the ideal packing of the O^{-2} ions. Because of this, the six O^{-2} ions are not equivalent in bonding strength. The structure and characteristics of some low index planes likely to appear at the surface of RuO_2 samples are reported in Figure 11 and in Table IV. An inspection of these structures shows the different types of O_2 ions. Thus, the base plane (001) has two O^{-2} ions lying closer to the center Ru^{+4}, while two additional O^{-2} ions are located at a greater distance. In addition, for Ru^{+4} ions lying in this plane, octahedral coordination is restored by the addition of two O^{-2} ions of the tight bind type. Similarly, in the (110) plane there are two kinds of Ru^{+4} ions. In one type, only one O^{-2}

Table IV: Atomic Characteristics of Some Crystal Planes in RuO_2[a]

Plane	Area of plane,[b] cm.^{2}	Average composition	Atomic density, atom cm.$^{-2}$	Adsorption site cation	Distance of adsorption site from cation, Å.
(100)	20.2×10^{-16}	2 O 1 Ru	1.5×10^{15}	2	2.01
(110)	19.8×10^{-16}	2 O 2 Ru	2.0×10^{15}	1 1	1.91 2.01

[a] Calculated with: Ru atoms at ($1/2$, $1/2$, $1/2$); (0, 0, 0); O atoms at (u, u, 0); $\pm(u + 0.5, 0.5 - u, 0.5)$; $u = 0.3$ [b] Per unit cell.

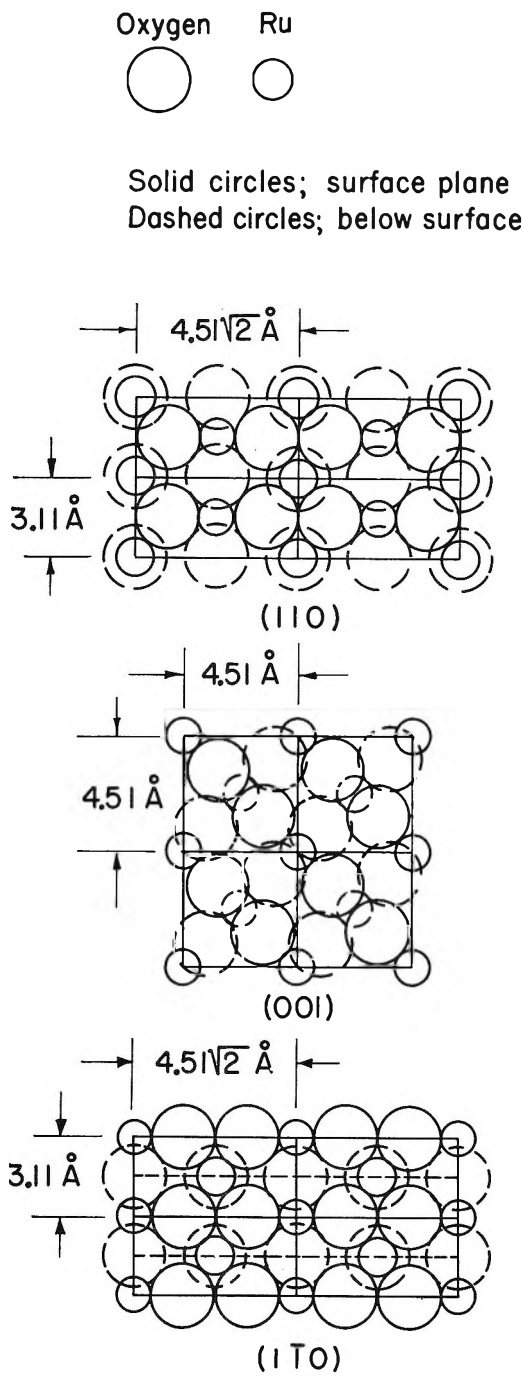

Figure 11. Structure of some low index planes in RuO_2.

(12) G. Parravano, *Gazz. chim. ital.*, 91, 467 (1961).

ion (tight bind) per Ru^{+4} can restore the octahedral coordination of the metal ion, while in the second case two O^{-2} ions are needed per Ru^{+4} ion. The above idealized picture gives an indication of the presence of adsorption sites for oxygen possessing different strength and accommodating different numbers of adatoms. In real surfaces, the situation is more complex and additional possibilities exist for the accommodation of more adatoms around the same center. In the case of ruthenium compounds, this latter effect is facilitated by the fact that there is not a large difference in stability between the ligand structures of Ru^{+}, Ru^{+2}, Ru^{+3}, and Ru^{+4}. In general, the electronic configuration of Ru^{+3} shows no coordination preference, while configurations for valence states >4 have a tendency for a tetrahedral environment.[13] O_2 adsorption on a RuO_2 surface can then be looked upon as the formation of surface groups $Ru(O)_x$. This, of course, is a simplification since each O^{-2} ion in the RuO_2 structure is coordinated with two Ru^{+4} ions. It should also be noted that the value of x in $Ru(O)_x$, controlling the reduction–oxidation state of surface reactions, depends upon temperature and O_2 pressure. It is also well known that low or high valence states of the metal ion can be stabilized by the presence of foreign substances.

The $Ru(O)_x$ surface groups are essentially surface defects. There is no experimental evidence to decide upon the nature of bulk solid state defects in RuO_2. However, it is quite probable that RuO_2 in the temperature range investigated displays a ratio $Ru/O < 1/2$. Thus, one may conceive the presence of cation vacancies in bulk RuO_2 and O_2 adsorption can be described as

$$O_2(g) = V_0 + \text{crystal} \quad (17)$$

$$V_0 = V_0^{-4} + 4e^{+} \quad (18)$$

where V_0, V_0^{-4}, and e^{+} are neutral cation vacancy, ionized cation vacancy, and a free hole, respectively. Then the amount of adsorbed O_2 should be proportional to V_0^{-4}. From eq. 17 and 18

$$\theta \propto [V_0^{-4}] = K' p_{O_2}^{1/6}$$

where K' is a constant. This expression is similar to that found to hold at high temperature (Table III), where equilibria 17 and 18 could conceivably be easily established.

It was seen earlier (Figure 3) that the isosteric heats of adsorption increase from constant values in the temperature range 300–385° to larger values as the temperature is decreased. For example, for $q = 1$ cc. the adsorption heat is -27 kcal. mole^{-1} in the temperature range 300–385°, but it averages -75 kcal. mole^{-1} in the temperature range 220 to 300°. This type of behavior has sometimes been rationalized, in the case of transition metal oxides, by changes in the band structure at the oxide surface as the temperature is increased. Another interpretation has been proposed[14] suggesting that, on proceeding from low temperatures at which the adsorbed species has just sufficient mobility to maintain the equilibrium configuration to higher temperatures where it begins to resemble a two-dimensional gas, the isosteric heat of adsorption should be diminished by an amount equal to the activation energy for surface diffusion. The latter, however, are generally of the order of a few kcal. mole^{-1} and can hardly account for the larger variation of the adsorption heat found in this study. The effect of temperature-induced changes in the structure of the adsorbed species upon its specific heat has also been considered; these effects alone can only account for a diminution of approximately 5 kcal. mole^{-1} in the isosteric heat of adsorption as the temperature is increased from room temperature to 1000°K.[15]

Desorption Kinetics. Additional information on the nature of the adsorbed oxygen species on the RuO_2 surface can be obtained by an application of the theory of absolute reaction rates to the observed desorption kinetics. In order to perform these calculations, the average surface density of ruthenium atoms was taken as 0.75×10^{15} atoms cm.$^{-2}$. Assuming that there are on the average two adsorption sites per Ru atom, the average surface site concentration, L, is 1.5×10^{15} sites cm.$^{-2}$. If O_2 adsorption is dissociative and mobile, the rate, V, is given by

$$V \exp\left\{\frac{E}{RT}\right\} = L^2\theta^2 \left(\frac{\pi IkT}{2}\right)^{1/2} \left(\frac{2}{M}\right)$$

where I and k are the moment of inertia of O_2, k the Boltzmann constant, and M the mass of adsorbed particle, respectively. Taking $I = 19.3 \times 10^{-40}$ (g. cm.^{2}), the comparison between calculated and experimental rates is reported in Table V.

The agreement between experimental and theoretical rates can be considered satisfactory, since slight variations with temperature and surface coverage of the experimental values are the result of neglecting variations in the pre-exponential factor for the rate of desorption in the correlation of the desorption rate data. It should also be noted that configurations of the activated complex, different from the above, gave values of

(13) L. E. Orgel, "An Introduction to Transition-Metal Chemistry," John Wiley and Sons, Inc., New York, N. Y., 1960.

(14) E. F. Rideal and F. Sweett, *Proc. Roy. Soc.* (London), **A257**, 291 (1960).

(15) G. Ehrlich, *J. Chem. Phys.*, **36**, 1499 (1962).

Table V: Experimental and Theoretical Desorption Rates (molecules, cm.$^{-2}$, sec.$^{-1}$) for O_2 on RuO_2

Temp., °C.	q, cc. (STP)	θ	Exptl. rate × $\exp\{E/RT\}$ × 10^{-24}	Theor. rate × $\exp\{E/RT\}$ × 10^{-24}
300	0.2	0.0155	2.6	0.62
300	0.4	0.0310	2.1	2.40
300	0.6	0.0465	1.7	5.5
350	0.2	0.0155	1.7	0.66
350	0.4	0.0310	1.5	2.60
350	0.6	0.0465	1.3	5.80
385	0.2	0.0155	1.8	0.66
385	0.4	0.0310	1.6	2.70
385	0.6	0.0465	1.4	6.00

calculated rates several orders of magnitude different from the experimental values.

The conclusion, regarding the dissociative nature of the chemisorption, is supported by the observed value of the activation energy of desorption at zero coverage (50.1 kcal. mole^{-1}). This value is close to that of the heat of formation of bulk RuO_2 (50–75 kcal. mole^{-1}).[3] It should also be noted that the isosteric activation energies for desorption increase with decreasing temperature as the latter is diminished below a value of 275° (Figure 3); the similarity of this behavior to that of the isosteric heats of adsorption (Figure 7) is readily apparent.

The results of the calculations of the activation energy of desorption and heat of adsorption as functions of surface coverage, in the temperature range 300 to 385°, are plotted in Figure 12. The resulting activation energy of adsorption shows a negative value for $\theta < 6 \times 10^{-2}$. This conclusion should be considered together with similar results previously reported in kinetic studies of adsorption[16] and catalytic reactions.[17] Several suggestions for the apparent negative value of the activation energy have been put forward. These assume the simultaneous occurrence of chemisorption processes with different activation energies. The former could be due to the presence of (a) "inactive" surface parts,[16] (b) surface centers with slow activation from the solid,[18] (c) desintering as a result of adsorption,[19] (d) chemisorptions differing in the nature of the electronic binding mechanism,[20] and (e) large variations in surface coverage with temperature.[21] On the basis of our experimental results, it is not possible to indicate with sufficient justification which of these results may have been responsible for the reported negative value of the adsorption activation energy. In a general fashion, however, this result further corroborates the picture of a highly nonuniform energy distribution on the surface of RuO_2, as it has emerged from considerations presented in the previous sections of this communication.

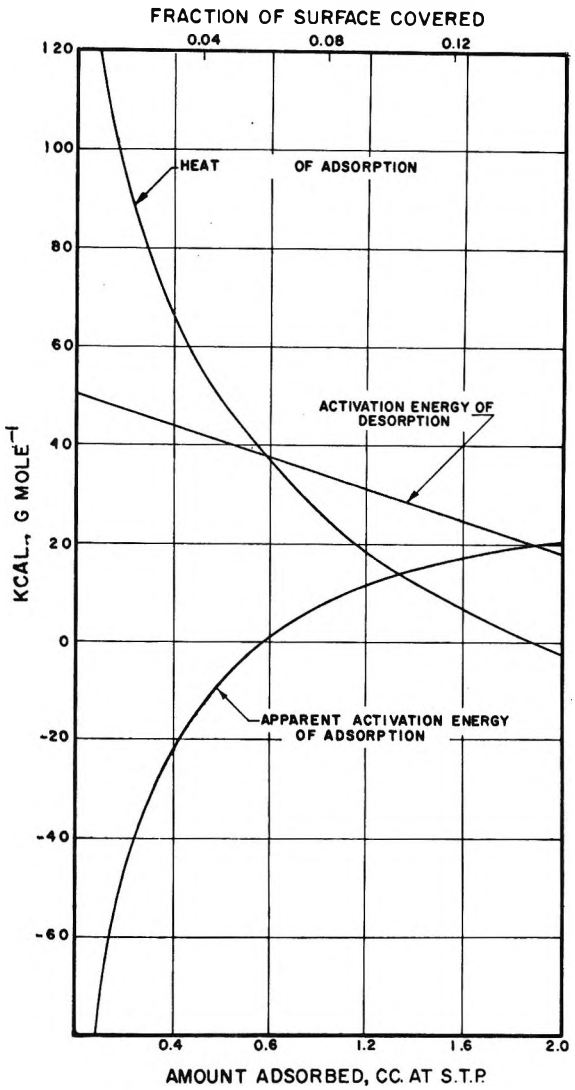

Figure 12. Heat of adsorption, activation energy of desorption, and apparent activation energy of adsorption of O_2 on RuO_2 as functions of the surface coverage in the temperature range 300 to 385°.

(16) H. S. Taylor and S. C. Liang, *J. Am. Chem. Soc.*, 69, 1306, 2989 (1947); H. S. Taylor and H. Sadek, *ibid.*, 72, 1168 (1950); E. K. Rideal and B. M. U. Trapnell, *J. chim. phys.*, 47, 126 (1950).

(17) H. zur Strassen, *Z. physik. Chem.*, A169, 81 (1934); G.-M. Schwab, *ibid.*, A171, 421 (1935); E. Molinari and G. Parravano, *J. Am. Chem. Soc.*, 75, 5233 (1953).

(18) M. Boudart and H. S. Taylor, L. Farkas Memorial Volume, Research Council of Israel, Special Publication No. 1, Jerusalem, 1952, p. 223.

(19) J. H. DeBoer, *Advan. Catalysis*, 8, 137 (1956).

(20) J. H. DeBoer, *ibid.*, 8, 138 (1956).

(21) J. Horiuti, *Catalyst*, 2, 1 (1947); T. Kwan, *Advan. Catalysis*, 6, 116 (1954).

Conclusions

The following results have been obtained from a study of the chemisorption of O_2 on RuO_2.

1. The adsorption-equilibrium data for this system in the temperature range 100–385° and pressure range of 0.01–500 μ can be expressed by a Freundlich equation, while the desorption-rate data in the temperature range 200–385° were found to satisfy an exponential relationship.

2. The heat of adsorption decreases linearly with the logarithm of the surface coverage in the temperature range 300–385° and a value greater than 120 kcal. mole^{-1} of O_2 is indicated at zero surface coverage. In the same temperature range, the activation energy for desorption decreases linearly with surface coverage and is equal to 50.1 kcal. mole^{-1} at zero coverage. At temperatures below 300° both the isosteric heats of adsorption and the isosteric activation energies of desorption appear to increase with decreasing temperature.

3. The adsorption equilibrium function is dependent upon the amount of surface covered. A numerical distribution of the adsorption equilibrium function has been calculated and shows a hyperbolic decrease with increasing values of the equilibrium function. A simple geometrical model, envisioning the possibility of various trapping levels for each surface adsorption site, can be used qualitatively to interpret the results.

4. An application of the theory of absolute reaction rates to the desorption kinetics, in the temperature range 300-385° and at low surface coverages, indicates that the adsorbed species are both mobile and dissociated.

Acknowledgment. This work was supported in part by a grant from the International Nickel Company. The authors gratefully acknowledge this support.

Appendix

Calculation of Possible Effects of Knudsen Diffusion on Desorption Kinetics

A. Pressure Drop through Tubing between Sample Container and Pump. At 300°K., the condition for Knudsen diffusion in cylindrical channels of mean diameter d_c [T (°K.)/P (atm.)] > d_c (Å.) shows that diffusion limitations will set in for $P \lesssim 1.5 \times 10^{-6}$ atm. The molar gas flow rate is

$$\dot{m} = -D_K A \frac{\partial c}{\partial x} \cong -D_K A \frac{\Delta c}{\Delta x} \qquad (19)$$

where D_K, A, c, and x are the Knudsen diffusion coefficient, average cross-sectional area, molar concentration of the gas, and distance measured in the direction of gas flow, respectively. For O_2 at 300°

$$D_K = \frac{2r}{3}\sqrt{\frac{8RT}{\pi M}} = 2.99 \times 10^4 \text{ cm.}^2/\text{sec.}$$

with $r = 1.0$ cm. It follows that $D_K A = 9.45 \times 10^4$ cm.^{4}/sec. Since the maximum desorption rate observed was approximately 0.1 cc. (STP) min.$^{-1}$ or 7.44×10^{-8} mole of O_2 sec.$^{-1}$, from eq. 19 one gets

$$\frac{\Delta c}{\Delta x} = \frac{7.44 \times 10^{-8}}{9.45 \times 10^4} = 7.87 \times 10^{-13} \text{ mole cc.}^{-1} \text{ cm.}^{-1}$$

or $\Delta P/\Delta x = 1.47 \times 10^{-2}$ μ cm.$^{-1}$. The total length of connecting tubing was about 200 cm., corresponding to a total pressure drop at the maximum desorption rate of about 3 μ.

B. Pressure Drop through the Adsorbent Bed. The RuO_2 bed used in the adsorption experiments had the following characteristics: true density = 6.97 g. cc.$^{-1}$, theoretical bed volume = 13.34/6.97 = 1.91 cc., actual bed volume = 6.8–7.0 cc., packing fraction = 0.27–0.28, specific surface area (B.E.T.) = 3.80 m.^{2} g.$^{-1}$, average particle diameter = 2.26×10^{-5} cm., total number of particles = 3.14×10^{14}. Assume that the bed consists of spherical agglomerates, packed in cubic fashion, with an average diameter of 50 μ. In each agglomerate RuO_2 particles are packed with cubic symmetry. Since the cubic packing fraction is $\pi/6 = 0.524$, the packing fraction of the model assumed here $(0.524)^2$ is in good agreement with the experimental value.

Assume the total pressure drop during desorption results from flow through interstices between agglomerates and through spaces between adjacent particles in an individual agglomerate. With the help of a simple cubic arrangement of the spherical particles, the average radius of the channel between adjacent agglomerates is found to be 1.95×10^{-3} cm. In these channels Knudsen diffusion is the primary means of gas transport at all pressures <1 mm.; then $D_K = 85.8$ cm.^{2} sec.$^{-1}$ and $D_K A = 1.02 \times 10^{-3}$ cm.^{4} sec.$^{-1}$. The number of channels opening onto the surface of the bed is equal to the number of agglomerates in the plane of the bed surface. Each agglomerate (including void space) contributes a projected area of $(5 \times 10^{-3} \text{ cm.})^2 = 2.5 \times 10^{-5}$ cm.^{2} to the surface. Since the area presented by the bed at its surface was calculated at 7.06 cm.^{2}, the total number of channels opening onto the surface is $(7.06/2.5) \times 10^5 = 2.85 \times 10^5$.

Each agglomerate with associated void volume occupies a volume of $(5 \times 10^{-3} \text{ cm.})^3 = 1.25 \times 10^{-7}$ cm.^{3} and the total number of agglomerates with an average diameter of 50 μ is $(69.2/1.25) \times 10^7 = 5.54 \times$

10^8. Thus, the number of agglomerates desorbing into one channel becomes $(5.54 \times 10^8)/(2.82 \times 10^5) = 1.96 \times 10^3$. The maximum flow rate through a given channel is merely one-half of the maximum desorption rate multiplied by the fraction of the total agglomerates desorbing into one channel (the factor of one-half is necessary since the maximum flow rate occurs only at the top of the bed while at the bottom it is essentially zero), or

$$\dot{m} = \frac{7.44 \times 10^{-8}}{2} \times \frac{1.96 \times 10^3}{5.54 \times 10^8} = 1.32 \times 10^{-13} \text{ mole sec.}^{-1}$$

The linear concentration gradient is, according to eq. 19

$$\frac{\Delta c}{\Delta x} = \frac{1.32 \times 10^{-13}}{1.02 \times 10^{-3}} = 1.29 \times 10^{-10} \text{ mole cc.}^{-1} \text{ cm.}^{-1}$$

or

$$\frac{\Delta P}{\Delta x} = 5.29\ \mu \text{ sec.}^{-1}$$

Since the average bed height was 0.92 cm., the pressure drop through the interstices between agglomerates is about 5.3 μ at the maximum rate of desorption.

The pressure drop through individual agglomerates is readily computed in a similar fashion. The average diameter of each particle was calculated to be 2.26×10^{-5} cm., with an associated void volume of $(2.26 \times 10^{-5})^3 \times 0.476 = 5.49 \times 10^{-15}$ cc. The average cross-sectional area normal to flow is $(5.49 \times 10^{-15})/(2.26 \times 10^{-5}) = 2.43 \times 10^{-10}$ cm.^{2} with a radius of 8.80×10^{-4} cm. At 385°, $D_K = 0.387$ cm.^{2} sec.$^{-1}$ and $D_K A = 0.940 \times 10^{-10}$ cm.^{4} sec.$^{-1}$. Approximating the flow out of the surface of the sphere in all directions with a flow in one direction only, *e.g.*, vertical, the maximum pressure drop will occur in the channel originating at the center of the sphere. The number of particles desorbing into this channel is $(2.5 \times 10^{-3})/(2.26 \times 10^{-5}) = 1.11 \times 10^2$. At an average rate of desorption of 0.1 cc. (STP) min.$^{-1}$, the flow rate through this channel is $[7.44 \times 10^{-8}/2] \times [(1.11 \times 10^2)/(3.16 \times 10^{14})] = 1.31 \times 10^{-20}$ mole sec.$^{-1}$. The resulting pressure gradient (at 385°) is 5.7 μ cm.$^{-1}$ and for a channel 2.5×10^{-3} cm. in length a pressure drop of about 0.014 μ.

Thus the maximum pressure drop that will occur in the adsorbent bed at the highest desorption rates observed will be ≤ 10 μ. At the highest desorption rates the rate of adsorption was small (<0.1 cc. min.$^{-1}$), and the effect of simultaneous adsorption on desorption measurements is negligible. Simultaneous adsorption could become a factor at low degree of surface coverage, where the measured desorption rates are of the order of 1×10^{-4} to 1×10^{-2} cc. min.$^{-1}$. However, the pressure in the adsorbent bed should be diminished by this time to 1×10^{-2} or 1×10^{-1} μ and it is probable that the rate of adsorption at these pressures is quite small. A pressure of 10 μ would correspond to a negligible amount of gas trapped in the small void volume of the bed. A pressure drop of 3 μ through the connecting tubing, however, would lead to a slight but significant amount of gas not recorded by the thermocouple gauge of the desorption gas reservoir. However, this would be a problem only at the very first stages of desorption and would be negligible during subsequent measurements where the observed rates are only $^1/_{1000}$ to $^1/_{10}$ as large as the maximum rate.

Flow in Thin Liquid Films

by J. Lyklema, P. C. Scholten, and K. J. Mysels

Chemistry Department, University of Southern California, Los Angeles, California 90007 *(Received June 12, 1964)*

An improved experimental method for studying vertical soap films slowly pulled out of a solution is described, and the interpretation of the optical thickness measurements is discussed. The behavior of mobile films presents complications which can be explained but prevent a quantitative interpretation. Rigid films, on the other hand, give results for films thicker than 800–1100 Å., which agree very closely with Frankel's law relating film thickness to the velocity of pullout (eq. 1). Since Frankel's law is derived on the assumption that the viscosity is constant up to the monolayer, this finding is not compatible with the existence of any thick, rigidified water layers (or of slip) in the neighborhood of the surface.

Whether the properties of liquids change in the neighborhood of a phase boundary and, if so, to what depth does any effect extend are old problems. In particular, there is considerable disagreement about the viscosity of water near a charged surface. The generally accepted present-day picture of dilute solutions of electrolytes and macromolecules is based on the assumption that the viscosity is constant to within a few molecular diameters from the particle considered. The possibility of an increased viscosity in a very thin layer of the order of 5 Å. caused by a high, local, electric field intensity near a charged surface has been examined by Lyklema and Overbeek.[1]

In contrast to the preceding approach which depends on underlying structural assumptions, the macroscopic approach based on direct observations of flow along surfaces provides much evidence for the existence of thick, rigid layers of water as shown, for example, in the review of Henniker.[2] However, macroscopic approaches involving solid walls are always made uncertain by the disturbing effect of any surface roughness and of a contaminating dust or microbial growth. For example, the peculiar results obtained by one of us[3] were certainly due mainly to microorganisms growing in the pores of sintered glass. Much more promising seems to be the study of water near a monolayer surface because of the relatively well-understood structure of the latter, along with its perfect smoothness, its easy renewal, and its ability to conform to any contaminating dust. For such systems the postulate of absence of slip and of normal viscosity, *i.e.*, the applicability of standard hydrodynamics up to the surface monolayer, was made explicitly by Harkins and Kirkwood[4] in 1938. Crisp[5] confirmed it experimentally, but the precision of his measurements could not preclude drastic changes of viscosity within the last few tenths of a millimeter next to the surface. More recently Goodrich[6] found evidence of slip. In both cases trough techniques involving a single monolayer surface were used.

A further step in this direction is the study of flow between two monolayers. This type of flow determines the thickness of a soap film pulled out of bulk solution. Measurements of Mysels and Cox[7] confirmed the postulate of constant viscosity down to within about 100 Å. of the surface of both mobile and rigid films.[8] Soap films are of particular interest because they have also been used[9–11] for direct measurements of

(1) J. Lyklema and J. Th. G. Overbeek, *J. Colloid Sci.*, **16**, 501 (1961).

(2) J. C. Henniker, *Rev. Mod. Phys.*, **21**, 322 (1949).

(3) K. J. Mysels and J. W. McBain, *J. Colloid Sci.*, **3**, 45 (1948).

(4) W. D. Harkins and J. G. Kirkwood, *J. Chem. Phys.*, **6**, 53, 298 (1938).

(5) D. J. Crisp, *Trans. Faraday Soc.*, **42**, 619 (1946).

(6) F. C. Goodrich, *J. Phys. Chem.*, **66**, 1858 (1962).

(7) K. J. Mysels and M. C. Cox, *J. Colloid Sci.*, **17**, 136 (1962).

(8) Rigid films have a high surface *shear* viscosity or a yield value which is absent in mobile films.

(9) B. V. Deryagin and A. S. Titievskaya, *Discussions Faraday Soc.*, **18**, 27 (1954).

double-layer repulsion and van der Waals attraction. The results of these measurements would be greatly affected if any rigidified layers extended over the whole thickness of the soap film and, thus, could affect (or even determine) its ultimate thickness. Present evidence on the existence of such layers is contradictory. Thus, Dasher and Mabis[12] presented X-ray evidence for a hydrous gel structure in rigid films, and Deryagin and Titievskaya[9] postulated a structure of the solvent which prevents complete drainage of thin films. Yet, Mysels, Shinoda, and Frankel[13] accounted semiquantitatively for the drainage of rigid vertical films using a constant viscosity, and Sheludko and Exerova[10] found experimental agreement with a hydrodynamic approach which applies Reynold's formula for solid pistons to small horizontal films. There is, however, some question about the validity of the piston model for soap films.[14]

The present paper reports a considerable experimental refinement of the technique of Mysels and Cox,[7] which was necessary in order to study the effect of double-layer and van der Waals forces, to be reported elsewhere.[15] The results presented here deal with a verification of the applicability of the simple hydrodynamic approach for films as thin as 1000 Å. or less with a precision which gives an upper limit of some 10 Å. for the thickness of the water layer which may be effectively rigidified. This eliminates the possibility that such rigid layers can affect equilibrium thicknesses exceeding some 50 or 100 Å.

I. Frankel's Law

Let us consider an inverted U-shaped frame being withdrawn at a constant rate v from a film-forming solution as shown in Figure 1. The experimentally measurable thickness δ of the film thus formed is related to the velocity v at which it is formed, the surface tension γ of the solution, its viscosity η, its density ρ, and the acceleration of gravity g. Assuming that the viscosity remains constant up to the surface and that the latter is completely inextensible, Frankel[16-18] derived the expression

$$\delta = 1.88\frac{v^{2/3}\eta^{2/3}}{\gamma^{1/6}\rho^{1/2}g^{1/2}} \qquad (1)$$

by purely hydrodynamic considerations. The effect of introducing double-layer repulsion and van der Waals attraction into this simple picture has been discussed by Overbeek.[19]

II. Apparatus and Materials

Frame. The construction of the frame used in our measurements is shown in Figure 2. The wire used had

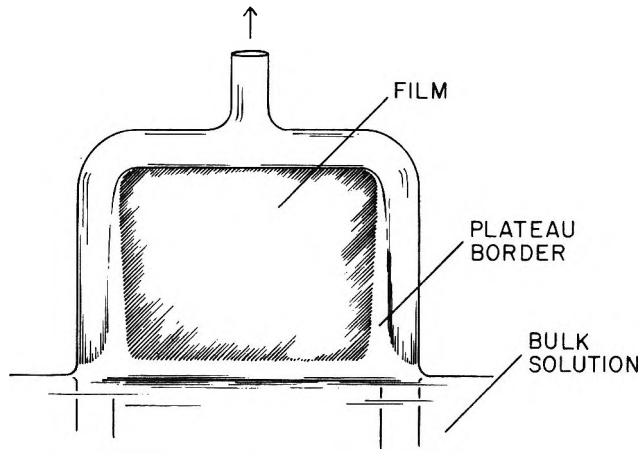

Figure 1. Film formed by a frame pulled out of a solution.

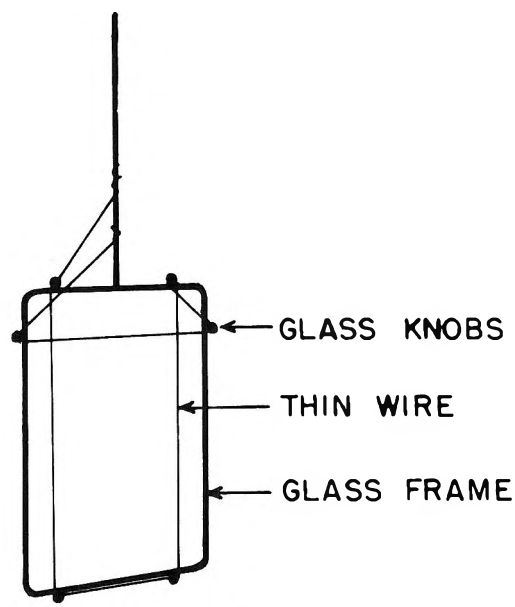

Figure 2. Thin-wire frame.

(10) A. Sheludko and D. Exerova, *Kolloid-Z.*, **165**, 148 (1959); **168**, 24 (1960); A. Sheludko, *Proc. Koninkl. Ned. Akad. Wetenschap.*, **B65**, 76 (1962).

(11) E. M. Duyvis, Thesis, University of Utrecht, 1962.

(12) G. J. Dasher and A. J. Mabis, *J. Phys. Chem.*, **64**, 77 (1960).

(13) K. J. Mysels, K. Shinoda, and S. P. Frankel, "Soap Films—Studies of their Thinning and a Bibliography," Pergamon Press, New York, N. Y., 1959.

(14) S. P. Frankel and K. J. Mysels, *J. Phys. Chem.*, **66**, 190 (1962).

(15) J. Lyklema and K. J. Mysels, to be published.

(16) See ref. 13, p. 55.

(17) It has recently come to our attention that Derjaguin[18] has derived a very similar relation for the thickness of a photographic emulsion layer deposited on a film base. In contrast to Frankel's approach this derivation assumes complete extensibility of the free liquid surface.

(18) B. V. Deryagin and S. M. Levi, "Fiziko-khimiya Naneseniya Tonkikh Sloev na Dvizhushchuyusya Podlozhki," USSR Acad. Sci., Moscow, 1959; B. V. Deryagin, *Zh. Eksp. i Teor. Fiz.*, **15**, 9 (1945).

(19) J. Th. G. Overbeek, *J. Phys. Chem.*, **64**, 1178 (1960).

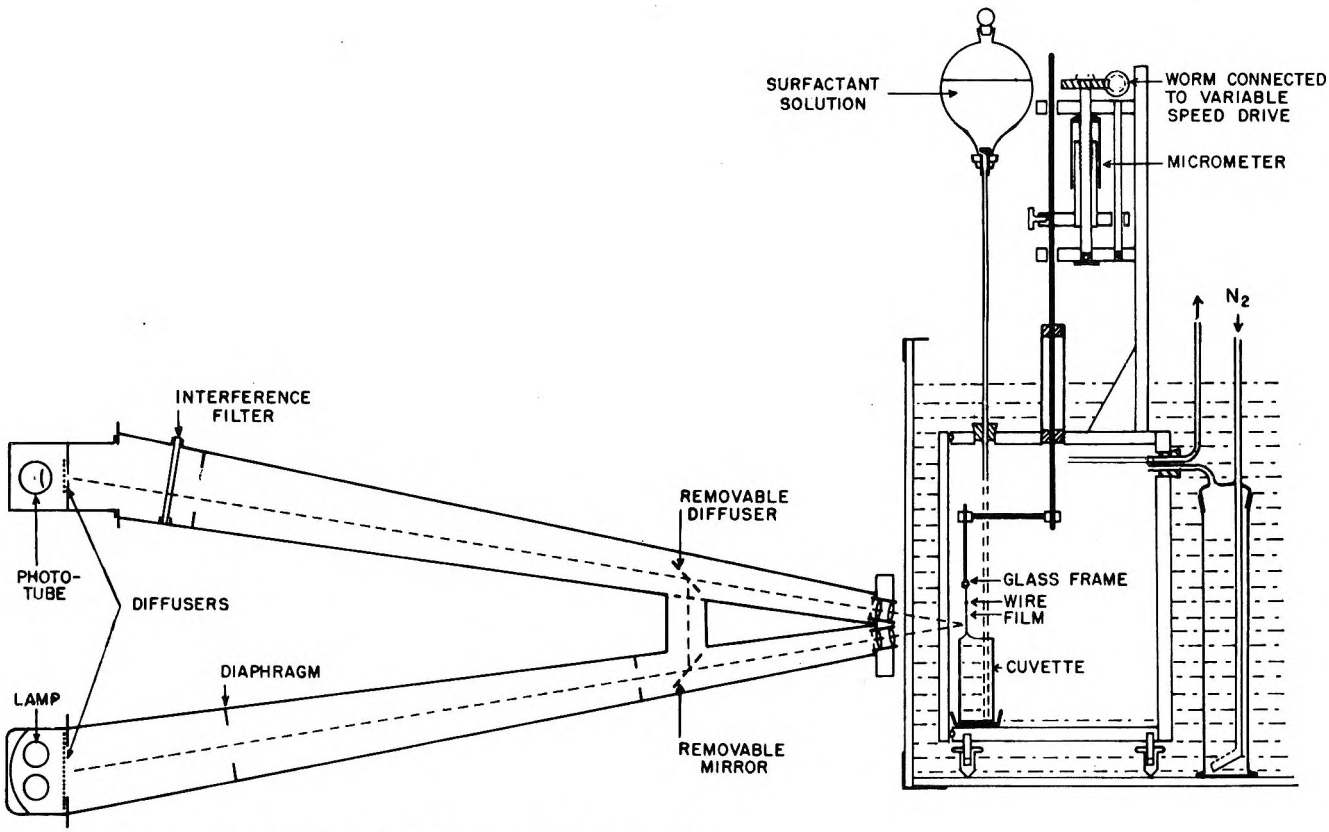

Figure 3. Apparatus for measuring the thickness of slowly formed films.

a diameter of 12.5 μ and was made of "Evenohm" chromium–nickel alloy. This elaborate construction of the frame was chosen to reduce the rate of thinning of the films. This in turn reduces the uncertainty about any difference between the rate at which the frame rises and that at which the film is being pulled out of the solution. The effectiveness of the very thin frames in this respect will be discussed elsewhere.[20] The choice of the 12.5-μ size was dictated by preliminary experiments on mobile films which showed that there was no observable difference between the thicknesses of films produced in frames made of 5-μ and of 12.5-μ wires, whereas the thicknesses were very slightly lower when the wire diameter was 50 μ and about 200 Å. lower for a wire diameter of 200 μ. In the following analysis we therefore assume that the velocity of the frame and that of the film are equal. This is additionally justified by the fact that the thickness of rigid films just pulled out was independent of the total height of the film already present.

Mechanical Part. (See Figure 3.) The films were made inside a brass box completely submerged in a water bath thermostated to better than 0.01° and kept at 25°. The box had two large glass windows for observation and easy access. Close to the window used for measurements was a cuvette with surfactant solution. The cuvette could be filled (and the surface renewed by overflow) from outside through a narrow glass tube and a Teflon valve. Surface creep of contaminants (*e.g.*, copper salts) into the cuvette was prevented by placing it in a Teflon cup. Behind the frame were two black glass plates (not shown in the figure) forming a light trap for the transmitted beam. The bottom of the chamber was always covered with a layer of the solution studied, and a slow stream of nitrogen saturated with water vapor maintained a slight excess pressure within the chamber in order to keep out dry air and, thus, prevent evaporation. Since the equilibrium films maintained their thickness for days, we are quite sure that evaporation did not occur.

The rod supporting the frame passed through two Teflon collars in a chimney on top of the chamber and was connected to the body of a micrometer. A multiple-speed gear transmission connected to a variable-speed d.c. motor was used to drive the spindle of this micrometer *via* a fine worm gear. This enabled us to move the frame at any speed between 40 Å./sec. and

(20) P. C. Scholten, K. J. Mysels, and J. Hotchkiss, unpublished.

500 μ/sec. A constant voltage transformer assured constancy of speed at any setting.

Optical Part. (See Figure 3.) The light source was a fluorescent mercury lamp operated from a stabilized but variable voltage supply. This lamp was screened except for a circular area 3 cm. in diameter. A tenfold reduced image of this area was projected onto the film by means of small lens of 5-cm. focal length. An identical system projected a tenfold enlarged image of the illuminated area of the film onto a photomultiplier tube. A diaphragm in front of the photomultiplier had an opening of 0.4 × 3 mm.; thus, out of the 3-mm. illuminated circle on the film, a 0.04 × 0.3-mm. rectangle was selected. Most measurements were made with the lower edge of the observed rectangle 0.2 mm. above the meniscus, but in some experiments on mobile films this distance was reduced to 0.05 mm. In this case the part of the lamp illuminating the meniscus was screened off in order to avoid stray light.

The phototube was mounted in lieu of a camera on a Leitz "focaslide" so that it could easily be replaced by a ground glass for visual inspection, focusing, and adjustment. The intensity of the light source could be measured directly through a bypass in the optical system. It appeared to be constant after a few hours of operation.

Interference filters in front of the phototube allowed selection of the 546- or 436-mμ wave length for measurement. Stray light from outside was kept out effectively by shields around the light paths. Inner reflections were reduced by suitably placed diaphragms. The photomultiplier was a 1PN1, powered by a stack of dry cells. Its signal was amplified by a Hewlett–Packard Model 425 A microvolt-ammeter and recorded by a 10-mv. Leeds and Northrup recorder.

Materials. Pure dodecyl alcohol was obtained from Applied Science Laboratories, State College, Pa. The preparation of the sodium dodecyl sulfate used has been described.[18] The sodium dodecylbenzene sulfonate was a commercial high purity sample, freed of inorganic salts and nonionic materials, obtained through the courtesy of the Colgate Palmolive Peet Co. Inorganic salts were of reagent purity. Distilled water was used for the preparation of the solutions.

III. Thickness Measurements

At the beginning of most experiments the horizontal top wire of the frame was submerged. It was then raised at the desired speed which was checked by timing the motion of the micrometer. For rigid films the record of the photomultiplier current showed a maximum or a shoulder corresponding to the passage of the wire frame and then a constant intensity giving the thickness of the film. The same was true for very thin mobile films. For thicker mobile films the frame signal was always followed by a minimum, corresponding to a layer of film which had already thinned out greatly in the time required to rise from the meniscus to the field of view. This was followed by a region of small slope corresponding to a film whose thickness was changing slowly by the various processes involved in thinning. This thickness was extrapolated to the moment when the frame left the field of view to give as closely as possible the actual initial thickness of the film. (The first observed film thicknesses, which are often appreciably different, are reported by one of us elsewhere.[21]) This correction was generally minor and did not affect the over-all result for these mobile films.

The determination of the thickness of a film involves two steps. One is the optical measurement which in our case was the determination of the ratio of intensity I of light reflected by the film to that, I_0, obtained when the film thickness δ corresponds to maximum reflection ($\delta \approx \lambda/4$). The second step involves the computation of a material thickness from this measurement after taking into account the structure and optical properties of the film.

Optical Measurement. In order to obtain the reflected intensity, the measured light intensity must be corrected for stray light. As stated previously, outside stray light presented no problem. Stray light within the system in the absence of a film was not perceptible. However, once a film was formed, the presence of the meniscus could modify the background and introduce stray light. An upper limit for this factor is found by measuring the intensity of the reflected light at the first reflection minimum ($\delta \approx \lambda/2$). This was done repeatedly and found to be of the same order as the noise, which was less than 2% of the reflection from the thinnest film measured, and, therefore, also negligible.

Another source of stray light lies in the illuminated surface surrounding the measured area. This was estimated by focusing the slit on a dark portion just below the meniscus and pulling out a film close to the maximum reflectivity. The effect amounted to less than 1% of this maximum. As the thickness of most films measured is quite uniform near the measured area, this last kind of stray light introduces a correction which is not only small but also proportional to the intensity measured and can, therefore, be neglected in the I/I_0 ratio. An advantage of the thin wire frames used is that their contribution to the stray light is negligible.

For rigid films the maximum reflected intensity I_0

(21) J. Lyklema, *Rec. trav. chim.*, **81**, 890 (1962).

was generally measured by pulling out films at a number of speeds around the expected maximum until the maximum value was well defined. For mobile films I_0 was usually found by producing a film of greater thickness, stopping the frame, and recording the maximum through which the intensity passed. Occasionally a further confirmation was obtained from the second maximum ($\delta \approx 3\lambda/4$), but, here, the more rapid drainage made the measurements less accurate.

The measurements depended also on the linearity of the photomultiplier, amplifier, and recorder which were not further tested. The consistency of the data and especially the fact that measurements using two different wave lengths and, therefore, involving very different absolute intensities and different I/I_0 ratios, agreed to better than 6% indicates that the total accuracy was at least of that order. It should be noted that because two such sets of measurements at different wave lengths were always performed on different films and with independent standardization, they really test the over-all experimental reproducibility. All reported measurements were made in green light of 546 mμ because of greater precision and convenience.

Computation. The conversion of the optical quantity I/I_0 into a material thickness δ is still an incompletely solved problem because of the uncertainty about the optical properties of the film. However, a sufficiently good estimate can be obtained by examining two successive approximations.

As a first approximation, we assume that the film is a homogeneous aqueous structure. A convenient thickness unit for the system is the thickness, l, of the film which gives maximum reflection, *i.e.*, for which the optical thickness is a quarter wave length. For such a homogeneous film it is given by

$$l = \lambda/4n \cos \phi \qquad (2)$$

where n is the refractive index of the film, λ the wave length under vacuum of the light used, and ϕ the refracted angle. The desired relation is

$$I/I_0 = F \sin^2 (\delta/l) \qquad (3)$$

in which the angle is measured in quadrants (*i.e.*, 90° = 1). F is a correction factor taking into account secondary reflections. If these are neglected, $F = 1$. Secondary reflections depend on the reflectivity, r^2, of the surface of the film where r is the Fresnel reflection coefficient. For unpolarized light going from medium 1 into medium 2 and for angles that are not too large (<30°) r is given[22] by

$$r_{12} = \frac{n_1 - n_2}{n_1 + n_2} \qquad (4)$$

For the air–water interface its value is 0.1427 so that $r^2 = 0.0204$ and $r^4 = 4 \times 10^{-4}$. The factor F is given by

$$F = \frac{1 + 2r^2 + 4r^4}{1 - 2r^2 \cos 2(\delta/l) + r^4} \qquad (5)$$

Taking F into account changes the calculated value of δ by −8.5% if $\delta \approx 0$ and by 0% if $\delta \approx l$. For green light the effect is, at most, minus 11–15 Å. for film thicknesses in the range of 300–700 Å. (it is less in violet light).

A soap film, however, is clearly not homogeneous but presumably formed by two surfaces with an intralamellar solution having essentially bulk concentration as already postulated by Gibbs and recently demonstrated by Corkill and co-workers.[23] To this layered structure must correspond a symmetrical but complicated variation of the refractive index. Hence, as a second approximation we can consider the film to be a sandwich of three homogeneous layers, the two outer ones having a small constant thickness and a higher refractive index than the central core of variable thickness (see Figure 4). Reflection from any three transparent layers has been calculated explicitly by Crook,[24] but the implicit expressions given by Vašiček[25] are more useful. Reduced to our symmetrical case, as outlined in the Appendix, they show that the outer layers of small and fixed thickness introduce a constant phase change which results in an apparent change of the thickness of the film by a *constant* amount, whereas the change in the reflectivity of each side of the film is quite small.

In order to estimate the magnitude of this effect we consider two realistic models. One, based on fully extended C_{12} chains plus a sulfate group, assumes a thickness d_1 of 16 Å. for each outer layer and is applicable to rigid films. The other, based on an area of 52 Å./molecule (as estimated by van Voorst Vader[26]) and a density of 1.0, assumes a corresponding thickness of 8.5 Å. and is applicable to mobile films. In both models the refractive index n_1 is assumed to be 1.45. This is somewhat higher than that corresponding to normal hydrocarbons in order to take into account the effect of the sulfate group. In both cases the core of varying thickness d_2 is assumed to have the refractive index of water, 1.333.

(22) C. J. Vašiček, "Optics of Thin Films," North-Holland Publishing Co., Amsterdam, 1960, p. 49.

(23) J. W. Gibbs, "Collected Papers," Longmans Green and Co., New York, N. Y., 1931, p. 300; J. M. Corkill, J. F. Goodman, D. R. Glaisman, and S. P. Harwood, *Trans. Faraday Soc.*, **57**, 821 (1961).

(24) A. W. Crook, *J. Opt. Soc. Am.*, **38**, 954 (1948).

(25) See ref. 22, p. 185.

(26) F. van Voorst Vader, *Trans. Faraday Soc.*, **56**, 1067 (1960).

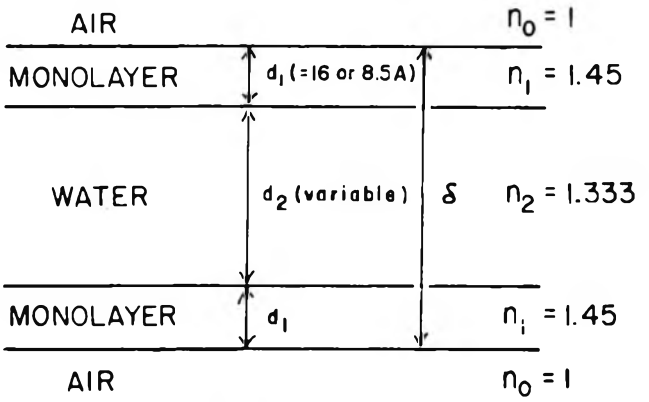

Figure 4. Assumed sandwich structure of film.

Applications of eq. 12 (Appendix) show that the real thickness of the film is less than that computed, neglecting the effect of the surface layers, by 7.25 Å. for mobile films and by 13.5 Å. for rigid films. There is no significant difference between measurements in green and in violet light. These results are consistent with those obtained using different approaches by Duyvis[11] and by Frankel.[27]

Thus, a realistic sandwich structure produces a correction which is significant, especially for thinner films. In view of the fact that the two extreme models give corrections differing by only 6 Å., it is likely that each differs from reality by less than this amount. As our picture of the structure of soap films becomes more refined, it should be possible to narrow down this uncertainty further and to improve somewhat the interpretation of experimental data.

IV. The Behavior of Mobile Films

Our first measurements were made on mobile films of a solution about 10^{-2} M in alkylbenzene sulfonates and 9×10^{-2} M in lithium chloride. A typical result is shown in Figure 5 by open circles, along with the straight line based on Frankel's theory. At high velocities the agreement is good, but below about 5 μ/sec. the deviations become large. At very low velocities the thickness is essentially constant, which shows that it is not determined by hydrodynamic and rate-dependent factors but is an equilibrium value. This will be discussed in another article.[16] At intermediate velocities, films are much thicker than predicted by Frankel's law. Visual observation of these films showed that the very thin equilibrium "black" film was always forming spontaneously just above the field of view of the photomultiplier. As has been described qualitatively in the past,[13,19] the black film increases in area at the expense of the neighboring thicker film. The excess liquid collects in a still thicker welt at the boundary. Under

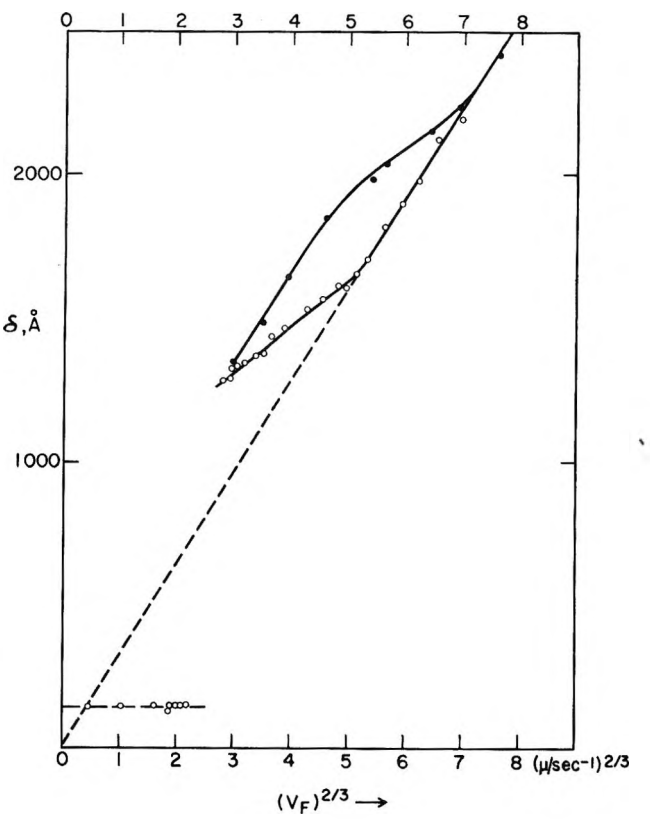

Figure 5. Mobile films: variation of observed thickness with rate of pullout. Open circles, experiments beginning with submerged frame; filled circles, experiments beginning with a black film.

the influence of gravity this welt then flows down. Thus, in the deviation region it was the thickness of the welt that was being measured. At higher velocities the measurements were more representative of the real thickness of pulled out film because the black film formed later in the thicker films, and the rapidly rising film carried the welt out of the field of view.

To verify this explanation another series of measurements was made. It is represented by filled circles in Figure 5. In this series the frame was first raised about 1 mm. above the meniscus, and the film was allowed to thin in this position until all of it became black. The frame was then raised at the desired uniform velocity. This permitted immediate formation of the welt, whereas in the original measurements, in which the frame was submerged at the beginning, this occurred only after a certain delay required by the thinning of the upper part of the film. As may be seen, the two series agree at lower velocities where the delay is insignificant compared to the time needed to produce a film, but the large deviations from Frankel's law extend

(27) S. P. Frankel, unpublished.

Table I: Frankel's Law Results Obtained with Solutions Giving Rigid Films[a]

Solution			No. of	Least-squares Frankel's law line		
NaLS, $M \times 10^3$	LiCl, $M \times 10^3$	γ, dynes cm.$^{-1}$	observations	Numerical constant	Intercept, Å.	Std. dev., Å.
1.59	100	21.3	20	1.78	18	28
2.83	100	21.3				
3.7	16	24.6	9	1.83	50	31
4.0	1.92	27	17	1.86	46	18
3.58	...	26.8	7	1.93	−35	29
0.87	...	32.1	7	1.75	83	19
				Av. 1.83 ± 0.055	32 ± 16	24

[a] Many of these solutions were clearly supersaturated with respect to the alkyl sulfate–alcohol compound (adduct). When this precipitated after some time, the films became mobile and the solutions had to be replaced. In all cases the dodecyl alcohol content was 2.5% by weight of the dry sodium dodecyl sulfate (NaLS).

to much higher velocities in the absence of the delay. At the highest velocities, when most of the welt is carried upward by the rising film and does not affect the measurement, there is again agreement between the two series.

An attempt to obviate these difficulties by bringing the field of view still closer to the meniscus (0.05 to 0.15 mm.) did not change the results appreciably.

Thus, the results at higher frame velocities confirm that mobile films conform closely to Frankel's law, but the complications due to formation and flow of the welt distort the results at lower velocities and prevent the use of these mobile films in a more refined test. All the results reported below were therefore obtained with rigid films.

V. Results with Rigid Films

Figure 6 shows the results obtained for rigid films made from a series of solutions of varying ionic strength. Table I gives the exact composition of each solution. The solid lines of the figure are fitted to the points through which they pass by the method of least squares. The dotted parts are extrapolations. As may be seen from Table I, the slopes of these lines are very close to the value 1.88 predicted by Frankel's law, whereas the intercepts are close to zero.

When the thickness of the film is below 500–1100 Å., definite deviations from Frankel's law appear in qualitative agreement with Overbeek's prediction.[19] At low ionic strengths double-layer repulsion between the ionized surfaces predominates and causes deviations toward larger thicknesses. At higher ionic strengths the double layers are thinner so that van der Waals forces can become important and cause gradual or abrupt deviations toward thinner films. In all cases an equilibrium thickness is reached at sufficiently low speeds.

These deviations will be considered in detail elsewhere,[15] but their conspicuous presence justifies confining the quantitative application of our purely hydrodynamic considerations to thicker films in which double-layer and van der Waals effects are negligible. For the most dilute solution, in which the double layer "thickness,", $1/\kappa$, is 111 Å., the limit seems to be about 1100 Å.; for the others, about 800 Å.

Above this range and up to the limit of our measurements at about 2200 Å. the experimental points lie on straight lines with a standard deviation varying from 18 to 42 Å. for the different solutions.

From the slopes of the lines fitted to the experimental points by the method of least squares the numerical coefficients of Frankel's equation (eq. 1) were calculated using the proper surface tension value for each solution. These values range from 1.75 to 1.93 with a weighted average of 1.83 ± 0.055 as compared with the theoretical value of 1.88. This provides strong evidence that the hydrodynamic model used is correct and confirms the older results[7] which covered a much wider range but were less accurate.

The vertical intercepts of the lines vary between the extreme values of −35 and +83 Å., with a weighted average of 32 Å. and a standard deviation of 16 Å. This indicates that a layer of only about 15 Å. on each side of the film is rigid and does not participate in the viscous flow determining the thickness of the film. This corresponds very well to the thickness of the surfactant monolayer in these rigid films as estimated in section 3, *i.e.*, 16 Å. It is between these monolayers that flow occurs during pullout. Thus, our results provide an independent confirmation of the generally accepted sandwich structure of these films and of the physical reality of monolayers.

One may also conclude that, within the accuracy of our measurements, *i.e.*, some 10 Å. for each surface,

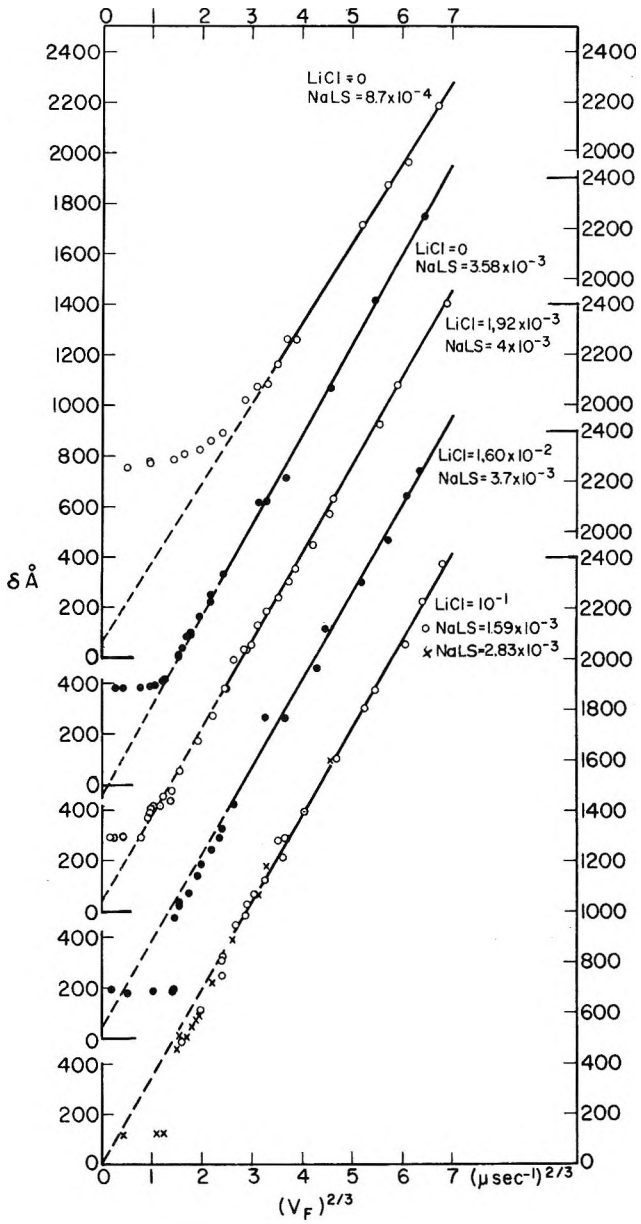

Figure 6. Rigid films: variation of thickness with rate of pullout for solutions of ionic strengths indicated. For clarity, scales corresponding to different solutions are displaced vertically in steps of 500 Å.

there are no rigidified layers of water near the surfaces of our systems. The absence of such thick, rigidified water layers on these highly charged and strongly hydrophilic surfaces suggests strongly that such layers are not generally present in soap films and play no direct role in determining their equilibrium thickness.

Acknowledgment. This work was supported, in part, by the Air Force Office of Scientific Research. We are indebted to Professor Overbeek for stimulating discussions leading to this work and for calling our attention to the importance of the optical corrections. We are also grateful to Dr. Duyvis and Dr. Frankel for making available to us their unpublished optical calculations.

Appendix

For our symmetrical model, the general results given by Vašiček[25] reduce to

$$x_1 = 2d_1/l_1 \tag{6}$$

$$r^2 = \frac{r_1^2 + r_2^2 - 2r_1r_2 \cos x_1}{1 + r_1^2r_2^2 - 2r_1r_2 \cos x_1} \tag{7}$$

$$\tan \zeta_1 = \frac{r_2 \sin x_1}{r_1 - r_2 \cos x_1} \tag{8}$$

$$\tan \zeta_2 = \frac{r_1 \sin x_1}{-r_2 + r_1 \cos x_1} \tag{9}$$

$$\tan \eta = \frac{r_1r_2 \sin x_1}{1 - r_1r_2 \cos x_1} \tag{10}$$

$$\alpha = (d_2/l_2) + (d_1/l_1) + \eta + (\zeta_1 + \zeta_2)/2 = \frac{\delta - d_1[2 - (l_2/l_1)] + l_2[\eta + (\zeta_1 + \zeta_2)/2]}{l_2} \tag{11}$$

where $r_1 = |r_{01}|$ and $r_2 = |r_{12}|$ and α replaces δ/l in formula 3. The terms beyond δ are constant for a given d_1 and give the correction to be applied (with opposite sign) to the thickness computed by formula 3, neglecting any surface layers.

For our model in which x_1 is small and r_1 is moderate, an error of 0.1 Å. is made by neglecting the differences between an angle and its tangent or sine, and between its cosine and unity, which gives

$$\alpha = \frac{\delta - 2d_1\left[1 - \frac{l_2r_1(1 - r_2^2)}{l_1(1 - r_1r_2)(r_1 - r_2)}\right]}{l_2} \tag{12}$$

The correction term beyond δ involves only the ratio of the l_i values. It depends on the refractive indices but not otherwise on the wave length.

Neglecting higher terms, which involves an error of less than 0.5 Å., one obtains simply, in terms of refractive indices

$$\alpha = \frac{\delta - d_1(n_1 - n_2)(1 - n_1 - 2n_2)/n_2(n_2 - 1)}{l_2} \tag{13}$$

The correction term is, therefore, sensitive to the difference of refractive indices between the surface and the bulk, as would be expected, but, otherwise, is not significantly affected by usual variations of refractive index with wave length in the visible.

The Bismuth Iodide–Iodine Phase Diagram[1]

by Ferenc E. Rosztoczy and Daniel Cubicciotti

Stanford Research Institute, Menlo Park, California 94025 *(Received June 20, 1964)*

The BiI_3–I_2 phase diagram was determined. It is of the simple eutectic type, the eutectic composition being very close to pure I_2. The shape of the liquidus is very close to that calculated on the basis that BiI_3 and I_2 are the species in the melt.

Introduction

There are two ways in which bismuth(III) iodide and iodine might react to form a compound: (a) if iodine is a sufficiently strong oxidizing agent, a higher oxidation state of bismuth might be formed; (b) iodine might combine with the iodide ions to form polyiodide ions (*i.e.*, I_3^-). Oxidation states for bismuth greater than three have been obtained through oxidation by fluorine to BiF_5 and by chlorine to $BiCl_4$. The formation of polyiodides is well known for the heavier alkali iodides, but no polyiodides seem to have been reported for the less ionic iodides. As may be seen below, the present thermal analysis of the BiI_3–I_2 system indicated no compound formation in this system; hence, the problem concerning the type of compound does not arise.

Experimental

Thermal Analysis. Two types of sealed capsules were used for thermal analysis. One consisted of a Pyrex test tube (25-mm. o.d., 75 mm. long) with a reentrant thermocouple well in the bottom. Such cells were often found to be cracked after a cooling curve. The other type consisted of a bundle of three separate heavy-wall Pyrex tubes (each 16-mm o.d., 10 cm. long). The measuring thermocouple was placed in the channel created in the center of the bundle of three tubes. This latter type of cell was much more resistant to the stresses in the system.

The capsules were filled with weighed samples of Bi and I_2 and sealed under vacuum. The sealed capsules were then heated to above 410°. The heating was gradual enough so that the reaction was not vigorous. (Capsules heated too rapidly exploded.) After several cooling curves had been obtained on a sample of a given composition, the capsule was opened, Bi or I_2 added to change the composition, and the capsule resealed under vacuum. When the capsule was full it was discarded and a new one filled. The amount of sample ranged from 40 to 60 g. (for one large or three small tubes).

The sample capsule or bundle was placed in the center of a heavy nickel tube (72-mm. o.d., 61-mm. i.d., 22 cm. long) and insulated from it with Fiberfrax wool. The entire assembly was placed in a tube furnace and a constant temperature difference was maintained between the sample capsule and the nickel tube during a heating or cooling operation. The constant temperature difference was obtained by controlling the temperature of the furnace with a differential thermocouple between the capsule and the nickel tube which actuated a controller. The heating or cooling rate was approximately 0.5°/min. The temperature was measured with a Pt—Pt–10% Rh thermocouple checked against a similar thermocouple calibrated by the National Bureau of Standards. The output of the thermocouple was recorded on a strip-chart potentiometer recorder with a span of 1 mv./25 cm.

Conductivity Measurements. These measurements were made by a four-probe method. A fused-quartz cell was made having two bulbs connected by a tube (3-mm. i.d., 9 cm. long) which was the resistance path. Each bulb had two graphite-rod electrodes emerging from the top through closely fitting quartz tubes sealed outside the heated zone with epoxy cement. The cell was fitted with an auxiliary bulb containing iodine. The temperature of the auxiliary bulb could be varied independently of that of the main cell so that the amount of iodine in the cell (hence, the composition of the Bi–I_2 sample) could be varied. The

(1) This work was made possible by the support of the Research Division of the U. S. Atomic Energy Commission under Contract No. AT(04-3)-106.

main cell was initially loaded with BiI_3 made from the elements in another container. The resistance of the sample was measured by determining the potential drop across one pair of graphite electrodes while a measured direct current of 2 to 5 ma. was being passed through the other pair of electrodes. The conductivity of the melt was determined at 430° with the iodine bulb at 130, 210, 265, and 310° (measurements at lower iodine temperatures were erratic and were discarded). The cell constant of the conductance cell was measured with mercury at 25°.

Materials. Bismuth triiodide was synthesized by direct combination of the elements. Special high-purity (99.999+%) bismuth (Asarco, South Plainfield, N. J.) was melted and heated under H_2 in a fused-quartz tube to remove oxide. Iodine U.S.P. resublimed crystals (Mallinckrodt) were used. The residue on resublimation was less than 0.01%.

Results and Discussion

The cooling curves had the following general characteristics. For pure BiI_3 the curves showed an arrest of about 70-min. duration with an initial supercool region of a few minutes followed by a flat region (taken as the freezing point) that dropped only 0.1° for the first 10-min. duration. There were no heat effects below the freezing point down to 70°. For pure I_2 the curve was similar except the over-all duration was about 40 min. For compositions from 75 atom % I (*i.e.*, BiI_3) to 85 atom % the curves showed, at the upper thermal effect, an initial supercool followed by a curve that was initially almost horizontal and then curved downward. This almost horizontal portion became less and less horizontal with increasing iodine content. The supercool made it difficult to determine the temperature of the beginning of the thermal effect more precisely than ±1°. From 90 to 98 atom % I the curves showed no supercool; however, the change in slope, due to the heat effect, was small, and the beginning of the heat effect could be established with the same accuracy. A eutectic halt was observed at about 113° for all compositions other than I_2 and BiI_3. The length of the halt increased with iodine content indicating the eutectic composition was close to pure I_2 The heating curves were in general agreement with the cooling curves but were not used to determine the temperatures of the thermal effects. The temperatures of the heat effects observed are given in Table I.

Our interpretation of the phase diagram based on these observations is the BiI_3–I_2 portion of the entire Bi–I_2 phase diagram in Figure 1. (The Bi–BiI_3 portion is from the work of Yosim, *et al.*[2]) The BiI_3–I_2 system is a simple eutectic one with the eutectic very close to pure I_2. There is no evidence for any compound formation (congruently or incongruently melting) since the eutectic halt occurs at the same temperature over the whole composition range. van Klooster[3] reported some measurements on the BiI_3–I_2 system. His results are much below those we reported above. His measurements were made in *open* tubes, and he reported heavy loss of I_2; therefore, we did not consider those data in constructing the phase diagram.

Table I: Thermal Effects Observed

Composition		Temp., °C.	
Atom % I	Mole % I_2	First break	Eutectic halt
75.0	0.00	408.5	...
75.44	3.50	405.3	112.1
75.87	6.70	402.4	112.4
76.31	9.94	399.4	112.7
77.05	15.2	394.0	112.9
77.97	21.3	388.4	113.0
79.06	27.9	381.0	113.1
81.00	38.7	366.4	112.9
83.50	50.7	349.0	113.1
86.00	61.1	332.7	113.1
88.00	68.4	319.4	113.1
90.00	75.0	304.8	112.8
92.00	80.9	291.9	113.1
94.00	86.4	275.4	113.2
96.00	91.3	251.5	113.0
96.78	93.1	239.1	112.8
98.00	95.8	208.6	113.0
100.00	100.00	113.3	...

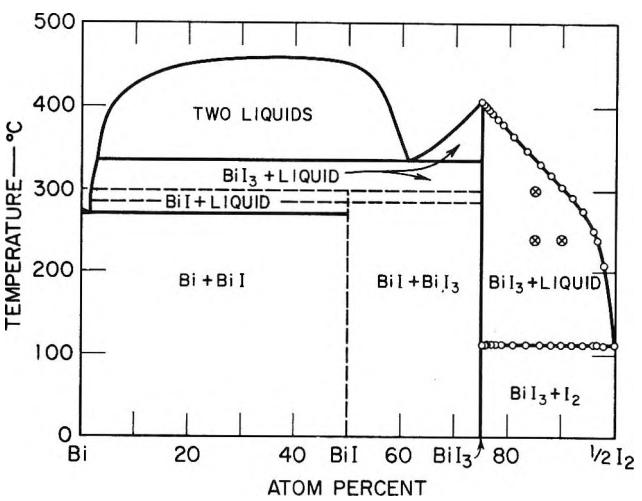

Figure 1. The Bi–I_2 phase diagram. Data to left of BiI_3 from Yosim, *et al.* Present data = points to right of BiI_3.

(2) S. J. Yosim, L. D. Ransom, R. A. Sallach, and L. E. Topol, *J. Phys. Chem.*, 66, 30 (1962).

(3) H. S. van Klooster, *Z. anorg. Chem.*, 80, 104 (1913.)

To substantiate this interpretation of the thermal data, three samples in sealed tubes were equilibrated for about 70 hr., quenched, and X-rayed. The compositions and temperatures of these equilibrations are marked by circled crosses in Figure 1. The patterns observed for all three samples were those of BiI_3 and I_2 with no unidentified lines.

Comparison of the experimental freezing point lowering of BiI_3 by I_2 with that expected for various solution models is shown in Figure 2. The freezing points expected for the several solution models were calculated from

$$\ln X(BiI_3) = -\frac{\Delta H_f}{R}\frac{T_0 - T}{T_0 T} \qquad (1)$$

The heat of fusion of BiI_3 (ΔH_f = 9.41 kcal./mole) was taken from Yosim, *et al.*[2] The effective mole fraction of BiI_3 (*i.e.*, $X(BiI_3)$) was calculated for the models assumed as in Table II.

Table II

Species assumed	$X(BiI_3)$[a]
BiI_3, I_2	$\frac{[BiI_3]}{[BiI_3] + [I_2]}$
Bi^{+3}, I^-, I_3^-	$\left(\frac{3[BiI_3] - [I_2]}{3[BiI_3]}\right)^3$
Bi_2I_6, I_2	$\frac{{}^1/_2[BiI_3]}{{}^1/_2[BiI_3] + [I_2]}$

[a] $[BiI_3]$ and $[I_2]$ represent moles of BiI_3 and I_2 originally introduced into sample.

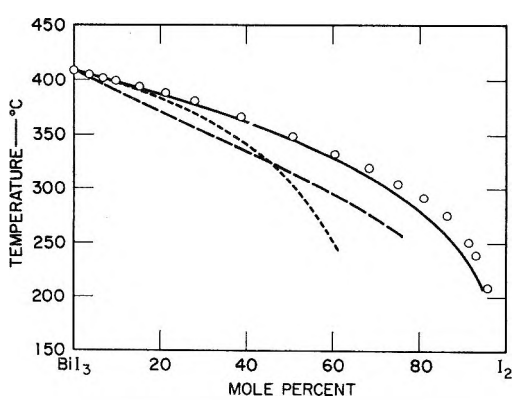

Figure 2. Comparison of experimental freezing points with various models for solution: ———, BiI_3, I_2; · · · ·, Bi^{3+}, I^-, I_3^-; – – – –, Bi_2I_6, I_2.

The curve calculated on the basis of BiI_3 and I_2 as the species in the melt agrees quite well with the experimental data.

The phase diagrams of three similar systems have been reported: AsI_3–I_2 and SbI_3–I_2 by Jaeger and Doornbosch,[4] and AlI_3–I_2 by Nizhnik.[5] These systems are also of the simple eutectic type. In Figure 3 the experimental freezing points for the liquidus in equilibrium with MI_3 are compared with curves calculated for the same types of solution models. For this purpose the heats of fusion of the iodides were determined by drop calorimetry. The values obtained were 5.21, 5.44, and 3.86 kcal./mole of AsI_3, SbI_3, and AlI_3, respectively.[6] It was also possible in these three systems to calculate the liquidus in equilibrium with solid I_2 since that branch of the curve was long enough to be measured. The heat of fusion[7] of I_2 was taken as 3.74 kcal./mole. The mole fractions of I_2 substituted in eq. 1 were calculated for the various solution models as in Table III.

Table III

Species assumed	$X(I_2)$
MI_3, I_2	$\frac{[I_2]}{[MI_3] + [I_2]}$
M^{+3}, I^-, I_2	$\frac{[I_2]}{[I_2] + 4[MI_3]}$
M_2I_6, I_2	$\frac{[I_2]}{[I_2] + {}^1/_2[MI_3]}$
MI_2^+, I^-, I_2	$\frac{[I_2]}{[I_2] + 2[MI_3]}$

The comparisons of Figure 3 indicate that the only solution model that fits both liquidus branches reasonably well for all three systems is the one in which the species are assumed to be MI_3 and I_2. This was also the case with BiI_3. (It may well be that at compositions near the pure components some other solution model would give a better representation of the properties. For instance, with small concentrations of I_2 in SbI_3 the latter may act as a dimer. However, the liquidus for the whole phase diagram is in each case in

(4) F. M. Jaeger and H. J. Doornbosch, *Z. anorg. Chem.*, **75**, 261 (1912). Phase diagrams for these systems have also been reported by E. Quercigh, *Atti accad. Lincei*, (5) **21**, 786 (1912), whose data are in general agreement with those of Jaeger and Doornbosch and also by E. Montignie, *Bull. soc. chim. France*, **8**, 542 (1941), who did not present his data points.

(5) A. T. Nizhnik, *Zh. Obshch. Khim.*, **7**, 1935 (1937).

(6) H. Eding and D. Cubicciotti, "Heat Contents for AsI_3, SbI_3, and AlI_3 above Room Temperature," to be published.

(7) F. D. Rossini, D. D. Wagman, W. H. Evans, S. Levine, and I. Jaffe, National Bureau of Standards Circular 500, U. S. Government Printing Office, Washington, D. C., 1952.

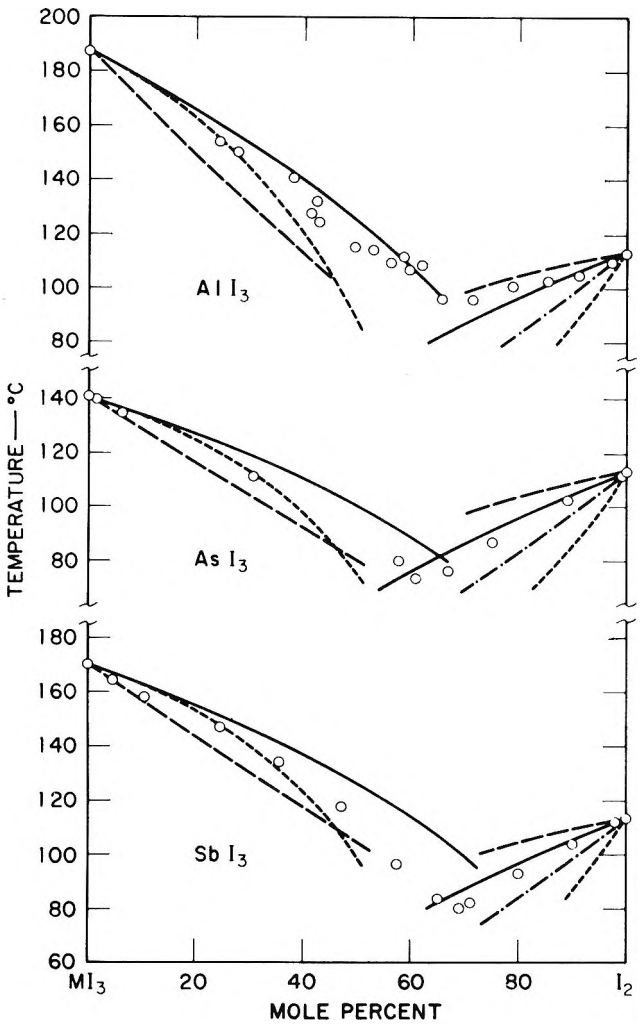

Figure 3. Comparison of freezing points of Jaeger and Doornbosch and Nizhnik with various solution models: ———, MI_3, I_2; – – – –, M^{+3}, I^-, I_2; — — —, M_2I_6, I_2; — · —, MI_2^+, I^-, I_2.

best accord with the assumption that MI_3 and I_2 are the species in solution.)

A brief investigation of the effect of added I_2 on the electrical conductivity of molten BiI_3 was made. The sample of BiI_3 was maintained at 430° and the I_2 bulb temperature increased from about 130 to 310°. The approximate composition of the melt was calculated from the I_2 pressure in the bulb assuming Raoult's

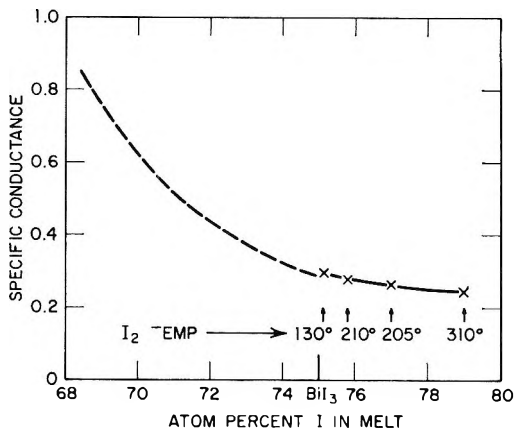

Figure 4. Electrical conductance of melts near BiI_3 composition at 430°. Dashed curve from data of Grantham and Yosim.

law for the melt. The results, which are to be considered as qualitative, are shown in Figure 4. The data show that the conductance of the melt decreases with increasing I_2 content; that is, the solution of I_2 in BiI_3 does not involve the production of appreciable concentrations of conducting species. Also, the data join reasonably well with those of Grantham and Yosim[8] and indicate that no abrupt change in conduction occurs at the composition of the compound BiI_3. In fact, the gradual decrease in conductance with increase in I_2 content is very similar to that observed in the melts of the Sb–S[9] and Bi–S[10] systems near the M_2S_3 composition with increasing S content.

As seen above, the species which can be considered to determine the thermodynamic properties of these solutions are BiI_3 and I_2. Since these are uncharged, there must also be some minor species in the melt to carry the current. The exact nature of these species is as yet unspecified; their concentration apparently decreased as I_2 was added to the melt.

Acknowledgment. The authors are grateful to Dr. J. W. Johnson for his contributions, especially in the conductance work.

(8) L. F. Grantham and S. J. Yosim, *J. Chem. Phys.*, **38**, 1671 (1963).

(9) F. S. Pettit, *J. Phys. Chem.*, **68**, 9 (1964).

(10) J. W. Johnson, "Electrical Conductance of Bi–S Melts," to be published.

The Kinetics of Ion Association in Manganese Sulfate Solutions. I. Results in Water, Dioxane–Water Mixtures, and Methanol–Water Mixtures at 25°

by Gordon Atkinson and S. K. Kor

Department of Chemistry, University of Maryland, College Park, Maryland *(Received June 23, 1964)*

Ultrasonic absorption has been measured in water, dioxane–water, and methanol–water solutions of $MnSO_4$ at 25°. The three-peak relaxation spectrum is interpreted by the three-step association between $Mn^{+2}(aq)$ and $SO_4^{-2}(aq)$ proposed by Eigen. All six rate constants for the three-step process are calculated by a straightforward method. Step I is diffusion controlled with a forward rate constant of $4.2 \times 10^{10}\ M^{-1}$ sec.$^{-1}$ in water while the step III forward rate (4.8×10^7 sec.$^{-1}$) seems controlled by the rate of exchange of solvent on the Mn^{+2} ion. The over-all equilibrium constant including the three ion-pair states is shown to be the same as the K_A determined by conductance both in water and the mixed solvents.

The classic model for electrolyte solution theories has been the continuum solvent model of Debye and Onsager. The great power of this approach in giving the low concentration equilibrium and nonequilibrium properties of solutions cannot be overlooked. For associated electrolytes, the continuum solvent models of Bjerrum and Fuoss have given much insight into electrolyte behavior.

Yet in recent years, it has become more and more apparent that the model was inadequate to describe many electrolyte systems. Corrections and additions that take a more specific and molecular view of the solvent have been either mathematically intractable or of very limited service. In some recent articles, Fuoss[1] has pointed up some cases where a molecular approach to the solvent seemed necessary. A few years ago Gilkerson[2] developed a more general approach to association to explain specific solvent effects. Ramsey[3] and Hyne[4] have also emphasized specific solvent effects in conductance behavior. In a very careful analysis of KCl conductance data, Petrucci[5] has demonstrated that a simple Stokes law approach is inadequate even for this uncomplicated salt. And in a series of papers[6] we have pointed out the great inadequacies of the simple model for 2–2 salts such as $MnSO_4$ and manganese *m*-benzenedisulfonate.

Besides these analyses from the viewpoint of classical solution measurements, other approaches and techniques have demonstrated the limitations of the continuum model. Frank and his co-workers have organized much data using the "structure-making" and "structure-breaking" concept.[7] The coordination chemists have consistently looked at many ions as having definite numbers of solvent molecules around them in solution and have developed ways of measuring the numbers in at least some cases.[8,9]

In our recent work on the conductance of $MnSO_4$ and manganese *m*-benzenedisulfonate (MnBDS) in various

(1) R. M. Fuoss and A. D'Aprano, *J. Phys. Chem.*, **67**, 1704, 1722 (1963).

(2) W. R. Gilkerson, *J. Chem. Phys.*, **25**, 1200 (1956).

(3) J. B. Ramsey and H. K. Bodenseh, *J. Phys. Chem.*, **67**, 140 (1963).

(4) J. B. Hyne, *J. Am. Chem. Soc.*, **85**, 304 (1963).

(5) S. Petrucci, *Acta Chem. Scand.*, **16**, 760 (1962).

(6) G. Atkinson, *et al.*, *J. Am. Chem. Soc.*, **83**, 3759 (1961); **84**, 721 (1962); **86**, 7 (1964).

(7) H. S. Frank and W. Wen, *Discussions Faraday Soc.*, **24**, 133 (1957).

(8) H. Taube and J. P. Hunt, *J. Chem. Phys.*, **19**, 602 (1951).

(9) R. E. Connick, "Advances in the Chemistry of the Coordination Compounds," S. Kirschner, Ed., Macmillan and Co., New York, N. Y., 1961, p. 15.

solvent mixtures, very specific solvent effects showed up in a number of ways. The classic log K_A *vs.* $[1/D]$ plot was not a single straight line for a given salt in any solvent but depended on the specific solvent mixture. The "mean distance of closest approach," a_J, changed with solvent composition in some cases. Finally, the Walden product, $\Lambda^0\eta^0$, exhibited specific dependence on solvent composition.

This led us to explore other techniques that would give us a more detailed view of ion–ion interaction in solution. The most promising development in many years has been the array of relaxation methods developed and utilized by Eigen and his co-workers.[10] Of the various methods used by Eigen, the most versatile for electrolyte work seemed to be the ultrasonic absorption technique. The excellent analyses of this technique presented elsewhere[11,12] make it unnecessary to go into it in detail here.

The particular system that we chose to examine was $MnSO_4$ ion association. In this system we had accurate conductance data in water and in a variety of mixed solvent systems. Furthermore, its ultrasonic relaxation spectrum was measurable with a single type of apparatus. Three previous groups of workers had reported various detailed experiments in ultrasonic absorption in $MnSO_4$ solutions. Eigen, Kurtze, and Tamm (EKT) had measured absorption over a wide frequency range as part of a very extensive program.[13] Smithson and Litovitz[14] (SL) had made some very accurate measurements in H_2O, D_2O, and H_2O–CH_3OH mixtures over a more limited frequency range. Verma and Kor[15] (VK) had made measurements in H_2O and water–dioxane mixtures over a still more limited frequency range. There were some curious inconsistencies in the three sets of data. EKT report relaxation peaks at approximately 3 and 200 Mc. in 0.1 *M* aqueous $MnSO_4$ while SL also report a distinct peak at about 30 Mc. The effect of methanol noted by SL seemed quite different from the effect of dioxane measured by VK. Furthermore, the effect of temperature on relaxation frequency seemed very different for SL and for VK.

In view of these inconsistencies we decided to measure ultrasonic absorption as a function of concentration in aqueous $MnSO_4$ and in dioxane–water and methanol–water mixtures. The best theoretical analysis of ultrasonic absorption in electrolytes is that given by Eigen and Tamm[16] and we have based our interpretation of data on their general approach.

Experimental

The equipment used for the ultrasonic measurements has been described in detail elsewhere.[17] It is based on the pulse technique which has proven to be the most accurate in the megacycle range.[18,19]

The basic frequency range of the main apparatus is 1–60 Mc. using a cell with a maximum path length of 1 m. For the range 60–250 Mc. a cell with a maximum path length of 5.08 cm. is used. The temperature of the solution being measured can be controlled to ±0.05° over the range 0–65°. The purification of $MnSO_4$ and the solvents have been described in the papers on conductance previously referenced.

The absorption coefficient α is defined by the equation $I_x = I_0 \exp(-2\alpha x)$ where I_0 = intensity of sound beam at 0, I_x = intensity of sound beam at x, and x = centimeters of path length. The relaxation spectra are usefully plotted as $[\alpha\lambda]^*$, the absorption per wave length in the solution minus the absorption per wave length in the solvent, *vs.* frequency.

Figure 1 shows the relaxation spectra of $MnSO_4$ in water at three different salt concentrations. It is quite apparent that the peak at approximately 30 Mc. reported by SL exists. Figure 2 shows the effect of increasing dioxane content on the relaxation spectra of

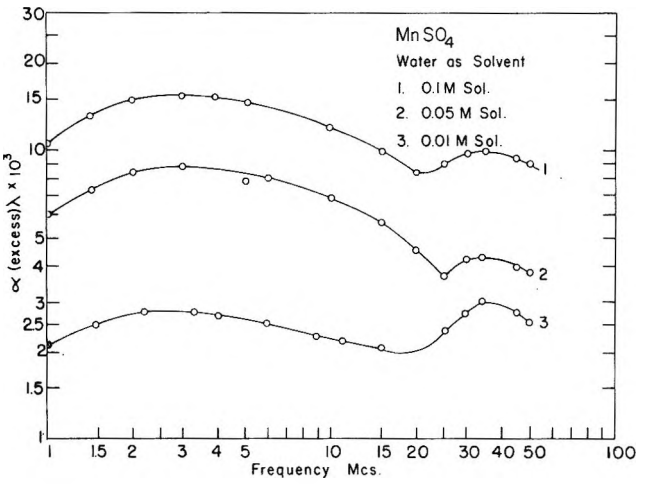

Figure 1.

(10) M. Eigen and L. De Maeyer, "Technique of Organic Chemistry," Vol. VIII, Interscience Publishers, New York, N. Y., Part 2, Chapter 18.

(11) G. S. Verma, *Rev. Mod. Phys.*, **31**, 1052 (1959).

(12) R. T. Beyer, *et al.*, *ibid.*, **23**, 353 (1951).

(13) M. Eigen, G. Kurtze, and K. Tamm, *Z. Elektrochem.*, **57**, 103 (1953).

(14) J. R. Smithson and T. A. Litovitz, *J. Acoust. Soc. Am.*, **28**, 462 (1956).

(15) S. K. Kor and G. S. Verma, *J. Chem. Phys.*, **29**, 9 (1958).

(16) M. Eigen and K. Tamm, *Z. Elektrochem.*, **66**, 93, 107 (1962).

(17) G. Atkinson, S. K. Kor, and R. L. Jones, *Rev. Sci. Instr.*, in press.

(18) J. R. Pellam and K. J. Galt, *J. Acoust. Soc. Am.*, **18**, 251 (1946).

(19) J. M. M. Pinkerton, *Proc. Phys. Soc.* (London), **B62**, 286 (1949).

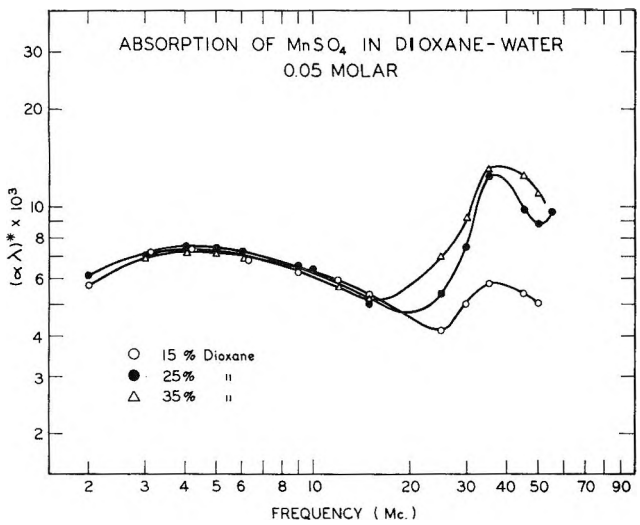

Figure 2.

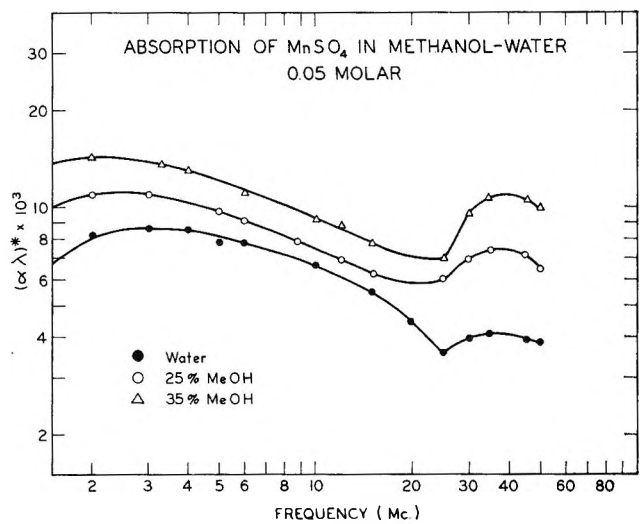

Figure 3.

one concentration of $MnSO_4$. Although the 30-Mc. peak is lower in amplitude than the 3-Mc. peak in water, it rapidly becomes higher as dioxane is added. Figure 3 shows the analogous effect upon adding methanol. Table I summarizes the relaxation frequencies and absorption maxima measured in this work. The frequencies were calculated from the measured excess absorption values using the Mikhailov technique.[20]

Data Treatment

Since measurements of the 200-Mc. peak were not available to us until very late in the work we have used the data of Kurtze and Tamm[21] for this peak.

The existence of three peaks (approximately 3, 30, and 200 Mc.) is very strong evidence for a three-step association process as postulated by Eigen and Tamm. Eigen has shown that other equilibria leading to relaxation peaks can be eliminated from consideration experimentally or theoretically. Various hydrolysis equilibria are easily eliminated by examination of pH dependence. Structural relaxation of the solvent itself must occur at a frequency much higher than 200 Mc., and ion-atmosphere relaxation is too small to account for the peaks in this frequency range.

Therefore, we have assumed a three-step association equilibrium between Mn^{+2} and SO_4^{-2} as a working hypothesis.

Table I: Ultrasonic Absorption of $MnSO_4$ Solutions at 25°[a]

Concn., *M*	ν_{II}*, Mc.	ν_{III}*, Mc.	$[\alpha\lambda]_{II}$* × 10⁴	$[\alpha\lambda]_{III}$* × 10⁴
		Water		
0.01	32	2.7	31.2	28.0
0.05	34	3.1	42.5	87.5
0.10	35	3.3	100.0	160.0
		15% (w./w.) dioxane		
0.01	33	3.5	48.0	26.0
0.05	35	4.2	58.8	73.0
0.10	36	4.5	160.0	140.0
		25% (w./w.) dioxane		
0.01	34	3.6	55.0	26.5
0.05	36	4.4	127.0	73.7
0.10	37	4.8	187.0	145.0
		35% (w./w.) dioxane		
0.01	35	3.9	73.5	26.5
0.05	37	4.65	132.0	75.3
0.10	38	5.1	218.0	160.0
		15% (w./w.) methanol		
0.01	34	2.4	36.0	29.3
0.10	37.5	3.2	103.0	202.0
		25% (w./w.) methanol		
0.05	38.5	2.6	74.2	110.0
0.10	40	2.9	120.0	202.0
		35% (w./w.) methanol		
0.01	37	1.9	38.7	35.0
0.05	39.5	2.5	105.0	137.0

[a] ν_{II}* = frequency of 2nd absorption maximum; ν_{III}* = frequency of 3rd absorption maximum; $(\alpha\lambda)_{II}$* = absorption per wave length at 2nd maximum (excess); $(\alpha\lambda)_{III}$* = absorption per wave length at 3rd maximum (excess).

(20) I. G. Mikhailov, *Dokl. Akad. Nauk SSSR*, **89**, 991 (1953).
(21) G. Kurtze and K. Tamm, *Acustica*, **4**, 380 (1953).

$$\begin{array}{ccc} \text{State } ① & \text{I} & ② \\ Mn^{+2}(\text{solvated}) + SO_4^{-2}(\text{solvated}) & \underset{k_{21}}{\overset{k_{12}}{\rightleftharpoons}} & [Mn^{+2}SO_4^{-2}] \\ & & k_{24}\downarrow\uparrow k_{42} \quad \text{II} \\ [Mn^{+2}SO_4^{-2}] & \underset{k_{43}}{\overset{k_{34}}{\rightleftharpoons}} & [Mn^{+2}SO_4^{-2}] \\ ④ & \text{III} & ③ \end{array}$$

Step I involves the approach of two completely solvated ions. Steps II and III are most probably the successive removal of solvent molecules from the region between the ions giving, finally, a contact ion pair.

For such a three-step process Eigen has shown that the relationships between the relaxation times and the rate constants are given by the equation

$$1/\tau_I = 2\pi\nu_{mI} = k_{21} + k_{12}' \tag{1}$$

where

$$k_{12}' = k_{12}^0 \alpha C \gamma_\pm^2 \left[2 + \frac{\partial \ln \gamma_\pm^2}{\partial \ln \alpha}\right] \tag{2}$$

$$1/\tau_{II} = 2\pi\nu_{mII} = k_{32} + \left[\frac{k_{12}'}{k_{12}' + k_{21}}\right] k_{23} = k_{32} + k_{23}' \tag{3}$$

$$1/\tau_{III} = 2\pi\nu_{mIII} = k_{43} + \left[\frac{k_{23}'}{k_{23}' + k_{32}}\right] k_{34} = k_{43} + k_{34}' \tag{4}$$

where α = degree of association in step I at C; $\gamma_\pm$ = mean activity coefficient of ions in state 1 at concentration C; C = equilibrium concentration of $MnSO_4$; ν_{mi} = frequency of maximum absorption for concentration C; τ_i = relaxation time for step i.

The more complete mathematical treatment using transformation matrices did not significantly alter the numerical results of this analysis. For data analysis we have made the following assumptions.

1. Step I can be described using the Fuoss–Bjerrum association model.[22] An equilibrium constant can be calculated for a given solvent system with the Bjerrum equation and a distance parameter equal to the sum of the ionic radii plus the diameter of two solvent molecules (the calculations are quite insensitive to the distance chosen).

2. The activity coefficient, $\gamma_\pm$, can be calculated using the extended Debye–Hückel equation. Brubaker[23] has shown that this is quite good for an unassociated 2–2 salt. The measured activity coefficients for $MnSO_4$ include a contribution from association and cannot be used.

3. Activity coefficients can be ignored for states 2, 3, and 4. With these assumptions we can define a quantity $\Theta[C]$ as

$$\Theta[C] = \alpha C \gamma_\pm^2 \left[2 + \frac{\partial \ln \gamma_\pm^2}{\partial \ln \alpha}\right]_C \tag{5}$$

and write

$$2\pi\nu_{mI} = k_{21} + k_{12}^0[\Theta[C]] \tag{6}$$

$$2\pi\nu_{mII} = k_{32} + \left[\frac{\Theta[C]}{K_{12} + \Theta[C]}\right] k_{23} = k_{32} + \Phi[C]k_{23} \tag{7}$$

$$2\pi\nu_{mIII} = k_{43} + \left[\frac{\Phi[C]k_{23}}{k_{32} + \Phi[C]k_{23}}\right] k_{34} \tag{8}$$

A small computer program is used to calculate $\Theta[C]$ for a given K_{12} and solvent. Plots of $2\pi\nu_{mi}$ *vs.* the quantities in brackets in eq. 6, 7, and 8 are straight lines yielding the rate constants for the given step as slope and intercept. The graphical method is very useful for smoothing the ν_m data.

Water Results. Table II summarizes the rate constant results in water. The most significant features can be summarized as follows. (1) k_{12} agrees very well with that predicted for a diffusion-controlled rate.[24] (2) k_{34} is very close to Connick's best estimate of the rate of exchange of water in the first coordination sphere of Mn(II).[25] This encourages our belief that the rate-determining step in the association is the replacement of a solvent molecule in the first coordination sphere by the ligand. (3) All three "ion-pair" states exist in reasonable quantities but state 3 is definitely less stable.

It is fruitful to compare the over-all constant for association

$$K_\Sigma = \frac{C_2 + C_3 + C_4}{C_1^2 \gamma_\pm^2} = 139$$

with the association constant determined by conductance measurements,[6] K_A = 133. This very close agreement, as well as the results noted in points 1 and 2 above, give us confidence in the general model chosen and in the method of data treatment.

Mixed Solvent Results. The change of step I rates (k_{12} and k_{21}) is what is expected from consideration of

(22) *E.g.*, R. M. Fuoss and C. A. Kraus, *J. Am. Chem. Soc.*, 79, 3301 (1957).

(23) C. H. Brubaker, Jr., and P. G. Rasmussen, *J. Phys. Chem.*, 67, 330 (1963).

(24) See ref. 10, pp. 1032, 1033.

(25) See ref. 9, p. 17.

Table II: Rate Constants for $MnSO_4$ Association in Water at 25°

$$k_{12} = 4.2 \times 10^{10}\ C^{-1}\ \text{sec.}^{-1}$$
$$k_{21} = 8.0 \times 10^{8}\ \text{sec.}^{-1}$$
$$K_{12} = 0.0192\ \text{l./mole}$$
$$k_{23} = 6.9 \times 10^{7}\ \text{sec.}^{-1}$$
$$k_{32} = 1.9 \times 10^{8}\ \text{sec.}^{-1}$$
$$K_{23} = \frac{C_2}{C_3} = 2.8$$
$$k_{34} = 4.8 \times 10^{7}\ \text{sec.}^{-1}$$
$$k_{43} = 1.4 \times 10^{7}\ \text{sec.}^{-1}$$
$$K_{34} = \frac{C_3}{C_4} = 0.29$$

the Debye equation for diffusion-controlled reactions. This reinforces our belief that the continuum model is perfectly adequate, as long as we are dealing with ions separated by two or more solvent molecules.

However, in steps II and III we start seeing the individual behavior of the different solvent mixtures. Figure 4 shows the change of the step II rate constants with added methanol or added dioxane. It is apparent that methanol has no effect on the rates implying that the ions do not distinguish between water molecules and methanol molecules in this step. The dioxane drastically increases the forward rate and decreases the reverse.

Figure 5 shows the effect of the added organic solvent on step III. Here both solvents have markedly different effects on the rate constants. With results on just one salt, molecular interpretation seems premature. There is no particular reason for plotting the constants against mole fraction organic in Figures 4 and 5. However, in step III if we consider k_{43} as a pseudo-first-order constant, $k_{43} = k_{43}^0[H_2O]$, and calculate k_{43}^0 we find that the dioxane line and the methanol line coincide. This implies a decided preference for water over the organic component by one (or both) of the ions in the pair.

This reinforces King's recent results on the preference of Cr(III) for water over methanol.[26]

In Figure 6 we have plotted the K_Σ calculated from the ultrasonic data on the same plot as the K_A values obtained from conductance work. The two sets of data agree very well. The difference between the methanol line and the dioxane line noted in the conductance work is found to result from the very different effects of the two organic solvents on steps II and III of the association process. We might also point out that, at least in the case of $MnSO_4$, conductance includes all three ion-pair states in the nonconducting group.

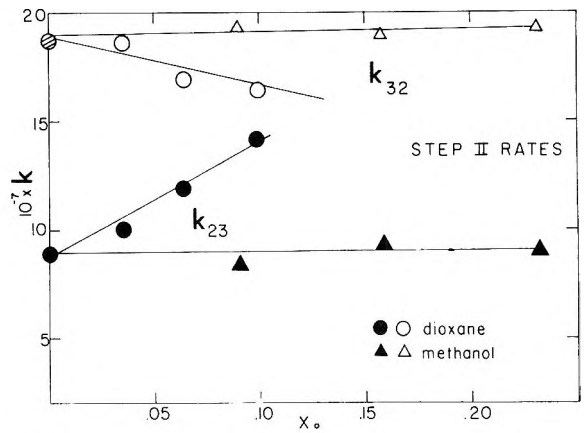

Figure 4.

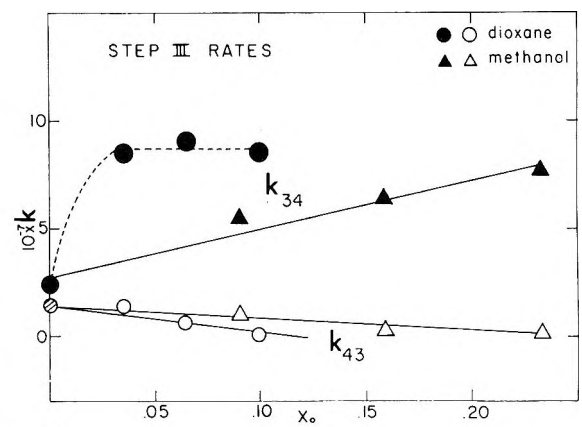

Figure 5.

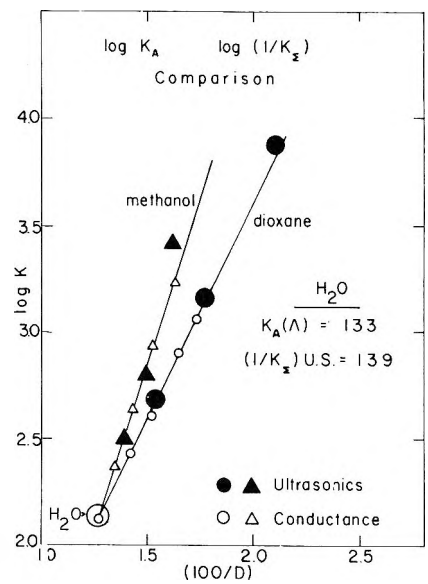

Figure 6.

(26) E. L. King, *et al.*, Proceedings of the 7th International Coordination Chemistry Conference, Paper 6BI, 1962.

Summary

The Eigen three-step mechanism for 2–2 salt association has been demonstrated to hold very accurately for $MnSO_4$, both in water and in dioxane–water and methanol–water mixtures. The first and fastest step is the diffusion-controlled interaction of ions with complete solvation spheres. The second and third steps most probably involve the successive removal of solvent molecules from between the ions, giving a contact ion pair in the final state. Only the first step can be adequately described using the classical continuum model. A theoretical description of the second and third steps must await a theoretical model recognizing the discrete structure of the solvent. In the final step the rate seems determined by the rate of exchange of solvent molecules on the cation. The dependence of the reverse rate constant of this final step (k_{43}) on the actual water concentration in the low organic content solvent mixtures examined implies a definite preference for a H_2O molecule on the part of the Mn(II) ion.

The over-all association constants calculated from the ultrasonic data agree very well with those previously obtained by conductance work. This means that for this salt, at least, none of the three ion-pair states contributes to the electrical conductance. Furthermore, the individual effects of different added organic solvents, so inexplicable by classical electrolyte theories, are the result of distinctly different solvent effects on the individual steps of the association reaction.

In a succeeding paper we shall report the effect of temperature on the relaxation spectra and examine the energetics of the individual steps of the association process.

Acknowledgment. The authors wish to acknowledge the generous support given this research by the Army Research Office (Durham) under Grant DAARO(D)-31-124-G175. They also wish to acknowledge the aid of Dr. Hiroyuki Tsubota in the preparation, purification, and analysis of the materials used, and the help of Mr. D. W. Ebdon in the computer programming.

The Exchange of Methanol between Solvated Cations and Solvent. II

by Terrence E. Rogers, James H. Swinehart, and Henry Taube[1]

George Herbert Jones Laboratory of the University of Chicago, Chicago 37, Illinois, and the Department of Chemistry, Stanford University, Stanford, California *(Received June 25, 1964)*

The exchange of methanol between solvated Co^{+2} or Ni^{+2} and methanol as solvent was studied by the isotopic dilution method. The enthalpy of activation, ΔH^*, for the exchange process is 11.5 ± 0.7 kcal./mole for Co^{+2} and 13.1 ± 0.7 kcal./mole for Ni^{+2}. Qualitative observations have been made on methanol–water solvation equilibria for Co^{+2} solutions in CH_3OH containing some H_2O. The "kinetic solvation number" is shown to be 6. Preliminary data for the $PrCl_3$–methanol system indicate that solvation of Pr^{+3} in CH_3OH can be studied by the isotopic dilution method. In this case it appears that H_2O in small amounts decreases the lability of the solvation methanol. Analysis of the isotopic dilution data for the perchlorate salts of Co^{+2}, Ni^{+2}, or Fe^{+3} shows that in certain cases the holdback of methanol for each mole of solute may exceed that ascribable to first coordination sphere interactions.

Introduction

This paper describes a study of the exchange of methanol between solvated Co^{+2}, Ni^{+2}, or Fe^{+3} and the solvent. Some preliminary data on the Pr^{+3}–methanol system are included. Since the preparation of the first paper in this series,[2] the nuclear magnetic resonance line broadening method for determining the rate of solvent exchange has been developed so that it is now possible by studying the line width as a function of temperature to determine which of two mechanisms causes the broadening of the n.m.r. line. Luz and Meiboom[3] have used the proton n.m.r. of mixed methanol–water solutions of Co^{+2} and Ni^{+2} to determine the rate of methanol exchange for various mixed complexes of these ions and have determined the solvation number of Co^{+2}. Recently, a complete study of the rate of water exchange between the solvated Mn^{+2}, Fe^{+2}, Co^{+2}, Ni^{+2}, and Cu^{+2}, and the solvent water appeared.[4] Eigen and his co-workers[5] have recently summarized the results of their studies on the rates of solvent replacement on many cations in aqueous solution; these rates are very close to those measured by the n.m.r. method.

Direct comparison of the rates obtained by the n.m.r. or by relaxation techniques with those we have determined is not possible, because the isotopic dilution technique for the labile ions is applicable only at low temperatures where the rates of exchange are quite slow. Nevertheless, comparison of the activation energies measured by this direct method with those obtained by methods capable of responding to rapid exchange rates is of interest. In principle, too, the isotopic dilution method can yield important information about the composition of the solvated complex.[6-9] Its full potential in this respect has not yet been realized for methanol solutions and awaits refinement of the experimental method.

Experimental

A detailed description of the procedure, including methods of analysis, preparation of solutions and reagents, and evaluation of errors, is found in a previous paper.[2] However, the preparations of the solutions of the particular salts studied in the present work are described.

(1) Department of Chemistry, Stanford University, Stanford, Calif. All reprint requests should be addressed to this author.

(2) J. H. Swinehart, T. E. Rogers, and H. Taube, *J. Chem. Phys.*, **38**, 398 (1963).

(3) Z. Luz and S. Meiboom, *ibid.*, **40**, 1058, 1066, 2686 (1964).

(4) T. J. Swift and R. E. Connick, *ibid.*, **37**, 307 (1962).

(5) M. Eigen and L. de Maeyer in "Technique of Organic Chemistry," A. Weissberger, Ed., Vol. VIII, Part II, Interscience Publishers, Inc., New York, N. Y., 1961, Chapter XVIII.

(6) H. W. Crandall, *J. Chem. Phys.*, **17**, 602 (1949).

(7) J. P. Hunt and H. Taube, *ibid.*, **18**, 757 (1950).

(8) J. P. Hunt and H. Taube, *ibid.*, **19**, 602 (1951).

(9) H. W. Baldwin and H. Taube, *ibid.*, **33**, 206 (1960).

$CoCl_2$ and $Co(ClO_4)_2$ Solutions. Anhydrous $CoCl_2$ was prepared from reagent grade hydrated $CoCl_2$ by heating the salt at 135° for several days. Anhydrous methanol was added to the anhydrous salt. A small amount of anhydrous HCl gas was added to repress acid dissociation. In several runs this stock $CoCl_2$ solution was used. Cobalt perchlorate solutions were prepared by adding the necessary amount of anhydrous $AgClO_4$ to give a slight excess of silver ion. In both the $CoCl_2$ and $Co(ClO_4)_2$ solutions the cobaltous ion was determined as $[Co(C_5H_5N)_4](CNS)_2$.[10] The precision of the analysis was ±2%. The acidity was determined to be 0.001 *m*. The water content could not be determined by the Karl Fischer reagent, but on the basis of the experience with other solutions, even for the perchlorates it is less than 2 moles of water/mole of cation.

$NiCl_2$ and $Ni(ClO_4)_2$ Solutions. The nickel solutions were prepared in the same way as the cobaltous solutions. Nickel was determined as the dimethylglyoxime by the standard procedure. The water content of the solutions is less than 2 moles of water/mole of cation.

$FeCl_3$ and $Fe(ClO_4)_3$ Solutions. Dry chlorine gas was passed through a heated Pyrex tube containing coils of high-purity iron wire. Ferric chloride condensed on the cooler parts of the tube.[11] The $FeCl_3$ was collected and stored in sealed Pyrex ampoules. Anhydrous methanol, freshly prepared by distillation from magnesium, was used to prepare solutions of the salt. A small amount of anhydrous HCl was bubbled into the solution to prevent acid dissociation of the solvated ferric ion. A ferric perchlorate solution was prepared by adding the necessary amount of anhydrous $AgClO_4$ to give a slight excess of silver ion.

The following analytical procedures were used for both $FeCl_3$ and $Fe(ClO_4)_3$–methanol solutions. The ferrous content was estimated by direct titration to a ferroin end point using ceric ammonium sulfate solution which had itself been standardized against pure iron wire. Total iron was determined by reducing weighed aliquots of solution on a Jones reductor and then titrating the solution with Ce(IV). The acidity of the solution was estimated by direct titration of a methanol solution diluted with water with standard base to pH 1 using cresol red as an indicator. The water content was estimated to be less than 2 moles of water/mole of cation.

$PrCl_3$ Solution. Hydrated $PrCl_3$ was heated at 180° for 5 hr. in a stream of HCl. Freshly distilled methanol was added. Water as determined by the Karl Fischer reagent was found to be present to the extent of 1 mole/mole of salt in a 1 *m* solution.[12] Praseodymium chloride was analyzed by evaporating the solution and then heating the residue at 230–250° for several hours in the absence of air to minimize the decomposition of $PrCl_3$ to PrOCl. The residue was assumed to be $PrCl_3$.

Results and Discussion

Definitions of Symbols. The symbols used to describe the results are the same as those of the previous paper.[2] For convenience, they are repeated here.

R_t represents the mass spectrometer value of [mass 34/(mass 32 + mass 33)] for the sample of solvent methanol taken at time *t*.

R_∞ represents the mass spectrometer value of [mass 34/(mass 32 + mass 33)] for the sample of solvent methanol taken at infinite time.

R_e and R_n represent the mass spectrometer values of [mass 34/(mass 32 + mass 33)] for oxygen-18 enriched methanol and methanol of normal isotopic composition.

R_∞^c represents [mass 34/(mass 32 + mass 33)] as calculated using b', R_n, and R_e for the solvent methanol at infinite time assuming random mixing.

R_0 represents the extrapolated mass spectrometer value at zero time of [mass 34/(mass 32 + mass 33)] for the solvent methanol. R_0 is determined from a plot of $(R_t - R_\infty)$ *vs. t*.

a represents the ratio of the number of moles of salt to the number of moles of methanol of normal isotopic composition in the solution before mixing with the oxygen-18 enriched methanol.

b represents the ratio of the number of moles of oxygen-18 enriched methanol to the number of moles of methanol of normal isotopic composition as calculated from R_∞, R_e, and R_n.

b' is *b*, but calculated from the weights of the component solutions in the mixture, *a*, R_e, and R_n.

q represents the "kinetic solvation number" calculated from R_0, *a*, *b*, R_e, and R_n.

Cobaltous Solutions. Table I summarizes the isotopic exchange results for $CoCl_2$–methanol solutions at −82.5°. The data indicate that the exchange is complete by the time of sampling, 0.5 min. If the chloride anion is replaced by perchlorate, the rate of exchange of methanol between the solvated cation and the solvent is observable. Thus the cobaltous species present in solution when chloride is the anion exchanges methanol more rapidly than the completely methanolated cobaltous species. The work of Katzin[13] on

(10) A. I. Vogel, "Textbook of Quantitative Inorganic Analysis: Theory and Practice," Longmans, Green and Co., Inc., New York, N. Y., 1951, p. 463.

(11) B. R. Tarr, *Inorg. Syn.*, **3**, 191 (1957).

(12) J. Mitchell, Jr., and D. M. Smith, "Aquametry, Application of Karl Fischer Reagent to Quantitative Analyses Involving Water," Interscience Publishers, Inc., New York, N. Y., 1948, p. 231, for the analysis of water in inorganic salts.

(13) L. I. Katzin, *J. Chem. Phys.*, **35**, 467 (1961).

Table I: Summary of Data for the Isotope Exchange Reaction of $CoCl_2$ Solutions (at $-82.5°$)[a]

Run no.	b	R_n	$R_\infty°$	R_t	t, min.
1	0.2521	0.02000	0.04644	0.04655	0.8
				0.04565	2.8
				0.04570	4.5
				0.04570	10.0
2	0.2591	0.02060	0.04544	0.04705	0.5
				0.04705	1.8
				0.04700	3.0
				0.04675	10.0

[a] $a = 0.03988$, $R_e = 0.14765$.

the absorption spectrum of the $CoCl_2$–methanol system indicates that an octahedral form of Co^{+2} containing chloride predominates at the low temperature of our experiments. In view of the results obtained for $Co(ClO_4)_2$ (*vide infra*) we can conclude that addition of chloride to the coordination sphere of octahedral cobaltous increases the rate of exchange of the bound methanol; it may do this by increasing the rate of the octahedral–tetrahedral transformation for Co^{+2}.

The quality of the exchange data obtained for $Co(ClO_4)_2$ in CH_3OH is similar to that for $Mg(ClO_4)_2$[2] and the exchange curves are not reported in detail. Table II summarizes the results for cobaltous perchlorate solutions.

In appraising the data shown in Table II, it must be appreciated that the amount of adventitious water is not constant from experiment to experiment; thus the results tend to be somewhat erratic. However, even with the limitations on precision which this imposes, certain conclusions are suggested by the data recorded in Table II.

(i) Comparison of runs 3–9 at $-97°$ shows that for solutions with a constant amount of water (less than 2 moles of water/mole of Co^{+2}) the "kinetic solvation number" usually increases with the cooling time.

(ii) The addition of excess water to the $Co(ClO_4)_2$ solution before mixing with the oxygen-18 enriched methanol yields results which depend on the cooling time. (iia) If the amount of water added is about 1 mole/mole of Co^{+2} and the cooling time is short, the exchange is complete within the time of the second sampling, 1.5 to 2.0 min., and the "kinetic solvation number" is small compared to the value generally observed (runs 10 and 11). (iib) If less than 1 mole of water/Co^{+2} is added and the cooling time is short or about 1 mole of water is added and the cooling time is longer, normal kinetics and nearly normal solvation numbers are observed (runs 12 and 13).

(iii) The addition of excess water to the oxygen-18 enriched methanol before mixing with the $Co(ClO_4)_2$ solution has no effect on the solvation number of isotopic exchange rate (run 14). It should be noted that when the experiment is done in this way, the excess water is not introduced into Co^{+2} solution until the solutions are cooled to the temperature of the experiments.

The observations cited indicate that there is a slow re-equilibration of water in the solution at $-97°$ and that as time progresses a water-containing Co(II) species which exchanges methanol rapidly transforms to a Co(II) species containing less water and exchanging methanol slowly. The labilization of methanol by water in mixed methanol–water complexes of Co^{+2} has also been observed by Luz and Meiboom.[3]

The presence initially of a water-containing species which exchanges methanol rapidly is indicated by several items of evidence. First, at room temperature there is definitely a preference for water over methanol in the first coordination sphere of Cr^{+3} and Eu^{+3}.[14,15] Bjerrum and Jørgensen have shown that there is a preference for water over ethanol in the first coordination sphere of the cobaltous ion,[16,17] and there is no reason to believe that the situation will be different in the case of methanol–water solutions of cobaltous ion. Second, the coordinated water must be uniformly distributed over the cobaltous ions initially at $-97°$ in order to explain the difference between (iia), where the addition of about 1 mole of water/mole of Co^{+2} results in rapid exchange of all the bound methanol and (i) where normal exchange is observed.

The evidence for the re-equilibration of water in the solution is the fact pointed out in (i) that the longer the cooling time the larger the solvation number observed, and the difference in the behavior noted under (iia) and (iib). It is possible for this re-equilibration to occur in two ways. The water can be redistributed on cooling in such a manner so as to yield a slowly exchanging cobaltous species with little or no water and a rapidly exchanging species enriched in water, or water may be transferred to the solvent during the redistribution process. Experiment 14 indicates that external H_2O only slowly enters the coordination sphere at low temperatures. Since direct transfer of H_2O from one Co^{+2} complex to another is

(14) E. L. King, private communication.

(15) E. V. Sayre, D. G. Miller, and S. Freed. *J. Chem. Phys.*, **26**, 109 (1957).

(16) J. Bjerrum and C. K. Jørgensen, *Acta Chem. Scand.*, **7**, 951 (1953).

(17) C. K. Jørgensen, *ibid.*, **8**, 175 (1954).

Table II: Summary of Isotopic Exchange Data for $Co(ClO_4)_2$–Methanol Solutions

Run no.	Temp., °C.	Cooling time, hr.	a	b	R_n	R_e	R_0	q	$t_{1/2}$, min.
3	−97	1.5	0.02421	0.1420	0.02115	0.14765	0.03790	2.9	10.3[a]
4	−97	1.2	0.02912	0.1490	0.02041	0.14765	0.03936	3.2	9.4[a]
5	−97	1.5	0.01675	0.1786	0.02070	0.14979	0.04206	3.7	11.6[a]
6	−97	3.5	0.02999	0.1995	0.02092	0.14765	0.04590	6.3	10.0[a]
7	−97	4.0	0.02442	0.1352	0.02085	0.14765	0.03798	5.5	12.4[a]
8	−97	4.5	0.03988	0.2497	0.02031	0.14765	0.05019	4.7	10.0[a]
9	−97	7.3	0.02763	0.2176	0.02077	0.14979	0.04589	3.6	12.0[a]
10	−97	2.0	0.02587	0.1967	0.02083	0.14979	<0.04279	<1.6[b]	
11	−97	2.0	0.03988	0.2491	0.02045	0.14765	<0.04700	<1.0[b]	
12	−97	2.0	0.02649	0.1935	0.02102	0.14979	0.04190	~3.6	(11.6)[c,h]
13	−97	5.8	0.02853	0.2244	0.02060	0.14979	0.04575	~3.1	(11.2)[d]
14	−97	2.0	0.02991	0.2308	0.02093	0.14979	0.04829	~4.8	(10.0)[e]
15	−97	1–4	0.03988	0.2517	0.02072	0.14765	>0.05624	>8.8	(>18.6)[f]
16	−97	1–4	0.03988	0.1951	0.02040	0.14765	>0.05117	>12.6	(>20.0)[f]
17	−97	1–4	0.03988	0.2122	0.02070	0.14765	>0.05293	>9.6	(>10.0)[f]
18	−82.5	1–4	0.02988	0.2663	0.02102	0.14765	0.05345	6.2	0.85[a]
19	−82.5	1–4	0.03988	0.2786	0.02017	0.14765	0.05620	5.8	0.75[a]
20	−82.5	1–4	0.03988	0.2479	0.02068	0.14765	0.05470	8.1	0.85[a]
21	−101.5	1–4	0.02989	0.2469	0.02021	0.14979	0.04935	5.0[f,g]	25.5[f,g]

[a] H_2O/Co^{+2} estimated as <2. [b] H_2O added to Co^{+2} solution, 1.1 moles/mole of Co^{+2}. [c] H_2O added to Co^{+2} solution, 0.66 mole/mole of Co^{+2}. [d] H_2O added to Co^{+2} solution, 1.2 moles/mole of Co^{+2}. [e] H_2O added to CH_3OH enriched in O^{18}, 1.2 moles/mole of Co^{+2}. [f] Curvature in the exchange plots. [g] Based on last linear portion; $q_{initial} = 11.6$. [h] $t_{1/2}$ values which are bracketed are not used in the calculation of ΔH^* or ΔS^*.

unlikely, we conclude that the redistribution takes place, as with Mg^{+2},[2,18] by H_2O leaving the solvated complex as the temperature is lowered.

The "kinetic solvation number" is not unambiguously fixed by the experiments. However, the data in runs 3–9, 18–20, and 21 suggest that it is probably 6, as it has been shown to be by Luz and Meiboom.[3]

An interesting deviation from normal kinetic behavior was noted in several experiments. At −97° concentrated solutions sometimes exhibit an anomalous behavior both as to the rate of exchange and initial holdback (compare runs 15–17 with runs 3–14). The rate of isotopic exchange is not pseudo-first-order and the initial holdback is much larger than normally observed. This behavior can be attributed to the formation of structure within the solution but it is not certain whether these structures are of the "iceberg" type that Miller[19] has suggested for aqueous solutions of rare earth ions or whether crystals actually form. Filtration of a concentrated $Co(ClO_4)_2$ solution (a = 0.03988) at −97° through a medium-mesh sintered glass filter after cooling for 4 hr. showed no residual solid. Visually, the solutions are clear with no sign of solid and the viscosity of those showing anomalous holdback is not obviously greater than for those exhibiting normal behavior. Thus it appears that very small crystals or ordered regions of the solution are causing the anomalous behavior.

If experiments such as 15, 16, and 17 are excluded—and the anomalous behavior they feature is easily recognized—we find that the specific rate of exchange at a fixed temperature is independent of the value of q. Thus it is likely that the exchange of a single species is observed, its abundance being affected by the water content and cooling time. Taking into account experiments such as runs 6 and 7, we can conclude that this species is $Co(CH_3OH)_6^{+2}$. The average pseudo-first-order rate constants ($\ln 2/t_{1/2}$) for the exchange of methanol between the solvated cobaltous ion of coordination number 6 and the solvent are 8.5×10^{-2} sec.$^{-1}$, 6.5×10^{-3} sec.$^{-1}$ and 2.7×10^{-3} sec.$^{-1}$ at −82.5, −97, and −101.5°, respectively. The enthalpy of activation, ΔH^*, is calculated as 11.5 ± 0.7 kcal./mole. The entropy of activation, ΔS^* is −4 e.u.

Solutions Containing Ni^{+2}. Table III summarizes the data obtained for solutions of $NiCl_2$ in CH_3OH. The data at 82.5° yield quite reasonable values of q and of the coordination number of Ni^{+2} for CH_3OH.

(18) J. H. Swinehart and H. Taube, *J. Chem. Phys.*, **37**, 1579 (1962).
(19) D. G. Miller, *J. Am. Chem. Soc.*, **80**, 3576 (1958).

Table III: Summary of Isotopic Exchange Data for $NiCl_2$–Methanol Solutions[a]

Run no.	Temp., °C.	Cooling time, hr.	b	R_n	R_e	R_0	q	$t_{1/2}$, min.
22	−97	1.5	0.3633	0.02094	0.15507	0.06218	4.8	420
23	−97	2.0	0.3387	0.02088	0.15507	0.05985	4.6	375
24	−97	2.0	0.3408	0.02160	0.15507	0.06033	4.6	430
25	−97	1.5	0.3023	0.02090	0.15507	0.06004	4.9	415
26	−82.5	1.5	0.3596	0.02220	0.15507	0.06394	5.8	21
27	−82.5	2.2	0.2298	0.02145	0.15507	0.05340	6.0	26
28	−82.5	1.7	0.3478	0.02154	0.15507	0.06300	6.0	23
29	−82.5	1.7	0.3042	0.02135	0.15150	0.05781	6.0	21

[a] $a = 0.03816$.

Table IV: Summary of Isotopic Exchange Data for $Ni(ClO_4)_2$–Methanol Solutions (at −82.5°)[a]

Run no.	Cooling time, hr.	b	R_n	R_e	R_0	q	$t_{1/2}$, min.
30	2.0	0.4200	0.02181	0.15120	0.06648	4.2	28
31	2.5	0.4448	0.02185	0.15120	0.06831	4.2	25
32	2.3	0.2671	0.02170	0.15125	0.05470	4.5	27
33	1.0	0.3436	0.02120	0.15125	0.06145	4.9	30

[a] $a = 0.04822$.

However, the substantially lower value observed at −97° causes some difficulty. Unfortunately, the effect of varying the water content and the cooling time was not studied systematically for the $NiCl_2$ solutions. The initial water content was varied in the isotopic dilution experiments done with $Ni(ClO_4)_2$ solution (*cf.* Table IV). In two of the three experiments in which the initial ratio of H_2O/Ni^{+2} was set at 4.0, anomalous holdback of methanol of the type described for the $Co(ClO_4)_2$ solution was observed. In the third experiment, normal exchange behavior was noted, and the initial holdback was less than it was for the other experiments of the series. Thus it seems likely that the reduced holdback shown at −97° is again a result of the water content, but whether the defect from 6.0 represents direct replacement or loss from the holdback effect of all species containing at least one H_2O/Ni complex is not settled by our data, but the work of Luz and Meiboom[3] supports the second alternative.

In Figure 1 are displayed typical exchange data for solutions of $NiCl_2$. The results of an experiment in which anomalous initial holdback is observed are included. The observations for $Ni(ClO_4)_2$ differ in that the anomalous behavior occurs with much greater frequency, and the anomalous holdback extends over much longer time periods.

Table IV summarizes the results obtained for solutions of $Ni(ClO_4)_2$ in those few instances in which the anomalous holdback effect did not appear. Comparison with the results of the experiment with $NiCl_2$ at the same temperature shows the the holdback is less than it is for $NiCl_2$. This may be a result of an increased water content caused by the additional handling required in the double decomposition of $NiCl_2$ with $AgClO_4$, or it may be an intrinsic effect. The affinity of Cl^- for H_2O is probably greater than that of ClO_4^- for H_2O; thus in the former solutions there may be less tendency for H_2O to enter the first coordination sphere of the cation.

Using the data of Table III, the specific rates of CH_3OH exchange between CH_3OH and $Ni(CH_3OH)_6^{+2}$ are 2.8×10^{-5} sec.$^{-1}$ at −97° and 5.1×10^{-4} sec.$^{-1}$ at −82.5°. The value of ΔH^* is 13.1 ± 0.7 kcal./mole.

Comparison of the activation enthalpies for H_2O and CH_3OH are of some interest. These are for Ni^{+2} and Co^{+2} in water,[4] 11.6 and 8.0 kcal., respectively; for the same ions in CH_3OH, they are 13.1 and 11.5. The latter values can be compared with those of Luz and Meiboom,[3] 15.8 kcal. for Ni^{+2} and 13.8 kcal. for Co^{+2}.

Ferric Solutions. Table V presents the isotopic dilution data for $Fe(ClO_4)_3$–methanol solutions at

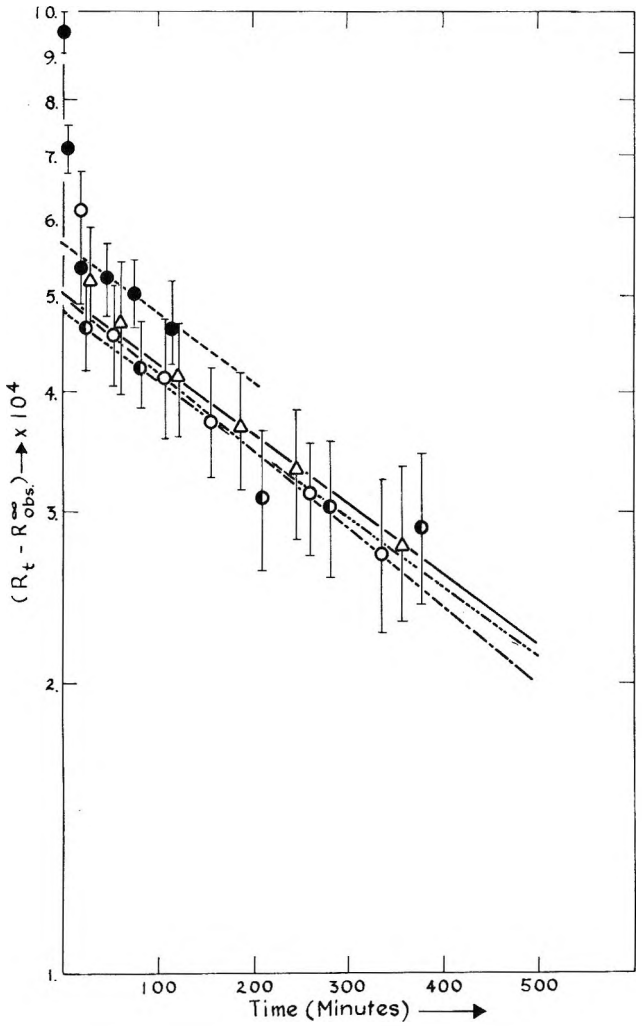

Figure 1. Exchange between solvated Ni^{+2} and solvent (methanol) at −97° (*cf.* Table III): ●, ---------, expt. 22; ○—·—·—·—, expt. 23; ◐—·--·—·--, expt. 24; △ ———, expt. 25.

Table V: Isotopic Dilution Data for $Fe(ClO_4)_3$–Methanol Solutions (at −97°)

Run no.	t, min.[a]	$\frac{[MeOH]_{total}}{[Fe(ClO_4)_3]}$[b]	$\frac{[MeOH]_{initial}}{[Fe(ClO_4)_3]}$[c]	q
	2.0			35.4
	3.8			35.6
34	5.5	46.6	36.0	35.3
	15.0			35.2
	∞			0
	1.0			28.1
	2.8			25.6
35	4.8	50.7	36.0	24.7
	15.0			22.1
	∞			...
	0.8			26.3
	2.3			25.2
36	3.8	48.0	36.0	24.6
	15.0			21.3
	∞			0
	0.7			26.4
	4.8			18.0
37	6.5	65.1	49.9	12.7
	15.5			10.4
	∞			0
	0.6			21.4
	2.2			13.7
38	4.2	72.8	56.0	7.7
	10.0			5.5
	∞			0
	0.8			19.3
	2.5			12.8
39	4.8	83.6	68.1	7.5
	10.3			4.7
	∞			0

[a] Time after mixing at which samples were taken. [b] After dilution by O^{18}-enriched CH_3OH. [c] Before dilution by O^{18}-enriched CH_3OH.

−97°. All runs (34–39) show an anomalously high initial "kinetic solvation number." As the ratio of the total methanol per ferric ion is increased, exchange takes place more rapidly and the initial solvation numbers are smaller. In none of the experiments summarized was solid detected in the solution. A simple calculation shows that in the concentrated solution there is probably no more than one methanol between the solvated cation and unsolvated anion. Taken at face value, the results suggest that there is some sort of well-ordered structure outside of the first coordination sphere of the cations, which is fairly inert to solvent exchange until the structure is destroyed by dilution. These characteristics are not observed in the experiments with $FeCl_3$–methanol solutions (the results obtained for these systems are not described in detail). Even though the solutions are more concentrated, normal kinetics are observed. The "kinetic solvation number" is about 6 ± 1. It is likely that the chloride enters the first coordination sphere of the ferric ion and thus the value of the kinetic solvation number seems somewhat too high to represent the direct coordination of Fe^{+3} to CH_3OH. The half-life of the exchange in the $FeCl_3$–methanol solution is about 2–3 min. at −97°.

Whenever both the perchlorate and chloride salts of a given metal ion were studied, the anomalous hold-back was observed more frequently for the perchlorates. This difference may be related to differences in "structure breaking" properties of the two anions in methanol, as described by Frank and Evans[20] for aqueous solutions.

(20) H. S. Frank and M. W. Evans, *J. Chem. Phys.*, **13**, 507 (1945).

$PrCl_3$ Solutions. The exchange of methanol between the solvated cation and the solvent is observable at $-82.5°$. However, this system also is complicated by effects which are caused by water, but in contrast to the behavior of Co^{+2} and Mg^{+2}, here it appears that holdback is observed only if some water is present in the solution. Problems of solvation for rare earth ions are of especial interest and these systems merit further study.

Acknowledgments. The authors wish to acknowledge financial support from the National Science Foundation and the U. S. Atomic Energy Commission.

Elasticity of Semicrystalline Polymers[1]

by D. Puett, K. J. Smith, Jr., and A. Ciferri

Chemstrand Research Center, Inc., Durham, North Carolina *(Received June 26, 1964)*

In order to investigate how the elastic properties of a rubber change as the degree of crystallinity of the system is increased up to the extreme of a fully crystalline substance, stress–strain–temperature analysis was performed using ethylene–propylene block copolymers of varying degrees of crystallinity, nylon and keratin samples. Stress–strain isotherms of all samples show a peculiar behavior: if a polymer sample is first stretched to an elongation α^I and then released, the subsequent stress–strain isotherm shows an abrupt change of course at an elongation corresponding to α^I. The portion of the isotherm at elongations greater than α^I is unaffected by the mechanical treatment. A similar effect is shown by filled rubber samples, polyurethane elastomers, cellulose filaments, and metals such as aluminum and copper. From a phenomenological viewpoint two conditions were found necessary for the occurrence of the phenomenon, namely, (1) the structure resulting from strain at a given α^I should be permanent and (2) the constraints which hinder deformation above α^I should not be relieved by the previous mechanical treatment. From a structural viewpoint the occurrence of the phenomenon was explained, for substances possessing low degrees of order, in terms of ability of amorphous chains to pull loose from pseudo-crystalline regions and, for crystalline substances, in terms of crystal–crystal transformations and of crystalline orientation accompanied by plastic flow. This description accounts for the small set and large softening caused by the mechanical treatment on samples with low degree of order and for the large set and hardening caused, instead, for crystalline substances. The stress–temperature analysis for the block copolymer samples also reveal a peculiar effect. Negative stress–temperature coefficients are exhibitied when data obtained from isothermal stretching are considered. However, positive coefficients are exhibited when isotherms obtained from stress–temperature data at constant length are considered. The phenomenon is explained on the basis that the melting distribution of the crystalline component is, even in absence of strain, within the range where experimental analysis was performed. Recrystallization in state of strain results in a *decrease* of stress while recrystallization in a state of null strain results in an *increase* of modulus.

I. Introduction

Large, reversible deformations and positive temperature coefficients of the stress are well-known properties of cross-linked, amorphous polymer networks. The success of the rubber elasticity theory in describing the behavior of these networks is well established.[2] Elasticity exhibited by macromolecular systems is not, of course, limited to the behavior of amorphous rubbers. Consideration of the variety of "states" in which a macromolecular network may exist clearly suggests a variety of elastic behaviors and elastic mechanisms. A fully crystalline (oriented) fiber may, for instance, exhibit short-range elasticity, common among crystalline substances, or a long-range elasticity if a crystal–crystal transition takes place.[3] Intermediate to the fully crystalline and the amorphous state, there exists a variety of semicrystalline states that are common among macromolecular systems. The study of the elastic behavior of semicrystalline systems is the subject of the present paper.

(1) From a thesis submitted by D. Puett to the Graduate School of the University of North Carolina, 1964, in partial fulfillment of the requirements for the degree of Master of Science.

(2) A. Ciferri, *J. Polymer Sci.*, **54**, 149 (1961).

(3) A. Ciferri and K. J. Smith, Jr., *ibid.*, **A2**, 731 (1964).

In spite of the great technological interest associated with systems possessing elastic properties ranging between those of rubbers and those of crystalline substances, fundamental studies of the elastic behavior of semicrystalline systems (of varying degree of crystallinity) have been relatively scarce. A reason for this is probably the lack of adequate models and theories for such structurally complex systems. A model which has long been considered is the fringed micelle structure whereby submicroscopic crystallites are imbedded in an amorphous matrix. Since a given chain may traverse one crystallite, pursue an irregular pattern through an amorphous region, and then re-enter the same or a different crystallite, the chains in the amorphous regions are generally limited in length and constrained in position. For homopolymers, such as nylon under ordinary conditions, these constraints may become so important that it is no surprise that several attempts to describe the elastic properties of such systems primarily in terms of elasticity of amorphous regions (crystallites being regarded as giant cross linkages or as inert fillers having a much larger modulus than the amorphous matrix) have met with very limited success. In fact, recently, the view that another model may better describe the properties of a polymer such as nylon has gained consideration.[4] According to this model, nylon, at least, is regarded as a typical crystalline substance. Dislocations are considered to be the analog of the amorphous regions of the fringed micelle model. Experimental data appear to substantiate the view that deformations take place in the crystal through the motion of the dislocations, rather than in the amorphous regions themselves. There is, however, a class of polymeric systems where the fringed micelle model can be conceptually applied with less reservations than for nylon. This is the class of block copolymers, for instance, one where each macromolecule is constituted by regular sequences of a monomer A alternated with sequences where monomers A and B are randomly distributed. *i.e.*, . . . AAAAAAABABBABAAAAAAA . . . The A sections may crystallize while the AB sections have typical rubber behavior. Thus, the amorphous regions are not merely prevented from crystallizing by the restraints exerted by adjacent crystalline regions but are intrinsically uncrystallizable. Clearly, by increasing the amount of crystalline regions, though adequate variations of the A/B ratio, a range of polymers having elastic properties intermediate between those of a rubber and those of a crystalline substance can be obtained. This approach is followed here, using mainly ethylene–propylene block copolymers, in an attempt to explore how the salient features of the elastic behavior of rubbers are modified as the crystallinity of the system is increased.

II. Experimental

A. Materials. Two unfilled, uncross-linked ethylene–propylene block copolymer films were kindly supplied by Dr. E. G. Kontos of the Naugatuck Chemical Division of the U. S. Rubber Co. Details concerning the preparation and characterization of the polymers have been discussed in the original paper by Kontos, Easterbrook, and Gilbert.[5] Characteristics of the samples, also supplied by Dr. Kontos, are reported in Table I. The structural scheme is suggested by the polymerization procedure and by additional characterization.[5] It does not imply that minor variations are not present. Sample A, having lower modulus and lower crystallinity than sample B, is of the "crystallizable" type,[6] *i.e.*, apparently amorphous in the undeformed state (as detected by X-ray analysis) but able to crystallize when stretched to about four to five times the original length giving a polyethylene-type diffraction pattern. Sample B is of the "semicrystalline" type,[5] *i.e.*, showing a low crystallinity content in the unstretched state.

Strips $\approx$4 cm. long and $\approx 10 \times 10^{-3}$ cm.^{2} in cross-sectional area were used for the experiments. Data reported for sample A in Figures 1–4 and also for sample B were obtained with strips annealed to about 85° for 3 hr. (under vacuum) followed by slow cooling.

The stress–strain curves for nylon reported in Figure 5, kindly supplied by Dr. D. A. Zaukelies of this laboratory, were obtained with undrawn samples of nylon 66 (single filaments of cross-sectional area $\approx 8.7 \times 10^{-5}$ cm.^{2}).

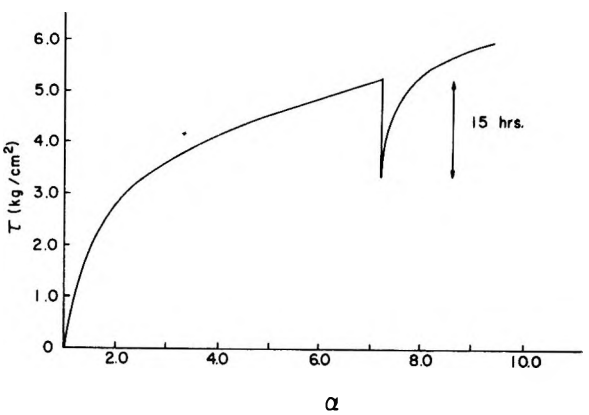

Figure 1. Master stress–strain curve for sample A at $T = 30°$ including a 15-hr. relaxation period at $\alpha = 7.0$.

(4) D. A. Zaukelies, *J. Appl. Phys.*, **33**, 2797 (1962).

(5) E. G. Kontos, E. K. Easterbrook, and R. D. Gilbert, *J. Polymer Sci.*, **61**, 69 (1962).

Table I: Physical Properties of Stereoblock α-Olefin Copolymers

	Sample A	Sample B
Class of material	Crystallizable	Semicrystalline
Structure according to polymerization procedure	$(E)_{x_1} - (EP)_y - (E)_{x_2}$	$(EP)_{x_1} - (E)_{y_1} - (EP)_{x_2} - (E)_{y_2} - (EP)_{x_3} - (E)_{y_3} - (EP)_{x_4}$
Average E/P weight ratio	52:48	73:27
Crystallinity, %, by X-ray;		
(a) unstretched	0	25
(b) stretched 500%	E crystallization	E orientation with additional crystallization
Density, g./ml., at 24°	0.856	0.905

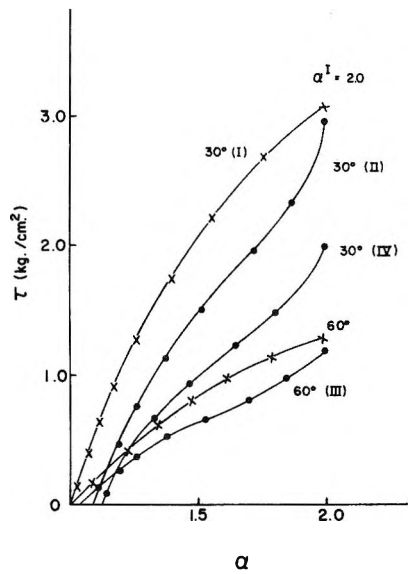

Figure 2. Two master stress–strain curves for sample A at T = 30 and 60°. Second, third, and fourth isotherms were performed in the order and at the temperature indicated using the sample for which the master curve was performed at 30°.

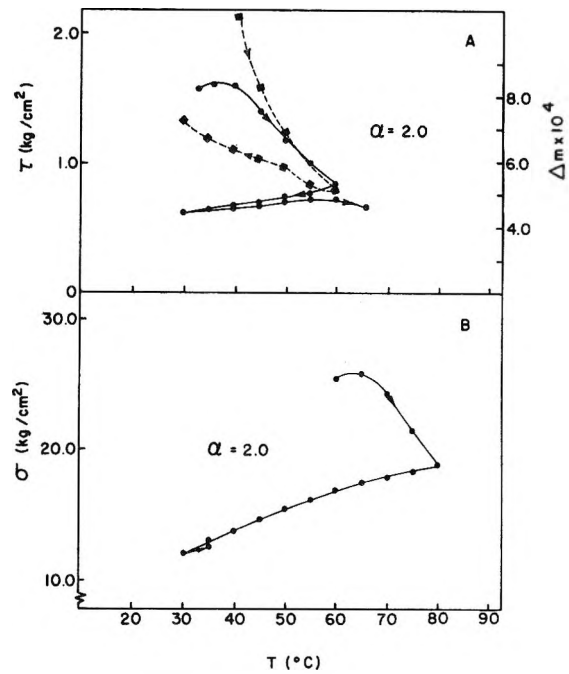

Figure 3. Stress–temperature curves for samples A and B at the indicated elongation (measured at the lowest experimental temperature). Broken lines represent the corresponding variation of birefringence with temperature. Arrows indicate the sequence of heating and cooling.

Corriedale wool fibers (unmedulled) of uniform cross-sectional area ($\approx 1.7 \times 10^{-5}$ cm.^{2} ± 5%) were kindly supplied by Dr. M. Feughelman of the Division of Textile Physics of the C.S.I.R.O., Australia.

B. Dynamometry. Most stress–strain and stress–temperature data were obtained according to techniques described elsewhere.[6] For sample A the force was recorded at 10-min. intervals during the standardized stepwise procedure for obtaining the stress–strain isotherm. For the keratin sample, which was analyzed while immersed in water, 3-min. intervals were used. Stress–strain curves for sample B and for the nylon sample were obtained at 23° and 65% relative humidity. Data in Figures 1, 2, and 5–9 include the first stress–strain isotherm performed on a sample which had no previous mechanical treatment. This isotherm, referred to as the "master isotherm," was extended to the maximum elongation for each sample and is represented throughout with crosses (×) to distinguish it clearly from the isotherms, represented with closed circles, referred to as "second isotherms" which were obtained with independent similar strips (or fibers) previously lengthened (according to the standard procedure) to elongations characterized by the value of α^I.

In all cases a cycle was performed, *i.e.*, after the elongation α^I was attained, the elongation was decreased according to the stepwise procedure outlined above (the recovery part of the cycle is not always represented in the graphs). In the case of sample A and the keratin fiber (Figures 6, 7, and 9) a period of 16

(6) K. J. Smith, Jr., A. Greene, and A. Ciferri, *Kolloid-Z.*, **194**, 49 (1964).

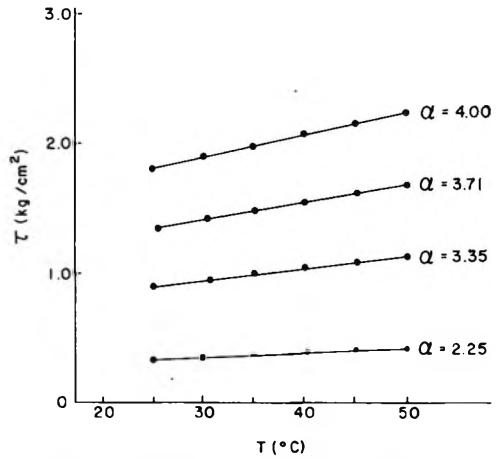

Figure 4. Stress–temperature curves for sample A at the indicated elongations.

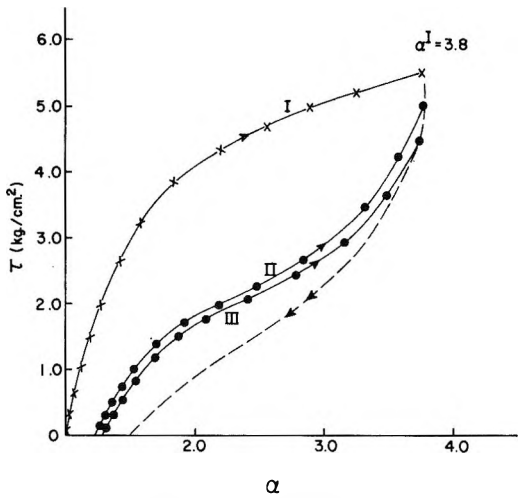

Figure 6. Master, second, and third stress–strain curves for sample A at $T = 30°$: ———, increasing elongation; – – – –, decreasing elongation.

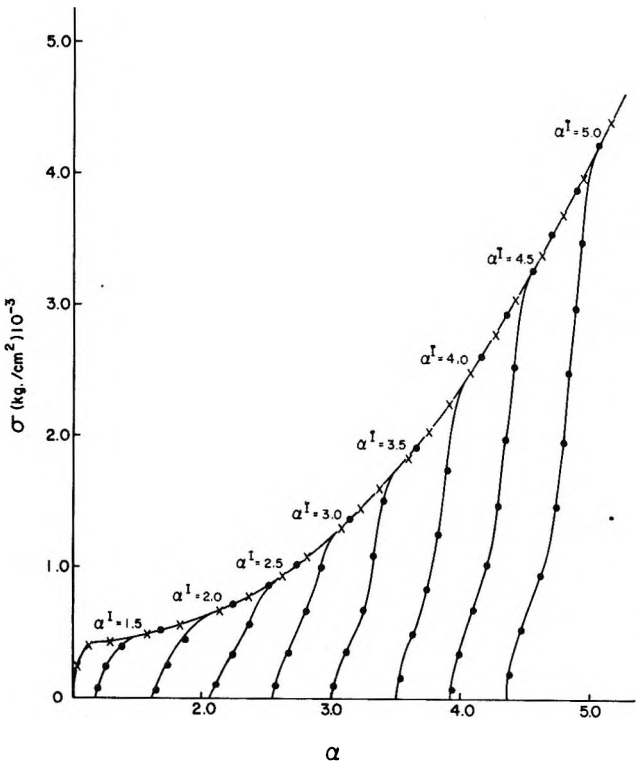

Figure 5. Master and second isotherms at $T = 23°$ for the nylon sample. The second isotherms were performed using a single fiber carried through successive α^I values.

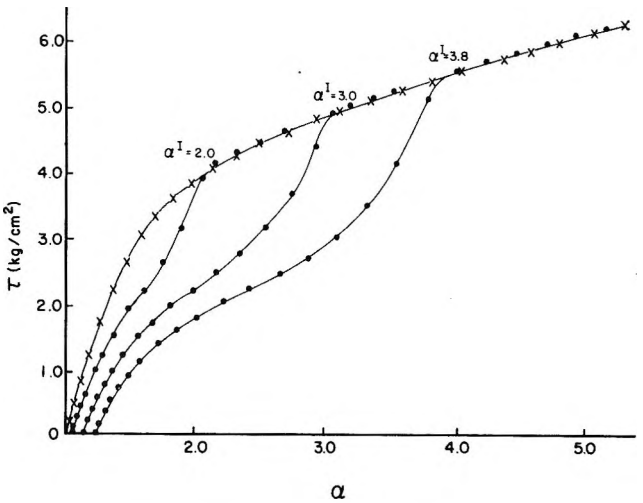

Figure 7. Master and second isotherms at $T = 30°$ for sample A performed on independent strips previously elongated to $\alpha^I = 2.0$, 3.0, and 3.8.

hr. was allowed before the performance of the next stress–strain isotherm; for sample B and for the nylon sample no time was allowed to elapse between consecutive cycles. No difference was observed using independent strips which were stretched to different α^I values or using a single strip (or fiber) which was carried through successive α^I values.

In all cases, the extension ratio (α) is referred to the original rest length of the sample before any mechanical treatment was performed. The stress (τ) is usually referred to the original cross-sectional area of the dry sample. However, in the case of sample B (Figure 8) and the nylon sample, values of the true stress (σ) are plotted, *i.e.*, the force divided by the actual cross-sectional area at the given elongation. The "Mullins effect" is evident irrespective of whether stress or true stress is plotted.

For the stress–temperature data, reported in Figures 4 and 10, long times (up to 24 hr.) of relaxation at the highest temperature were required before the force at-

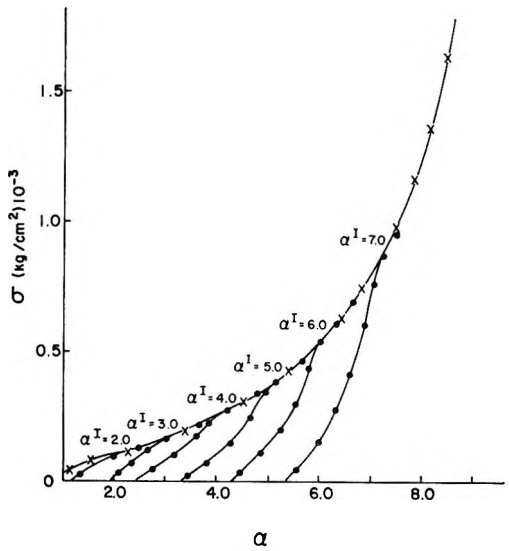

Figure 8. Master and second isotherms of $T = 23°$ for sample B. The second isotherms were performed using a single strip carried through successive α^I values.

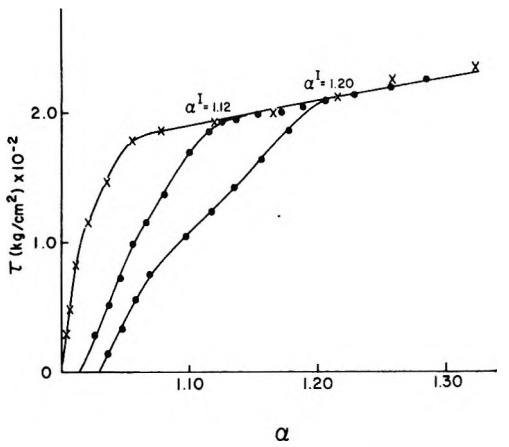

Figure 9. Master and second isotherms at $T = 83°$ in water for Corriedale wool fibers. The second isotherms were performed using a single fiber carried through successive α^I values.

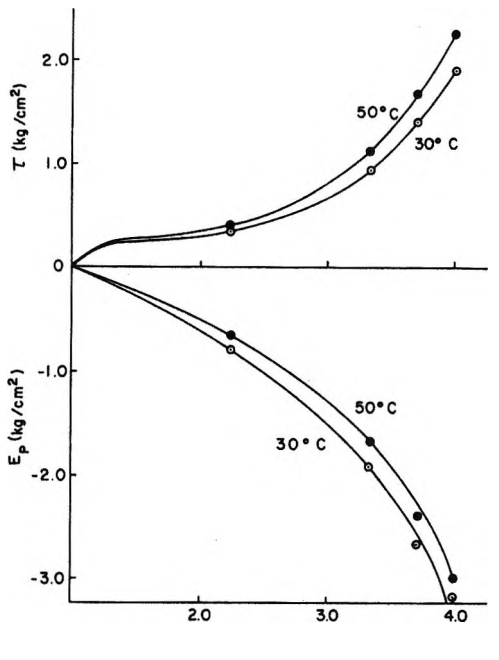

Figure 10. The energy component E_P and the isothermal stress–strain curves at $T = 30$ and 50° obtained from the data in Figure 4.

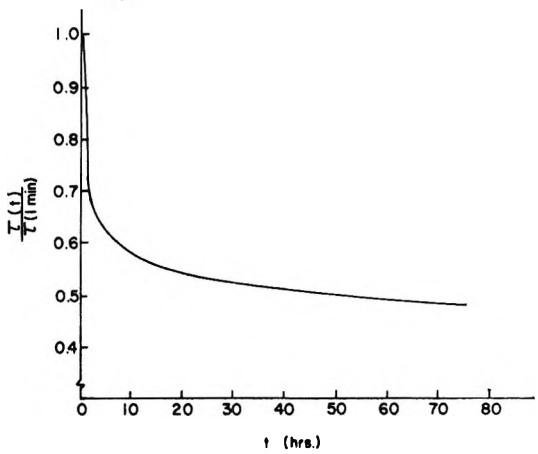

Figure 11. Stress–relaxation for sample A at $\alpha = 3.8$ and $T = 30°$.

tained sensibly constant values. Thereafter, the temperature was lowered at a rate of 5°/20 min. which appeared satisfactory for obtaining stress–temperature cycles with negligible hysteresis.[6]

The birefringence (Figure 3) was measured simultaneously with the measurement of the stress according to the technique described in detail elsewhere.[7] Other details of stress–temperature measurements are given in section IIIB.

III. Results and Discussion

A. Isothermal Behavior. Relaxation and Conditioning Attempts. Figure 11 shows the large relaxation exhibited by sample A, and Figure 6 shows the large hysteresis presented by the master stress–strain isotherm and the large difference between the master and the second isotherm. The set at the end of the first cycle is not permanent. In the case of Figure 6, it corresponds to an extension ratio of $\alpha \approx 1.4$ at the end of the cycle which was then reduced to $\alpha \approx 1.2$ after 16-hr. standing (when the second cycle was initiated). The elastic behavior exhibited by the second stress–strain isotherm more closely approaches that of a

(7) To be published.

rubber-like network. The modulus is lower, and, while some hysteresis still persists, the third and the following isotherms are very close to the second one, provided the limiting elongation α^I reached during the first cycle is not exceeded (cases where the elongation α^I is exceeded are reported in Figures 7 and 8).

Thus, in spite of the large initial time effects, the system appears to possess an "equilibrium" elastic component which, since the system is not chemically cross-linked, is probably due to pseudo-crystalline aggregates (not revealed by wide angle X-ray measurements) which resist the rearrangement of structure evident during the first stages of relaxation.

Figure 1 illustrates a master curve for sample A. At $\alpha \approx 7$ a relaxation period of 15 hr. was allowed. It is seen that on increasing the strain after the long relaxation period the stress rises abruptly, and the course of the master curve is resumed (this coincides with an independent master curve for which no long relaxation period was allowed). This fact may be interpreted as indicating that, in spite of the relaxation which occurred in the course of 15 hr. at $\alpha \approx 7.0$, there are restraints to the deformation which remain largely ineffective at $\alpha \approx 7.0$ but which become effective as soon as the elongation is increased past $\alpha \approx 7.0$. This interpretation will receive further substantiation and clarification from the data subsequently presented.

In an attempt to eliminate the difference between the master and the second isotherm several approaches were used, namely, (1) performing stress–strain isotherms at high temperature (60°), (2) annealing the sample at 85° for 3 hr. (under vacuum) and then slowly cooling it, and (3) allowing permeation of a limited amount of xylene which was subsequently pumped off. Invariably, these attempts resulted in a large decrease of the stress (up to 50%) at all elongations for both the master and the second isotherm. The difference between the two curves remained large, however, and the "Mullins effect" was never eliminated. X-Ray analysis did not reveal significant development of the crystallinity of unstretched samples after the various treatments.

A more detailed analysis of the effect of temperature on the sequence of the isotherms is presented in Figure 2. Two independent master curves, one at 30° and the other at 60°, reveal the great effect of temperature in reducing the stress. For the sample which was stretched at 30°, a series of consecutive isotherms (16-hr. intervals were allowed among the various isotherms) are represented. The second isotherm at 30° again reveals the difference exhibited also in Figure 6; the third isotherm was performed at 60°, and it is seen to fall below the independent master curve at 60° (had the second isotherm at 60° been plotted for the latter, it would have been indistinguishable from the one reported). The fourth isotherm was performed at 30°; although the master isotherm could not be regenerated, a partial reversibility is clearly indicated which could have been improved by allowing longer recovery or using somewhat different conditions. The fact that the isotherm at 30° lies above the one at 60° appears to be in contrast to the behavior of rubbers. The origin of this behavior will be discussed in connection with the stress–temperature analysis in section IIIB. In the following part, attention is devoted to the analysis of the difference, so generally exhibited, between the master and the second isotherm.

The Mullins Effect. In both Figures 2 and 6 the elongation α^I of the master isotherm is not exceeded during the subsequent isotherm. The shape of the second isotherm clearly indicates an upturn of the stress which tends to coincide, when α^I is reached, with the value of the master curve. Figures 7 and 8, for samples A and B, respectively, clearly indicate this trend and also the sudden change of course of the second isotherm, past α^I, which henceforth coincides with the master curve. The phenomenon is seen to be general for different α^I values and for the two different samples. As has been reported in a preliminary communication,[8] the phenomenon is seen to be superficially similar to that described by Holt, Mullins, and Bueche[9] for "filled" natural rubber vulcanizates (the filler being, for instance, carbon black) and has been often called the "Mullins effect." Mullins has presented a general interpretation of the phenomenon in terms of soft and hard regions connected in series, the hard regions converting to soft as a result of stretching. Bueche has presented a somewhat more elaborate model whereby the filler particles are regarded as giant (secondary) cross linkages undergoing quasi-affine deformations with the result that chains, which at a given α^I value happen to be highly strained, will pull loose from the filler particle, thus, decreasing the stress during the second stress–strain isotherm for elongations which do not exceed α^I. According to Bueche, in an unfilled network a similar softening phenomenon will be comparatively negligible since the network junctions do not undergo an affine deformation in the vicinity of a highly strained chain. As in the case of our samples (*cf.* Figure 6 and Table II), the lower modulus persists in a filled rubber even when the material is allowed to

(8) D. Puett, K. J. Smith, Jr., A. Ciferri, and E. G. Kontos, *J. Chem. Phys.*, **40**, 253 (1964).

(9) W. L. Holt, *Rubber Chem. Technol.*, **5**, 79 (1932); L. Mullins, *ibid.*, **21**, 281 (1948); F. Bueche, *J. Appl. Polymer Sci.*, **4**, 107 (1960).

Table II: The Dependence of Set and Modulus on α^I

α^I	A. *E/P* 52/48		B. *E/P* 73/27		Keratin		Nylon 66	
	α_s[a]	*Y*, kg./cm.^{2}	α_s	*Y*, kg./cm.^{2}	α_s	*Y*, kg./cm.^{2}	α_s	*Y*, kg./cm.^{2}
1.0	..	7.7	..	3.3×10^2	..	6.8×10^3	..	1.8×10^4
1.1	..	...	..	...	1.02	2.3	..	...
1.2	..	...	..	...	1.03	2.0	..	...
2.0	1.06	5.6	1.20	2.8	..	...	1.60	1.6
3.0	1.14	4.8	1.85	2.5	..	...	2.55	1.3
3.8	1.23	4.7	..	...	..	...	..	...
4.0	..	...	2.45	2.3	..	...	3.50	1.2

[a] α_s is the ratio of the rest length before the performance of the second isotherms to the initial rest length.

relax for many days at room temperature (the rubber recovers its original high modulus if it is allowed to rest at about 100° while our master isotherms could be regenerated after complete melting and reformation of the fibers according to the original procedure).

As stated in the introductory section, our samples are expected to conform ideally to the fringed micelle model; the presence of relatively large "regions" where the crystallizable $(E)_x$ portion of the macromolecules occurs in more or less perfect crystalline arrangements is expected. A superficial analogy of these "regions" to filler particles is, therefore, suggested. A main difference is, however, the fact that, while, in the case of rubber, the filler particle is of a chemical nature different from the network, in our samples, A and B, selected sections of only one macromolecular species form these regions. It is, consequently, more difficult to specify the nature of the bonds which are broken during the first stretching. A quantitative description of the original structure would be extremely difficult unless drastic simplifications are introduced. Thus, we believe that a qualitative description will have to suffice. The structure prevailing in the original unstretched samples A and B is probably very different from the ideal fringed micelle picture where all crystallites are relatively perfect and well delimited from the adjacent amorphous regions. Rather, we suspect a gigantic chaotic array where strong interactions are more evenly distributed throughout the sample than is expected for the model. The complexity of this structure could, by certain treatment, perhaps, be simplified to the state where each crystalline region is clearly delimited from the matrix (if the chemical structure has the necessary regularity). The preliminary conditioning attempts (to anneal or to allow a diluent to increase the mobility of the macromolecules), as well as the mechanical conditioning achieved by the first stretching, have probably helped the formation of a less disordered structure. The Mullins effect has not, however, disappeared as a result of these conditioning attempts, which is not surprising since it may be expected that this effect exists also in the ideal fringed micelle structure; *i.e.*, amorphous chains, which at a given α^I happen to be highly strained, could rupture if the matrix as a whole undergoes affine deformation. While for a typical rubber vulcanizate the elastic properties are determined by a given network structure which is stable at all degrees of deformation, a block copolymer, such as sample A, possesses in the original undeformed state no definite network structure. Rather, the network structure which assures elastic behavior during the second isotherm is formed in the first stretching and depends upon the particular α^I at which the sample is mechanically conditioned. This network structure is then stable for all elongations below the particular α^I, but it can be modified (in one of lower modulus, *cf.* Table II) just by exceeding this given α^I value. It is this possibility of establishing a network structure which depends upon the α^I value and upon the presence of strong intermolecular interactions, which assures this system of a high modulus and long-range extensibility which may considerably exceed those exhibited by an amorphous vulcanizate where the molecular network is structurally stable.

Inspection of Figures 7 and 8 and of the data collected in Table II indicates that the Mullins effect persists, in spite of great variations of the set and of the modulus (or the general shape) of the second isotherm (at each α^I value), which suggest that these factors are not essential to the occurrence of the effect (negligible set was observed for filled rubber vulcanizates[9]). The generality of these conclusions is illustrated by the data in Figures 5 and 9, which show the occurrence of the Mullins effect in the case of an undrawn nylon sample and in the case of a wool fiber. In the case of nylon, the stretching is equivalent to a cold drawing (performed under conditions under which no necking was likely to occur). The structure which is formed by stretching at

a given α^I is that of the partially oriented fiber, as is evident from the change in the X-ray diffraction pattern.[10] This oriented structure does not spontaneously revert to the original unoriented state. The set is particularly large, as is the modulus of the set sample. This modulus does not increase with increasing set (*cf.* Table II) because of the high rate of stretching which was used; under conditions where longer intervals between consecutive stretchings is allowed, the modulus, as is well known, increases with set. In fact, although the set and the shape of the second isotherm are not essential for the Mullins effect, there are evident connections between them. The transition from a rubber to a crystalline substance on increasing the degree of crystallinity is quite evident from the set and the elastic properties of the second isotherm when data in Table II for a given α^I value for different samples are considered. A smaller set, necessarily associated with a longer range of elastic behavior up to the given α^I, corresponds to a lower Young's modulus. For sample A the modulus appears, in fact, to decrease with α^I when also the set/α^I ratio decreases. The fact that, on increasing α^I, a sample with low crystallinity is progressively softened (while a sample with a high degree of crystallinity is progressively hardened) is not unexpected since, for the former sample, the part played by the amorphous network is preponderant, and this, according to Bueche's description, will contain a smaller number of constrained chains the higher α^I is (to what extent the elastic behavior of the resulting network is rubber-like will be discussed in section IIIB).

In the case of the keratin fiber immersed in water, it is well known that a certain value of the stress is required in order to initiate the $\alpha \rightleftarrows \beta$ transformation.[11] This stress value is usually attained when an elongation of about 5% is reached. However, at ordinary temperatures the transformation is quickly reversible and no Mullins effect was observed in these conditions. It is, however, well known that, at higher temperatures where the transformation is no longer reversible, the fiber can be permanently set in the β-form, probably because of chemical changes (elimination or displacement of some chemical cross linkages[10]). Accordingly, stress–strain curves performed at 83° reveal the Mullins effect. The large set is attributed to the permanence of the β-structure at zero force; the set increases with α^I since the amount of α transformed into β depends upon α^I (*cf.* ref. 11). The lower modulus of the second isotherm (with respect to the one exhibited by the master curve, *cf.* Table II) does not necessarily reflect a difference in the modulus of the α- and β-form but, very likely, a general breaking down due to prolonged exposure at high temperature.

For other materials the occurrence of a Mullins effect has been reported. Effects similar to those described in Figure 1 have been observed by Hermans[12] using cellulose filaments, and the occurrence of stress–strain curves similar to those reported in Figure 7 was reported by Trick[13] using polyurethane elastomers. The occurrence of the Mullins effect is not limited to polymeric materials. Stress–strain curves for metals such as aluminum, copper, etc., also reveal a Mullins effect associated with the occurrence of orientation and large plastic flow.[14] When the variety of conditions under which the Mullins effect is observed is considered, some generalizations can be made. Two requirements appear necessary for its occurrence. One requirement is that whatever structure results from strain at a given α^I (a network with fewer constrained chains or the β-form for a polypeptide chain or a crystalline orientation accompanied by plastic flow) is permanent or, at least, very slowly reverts to the original form. The second requirement is that the constraints which hinder deformation above α^I should not be relieved by the previous mechanical history and relaxation of the sample at elongations less than α^I. The preceding examples give a clear illustration of this latter requirement. In the case of sample A, the constraints which limit elongation above α^I can be conveniently regarded, extending Bueche's model for filled rubber, as chains which are near full extension. Thus, a relaxation at α^I (*cf.* Figure 1) cannot contribute appreciably to the relief of these constrained chains; the largest part of the time effects should be ascribed to other viscoelastic processes. In the case of the keratin fiber, if the solid–solid transition theory[11] is accepted and the strain in the yield region (*cf.* Figure 9) reflects the $\alpha \rightleftarrows \beta$ transformation, then it is clear that a critical value of the stress has to be reached in order for additional $\alpha \rightleftarrows \beta$ transformation to occur. This critical stress value is strictly related to the thermodynamic heat of transformation of the α- into the β-form. In the case of metals, the constraints which hinder deformation above α^I are essentially related to the interaction of the dislocations with lattice vacancies and other dislocations.

While from a phenomenological point of view the Mullins effect has been shown to be a quite common phenomenon among semicrystalline and crystalline

(10) R. Meredith, "The Mechanical Properties of Textile Fibres," North-Holland Publishing Co., Amsterdam, 1956.

(11) A. Ciferri, *Trans. Faraday Soc.*, **59**, 562 (1963).

(12) J. J. Hermans, *Rec. trav. chim.*, **65**, 624 (1946).

(13) G. S. Trick, *J. Appl. Polymer Sci.*, **3**, 252 (1960).

(14) H. G. Van Bueren, "Imperfections in Crystals," North-Holland Publishing Co., Amsterdam, 1961.

substances, we have found it expedient to interpret its occurrence and the consequent softening effect for samples having a low degree of crystallinity in terms of restrained chains pulling out from more ordered pseudo-crystalline regions. As the degree of crystallinity is increased, deformations within the crystallites become predominant so that ultimately an interpretation in terms of dislocation motions must be offered. The transition from a rubber to a crystalline substance will involve a transition from a case where the former effect prevails to a case where the latter effect is predominant. It should be emphasized that this interpretation represents a preliminary descriptive attempt—more refined descriptions can be expected.

B. Stress–Temperature Behavior. Figure 3 illustrates stress–temperature data for samples A and B held at constant length. Sample A was first stretched at 30°, and at the end of a 24-hr. relaxation, when the stress attained a sensibly constant value (*cf.* Figure 11), the temperature was raised at a rate of 5°/20 min. According to this schedule the temperature was raised to 60°, lowered, and then raised again. The birefringence was measured following a similar schedule. For sample B a similar approach and a somewhat different temperature range were used. It is seen that the initial decrease of the stress between 30 and 60° is not reversible; when the elongated sample is cooled, a positive stress–temperature coefficient is exhibited. As for rubbers, a cycle of cooling and heating can be performed showing negligible hysteresis.

This surprising behavior can be explained on a basis which also accounts for the relative position of the isotherms at 30 and 60° illustrated in Figure 2. In fact, though wide angle X-ray analysis gave no evidence of crystallinity for the unstretched sample A, the analysis of the preceding section (*cf.* the similarity of behavior with sample B which is crystalline in the rest state) indicates the occurrence of pseudo-crystalline aggregates. Viewed under a polarizing microscope, sample A (unstretched) reveals considerable depolarization which is indicative of crystallization. On increasing the temperature up to 60° this depolarization was almost eliminated while it reappeared when the sample was cooled again. Thus, in the case of Figure 2 the modulus at 60° is lower than the modulus at 30° essentially because at the higher temperature less "crystallinity" is present. This reduction of crystallinity overshadows the rubber-like behavior according to which the curve at 60° should exhibit a larger modulus. Further, when a sample examined at 60° is relaxed and subsequently examined at 30°, the re-increase of modulus testifies to the reversibility of melting. The redevelopment of crystallinity in the relaxed state is, however, to be clearly distinguished from the redevelopment of crystallinity on cooling a sample held stretched at constant length. In fact, in the latter instance a preferential orientation in the direction of stretch will be assumed by the growing crystallites, and this, as is well known, will generally decrease the stress.[6] Thus, the initial decrease of stress on heating a stretched sample (Figure 3) is due to the melting of crystallites which were not formed in an oriented state while a subsequent recrystallization in the oriented state will not overshadow, but rather emphasize, the positive stress–temperature coefficient due to the network. Redevelopment of crystallinity on cooling the elongated sample is unmistakably proved by the concomitant increase of birefringence (*cf.* Figure 3). Thus, in spite of the mechanical conditioning at a given temperature, the crystallites have not attained the degree of orientation that can be achieved by cooling an oriented specimen. For a typical rubber vulcanizate the decrease of stress with temperature illustrated in Figures 2 and 3 is not observed only because no crystallinity is present (under ordinary conditions) in the unstretched state.

In the preceding section it has been emphasized that the network structure which assures elastic behavior during the second isotherm is formed and depends upon the particular α^I value at which the sample is mechanically conditioned. The results illustrated in this section add a further restriction to the stability of this network structure: the structure stabilized during the mechanical treatment at α^I will be essentially stable only at a given temperature. In Figure 4 several stress–temperature data at constant length are reported. In obtaining these curves, in accordance with the above observation, the sample was conditioned with respect to α^I and temperature, *i.e.*, the sample was mechanically conditioned at $\alpha^I = 4$ and allowed to relax at the highest experimental temperature. At the end of a stress–temperature cycle the elongation was decreased so that the original α^I value was in no case exceeded. Under these conditions the elastic contribution of the network should be best observed. The curves in Figure 7 are practically linear, and good reversibility is exhibited (*cf.* also Figure 3). The value of the stress at 50 and 30° and the corresponding energy component E_p (derived from the relation[6] $\tau = E_p + T(\partial\tau/\partial T)_L$) obtained from the data in Figure 4 are reported in Figure 10. The large decrease of E_p with α can be associated with crystallization as evidenced by the increase of birefringence (*cf.* Figure 3). It is remarkable, though not unjustified,[15] that the stress–

(15) A. J. Wildschut, *J. Appl. Phys.*, **17**, 51 (1946).

temperature curves (Figures 3 and 4) are essentially linear and hysteresis-free, even under these conditions.[6] In contrast to the data in Figure 2, the curve at 50° lies above the curve at 30° in Figure 10 which is coherent with the fact that, once the main variation of crystallinity with temperature takes place in the oriented state, the rubber-like network contribution can be observed. The shape of the isotherms is similar to the shape expected for a nongaussian network. However, we believe that the present results do not offer compelling evidence for concluding that the shape of these curves is exclusively due to nongaussian behavior. The problem of analyzing the shape of stress–strain isotherms in terms of nongaussian behavior and stress-induced crystallization has been dealt with, in much detail, elsewhere.[6] The upturn exhibited by the isotherms obtained from stress–temperature data can be safely attributed to nongaussian behavior, only if it is possible to stretch a network at temperatures where crystallization and large, negative energy components are absent. These conditions are clearly not fulfilled by the present system.

In spite of the large difference for the degree of crystallinity of samples A and B, the stress–temperature analysis reported above is characteristic of samples having a melting distribution within the temperature range where the experiments were performed. From the point of view of discussing the behavior of semicrystalline polymers in general, it would be desirable to study cases where the melting range is above the temperature range investigated, this for polymers having different degrees of crystallinity. On the basis of the present results, some predictions about the stress–temperature behavior of these substances can be made. If the degree of crystallinity is low, small energy components and positive stress–temperature coefficients should be observed. If viscoelastic effects are not too severe, the conventional stress–strain isotherms should exhibit increased modulus at higher temperatures. On increasing the degree of crystallinity, the elongation at which positive stress–temperature coefficients are observed should increase because of the opposite effect associated with the crystalline component. This has been, in fact, observed in the stress–temperature analysis of nylon samples.[16,17]

Acknowledgment. Pleasure is taken in acknowledging the kindness of Dr. E. G. Kontos for supplying the copolymer samples, for their characterization, and for his interest in this work. Acknowledgment is also due to Dr. D. A. Zaukelies, who kindly supplied the data on the nylon sample and contributed interesting and clarifying discussions, and to Dr. M. Feughelman for kindly supplying the wool fibers. The authors are particularly indebted to Professor J. J. Hermans for his great interest and guidance throughout the course of this work.

(16) M. L. Williams, *Trans. Soc. Rheol.*, **4**, 297 (1960).

(17) NOTE ADDED IN PROOF. After the manuscript was completed, we found that R. S. Stein and A. V. Tobolsky (*Textile Res. J.*, **18**, 201 (1948)) found similar force–temperature behavior for elastic polyamides.

Heats of Immersion in the Thorium Oxide–Water System[1,2]

by H. F. Holmes and C. H. Secoy

Reactor Chemistry Division, Oak Ridge National Laboratory, Oak Ridge, Tennessee *(Received July 2, 1964)*

Heats of immersion in water at 25.0° have been measured for four samples of thorium oxide whose specific surface areas ranged from 2.2 to 14.7 m.²/g. Pretreatment consisted of vacuum outgassing for 24 hr. at temperatures ranging from 100 to 500°. Results were reproducibly dependent on the sample and outgassing temperature involved with the measured heat of immersion varying from 430 to 1120 ergs/cm.². Large heats of immersion and their dependence on outgassing temperature are attributed to chemisorption of water on the thorium oxide surface with net heats of adsorption as large as 22 kcal./mole. Three of the samples exhibited a slow heat of immersion with the rate-determining step ascribed to diffusion of water into the porous structure of the particles.

Introduction

Although thorium oxide has long been of interest as a catalyst and, in recent years, because of the nuclear properties of thorium, no exhaustive study of the thorium oxide–water interface has been made. Winfield[3] has made some water adsorption studies on one sample of thorium oxide over the temperature range from 50 to 200°. Draper and Milligan[4] have also studied the adsorption of water on thorium oxide. Water adsorption on the surface of thorium oxide at high temperatures (500 to 700°) has been measured by Oblad, Weller, and Mills.[5] Wadsworth, *et al.*,[6] have made an infrared study of the surface hydroxyl content of thorium oxide over the temperature range of 150 to 1050°.

The utility of and the thermodynamics involved in heats of immersion have been treated in detail[7] and need not be reviewed here. More recently, a useful criticism[8] of current experimental techniques and data interpretations involved in heats of immersion has appeared. However, the usefulness of the information available from and the fundamental relationships involved in heats of immersion are so well founded as to warrant inclusion of this technique in any fundamental study of a solid–liquid interface.

Experimental

Calorimeter. Figure 1 is a section view of the calorimeter used in this study. With the exception of the stirrer and sample holder, which are brass, the entire calorimeter was constructed of copper. In order to protect against corrosion and to reduce radiant heat transfer, the interior and exterior surfaces of the calorimeter were gold plated. Nylon sections in the stirrer and sample holder shafts served to further reduce heat transfer between the calorimeter and its surroundings. Inlet and exit connections to the cooling coil were made with thin-walled rubber tubing. The "O" rings shown in Figure 1 provided effective airtight seals as evidenced by no difficulty with evaporation or condensation. The calorimeter stirrer was driven directly by a 300-r.p.m. synchronous motor. All interior parts of the calorimeter were attached to the lid of the calorimeter which, in turn, was attached to the lid of the submarine jacket. This arrangement facilitated cleaning and assembly of the calorimeter. Total internal volume of the calorimeter (including metal parts) was 297 cm.³. For immersion experiments, the calorimeter was loaded

(1) Research sponsored by the U. S. Atomic Energy Commission under contract with the Union Carbide Corp.

(2) Presented in part at the 14th Annual Southeastern Regional Meeting of the American Chemical Society, Gatlinburg, Tenn., Nov. 1962.

(3) M. E. Winfield, *Australian J. Sci. Res.*, **3A**, 290 (1950).

(4) A. L. Draper and W. O. Milligan, "Structure and Surface Chemistry of Thorium Oxide." The Rice Institute, Houston, Texas, 1959.

(5) A. G. Oblad, S. W. Weller, and G. A. Mills, "Proceedings of the Second World Congress on Surface Activity," Vol. II, Academic Press, New York, N. Y., 1957, p. 309.

(6) M. E. Wadsworth, *et al.*, "The Surface Chemistry of Thoria," Progress Report, University of Utah, Salt Lake City, Utah, Jan. 31, 1959.

(7) J. J. Chessick and A. C. Zettlemoyer, *Advan. Catalysis*, **11**, 263 (1959).

(8) J. J. Chessick, *J. Phys. Chem.*, **66**, 762 (1962).

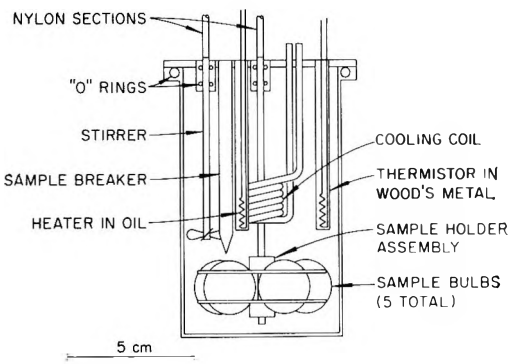

Figure 1. Calorimeter for heat-of-immersion studies.

with 230 cm.^{3} of water which brought the water level to within about 1.5 cm. of the lid. An immersion experiment was initiated by manually lifting the sample holder assembly, which broke a sample bulb against the sample breaker. Any one of the five samples could be selected by reference to a scale and pointer assembly mounted on one of the exit tubes of the submarine jacket. Vertical motion of the sample holder assembly was limited to about 8 mm. by a mechanical stop on the nylon section. This arrangement was necessary to prevent breaking more than one sample bulb per experiment.

The calorimeter was suspended by four nylon rods inside a brass submarine jacket whose inside surface was gold plated. The calorimeter was separated from the submarine jacket by a 4-cm. dead-air gap. The lid of the submarine jacket was fitted with appropriate exit tubes for electrical and mechanical connection to the calorimeter. These tubes were 7 cm. long and extended 1 cm. above the level of the constant temperature water bath. The entire assembly was suspended from an aluminum plate mounted on top of the constant temperature bath. The aluminum plate also served as a mount for the stirring motor.

The constant temperature bath consisted of a well-stirred, insulated, 30-l. water bath operated at 25.0°. Control was accomplished by a nickel resistance thermometer used with a proportional controller having reset action (Hallikainen Instruments Thermotrol, Model 1053 A). This combination gave short-term control to better than ±0.001° with long-term drift less than 0.001°/24 hr. Some of the experiments were done with the bath controlled by a mercury thermoregulator and an electronic relay. Bath control to ±0.003° was obtained with no apparent loss in accuracy or precision of the calorimetric measurements.

Electrical Circuits. The electrical circuits consist essentially of two separate circuits, the temperature-measuring and the electrical calibration circuits. The temperature-sensing element was a nominal 100-ohm bead-type thermistor enclosed in a glass probe (Victory Engineering Corp., thermistor No. 21A4). The thermistor was aged in a 150° oven for 400 hr. Following this, a current of 7.5 ma. (five times the measuring current) was passed through the thermistor for 70 hr. Stability of the thermistor after this treatment has been demonstrated by a constant calibration factor with no detectable long-term drift. Thermal contact with the calorimeter was made by imbedding the thermistor in Wood's metal inside the thermistor well of the calorimeter. Copper thermocouple wire was used to connect the thermistor to the resistance bridge as a three-lead thermometer.

A Leeds and Northrup Model G-2 Mueller bridge served as the primary resistance-measuring instrument. Two volts from a 6-v. lead storage battery served to supply the bridge current. The unbalance potential of the bridge was amplified by a Beckman Model 14 breaker–amplifier. The output of the amplifier was used to derive a zero-center Brown recorder having a full scale range of 100 mv. and operating at a chart speed of 30 in./hr. In normal use the gain of the amplifier was adjusted so that full scale on the recorder was 5×10^{-3} ohm (approximately 1.6×10^{-3}°).

The electrical calibration heater was 10 ohms of enameled 36-gauge Manganin wire wound noninductively on a 2-cm. length of 4-mm. Pyrex tubing. Thermal contact with the calorimeter was made by placing a small amount (to cover the heater) of light mineral oil in the heater well. Potential leads were connected halfway between the calorimeter and the submarine jacket. An identical heater placed in the constant temperature bath served as the dummy heater. The heating circuit, which consisted of a variable resistor, a 10-ohm standard, and the calibration heater, was powered by four 6-v. lead storage batteries connected in parallel. The batteries were always discharged through the dummy heater for at least 1 hr. prior to a calibration experiment. Potential drops across the heater and the standard resistor were measured with a Leeds and Northrup K-3 potentiometer using a Leeds and Northrup electronic null detector.

Duration of the heating period was measured with an electronic frequency counter (Northeastern Engineering, Model 13–20). The triggering circuit of the counter was connected directly across the batteries and the calibration heater so that it was energized with the same switch contact as the calibration heater. Periodic checks of the accuracy of the internal oscillator were made by comparing it with the standard frequency broadcast by station WWV. In normal calorimetric

usage the counter was used to measure heating periods up to 1000 sec. in duration with an accuracy of 0.001 sec.

Operation. Prior to an experiment, the temperature of the calorimeter was adjusted, if necessary, with the heater or cooling coil to give the desired drift rate depending on the estimated temperature rise for that experiment. Drift rates never exceeded 1.5×10^{-4} deg./min. and were usually much less as the calorimeter was never operated more than 0.05° from bath temperature. Cooling of the calorimeter was accomplished by blowing dry air through a coil immersed in liquid nitrogen and then through the calorimeter-cooling coil.

The temperature rise for an experiment was evaluated by a simple extrapolation of the fore and after drift rates. Electrical noise of the recorder trace was about 1.8×10^{-5}° peak-to-peak and did not contribute any uncertainty to the measurements. Total heat evolution for an immersion experiment varied from about 3 to 50 joules, depending on the sample and the outgassing temperature. Three corrections were applied to the observed heat from an immersion experiment. These were the heat of bulb-breaking (see below), the heat produced by the mechanical motion of the sampler holder (~0.05 joule), and the correction for the vaporization of water into the previously evacuated void space in the sample bulb (~0.2 joule). The heat of vaporization correction was calculated from the properties of water and the measured void volume in the sample bulb. The other two corrections were determined experimentally.

Some characteristics of the loaded calorimeter and its associated instrumentation are a thermal leakage constant of approximately 2.5×10^{-3} min.$^{-1}$, attainment of an isothermal condition internally 2 min. after cessation of heating within 1 part in 10^4, and a short-term sensitivity of approximately 0.008 joule ($\sim 8 \times 10^{-6}$°). For a reaction period of 1 hr., maximum uncertainty in the calorimetric results was no more than 0.2 joule.

Six to eight electrical calibrations and five heat-of-immersion experiments were made for each loading of the calorimeter. In general, the electrical calibrations always agreed to better than 0.1% and were independent of the rate of heating, the total heat input, and the duration of the heating period. Reproducibility of the heat-of-immersion results for a given sample was generally about 2%. Accuracy of the heat measurements was about 1% for all of the samples being limited by the small temperature rise in the case of samples with small specific surface areas, and by the extended reaction period in other cases.

Materials. The thorium oxide samples were prepared[9] by the thermal decomposition of thorium oxalate obtained by precipitation from a nitrate solution with oxalic acid. Four samples were prepared from the same lot of thorium oxalate. The entire lot was first calcined at 650° for 4 hr. Portions of this were then calcined at 800, 1000, and 1200° for an additional 4 hr.

Physical properties and impurities are given in Table I.[10] Particle sizes given in Table I were determined by sedimentation rates and represent the equivalent Stokes diameter for a sphere. It is apparent from the geometric standard deviation that each of the samples has a wide distribution of particle sizes. Specific surface areas of the samples, as determined by nitrogen adsorption at 77°K., are much too large to be related to the size of the particles. This has been attributed to the oxide particles retaining the relic structure of the oxalate crystal with the oxide particles consisting of much smaller crystallites of thorium oxide.[11] This is in agreement with the crystallite sizes quoted in Table I. General characteristics of this type of thorium oxide preparation have been discussed.[12]

Table I: Properties of ThO_2 Samples[a]

	Sample			
	A	B	C	D
Calcining temp., °C.	650	800	1000	1200
Calcining time, hr.	4	4	4	4
Nitrogen surface area, $m.^2/g.$	14.7	11.5	5.64	2.20
Geometric mean particle diameter, μ[b]	2.63	2.67	2.72	2.97
Geometric std. dev.	1.37	1.37	1.38	1.39
Crystallite size, Å.[c]	194	220	682	1700

[a] Impurities (in p.p.m.): F, <10; NO_3, <10; SO_4, 140; PO_4, 15; Si, <10; Cl, <10; Fe, <10; Ni, <10; Cr, <10; Pb, <10; Na, 20; K, <10; Li, <10; Ca, 51; Ba, 0; Al, 2. [b] See ref. 12 for method. [c] Crystallite sizes were determined from X-ray line broadening. Uncertainty is about 5% below 500 Å. and 10% above 500 Å.

Water for the immersion experiments was prepared by passing distilled water through a mixed bed, ion-exchange column. This water had a pH of approxi-

(9) ORNL Lot No. DT-37-100 prepared by the Chemical Technology Division of Oak Ridge National Laboratory.

(10) The data in Table I were obtained by the Analytical Chemistry Division of Oak Ridge National Laboratory.

(11) R. Beckett and M. E. Winfield, *Australian J. Sci. Res.*, **4A**, 644 (1951).

(12) V. D. Allred, S. R Buxton, and J. P. McBride, *J. Phys. Chem.*, 61, 117 (1957).

mately 6.9 and a specific electrical conductivity of $<4.5 \times 10^{-7}$ ohm^{-1} cm.$^{-1}$. Several duplicate experiments were made with distilled water (specific electrical conductivity $\sim 1 \times 10^{-6}$ ohm.$^{-1}$ cm.$^{-1}$) with no detectable difference in the results obtained.

Sample Bulbs. The sample bulbs were blown from 4-mm. Pyrex tubing and had a diameter of 2 cm. Size of the bulbs was controlled by shaping them in a hemispherical graphite mold during the blowing operation. In this manner the wall thickness of the bulbs was controlled between the limits of 0.0076 to 0.015 cm. The bulbs had an internal volume of approximately 3.2 cm.^{3}, were able to withstand vacuum outgassing to 500°, and were easily broken in the calorimeter.

The heat released on breaking an evacuated glass sample bulb has been a source of difficulty in precise measurements of small quantities of heat.[13] To determine the magnitude and reproducibility of the correction for the heat of bulb-breaking, a series of five evacuated sample bulbs were broken in the calorimeter. The average value, after correcting for the heat of vaporization of water and mechanical motion of the sample holder assembly, was 0.513 ± 0.016 joule. The significance of this correction varied inversely with the specific surface area of the sample, amounting to about 15% for sample D. However, the uncertainty in the correction was only twice as large as the ultimate calorimetric sensitivity.

Sample Pretreatment. Prior to loading with the sample, the sample bulbs were sealed to glass "O" ring seals to facilitate connection to the vacuum system consisting primarily of an oil diffusion pump and a liquid nitrogen trap. Samples were outgassed for 24 hr. at temperatures ranging from 100 to 500° to a pressure of approximately 1×10^{-5} mm. Ultimate pressure was attained within 1 to 2 hr. after the sample reached outgassing temperature. Outgassing temperatures were controlled to ±3° and the samples were sealed off under vacuum at the end of the outgassing period. Weighing of the component parts of the sample bulb-joint assembly, coupled with the initial weights, gave the evacuated sample weight and the weight loss on outgassing. Void volumes in the sample bulbs (necessary for the heat of vaporization correction) were determined by weighing in air and in water.

A gray coloration was observed on the top portion of some of the samples after outgassing. The coloration was more noticeable with the low specific surface area samples outgassed at the higher temperatures. The presence of coloration was not reproducible under apparently identical outgassing conditions. No detectable difference was ever observed between the heats of immersion of samples showing the coloration and those in which it was absent. A gray coloration in thorium oxide has been attributed to a defect structure.[6]

Chessick[8] has criticized the use of high-temperature activated solids in heat of immersion studies. This criticism was based primarily on Hollabaugh and Chessick's experience with the surface of rutile.[14] Their study indicated reduction of the solid surface by organic contaminants present in the vacuum system and/or on the solid surface. In view of this possibility a series of thorium oxide samples were given the usual outgassing treatment at 500°. Following this, they were treated with oxygen at 500° according to the procedure of Hollabaugh and Chessick.[14] Although the presence of sample coloration was questionable before the oxygen treatment, there was definitely no coloration present after the oxygen treatment. Subsequent measurement of the heat of immersion of these samples gave the same values as obtained for the untreated samples. Any chemical reduction of the oxide which may have occurred during normal outgassing does not have a measurable effect on the heat of immersion. The possibility that the gray coloration is due to carbon has not been eliminated. Carbon has been observed on the surface of thorium oxide used as a catalyst in dehydration reactions.[3] Small quantities of carbon would not be detected in the immersion experiments because of the hydrophobic nature of the carbon surface.

Results and Discussion

The heats of immersion of these samples of thorium oxide are shown in Figure 2 as a function of the outgassing temperature. The experimental heat data were reduced to a unit area basis by means of the measured nitrogen surface areas. Two important points are obvious from Figure 2. The first of these is the general increase of the heat of immersion with increasing outgassing temperature. The second obvious point is the fact that the four samples have remarkably different energetics with respect to the solid–water interface. This is especially true with respect to sample D, whose heat of immersion is lower and much less dependent on outgassing temperature than that of the remaining three samples.

If the only function of the outgassing procedure was to remove physically adsorbed water, then the heats

(13) (a) W. H. Wade, R. L. Every, and N. Hackerman, *J. Phys. Chem.*, **64**, 355 (1960); (b) C. A. Guderjahn, D. A. Paynter, P. E. Berghausen, and R. J. Good, *J. Chem. Phys.*, **28**, 520 (1958).

(14) C. M. Hollabaugh and J. J. Chessick, *J. Phys. Chem.*, **65**, 109 (1961).

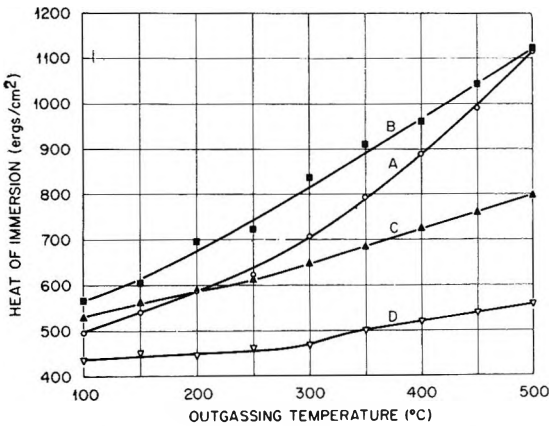

Figure 2. Heat of immersion of ThO_2 in water at 25.0°.

of immersion should be practically independent of the outgassing temperature over this entire range, for there should be no physically adsorbed water remaining under these outgassing conditions. To check on the possibility of a variable surface area, the nitrogen surface area of sample A was measured after outgassing under the conditions used in the preparation of calorimetric samples. Within experimental error the surface area was independent of the outgassing conditions. A much more plausible explanation is that we are progressively removing more strongly bound chemisorbed water as we increase the outgassing temperature. On subsequent exposure to liquid water during the immersion process this chemisorbed water is replaced with a large net heat of adsorption. Indeed, heats of adsorption as large as 45 kcal./mole have been observed[5] for water on thorium oxide which was dehydrated at 593°. These high heats of adsorption are in line with the generally held belief that the surface of polar oxides is populated with surface hydroxyl groups. In this respect Wadsworth, *et al.*,[6] have shown that temperatures as high as 1300°, under atmospheric conditions, are required to reduce the surface hydroxyl content of thorium oxide to the point where it is no longer detectable by infrared spectroscopy. This mechanism, involving surface hydroxyl groups, may not be as operative in the case of sample D because of the fact that the heat of immersion of this sample is relatively independent of outgassing temperature.

By making a number of assumptions[8] one can estimate the net integral heat of adsorption for a monolayer of water on the surface of thorium oxide from the observed heat of immersion data. Perhaps the most risky assumption in the present case involves the estimation of the water monolayer capacity from the measured nitrogen surface areas. Water surface areas of thorium oxide have been measured[3] which were approximately twice as large as those obtained with nitrogen as the adsorbate. Recognizing the assumptions involved, the net integral heat of adsorption of water on thorium oxide, estimated from the present heat of immersion data, varies from about 7 to 22 kcal./mole, depending on the sample and outgassing temperature. This is a qualitative estimate and is significant only in that it substantiates the postulated chemisorption mechanism and is in general agreement with net heats of adsorption calculated from rather limited adsorption data.[3–5]

There is no obvious correlation of the observed heats of immersion with the physical properties listed in Table I. At outgassing temperatures greater than about 250° there is, with the exception of sample B, a decrease in the heat of immersion with increasing crystallite size or decreasing surface area. Experimentally there is not enough difference in the particle sizes to draw any correlations. Neither could impurities account for the observed differences in the heats of immersion since all of the samples were prepared from the same lot of material. One can calculate an expected surface area from the crystallite sizes in Table I by assuming spheres or cubes. In all cases the calculated surface areas are too large, but the ratio of the calculated to the measured surface area is largest for sample B. From the data in Table I, one can infer that significant crystallite growth is just beginning to occur at 800°. A simple model would be that crystallite growth is occurring by fusion of smaller crystallites. This would lead, in the case of sample B, to a larger percentage of the surface being in the form of edges, corners, and boundaries between adjacent crystallites. These more energetic sites could then account for the anomalous behavior of sample B.

The behavior of the present system can be contrasted with reported heat-of-immersion measurements for SiO_2,[13a,15,16] TiO_2,[17] and Al_2O_3[18] in water. For all of these cases a general decrease in the heat of immersion with increasing specific surface area was observed. This is exactly the opposite of the behavior of the present system. In the case of SiO_2, the decrease in the heat of immersion with increasing specific surface area was explained by the hypothesis that the mechani-

(15) A. C. Makrides and N. Hackerman, *J. Phys. Chem.*, **63**, 594 (1959).

(16) J. W. Whalen, Advances in Chemistry Series, No. 33, American Chemical Society, Washington, D. C., 1961, p. 281.

(17) W. H. Wade and N. Hackerman, *J. Phys. Chem.*, **65**, 1681 (1961).

(18) W. H. Wade and N. Hackerman, *ibid.*, **64**, 1196 (1960).

cal grinding used in preparing the samples imparted an amorphous character of the surface. This argument could not be extended to the TiO_2 and Al_2O_3 systems. Samples used in the present study have not been subjected to any mechanical treatment; rather, the gross particles are agglomerates of smaller crystallites formed during the calcination process. It is quite probable that in the present thorium oxide–water system the relative heats of immersion are dictated by the relative proportions of the more energetic crystalline edges, corners, and boundaries included in the available surface.

In one respect this system behaves more like the Al_2O_3 system and less like the SiO_2 and TiO_2 systems. Heats of immersion in the TiO_2[17] and SiO_2[15] systems were observed to initially increase with increasing outgassing temperature, pass through a maximum, and subsequently decrease. This was attributed to the irreversible dehydration of surface hydroxyl groups. "Irreversible" as used here means that the surface oxide groups resulting from the dehydration were not rehydrolyzed during the time involved in the immersion experiments. Neither the Al_2O_3 system[18] nor the present system exhibited this type of variation with outgassing temperature. Apparently the dehydration of surface hydroxyl groups on Al_2O_3 and thorium oxide is a reversible process within the time scale of the calorimetric measurements. It should be pointed out that the immersion process produces no irreversible change in the surface of the samples used in the present study. This was evident from the fact that samples soaked in water for 2 to 3 weeks prior to the outgassing pretreatment gave the same heat of immersion as unsoaked samples.

The vast majority of reported heat-of-immersion measurements are rapid processes, *i.e.*, they are considered to be instantaneous within the measurement capabilities of the calorimeters used. Such was not the case for samples A, B, and C of the present study. Figure 3, showing the typical behavior observed on immersing these samples in water, is essentially a semilog plot of the unreleased heat as a function of time after initiating the immersion reaction. Detectable quantities of heat continued to be liberated for periods of time as long as 90 min. in the case of sample B. Linearity of the semilog plots extended over practically the entire period in all cases. Extrapolation of the semilog plots back to the time of immersing the sample gives a value which we refer to as the slow heat of immersion. Half-lives for the slow heats of immersion were 7.2, 10.7, and 5.3 min. for samples A, B, and C, respectively. Within experimental uncertainty, the half-lives were independent

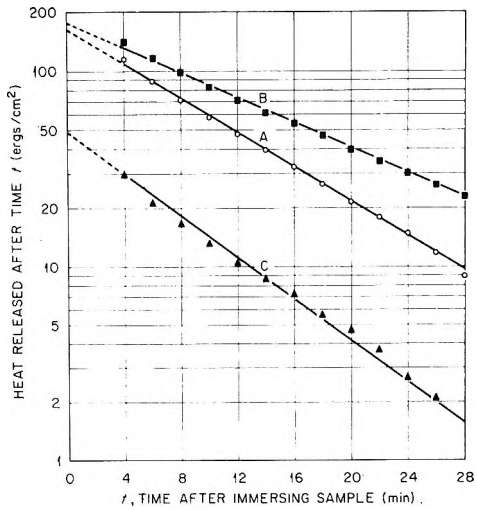

Figure 3. Time dependence of the slow heat of immersion of ThO_2 in water at 25.0° (samples outgassed at 450°).

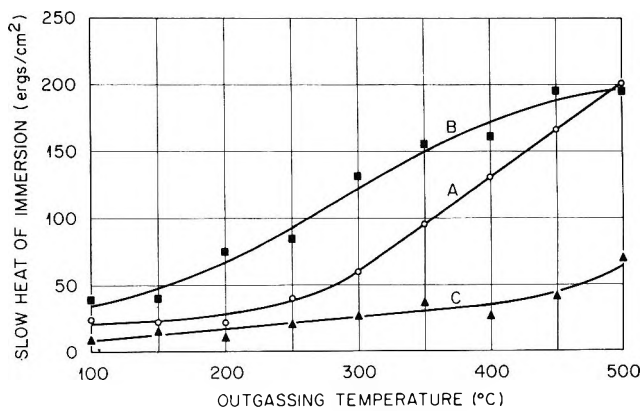

Figure 4. Slow heat of immersion of ThO_2 in water at 25.0°.

of the outgassing temperature. In contrast the magnitudes of the slow heats of immersion were dependent on the outgassing temperature.

Figure 4 shows how the slow heats of immersion for samples A, B, and C vary with the outgassing temperature. Within the experimental capabilities, no slow heat was ever observed with sample D. The fraction of the total heat of immersion which appears as slow heat varies from about 4 to 18% and increases with outgassing temperature. This fraction is generally larger for sample B which again is out of line with respect to surface area and crystallite size.

Slow heats of immersion have previously been reported for the immersion of Al_2O_3[19] and SiO_2[16,19] in water. For the Al_2O_3–water system[19] the quantity of

(19) C. A. Guderjahn, D. A. Paynter, P. E. Berghausen, and R. J. Good, *J. Phys. Chem.*, **63**, 2066 (1959).

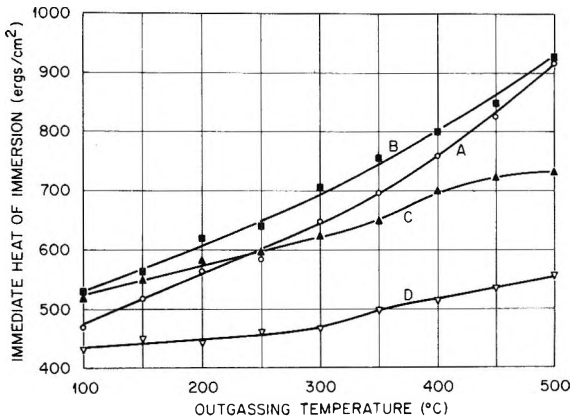

Figure 5. Immediate heat of immersion of ThO_2 in water at 25.0°.

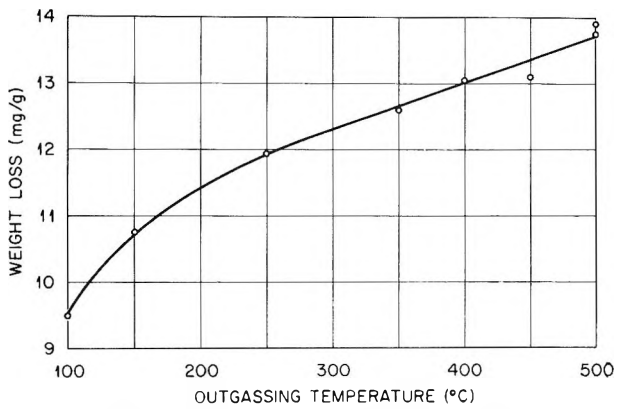

Figure 6. Weight loss on outgassing ThO_2 (sample A).

slow heat and its half-life increased with outgassing temperature. Corresponding data were not given for the SiO_2–water system. For both systems the slow heat phenomena were attributed to a slow rehydration of surface oxide groups resulting from the outgassing procedure. If the slow step in the immersion process was rehydration of surface oxide groups, one would expect[19] the half-life of the slow heat to vary with outgassing temperature. The fact that the half-life of the slow heat in the present system is independent of outgassing temperature is evidence that the rate-controlling step is also independent of the outgassing temperature. In view of this we are led to postulate that the rate-controlling step for the slow heat must be slow diffusion of water into the porous structure of the thorium oxide particles. However, the dependence of the magnitude of the slow heat on the outgassing temperature must be due to the removal of chemisorbed water from the internal surface of the particles during the outgassing process.

By a simple subtraction one can obtain the heat which is released immediately on immersing the samples. These data are shown in Figure 5 as a function of the outgassing temperature. Data for sample D are identical with those in Figure 2 and are included for comparison. Apart from the obvious fact that the immediate heats of immersion are dependent on the outgassing temperature and sample, the significant feature of Figure 5 is that the immediate heats of immersion for samples A, B, and C are more nearly equal than the corresponding total heats of immersion. This is particularly true in the case of samples A and B and is in line with the postulated mechanism to account for the behavior of sample B. If sample B contains a larger percentage of edges, corners, and boundaries because of the manner in which crystallite growth takes place, then many of these energetic sites would be located in cracks or crevices between adjacent crystallites. During the immersion process the energy involved in these sites would appear in the slow heat fraction due to the slow diffusion of water into these cracks and crevices

Weight loss data from the preparation of calorimetric samples were found to be very dependent on the ambient atmosphere. This, plus the fact that the procedure was not designed for accurate weight loss measurements, precluded general use of the weight loss data for purposes of interpretation. However, by chance, a group of calorimetric samples were prepared from sample A during the same period of time, *i.e.*, under constant ambient conditions. Weight loss data for this group of samples are shown in Figure 6. There is no indication that this sample has reached a constant weight, independent of outgassing temperature, at 500°. This is in agreement with the infrared measurements of Wadsworth, *et al.*,[6] which showed the presence of surface hydroxyl groups on thorium oxide after calcining at temperatures as high as 1050°. From the lattice parameter of the thorium oxide crystal one can calculate the theoretical maximum concentration of surface hydroxyl groups on thorium oxide. The maximum theoretical concentration is 12.8 surface hydroxyls for 100 Å.^{2} of surface, equivalent to 2.8 mg. of water/g. of thorium oxide for this sample. The range of weight losses shown in Figure 6 is much larger, indicating that surface hydroxyl groups on thorium oxide are probably not removed below an outgassing temperature of approximately 250°. If one assumes that all of the weight loss between 250 and 500° is due to the loss of surface hydroxyls, one can calculate from the heat of immersion data that the average net heat of adsorption of water in this range of surface coverage is 18 kcal./mole. Winfield[3] estimated 24 kcal./mole for the first water molecules adsorbed on a

water-free thorium oxide surface. Weight loss data for the remaining three samples indicate the same general trend although the uncertainty in the data does not permit any quantitative conclusions to be drawn.

Further elucidation of the energetics and mechanism of the interaction of water with the surface of thorium oxide must await precise and accurate water adsorption and weight loss data for these and additional samples. These experiments are currently in progress.

The Oxidation of Titanium Monoxide at High Temperatures

by D. E. Poland, A. K. Kuriakose, and J. L. Margrave[1]

Department of Chemistry, University of Wisconsin, Madison, Wisconsin *(Received July 3, 1964)*

The rates of oxidation and the nature of the scales formed on single crystal samples of $TiO_{1.2}$ have been studied at 1 atm. oxygen pressure, between 802 and 924°. The reaction follows a parabolic rate law with an activation energy of 45 kcal./mole, after an initial apparently linear rate law region. X-Ray diffraction studies show that the product layer consists of rutile, although formed in two distinctive layers. The oxidation of both Ti metal and $TiO_{1.2}$ seems to have a common mechanism of scale growth since the two processes have nearly equal activation energies in the same temperature range.

There have been nearly a hundred studies of the kinetics and mechanism of the oxidation of titanium metal cited in the various recent books and review articles[2-6] on the subject. Complete agreement among the various authors is not found, partly due to the variations in subtle experimental factors and partly due to the real complexity of the process, when examined closely. There is general agreement in that the main product is rutile with the innermost layer consisting of a solution of oxygen in the metal lattice. X-Ray investigations by Kofstad and co-workers[7] show that at 900° this solution tends toward a limiting composition of $TiO_{0.35}$, although Hurlen[8] finds that its composition corresponds to Ti_6O at 700°. Hurlen's study shows that below 550° the oxidation of titanium follows a logarithmic rate law while above 600° it follows a parabolic rate expression. Kofstad, *et al.*,[7] report that above 800°, the oxidation initially obeys a parabolic rate law which eventually gives way to a linear rate.

A study of the oxidation kinetics of titanium monoxide was undertaken in the present investigation in order to complement the data on the oxidation of titanium metal and to allow comparison of the kinetics and energetics of the two processes.

Experimental

The samples of titanium monoxide used were thin slabs of nearly elliptical cross section, cut from a single crystal boule obtained from the Linde Company. The stoichiometry was established by reaction with fluorine as $TiO_{1.2}$ and the structure was NaCl-cubic.

(1) Department of Chemistry, Rice University, Houston 1, Texas.

(2) (a) A. D. McQuillan and M. K. McQuillan, "Titanium," Butterworth and Co., Ltd., London, 1956; (b) U. R. Evans, "The Corrosion and Oxidation of Metals," Edward Arnold, London, 1960.

(3) O. Kubaschewski and B. E. Hopkins, "The Oxidation of Metals and Alloys," Butterworth and Co., Ltd., London, 1953.

(4) K. Hauffe, "Oxidation von Metallen und Metallegierungen," Springer-Verlag, Berlin, 1956.

(5) P. Kofstad, K. Hauffe, and H. Kjöllesdal, *Acta Chem. Scand.*, 12, 239 (1958).

(6) P. Kofstad and K. Hauffe, *Werkstoffe Korrosion*, 7, 642 (1956).

(7) P. Kofstad, P. B. Anderson, and O. J. Krudtaa, *J. Less-Common Metals*, 3, 89 (1961).

(8) T. Hurlen, *J. Inst. Metals*, 89, 128 (1960).

Trace impurities of aluminum, iron, and lead were present to the extent of 1–10 p.p.m. An emission spectroscopic analysis indicated the presence of trace amounts of aluminum, calcium, magnesium, copper, and silicon. The specimens were ground flat with 400-grit alumina paper, polished with crocus cloth, washed in a sequence of distilled water, trichloroethylene, acetone, and methanol, and dried. They had a brass-like appearance and their surface areas were calculated from their measured geometrical dimensions.

The technique used for the kinetic study was similar to the one for the oxidation kinetics of ZrC and ZrB_2 reported earlier.[9] The cleaned samples were suspended from a calibrated quartz helical spring enclosed in a glass tube, into the hot zone of a Vycor-tube furnace, down which was passed a stream of dried, commercial tank oxygen at a flow rate of 60 ml./min. A timer was started immediately and the weight gain of the samples with time was recorded by noting the extension of the spring using a cathetometer, at suitable intervals. The temperature of the furnace was measured with a calibrated Pt *vs.* Pt–10% Rh thermocouple, and was maintained within 2–3° of the reported value throughout the run. Corrections were applied for the slight furnace temperature gradient. The atmospheric pressure was measured prior to each experiment and it ranged between 737 and 743 torr over the entire set of experiments.

After oxidation of the sample, an X-ray diffraction pattern of the oxidized surface was taken and then it was fractured for microscopic examination of the layers.

Results and Discussion

Between 300 and 500° an initial change of color of the specimen from brassy yellow to violet and blue-black, indicating the formation of higher oxides,[10] was observed, although without any measurable weight gain in these short times. X-Ray analysis of the various colored surfaces indicated nothing but TiO until the slate-gray TiO_2 layer was formed. Probably these early layers were very thin and epitaxially formed on the surface of the TiO single crystal, whereas the gray TiO_2 layers were sufficiently crystalline to yield good rutile powder patterns.

The weighable oxide layer formed on all of the samples during the kinetic studies was found by X-ray analysis to be only rutile, although it consisted of two distinctive layers—a marble-white inner and a silvery-white outer—when examined after fracturing the specimens. The outer surface of the specimens had a slate-gray color indicative of a nonstoichiometric composition, except in the case where the run was continued for a long time (180 min. at 844°) and the run at 924°, where the product layer was yellowish white. This double-layered structure of rutile coatings has also been observed by other workers. Kofstad, *et al.*,[7] attribute one layer to a recrystallization of the rutile, though in their work double-layer formation was observed only above 900°. In this work, slight differences in the X-ray diffraction patterns were noticed between the two layers which could indicate some recrystallization.

Plots of the weight gain of the TiO samples per unit area with time were apparently linear during the initial stages of the reaction, after which the lines tended toward a parabolic behavior. In general, parabolic plots of the data (*cf.* Figures 1 and 2) were more consistent after an initial period of erratic behavior.

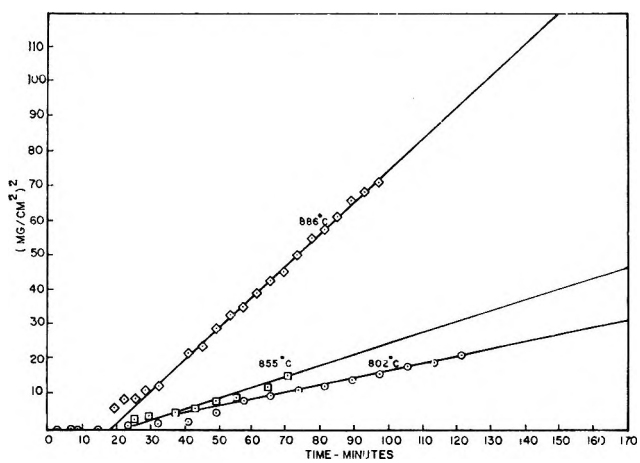

Figure 1. Oxidation of TiO (parabolic plot).

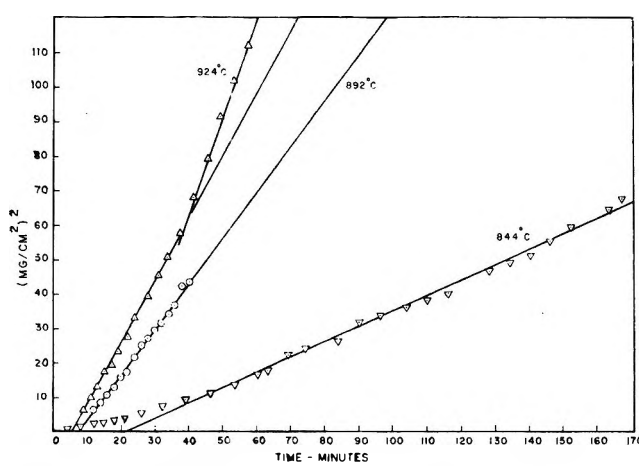

Figure 2. Oxidation cf TiO (parabolic plot).

(9) A. K. Kuriakose and J. L. Margrave, *J. Electrochem. Soc.*, **111**, 827 (1964).

(10) P. Ehrlich, *Z. Elektrochem.*, **45**, 362 (1939).

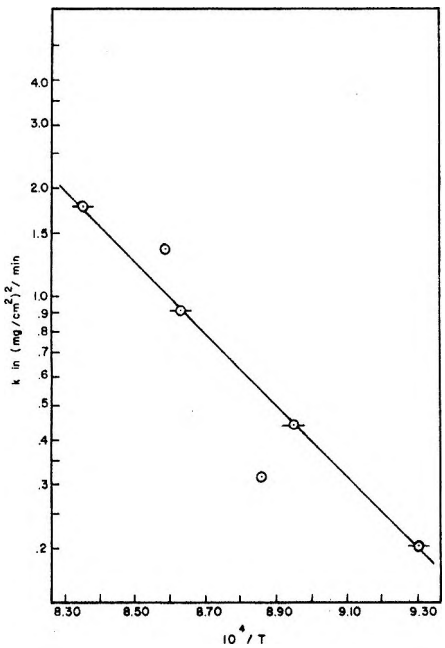

Figure 3. Arrhenius plot of the parabolic rate constants.

Hence, the reaction rate constants were calculated based on a parabolic rate law. The initial deviation could be attributed to either a short-time linear reaction process or to nonequilibrium temperature conditions. The break in the plot of the data at 924° may be due to a change to linear reaction kinetics as reported by Kofstad, *et al.*,[7] to occur after a region of parabolic behavior in the oxidation of titanium metal.

A least-squares fit of the data in the parabolic region gives the rate constants presented in Table I at the various temperatures. Figure 3 is an Arrhenius plot of the rate constants. The points for 855 and 892° involve greater uncertainties in the oxidation temperatures than the others, since these were two of the initial experiments. An activation energy of 45.3 ± 0.6 kcal./mole is obtained by a least-squares method after eliminating the two erratic points (49 ± 4 kcal./mole if they are included), and this value is comparable to the values 50 and 51 kcal./mole obtained, respectively, by Hurlen[8] and Kofstad, *et al.*,[7] for the parabolic region of the oxidation of titanium metal. Since the activation energies are about the same, it may be assumed that the rate-limiting process is the formation of TiO_2 for the oxidation of both titanium metal and titanium monoxide.

There has been a controversy in the literature regarding the identity of the diffusing ionic species in the oxide scales. Kofstad, *et al.*,[7] interpret their work as if oxygen ions were the mobile species, while Kinna and Knorr,[11] Hurlen,[8] and Gulbransen and Andrew[12] favor Ti ion transport. This discrepancy has been explained by Kofstad, *et al.*,[7] as being the result of "plastic flow" of the layers during the crystallization process. Then experimental techniques and temperatures may determine the position of markers after oxidation, independent of which ion is more mobile.

Table I: Kinetic Data for the Oxidation of $TiO_{1.2}$

Temp., °C.	Parabolic rate constant, mg.²/cm.⁴ min.⁻¹
802	0.20 ± 0.01
844	0.44 ± 0.01
855	0.32 ± 0.02
886	0.91 ± 0.01
892	1.36 ± 0.03
924	1.77 ± 0.03

One of the ways to predict the more mobile ionic species is to compare the diffusion coefficients of oxygen and titanium in rutile but comparable data seem to be unavailable. Haul and Dumbgen[13] recently reported the results of oxygen isotope exchange with single crystal rutile. For the temperature range 710 to 950° they found that the exchange rate is controlled not only by the rate of oxygen diffusion in the solid, but also by a phase boundary reaction involving activation energies of 75 and 61 kcal./mole, respectively. Therefore if oxygen diffusion alone were the rate-determining step in the oxidation of Ti and TiO, then the activation energy should be nearer to 75 kcal. Since the observed value is much smaller, it seems reasonable to assume that a titanium ion is the predominantly diffusing species in the oxidation rather than the oxygen ions. Carnahan and Brittain[14] have recently reported internal friction studies of nonstoichiometric TiO_2 crystals and suggested that the dominant nonstoichiometric defect in rutile is a Ti interstitial, in agreement with this conclusion.

Acknowledgments. The authors are pleased to acknowledge the support of this work by the United States Atomic Energy Commission.

(11) W. Kinna and W. Knorr, *Z. Metallkunde*, **47**, 594 (1956).

(12) E. A. Gulbransen and K. F. Andrew, *Trans. AIME*, **185**, 741 (1949).

(13) R. Haul and G. Dumbgen, *Z. Elektrochem.*, **66**, 636 (1962).

(14) R. D. Carnahan and J. Brittain, *J. Appl. Phys.*, **34**, 3095 (1963).

Degradation of Polymers by Controlled Hydrodynamic Shear[1]

by R. E. Harrington

Department of Chemistry, University of Arizona, Tucson, Arizona 85721

and B. H. Zimm

Department of Chemistry, University of California, San Diego, La Jolla, California 92038 *(Received July 7, 1964)*

The mechanical degradation of polystyrene in both "good" and "poor" solvents, and of DNA in two solvents, is studied using (1) a high pressure capillary, (2) a special device to force fluid at high pressure through the narrow annular region between a close-fitting piston and cylinder, and (3) several laboratory homogenizers. Solvents are chosen to span a considerable range of viscosity. Degradation is observed to follow roughly a first-order rate law in all cases. For the first two devices mentioned, maximum shear rates are obtained which are used to estimate the critical shear stress for degradation by means of a semiempirical relation. Estimated critical stresses are 3.5×10^{-6} dyne for polystyrene in "good" solvents, 4.0×10^{-7} dyne in "poor" solvents, and greater than 2.7×10^{-5} dyne for DNA in phosphate buffer solution. These values are roughly two orders of magnitude smaller than a simple theoretical estimate (based on bond strengths) for polystyrene and too small by a factor of 30 for DNA. Possible reasons for this discrepancy are given.

Introduction

It has been known for some time that long-chain molecules can be broken mechanically, both in solution and in the bulk phase. In dilute solutions, degradation evidently occurs as a result of molecular stresses developed by hydrodynamic shear, but the process is, in the usual case, accompanied by turbulence. Under these conditions, not only is a quantitative treatment of the hydrodynamic problem difficult, but additional complications may enter such as local intense adiabatic heating due to cavitation. Such effects create the possibility of chain scission by a thermal mechanism. Apart from difficulties of this nature, a quantitative discussion of the problem is primarily limited by the absence of an adequate theory of non-Newtonian flow under conditions of high shear and frequently by uncertainties in the rheology of the apparatus used as well. Consequently, in spite of the relatively abundant literature on hydrodynamic shear degradation, the process is not well understood.

Ultrasonic irradiation techniques have been used by a variety of workers[2-6] to degrade polymer molecules in solution, but the mechanism responsible for chain scission is not known and is probably complicated. Analyses of the kinetics of ultrasonic degradation by Jellinek[4] and by Ovenall[7] appear to indicate that bond rupture occurs within a central region of the molecule. This would be qualitatively consistent with the expected distribution of stresses on the polymer molecules due to a shear gradient, but quantitative information is largely lacking, and the additional effects of cavitation and of adiabatic heating are difficult to assess.

(1) The authors gratefully acknowledge the financial support of this work provided by Grants No. GM 11916-01 and GM 10491-01 and -02 from the U. S. Public Health Service, and Grant No. G18936 from the National Science Foundation.

(2) G. Schmid and O. Rommel, *Z. physik. Chem.* (Leipzig), **A185**, 97 (1939).

(3) G. Schmid, *ibid.*, **A186**, 113 (1940).

(4) H. H. G. Jellinek, "Degradation of Vinyl Polymers," Academic Press, New York, N. Y., 1955.

(5) H. H. G. Jellinek and G. White, *J. Polymer Sci.*, **6**, 745, 757 (1951).

(6) P. E. M. Allen, G. M. Burnett, G. W. Hastings, H. W. Melville, and D. W. Ovenall, *ibid.*, **33**, 213 (1958).

(7) D. W. Ovenall, G. W. Hastings, and P. E. M. Allen, *ibid.*, **33**, 213 (1958).

Recently, a considerable number of papers[8-12] have appeared dealing with shear degradation of both synthetic and biological macromolecules, in which a variety of shearing devices have been employed. Unfortunately, in these studies, it is not possible to estimate the magnitudes of the shearing stresses leading to chain scission because of the large number of variables involved. The only studies of controlled polymer degradation available at the present time have been reported by Levinthal and Davison.[13] These authors have sheared DNA from T2 bacteriophage in a capillary under apparently well-controlled conditions and have reported a critical force for the transverse breakage of the DNA helix. Although their calculation of shear stress is necessarily a highly approximate one, information of this type is of considerable general interest, and for those systems which degrade by an elementary chain-scission mechanism, a comparison of the critical force required to cause dissociation with a theoretical value predicted from a potential energy function can permit a rough quantitative assessment of the molecular deformation associated with non-Newtonian flow behavior, and can also provide some insight into the effect of solvent in stabilizing or destabilizing the polymer in solution.

It was decided in the present work to study the degradation of relatively well-characterized polymers in dilute solutions, using apparatus in which the shear rates can be calculated with reasonable confidence. Critical molecular shear stresses can then be obtained by extrapolating a semiempirical expression, such that only experimental quantities are involved. Although interpretation of the results, obtained under otherwise ideal conditions, is still complicated by non-Newtonian flow characteristics of the solution, the effects of the latter upon the critical stress for chain scission are relatively small in comparison to those due to turbulence.

Experimental

Materials. Polystyrenes of viscosity-average molecular weights 1.04×10^7 and 3.72×10^6 were prepared by ultraviolet-initiated emulsion polymerization at 0°. No attempt was made to determine the relative molecular weight dispersions in the samples, but the method of preparation was similar to that of a sample that was analyzed in a previous publication[14] and which had a typical distribution for a vinyl polymer.

Solvents used in preliminary studies were redistilled reagent grade toluene, benzene, and methyl ethyl ketone. A comparison of equivalent data on the degradation of these early solutions with those on later solutions using reagent solvents without additional purification detected no differences within experimental error. Consequently, no further purification of reagent grade solvents was undertaken in the studies reported here.

Calf thymus DNA, obtained from Nutritional Biochemicals Corp. and dissolved in standard saline citrate buffer, was used in some of the earlier studies. No attempt was made to fractionate this material. Subsequent studies were made on DNA from T2 bacteriophage dissolved in a sodium chloride, phosphate, EDTA buffer (BPES), 0.1 *M* in sodium chloride at pH 6.8. This bacteriophage DNA is known to have a high degree of intermolecular and intramolecular homogeneity.[11]

The free-radical scavenger 2,2-diphenyl-1-dipicrylhydrazyl was obtained from Distillation Products Industries of Eastman Kodak Co. It was used directly as received.

Apparatus and Equipment. Capillary Cell. High shear rates are developed by forcing fluid through a capillary using high driving pressures of inert gas. A Pyrex reservoir is attached to the capillary through a coarse sintered glass filter (2-cm. diameter, nominal pore size 40 μ), and this is encased in a stainless steel pressure jacket equipped with gas inlet and outlet valves. A double "O" ring pressure seal is used to hold the glass assembly in place and to provide a gastight seal with the pressure jacket.

It was necessary to place the sintered glass filter in an ultrasonic cleaning apparatus for several hours at high field intensity and then to pass quantities of pure water through it at moderate pressures (25 p.s.i. gas driving pressure) in order to displace and remove loose particles of glass. Prior to this rather harsh treatment, the filter would "shed" small pieces of glass of sufficient size to obstruct the capillary.

The capillary used in the present work was drawn from 0.4-mm. bore stock Pyrex capillary, using a specially constructed jig to permit rapid drawing to the desired diameter. Although capillaries drawn in this way were found to have a bell-shaped flare

(8) W. R. Johnson and C. C. Price, *J. Polymer Sci.*, **45**, 217 (1960), have given an adequate summary of previous work on the hydrodynamic degradation of synthetic polymers.

(9) P. F. Davison, *Nature*, 185, 915 (1960).

(10) L. F. Cavalieri and B. H. Rosenberg, *J. Am. Chem. Soc.*, **81**, 5136 (1959).

(11) A. D. Hershey and E. Burgi, *J. Mol. Biol.*, **3**, 674 (1961).

(12) G. S. Rosenberg and G. Bendich, *J. Am. Chem. Soc.*, **82**, 3198 (1960).

(13) D. Levinthal and P. F. Davison, *J. Mol. Biol.*, **3**, 674 (1961).

(14) J. P. Bianchi, F. P. Price, and B. H. Zimm, *J. Polymer Sci.*, **25**, 27 (1957). (The 1.04×10^7 molecular weight polystyrene sample, upon which most results for polystyrene in this study are based, duplicated as closely as possible sample 48.)

on either end, with proper rapid drawing technique a relatively uniform section 10 mm. in length could be obtained between the ends. This flare appeared to provide a more efficient coupling between the regions of high and low linear flow velocity, and was probably the principal reason that turbulence was not observed in these experiments until Reynolds numbers far in excess of those usually quoted for smooth pipes[15] were attained.

Measurement of diethyl phthalate flow at 25°, over a range of pressures, led to a value of 47.3 μ for the capillary radius and also provided calibration of the pressure. When this viscous liquid was used in the capillary, the kinetic energy correction was negligible.

In spite of prefiltering the solutions, considerable difficulty was experienced with capillary plugging, and several units were drawn and installed before one was obtained which did not plug. This was evidently a matter of removing, by use, all traces of foreign material from the region between the prefilter and the capillary itself.

The polymer solutions were forced through the capillary by nitrogen gas pressure obtained from a tank through a high-pressure, two-stage regulator. Gas flow into and out of the cell was controlled by means of stainless steel needle valves, and the gas manifold was designed so that the cell could be pressurized and depressurized very rapidly. No attempt was made to purify the tank nitrogen gas, which typically contained about 2% oxygen. The maximum pressure used in the apparatus was 200 p.s.i.; the pressure jacket and seals were not designed to withstand greater pressures than this, and, in any case, the less viscous polymer solutions were forced through the capillary under conditions bordering on turbulent flow at this pressure.

Maximum shear rates obtainable under flow conditions which could definitely be characterized as nonturbulent were on the order of 10^6 sec.$^{-1}$.

The rheology of the capillary is well known, and the calculation of the maximum Newtonian shear rate developed in capillary flow presents no special problems, as long as corrections for the kinetic energy and end effect are small.[16] The experimental variables may be either the pressure difference across the capillary or the volume flow rate. However, the rather uncertain kinetic energy correction to the pressure (*i.e.*, the Bernoulli pressure drop) becomes considerable at higher driving pressures for the capillary used here and must be taken into account in some way. The use of volume flow rate data eliminates the kinetic energy effect, as well as the end effect from explicit consideration, and maximum shear rates were, therefore, calculated on this basis in the present study.

In terms of the volume flow rate, the shear rate at the wall of a smooth capillary may be calculated from the relation

$$G = \frac{4}{\pi r^3}\frac{dV}{dt} \qquad (1)$$

where G is the maximum (wall) shear rate, dV/dt is the observed volume flow rate, and r is the radius of the capillary.

Piston and Cylinder. A second piece of equipment used was a modification of the penetrometer, designed to produce high shear rates within the very narrow annular region between a closely fitted piston and cylinder. The assembly was made from a 1-cc. glass tuberculin syringe with the outlet tip cut off and sealed. The effective length of the piston was maintained constant by etching all but the bottom 2 cm. of the syringe piston sufficiently to provide a gap large compared to the shearing annulus. To provide the additional strength necessary to withstand relatively high pressures produced within the apparatus, the syringe barrel was mounted in a brass housing with epoxy resin.

In use, the syringe was inserted in a rigid support. A rod, operating in a low friction sliding bearing, connected the glass piston with the weight pan. The desired weights were then placed in the pan by means of a hoist, the apparatus was filled with polymer sample, and the weights were released. Piston velocity was automatically timed by means of a microswitch arrangement operating an electric stopwatch. The sample was removed as it flowed out around the piston by means of a large stainless steel hypodermic needle located in a small depression ground between the piston and the open end of the syringe barrel. Since the device would shear only about 0.75 cc. of sample per pass, it was necessary to make a large number of strokes for each sample. The apparatus was carefully rinsed with solvent and dried with compressed air between strokes.

As can be seen from a comparison of the data of Table I, the extent of polymer degradation per pass was greatly increased by scoring a number of grooves laterally in the piston surface. Twelve narrow circumferential grooves were equally spaced over the length of the piston. The explanation for the in-

(15) H. Lamb, "Hydrodynamics," Dover Publications, New York, N. Y., 1932, p. 664.

(16) S. Oka in "Rheology," Vol. III, F. R. Eirich, Ed., Academic Press, New York, N. Y., 1960.

Table I: Degradation of α-Methylnaphthalene Solutions of Polystyrene (Initial Molecular Weight 10.4 × 10^6) by Repeated Passage through the Piston–Cylinder Apparatus. Results Are Shown before and after Scoring the Piston

Pass	Pressure, dyne/cm.² × 10^{-8}	Concn., g./cm.³ × 10^4	Mol. wt. × 10^{-6}	k, sec.$^{-1}$ × 10^4	$\langle f \rangle_{av}$, dynes × 10^6
		Unscored piston			
1	2.21	5.67	5.04	...	...
2	2.21	5.67	3.30	...	...
3	2.21	5.67	2.47	...	...
		Scored piston			
1	1.22	5.99	4.46	4.07	4.18
2	1.22	5.99	2.79	1.51	2.66
3	1.22	5.99	2.09	...	1.99
1	1.83	5.49	3.78	10.9	5.35
1	2.21	5.99	3.45	17.3	6.46
2	2.21	5.99	2.17	5.01	4.13
3	2.21	5.99	1.62	2.56	3.05

creased degradation rate due to these grooves is evidently to be found in the laminar flow pattern of fluid through the annular region between the unscored piston and syringe barrel wall. Principal shearing takes place at the walls, and molecules in a region of high shear rate are degraded to a limiting molecular weight which is a function of local shear rate and molecular size. This process evidently occurs in a time short compared to the time of travel of the molecule (near the wall) through the device. If the flow is laminar, little mixing can ocur in the direction normal to the liquid flow. The scored grooves, then, apparently provide periodic mixing of the sample, and one stroke of the scored piston is equivalent to several strokes of an unscored but otherwise identical piston.

The advantages of the piston and cylinder apparatus over the simple capillary are principally that the narrow annular width definitely precludes turbulent flow under any experimental conditions reported here, and the fact that the correction to the shear rate, due to kinetic energy of the emerging liquid, is significantly less. In this connection, the flow of liquid out of the device is analogous to flow through a slit (although a special type of slit in which one side moves relative to the other). Thus, for a reasonable total flow rate, the rheology of the sample is not only less subject to complications as just discussed, but there is the practical advantage that plugging is eliminated.

The maximum driving force which could be applied to the glass syringe was 100 lb. This produced a pressure of 3200 p.s.i. on the fluid. Because of this pressure limitation, studies could only be made on solutions in an intermediate viscosity range; it was necessary that flow through the annulus be rapid enough that the piston would remain centered in the syringe barrel by hydrodynamic forces and yet not exceed the limiting Reynolds number for laminar flow. In terms of these considerations, α-methylnaphthalene appeared to be nearly an ideal solvent for studies of polystyrene degradation. Little information could be obtained using diethyl phthalate as a solvent, however, since these solutions were so viscous that failure of the piston to remain centered during its downward travel (as evidenced by sticking and grabbing) became a serious problem.

The rheological theory for several types of penetrometers has been discussed by Bikermann[17] and Oka,[16] and a general treatment has been given by Smith, *et al.*,[18] which includes as a special case an earlier treatment by Lawaczeck,[19] for which the annular gap becomes limitingly small (the case considered here). The following basic equations for the penetrometer are largely due to Smith, *et al.*

The maximum shear rate developed in a piston and cylinder device of the type considered can be calculated as a function of either piston velocity or driving force. In the present work, the piston travel time per stroke was relatively short (on the order of 1 to 2 sec., typically) and, hence, difficult to measure with precision comparable to the remainder of the experiment. All results were therefore calculated using the piston driving force as the experimental variable since this involved only a knowledge of the weights used. A comparison showed the two types of calculations were in agreement within estimated experimental error, and this was taken as evidence that the kinetic energy correction was negligible in these studies.

For a cylinder of radius b and a piston of radius a, with effective piston length L, the shear rate at the walls is given as

$$G = \frac{v}{a} A \tag{2}$$

and the driving force as

$$\Phi = \frac{2\pi\eta L v a}{(b - a)} (A + 1) \tag{3}$$

where

(17) J. J. Bikermann, *J. Colloid Sci.*, **3**, 75 (1948).

(18) T. L. Smith, J. D. Ferry, and F. W. Schoemp, *J. Appl. Phys.*, **20**, 144 (1949).

(19) T. Lawaczeck, *Z. Ver. deut. Ing.*, **43**, 677 (1919).

$$A = \frac{b^2 - a^2}{(b^2 + a^2) \ln b/a - (b^2 - a^2)} \quad (4)$$

and v and η are the piston velocity and the Newtonian viscosity of the solution, respectively. Thus, the shear rate can be expressed as a function of Φ.

$$G = \frac{\Phi(b - a)A}{2\pi\eta La^2(A + 1)} \quad (5)$$

For small annular gap, $b/a \cong 1$, and it can be easily shown that A is a large number such that $A \cong (A + 1)$. For this case, the expression for the shear rate can be simplified.

$$G = \frac{\Phi(b - a)}{2\pi\eta La^2} \quad (6)$$

The dimensions of the apparatus used in the present work are as follows: the piston length L, 2.0 cm., exclusive of the scored grooves; the piston radius, 0.236 cm.; the annular gap, 20×10^{-4} cm. The maximum (Newtonian) shear rate developed by the apparatus with 100-lb. driving force on α-methylnaphthalene is therefore 4.4×10^6 sec.$^{-1}$.

Sintered Disk. Solutions of polystyrene in toluene were degraded by forcing them through Pyrex sintered disks (nominal pore diameter 14 μ). The disks were mounted in a high-pressure gas cell, similar in design and operation to that described in connection with the capillary.

It is possible to degrade high molecular weight polystyrene effectively at high flow rates through the Pyrex disk, but interpretation of the results is impossible because of an apparent adsorption of the polymer to the glass, resulting in a substantial decrease in apparent pore size. We have found that the amount of polymer adsorption in a clean sintered glass disk is proportional to the surface area of the disk, using as a model a hexagonal, closest-packed arrangement of glass spheres of such size that the radius of the circle inscribed between three spheres in contact corresponds to the nominal pore size of the disk. This plugging of the disk is also a strong function of polymer molecular weight at molecular weights above 10^6 and corresponds to a (calculated) reduction in nominal pore size by a factor of 5 in the case of the highest molecular weight polymer studied (1.04×10^7). The effect becomes very much less significant at lower molecular weights but is observable for polystyrene of molecular weight as low as 10^5. Corresponding effects were noted with high molecular weight DNA. Curiously enough, the effect persists even at the highest shear rates attainable in these studies although it is noticeably shear rate dependent. Furthermore, once plugged, a disk can only be returned to its original pore size by chemical cleaning using strong oxidizing agents, such as hot chromic acid cleaning solution.

The anomalous plugging of sintered glass disks because of the apparent adsorption of high polymers will be discussed more fully in a forthcoming paper on the subject, and the experimental study of this phenomenon will be presented in detail. Because of this effect, however, it is impossible to calculate shear rates which can be sensibly correlated with molecular degradation rates. Thus, although no quantitative information can be obtained from the shearing experiments in sintered glass disks reported here, the results are included because the disk will certainly be useful, in many circumstances, for the rapid bulk degradation of polymers in dilute solutions.

Degradation by High-Speed Stirring. Preliminary studies on degradation of polystyrene in toluene and diethyl phthalate and of calf thymus DNA (original molecular weight on the order of 10^7) by high speed stirring employed a Gifford–Wood Minimill. This was a high-speed rotary homogenizer which developed high rates of shear in an annular region between a rotor and stator, and also at the edges of rotating impeller blades. The annular width in this device was continuously variable from 0.0076 cm. to approximately 0.3175 cm. The maximum rotor speed was 22,000 r.p.m. It was found that the rate of polymer degradation was not dependent upon the width of the annulus over its entire range of adjustment, so that all degradation evidently occurred at the impeller blades. For all runs, therefore, annular spacing was set at 0.038 cm., and the motor was operated at full speed.

A Virtis "45" Macro homogenizer was employed in which blades 3.85 cm. in diameter rotated at speeds up to 40,800 r.p.m. under conditions of load. This corresponds to a maximum blade-tip velocity of 8220 cm./sec. The large 250-ml. sample flask and double-blade assembly were used in all cases. Water from a thermostat was constantly circulated through the cooling cup to maintain temperature control during a run.

An ultra-high-speed air turbine motor, constructed especially for the polymer degradation studies, was able to rotate blades 2.95 cm. in diameter at speeds up to 80,000 r.p.m., corresponding to tip velocities of 12,500 cm./sec. Unfortunately, because of difficulties with the bearings (mechanical bearings were required because of the lateral thrust of splashing liquid against the blades), the turbine was not able to maintain speeds in excess of 65,000 r.p.m. for prolonged periods of time, so that blade speeds of 10,000 cm./sec. were

the practical maximum for this device. Both the Virtis homogenizer and the air turbine developed higher maximum shear rates (as is evidenced by the more rapid and extensive polymer degradation shown in Figure 1) than could be obtained from the Minimill. Because of the complicated shearing action of these devices, however, quantitative interpretation of results is not attempted, and the molecular weight *vs.* running time curves in Figure 1 are given for comparative purposes only.

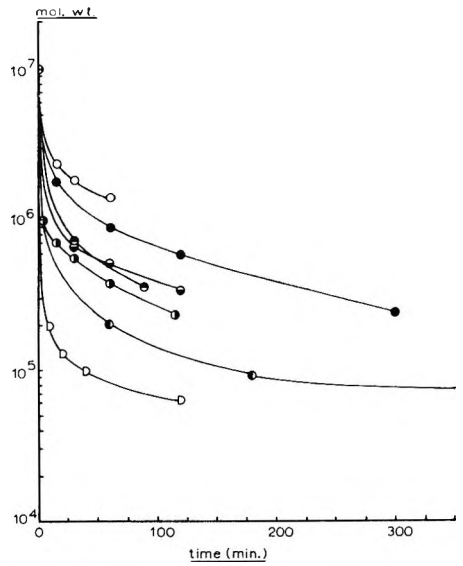

Figure 1. Molecular weight falloff with time for various rotating-blade shearing devices: O, polystyrene in toluene, Minimill; ●, calf thymus DNA in SSC buffer, Minimill; ◒, T2 bacteriophage DNA in BPES buffer, Virtis homogenizer, 8000 cm./sec. blade speed; ◓, T2 bacteriophage DNA in BPES buffer, air turbine homogenizer, 10,000 cm./sec. blade speed; ◑, T2 bacteriophage DNA in 50% glycerine–BPES solvent, Virtis homogenizer, 8000 cm./sec. blade speed; ◐, polystyrene in diethyl phthalate, virtis homogenizer, 8000 cm./sec. blade speed; O, polystyrene in diethyl phthalate, air turbine homogenizer, 10,000 cm./sec. blade speed.

The kinetics of shear degradation in the rotary homogenizers showed a strong dependence upon design of the sample vessel. Degradation to the nearly horizontal region of the molecular weight *vs.* time curve occurred most rapidly in the Minimill, where the sample was constantly circulated through the blades by the strong centrifugal pumping action of the conical shaped rotor–stator assembly. In spite of the high shear rates developed in the turbine homogenizer, degradation proceeded relatively slowly until Teflon fins were installed to direct the sample flow onto the blade tips. With the rate of sample mixing thus improved, the falloff rate of molecular weight in the turbine apparatus became comparable to the two commercial homogenizers.

Procedure. The degradation studies were conducted at the temperature of the laboratory, which was maintained at 25 ± 2°. No attempt was made to control the sample temperature accurately since preliminary studies of polystyrene degradation at temperatures from 15 to 45° showed a negligible temperature effect.

Polymer degradation was followed by means of viscosity-average molecular weight changes. The viscometer used was a capillary type with maximum shear rate less than 250 sec.$^{-1}$.

Several early studies were made using the stable free radical 2,2-diphenyl-1-dipicrylhydrazyl (DPPH) to determine the effects of a known free-radical scavenger upon the degradation kinetics, and to measure directly the number of chain scissions in polystyrene dissolved in toluene. The colorimetric method described by Allen, *et al.*,[6] was used to detect DPPH concentration changes as a result of polymer bond rupture. The results of these studies were substantially in accord with those of Johnson and Price,[8] who found good agreement between the number of chain scissions calculated from viscosity-average molecular weight falloff data and a direct determination of iodine uptake. As a result of these findings, subsequent data, including those reported here, are based entirely upon viscosity molecular weight determinations.

Interpretation of Shear Degradation Data

An attempt was made to reduce the important kinetic variables so that a comparison of results between polystyrene and DNA and also among solutions of polystyrene in different solvents could be made without ambiguity.

Studies of the degradation reactions of various polymers by ultrasonic irradiation[5,6] have demonstrated that these processes can be adequately described by simple first-order kinetics in the number of bonds.[5,7] Although the mechanism of ultrasonic degradation is not well understood and may be complicated by thermal effects due to cavitation, the predominant mechanism (insofar as it affects the kinetics) is probably essentially similar to the hydrodynamic shear process employed here. Thus, our experimental rate should also be characterized rather well by an expression of the type

$$\frac{d\bar{x}}{dt} = kx \qquad (7)$$

where

$$\bar{x} = cN\left(\frac{1}{M} - \frac{1}{M_0}\right) \tag{8}$$

is the number of broken bonds per unit volume, starting with polymer of molecular weight M_0 to form polymer of molecular weight M, and

$$x = cN\left(\frac{1}{M_L} - \frac{1}{M}\right) \tag{9}$$

is the number of bonds available for breakage per unit volume, assuming limiting degradation to molecular weight M_L. One has, then, for extensive degradation

$$\frac{d(1/M)}{dt} = k\left(\frac{1}{M_L} - \frac{1}{M}\right) \tag{10}$$

and for moderate degradation (*i.e.*, $M >> M_L$)

$$M_L \frac{d(1/M)}{dt} = k \tag{11}$$

The above expressions ignore the effects of polydispersity in the polymer sample and are mainly useful to provide a semiempirical fit to the experimental data. Nevertheless, the time and molecular weight parameters can be related to theory in a reasonable way.

The constant k is seen to be the fraction of available bonds broken per unit time, but it is difficult to define a suitable time scale. In the capillary and piston–cylinder apparatus, the velocity distribution will be parabolic with the radius (apart from non-Newtonian flow effects) so that only a very small fraction of the molecules in the device at a given instant of time will be near the walls, in a region of high shear rate. In spite of this, an effective time can be defined as the reciprocal of the observed flow rate times the volume of the capillary or the annular region in the piston–cylinder apparatus. This experimental quantity therefore measures the average time (averaged over the appropriate non-Newtonian velocity distribution) that a molecule spends in the device and, assuming laminar flow, will be proportional to, and not too different from, the average time spent in the region of critical shear stress. One notes, however, that the particular definition of the time scale does not affect the principal conclusions of this work since only the relative rates of degradation are of interest.

The distribution of stress in a straight rod in shear flow is parabolic with the peak at the center.[13,20] Thus, in the case where the shear rate only slightly exceeds the critical value, the breaking points will be narrowly localized in the center and the broken pieces will be nearly perfect half-molecules. This ideal situation was probably closely approached in the degradation of T2 DNA by Hershey and Burgi.[11] More commonly, the picture is complicated by two factors. In the first place, the molecule may not be a straight rod but some partially extended form of a random coil or one of the special coils seen at high shear rates by Mason and co-workers.[21–23] It is not then immediately obvious that the highest stress will occur exactly in the center. In the second place, if the initial distribution of chain sizes is broad, the product cannot have a perfectly sharp distribution. In such a case, the largest molecules may be broken repeatedly at or near the center until the resulting fragments are below the size at which the stress is sufficient to break them; a molecule just above the critical size is broken while one only slightly smaller is not. Thus, a distribution arises in which the largest molecules are approximately twice the length of the smallest. Even such a distribution is relatively narrow in comparison to the distributions of the common synthetic polymers. It is likely, therefore, that the distribution of molecular sizes is not an important complication in the present work.

Since we believe that the mechanical stress on the molecule is the primary cause of breakage, it is important to relate this to other more easily observed quantities. This may be done in the following way for the *average* stress. The shearing stress, the force transmitted across a unit area perpendicular to the velocity gradient, is ηG, where η is the viscosity and G is the shear rate. In a dilute solution in which the volume occupied by the polymer molecules may be neglected, the quantity $\eta_0 G$, where η_0 is the viscosity of the pure solvent, is the part of the force transmitted by the solvent alone. The difference, $(\eta - \eta_0)G$, is then the force transmitted by the long-chain molecules of the solute that cross the unit area. If the average number of such molecules that cross the unit area is known, it then becomes a simple matter to get by division the average force per molecule. By a well-known theorem, used frequently in the kinetic theory of gases, the number of molecules crossing the unit area is equal to the number per unit volume, n, times the average of the reciprocals of the projections of their end-to-end lengths on the normal to the area, which is the direction of the velocity gradient; we call this projection z. The average force sustained by one long-chain solute molecule then is given by

(20) J. Frenkel, *Acta Physiochim. URSS*, **14**, 51 (1944).
(21) O. L. Forgacs and S. G. Mason, *J. Colloid Sci.*, **14**, 473 (1959).
(22) O. L. Forgacs and S. G. Mason, *ibid.*, **14**, 457 (1959).
(23) W. Bartok and S. G. Mason, *ibid.*, **14**, 13 (1959).

$$\langle f \rangle_{av} = \frac{G(\eta - \eta_0)}{nz} \tag{12}$$

This is the average force per molecule. The actual force is not uniform over a given chain but is parabolic in form with the maximum in the center, as Frenkel[20] showed. However, the height of the maximum should be proportional to the average force, eq. 12.

All quantities in eq. 12 are, in principle, directly accessible experimentally. In practice, the measurements of both η and z are difficult at high flow rates. We are going to assume in this paper that z has the same value in the flowing solution as it has in the molecule at rest, where it is $3^{-1/2}$ times the r.m.s. end-to-end length, a quantity which is directly measurable by light scattering. (Actually, since the average of the reciprocal is involved, a slightly different numerical factor should be used, but we ignore this in view of the presence of more serious approximations.) We also assume that η has the same value as at rest. The justification for the above assumptions is that they become exact in the ideal limiting case of a chain that is extensible and which also perfectly obeys gaussian statistics.[24] In real molecules with limited extensibility, η and z are certainly less in a strong velocity gradient than with the solution at rest. This point will be discussed again in a later section in connection with the actual data.

Another difficulty arises from the fact that the end-to-end length is determined by light scattering for molecules at infinite dilution. It is known that this distance should decrease with increasing concentration, particularly in good solvents. We shall ignore this effect in this paper, since we are working with dilute solutions and since other errors are probably more significant.

Since it is the maximum values of the stretching force that are of principal interest in polymer degradation, the shear rate at the interface between the moving liquid and the wall of the apparatus is appropriate. The maximum shear rates for the experimental equipment used here have been given previously. One can then calculate the average shearing stress for the capillary from eq. 12 as

$$\langle f \rangle_{av} = \frac{4\eta_{sp}\eta_0 M}{\pi r^3 cNz} \frac{dV}{dt} \tag{13}$$

where M is the molecular weight of the (unsheared) polymer, c is the concentration, and N is Avogadro's number. For the piston–cylinder apparatus, the expression becomes

$$\langle f \rangle_{av} = \frac{M\Phi(b - a)\eta_{sp}}{2\pi La^2 cNz\eta_{rel}} \tag{14}$$

where η_{rel} is the relative viscosity of the polymer solution.

Results and Discussion

The degradation reaction as observed here represents a chemical process for which the activation energy is supplied mechanically. However, it is difficult, from hydrodynamic shear experiments alone, to obtain an activation energy which can be compared directly with the dissociation energy of the reaction coordinate in a thermodynamic sense. This is because one cannot be certain of the range over which a force such as that given by eq. 12 must operate in order for chain scission to occur. Moreover, for molecules partially extended by a hydrodynamic shear gradient, the observed energy would also be a function of the number of bonds simultaneously (or nearly so) involved in the chain scission event.

One can, however, compute the average tensile force on a polymer molecule in a shear gradient (apart from effects due to distortion of configuration of the molecule at high rates of shear) as discussed above, and by extrapolating this value to zero rate, one can obtain an experimental critical stress for chain rupture.

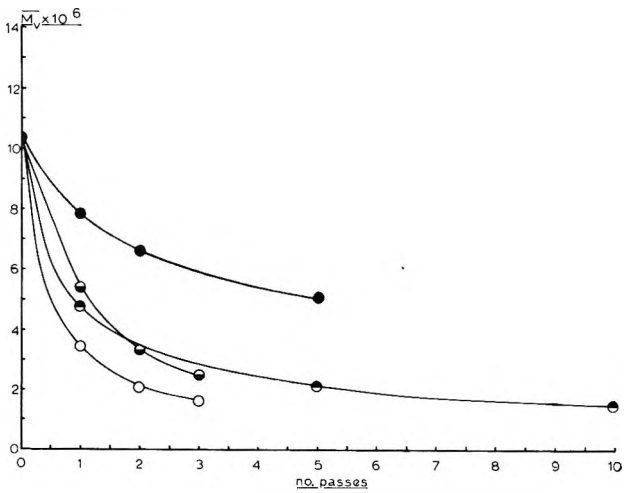

Figure 2. Comparison of molecular weight falloff with number of passes through controlled shearing devices: ●, polystyrene in toluene, capillary, 200 p.s.i. driving pressure; ◓, polystyrene in toluene, sintered glass disk, 200 p.s.i. driving pressure; ◒, polystyrene in α-methylnaphthalene, unscored piston–cylinder apparatus, 3200 p.s.i. driving pressure; ○, polystyrene in α-methylnaphthalene, scored piston–cylinder apparatus, 3200 p.s.i. driving pressure.

(24) B. H. Zimm, *J. Chem. Phys.*, **24**, 269 (1956).

Table II: Capillary Degradation of Polystyrene (Initial Molecular Weight 10.4 × 10^6) in Good (Toluene) and Poor [Methyl Ethyl Ketone (MEK)] Solvents at Different Driving Pressures. Properties Given Are Those Observed after the Indicated Number of Successive Passes of the Polymer Solutions through the Capillary; Zero in the Pass Column Indicates the Solution before Shearing

Solvent	Pass	Pressure, dyne/cm.² × 10^{-6}	η_{sp}	Flow rate, cm.³/sec.	Concn., g./cm.³ × 10^4	z, cm. × 10^6	Mol. wt. × 10^{-6}	k, sec.$^{-1}$ × 10^4	$\langle f \rangle_{av}$, dynes × 10^6
MEK	0	6.21	0.174	0.151	5.30	3.10	10.4	85.5	1.34
MEK	1	6.21	0.120	0.148	5.55	2.20	8.34	47.7	0.983
MEK	2	6.21	0.110	0.152	5.92	2.06	7.31	38.5	0.810
MEK	3	6.21	0.105	0.150	6.40	1.90	6.25	31.2	0.653
MEK	0	2.76	0.174	0.045	5.30	2.56	10.4	8.21	0.484
MEK	1	2.76	0.173	0.045	5.59	2.54	10.3	3.75	0.463
MEK	2	2.76	0.165	0.047	5.71	2.41	9.82	1.50	0.447
MEK	3	2.76	0.161	0.046	5.81	2.39	9.74	0.625	0.420
Toluene	0	13.8	0.644	0.245	4.49	4.30	10.4	127	9.39
Toluene	1	13.8	0.515	0.260	4.47	3.62	7.88	104	7.27
Toluene	1	13.8	0.516	0.260	4.46	3.63	7.88	104	7.26
Toluene	2	13.8	0.454	0.263	4.52	3.32	6.62	86.1	5.87
Toluene	5	13.8	0.367	0.266	4.49	2.88	5.08	45.1	4.26
Toluene	0	6.21	0.648	0.120	4.47	4.30	10.4	21.1	4.70
Toluene	1	6.21	0.608	0.125	4.46	4.15	9.74	8.85	4.46
Toluene	2	6.21	0.603	0.128	4.56	4.00	9.29	7.10	4.38
Toluene	3	6.21	0.593	0.129	4.55	3.95	9.14	6.21	4.34
Toluene	5	6.21	0.571	0.131	4.60	3.85	8.59	4.91	4.06
Toluene	0	6.89	0.644	0.138	4.49	4.30	10.4	14.5	5.28
Toluene	1	6.89	0.605	0.145	4.47	4.06	9.61	13.8	5.17
Toluene	2	6.89	0.575	0.149	4.45	3.95	9.08	13.1	4.92

Experimental molecular weight falloff data for various polymer solutions in the capillary and piston–cylinder devices are given in Tables I through V, and are summarized in Figure 2. For these apparatus, effective experimental and average force values are calculated using eq. 13 and 14 as discussed previously. The rate constants are obtained by graphical differentiation of reciprocal molecular weight *vs.* effective time plots because of the relatively considerable molecular weight change associated with each pass.

The degradation studies of several polymer systems by high-speed stirring are summarized in Table VI and Figure 1. Although the degradation process occurs more slowly here than in the controlled shear devices, this undoubtedly is due to the lesser efficiency of the rotating blade equipment in subjecting a given number of polymer molecules to critical or greater shearing stresses per unit of time. The limiting molecular weights of polymers sheared by high-speed stirring are lower than those of polymers sheared in either the capillary or piston–cylinder apparatus, indicating that maximum shear rates developed in the stirrers must be higher. However, because of the virtual certainty of turbulence at the high blade speeds used, and the inherent difficulty in applying hydrodynamic theory to the calculation of maximum shear rates, as discussed later, no attempt is made to estimate critical force values from these experiments.

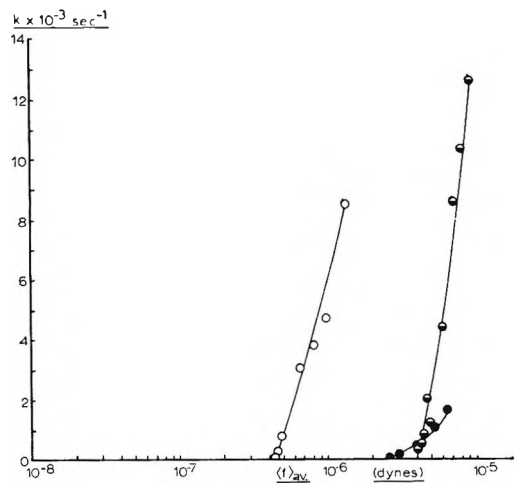

Figure 3. Degradation rate *vs.* average tensile stress, multiple pass data ◒, polystyrene in toluene, capillary; ○, polystyrene in methyl ethyl ketone, capillary; ●, polystyrene in α-methylnaphthalene, scored piston–cylinder apparatus.

Table III: Capillary Degradation of Polystyrene in Good [Toluene and α-Methylnaphthalene (α-MN)] and Poor [Methyl Ethyl Ketone (MEK) and Diethyl Phthalate (EP)] Solvents Which Span a Considerable Range of Solvent Viscosity. Degradation Resulting from a Single Pass through the Capillary Is Given at Various Driving Pressures. The Initial Molecular Weight of the MEK Solution of Polystyrene was 3.72×10^6; That of the Remainder of the Solutions Was 10.4×10^6

Solvent	Pressure, dyne/cm.^{2} $\times 10^{-6}$	η_{sp}	Flow rate, cm.^{3}/sec.	Concn., g./cm.^{3} $\times 10^4$	z, cm. $\times 10^5$	Mol. wt. $\times 10^{-6}$	k, sec.$^{-1}$ $\times 10^4$	$\langle f \rangle_{av}$, dynes $\times 10^6$
MEK	13.8	0.095	0.278	4.19	1.42	2.96	281	1.06
MEK	8.27	0.103	0.212	4.20	1.53	3.37	85.0	0.926
MEK	5.52	0.105	0.152	4.22	1.56	3.48	39.0	0.683
MEK	2.76	0.108	0.080	4.17	1.62	3.72	...	0.383
EP	10.3	0.272	0.016	4.73	2.50	8.50	7.87	0.884
EP	6.89	0.283	0.011	4.73	2.61	9.16	2.01	0.455
EP	13.8	0.264	0.022	4.73	2.47	8.25	13.8	1.33
Toluene	13.8	0.434	0.272	3.95	3.60	7.62	124	7.04
Toluene	8.27	0.500	0.165	3.89	4.01	9.26	75.5	5.44
Toluene	5.52	0.538	0.112	3.95	4.18	9.95	49.1	4.05
Toluene	2.76	0.572	0.089	3.75	4.28	10.4	...	3.68
Toluene	13.8	0.754	0.232	6.14	3.71	7.93	83.7	6.79
Toluene	8.27	0.859	0.150	6.21	3.98	9.08	58.4	5.25
Toluene	5.52	0.902	0.105	6.22	4.08	9.58	39.3	3.98
Toluene	2.76	0.951	0.087	6.19	4.27	10.2	0.802	3.59
Toluene	13.8	0.516	0.260	4.47	3.62	7.88	104	7.27
Toluene	13.8	0.518	0.263	4.52	3.62	7.88	109	7.30
Toluene	6.21	0.608	0.125	4.45	4.15	9.74	12.4	4.46
Toluene	2.76	0.685	0.088	4.40	4.27	10.2	0.942	3.65
Toluene[a]	6.89	0.585	0.145	4.52	4.08	9.65	16.4	4.94
α-MN	13.8	0.732	0.073	6.00	3.85	8.60	21.9	10.9
α-MN	6.84	0.763	0.033	6.00	3.98	9.05	7.01	5.39
α-MN	3.45	0.811	0.024	6.00	4.10	9.68	1.12	4.34

[a] Run with 1.4×10^{-4} g./ml. of DPPH.

Table IV: Degradation of a Polystyrene Solution by Repeated Passage through a Sintered Glass Disk (Nominal Pore Size 14 μ)

Pass	Pressure, dyne/cm.^{2} $\times 10^{-6}$	Concn., g./cm.^{3} $\times 10^4$	Mol. wt. $\times 10^{-6}$
0	13.8	6.30	10.4
1	13.8	6.33	4.76
5	13.8	6.39	2.11
10	13.8	6.55	1.47
25	13.8	6.78	0.882
100	13.8	9.64	0.538

Data of Tables I and II are summarized in Figure 3, where experimental rates for repeated passes of one sample through the apparatus are shown plotted against calculated molecular force values. An apparent curvature of all lines toward smaller molecular forces, particularly at low rates of degradation, is observed. This effect is particularly pronounced in the studies upon the polystyrene–α-methylnaphthalene system in the piston–cylinder apparatus and is probably an artifact associated with changes in the molecular weight distributions.

Since the molecular weight distributions certainly undergo relatively large changes, especially during initial degradation of the samples, it is more satisfactory to vary the rate of degradation by changing an external variable such as the driving pressure or force. This type of representation is shown in Figure 4, which is based upon the data of Tables I and III, except that here the rates and stress values are computed on the basis of the *initial pass* of the polymer solution through the apparatus. Although the curves of Figure 4 are still not completely independent of the effect of changing molecular weight distribution, they are, nevertheless, largely *self-consistent* with respect to these molecular weight changes and certainly permit the experimental results to be more easily in-

Table V: Degradation of T2 Bacteriophage DNA (Initial Molecular Weight 120 × 10^6) in BPES Buffer by Repeated Passage through the Scored Piston–Cylinder Apparatus. Average Tensile Force Values Are Based upon Radii of Gyration Determined from a Consensus of Light-Scattering Values (See Text)

Pass	Pressure, dyne/cm.^{2} × 10^{-8}	Concn., g./cm.^{3} × 10^4	η_{sp}/η_{rel}	Mol. wt. × 10^{-6}	k, sec.$^{-1}$ × 10^4	ρ(r.m.s.)/$\sqrt{3}$, cm. × 10^5	$\langle f \rangle_{av}$, dynes × 10^5
1	1.22	2.5	0.694	6.8	12	2.8	3.0
2	1.22	2.5	0.601	5.9	3.9	2.35	2.92
3	1.22	2.5	0.572	5.3	1.0	2.06	2.84

Table VI: Degradation of Various Polymer Systems by High-Speed Rotary Stirring. Systems: Polystyrene in Toluene; Calf Thymus DNA in Standard Saline Citrate Buffer; Polystyrene in Diethyl Phthalate; T2 Bacteriophage DNA in BPES Buffer; T2 Bacteriophage DNA in 50% Glycerol-BPES Buffer Solution (See Text)

Apparatus	Polymer	Solvent	Concn., g./cm.^{3} × 10^4	Time, hr.	Mol. wt. × 10^6	Blade velocity, cm./sec.
Minimill	PST	Toluene	4.20	0.25	2.38	...
Minimill	PST	Toluene	4.20	0.5	1.83	...
Minimill	PST	Toluene	4.20	1	1.41	...
Minimill	CT/DNA	SSC	5	0.25	1.8	...
Minimill	CT/DNA	SSC	5	1	0.90	...
Minimill	CT/DNA	SSC	5	2	0.60	...
Minimill	CT/DNA	SSC	5	5	0.25	...
Virtis	PST	EP	12	1	0.21	8,000
Virtis	PST	EP	12	3	0.095	8,000
Virtis	PST	EP	12	6	0.079	8,000
Virtis	PST	EP	12	7	0.076	8,000
Virtis	T2/DNA	BPES	1.25	0.5	0.67	8,000
Virtis	T2/DNA	BPES	1.25	1	0.52	8,000
Virtis	T2/DNA	BPES	1.25	2	0.34	8,000
Virtis	T2/DNA	BPES	1.25	3	0.28	8,000
Virtis	T2/DNA	50%G-BPES	0.83	0.083	1.00	8,000
Virtis	T2/DNA	50%G-BPES	0.83	0.25	0.72	8,000
Virtis	T2/DNA	50%G-BPES	0.82	0.5	0.56	8,000
Virtis	T2/DNA	50%G-BPES	0.83	1	0.38	8,000
Virtis	T2/DNA	50%G-BPES	0.83	2	0.24	8,000
Turbine	T2/DNA	BPES	2.5	0.5	0.72	10,800
Turbine	T2/DNA	BPES	2.5	1.5	0.37	10,800
Turbine	PST	EP	4.2	0.16	0.20	10,000
Turbine	PST	EP	4.2	0.33	0.13	10,000
Turbine	PST	EP	4.2	0.66	0.099	10,000
Turbine	PST	EP	4.2	2	0.064	10,000

terpreted. (Unfortunately, since the data of Figure 4 are based upon initial passes through the degradation apparatus where the molecular weight changes are largest, the effects of molecular weight distributions, although self-consistent, are maximized.)

Limiting Degradation of Polystyrene. In Figures 3 and 4, the experimental degradation rate as a function of tensile stress is extrapolated to zero degradation rate. (The polystyrene sample had an initial molecular weight of 1.04 × 10^7 in all solvents except methyl ethyl ketone; in this solvent, the molecular weight was 3.72 × 10^6, but the sample was, otherwise, similar to the higher molecular weight preparation.) Our guiding principle here is that there is a critical force per molecule, above which degradation occurs. This critical force should be the value at which the curves of degradation rate meet the force axis.

We see in Figures 3 and 4 that the degradation curves do meet the force axis in a well-defined manner, supporting our expectations about the existence of a

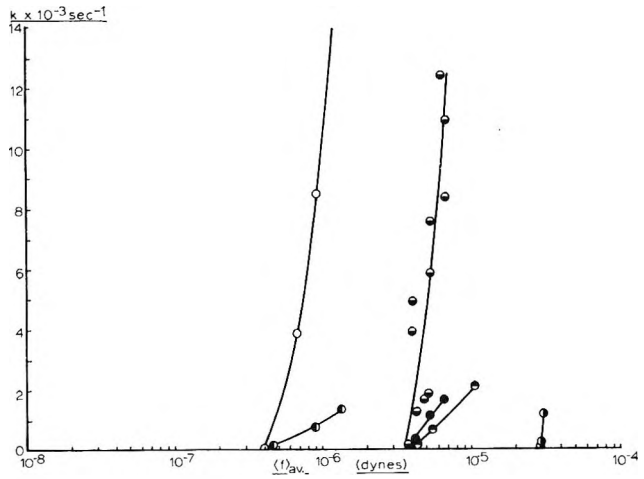

Figure 4. Degradation rate *vs.* average tensile stress, single pass data: ◒, polystyrene in toluene, capillary; O, polystyrene in methyl ethyl ketone, capillary; ●, polystyrene in α-methylnaphthalene, scored piston-cylinder apparatus; ◓, polystyrene in α-methylnaphthalene, capillary; ◐, polystyrene in diethyl phthalate, capillary; ◑, T2 bacteriophage DNA in BPES buffer, scored piston-cylinder apparatus.

critical force. The critical forces obtained from Figures 3 and 4 are in essential agreement for any given solvent; however, this force seems to vary over nearly a factor of 10 in going from one solvent to another.

The projected extension, z, for polystyrene in the two poor solvents, methyl ethyl ketone and diethyl phthalate, in which the intrinsic viscosity is similar, is taken as $3^{-1/2}$ times the r.m.s. end-to-end length from light-scattering studies on nonflowing solutions of the polymer in methyl ethyl ketone.[25,26] The extension for polystyrene in good solvents, toluene and α-methylnaphthalene, is estimated from the light-scattering data for the polymer in toluene and dichloroethane.[25] The viscosities of the solutions are taken to be the same at high shear as they are at low shear. These assumptions, which might be valid for ideal gaussian coils, are seriously in doubt when the molecules are extended to near their maximum lengths. We are, therefore, led to calculate the degree of extension under shear and to compare this to the contour lengths of the chains. This calculation is easily carried out in the following approximate way, which, though oversimplified, is sufficient to show the nature of the true situation.

The distribution function of the components, x, y, and z, of the end-to-end length of a gaussian coil is the function

$$W(x,y,z) = C \exp[-3(x^2 + y^2 + z^2)/2L^2] \quad (15)$$

where C is a constant and L is the r.m.s. end-to-end length. This is the distribution function of the coil in the undisturbed state. By a well-known theorem of statistical mechanics, the average force on the ends of the chain when it is stretched so that it has a component of length x along the x-axis is given by

$$\langle F \rangle_{av} = -kT \ln \left(\frac{\partial \ln W}{\partial x} \right) = -\frac{3kTx}{L^2} \quad (16)$$

The mean force per molecule, $\langle f \rangle_{av}$, which we have already estimated, is directed mainly along the streamlines under these extreme flow rates. We, therefore, insert it in place of $\langle F \rangle_{av}$ in eq. 16 and find x to be the calculated projected extension of a gaussian coil on the direction of flow. This quantity can then be compared with the contour length, l, the maximum possible extension of the real chain. The results are shown in Table VII, where the critical force intercepts from Figure 4 are used for $\langle f \rangle_{crit}$.

Table VII: Molecular Extensions Calculated from the Gaussian Formula Compared to the Contour Lengths of Polystyrene under Shear in Various Solvents. $\langle f \rangle_{crit}$ is the Limiting Breaking Force from the Intercepts of Figure 5; L is the r.m.s. End-to-End Length; x is the Component of Length on the Streamlines under Shear Calculated from Eq. 16; the Contour Length, l, is Estimated from the Molecular Weights Taken from Table III for the Appropriate Samples

Solvent	$\langle f \rangle_{crit}$	L	x	Mol. wt. × 10⁻⁶	l	x/l
Toluene	3.5×10^{-6}	0.74	1600	10.4	26	62
Methylnaphthalene	3.5×10^{-6}	0.74	1600	10.4	26	62
Methyl ethyl ketone	4.0×10^{-7}	0.28	26	3.72	9.3	2.8
Ethyl phthalate	4.0×10^{-7}	0.45	66	10.4	26	2.5

The results show that the calculated values of x are absurdly large, in all cases greater than the contour lengths. The last column of Table VII shows the ratio of x to l. Since the numbers all exceed 1, it is obvious that the gaussian coil model is no longer possible. In actual fact, eq. 16 is no longer valid when the coil is extended to near the contour length, so that the calculated values of x are fictitious. Correspondingly, the constancy of η and z that is found with gaussian coils is no longer to be expected.

(25) P. Outer, C. I. Carr, and B. H. Zimm, *J. Chem. Phys.*, **18**, 830 (1950).

(26) R. H. Boundy and R. F. Boyer, "Styrene, Its Polymers, Copolymers, and Derivatives," Reinhold Publishing Corp., New York, N. Y., 1952.

Unfortunately, there is no reliable theory with which one can use measurements at low rates of shear to calculate the force under conditions so extreme that the gaussian approximation breaks down. The measurement of z, and, to some extent, η under such conditions would pose serious technical problems. We must, therefore, conclude that there is little that we can do with existing measurements or theories to improve the accuracy of the critical forces calculated by means of eq. 12.

Having accepted these limitations, what then can be concluded from the results? In the first place, it appears that we have been able to rationalize the effect of solvent viscosity by the use of eq. 12. The critical forces found in the good solvents (toluene and α-methylnaphthalene) and in the poor solvents (methyl ethyl ketone and diethyl phthalate) are in each case unaffected by the large differences in the solvent viscosity. The important quantity is shear rate times viscosity, which is proportional to shear stress and, in the case of negligible kinetic energy, proportional also to the driving pressure. Thus, the degradation in methyl ethyl ketone and in diethyl phthalate is similar at the same driving pressure in spite of the 26-fold ratio of the viscosities.

Solvent power remains a variable that has a decided effect on the breaking force and one that is not well interpreted by our formalism. It is obvious from Table VII that the breaking situation in good solvents is very far from the region in which the gaussian statistics, on which eq. 12 is based, are valid. We might, thus, expect that the resulting critical breaking force should appear to be different from that calculated from the data on poor solvent systems, wherein gaussian statistics are more nearly obeyed. Even so, it is difficult to understand, on purely mechanical grounds, why it is necessary to force good solvent systems to higher shear rates in order to achieve the degradation rate found in poor solvent systems at lower shear rates and with lower specific viscosities. It is possible that the chemical nature of the solvent is important here; this point is discussed in more detail below. In any case, the absolute value of the critical force found in poor solvents should be more reliable since Table VII shows that gaussian statistics are much more nearly obeyed.

It is interesting that the degradation of the α-methylnaphthalene solution of polystyrene occurs at a greater rate for equivalent calculated molecular force in the scored piston apparatus than in the capillary. This is probably the result of the narrow annular gap and efficient mixing of the latter device. The same kind of result can be seen in Figure 2, where the falloff of molecular weight is shown for toluene solutions sheared in the capillary and in the disk, and for α-methylnaphthalene solutions in the unscored and scored piston devices. Thus, the experimental degradation rate "constant," a measure of the number of bonds broken per unit time, is dependent on the apparatus since the time that a polymer molecule spends in the region of strong shear is clearly a function of the apparatus. Although no fundamental significance can be attached to this constant, this fact in no way detracts from its utility as a relative measure of the degradation rate in the same apparatus.

A comparison can be made between the experimental critical molecular force for chain scission and the derivative at the inflection point of a theoretical potential energy function. Such an estimate has been given by Levinthal and Davison,[13] who calculate a maximum stretching force of 8.1×10^{-4} dyne for a single bond. This estimate is based upon a potential function due to Lippincott and Schroeder.[27] We see that the experimental critical stresses for polystyrene are at least one-hundredth of this theoretical estimate. It seems very unlikely that the experimental critical stresses can be a hundred times in error, especially since the errors to be expected from the known decrease of viscosity with shear rate should make them too high rather than too low. (This expectation is strengthened by the fact that the calculated critical stresses in the good solvents, where the theory is most greatly overextended, are the highest.)

It is tempting to think that the actual effect of the mechanical stress is to lower the activation energy of the thermal bond-breaking process; if this is the case, it is not necessary to assume that the mechanical stress is great enough to pull a bond to the inflection point in its potential curve. We believe that this interpretation is untenable for several reasons. In the first place, shearing experiments in the capillary, conducted over the temperature range from 15 to 45°, disclosed no evidence for a temperature dependence of the degradation process. Although such experiments should ideally span a greater range of temperature, this was not possible with the apparatus and polymer–solvent systems used here, and, in any case, a temperature dependence of the degradation process, if it exists, must be very small. Furthermore, the temperature at which thermal degradation of polystyrene becomes appreciable (the "ceiling temperature" of polymerization[28]) is about 276°C. or 549°K., about twice

(27) E. R. Lippincott and R. Schroeder, *J. Chem. Phys.*, **23**, 1131 (1955).

(28) F. G. Dainton and K. J. Ivin, *Trans. Faraday Soc.*, **46**, 331 (1950).

room temperature. In order for the degradation process to proceed at an appreciable rate at room temperature, the activation energy for carbon–carbon bond breakage would therefore have to be reduced by roughly a factor of 2. Using the Lippincott and Schroeder potential function,[27] the bond distance for the breaking carbon–carbon bonds in the polystyrene chain must be increased from Pauling's value[29] of 1.53 to almost 2.0 Å. in order to decrease the dissociation energy to one-half its maximum value. Since the bond extension corresponding to maximum tensile stress (*i.e.*, the inflection point on the potential energy curve) occurs at about 1.9 Å., it is clear that, if this potential function is correct, tensile stressing of the polymer chain cannot appreciably enhance the thermal degradation process. Finally, our average critical force values, which are two to three orders of magnitude smaller than the simple theoretical estimate, would result in a bond extension of less than 0.01 Å., with a corresponding reduction in the bond dissociation energy of less than 50 cal./mole, again estimated from the potential function used above.

We are inclined to think that the hydrodynamic chain-scission process is far more complicated than a simple stretching of a bond to the rupture point. It is likely that considerable solvent interaction with the reaction coordinate occurs, and that the estimated critical stress given by Levinthal and Davison,[13] while entirely valid for a gas-phase process, is not applicable here. This view is supported by the well-known fact that polystyrene in certain solvents, methyl ethyl ketone among them, tends to degrade spontaneously upon standing over a period of time. It is clearly necessary to study the shear degradation of model polymers in chemically distinct solvents, since, unfortunately, both our "good" solvents for polystyrene are aromatic hydrocarbons, and both "poor" solvents contain carbonyl groups. Other solvents of different chemical characteristics, such as chlorinated and cyclic hydrocarbons, nitro compounds, and others, must be examined.

Limiting Degradation of DNA. The hydrodynamic behavior of DNA is not as easily interpreted as that of a flexible, random-flight polymer such as polystyrene. High molecular weight native DNA shows anomalous viscosity behavior in many ways but, generally, seems to act as an easily distorted coil having unusually large statistical segment length.[30]

The limiting degradation behavior of native T2 bacteriophage DNA in the scored piston apparatus is given in Table V. Experimental values of parameters for various numbers of passes through the apparatus are averages, based upon several separate and identical runs. The experimental degradation rate k is calculated as with polystyrene, but, because of the extremely non-Newtonian flow behavior of DNA solutions, a serious uncertainty exists in the average tensile force. Nevertheless, the ratio η_{sp}/η_{rel} is fairly insensitive to shear rate even for DNA, and it is computed from experimental viscosity measurements at low shear. Average tensile force values were computed in which the mean extensions, z, were obtained from experimental light-scattering radii of gyration of calf thymus DNA compounds of different molecular weights.[30] Such data provide probably the most reasonable values of this parameter. The tensile forces are plotted against the experimental degradation rate in Figure 4, and the critical shear stress for DNA extrapolates to about 2.7×10^{-5} dyne on this basis. (The T2 bacteriophage DNA had an initial molecular weight of 130×10^6 as determined by autoradiographic methods.[31,32])

Levinthal and Davison[13] found good correlation between calculated and experimental critical shear stresses, where the latter were obtained by measurement of limiting flow conditions through a capillary, such that DNA, in dilute solution, could just be broken by chain scission. The theory used by these authors to calculate experimental stresses on the DNA molecule requires the *a priori* assumption that the molecule behaves as a rigid rod in a shear gradient. This assumption is generally at variance with the present work and with available viscosity data on high molecular weight DNA.[33–35] The fiber model experiments of Forgacs and Mason[21] have demonstrated that orientation of the major axis of a rod showing some flexibility may occur at angles considerably less than 45°, with respect to the direction of flow under conditions of severe tensile stress. There may be, in addition, severe bending at extreme shear rates; this can take the form of an S-shaped twist normal to the direction of flow, in which the molecule is bent sharply, but with most of its length at any given instant lying essentially parallel to the direction of solvent flow, and, associated with this, a torsional motion which at

(29) L. Pauling, "The Nature of the Chemical Bond," Cornell University Press, Ithaca, N. Y., 1960, p. 222.

(30) E. P. Geiduschek and A. Holtzer, *Advan. Biol. Med. Phys.*, **6**, 490 (1958).

(31) I. Rubenstein, C. A. Thomas, Jr., and A. D. Hershey, *Proc. Natl. Acad. Sci. U. S.*, **47**, 1113 (1961).

(32) P. F. Davison, D. Freifelder, R. Hede, and C. Levinthal, *ibid.*, **47**, 1123 (1961).

(33) D. M. Crothers, Thesis, University of California, San Diego, Calif., 1963.

(34) V. N. Schumaker and C. Bennett, *J. Mol. Biol.*, **5**, 384 (1962).

(35) J. Eigner, Thesis, Harvard University, Cambridge, Mass., 1960.

high shear rates manifests itself as helical twisting. One notes that torsional stresses of this type are not included in the theoretical estimate of Levinthal and Davison[13] for carbon–carbon bond rupture.

The calculation employed by Levinthal and Davison[13] to obtain an experimental critical stress for DNA differs from ours in a significant way. In their calculations, it was necessary to assume a molecular model and configuration (a rigid, solvent-impermeable rod, oriented at an angle of 45° to the streamlines of flow) and to estimate a frictional resistance per unit length based upon this model. Our eq. 12, on the other hand, is independent of model and requires as parameters, apart from the shear rate term common to both treatments, only the viscosity increment and z extensions of the polymer molecules. The considerable (10^2- to 10^3-fold) difference between the two calculations must therefore be due to inadequacies in Levinthal and Davison's molecular model and, consequently, in their frictional resistance term, and in our estimation of z. Although it is likely that the z extension is significantly reduced over the zero-shear value at the extreme shear rates employed here, this fact alone cannot possibly account for such a large discrepancy between the two calculations, and it is, therefore, virtually certain that the coiled configuration and solvent permeability of the DNA molecule are also important factors. The change of these characteristics with concentration may be the origin of the "self-protection effect" observed in DNA solutions by Burgi and Hershey.[36]

As is the case with polystyrene, a comparison of the experimental critical stress with a simple gas-phase calculation is interesting, but mainly serves to point up the complex nature of the degradation process. It would seem remarkable that DNA in aqueous solution could degrade without considerable interaction of water with the rupturing bond. If hydrolysis or incipient hydrolysis plays a significant role in the mechanical degradation of DNA, the theoretical estimate of 8.1×10^{-4} dyne for carbon–carbon bond scission in DNA given by Levinthal and Davison[13] may well be too large and represent only an upper limit to the true critical stress.

Degradation in High-Speed Homogenizers. Molecular weight falloff curves for various polymer solutions in laboratory homogenizers are given in Figure 1. Molecular force values are not directly calculated from the high-speed stirring data because of the uncertainty in the thickness of the boundary layer of fluid on the blades near the leading edges. Thus, the shear stress calculated assuming laminar flow in the boundary layer approaches infinity at the leading edge,[15,37] but the boundary layer thickness also decreases, with the result that shear stress will be maximum at a point near the leading edge.[37] However, this point will depend strongly upon the geometrical shape of the blade, and no attempt was made to calculate this quantity for an irregularly shaped blade, such as is used in the laboratory homogenizers.

In general, shearing in the Gifford–Wood Minimill was less rapid and less extensive than in either the Virtis homogenizer or the air turbine apparatus. This is undoubtedly due to the lower speed and smaller blade size of this machine. Apart from this, the degradation kinetics are similar, and molecular weight falloff is seen to increase, as expected, with blade speed and with solvent viscosity. In this connection, the most extensive degradation of polystyrene occurred in the high-viscosity, poor solvent, diethyl phthalate. Similarly, DNA was degraded more extensively in a 50% glycerol solution (with viscosity 5.7 times that of the buffer) at a blade speed of 8000 cm./sec. than in pure buffer at 10,000 cm./sec. The fact that DNA does not denature at glycerol concentrations of this magnitude has been reported by Duggan[38] and was verified separately for each sample here by observing the 259-mμ absorption maximum.

Conclusions

Full interpretation of these results is impossible without more exact information about the actual mechanical stress in the rapidly flowing solutions and about the dimensions of the chain molecules under these extreme conditions. The molecular nature of the process of bond breaking and the effect of solvent character thereon remain obscure. However, even with the use of information obtained at low shear rates, it has been possible to rationalize the effects of changing solvent viscosity and solute size.

Acknowledgment. The authors wish to acknowledge the assistance of Mr. John Emrich in obtaining much of the data pertaining to DNA and his help with much of the computational work. Thanks are also due to Dr. Donald M. Crothers for kindly supplying the T2 bacteriophage DNA used in this study.

(36) E. Burgi and A. D. Hershey, *J. Mol. Biol.*, **4**, 315 (1962).

(37) L. Prandtl and O. G. Tietjens, "Applied Hydro- and Aeromechanics," Dover Publications, Inc., New York, N. Y., 1934, p. 67.

(38) E. L. Duggan, *Biochem. Biophys. Res. Commun.*, **6**, 93 (1961).

The Kinetics of the Reaction between Vanadium(II) and Uranium(VI)[1]

by T. W. Newton and F. B. Baker

University of California, Los Alamos Scientific Laboratory, Los Alamos, New Mexico *(Received July 7, 1964)*

Uranium(VI) has been found to catalyze the reaction between V(II) and V(IV) in aqueous perchlorate solutions. The rate of the catalyzed reaction is limited by that of the reaction between V(II) and U(VI), the kinetics of which have been studied from 0.6 to 36.8°, from 0.05 to 2.0 *M* $HClO_4$, and from 0.08 to 2.0 *M* ionic strength. The only important term in the rate law is $k_1[V(II)][U(VI)]$. Values of ΔS^* and ΔH^* for this term are -26.1 ± 0.4 e.u. and 7.1 ± 0.1 kcal./mole at $\mu = 2.0$ *M* and -33.7 e.u. and 6.7 kcal./mole extrapolated to $\mu = 0$. Both chloride and sulfate ions catalyze the reaction.

Introduction

The reaction between V(II) and U(VI) has been studied for comparison with the analogous reactions between Cr(II) and U(VI)[2] and between Fe(II) and Pu(VI).[3] The oxidation potentials[4] in acid solution are such that when V(II) and U(VI) are mixed, the reaction

$$V(II) + U(VI) = V(III) + U(V) \quad (1)$$

can occur, followed by

$$V(II) + U(V) = V(III) + U(IV) \quad (2)$$

$$2U(V) = U(IV) + U(VI) \quad (3)$$

and

$$V(III) + U(V) = V(IV) + U(IV) \quad (4)$$

Reactions 2, 3, and 4 occur at rates which make it very difficult to determine the rate of (1) from the behavior of V(II)–U(VI) mixtures. In order to avoid this difficulty, reaction 1 was studied in the presence of an excess of V(IV) so that the U(V) is reoxidized

$$V(IV) + U(V) = V(III) + U(VI) \quad (5)$$

It is shown later in this paper that (5) is much faster than (2), (3), or (4), so that the over-all process may be described as the U(VI)-catalyzed reaction between V(II) and V(IV). The uncatalyzed reaction has been found to be relatively slow.[5]

Experimental

Reagents. The vanadium stock solutions were prepared and analyzed as before[5] except that equimolar amounts of V_2O_3 and V_2O_5 were dissolved in $HClO_4$ to give the V(IV) perchlorate. The U(VI) stock solution was prepared by the dissolution of pure U_3O_8 in fuming $HClO_4$ and recrystallization twice from water. It was analyzed by reduction to U(IV) and titration with standard Ce(IV). $La(ClO_4)_3$ was prepared by fuming the nitrate (A. D. MacKay, Inc.) with $HClO_4$ and recrystallizing three times from water. Total ClO_4^- was determined by the use of a cation-exchange resin and the free acid was determined by titration after removing the La^{+3} as the oxalate. The water and the solutions of $HClO_4$, $LiClO_4$, and $NaClO_4$ were prepared and analyzed as before.[3] The concentration units are moles per liter, *M*, at 23°.

Procedure. The reaction was followed spectrophotometrically at 7600 Å. where the absorption is due primarily to V(IV). Appropriate amounts of U(VI), V(IV), salt, and acid were brought to temperature in stirred absorption cells which were positioned in a small water-filled thermostat in the light beam of the Cary recording spectrophotometer, Model 14.[5] The reaction was started by injecting a solution of V(II) by means of a hypodermic syringe with a Teflon needle.

Catalytic Impurities. The use of $LiClO_4$, $NaClO_4$, $La(ClO_4)_3$, or $UO_2(ClO_4)_2$, which had been given an

(1) Work done under the auspices of the U. S. Atomic Energy Commission.

(2) T. W. Newton and F. B. Baker, *Inorg. Chem.*, **1**, 368 (1962).

(3) T. W. Newton and F. B. Baker, *J. Phys. Chem.*, **67**, 1425 (1963).

(4) W. M. Latimer, "Oxidation Potentials," 2nd Ed., Prentice-Hall, Inc., New York, N. Y., 1952.

(5) T. W. Newton and F. B. Baker, *J. Phys. Chem.*, **68**, 228 (1964).

additional recrystallization, gave essentially the same rates as were obtained by the use of the reagents described above. Zn(II) at a concentration 30 times that ordinarily introduced with the V(II) was found to be without effect on the rate. Oxygen from the air can increase the rate by as much as 10%, so all solutions and absorption cells were thoroughly swept with purified argon before and during the runs.

Results

Stoichiometry. No spectrophotometrically detectable U(IV) is formed during the U(VI)-catalyzed reaction between V(II) and V(IV). This was shown in experiments at 23° in which the initial concentrations ranged from (1.5 to 4.0) $\times 10^{-3}$ *M* V(II), (3.0 to 4.2) $\times 10^{-3}$ *M* V(IV), (3.5 to 4.1) $\times 10^{-3}$ *M* U(VI), and 0.05 to 1.9 *M* $HClO_4$ in solutions with ionic strength of 2.0. These results show that reactions 2, 3, and 4 are unimportant with respect to reaction 5.

The stoichiometry of the reaction in the absence of V(IV), however, is not in accord with the simple equation

$$U(VI) + 2V(II) = U(IV) + 2V(III) \quad (6)$$

Spectrophotometric analyses for U(IV) and V(IV) after the completion of the reaction in the presence of excess U(VI) showed that the ratio of moles of U(IV) produced to moles of V(II) added is greater than 0.5. Values of the ratio obtained from solutions with $\mu = 2.0$ *M* ($LiClO_4$) at 23° which were 1.0, 0.2, and 0.05 *M* in $HClO_4$ were 0.50, 0.53, and 0.68, respectively. Increasing the concentration of V(III) was found to increase the ratio. These results indicate that reaction 4 becomes competitive with reaction 3 at low acid concentrations.

Evidence has been found for a very slow reaction between V(III) and U(VI); the apparent second-order rate constant was found to be about 3 $\times 10^{-4}$ M^{-1} sec.$^{-1}$ at room temperature in a solution which was 1 *M* $HClO_4$, 0.1 *M* U(VI), and 0.02 *M* V(III). This reaction is too slow to have any effect on the rate of the U(VI)-catalyzed reaction between V(II) and V(IV).

Since the reactions between Cr(II) and U(VI)[2] and between Fe(II) and Pu(VI)[3] have been shown to involve binuclear intermediates, it was of interest to see whether evidence could be found for a similar intermediate in the present reaction. In both 0.1 and 1.0 *M* $HClO_4$, the rate of formation of U(IV), in the absence of V(IV), was essentially the same whether Eu(II) or V(II) was added to an excess of U(VI). Since U(V) is produced when U(VI) is reduced by Eu(II), this observation indicates that if an intermediate is formed in reaction 1, it reacts rather quickly to give U(V), or that by an unlikely coincidence the rates of disproportionation of U(V) and of the intermediate are essentially the same.

The Rate Law. Absorbance *vs.* time data for all the rate runs were in close agreement with the rate law

$$-d[V(IV)]/dt = -d[V(II)]/dt = k_0[V(II)][V(IV)] + k_1[V(II)][U(VI)] \quad (7)$$

The k_0 and k_1 terms apply to the uncatalyzed and catalyzed paths, respectively. The procedure used in testing this rate law and in determining k_1 was the following. Equation 7 was integrated to give

$$A = \frac{A_\infty(k_0b + k_1c)(1 - \exp\{[k_0(b - a) + k_1c]t\}) - A_0[k_0(b - a) + k_1c]}{k_0a - (k_0b + k_1c)\exp\{[k_0(b - a) + k_1c]t\}} \quad (8)$$

where A, A_0 and A_∞ are the absorbance values at time t, time zero, and infinite time, respectively, and a, b, and c are the initial concentrations of V(II), V(IV), and U(VI). A nonlinear least-squares program for the IBM 7094[6] was used to find the best values of k_1 for each set of data. The values used for a, b, and c were calculated from the amounts and concentrations of the stock solutions, values for k_0 were from the previous work,[5] and A_0 and A_∞ were computed by the program. Data were taken until the reaction was at least 98% complete and were reproduced by eq. 8 with an average root-mean-square deviation of 0.0013.

Rate law 7 was further tested by varying the U(VI) and V(IV) concentrations widely. The results of these experiments are summarized in Tables I and II. The data in Table I show that k_1 is essentially independent of the U(VI) concentration from 5 $\times 10^{-5}$ *M* to 1 $\times 10^{-3}$ *M*, in accord with (7). Except at the lowest concentrations of U(VI), the k_0 term in (7) amounts to a minor correction; at 10^{-4} *M* U(VI),

Table I: The Dependence of k_1 on the U(VI) Concentration. Conditions: 25°, 1 *M* $HClO_4$, $\mu = 2.0$ *M* ($LiClO_4$), 0.0020 *M* V(II), 0.00255 *M* V(IV), $k_0 = 1.6$ M^{-1} sec.$^{-1}$

[U(VI)] $\times 10^4$, *M*	0.50	1.00	2.51	3.52	5.02	10.04
k_1, M^{-1} sec.$^{-1}$	65.2	71.2	71.0	71.3	71.2	70.9
	69.9	71.2	71.9	72.9	74.1	72.5

(6) We are indebted to R. H. Moore in the Statistical Section of the Laboratory for writing this program. It is based on R. H. Moore and R. K. Zeigler, Los Alamos Scientific Laboratory Report, LA-2367, Oct. 15, 1959, available from Office of Technical Services, U. S. Department of Commerce, Washington, D. C.; $2.25.

decreasing the value assumed for k_0 by 6% increased the calculated value of k_1 by 2.5%; the corresponding figure for 10^{-3} M U(VI) is 1.4%.

Table II: The Dependence of k_1 on the V(IV) Concentration. Conditions: 25°, 1 M $HClO_4$, μ = 2.0 M ($LiClO_4$), 0.0015 M V(II), 0.00116 M U(VI)

[V(IV)] × 10^3, M (initial)	1.64	3.29	4.93	6.47	8.22
k_1, M^{-1} sec.$^{-1}$	71.1	71.5	73.8	73.6	76.5
	72.7	73.2	74.4	76.2	76.4
	73.3				75.0
$k_{1\,calcd}$[a]	72.0	74.1	74.5	74.7	74.9

[a] Calculated using eq. 9 with k_1 = 75.3 M^{-1} sec.$^{-1}$ and k_1/k_5 = 0.054.

The data in Table II show that k_1 probably depends slightly on the V(IV) concentration. This dependence is readily explained in terms of eq. 1 and 5. The steady-state concentration of U(VI) should be less than the stoichiometric value and the apparent value of k_1 is given by

$$k_{1\,obsd} = k_1(1 + k_1[V(II)]/k_5[V(IV)])^{-1} \quad (9)$$

where k_5 is the rate constant for eq. 5. The data in the table are not inconsistent with this expression and indicate that the [V(II)]/[V(IV)] ratios used in most of the other experiments lead to apparent k_1 values which are several per cent low.

The reaction product, V(III), was found to have essentially no effect on the rate. Substitution of 0.01 M V(III) for 0.01 M La(III) at a constant ionic strength of 2.0 M at 25° leads to a reduction in the rate constant of only 2.8%. This difference is within the experimental error, so it has been concluded that the concentration of V(III) is not involved in the rate law.

Hydrogen Ion and Temperature Dependences. Rate constants were determined at seven hydrogen ion concentrations ranging from 0.05 to 2.0 M and at four temperatures from 0.6 to 36.8°. Although the hydrogen ion dependence is very small, the data were fit to the empirical equation

$$k_{1\,obsd} = A + B[H^+] + C[H^+]^{-1} \quad (10)$$

The values of the parameters and their standard deviations were determined by least squares and are summarized in Table III.

These results show that the B and C terms are relatively small and usually not significant statistically.

Chloride Ion Dependence. The rate constant, k_1, was determined as a function of chloride ion concentration at 0.6 and at 25.1°. The results are summarized in Table IV. Values for k_0 were obtained from the previous work.[5]

Table III: Hydrogen Ion and Temperature Dependences; μ = 2.0 M ($LiClO_4$)

Temp., °C.	No. of points	A,[a] M^{-1} sec.$^{-1}$	Std. dev.	B, M^{-2} sec.$^{-1}$	Std. dev.	C, sec.$^{-1}$	Std. dev.
0.6	14	22.8	0.15	0.315	0.13	0.0044	0.012
13.7	14	42.3	.4	.78	.32	.033	.032
25.1	14	73.0	.8	.80	.63	.25	.06
36.8	14	121.0	1.55	1.24	1.27	.15	.11

[a] The values of the parameters and the standard deviations were determined by least squares.

Table IV: Effect of Chloride Concentration on k_1, 1.0 M Acid, μ = 2.0 ($LiClO_4$)

0.6°			25.1°		
[Cl$^-$], M	$k_{1\,obsd}$, M^{-1} sec.$^{-1}$	$k_{1\,calcd}$,[a] M^{-1} sec.$^{-1}$	[Cl$^-$], M	$k_{1\,obsd}$, M^{-1} sec.$^{-1}$	$k_{1\,calcd}$,[b] M^{-1} sec.$^{-1}$
0.000	22.6, 22.7	22.5	0.000	72.6, 73.0, 74.0	73.3
.190	27.1, 27.5	27.6	.192	97.3, 100	99
.380	32.2, 32.5	32.2	.383	123, 124	122
.570	36.2, 36.5	36.4	.575	143, 142	144
.759	39.3, 41.1	40.1	.766	167, 162	164
.949	43.3, 44.0	43.7	.958	181, 184, 187	180

[a] Calculated using k_1 = (22.5 + 39.2[Cl$^-$] + 3.6[Cl$^-$]^2)·(1 + 0.465[Cl$^-$])$^{-1}$. [b] Calculated using k_1 = (73.3 + 206.7·[Cl$^-$] + 73.7[Cl$^-$]^2)(1 + 0.88 [Cl$^-$])$^{-1}$.

Table V: The Effect of Sulfate Concentration on k_1, 25.1°, $\mu \cong 0.8$ M

No.	[H_2SO_4], M	[$HClO_4$], M	[Na-ClO_4], M	[H^+], M	[HSO_4^-], M	[SO_4^{-2}],[a] M	k_1,[b] M^{-1} sec.$^{-1}$
1	0.00	0.467	0.298	0.467	0.00	0.00	40.5
2	.0055	.467	.298	.473	.00455	.00096	137
3	.0110	.774	.238	.786	.0098	.0012	186[c]
4	.0220	.467	.298	.493	.018	.004	388

[a] Concentrations of H^+, HSO_4^-, and SO_4^{-2} were calculated under the assumption that K_a of HSO_4^- is 0.1 M. [b] k_0 from ref. 5. [c] For this run, $\mu \cong 1.0$ M.

Sulfate Ion Dependence. A rather large effect of sulfate was found in a short series of experiments which are summarized in Table V. Plots of the value of k_1 from runs 1, 2, and 4 *vs.* [HSO_4^-] and *vs.* [SO_4^{-2}] were both nearly linear, while the point from run 3

Table VI: Ionic Strength Dependence; 25.1°, 0.05 *M* $HClO_4$

$LiClO_4$ solutions			$NaClO_4$ solutions			$La(ClO_4)_3$ solutions		
μ, *M*	k_1 obsd, M^{-1} sec.$^{-1}$	k_1 calcd,[a] M^{-1} sec.$^{-1}$	μ, *M*	k_1 obsd, M^{-1} sec.$^{-1}$	k_1 calcd,[a] M^{-1} sec.$^{-1}$	μ, *M*	k_1 obsd, M^{-1} sec.$^{-1}$	k_1 calcd,[a] M^{-1} sec.$^{-1}$
0.073	12.7	12.9	0.073	12.7	12.6	0.081	13.2	12.3
	12.6			12.7			13.2	
.190	19.8	19.8	.190	19.3	19.0	.281	19.2	20.1
	19.7		.200	19.9	19.4		19.9	
.384	27.2	27.7	.385	26.1	26.0	.480	25.0	25.1
	28.5		.410	26.7	26.8		25.0	
.656	35.9	36.4	.658	33.2	33.2	.879	32.4	33.2
	36.9		.706	33.7	34.4		32.6	
1.04	48.0	47.3	1.05	41.4	41.7	1.28	39.9	40.4
	46.7		1.13	42.0	43.3		40.8	
1.34	55.2	55.3	1.44	49.8	49.4	1.68	48.3	47.7
1.43	58.3	57.8	1.55	52.4	51.5		47.6	
2.02	75.0	74.4	2.02	59.6	60.6	2.08	56.1	55.4
	73.1		2.18	65.0	63.7		55.6	

[a] Calculated using eq. 18 and the values of the parameters in Table VII with log k_1^0 fixed.

(higher acid and higher ionic strength) fell 28.5% below the former plot and 16% above the latter. Since correction for the ionic strength difference should bring the value for run 3 closer to the plot *vs.* $[SO_4^{-2}]$ and farther from the plot *vs.* $[HSO_4^-]$, it has been concluded that the rate is essentially independent of the concentration of HSO_4^-.

Ionic Strength Dependence. The effect of ionic strength on the rate constant was investigated at 25.1° in $LiClO_4$, $NaClO_4$, and $La(ClO_4)_3$ solutions; the results are summarized in Table VI. Additional short series of runs in $LiClO_4$ and $NaClO_4$ solutions at 0.1° are summarized in part II of Table VII.

Discussion

The Net Activation Process. The observed rate law (7) and the fact that the hydrogen ion dependence of k_1 is essentially zero indicate that the principal net activation process is

$$UO_2^{+2} + V^{+2} = (UO_2 \cdot V^{+4})^* \qquad (11)$$

Values of ΔS^* and ΔH^* for this process were computed under various assumptions with respect to B and C, the minor terms in (10). First, B and C were ignored completely so that $k_{1\,obsd} = A$, and it was assumed that

$$k_1 = (k_B/h)T \exp(\Delta S^*/R) \exp(-\Delta H^*/RT) \qquad (12)$$

according to Eyring's absolute reaction rate theory. A least-squares procedure based on per cent deviations was used to find that $\Delta S^* = -25.85$ e.u. (cal. mole^{-1} deg^{-1}), std. dev. = 0.10, and $\Delta H^* = 7.20$ kcal./mole, std. dev. = 0.03. These parameters reproduce the experimental data with a root-mean-square deviation of 2.63%.

In an alternate calculation, the temperature dependences of the apparent rate constants, B and C, were also assumed to have the form of (12) and the data were used in a least-squares procedure for the simultaneous determination of all six parameters.[6] The use of six rather than two parameters reduced the root-mean-square deviation slightly to 2.47%. The values of the parameters for the two minor terms are probably without physical significance, but those for the major term are essentially the same as before: $\Delta S^* = -26.21$ e.u. and $\Delta H^* = 7.10$ kcal./mole.

This discussion and a correction for the small systematic error mentioned in connection with the V(IV) dependence lead us to the following values for process 11: $\Delta S^* = -23.1 \pm 0.4$ e.u. and $\Delta H^* = 7.1 \pm 0.1$ kcal./mole. Taking $S^0_{UO_2^{+2}}$ to be -17 e.u.[4] and estimating $S^0_{V^{+2}}$ to be -23 e.u., we calculate -66 e.u. for the formal ionic entropy of the activated complex. This value is in good agreement with those found for other activated complexes with a +4 charge.[3,5,7]

Since no evidence was found for a binuclear intermediate, it cannot be stated whether the activated

(7) N. A. Daugherty and T. W. Newton, *J. Phys. Chem.*, **67**, 1090 (1963).

Table VII: Ionic Strength Dependence; Parameters in Eq. 18

Salt	log k_1^0	D, $M^{-1/2}$	E, M^{-1}	R.m.s. dev., %[a]	
		Part I: 25.1°, α = 0.5092 M^{-1}			
$LiClO_4$	0.4651 ± 0.0082[b]	2.737 ± 0.053	0.1094 ± 0.0063	1.3	Best values
$NaClO_4$	.4913 ± 0.0109	2.988 ± 0.077	.0952 ± 0.0079	1.7	Best values
$La(ClO_4)_3$	.5488 ± 0.0132	3.809 ± 0.121	.1437 ± 0.0072	1.6	Best values
$LiClO_4$	.4756	2.801	.1159	1.4	log k_1^0 fixed
$NaClO_4$	.4756	2.877	.0836	1.6	log k_1^0 fixed
$La(ClO_4)_3$	.4756	3.230	.1105	3.3	log k_1^0 fixed
		Part II: 0.1°, α = 0.488 M^{-1}			
$LiClO_4$	−0.0153 ± 0.0023	2.606 ± 0.014	0.0988 ± 0.0018	0.2	Best values
$NaClO_4$	+0.0081 ± 0.0082	2.780 ± 0.055	.0776 ± 0.0061	0.7	Best values
$LiClO_4$	−0.01022	2.637	.1020	0.3	log k_1^0 fixed
$NaClO_4$	−0.01022	2.667	.0667	1.0	log k_1^0 fixed

[a] Root-mean-square per cent deviation between observed and calculated rate constants. [b] The uncertainties listed are the standard deviations calculated by the least-squares program.

complex shown in (11) is inner-sphere or not. It is interesting, however, that the value for $S^0_{complex}$ is in excellent agreement with that for the inner-sphere complex found in the Fe^{+2}–PuO_2^{+2} reaction.[3]

Chloride Ion Dependence. The data in Table IV show that 1 M Cl^- more than doubles the rate of the V(II)–U(VI) reaction at 25°. A quantitative interpretation requires that account be taken of the Cl^- complexing of the reactants. For UO_2^{+2} we have used the data of Day and Powers[8]; complexing between V^{+2} and Cl^- is expected to be less important and has been neglected. The data are consistent with the expression

$$k_{1\,obsd} = (k_1 + k_1'[Cl^-] + k_1''[Cl^-]^2)(1 + \beta[Cl^-])^{-1} \quad (13)$$

where $\beta = [UO_2Cl^+]/[UO_2^{+2}][Cl^-] = 0.88\ M^{-1}$ at 25° and 0.465 M^{-1} extrapolated to 0.6°. This rate law suggests paths involving one and two Cl^- in the activated complexes. This result is to be contrasted with that for the Sn(II)–Pu(VI) reaction where paths involving three and four Cl^- were the only ones found.[9]

The observed data, k_1 *vs.* $[Cl^-]$ and temperature, were treated by least squares to obtain the following values for the thermodynamic quantities of activation

$$UO_2^{+2} + V^{+2} + Cl^- = (UO_2 \cdot V \cdot Cl^{+3})^*;$$
$$\Delta S^* = -12.4 \pm 1 \text{ e.u.}; \ \Delta H^* = 10.6 \pm 0.3 \text{ kcal./mole} \quad (14)$$

$$UO_2^{+2} + V^{+2} + 2Cl^- = (UO_2 \cdot V \cdot 2Cl^{+2})^*;$$
$$\Delta S^* = 11 \pm 8 \text{ e.u.}; \ \Delta H^* = 18.1 \pm 2.4 \text{ kcal./mole} \quad (15)$$

The indicated uncertainties are the standard deviations. The actual uncertainties are greater than the statistical ones since medium effects are included in the k_1' and k_1'' terms. Subtracting (11) from (14) gives

$$(UO_2 \cdot V^{+4})^* + Cl^- = (UO_2 \cdot V \cdot Cl^{+3})^*;$$
$$\Delta S^* = 14 \text{ e.u.}; \ \Delta H^* = 3.5 \text{ kcal./mole} \quad (16)$$

It is interesting to compare this with the analogous process

$$UO_2^{+2} + Cl^- = UO_2Cl^+; \ \Delta S = 12 \text{ e.u.};$$
$$\Delta H = 3.8 \text{ kcal./mole}^8 \quad (17)$$

The agreement between these sets of heat and entropy values suggests that the Cl^- does not play a special role in the activated complex.

The effect that Cl^- has on a reaction rate is expected to depend on whether it is in (a) a ligand position of an inner-sphere activated complex, least effect, (b) a ligand position of an outer-sphere activated complex, or (c) a bridging position in an inner-sphere activated complex, largest effect.[10,11] In the present reaction $k_1'/k_1 = 2.6$, a value small enough to make (c) unlikely, although a distinction between (a) and (b) is not possible on this basis.

Ionic Strength Dependence. Rates in solutions of $LiClO_4$, $NaClO_4$, or $La(ClO_4)_3$ with ionic strengths ranging from about 0.08 M to about 2.0 M are con-

(8) R. A. Day, Jr., and R. M. Powers, *J. Am. Chem. Soc.*, **76**, 3895 (1954).

(9) S. W. Rabideau and B. J. Masters, *J. Phys. Chem.*, **65**, 1256 (1961).

(10) A. Zwickel and H. Taube, *J. Am. Chem. Soc.*, **83**, 793 (1961).

(11) G. Dulz and N. Sutin, *ibid.*, **86**, 829 (1964).

sistent with an extended form of the Debye–Hückel equation

$$\log k_1 = \log k_1^0 + \frac{\alpha \Delta z^2 \mu^{1/2}}{1 + D\mu^{1/2}} + E\mu \qquad (18)$$

For each set of data a least-squares procedure was used to find best values for the three parameters, log k_1^0, D, and E. A value of α appropriate to the temperature[12] was used and Δz^2 was taken as 8. The results of these calculations are summarized in Table VII. Ideally, the log k_1^0 terms should be independent of the added salt; actually small differences were found. This is probably due in part to inadequacy of (18) and in part to the fact that the points at the lowest ionic strengths contain no added salt.

Recalculations were made in which log k_1^0 was fixed at the weighted average of the $LiClO_4$ and $NaClO_4$ values. The best values then found for the other parameters are shown in Table VII. These alternative values reproduce the data less well than the best values but the root-mean-square per cent deviations show that the fit is still satisfactory.

The $La(ClO_4)_3$ results show that the rate depends primarily on the ionic strength and not on the concentration of the ion of opposite sign, the $[ClO_4^-]$. This provides an example counter to the recent generalization that for reactions between ions of like sign, a Debye–Hückel equation in terms of ionic strength is usually inapplicable and that it is the concentration of ions of opposite sign which is important.[13]

Thermodynamic quantities of activation applicable at zero ionic strength were calculated from the averaged log k_1^0 values given in Table VII; the results are: $\Delta S_0^* = -33.7$ e.u., a decrease of 7.6 e.u., and $\Delta H_0^* =$ 6.7 kcal./mole, a decrease of 0.4 kcal./mole.

Acknowledgment. The authors wish to acknowledge many helpful discussions with Dr. J. F. Lemons, under whose general direction this work was done.

(12) R. A. Robinson and R. H. Stokes, "Electrolyte Solutions," Butterworth and Co., Ltd., London, 1955.

(13) B. Perlmutter-Hayman and G. Stein, *J. Chem. Phys.*, **40**, 848 (1964).

Investigation of the Colloidal Hydrated Calcium Silicates. II.

Solubility Relationships in the Calcium Oxide–Silica–Water System at 25°

by S. A. Greenberg[1] and T. N. Chang

Portland Cement Association, Skokie, Illinois *(Received July 10, 1964)*

The solubilities of reaction mixtures of calcium oxide, silica, and water, and hydrated tricalcium silicate in water were investigated. It was concluded from the results that several solid phases exist in the system $CaO–SiO_2–H_2O$ at 25°: (1) silica and silica that has partially reacted with calcium hydroxide at $CaO–SiO_2$ mole ratios less than 0.14, (2) partially reacted silica and CaH_2SiO_4 at mole ratios between 0.14 and 1, (3) CaH_2SiO_4 with varying amounts of calcium hydroxide dissolved in it for over-all $CaO–SiO_2$ mole ratios greater than 1, and (4) $CaH_2SiO_4 \cdot nCa(OH)_2$ and calcium hydroxide at over-all $CaO–SiO_2$ ratios above about 1.75. The evidence for a phase $Ca(H_3SiO_4)_2$ is not conclusive. The solubility product for CaH_2SiO_4 and the ratio of the activity of the calcium hydroxide dissolved in CaH_2SiO_4 (in moles of calcium hydroxide per mole of CaH_2SiO_4) to that in the solution are constants which describe the system in the $CaO–SiO_2$ mole ratio range 1–1.75.

Introduction

The hydrated calcium silicates are the colloidal products of the reaction of mixtures of calcium oxide, silica, and water, and of the hydration of the tricalcium and dicalcium silicates found in portland cement.[2] These poorly crystallized products are the chief cementing agents in concrete and lime–silica products.[3] Although a great deal of information about the structures and solubilities of these substances has been reported, their physicochemical natures are not completely understood.[4–8] Brunauer[9] has recently written an excellent review of the subject.

In a previous investigation of this series,[10] it was demonstrated that, in spite of the colloidal nature of the products in the $CaO–SiO_2$ mole ratio range 1–1.5, the solubility of reaction mixtures of calcium oxide, silica, and water could be explained by the reactions

$$CaH_2SiO_4(c) + nH_2O(l) = Ca^{+2}(aq) + H_2SiO_4^{-2}(aq) \quad (1)$$

$$CaH_2SiO_4(c) + nCa^{+2}(aq) + 2nOH^-(aq) = CaH_2SiO_4 \cdot nCa(OH)_2(c) \quad (2)$$

For the reaction in eq. 1 the constant K_{sp_1} equal to $a_{Ca^{+2}}a_{H_2SiO_4^{-2}}$ was found to be 10^{-7}. The constant for eq. 2 was not evaluated. However, eq. 2 was necessary to explain the difference in compositions of the aqueous and solid phases. Evidence for a phase $Ca(H_3SiO_4)_2$ was not conclusive.

The present investigation was conducted to evaluate the constant for eq. 2 and to examine the factors that control solubility in the $CaO–SiO_2–H_2O$ system for $CaO–SiO_2$ mole ratios less than 1 and above about 1.75.

Experimental

The hydrated calcium silicate products were produced by two methods. First, mixtures of silica gel and water with increasing amounts of calcium oxide were allowed

(1) Mechrolab, Inc., Mountain View, Calif.

(2) For review, see S. Brunauer and S. A. Greenberg, Proceedings of the Fourth International Symposium on the Chemistry of Cements, Washington, D. C., 1960, Vol. I, p. 135.

(3) J. D. Bernal, J. W. Jeffery, and H. F. W. Taylor, *Mag. Concrete Res.*, **11**, 49 (1952).

(4) H. H. Steinour, *Chem. Rev.*, **40**, 391 (1947).

(5) H. H. Steinour, *Proc. Intern. Symp. Chem. Cements, 3rd, London*, 261 (1952).

(6) H. F. W. Taylor, *J. Chem. Soc.*, 3682 (1950).

(7) G. L. Kalousek, *Proc. Intern. Symp. Chem. Cements, 3rd, London*, 296 (1952).

(8) E. P. Flint and L. S. Wells, *J. Res. Natl. Bur. Std.*, **12**, 751 (1934).

(9) S. Brunauer, *Am. Scientist*, **50**, 210 (1962).

(10) S. A. Greenberg, T. N. Chang, and E. Anderson, *J. Phys. Chem.*, **64**, 1151 (1960).

Table I: Compositions of the Aqueous Phases (CaO, SiO_2, and H_2O Reaction Mixtures)

Expt. no.	pH	$(Ca)_F$, moles/l. $\times 10^3$	$(SiO_2)_F$, moles/l. $\times 10^3$	$(CaO:SiO_2)_L$	$(CaO:SiO_2)_S$	$(Ca(OH)_2)_I$, moles/l.	pK_{sp_2}	pK_{sp_1}	pK_{sp_3}	log C_S/a_L	log M_S/a_L
a	7.06	0.11	1.65	0.067	~0	0.0001	...	..	...	...	...
b	9.32	0.74	2.31	0.32	0.054	0.008	...	..	...	..	...
c	9.16	0.93	2.60	0.36	0.067	0.01	...	..	...	..	...
d	9.65	1.47	3.40	0.43	0.14	0.02	...	..	...	...	...
						Initial CaO, g.					
1	9.75	1.68	4.33	0.39	0.23	0.1764	8.29	7.62	11.40	..	10.76
2	9.80	1.90	4.07	0.47	0.32	0.2428	8.26	7.53	11.25	..	10.76
3	9.98	1.95	3.90	0.50	0.41	0.3092	8.14	7.28	10.88	..	10.50
4	10.02	1.97	3.87	0.51	0.43	0.3756	8.11	7.23	10.79	..	10.43
6	10.26	2.00	3.77	0.53	0.68	0.5084	8.28	7.07	10.31	..	10.14
7	10.48	1.75	1.47	1.19	0.76	0.5748	8.81	7.14	9.92	..	9.80
9	11.40	2.13	0.253	8.42	0.93	0.7076	10.24	7.39	8.01	..	7.97
10	11.77	3.90	0.090	43.3	1.01	0.7740	11.56	7.07	7.04	5.04	4.63
11	11.92	5.28	0.062	85.2	1.08	0.8404	11.12	7.15	6.64	5.05	4.06
12	11.90	4.71	0.065	73.0	1.17	0.9068	11.95	7.11	6.72	5.10	4.39
13	11.95	5.72	0.043	132	1.25	0.9732	12.32	7.21	6.55	5.10	4.31
14	12.10	7.42	0.029	258	1.33	1.040	13.04	7.28	6.16	5.07	4.03
15	12.10	6.45	0.033	199	1.43	1.106	10.77	7.26	6.21	5.08	4.02
16	12.14	9.42	0.022	434	1.49	1.172	11.11	7.33	6.00	5.07	3.98
17	12.16	10.50	0.025	425	1.57	1.239	13.07	7.28	5.94	5.07	3.96
18	12.25	15.00	0.018	833	1.63	1.305	12.43	7.30	5.62	5.04	3.80
19	12.40	18.50	0.015	1233	1.69	1.372	12.83	7.32	5.26	5.10	3.53
20	12.33	16.40	0.016	1025	1.79	1.438	12.64	7.31	5.44	5.03	3.66

Table II: Compositions of the Aqueous Phases (Hydrated Tricalcium Silicate)

Sample no.	pH	$(Ca)_F$, moles/l. $\times 10^3$	$(SiO_2)_F$, moles/l. $\times 10^5$	$(CaO:SiO_2)_S$	Reactants: Hyd. trical. silicate, g.	Reactants: Water, g.	pK_{sp_1}	pK_{sp_3}	log C_S/a_L
1	12.46	19.3	0	2.47	1.0054	100	..	5.13	5.30
2	12.60	19.2	0	2.33	0.7926	100	..	4.85	4.97
3	12.45	19.2	0.66	2.12	0.6028	100	7.63	5.15	5.20
4	12.50	18.3	1.67	1.75	0.8087	200	7.27	5.07	4.95
5	12.46	14.5	0.83	1.68	0.9039	300	7.62	5.22	5.05
6	12.40	10.0	7.49	1.65	0.8070	400	6.78	5.46	5.27

to react. Second, samples of completely hydrated tricalcium silicate were added in decreasing quantities to water to produce solids with decreasing CaO–SiO_2 ratios in equilibrium with the aqueous phases. This procedure of approaching a steady-state composition of solid and aqueous phases from two directions was considered a reasonable test for equilibrium.

Materials. For this study Standard Luminescent grade (S.L.) silica obtained from the Mallinckrodt Chemical Co., St. Louis, Mo., was employed. This is chemically pure (>99.9% SiO_2 on ignited basis) silica with a water content of 19.5% and a nitrogen surface area of 820 $m.^2/g.$ of anhydrous silica.[11] The calcium oxide was prepared by a 2-hr. ignition at 1050° of Baker A.R. calcium carbonate (56.5% CaO).

The sample of hydrated tricalcium silicate was prepared by hydration of a tricalcium silicate suspension (0.7 g. of water/g. of tricalcium silicate) for 400 days at 25°. The ignition loss of the sample was 17.26% and the free calcium hydroxide was 31.30% after the sample was vacuum dried at the vapor pressure of ice at −78° which is 10^{-4} mm.[9]

Procedures. Experiments a through d (Table I) were conducted with 100-ml. solutions of calcium hy-

(11) S. A. Greenberg, *J. Phys. Chem.*, **60**, 325 (1956).

droxide in the range of concentration 1×10^{-4} to 2×10^{-2} M (column 7, Table I) to which 1 g. of S.L. silica was added in each case. The mixtures were equilibrated at 25° for 90 days in rotated polyethylene bottles. For the remainder of the experiments (1–20, Table I) the mixtures contained 1 g. of S.L. silica (0.805 g. of SiO_2), 100 ml. of water, and calcium oxide additions of 0.1764 to 1.438 g. (column 7, Table I). The mixtures were placed in polyethylene bottles and rotated at 50° for 50 days. Then the samples were equilibrated at 25° for 34 days. The suspensions were filtered in a carbon dioxide-free box. . The solutions were analyzed for calcium and silicic acid, and the pH values of the solutions were measured.

The solid samples were vacuum dried at a water vapor pressure of 5×10^{-4} mm. until constant weight was attained. X-Ray diffraction patterns of the samples were obtained. The water contents of the samples were determined from the ignition loss at 1050° and from the carbon dioxide contents.

The hydrated tricalcium silicates were added to boiled distilled water in the quantities listed in Table II (see columns 6 and 7). The samples were rotated in polyethylene bottles for 150 days at 25°. After filtering the solutions in a carbon dioxide-free box the solutions were analyzed for calcium and silicic acid, and the pH values were measured. The compositions of the solid phases were evaluated from the differences between the total calcium and silica contents and the contents of the aqueous phases.

Equipment. The pH values were determined with a Leeds and Northrup pH meter, a glass measuring electrode, and a calomel reference electrode. A Beckman DU spectrophotometer was employed for the analysis of soluble silicic acid. The X-ray patterns were made with a Phillips diffractometer using copper radiation.

Analyses. Calcium concentrations were determined by titrating with Versene.[12] Analyses for silicic acid were made spectrophotometrically on the blue reduced form of the silicomolybdate complex following the procedure of Bunting.[13] The free calcium hydroxide was determined by extraction with acetoacetic ester and isobutyl alcohol.[14]

Results

CaO, SiO_2, and H_2O Mixtures. The pH values, calcium concentrations $(Ca)_F$, and silicic acid concentrations $(SiO_2)_F$ of the solutions at equilibrium are listed in columns 2, 3, and 4 of Table I. Columns 5 and 6 show the CaO–SiO_2 mole ratios in the liquid and solid phases, respectively. The pH values of the solutions may be seen to increase with the calcium oxide contents of the systems.

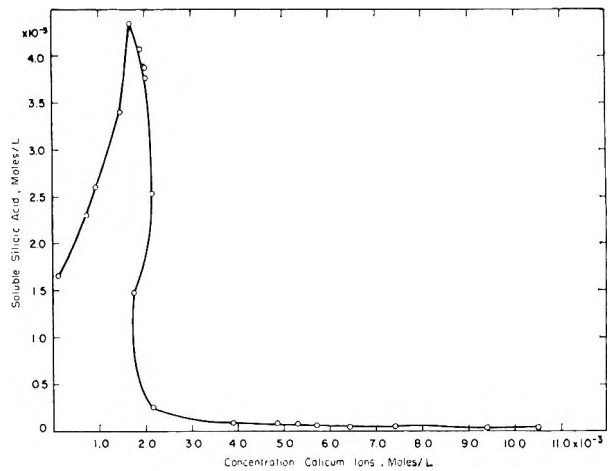

Figure 1. Solubility of silica as a function of calcium ion concentration.

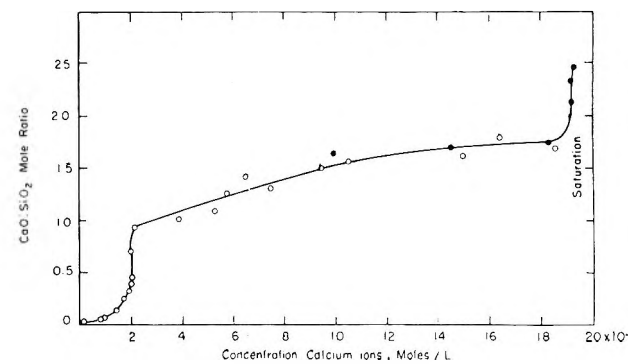

Figure 2. CaO–SiO_2 mole ratios in solids as a function of concentration of calcium ions. CaO, SiO_2, and H_2O mixtures (O) and hydrated tricalcium silicates (●).

In Figure 1 the silicic acid contents of the aqueous phases are plotted as a function of the calcium ion concentrations for the various mixtures. At zero calcium content the solubility of silica in water may be seen to be about 1.6×10^{-3} M. From the zero concentration of calcium ions the silicic acid concentration rises rapidly with calcium concentration (or pH) until a maximum is reached at a calcium concentration of 1.68×10^{-3} M. The solid at this point exhibits a CaO–SiO_2 mole ratio of 0.23. For mixtures with higher calcium oxide contents the silicic acid concentrations decrease, in general, with an increase in calcium ion concentration. It

(12) H. H. Willard, N. H. Furman, and C. M. Bricker, "Elements of Quantitative Analysis," 4th Ed., D. Van Nostrand Co., Inc., Princeton, N. J., 1956, p. 138.

(13) W. E. Bunting, *Ind. Eng. Chem., Anal. Ed.*, **16**, 6121 (1944).

(14) E. E. Pressler, S. Brunauer, D. L. Kantro, and C. H. Weise, *Anal. Chem.*, **33**, 877 (1961).

may be seen that, at a calcium ion concentration of 1.75×10^{-3} M, the silicic acid concentration deviates from this trend. The results of Flint and Wells[8] are very similar to those shown in Figure 1.

It is interesting to note that the CaO–SiO_2 mole ratios in the liquid rise from 0.067 (column 5, experiment a, Table I) to 1233 (experiment 19), but the mole ratios in the solids (column 6) rise only from approximately 0 to 1.79. It is clear that the solution phases are incongruent with respect to the solid phases.

Samples 11, 16, 17, 18, 19, and 20 exhibited free calcium oxide concentrations of 3.14, 9.38, 10.0, 9.04, 11.10, and 10.94% of the sample weight.

Figure 2 exhibits the relationship between the CaO–SiO_2 mole ratios in the solid phases and the calcium ion concentrations in the solutions. Similar results have been reported many times before.[4-8] In the present study an additional measurement of pH makes it possible to evaluate the equilibrium constants for these solid–liquid systems. It may be seen that the ratio rises rapidly to 0.93 over a concentration range from 0 to 2.13×10^{-3} M in calcium ion. A slow rise to a 1.79 mole ratio for CaO–SiO_2 is found between a 3.9×10^{-3} and 16.4×10^{-3} M concentration range of calcium ions.

The water contents of the solids were plotted as a function of CaO–SiO_2 mole ratio. It was noted that the water content increases from 10.13 to almost 13.4% in the CaO–SiO_2 mole ratio range 0.23 to 1. It is interesting to note that the theoretical water content of the CaH_2SiO_4 composition is 13.4%. At the mole ratio of 1 there may be seen an abrupt decrease of water content to about 11% from 13.4%. Thereafter, the water content rises to 13.92% at a CaO–SiO_2 mole ratio of 1.79.

X-Ray patterns of the solid phases with CaO–SiO_2 mole ratios of 0.32 to 1.63 were made. The three lines characteristic of hydrated calcium silicates were found at 3.06, 2.81, and 1.83 Å. The pattern for the sample with the 0.32 ratio was the least clear. Broad bands at 10 and 24° 2θ positions indicated the presence of silica gel. The sample with a 0.68 ratio did not exhibit these broad bands. Nevertheless, the sample probably contained partially reacted silica. The pattern for the sample with a 1.63 ratio was not as sharp as those for the samples with CaO–SiO_2 ratios between 0.68 and 1.32.

Evidence for 5.5- and 1.67-Å. spacings was found in the samples with mole ratios of 0.68 to 1.32, and the 5.5-Å. spacing was least distinct in the latter sample. The basal c-spacing was indistinct but seemed to increase from 9.0 to 10.6 Å. in the ratio range between 0.68 and 1.08 and then decreased to 9.81 Å. at the 1.32 ratio.

Heller and Taylor[15] have previously reported that no evidence was found for changes in the patterns of samples in the 0.8 to 1.5 mole ratio range. This subject has been reviewed recently by Brunauer.[9]

Hydrated Tricalcium Silicate. In columns 2, 3, and 4 of Table II the pH values, calcium concentrations $(Ca)_F$, and silicic acid concentrations $(SiO_2)_F$ in the solutions at equilibrium are listed. The silicic acid concentrations were very low; therefore, the absolute values are not completely reliable. The mole ratios of CaO–SiO_2 in the solids are given in column 5. It may be noted in Figure 2 that the CaO–SiO_2 values for the hydrated tricalcium silicate lie on the same CaO–SiO_2 *vs.* calcium concentration curve as those for the CaO, SiO_2, and H_2O reaction mixtures.

Discussion

Equilibria between Solid and Aqueous Phases. It will be profitable to describe first the various equilibria involved in the solubility relationships. For this purpose four regions will be proposed. In each of these regions one or more solid species exists: (1) silica at low calcium oxide contents with CaO–SiO_2 mole ratios of 0.14 and less; (2) partially reacted silica plus some hydrated calcium silicate in the CaO–SiO_2 mole ratio range between 0.23 and 1.0; (3) hydrated calcium silicate, CaH_2SiO_4, with a varying amount of calcium hydroxide dissolved in it in the over-all mole ratio range above 1 and less than about 1.75; (4) mixtures of the solid hydrated calcium silicate and solid calcium hydroxide for the over-all CaO–SiO_2 ratios above about 1.75.

It has been shown by Alexander, Heston, and Iler[16] that silica increases in solubility with pH because of the formation of $H_3SiO_4^-$ ions. It is possible to write the reaction

$$SiO_2(s) + nH_2O(l) = H_4SiO_4(aq) \qquad (3)$$

This reaction is written for silica in equilibrium with a saturated solution of monosilicic acid. The constant for this equilibrium is defined by

$$K = a_{H_4SiO_4} = (H_4SiO_4)f_{H_4} \qquad (4)$$

where a and f refer to the activity and activity coefficient of the species designated by the subscripts, and the quantity in parentheses is the concentration in moles/l. Since the activity constant for silicic acid K_{a_1} is defined by

$$K_{a_1} = \frac{a_H \cdot a_{H_3SiO_4^-}}{a_{H_4SiO_4}} \qquad (5)$$

(15) L. Heller and H. F. W. Taylor, "Crystallographic Data for the Calcium Silicates," Her Majesty's Stationery Office, London, 1956.

(16) G. B. Alexander, W. M. Heston, and R. K. Iler, *J. Phys. Chem.*, **58**, 453 (1954).

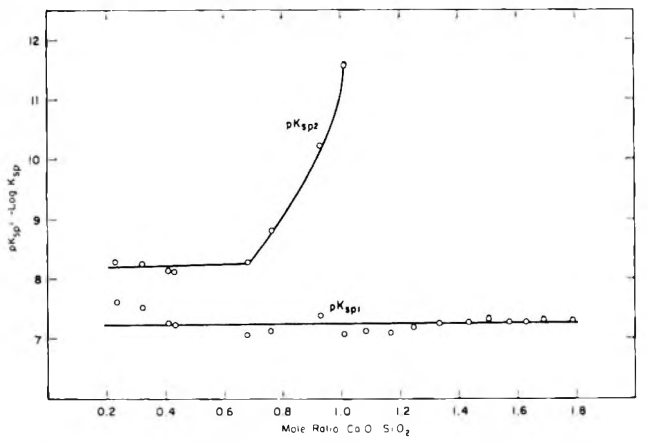

Figure 3. The pK_{sp_1} and pK_{sp_2} values as a function of $CaO–SiO_2$ mole ratio.

we may obtain the relationship

$$K^* = KK_{a_1} = a_{H^+}a_{H_3SiO_4^-} \quad (6)$$

by substituting K into eq. 5. It is apparent that, as the pH increases and the activity of the hydrogen ion decreases, the activity and concentration of the $H_3SiO_4^-$ ion must increase since K^* is a constant. Evidence for this is given in experiments a–d of Table I and in the initial portion of the curve in Figure 1. The soluble silicic acid content increases as the pH or calcium ion concentration increases.

In the mole ratio range 0.23 to 1 it will be assumed that the solid component is $Ca(H_3SiO_4)_2$, for which a solubility product K_{sp_2} may be written

$$K_{sp_2} = a_{Ca^{+2}}a^2_{H_3SiO_4^-} = (Ca^{+2})(H_3SiO_4^-)^2f_\pm^3 \quad (7)$$

where $f_\pm$ is the mean activity coefficient. The K_{sp_2} value may be evaluated by means of the experimental data, a knowledge of the dissociation constants of silicic acid, and the Debye–Hückel equation.[17]

$$-\log f_i = \frac{Z_i^2AI^{1/2}}{1 + d_iBI^{1/2}} \quad (8)$$

where Z_i is the valence of the ion, I is the ionic strength, d_i is the diameter of the aqueous ion, and the constants A and B are 0.509 and 0.320 at 25°, respectively. The values of d_i for calcium and silicate ions ($H_2SiO_4^{-2}$ and $H_3SiO_4^-$) were estimated to be 6 and 4 Å., respectively. The negative logarithms of the dissociation constants for silicic acid, pK_{a_1} and pK_{a_2}, are, at 25°, 9.7 and 11.77,[10,18] respectively. Since $pH = -\log a_{H^+}$, then $a_{OH^-} = K_w/a_{H^+}$ where K_w is the dissociation constant of water. The value of K_w at 25° is 1.008×10^{-14}. The ionic strengths of the aqueous phases were estimated from the concentrations of the calcium and silicic acid species, as well as the pH values.

It may be seen in Figure 3 and column 8 of Table I that pK_{sp_2} ($-\log K_{sp_2}$) values remain constant at about 8.25 at a $CaO–SiO_2$ mole ratio of 0.68 and then rise rapidly to 11.56 at a mole ratio of 1.01. Above the $CaO–SiO_2$ mole ratio of 1, the pK_{sp_2} values fluctuate between 10.77 and 13.07. In the previous paper in this series[10] it was shown that a solid with a mole ratio of about 0.8 exhibited a constant value for pK_{sp_2} of 8.5 ± 0.1 at 25°. However, it is clear that the pK_{sp_2} values in the present study are not constant in the range of over-all $CaO–SiO_2$ mole ratios 0.7 to 1.

In a previous paper[10] it was shown that, for hydrated calcium silicates with $CaO–SiO_2$ mole ratios of 1, 1.2, and 1.5, the solution equilibrium may be written as shown in eq. 1. For this reaction the constant is

$$K_{sp_1} = a_{Ca^{+2}}a_{H_2SiO_4^{-2}} \quad (9)$$

In the mole ratio range 1 to 1.5 the pK_{sp_1} values were 7.0 ± 0.1 at 25°. In Figure 3 the pK_{sp_1} values over the whole range of $CaO–SiO_2$ ratios are given. In the $CaO–SiO_2$ mole ratio range above 1 it may be seen that the pK_{sp_1} values rise from 7.07 to 7.31. The range of pK_{sp_1} values between 7.07 to 7.31 may perhaps be attributed to the errors in the method for evaluating the constants. Equation 8 decreases in reliability with increasing ionic strength. It will readily be noted that in the mole ratio range of $CaO–SiO_2$ less than 1 the pK_{sp_1} values fluctuate around an average value of 7.25.

The pK_{sp_1} values (column 8, Table II) for solutions in equilibrium with hydrated calcium silicate were not reliable. The very low silicic acid concentrations made it difficult to obtain accurate values for the $H_2SiO_4^{-2}$ concentrations. Nevertheless, the average of the four determined values, 7.32 (column 8, Table II), is the same as the value in column 9 of Table I at a $CaO–SiO_2$ mole ratio 1.69 (experiment 19), which indicates that the same hydration products were obtained in both reactions.

Because the ratio of $CaO–SiO_2$ is not the same in the liquid phase as it is in the solid phase, it is necessary to propose another equilibrium to explain this incongruent behavior. It will be assumed that for solids with $CaO–SiO_2$ mole ratios ≥ 1 the calcium hydroxide is distributed between a solid phase, CaH_2SiO_4, and a liquid water phase as described by eq. 2. For the thermodynamics of this reaction the procedure of Gibbs as amplified by Gaines and Thomas[19] will be followed.

The activity of the calcium hydroxide in solution is

$$K_{sp_3} = a_{Ca^{+2}}a^2_{OH^-} \quad (10)$$

(17) P. Debye and E. Hückel, *Physik. Z.*, **24**, 185, 305 (1923).
(18) S. A. Greenberg, *J. Am. Chem. Soc.*, **80**, 6508 (1958).
(19) G. L. Gaines and H. C. Thomas, *J. Chem. Phys.*, **21**, 714 (1953).

The chemical potentials of the calcium hydroxide species will be the same in the solid and liquid phases. K_{sp_3} is a constant only when the solution is in contact with crystalline calcium hydroxide. If we assume that the standard state of CaH_2SiO_4 is the pure solid, the equilibrium constant for the reaction in eq. 2 is

$$K_{D_1} = \frac{a_S}{a_L} = \frac{C_S f_S}{a_L} \quad (11)$$

where a_S and a_L are the activity of calcium hydroxide in the solid and liquid phases, C_S is the moles of calcium hydroxide per mole of CaH_2SiO_4, and f_S is an activity factor for calcium hydroxide in the solid phase. For lack of data it will be assumed that the activities of the solvent water and solid CaH_2SiO_4 do not change. The constancy of the K_{sp_1} value[10] is some indication that the activity of CaH_2SiO_4 does not change appreciably with the amount of calcium hydroxide dissolved in it. The activity of the calcium hydroxide a_L in the liquid phase will be given by eq. 10. Therefore, the ratios C_S/a_L may be evaluated. Column 11 of Table I gives the values of log C_S/a_L in the mole ratio range 1.01 to 1.79 for the calcium oxide, silica, and water reaction mixtures. The values range between 5.03 and 5.10. The log C_S/a_L values were plotted as a function of $I^{1/2}$. The value at the intercept (I where CaO–SiO_2 ratio = 1) is 5.1. It should be pointed out, however, that the values do not change appreciably with the activity of the calcium hydroxide in the liquid phase.

The log C_S/a_L values for the solutions in contact with hydrated tricalcium silicate fluctuate between 4.95 and 5.30 (column 10, Table II). For the mole ratios 1.68 and 1.75, the values are 5.05 and 4.95, respectively, which are within experimental error close to the 5.1 exhibited by the reaction mixtures of calcium oxide, silica, and water. The variations in log C_S/a_L values are due to the effect of small errors in pH determinations on the K_{sp_3} values (column 9, Table II) since pH = $-\log K_w/a_{OH^-}$.

In an effort to study the involvement of calcium hydroxide in mixtures with CaO–SiO_2 ratios less than 1 the following reaction was considered

$$SiO_2(s) + nCa^{+2}(aq) + 2nOH^-(aq) = SiO_2 \cdot nCa(OH)_2(s) \quad (12)$$

For this reaction we shall consider the ratio

$$K_{D_2} = \frac{M_S f_S}{a_L} \quad (13)$$

where M_S is the moles of calcium hydroxide per mole of SiO_2 in the solid, f is a sort of activity coefficient, and a_L is the activity of calcium hydroxide in the aqueous phase. It is evident from the results that more than silica is present as a solid phase. The log M_S/a_L values are listed in column 12 of Table I. It may be seen that the values are constant at 10.76 at the CaO–SiO_2 mole ratios of 0.23 and 0.32, and then the values decrease to 7.97 at a mole ratio of 0.93. It is thus apparent that the ease of entrance of calcium hydroxide into the silica structure decreases with an increase in the amount of calcium hydroxide in the solid phase.

Results have been reported[4-8] which show that, when the activity of the calcium hydroxide in the aqueous solution is the same as the equilibrium value for solid calcium hydroxide, 9.10×10^{-6} ($pK_{sp_3} = 5.09$) at 25°, the system contains two solid phases, calcium hydroxide and hydrated calcium silicate. The calcium hydroxide concentration which corresponds to a solid calcium hydroxide phase is less than 0.02 M in calcium hydroxide. If some of the calcium hydroxide consists of poorly crystallized crystals with small particle sizes, the concentration might temporarily rise above this value. In the present study the minimum pK_{sp_3} values for calcium hydroxide were 5.26 and 5.44 for calcium oxide, silica, and water reaction mixtures (column 10, Table I) even though the mole ratios of CaO–SiO_2 were between 1.69 and 1.79. The results indicate that the hydroxide is in a lower free energy state than normal crystalline calcium hydroxide.

The pK_{sp_3} values for hydrated tricalcium silicate solutions (column 9, Table II) approach the equilibrium value of 5.09 for CaO–SiO_2 mole ratios above 1.68.

In the present study the results indicate that the over-all mole ratios of CaO–SiO_2 in the solids are about 1.75 before the aqueous phase reaches the saturation solubility of crystalline calcium hydroxide. The solubility of calcium hydroxide which is part of the silicate structure was shown to exhibit a lower solubility than that of crystalline calcium hydroxide.

Nature of Solid Phases. The evidence for the nature of the various solid phases proposed in the previous section will now be considered.

For CaO–SiO_2 mole ratios less than 0.14 the system behaves like silica since the solubility increases with pH. However, above a CaO–SiO_2 ratio of 0.23 the concentration of silicic acid decreases with pH and calcium ion concentration. At a ratio of 0.23 "free" silica is no longer present because the solubility decreases with pH. Nevertheless, it has been shown[20] that the amount of the silica that dissolves in hydrochloric acid solution increases with calcium oxide content to 100% at a CaO–SiO_2 mole ratio of 1. It is possible to assume, therefore, that, in addition to the hydrated calcium sili-

(20) S. A. Greenberg, E. Pressler, and T. N. Chang, in preparation.

cate found by the X-ray measurements, there must be some partially reacted, stabilized silica species present in the mixtures with $CaO–SiO_2$ mole ratios less than 1. Even with a sample which has a $CaO–SiO_2$ mole ratio of 0.32, broad bands in the X-ray diffraction pattern demonstrate the presence of amorphous silica.

The evidence for a substance with the composition $Ca(H_3SiO_4)_2$ is not strong. The only evidence which indicates that such a compound exists is the apparent constancy of K_{sp_2} in the $CaO–SiO_2$ mole ratio range 0.23 to 0.68.

The evidence for a substance with a formula CaH_2SiO_4 in solids containing $CaO–SiO_2$ mole ratios ≥ 1 is fairly substantial. First a sharp break in water contents is found at a 1:1 mole ratio.[20] The water contents approach the theoretical value of 13.4%. At slightly more than a ratio of 1 the water content drops to about 11% to give a $CaO \cdot SiO_2 \cdot 0.8H_2O$ composition. Perhaps it is reasonable to conclude that a hypothetical compound with the formula CaH_2SiO_4 exists, but because of the colloidal nature of the solid—the high surface area and imperfect crystal lattice—the composition is not stoichiometric and exhibits the mole ratio $CaO \cdot SiO_2 \cdot 0.8H_2O$.

It has also been demonstrated[20] that products of the reaction of calcium oxide, silica, and water mixtures begin to dissolve completely in hydrochloric acid at a $CaO–SiO_2$ mole ratio of 1. Therefore, in the $CaO–SiO_2–H_2O$ system silica is completely depolymerized at this mole ratio.

In a study[21] of the reaction of aqueous solutions of calcium ions and monosilicic acid, the evidence indicates that the insoluble product forms by the reaction of Ca^{+2} and $H_2SiO_4^{-2}$ ions.

An analysis of the relationship between the calcium and water in the solid samples demonstrates that for samples with $CaO–SiO_2$ mole ratios greater than 1, 1.2 atoms of calcium enter the structure for every molecule of water.[20] Other investigators[2] have reported that equal quantities of each component go into the structure.

Taylor[6] and Kalousek[7] show a sharp rise in the $CaO–SiO_2$ ratio beginning at about 0.02 M calcium concentration and at an over-all $CaO–SiO_2$ ratio of 1.5. The rise was not found at this over-all ratio in the present study. The constancy of $\log C_S/a_L$ at 5.1 indicates that the calcium hydroxide distribution between the solid and liquid phase does not change with mole ratio up to about 1.75.

It should be recalled that this mole ratio includes the *free* calcium hydroxide. However, in this investigation the *free* calcium hydroxide exhibits a *lower* solubility than crystalline calcium hydroxide and, therefore, must be combined with the silicate structure, and is at a lower free energy state than crystalline calcium hydroxide.

On the other hand, the results of Taylor[6] and Kalousek[7] show a sharp rise in the mole ratio of the solids at a ratio of 1.5. It is apparent that some hydrated calcium silicate structures depending on the conditions of preparation can accommodate more calcium hydroxide than others.[9] Presumably beginning at a mole ratio of 1.5, the results of Taylor and Kalousek indicate that solid calcium hydroxide is present.

Acknowledgments. The authors wish to thank Dr. Stephen Brunauer for his many helpful suggestions and his careful reading of the manuscript. The X-ray patterns were made by Miss Elaine Anderson. The authors gratefully acknowledge a very helpful discussion of the X-ray results with Dr. D. L. Kantro. Thanks are due to Mr. C. H. Weise for the determination of free calcium hydroxide concentrations. The sample of hydrated tricalcium silicate was kindly supplied by Dr. D. L. Kantro and Mr. C. H. Weise.

(21) S. A. Greenberg and T. N. Chang, in preparation.

On the Degradation and Electron Spin Resonance Spectra of Irradiated Methacrylate Polymers[1]

by J. F. Kircher, F. A. Sliemers, R. A. Markle, W. B. Gager, and R. I. Leininger

Battelle Memorial Institute, Columbus 1, Ohio *(Received July 10, 1964)*

A study is reported of the degradation of irradiated methacrylate polymers, the formation and trapping of free radicals, and their electron spin resonance (e.s.r.) spectrum. Several different radicals are apparently formed and it seems necessary to assume that they are formed by different mechanisms. This is also suggested by a number of observations of main chain degradation and the ratio of chain scission to ester removal for several methacrylate polymers. It is probable that several mechanisms of degradation and radical formation are operative and the one which predominates is dependent on the pendant ester structure.

Introduction

At first glance, the problem of the origin of the 5–4 line e.s.r. spectrum in methacrylate polymers irradiated *in vacuo* appears rather straightforward. It has been shown that radicals trapped in polymerizing methyl methacrylate give a nine-line e.s.r. spectrum like that observed in irradiated polymethylmethacrylate (PMMA).[2] The propagating radical (I) then appears

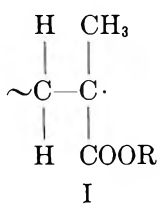

I

to be the one responsible in both cases. It has been shown that radical I could produce the observed e.s.r. spectrum through the interaction of the electron with the three methyl protons and either none or one of the methylene protons. This produces either a five- or four-line spectrum, depending on methylene group orientation, and the two components appear superimposed to provide the usual nine-line spectrum.[3a,b] However, it has not been conclusively demonstrated that this interpretation is correct. Further, it has been known for some time that, in the case of PMMA, approximately one ester scission occurs for each main-chain scission.[4,5] Moreover, the same general type of nine-line spectrum was observed for a number of other methacrylate polymers in addition to PMMA.[6–8] Therefore, most attempts to explain the origin of the spectrum invoke a mechanism that resulted in the loss of one ester group per main chain scission and left the propagating radical (I) on one end of the broken chain.[8] However, as more data became available from various laboratories it became increasingly apparent that this view was oversimplified.

Charlesby and Ormerod[9] and Campbell and Looney,[10] observing the decay of the usual nine-line spectrum, found that the five-line component appeared to decrease more rapidly than the four-line component. This has been confirmed in our own laboratories and is direct

(1) This work was supported by the Division of Isotope Development under AEC Contract W-7405-eng-92.

(2) G. K. Fraenkel, J. M. Hirshon, and C. Walling, *J. Am. Chem. Soc.*, **76**, 3606 (1954).

(3) (a) R. J. Abraham, H. W. Melville, D. W. Ovenall, and D. H. Whiffen, *Trans. Faraday Soc.*, **54**, 1133 (1958); (b) D. J. E. Ingram, M. C. R. Symons, and M. G. Townsend., *ibid.*, **54**, 409 (1958).

(4) P. Alexander, A. Charlesby, and M. Ross, *Proc. Roy. Soc.* (London), **A223**, 392 (1954).

(5) A. Todd, *J. Polymer Sci.*, **42**, 223 (1960).

(6) D. W. Ovenall, *ibid.*, **41**, 199 (1959).

(7) I. S. Ungar, W. B. Gager, and R. I. Leininger, *ibid.*, **44**, 295 (1960).

(8) I. S. Ungar, J. F. Kircher, W. B. Gager, F. A. Sliemers, and R. I. Leininger, *ibid.*, **A1**, 277 (1963).

(9) A. Charlesby and M. G. Ormerod, Fifth International Symposium on Free Radicals, Uppsala, Sweden, 1961.

(10) I. D. Campbell and F. D. Looney, *Australian J. Chem.*, **15**, 642 (1962).

evidence for the presence of more than one radical. We had reached a similar conclusion earlier from somewhat different considerations of radical decay data.[8] Lenk,[11] on the other hand, came to the same conclusions by observing that the five- and four-line portions of the e.s.r. spectrum did not grow at the same rate during irradiation. There can no longer be any doubt that more than one trapped radical is contributing to the normal nine-line e.s.r. spectrum from irradiated PMMA observed at room temperature or that these radicals have sufficient lifetimes to be readily detected many hours after irradiation. It is apparent that the formation and trapping of free radicals in irradiated PMMA is more complicated than first believed and it is probable that more than one mechanism is contributing.

Experimental

All experimental techniques have been described previously in some detail and will not be repeated here. The polymers were prepared by irradiation polymerization of carefully purified monomers. E.s.r. spectra were obtained with a Varian-4500 spectrometer from samples irradiated *in vacuo* by Co^{60} γ-rays at a dose rate of about 2×10^5 rads $hr.^{-1}$. Mass spectrometry and vapor phase chromatography were employed to determine the types and concentrations of the low-molecular weight radiolysis fragments by previously described techniques.[7,8,12]

Results and Discussion

It has been established in several investigations that approximately one ester group is removed for each chain scission in irradiated PMMA. However, our work with the isomeric butyl esters shows that this ratio is definitely influenced by the structure of the butyl ester group.[8] The ratio of ester removed to chain scission is shown in Table I. The concentration of ester removed was calculated from data on the products of radiation-induced decomposition and the chain scissions from the decrease in molecular weight for samples irradiated to 3×10^7 rads. The product distribution from the irradiated polybutylmethacrylates has been previously described.[8] The value of 0.7 for PMMA compares to about 0.8 obtained by Charlesby, *et al.*,[4] and Todd.[5] Among the butyl esters there was not a large change in the extent of chain scission but there was a large change in the amount of ester removal. This suggests that the mechanism of scission may change if the structure of the ester group is sufficiently altered or that it is not at all influenced by ester removal. If the pendant ester group is long enough, cross linking through the pendant ester predominates rather than the usual chain degradation. Graham showed that the *n*-heptyl methacrylate polymer forms a gel.[13] The effect of branching in the pendant alkyl was striking, however. Poly-*sec*-nonyl methacrylate did not gel even when irradiated to a dose almost three times that which produced gel in the *n*-heptyl polymer. These results are consistent with the frequent observation that branched hydrocarbons are more susceptible to radiation degradation than unbranched. Degradation in the pendant ester apparently tends to promote main chain scission in the methacrylates.

Table I: Events per Thousand Monomer Units at a Dose of 3.0×10^7 Rads

	PMMA	P-*n*-BMA	P-*i*-BMA	P-*sec*-BMA	P-*t*-BMA
Ester removal	2.5	2.7	3.9	5.3	9.6
Chain scission	3.5	10	11	7.1	13.6
Ratio	0.71	0.27	0.35	0.75	0.71

It has been shown previously that very pure PMMA and polyethylmethacrylate (PEMA) do not give the usual nine-line spectrum.[7] However, when small amounts of monomer were present, the spectrum was always the characteristic nine-line e.s.r. signal. It was also observed with these and other methacrylate polymers that continued irradiation caused the initially diffused spectrum to sharpen to the normal nine-line pattern.[12] This has been interpreted as being due to the initial formation of a radical formed by the loss of an ester group.

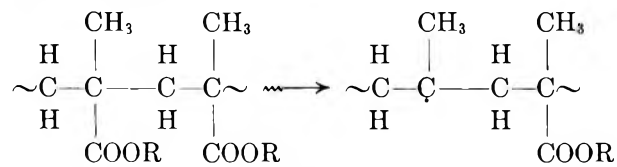

II

Depending on the orientation of the methylene groups, radical II would probably give rise to either a four-, five-, or six-line spectrum, the five-line spectrum being more probable than the other two. If all β-hydrogens interact equally, an eight-line spectrum would be expected. Such contributions could lead to the diffuse spectra observed with the very pure polymers. If monomer is present, radical II is of course converted to the propagating radical I. It was further suggested

(11) R. Lenk, *Czech. J. Phys.*, **B12**, 876 (1961).

(12) F. A. Sliemers, E. Gulbaran, W. B. Gager, J. F. Kircher, and R. I. Leininger, Second International Radiation Chemical Symposium, Harrogate, England, 1962; "Radiation Effects," M. Ebert and A. Howard, North Holland Publishing Company, Amsterdam, 1963.

(13) R. K. Graham, *J. Polymer Sci.*, **38**, 209 (1959).

that radical II leads to main chain scission by rupture of the C–C bond β to the radical site.

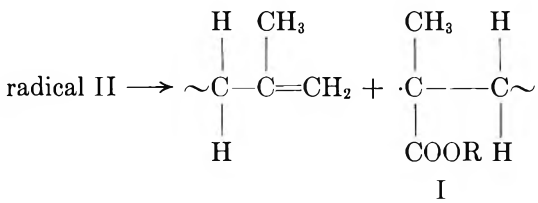

I

A reaction of this type produces free radical I again and accounts for the loss of an ester group. Because resolution of the e.s.r. spectrum from irradiated polymers very often is not extremely sharp, it would be difficult to discern the six- or eight-line component from radical II in the presence of a four-line component from two different radicals (I and II). However, it probably would not be lost from the mixture at the same rate as I and could explain in part some of the effects observed during postirradiation radical decay.

With the methacrylate polymers and polymethacrylic acid (PMAA), whenever the initial radiation event is on the main chain, it must be in the vicinity of a quaternary carbon which is well known to represent a weak point on the chain.[14] Moreover, when the "R" group is small (H or CH_3, for instance) and assuming the initial attack is random, then the vicinity of the quaternary carbon is the most likely place for the initial reaction. It is also known from studies of aliphatic acids that the carbonyl group is particularly susceptible to radiation decomposition, and, as has been pointed out by Todd, if the "R" group is removed by a radiation-induced reaction, then it is very likely that the small stable CO_2 would also be ejected. The net result is radical II either way and probably accounts for the fact that in PMMA main-chain scission is accompanied by ester removal at least 70–80% of the time.

As the alkyl portion of the ester becomes larger, the probability of having the initial act there increases. Since these events will not always lead to ester scission, the probability of ester removal should decrease with respect to the number of initial acts. If ester removal is necessary for main chain degradation, then degradation should decrease proportionally and the ratio of main chain scission to ester removal should remain about the same. In the case of the butyl methacrylate polymers, it is seen that this is not the situation even when the increased energy absorbed per monomer unit is taken into account (see Table I). With these polymers there are four carbons and nine hydrogens on the ester and only four carbons and five hydrogens in the rest of the monomer unit, so one might expect at least half the initial acts to occur on pendant alkyl groups. However, the rate of chain scission does not decrease in proportion to the increase in ester size; it actually increases. The two facts seem to indicate that another mechanism is leading to chain degradation.

If the initial act on the pendant alkyl group results in formation of a radical on that group, the radical is in a good position to abstract a hydrogen from a neighboring polymer chain and perhaps thereby initiate chain scission. Designating the alkyl radical R·, we envision a sequence of reactions such as

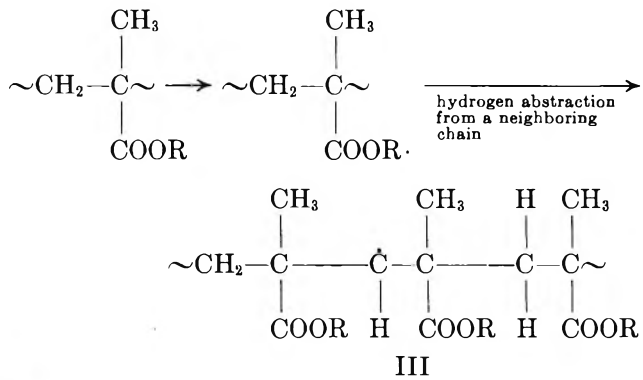

III

or

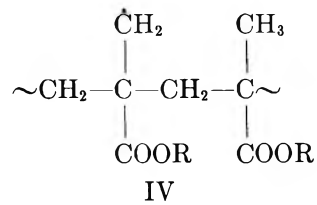

IV

followed by chain degradation.

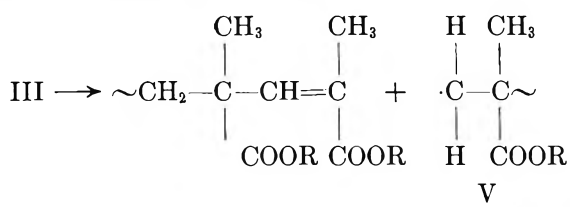

V

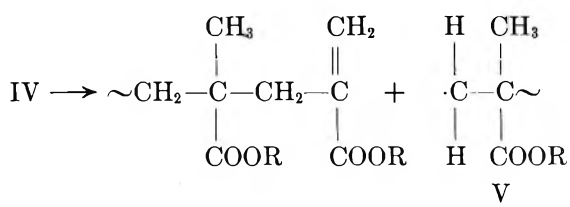

V

Hydrogen atoms or alkyl radicals which are always present during irradiation would also be able to start the same sequence of events. These may account in part for the 20–30% of the chain scissions which apparently occur without ester removal even in the case of PMMA. Radicals formed on the pendant alkyl group

(14) A. N. Pravednikov, E. N. Teleshov, I. M. Shen-Kan, and S. J. Medvedev, *J. Polymer Sci.*, **58**, 1039 (1962).

probably also account for the results obtained by Graham.[13]

Todd[5] has suggested that radical V ejects an ester to form a stable chain end.

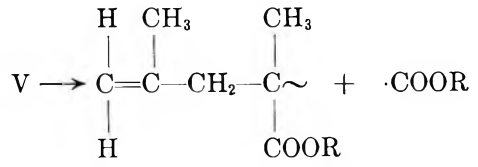

However, it does not seem that it can make a major contribution, at least in the case of the butyl methacrylate polymers since this reaction would always lead to an ester removal for each chain scission. However, radical V could possibly abstract a hydrogen from a neighboring butyl group to initiate further chain scission as described above. This could account in part for the increase in scission without corresponding loss of ester as shown in Table I. It must also be remembered that radicals I and V can be formed by direct chain cleavage and initiate the same reactions.

Another, but perhaps less likely, way in which scission could occur without loss of an ester group is by the formation of radical VI, which can then decompose to give radical I and chain scission.

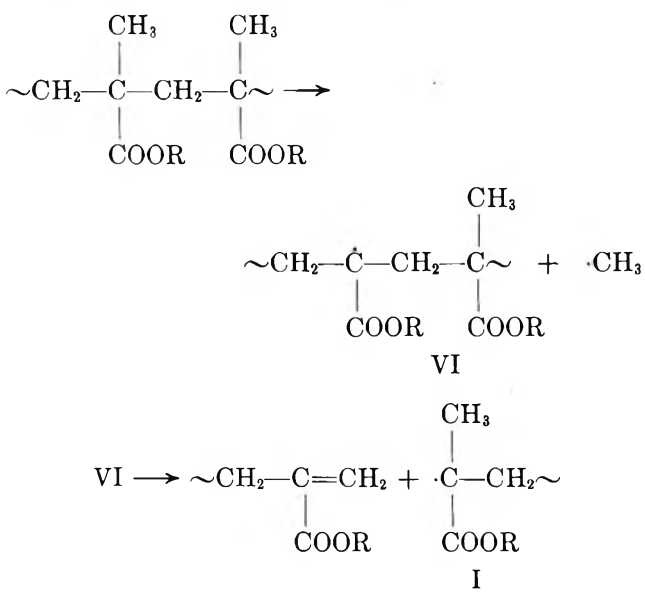

This requires the formation of $CH_3\cdot$ which should be accounted for in the volatile products measured after irradiation. In the case of PMMA, it was found that there are more methyl radical-derived products than can be accounted for on the basis of methyl radicals from ester group scission, which suggests such a mechanism is occurring to some extent.[12] This is not true in the case of the isomeric butyl esters. However, in those cases, it is possible that some products of very low volatility, *e.g.*, the methyl butyrates, were formed but not detected in the analyses. Also, it seems quite likely that as the pendant ester group is made larger, reaction at the α-methyl group becomes less probable.

Radical III would be expected to produce a two-line e.s.r. spectrum, radicals IV and V three-line spectra, and radical VI one, two, or three lines. How easy it would be to see these in the presence of other radicals giving four- and five-line e.s.r. spectra is open to question. Radicals IV and V would be expected to be very reactive and might not remain trapped in the solid as long as III or some other radical somewhat sterically protected. It must also be remembered that many of the polymers used in studies reported in the literature contain some unreacted monomer. Radicals such as IV or V would then be converted to I, increasing the contribution of the latter radical to the five–four-line spectrum.

From an analysis of the volatile products arising from the radiation-induced reactions, it is possible to make several statements regarding the positions on the polymer chain where radicals are likely to be formed. Some data from previous work are given in Table II for convenience.[8,12] It is seen that, when R is small (methyl) or branched adjacent to the carbonyl position (*sec* or *tert*), half or more of the events apparently lead to the removal of an ester group. These are the same polymers where the ratio of ester removal to chain scission is high. One would expect that the influence of the ester group structure would become more significant as the size of the group was increased. In the case of the *n*-

Table II: Estimated Concentrations of Free Radical Sites in Irradiated Methacrylate Polymers[a]

	Sites per thousand and monomer units					
Radical	PMAA	PMMA	P-*n*-BMA	P-*i*-BMA	P-*sec*-BMA	P-*t*-BMA
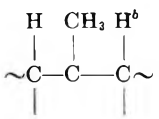	5.4	2.5	2.7	3.9	5.3	9.6
Formed by H atom extraction from backbone of ester[c]	...	2.7	4.7	5.0	5.4	3.6
Total	5.4	5.6	7.7	8.9	11.0	13.2

[a] After exposure to a dose of 3.0×10^7 rads. [b] Calculated from sum of concentrations of CO, CO_2, and ester. [c] Calculated from sum of concentrations of hydrocarbon (excluding isobutene in the case of the *t*-butyl polymer), hydrogen, alcohol, and formate.

butyl and isobutyl polymers, less than half of the products arise from the removal of an ester group. One might reasonably expect that some radicals could be trapped on the butyl group and thereby further confuse the e.s.r. pattern. Several different structures are possible which could lead to four-, five-, or six-line spectra, for instance.

Table III: Concentration of Free Radical Sites in Irradiated Methacrylate Polymers as Determined by Different Methods

	Sites per thousand monomer units[a]			
	From total product analysis	From molecular weight change	From e.s.r. signal	Initial G-value[b]
PMAA	5.4	n.d.	1.3	2.4
PMMA	5.6	3.5	0.8	2.4
P-*n*-BMA	7.7	10.0	0.06	1.6
P-*i*-BMA	8.9	11.0	0.2	3.4
P-*sec*-BMA	11.0	7.1	0.6	2.9
P-*t*-BMA	13.2	13.6	0.6	2.5

[a] Following irradiation to a dose of 3×10^7 rads. [b] Calculated from e.s.r. data at low doses.

From an analysis of the products of radiolysis, it is possible to estimate the number of bonds which must have been broken and hence the number of radicals which could be trapped in the polymer.[8] Another estimate of maximum trapped radicals can be obtained from the decrease in molecular weight by assuming a certain fraction of chain ends are trapped as free radicals. E.s.r. provides a more direct measure of these trapped radicals at any given dose. However, the trapping efficiency is not 100% in any case and, consequently, somewhat lower free-radical concentrations are to be expected from the e.s.r. data. The e.s.r. data, at low doses, can also be used to determine rate of formation or trapping of the radicals. Such data are briefly summarized in Table III. Generally, it can be seen that the apparent rate of radical formation and trapping does not vary among the different polymers to any great extent, and this is to be expected. The most obvious variation attributable to methacrylate structure is in the free radical concentration as observed by e.s.r. after an exposure of 3×10^7 rads. However, it should be pointed out that this may be primarily due to the influence of ester structure on the physical properties of the polymer (particularly glass-transition temperature) rather than the chemical reactions undergone during irradiation. From the data of Graham[13] and Shetter,[15] it appears that all of our experiments were performed below T_g for all materials except possibly the P-*n*-BMA. T_g for P-*n*-BMA is about 19–20°, and the experiments were conducted at 21–22°. The trapping efficiency is expected to be less above T_g; therefore, the results shown in Table III are not unreasonable, since a lower trapping efficiency means the concentration of radicals seen by e.p.r. at any time after irradiation will be low. However, T_g would not be expected to have this effect on radical concentrations calculated from molecular weight changes or product formation.

Summary

From the evidence accumulated in this and other studies, it appears that a number of radical species are being formed and trapped when polymethacrylates are irradiated. It seems necessary to assume that more than one mechanism is producing main chain degradation and radicals that can be trapped. In the case of PMMA, 70–80% of the degradation is accompanied by ester group loss. The five–four-line e.s.r. spectrum has been seen in almost every study and one of the major reasons for this may be unreacted monomer present in the methacrylate polymer sample. In those cases where the polymer was stringently purified, some change was usually observed in the e.s.r. pattern. It is also possible that the propagating radical is the most efficiently trapped and stable radical so that its relative concentration tends to increase with exposure time. The concentration of radicals seen by e.s.r. at a given dose is influenced by ester group structure in the polymethacrylates. However, this influence is predominantly through the effect on T_g and hence the efficiency of radical trapping rather than radical formation.

(15) J. A. Shetter, *Polymer Letters*, 1, 209 (1963).

Radical Yields in the Radiolysis of Unsaturated Hydrocarbons[1a]

by R. A. Holroyd[1b] and G. W. Klein

Radiation Research Laboratories, Mellon Institute, Pittsburgh, Pennsylvania *(Received July 10, 1964)*

A radical sampling technique utilizing carbon-14-labeled methyl radicals is applied to the determination of the individual radical yields in the radiolysis of several olefins. The major radicals and yields for propylene are allyl (45%), isopropyl (33%), and *n*-propyl (12%). In 1-butene the major radicals and corresponding yields are 1-methylallyl (42%), 3-butenyl (6%), *sec*-butyl (25%), and *n*-butyl (11.5%), showing that the loss of an allylic hydrogen atom occurs 11 times more readily than loss of a primary hydrogen atom. The 1-methylallyl radicals observed from *trans*-2-butene are 96% in the *trans* configuration,

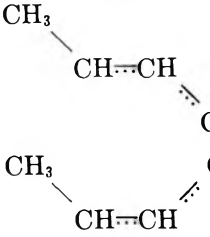

whereas from *cis*-2-butene 80% are in the *cis* configuration,

This retention of structure suggests that a highly excited species is not responsible for formation of allylic radicals. Approximately two-thirds of the combinations of methyl with 1-methylallyl radicals occur at the terminal carbon atom. The major radical species found in isobutene is 2-methylallyl. The precursor of the *n*-propyl radicals from propylene, the *n*-butyl radicals from 1-butene, and >60% of the *sec*-butyl radicals observed in *cis*-2-butene is not a thermal hydrogen atom. The effect of $^{14}CH_3I$ concentration on the relative radical yields suggests that the major source of $^{14}CH_3$ radicals is *not* abstraction of iodine atoms from $^{14}CH_3I$ by thermal hydrogen atoms.

Introduction

Recent studies of the radiolysis of liquid olefins have been concerned to a large extent with the nature and importance of ion–molecule reactions.[2-4] On the other hand, these and other studies have also demonstrated the presence of free radicals in the radiolysis of these substances. Recent investigations[5-7] of the radiolysis of ethylene have shown that free radical and molecular processes are of comparable importance. In the case of propylene, allyl, isopropyl, and *n*-propyl radicals have been shown to be intermediates in the radiolysis of the liquid[2] and the allyl radical has been observed in irradiated samples of the solid.[8]

An extensive study of the products formed in the radiolysis of various straight-chain butenes has been made.[3] The carbon skeletons of the dimer products suggested that *sec*-butyl and methylallyl radicals are present. In irradiated liquid isobutylene, the principal radical species present is believed to be 2-methylallyl.[9,10] It has been proposed[11] that this radical is formed by the

(1) (a) Supported, in part, by the U. S. Atomic Energy Commission; (b) Atomics International, Canoga Park, Calif.

(2) C. D. Wagner, *Tetrahedron*, **14**, 164 (1961).

(3) P. C. Kaufman, *J. Phys. Chem.*, **67**, 1671 (1963).

(4) F. Collinson, F. S. Dainton, and D. C. Walker, *Trans. Faraday Soc.*, **57**, 1732 (1961).

(5) R. A. Holroyd and R. W. Fessenden, *J. Phys. Chem.*, **67**, 2743 (1963).

(6) R. W. Fessenden and R. H. Schuler, *J. Chem. Phys.*, **39**, 2147 (1963).

(7) R. A. Holroyd and G. W. Klein, *J. Appl. Radiation Isotopes*, in press.

(8) B. Smaller and M. S. Matheson, *J. Chem. Phys.*, **28**, 1169 (1958).

(9) E. Collinson, F. S. Dainton, and H. A. Gillis, *J. Phys. Chem.*, **63**, 909 (1959).

(10) G. Porter, "Progress in Reaction Kinetics," Pergamon Press, New York, N. Y., 1961, Chapter 3, ref. 73.

(11) F. W. Lampe, *J. Phys. Chem.*, **63**, 1986 (1959).

ion–molecule reaction

$$C_4H_8^+ + C_4H_8 \longrightarrow C_4H_9^+ + C_4H_7 \qquad (1)$$

observed in mass spectrometer studies.[12] A total yield of 2-methylallyl radicals of $G = 4.2$ for isobutene has been calculated[11] by assuming that each ionization event leads to one radical and a *t*-butyl carbonium ion. This agrees with the observed total radical yield $G = 3.7$,[9] determined by the yield of disappearance of DPPH.

Thus in general terms the existence of free radicals in the radiolysis of liquid olefins has been established. However, specific information as to the individual yields of radicals and their identity is needed. This information had not been obtained previously largely because of the lack of a suitable chemical scavenger. In this study the ^{14}C-labeled methyl radical sampling technique[7] which was developed for use in such reactive solutes is employed.

The principle of the method is generation of methyl-^{14}C radicals *in situ* from a trace amount of added $^{14}CH_3I$ (reaction 2). The $^{14}CH_3$ radicals subsequently react

$$X + {}^{14}CH_3I \longrightarrow {}^{14}CH_3 + Y \qquad (2)$$

with the radical intermediates by combining (C) and disproportionating (D)

$$R + {}^{14}CH_3 \longrightarrow R-{}^{14}CH_3 \qquad (3)$$

$$R + {}^{14}CH_3 \longrightarrow {}^{14}CH_4 + R(-H) \qquad (4)$$

In reaction 3, labeled hydrocarbons which characterize the radical intermediates are formed. Further, if either high dose rates or low temperatures are employed so that bimolecular combination of radicals is favored, then the yields of labeled hydrocarbons are a quantitative measure of the corresponding radical yield[7]; that is

$$G_{R_1}/G_{R_2} = \frac{R_1-{}^{14}CH_3(1 + D_1/C_1)}{R_2-{}^{14}CH_3(1 + D_2/C_2)}$$

Absolute yields may be determined since the above relationship applies also to the yield of methyl-^{14}C radicals ($G_{^{14}CH_3}$) which is measured by the yield of ethane-^{14}C formed by recombination of $^{14}CH_3$ radicals, for example G_{R_1} is given by

$$G_{R_1} = G_{^{14}CH_3} \times \frac{R_1-{}^{14}CH_3(1 + D_1/C_1)}{2\,{}^{14}C_2H_6}$$

and $G_{^{14}CH_3}$ is defined as the sum of the yields of all labeled hydrocarbons plus the yield of $^{14}CH_4$ formed by disproportionation, reaction 4.

Experimental

The hydrocarbons (Phillips research grade) were dried and degassed prior to use. The 1-butene was further purified by gas chromatography to remove a trace butadiene impurity. The $^{14}CH_3I$ (specific activity ~0.3 mc./mmole), supplied by New England Nuclear Corp., was also purified by gas chromatography.

The preparation, irradiation, and analysis of samples was as described previously.[5,7,13] The temperature of the sample was regulated to $\pm 1°$ during radiolysis. The electron beam (2.8-Mev. electrons) from a Van de Graaff accelerator was used, estimated dose rate 3×10^{18} e.v. ml.$^{-1}$ sec.$^{-1}$. The methyl iodide-^{14}C was assumed to be entirely dissolved at the low temperatures employed and its mean concentration was determined from the total activity, including unreacted methyl iodide, in the sample when analyzed. The sample size was generally 0.1 to 0.2 ml. and each sample received a dose corresponding to ~0.3% conversion of the olefin and from 10 to 50% conversion of the $^{14}CH_3I$.

The total dose received by each sample was needed for the determination of absolute radical yields. This required measurement of the dose input from the electron beam to samples of ~0.1-ml. volume. Because of the small size of the sample, either a differential energy loss or internal standard method had to be used. The former method was used for propylene and calibration was based on $G_{H_2} = 3.7$ from liquid ethane,[14] samples of which were irradiated at $-120°$ in the irradiation cells. The internal standard technique was found to be quite reliable. This was based on measurement of the amount of a product not formed from radicals, such as ethylene, found in the sample upon analysis. This method was used for 1-butene, based on $G_{C_2H_4} = 0.30$,[3] and for *cis*-2-butene, based on $G_{C_3} = 0.14$.[3]

Results and Discussion

Propylene. Propylene was studied at temperatures below $-100°$ and at methyl iodide-^{14}C concentrations from 1 to 55 m*M*. Besides $^{14}CH_4$, the labeled products observed (and corresponding radical precursors) were ethane ($^{14}CH_3$ and CH_3),[15] 1-butene (allyl), isobutane (isopropyl), and *n*-butane (*n*-propyl).

For the purpose of establishing trends in relative

(12) V. L. Tal'roze and A. K. Lyubimova, *Dokl. Akad. Nauk SSSR*, **86**, 909 (1952).

(13) R. A. Holroyd and G. W. Klein, *J. Appl. Radiation Isotopes*, **13**, 493 (1962).

(14) H. A. Gillis, *J. Phys. Chem.*, **67**, 1399 (1963).

(15) The relative yield of methyl radicals is proportional to the yield of $^{14}C_2H_6$(cor.), reaction a, which contains only one $^{14}CH_3$ de-

$$^{14}CH_3 + CH_3 \longrightarrow {}^{14}C_2H_6(\text{cor}). \qquad (a)$$

$$^{14}CH_3 + {}^{14}CH_3 \longrightarrow {}^{14}C_2H_6 \qquad (b)$$

rived from the methyl iodide-^{14}C solute. Labeled ethane is also formed by reaction b and this becomes increasingly important at higher concentrations of $^{14}CH_3I$ (see figures). The yield of $^{14}C_2H_6$-(cor.) is readily derived from the ratio of concentrations $(CH_3)/(^{14}CH_3)$.

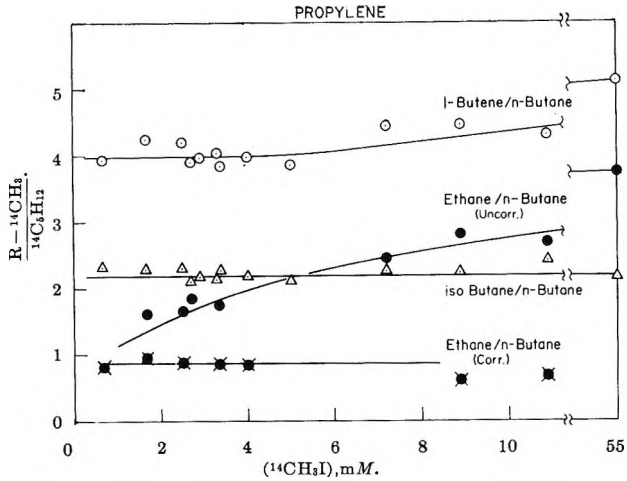

Figure 1. Yields of labeled hydrocarbons relative to the yield of n-$^{14}C_4H_{10}$ *vs.* $^{14}CH_3I$ concentration in liquid propylene; temperature, −102°: ⊙, 1-butene-^{14}C:-n-butane-^{14}C; △, isobutane-^{14}C : n-butane-^{14}C; ●, ethane-^{14}C (total):n-butane-^{14}C; ✦, ethane-^{14}C(cor.):n-butane-^{14}C.

yields, the data are presented as ratios of the yield of the labeled product to the yield of n-butane-^{14}C (Figure 1). The ratios are constant at concentrations of $^{14}CH_3I$ from 1 to 5 mM and the isobutane-^{14}C:n-butane-^{14}C ratio is constant at 2.2 throughout the entire concentration range studied. The 1-butene-^{14}C/n-butane-^{14}C ratio does increase slightly from its low concentration average value of 3.96 to 5.1 at 55 mM. The ratios are also independent of dose rate from 3×10^{17} to 10^{20} e.v. ml.$^{-1}$ sec.$^{-1}$. Lowering the temperature of the sample to −175° during irradiation changes only the isobutane-^{14}C/n-butane-^{14}C ratio from 2.2 to 1.3 (this effect is attributed to enhanced disproportionation at the lower temperature[16,17]). It was expected that at −175° vinyl radicals would be observed as was the case in studies of ethylene radiolysis.[5-7] However, no $^{14}C_3H_6$ was formed. Consequently, either vinyl radicals are not formed or they very readily abstract an allylic hydrogen atom from propylene to form ethylene (the lack of observation of a $C_5H_9\cdot$ radical which would be expected from vinyl radical addition to propylene further confirms this conclusion).

The amount of methane-^{14}C formed was approximately 36% of the total activity yield at all concentrations of methyl iodide-^{14}C. $G_{^{14}CH_4}$ increases to 0.29 at 55 mM $^{14}CH_3I$, an effect which is believed to be related to the observed increase in G_{allyl} at higher concentrations (see discussion under Effect of Concentration of $^{14}CH_3I$). Only 20% of the $^{14}CH_4$ can be attributed to disproportionation (reaction 4).

The relative radical yields are obtained from the relative yields of labeled products at low (<5 mM) concentration of methyl iodide where $G_{^{14}CH_3}$ is small and the system is not grossly perturbed by the presence of $^{14}CH_3I$ (that is, $G_{^{14}CH_3}$ is less than 0.3). A knowledge of disproportionation to combination ratios, D/C, is needed for this calculation. In general, these ratios are known in the gas phase; however, some recent work indicates that disproportionation becomes more important with decreasing temperature.[16,18] For example, when the radical, R, is C_2H_5, D/C increases to 0.9 at −95° in 2,2,4-trimethylpentane solution.[16] The data were found to fit the empirical relationship: log $D/C = 70.1/T$ + constant, corresponding to an "apparent" activation energy difference of 320 cal./mole (valid at $T > -100°$). In the present study, the value of $D/C = 0.09$ is assumed for all normal-type radicals encountered. A similar relationship was observed for the temperature dependence of disproportionation in a study of the reaction $C_2H_5 + C_2H_5 \rightarrow$, in 2,2,4-trimethylpentane solution.[18] Apparently, this effect is quite general and the above equation has been used to estimate values of D/C for other radicals at low temperatures. In this way the value of D/C for R = isopropyl is found to be 0.33 at −100°.[19] The ratio of D/C for allyl is assumed to be zero.[20] The resulting relative radical yields are given in column 5 of Table I.

Absolute yields are based on G_{CH_3} which is the product of $G_{^{14}CH_3}$ and the ratio of concentrations $(CH_3)/(^{14}CH_3)$.[21]

Table I: Radical Yields in Propylene

R	Relative yield of R-$^{14}CH_3$[a] Exptl. ratio	%	$1 + D/C$	G_R Relative yield of R, %	G_R Obsd., present study	G_R Calcd.[b] from product analysis
CH_3	0.88	10.9	1.0	9.9	0.20	..
n-C_3H_7	1.00	12.4	1.09	12.3	0.25	0.27
i-C_3H_7	2.20	27.4	1.33	33.0	0.67	0.58
Allyl	3.96	49.3	1.0	44.8	0.91	0.78

[a] Results are based on nine determinations at methyl iodide-^{14}C concentrations less than 5 mM (*cf.* Figure 1). [b] These values are derived from reported product yields given in ref. 2.

(16) P. S. Dixon, A. P. Stefani, and M. Szwarc, *J. Am. Chem. Soc.*, **85**, 3344 (1963).

(17) R. Klein, M. D. Scheer, and R. Kelley, *J. Phys. Chem.*, **68**, 598 (1964).

(18) P. S. Dixon, A. P. Stefani, and M. Szwarc, *J. Am. Chem. Soc.*, **85**, 2551 (1963).

(19) This ratio is based on a gas phase value of 0.22 at 25°; *cf.* J. A. Kerr and A. F. Trotman-Dickenson, *J. Chem. Soc.*, 1609 (1960).

(20) This is supported by a study of the pyrolysis of allyl iodide [F. P. Lossing, K. U. Ingold, and J. H. S. Henderson, *J. Chem. Phys.*, **22**, 621 (1954)] at 150° in which 1,5-hexadiene was found, but the yield of allene and propylene (the disproportionation products) was 1% of the 1,5-hexadiene.

(21) See ref. 7 for details of this method.

Table II: Yields of Methyl-^{14}C, Methyl, and Methane-^{14}C

Olefin	T, °C.	($^{14}CH_3I$), mM	Dose, e.v. $\times 10^{-19}$	$G_{^{14}CH_3}$	$(CH_3)/(^{14}CH_3)$	G_{CH_3}	$G_{^{14}CH_4}$[a]
Propylene	−102	4.0	3.0	0.15	1.33	0.19	0.046
Propylene	−102	1.7	3.8	0.17	1.41	0.24	0.072
Propylene	−102	2.5	4.0	0.165	1.13	0.19	0.069
Propylene	−102	3.4	3.5	0.27	0.72	0.19	0.089
Propylene	−103	55.0	3.3	0.66	..	..	0.29
1-Butene	−91	0.8	6.8	0.08	..	..	0.02
1-Butene	−88	~6.0	3.8	0.61	0.29	0.18	..
1-Butene	−88	~2.0	6.0	0.29	0.27	0.08	..
1-Butene	−88	~6.0	6.8	0.50	0.27	0.14	..
1-Butene	−86	6.5	6.6	0.50	0.18	0.09	0.25
1-Butene	−86	9.5	3.9	0.59	0.15	0.09	0.27
1-Butene	−88	18.0	1.56	1.22	0.07	0.09	0.53
1-Butene	−87	41.0	0.96	1.6	..	..	0.84
cis-2-Butene	−89	2.8	3.9	0.20	0.59	0.12	0.33
cis-2-Butene	−88	18.9	1.2	1.1	0.15	0.16	0.9

[a] Yield in excess of that formed by disproportionation.

The latter is derived in this case from the total and labeled yield of 1-butene. The results are shown in Table II. The average value of G_{CH_3} is 0.20 ± 0.02.

The other radical yields were calculated from the average relative ratios of labeled hydrocarbons observed at low $^{14}CH_3I$ concentrations[15] at −102°, and the value of $G_{CH_3} = 0.2$. The results are given in column 6 of Table I.

These values may be compared with radical yields which have been derived from product yields reported for the radiolysis of liquid propylene at −50°.[2] Such a calculation is complicated since it requires a knowledge of the percentage of each major product formed by a free radical process and also certain disproportionation ratios. If gas phase data are assumed for the latter, the yields of isopropyl, *n*-propyl, and allyl given in the final column of Table I can be derived from Wagner's data.[2] The agreement in the two sets of values demonstrates that radical yields determined with the $^{14}CH_3$ radical sampling technique in the presence of $^{14}CH_3I$ are in good agreement with yields obtained for the radiolysis of the pure olefin.

The major radical species is allyl, formed with a yield approximately equal to the sum of the yields of *n*-propyl and isopropyl radicals. An unusual feature of the radiolysis of propylene is the formation of *n*-propyl radicals. Since thermal hydrogen atom addition to propylene in the liquid phase at 25° gives 87% isopropyl radicals and only 9% *n*-propyl radicals,[13] processes other than thermal hydrogen atom addition must be invoked to explain the formation of some of the propyl radicals. Wagner has proposed that allyl radicals are formed by reaction 5

$$C_3H_6^+ + C_3H_6 \longrightarrow C_3H_7^+ + C_3H_5 \qquad (5)$$

and propyl radicals result from stabilization of the excited $C_3H_7^*$ radical formed on neutralization of the $C_3H_7^+$ ions. The presence of methyl radicals and the complete absence of vinyl radicals shows that simple cleavage of the carbon–carbon single bond does not occur. The formation of methyl radicals could be attributed to the decomposition of the activated *n*-propyl radicals.[22]

$$n\text{-}C_3H_7^* \longrightarrow CH_3 + C_2H_4 \qquad (6)$$

Although stabilization would be expected to occur readily, there is evidence[23] that decomposition also occurs in the liquid phase.

1-Butene. Of all of the olefins studied 1-butene was found to have the most radical intermediates and the analysis required the separation and identification of ten labeled products, of which six were C_5 compounds. Most of the irradiations were at −88°. The $^{14}CH_3I$ concentration varied from 1 to 40 mM. The labeled hydrocarbons (and corresponding radicals) observed were ethane ($^{14}CH_3$ and CH_3),[15] propane (C_2H_5), 1-butene (allyl), isopentane (*sec*-butyl), *n*-pentane (*n*-butyl), 1-pentene (3-butenyl), *trans*-2-pentene (*trans*-1-methylallyl or 1-butenyl), *cis*-2-pentene (*cis*-1-methylallyl or 1-butenyl), and 3-methyl-1-butene (both *cis*- and *trans*-1-methylallyl). Two isomers of the 1-methylallyl radical are expected (and both are observed in 1-butene) since the allyl structure is nonlinear.[24] Since there are two reactive sites on each radical, four reactions with $^{14}CH_3$ may occur yielding three distinguishable products

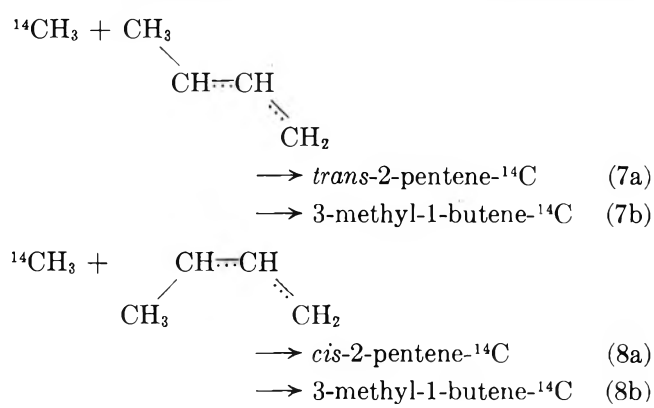

(22) W. A. Noyes, Jr., G. S. Hammond, and J. N. Pitts, Jr., "Advances in Photochemistry," Vol. I, Interscience Publishers, Inc., New York, N. Y., 1963, p. 155.

(23) E. K. C. Lee and F. S. Rowland, *J. Chem. Phys.*, **36**, 554 (1962).

(24) The stereochemistry of 1-methylallyl radicals has been demonstrated in the case of chlorine abstraction reactions; *i.e.*, these radicals retain their *cis* or *trans* structure and yield the corresponding *cis*- or *trans*-chlorobutene; *cf.* C. Walling and W. Thaler, *J. Am. Chem. Soc.*, 83, 3877 (1961).

In the case of 1-butene, 2-pentene-^{14}C is also derived to some extent from 1-butenyl radicals. However, most of this product is attributed to the 1-methylallyl radical since the ratio of the yields 2-pentene-^{14}C:3-methyl-1-butene-^{14}C is only slightly larger than the average values of k_{7a}/k_{7b} and k_{8a}/k_{8b} determined for *trans*- and *cis*-1-methylallyl radicals (see section on Reactions of 1-Methylallyl Radicals).

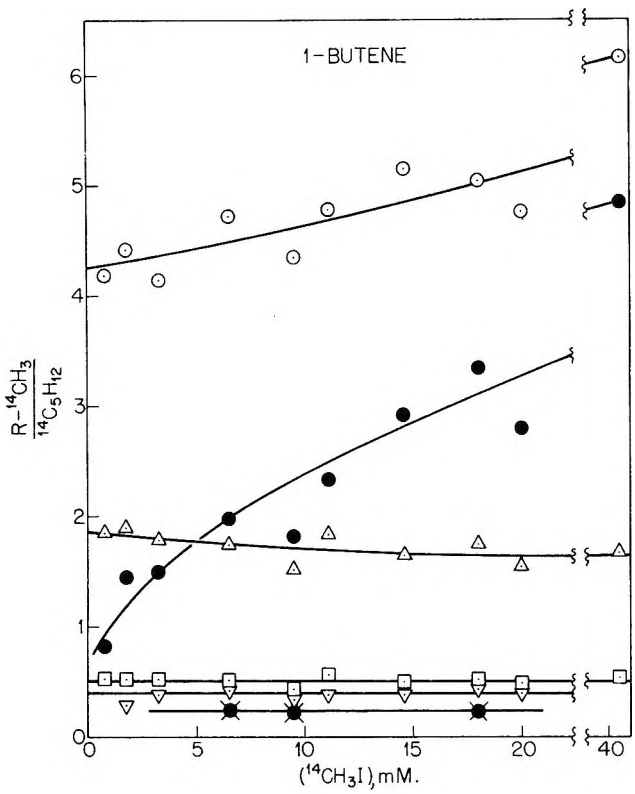

Figure 2. Yields of labeled hydrocarbons relative to the yield of n-$^{14}C_5H_{12}$ *vs.* $^{14}CH_3I$ concentration in liquid 1-butene; temperature, −90°: ⊙, (*cis* and *trans*-2-pentene + 3-methyl-1-butene):n-$^{14}C_5H_{12}$; △, isopentane-^{14}C:n-$^{14}C_5H_{12}$; ▽, 1-butene-^{14}C:n-$^{14}C_5H_{12}$; □, 1-pentene-^{14}C:n-$^{14}C_5H_{12}$; ●, ethane-^{14}C(total):n-$^{14}C_5H_{12}$; ✦, ethane-^{14}C(cor.):n-$^{14}C_5H_{12}$.

The effect of $^{14}CH_3I$ concentration on the relative yields is shown in Figure 2. The results are presented in terms of the ratio of the yield of a labeled product to that of n-pentane-^{14}C. The product ratios which are independent of concentration are: $^{14}C_2H_6$(cor.)/n-$^{14}C_5H_{12}$ = 0.24 ± 0.01,[15] $^{14}C_3H_8/n$-$^{14}C_5H_{12}$ = 0.38 ± 0.05, 1-$^{14}C_4H_8/n$-$^{14}C_5H_{12}$ = 0.40 ± 0.05, and 1-$^{14}C_5H_{10}/n$-$^{14}C_5H_{12}$ = 0.52 ± 0.03. The ratio i-$^{14}C_5H_{12}/n$-$^{14}C_5H_{12}$ is 1.8 ± 0.1 at low $^{14}CH_3I$ concentration and decreases slightly to 1.65 at higher concentrations. The combined yield of *cis*- and *trans*-2-pentene-^{14}C and 3-methyl-1-butene-^{14}C relative to that of n-pentane-^{14}C increases from 4.25 at low $^{14}CH_3I$ concentration to a maximum value of 6.1 at 41 mM. One experiment at −175° performed to determine the vinyl radical yield showed a small yield of $^{14}C_3H_6$, corresponding to $G_{vinyl} \cong 0.03$.

The methane-^{14}C yield was in all cases 38% of the total activity yield, similar to the result found for propylene. Only 12% of this yield can reasonably be attributed to disproportionation. $G_{^{14}CH_4}$ increases from 0.02 at 1 mM to 0.8 at 40 mM.

The yields of labeled hydrocarbons relative to that of n-$^{14}C_5H_{12}$ obtained at low $^{14}CH_3I$ concentration (<3 mM) where $G_{^{14}CH_3}$ is less than 0.3 are given in Table III, column 2. The disproportionation factors used in deriving radical yields from these ratios are given in column 4. The value of D/C at −88° for R = *sec*-butyl is taken as 0.27.[25] For n-butyl and 3-buteny radicals a value of D/C of 0.09 is assumed. For the 1-methylallyl radicals a correction for disproportionation is applied only to the yield of 3-methyl-1-butene. These disproportionation factors do not affect the relative yields by more than a few per cent (compare hydrocarbon yields in column 3 to radical yields in column 5).

Table III: Radical Yields in 1-Butene

R	Relative yield of R-$^{14}CH_3$[a] Exptl. ratio	%	1 + D/C	Relative yield of R, %	G_R
CH_3	0.235	2.7	1.0	2.5	0.11
C_2H_5	0.38	4.5	1.09	4.4	0.19
Allyl	0.40	4.6	1.0	4.2	0.19
sec-Butyl	1.82	21.1	1.27	24.4	1.09
n-Butyl	1.00	11.6	1.09	11.5	0.51
3-Butenyl	0.524	6.1	1.09	6.0	0.27
1-Butenyl	[b]	5.4	1.0	4.9	0.22
trans-1-Methylallyl	1.66[c]	16.2	1.0	23.8	1.05
	1.32[d]	15.3	1.15		
cis-1-Methylallyl	1.27[e]	12.4	1.0	18.2	0.80

[a] Average of four determinations of the yields of R-$^{14}CH_3$ relative to n-$^{14}C_5H_{12}$ at <3 mM $^{14}CH_3I$. [b] The yield of this radical is deduced from the relative yield of 2-pentene. [c] Relative yield of *trans*-2-pentene. [d] Relative yield of 3-methyl-1-butene. [e] Relative yield of *cis*-2-pentene.

The absolute yields of radicals were determined for 1-butene from G_{CH_3} as given by the products of $G_{^{14}CH_3}$ and the ratio $(CH_3)/(^{14}CH_3)$. The latter was obtained from the ratio of yields: (total isopentane − i-$^{14}C_5H_{12}$)/

(25) Based on a gas phase value at 25° of 0.19 which is the average of 0.3 obtained by B. S. Rabinovitch and R. W. Diesen, *J. Chem. Phys.*, **30**, 735 (1959), and 0.08 obtained by M. Miyoski and R. K. Brinton, *ibid.*, **36**, 3019 (1962).

i-$^{14}C_5H_{12}$. The value of G_{CH_3} obtained is 0.11 ± 0.03.[26] The other radical yields were calculated from this value and the relative yields in column 5 of Table III. The total radical yield, G_{TR}, is 4.4 ± 1.2.

Approximately equal yields, 0.80 and 1.05 of *cis*- and *trans*-1-methylallyl radicals, respectively, are observed, which again indicates that 1-methylallyl radicals do not isomerize to a preferred structure. The total yield of 1-methylallyl radicals (G = 1.85) exceeds the total yield of butyl radicals (G = 1.6). Again it is noticed there is a significant yield of *n*-butyl radicals which would not be expected to be formed by thermal hydrogen atom addition to 1-butene. The 3-butenyl yield is only 0.27. Thus the allylic hydrogen atoms in 1-butene are approximately 11 times more readily removed than the primary hydrogen atoms and are comparable in reactivity to tertiary hydrogen atoms in saturated alkanes.[27] Fragmentation is much less important (11% of the total radical yield) in 1-butene than in saturated hydrocarbons. The methyl and allyl radical yields are comparable, suggesting a terminal C–C bond split

$$\text{1-butene} \xrightarrow{\sim} CH_3 + \text{allyl} \qquad (9)$$

The formation of ethyl radicals (G = 0.19) and the low yield of vinyl radicals (G = 0.03) are analogous to the results for propylene where methyl radicals but no vinyl radicals are observed and could be attributed to cracking of activated *n*-butyl radicals.[23,28] (See discussion of mechanism below.)

$$(n\text{-}C_4H_9)^* \longrightarrow C_2H_5 + C_2H_4 \qquad (10)$$

Effect of Concentration of $^{14}CH_3I$. Although the primary interest of this study was the results obtained at low concentrations of methyl iodide, the effect of concentration was studied in propene (Figure 1) and 1-butene (Figure 2) as an aid in understanding the mechanism of interaction of $^{14}CH_3I$. Relative yields of labeled hydrocarbons are expected to be proportional to radical yields at all concentrations but absolute yields may be somewhat in error at high concentrations owing to the lack of a quantitative measure of the yield of methyl-^{14}C radicals (some are lost by reaction with species Y formed in reaction 2, for example).

If the precursor of the $^{14}CH_3$ radical is a thermal hydrogen atom, then there should be a competition between reactions 2a and 11 in propylene and 2a and 12 in 1-butene. Reaction 11 yields mostly isopropyl radicals[13] and reaction 12 yields *sec*-butyl radicals.[29,30] Thus the yields of isopropyl and *sec*-butyl radicals should be sensitive to the methyl iodide concentration. However, the ratio of yields i-$^{14}C_4H_{10}$:n-$^{14}C_4H_{10}$ in propylene, which measures the ratio of the isopropyl to *n*-propyl radical yield, is invariant up to 55 mM $^{14}CH_3I$. Similarly, the ratio i-$^{14}C_5H_{12}$:n-$^{14}C_5H_{12}$ in 1-butene (Figure 2) is nearly constant from 1 to 40 mM. Thus this competition is not occurring to a large extent either because hydrogen atoms are not present or because reactions 11 and 12 are fast compared to reaction 2a, in which case $G_H \leqq G_{\text{isopropyl}}$ in propylene and $G_H \leqq G_{sec\text{-butyl}}$ in 1-butene. In either case it must be concluded that $^{14}CH_3$ radicals are generated in these systems by a process other than reaction 2a such as dissociative electron capture, reaction 2b. This reaction

$$e^- + {}^{14}CH_3I \longrightarrow {}^{14}CH_3 + I^- \qquad (2b$$

seems plausible in light of the recent observation of a 390-mμ absorption band, attributed to I^-, in irradiated alkane glasses containing methyl iodide as solute.[31]

The most pronounced effect of concentration of $^{14}CH_3I$ on the ratios (as shown in the figures) is an increase in the ratio of yields: allyl:*n*-propyl in propylene and 1-methylallyl:*n*-butyl in 1-butene. If for 1-butene this is considered to represent a change in the yield of 1-methylallyl radicals while $G_{n\text{-butyl}}$ remains constant, the increase is 0.8 molecule/100 e.v.; *i.e.*, from G = 1.9 at low methyl iodide to G = 2.7 at 40 mM methyl iodide. It is suggested that the explanation for this increase is related to the formation of methane[32] which increases from G = 0.02 at 1 mM to 0.8 at 40 mM. The agreement of these two increases suggests that a fraction ($\sim 1/3$) of the methyl-^{14}C radicals formed in reaction 2b have excess energy derived from the exothermicity of the reaction[33] and abstract an

$$H + {}^{14}CH_3I \longrightarrow {}^{14}CH_3 + HI \qquad (2a)$$

$$H + C_3H_6 \longrightarrow \begin{cases} \text{isopropyl} & (87\%) \\ n\text{-propyl} & (9\%) \\ \text{allyl} + H_2 & (4\%) \end{cases} \qquad (11)$$

$$H + \text{1-butene} \longrightarrow \textit{sec}\text{-butyl} \ (>95\%) \qquad (12)$$

(26) Although the relative yields are reliable to 5%, the absolute radical yields reported here are uncertain to ±25% as a result of this uncertainty in the measurement of G_{CH_3}. This arises largely from the fact that the methyl radical yield is small relative to $G_{^{14}CH_3}$ and the yield of i-$^{14}C_5H_{12}$ is close to that of the total isopentane as measured by the thermal conductivity detector. Thus a large uncertainty is introduced in determining the difference of the two yields in arriving at the ratio $(CH_3)/(^{14}CH_3)$.

(27) R. A. Holroyd and G. W. Klein, to be published.

(28) J. R. McNesby, C. M. Drew, and A. S. Gordon, *J. Chem. Phys.*, **24**, 1260 (1956).

(29) W. J. Moore and L. A. Wall, *ibid.*, **16**, 916 (1948); **17**, 1325 (1949).

(30) R. Klein and M. D. Scheer, *J. Phys. Chem.*, **67**, 1874 (1963).

(31) E. P. Bertin and W. H. Hamill, *J. Am. Chem. Soc.*, **86**, 1301 (1964).

(32) Only 12% of the methane is formed by disproportionation (see above).

(33) P. R. Geissler and J. E. Willard, *J. Am. Chem. Soc.*, **84**, 4627 (1962).

Table IV: Radical Yields in *cis*- and *trans*-2-Butene

R	Relative yield of $R-^{14}CH_3$[a] Exptl. ratio cis	trans	% cis	trans	1 + D/C	Relative yield of R, % cis	trans
CH_3	0.23	0.19	5.6	5.4	1.0	5.0	4.7
sec-Butyl	1.00	1.00	24.2	28.1	1.27	27.8	31.3
trans-1-Methylallyl	0.35	1.57	8.5	44.2	1.0	12.9	61.4
	1.09[b]	0.83[b]	26.4	23.4	1.15		
cis-1-Methylallyl	1.47	0.066	35.5	1.9	1.0	54.2	2.6

[a] The ratios given are averages of six determinations of the yields of $R-^{14}CH_3$ relative to that of $i-^{14}C_5H_{12}$ at concentrations of $^{14}CH_3I$ <3 m*M*. Average deviation <4%. [b] The ratio 3-methyl-1-butene-C^{14}: $i-^{14}C_5H_{12}$.

allylic hydrogen atom forming equal yields of $^{14}CH_4$ and

$$CH_3^* + \text{1-butene} \longrightarrow {}^{14}CH_4 + \text{1-methylallyl} \quad (13)$$

1-methylallyl radicals. The same effect is observed in propylene, *i.e.*, the yields of allyl radicals and $^{14}CH_4$ increase with methyl iodide concentration and this explanation quantitatively accounts for the results in that case also.

cis and trans-2-Butene. Since the loss of allylic hydrogens was shown to be a predominant process in 1-butene, it was of interest to investigate the 2-butenes where loss of an allylic hydrogen may also lead to 1-methylallyl radicals to see whether retention of configuration occurs. The 2-pentene-^{14}C produced in *cis*-2-butene was 80% *cis* and in *trans*-2-butene it was 96% *trans* (Table IV). Thus the 1-methylallyl radicals that are formed are mainly the *cis* isomer in *cis*-2-butene and almost exclusively the *trans* isomer in *trans*-2-butene, a fact which is significant to the consideration of mechanism of radical formation (see below) and which accounts for the observed differences in the C_8 products formed in the radiolysis of the two isomeric butenes.[3,34]

The only other labeled products at −88° are ethane and isopentane, indicating that methyl and *sec*-butyl radicals are also present making a total of only four radical intermediates in each of the 2-butenes. The relative radical yields in columns 7 and 8 of Table IV are derived from the yields of labeled hydrocarbons (columns 2 and 3) obtained at low $^{14}CH_3I$ concentration (<0.3 m*M*). The total radical yield for *cis*-2-butene is $G_{TR} = 2.8 \pm 0.7$ and for *trans*-2-butene it is $G_{TR} = 3.2 \pm 0.8$ (based on only two determinations in each case).

The formation of methyl and lack of formation of complementary 2-methylvinyl radicals suggests a process similar to that postulated for propylene radiolysis

$$(sec\text{-}C_4H_9)^* \longrightarrow CH_3 + C_3H_6 \quad (14)$$

For *cis*-2-butene the yield of propylene ($G = 0.13$)[3] is observed to be approximately equal to the yield of methyl radicals ($G = 0.14$, Table II). Reaction 14 has been shown to be an important mode of decomposition of chemically activated *sec*-butyl radicals in the gas phase.[35]

An attempt was made to see if thermal hydrogen atoms are present in irradiated *cis*-2-butene by adding isobutene as a scavenger. Hydrogen atoms react with isobutene to form mainly *t*-butyl radicals and $k_{15}/k_{16} \sim$

$$H + \text{isobutene} \longrightarrow t\text{-butyl} \quad (15)$$

$$H + cis\text{-2-butene} \longrightarrow sec\text{-butyl} \quad (16)$$

7 under the conditions of the experiment.[36] A 14 mole % solution of isobutene in *cis*-2-butene was irradiated and the ratio of radical yields *t*-butyl:*sec*-butyl was found to be 0.26. This ratio should have been approximately 1.0 for this solution if *sec*-butyl radicals were formed solely from thermal hydrogen atoms. Therefore, a significant fraction (at least 60%) of the *sec*-butyl radicals is formed by some other process and G_H is <0.4 molecule/100 e.v. for *cis*-2-butene.

Reactions of 1-Methylallyl Radicals. When $^{14}CH_3$ radicals react with 1-methylallyl radicals combination can occur at either of two positions (reactions 7 and 8) and if disproportionation occurs $^{14}CH_4$ and butadiene are formed. The results for *cis* and *trans*-2-butene show that *cis*-1-methylallyl radicals are slightly different from *trans*-1-methylallyl radicals. Roughly two-thirds of the combinations with methyl (at −88°) occur at the terminal carbon position for *trans*-2-butene since the yield of 2-pentene-^{14}C relative to that of 3-methyl-1-butene-^{14}C, *i.e.*, k_{7a}/k_{7b}, is 2.04 ± 0.02, but for *cis*-2-butene the corresponding ratio k_{8a}/k_{8b} is 1.67 ± 0.02. The higher value for the *trans* structure is attributed to steric effects. The fact that these ratios exceed unity is ascribed in part to enhanced disproportionation for $^{14}CH_3$ radical attack at the methyl-substituted carbon atom and in part to steric effects. As an independent check on these ratios, 1-methylallyl radicals were produced by irradiating a dilute (4×10^{-4} mole fraction) solution of butadiene in liquid ethane at −160°, in the presence of methyl iodide-^{14}C (2×10^{-4} mole frac-

(34) Although retention of configuration is observed in radical formation, a process occurring with high yield ($G \sim 4$ molecules/100 e.v.) during radiolysis is *cis–trans* isomerization of the olefin.

(35) B. S. Rabinovitch and R. W. Diesen, *J. Chem. Phys.*, **30**, 735 (1959).

(36) Although k_{15}/k_{16} is reported to be 4.4 at 24° in the gas phase, *cf.* K. R. Jennings and R. J. Cvetanović, *J. Chem. Phys.*, **35**, 1233 (1961), R. A. Holroyd and G. W. Klein (unpublished data) have observed that k_{15}/k_{16} is ~7 at −100° in liquid ethane. A recent study [T. T. Kassal and M. Szwarc, *J. Phys. Chem.*, **68**, 381 (1964)] showed that D-atom addition to isobutene is 8–10 times the rate of D-atom addition to 2-pentene in liquid propane at −183°.

tion). The labeled products were propane, *trans*-2-pentene, and 3-methyl-1-butene, formed with relative yields of 5.2, 1.9, and 1.0. Thus only *trans*-1-methylallyl radicals are formed by the addition of hydrogen atoms (from the radiolysis of C_2H_6) to butadiene and k_{7a}/k_{7b} is 1.9 at -160, confirming the value obtained above.

In 1-butene the ratio of 2-pentene-^{14}C to 3-methyl-1-butene-^{14}C was found to be 2.24 ± 0.08 and a ratio of ~1.86 (equal to the average of k_{7a}/k_{7b} and k_{8a}/k_{8b}) would be expected where both *cis*- and *trans*-1-methylallyl radicals are present in equal amounts. This difference is interpreted as evidence that 2-pentene-^{14}C is also formed in 1-butene by combination of $^{14}CH_3$ and 1-butenyl radicals.

Strikingly similar results for reactions of 1-methylallyl radicals were obtained in a study of allylic chlorination of olefins using *t*-butyl hypochlorite.[24] The analogous ratio of products 1-chloro-2-butene:3-chloro-1-butene formed on abstraction of a chlorine atom (1-methylallyl + *t*-BuOCl → 1-chloro-2-butene or 3-chloro-1-butene + *t*-BuO) was 1.72 for *cis*-1-methylallyl radicals, 2.73 for *trans*-1-methylallyl radicals, and 2.24 for a mixture of the two radicals obtained from 1-butene. Again the *trans* species was observed to be slightly more reactive than the *cis* at the terminal carbon position.

Isobutene. A few experiments were carried out to determine the nature of the radical intermediates in isobutene at $-90°$. The labeled hydrocarbons and relative yields observed at 10 m*M* $^{14}CH_3I$ were C_2H_6(cor.) (6%), *i*-C_4H_8 (2%), neo-C_5H_{12} (8%), *i*-C_5H_{12} (14%), and 2-methyl-1-butene (70%). The major radical species is indeed 2-methylallyl and the yield of 1-methylvinyl radicals is small, which confirms the e.s.r. studies.[10] The relative radical yields derived from these yields, assuming D/C is 1.4 for *t*-butyl at $-90°$, are methyl (6%), 1-methylvinyl (2%), *t*-butyl (18%), isobutyl (12%), and 2-methylallyl (62%).

The isobutyl radical yield is significant in that again its formation cannot be attributed to thermal hydrogen atom addition.[30,37] It is interesting that of the butyl radicals formed in isobutene, 40% are isobutyl and 60% are *t*-butyl, and in the radiolysis of neopentane 23% of the butyl radicals formed in the primary processes are isobutyl and 77% are *t*-butyl.[27] These may be unrelated observations; however, the similarity of the results suggests that the precursor of butyl radicals might be the same in both substances. The *t*-butyl carbonium ion, $C_4H_9^+$, has been suggested as an intermediate in both isobutene[9] and neopentane.[38] Perhaps on neutralization of this ion both isobutyl and *t*-butyl radicals are formed in approximately a 1:2 ratio.

Mechanism of Radical Production. From the results of this study of the characterization of radical intermediates in liquid olefins, several generalities emerge and some conclusions can be formed which apply to the mechanism of radical production. The major radicals observed correspond to either the gain or loss of a hydrogen atom from the parent olefin. The yield of methylallyl radicals is larger than the yield of butyl radicals in all of the butenes, and ≧80% retention of structural configuration is observed in the formation of 1-methylallyl radicals. Only 5–10% of the radicals arise from carbon–carbon bond cleavage and vinyl or substituted vinyl radicals have low yields.

There must be a process by which an olefin ultimately becomes an alkyl radical, which is not the addition of thermal hydrogen atoms, in order to account for *n*-propyl radicals in propylene, *n*-butyl radicals in 1-butene, isobutyl radicals in isobutene, and a large share of the *sec*-butyl radicals in *cis*-2-butene.

An excited molecule mechanism for the production of 1-methylallyl radicals would mean that the excited species must be energetic enough to dissociate the allylic carbon–hydrogen bond, in which case it would also have sufficient energy to isomerize rapidly. The observed retention of configuration in the 2-butenes argues against such a mechanism.

The ion–molecule reaction that has been proposed for isobutene[11] involves reaction 1. Analogous reactions have been postulated for propylene,[2] 1-hexene and 1-octene.[39] Further support for ionic intermediates comes from the observation of a 680-mμ absorption band in alkane–alkene glass at $-196°$ which was ascribed to the 2-methyl-1-pentene cation.[40] Formally, reaction 1 could be considered to be either a proton transfer or a hydrogen atom abstraction. Mass spectrometer studies tend to favor the former.[41] If proton transfer is involved, the 2-butene results require that the $C_4H_8^+$ molecule ion retains the configuration of the olefin from which it was formed and that subsequently in reaction 1 a proton is removed from the allylic position of the ion. Alternately, reaction 1 could be considered to be a hydrogen atom abstraction reaction as was postulated for 1-hexene.[39] Retention of configuration would certainly be expected for this mechanism. A cor-

(37) R. A. Holroyd, *J. Phys. Chem.*, **65**, 1352 (1961).

(38) T. F. Williams, *Trans. Faraday Soc.*, **57**, 755 (1961).

(39) P. C. Chang, N. C. Yang, and C. D. Wagner, *J. Am. Chem. Soc.*, **81**, 2060 (1959).

(40) J. P. Guarino and W. H. Hamill, *ibid.*, **86**, 777 (1964).

(41) It has been noted that known proton-transfer reactions have cross sections one order of magnitude larger than hydrogen atom transfer reactions (*cf.* ref. 10, p. 88).

sequence of this alternative is that the yields of radicals in mixtures of olefins should be related to the ease of hydrogen atom abstraction. Consideration of the present results does not allow one to conclude which of these mechanisms is the important one in radical formation in olefins.

It is postulated that subsequent neutralization of the $C_4H_9^+$ carbonium ion formed in reaction 1 leads to an excited butyl radical which may decompose (reactions 10 and 14), abstract to form *n*-butane (reaction 17), as well as stabilize to butyl radicals (reaction 18). Although the latter is most important in the liquid phase, decomposition is indicated for 1-butene and *cis*- and *trans*-2-butene and this process accounts for the yield of methylallyl radicals exceeding that of butyl radicals. Reaction 17 is proposed to explain the large yields ($G \sim 0.6$ to 1.0)[3] of *n*-butane, observed to be formed from 1-butene and 2-butene, which cannot be attributed solely to free radical reactions.

$$C_4H_9^* + C_4H_8 \longrightarrow C_4H_{10} + C_4H_7 \quad (17)$$

$$\longrightarrow C_4H_9 + C_4H_8 \quad (18)$$

Kinetics and Equilibria of the System Indium(III)–Indium(I)–Indium(0) in Acidic Solution

by Robert E. Visco

Bell Telephone Laboratories, Incorporated, Murray Hill, New Jersey *(Received July 13, 1964)*

The kinetics of the homogeneous oxidation of In(I) ion by H^+ in perchloric acid have been investigated using a dropping mercury electrode. The rate law for the disappearance of In(I) ion was found to be: rate $= -k[\text{In(I)}][H^+]$. The heat of activation is 11.4 kcal./mole and the entropy of activation is −33.8 e.u. Solutions of In(I) used in the kinetic studies were prepared *in situ* by electrochemical or chemical oxidation of indium metal or its amalgam. Equilibration of indium metal or its amalgam with In(III) ion in 0.70 *M* $HClO_4$ was also investigated. A potentiometric method has been used to evaluate the potential of the In(I)–In(0) couple. At 20° in 0.70 *M* $HClO_4$, the standard potential is −0.126 v. *vs.* n.h.e.

Introduction

Compounds of indium in the +1 oxidation state are well known in the solid phase. These compounds have the stoichiometry InX and $In(InX_4)$.[1,2] The experiments in aqueous solution designed to yield In(I) have been those associated with equilibration of In(III) solutions with indium metal.[3-5] After the equilibration, titrimetric or potentiometric investigations were carried out, and the soluble oxidizable species present were interpreted as In(I). In one study, In(II) was also presumed to be present.[3] Except for one polarogram of the equilibrated solution shown by Marple,[4] evidence other than titrimetry and potentiometry does not exist for intermediate indium oxidation states. It has recently been demonstrated that

(1) J. D. Corbett and R. K. McMullan, *J. Am. Chem. Soc.*, **78**, 2906 (1956); R. K. McMullan and J. D. Corbett, *ibid.*, **80**, 4761 (1958).

(2) J. D. Corbett, *Inorg. Chem.*, **2**, 634 (1963); *J. Electrochem. Soc.*, **109**, 1214 (1962).

(3) L. G. Hepler, Z Z. Hugus, Jr., and W. M. Latimer, *J. Am. Chem. Soc.*, **75**, 5652 (1953).

(4) L. W. Marple, Ph.D. Thesis, Massachusetts Institute of Technology, 1960.

(5) G. Biedermann and T. Wallin, *Acta Chem. Scand.*, **14**, 594 (1960).

the indous ion can be generated by electrochemical oxidation of indium amalgams or indium metal.[6] This paper is a report on some aspects of the solution chemistry of the indous ion.

Experimental

Three general types of experiments were performed to generate In(I) in solution. The first type involved the constant current anodization of indium metal or an amalgam several mole per cent in indium. The second type generated In(I) by a chemical oxidation of indium metal or its amalgam with nitrate ion which was added to perchloric acid electrolyte. Lastly, In(I) was generated by equilibration of In(III) solutions with indium metal or indium amalgam.

The electrodes used were either an indium metal or amalgam anode to generate In(I), a dropping mercury electrode used to study the decay of In(I), and two saturated calomel electrodes (s.c.e.), one used as a reference electrode and one used as a cathode during electrochemical generation of In(I). Additions of HCl and HNO_3 solutions were achieved by using syringe burets. The $NaClO_4$ used was prepared by neutralization of Na_2CO_3 with $HClO_4$, and the resulting solution was standardized by ion exchange and pH titration.

The potentiometric experiments were carried out in stirred solutions with and without added In(III). The potential of an indium metal electrode was recorded using a high impedance follower and strip chart recorder. An indium stick electrode was anodized and after a time sufficient to generate polarographically measurable quantities of In(I), the anodization was terminated. The potential decay was followed for some time and then the stirring was terminated in order to measure the polarographic current at −0.20 v. *vs.* s.c.e. Zero time potentials and polarographic currents, as well as potential decay rates, could be determined in this way.

The potential of the saturated calomel electrode employed was measured against a reversible hydrogen electrode, and the thermodynamic data presented herein reflect the shift of potentials to the normal hydrogen electrode scale. A complete description of the equipment used has been given elsewhere.[6]

Results

1. Homogeneous Disappearance of In(I). The dropping mercury electrode was used to follow the In(I) concentration as a function of time after termination of anodization or chemical oxidation of indium amalgams and indium metal. The current at −0.20 v. *vs.* s.c.e. corresponds to the oxidation of In(I) to

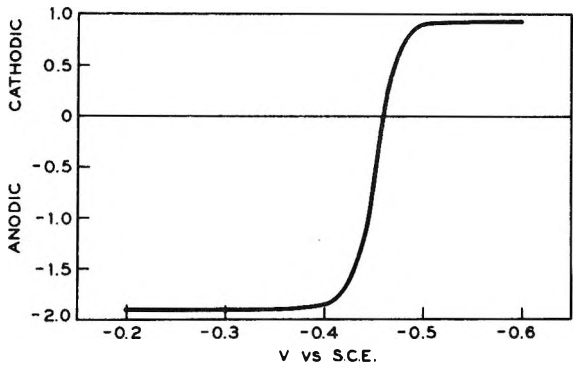

Figure 1. Polarographic wave for In(I) normalized to a common time after termination of anodization.

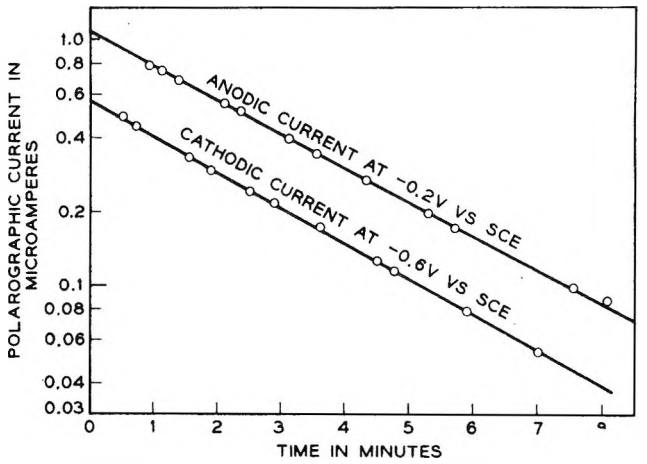

Figure 2. Time dependence of the polarographic current at −0.20 v. *vs.* s.c.e. and −0.60 v. *vs.* s.c.e. after anodization of a 2 mole % indium amalgam in 0.70 *M* $HClO_4$ at 20°.

In(III), while the current at −0.60 v. corresponds to the reduction of In(I) to the amalgam[6] (Figure 1).

The chemical reaction associated with the homogeneous disappearance of In(I) is of interest. It is observed that in acidic solution, the decay of In(I) is first order in the In(I) concentration for at least four half-lives (Figure 2). After the In(I) has decayed completely, the polarographic residual current anodic to −0.70 v. *vs.* s.c.e. is identical with that of the original $HClO_4$ solution. Cathodic to −0.70 v., the irreversible reduction of In(III) becomes important. The pseudo-first-order rate constant at constant anionic molarity (0.70 *M*) is dependent on the hydrogen ion concentration (Figure 3). It is also observed that a colorless gas is homogeneously liberated both during and after anodization. This gas is neither O_2 nor Cl_2 because after anodization no change in the polarographic

(6) R. Visco, *J. Electrochem. Soc.*, in press; paper No. 166, 125th Meeting of the Electrochemical Society, Toronto, Canada, 1964.

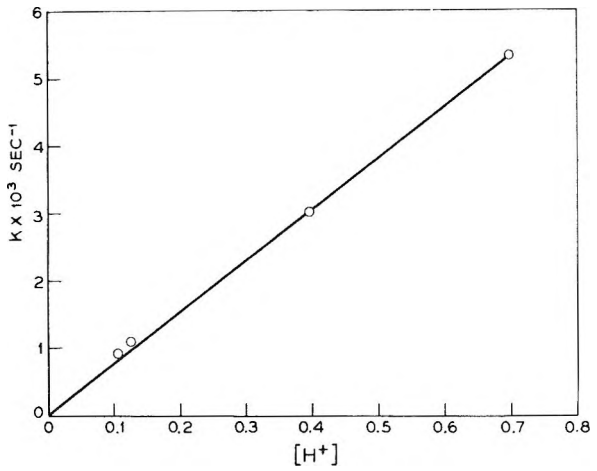

Figure 3. Acidity dependence of the first-order rate constant for In(I) disappearance at 20° in $HClO_4$ + $NaClO_4$ of 0.70 *M*.

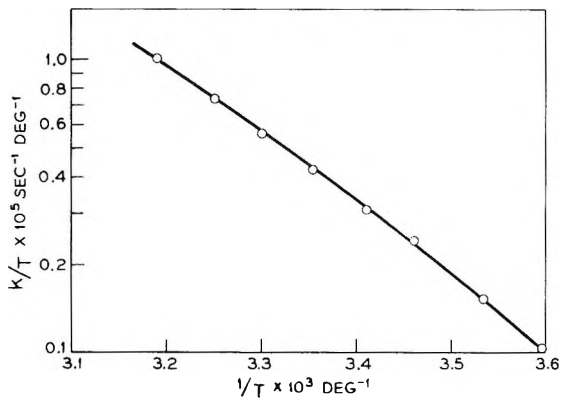

Figure 4. Temperature dependence of the first-order rate constant for In(I) decay in 0.105 *M* $HClO_4$ + 0.595 *M* $NaClO_4$.

residual current is observed. The gas is, therefore, presumed to be H_2. Homogeneous liberation of H_2 has been reported recently for the disappearance of Ga(I) in acidic solution[2] and has been postulated previously for In(I) decay.[5] The polarographic residual current anodic to 0 v. *vs.* s.c.e. is unaltered by successive anodizations; therefore, Cl^- from chemical attack on the perchlorate anion of the supporting electrolyte cannot be produced by the disappearance of In(I). The same observations concerning the production of chloride ion and hydrogen gas are true for those experiments where indium metal was chemically oxidized in perchloric acid solutions that were millimolar in nitrate ion.

The chemical reaction for the disappearance of In(I), therefore, must be

$$In(I) + 2H^+ \longrightarrow In(III) + H_2 \qquad (1)$$

The rate law for the disappearance of In(I) has the form

$$-\frac{d[In(I)]}{dt} = k[In(I)] = k_1[In(I)][H^+] \qquad (2)$$

The temperature dependence of k at 0.105 *M* H^+ was evaluated over the range from 5 to 40°. The plot of log k *vs.* the reciprocal of the absolute temperature is given in Figure 4. The energy of activation, ΔH^*, is calculated to be 11.4 kcal./mole, while ΔS^* is −33.8 e.u. The values of ΔS^* and ΔH^* were identical with those found in 0.70 *M* H^+ over a slightly narrower range of temperature.

The pseudo-first-order rate constant for In(I) decay is independent of added Cl^- up to the highest added Cl^- concentration investigated (3.9×10^{-3} *M*). This rate constant is also independent of added NO_3^- ion.

The concentration of In(I) after termination of the anodization varied depending on anode current and time of anodization. A typical zero time polarographic current for the oxidation of In(I) to In(III) was 0.2 μa. Assuming a diffusion coefficient for In(I) equal to that of Tl(I),[7] the concentration of In(I) is approximately 2.5×10^{-5} *M*. Solutions at least 10 times more concentrated in In(I) can be generated by NO_3^- oxidation of indium metal.

A comparison with other inorganic ions capable of reducing H^+ is difficult because of the lack of precise rate data. The Cr(II)-Cr(III) couple does liberate H_2 slowly from aqueous solution, but the rate seems to be dependent on impurities and is, therefore, markedly dependent on the method of Cr(II) preparation.[8] Since Cr(II) can be stored for a period of days to weeks and used as an oxidation–reduction titrant, the rate of liberation of H_2 must be significantly slower than that for In(I). The Eu(II)-Eu(III), Ti(III)-Ti(IV), and V(II)-V(III) couples are also slow to liberate H_2 since they, like Cr(II), also are used as oxidation–reduction titrants.[8] Corbett[2] has recently reported on the H_2 liberation reaction by Ga(I) in acidic solution. Precise rate data were not presented, but the Ga(I) reaction is fairly rapid and certainly the rate of hydrogen evolution is of the order of that for In(I).

2. In(I) by Equilibration of In(III) and In(0). An effort was made to repeat some of the equilibration experiments described by Latimer,[3] Marple,[4] and Biedermann.[5]

$$In(III) + 2In(0) \rightleftarrows 3In(I) \qquad (3)$$

(7) I. Shain and K. J. Martin, *J. Phys. Chem.*, 65, 254 (1961).

(8) H. A. Laitinen, "Chemical Analysis," McGraw-Hill Book Co., Inc., New York, N. Y., 1960, p. 447 ff.

Indium metal either as a 0.6-cm. diameter rod, with 5 cm.^{2} of exposed area, or as the 2.5 mole % amalgam with a 1-cm.^{2} area were equilibrated with solutions of In(III) ion in 0.70 M $HClO_4$. Polarographic evidence was obtained which demonstrated the presence of In(I) in these equilibrated solutions, but the magnitude of the current at either −0.20 or −0.60 v. *vs.* s.c.e. was severalfold smaller than that calculated using either Latimer's or Marple's values for the disproportionation constant, eq. 3, and a value of 18×10^{-6} cm.^{2} sec.$^{-1}$ for the diffusion coefficient of In(I). It was found that the quantity of In(I) formed depended both on stirring conditions and exposed area of the metal electrode. Since In(I) had been shown to exist under these conditions, and because of the difficulty in obtaining precise concentration data, an alternate approach was attempted to allow an evaluation of the equilibrium constant for reaction 3.

3. Potential–Time Curves on Indium Metal Electrodes. By electrochemical oxidation of indium metal, it is possible to generate solutions of In(I) in excess of the equilibrium concentration predicted by using the appropriate equilibrium constant for reaction 3. The return to equilibrium conditions can be followed by recording the potential of the indium metal electrode after the anodization is terminated. Since it is well established that the electrochemical exchange-current density for the In(III)–In(0) couple is quite low,[9-11] it may be expected that the electrode would respond to the In(I)–In(0) couple if the exchange-current density for this couple is sufficiently high. Since the rate law for the decay of In(I) in acidic solutions has already been established, the potential–time behavior of an indium metal electrode can, hopefully, be used to evaluate the standard potential of the In(I)–In(0) couple as well as supply qualitative information on the rate of attainment of the disproportionation equilibrium.

The Nernst equation for the In(I)–In(0) couple, where the In(I) concentration obeys the rate law described above, is shown in eq. 4.

$$E = E^\circ_{1/0} + \frac{RT}{nF} \ln [\mathrm{In(I)}^0] - \frac{RT}{nF} k_1[\mathrm{H}^+]t \quad (4)$$

The quantity $In(I)^0$ is the zero time value of the In(I) activity, that is, if time is measured from the termination of anodization, $In(I)^0$ becomes the activity of In(I) at the termination of anodization.

Equation 4 will be valid under only a very special set of circumstances, namely: (1) the exchange-current density for the In(III)–In(0) couple ($i^0_{3/0}$) is relatively low; (2) the exchange-current density for the In(I)–In(0) couple ($i^0_{1/0}$) is relatively high; and (3) the disproportionation reaction is slow with respect to the homogeneous path for In(I) decay under the mass transport conditions prevailing in the cell.

Table I: Calculation of the Formal Potential, $E^{\circ\prime}$, for the In(I)-In(0) Couple at 20° in 0.70 M $HClO_4$

	In(I) polarographic current, μa.[a]	$-E$ at termination of anodization *vs.* n.h.e., v.	$-E^{\circ\prime}$ *vs.* n.h.e., v.
I	21.5	0.304	0.150
II	12.0	0.319	0.150
III	19.0	0.307	0.150
IV	7.0	0.324	0.142
V	20.0	0.306	0.150
VI	11.7	0.316	0.146

[a] The concentration of In(I) was evaluated by using the simple Ilkovic equation with an assumed D^7, $n = 2$, and the values of m and τ appropriate to the capillary employed.

If $i^0_{3/0}$ is even comparable to $i^0_{1/0}$, then the electrode will not respond reversibly to the In(I)–In(0) couple since in these experiments the In(III) ion concentration is much greater than the In(I) ion concentration. If the disproportionation reaction is rapid, then the In(I) ion concentration at the electrode surface will be altered both by the homogeneous decay of In(I) and by the disproportionation reaction. Since the In(I) ion exceeds its equilibrium value, it will be consumed by the back reaction of eq. 3 and, therefore, the rate of change of potential should be greater than that predicted by only the homogeneous decay path. Changes in stirring would be expected to bring about changes in the potential of an indium metal electrode if, because of reaction 3, the surface concentration of In(I) ion differs to a significant extent from its bulk concentration.

It has been observed experimentally that changes in stirring do not alter the potential decay rate for the first two half-lives of In(I) decay when the initial In(I) ion concentration is greater than 2×10^{-5} M. The rate of change of electrode potential in 0.70 M H^+ is 8.0 mv./min., while that calculated using the appropriate value of k_1 is 8.05 mv./min. The extrapolated zero time value of the indium metal electrode potential is proportional to the logarithm of the zero time value of the In(I) polarographic current with a

(9) B. Lovrecek and V. Markovac, *J. Electrochem. Soc.*, **109**, 727 (1962).

(10) E. D. Moorhead and W. M. MacNevin, *Anal. Chem.*, **34**, 269 (1962).

(11) V. V. Losey and A. I. Molodov, *Electrochim. Acta*, **6**, 81 (1962).

proportionality constant corresponding to a one-electron change, Table I.

Therefore, it appears that all the special conditions prescribed above are fulfilled, namely, $i^\circ_{1/0} \gg i^\circ_{3/0}$, and that the rate of disappearance of In(I) *via* the disproportionation reaction is probably less than 10% of the rate of the homogeneous path for In(I) decay.

It remains only to calculate the standard potential ($E^\circ_{1/0}$) of the In(I)–In(0) couple using the measured zero time potentials and polarographic currents. With this, $E^\circ_{1/0}$ and the recently re-evaluated $E^\circ_{3/0}$ for the In(III)–In(0) couple,[12] a value for the disproportionation constant for reaction 3 can be stated with some certainty. In order to calculate $E^\circ_{1/0}$, the polarographic diffusion coefficient of In(I) is required as well as the value of the mean ionic activity coefficient of $InClO_4$. Neither of these quantities can be evaluated independently. A value of -0.126 v. *vs.* n.h.e. for $E^\circ_{1/0}$ can be calculated subject to reasonable assumptions and approximations. It has been assumed that the polarographic diffusion coefficient of In(I) is equal to that of Tl(I),[7] 17.9×10^{-6} cm.^{2} sec.$^{-1}$, and that the mean ionic activity coefficient of $InClO_4$ is 0.65. The value of the equilibrium constant for reaction 3 using a value of -0.338 v. *vs.* n.h.e.[12] for $E^\circ_{3/0}$ is then 1.3×10^{-11} mole^2 l.$^{-2}$.

4. Nitrate Oxidation of Indium Metal in $HClO_4$ Solutions. When stirred solutions of $HClO_4$ adulterated with HNO_3 on the millimolar level are brought in contact with indium metal, it is possible to demonstrate polarographically that In(I) is formed. The kinetics and stoichiometry of this oxidation–reduction reaction were not investigated in detail, but it was demonstrated that less than 3 moles of In(III) are eventually formed per mole of added NO_3^-. The polarographic current of In(I) was followed as a function of time at -0.20 v. *vs.* s.c.e. by periodically interrupting the stirring. At the particular stirring conditions employed, the In(I) current was proportional to the NO_3^- concentration and the current decayed exponentially with a half-life of 35 min. Such behavior is consistent with a mass transport limited NO_3^- oxidation of indium metal to give In(I) as one product. Using the above technique, it was possible to generate 2×10^{-4} *M* In(I) solutions from indium metal in solutions containing 2.7×10^{-3} *M* NO_3^-.

Marple[4] has demonstrated that the $Ce(ClO_4)_3$ electrolyte made in the manner described by Latimer contained NO_3^- as an impurity. Since it has been demonstrated above that In(I) is a product of NO_3^- oxidation of indium metal, and since a slow attainment of the disproportionation equilibrium is consistent with the potentiometric experiments herein described, there appears to be some doubt concerning the validity of direct equilibration of indium metal with In(III) in solutions adulterated with traces of NO_3^-.

Discussion

It has been shown that In(I) is produced during chemical or electrochemical oxidation of indium metal or its amalgam. The rate law for the decay of In(I) in acidic solutions is first order in both In(I) and H^+ with a ΔH^* of 11.4 kcal./mole and a ΔS^* of -33.8 e.u. Rechnitz and Catherino[13] have observed recently that in acidic solutions Ru(II) is oxidized by water to Ru(III). They observed no Cl^- or pH dependence on the rate, while an Arrhenius activation energy of 26.4 kcal./mole was calculated. The differences between the several one-electron couples of which Ru(III)–Ru(II) is but one example and the two-electron couples, In(III)–In(I) and Ga(III)–Ga(I), indicate that rates, and probably mechanisms, of homogeneous hydrogen ion reduction by inorganic cations seem to fall into two classes. A very slow, but sometimes readily catalyzed reaction, is typical of the several common one-electron oxidation–reduction couples, while a much more rapid reaction is observed with the two-electron reductants studied to date. The observation by Schug and Sadowski[14] that Ga(I) reduces ClO_4^- to give Cl^- does not seem to be true for the In(I) ion. The experiments with gallium were conducted in hot concentrated $HClO_4$ solutions which are the usual conditions necessary for perchlorate reactivity for its reduction to Cl^-.

By a potentiometric technique, it was possible to evaluate the standard potential for the In(I)–In(0) couple and to conclude that, under the experimental conditions employed here, the disproportionation of In(I) at an indium metal electrode is slow. Such a conclusion is consistent with the observation that in acidic noncomplexing media the electrochemical exchange-current density for the In(III)–In(0) couple is exceedingly low. Since the electrochemical measurements in noncomplexing media[9-11] indicate that the first electron addition to In(III) ion or the last electron removal in the oxidation of indium metal[9,10] is the rate-controlling step, it is suggested that the sluggishness in establishing the equilibrium in the system In(III)–In(I)–In(0) is due to a slow electron transfer between the In(III) ion and a transient In(II) state.

The several literature values for the disproportiona-

(12) A. K. Covington, M. A. Hakeem, and W. F. K. Wynne-Jones, *J. Chem. Soc.*, 4394 (1963).

(13) G. A. Rechnitz and H. A. Catherino, private communication.

(14) K. Schug and A. Sadowski, *J. Am. Chem. Soc.*, **83**, 3538 (1961).

tion constant for reaction 5 are, unfortunately, not directly comparable with the value of 1.3×10^{-11} reported here. Marple's values of 1.3×10^{-7} in 4.0 M Na_2SO_4 and 4.9×10^{-12} in 4.1 M $NaClO_4$ for the equilibrium quotient at 25° are difficult to correct for ionic strength. Latimer's value of $K^0 = 3.3 \times 10^{-11}$ in $Ce(ClO_4)_3$ ($\mu = 0.83$) with estimated values of the appropriate $\gamma_\pm$ is suspect[4] because of a probable NO_3^- impurity in the supporting electrolyte employed. The value of $K^0 = 4.0 \times 10^{-9}$ reported by Biedermann and Wallin[5] in 3.0 M $NaClO_4$ differs considerably from that reported here. These authors concluded that the reaction of In(I) with H^+ was less than first order in In(I) and has an inverse In(III) dependence in the rate law. They also concluded that In(I), to some extent, decayed by a heterogeneous path. Based on the work reported here and elsewhere,[6] the decay of In(I) appears to be a homogeneous first-order reaction in In(I) with no detectable inverse In(III) terms. These differences may be rationalized in terms of the differing acidities employed in the two studies. At the low acidities studied by Biedermann, the H^+ ion dependent homogeneous term in the rate law determined at the higher acidities may have become comparable to the heterogeneous term with an inverse In(III) dependence.

Thermodynamic Properties of Aqueous Solutions of Mixed Electrolytes. The Hydrochloric Acid–Potassium Chloride System from 40 to 0°

by J. H. Stern, C. W. Anderson, and A. A. Passchier

Department of Chemistry, California State College at Long Beach, Long Beach, California 90804
(Received July 18, 1964)

Heats of mixing, ΔH_m, of equimolal solutions of HCl and KCl at 2 and 3 m concentrations, respectively, were determined calorimetrically at 40, 25, 10, and 0° and fitted to an equation based on Harned's rule. Excess free energies, ΔF_m^E, were calculated from e.m.f. measurements and combined with ΔH_m to yield ΔS_m^E. The results are interpreted *via* the Brønsted–Guggenheim theory of specific interaction. Apparent molal heat capacities, $\Phi C_{p(2,3)}$, of mixed HCl–KCl and HCl–NaCl solutions at 25° are also given.

I. Introduction

Activity coefficients of binary components in ternary mixed strong 1–1 electrolytes have frequently been determined *via* e.m.f.[1] and isopiestic vapor pressure methods.[2] The activity coefficients express the deviation of observed behavior of each component from ideality. Components in many such mixtures have been found to obey Harned's rule

$$\log \gamma_2 = \log \gamma_{2(0)} - \alpha_{23}[m(1 - X_2)] - \beta_{23}[m(1 - X_2)]^2 \quad (1)$$

$$\log \gamma_3 = \log \gamma_{3(0)} - \alpha_{32}[m(X_2)] - \beta_{32}[m(X_2)]^2 \quad (2)$$

where γ_2 and γ_3 are the activity coefficients of electrolytes 2 and 3 in the presence of each other at solute mole fractions X_2 and $1 - X_2$, respectively, and total molality m. $\gamma_{2(0)}$ and $\gamma_{3(0)}$ are the activity coefficients of the pure binary electrolytes at molality m. The α and β terms are empirical coefficients independent of mole fraction, but are in general functions of the total

(1) H. S. Harned, *J. Phys. Chem.*, **64**, 112 (1960).
(2) R. A. Robinson, *ibid.*, **65**, 662 (1961).

molality m, temperature, and pressure. Very few systems have been studied at temperatures other than 25°.

Another related approach to the interpretation of physicochemical behavior of such mixtures is *via* excess thermodynamic properties. These determine the departure from ideality of the solution as a whole and characterize quantitatively the changes in interaction that occur as a result of the mixing process.

Earlier contributors reported on the investigation of the systems HCl–NaCl[3] from 40 to 0° and LiCl–NaCl and KCl–NaCl[4] at 25°. Direct heats of mixing, ΔH_m, of equimolal solutions of each of the two binary electrolytes were combined with excess free energies, ΔF_m^E, to obtain excess entropies of mixing, ΔS_m^E. The present study describes the excess thermodynamic properties of HCl–KCl at 2 and 3 m concentrations from 40 to 0° and follows the investigation of the activity coefficients by Harned *via* e.m.f. methods[1] over the same concentration and temperature ranges.

It can be shown[5] that for systems obeying eq. 1 and 2, ΔF_m^E takes the form

$$\Delta F_m^E = -2.303RT(X_2)(1 - X_2)m[(\alpha_{23} + \alpha_{32}) + \frac{2m}{3}(2\beta_{23} + \beta_{32}) - \frac{2mX_2}{3}(\beta_{23} - \beta_{32})] \quad (3)$$

Both electrolytes are initially at molality m and yield a final solution of total molality m with solute mole fractions X_2 and $1 - X_2$, respectively. ΔF_m^E can thus be obtained from experimentally determined Harned coefficients. ΔH_m per mole of solute may be obtained by combining eq. 3 and the Gibbs–Helmhotz equation

$$\Delta H_m = 2.303RT^2(X_2)(1 - X_2)m\frac{\partial}{\partial T}[(\alpha_{23} + \alpha_{32}) + \frac{2m}{3}(2\beta_{23} + \beta_{32}) - \frac{2mX_2}{3}(\beta_{23} - \beta_{32})] \quad (4)$$

At $X_2 = X_3 = 0.50$, eq. 4 reduces to

$$\Delta H_m = \frac{2.303RT^2m}{4}\frac{\partial}{\partial T}[(\alpha_{23} + \alpha_{32}) + m(\beta_{23} + \beta_{32})] \quad (5)$$

In all preceding equations, subscripts 2 and 3 refer to components HCl and KCl, respectively.

The excess functions will be examined briefly as deviations from the Brønsted–Guggenheim theory of specific interaction which has been discussed in two previous communications.[3,4] Systems with a common ion obeying this theory show zero values of all three excess thermodynamic functions.

II. Experimental

The calorimeter[6] and general experimental procedures[7] have been described elsewhere. The over-all estimated accuracy is ±4%.

Materials. The KCl, A.R. grade, was kept at 150° prior to weighing and was dissolved to the desired molalities with weighed quantities of triple-distilled water. The HCl was prepared from concentrated stock solutions and analyzed *via* NaOH previously standardized with KHP.

III. Results and Discussion

Observed values of ΔH_m for HCl–KCl as a function of the solute mole fraction X_{HCl} are shown in Figures 1 and 2, respectively. All heats are exothermic and ΔH_m is expressed as a polynomial function of X.

$$\Delta H_m = 2.303RT^2mX_2(1 - X_2)(A + BX_2) \quad (6)$$

The curves represent the fit of all data, by the method of least squares, to equations of this form. A and B are constants; these constants expressed in terms of eq. 4 are

$$A = \frac{\partial}{\partial T}\left[(\alpha_{23} + \alpha_{32}) + \frac{2}{3}m(2\beta_{23} + \beta_{32})\right] \quad (7)$$

$$B = \frac{\partial}{\partial T}\left[-\frac{2}{3}m(\beta_{23} - \beta_{32})\right] \quad (8)$$

A is related to the magnitude of ΔH_m; the parameter B pertains to the asymmetry of the curves in Figures 1 and 2. Values of A and B are shown in Table I. All

Table I: Summary of Parameters A and B

t, °C.	$-A \times 10^5$	$-B \times 10^5$
	Concn. = 2 m	
0	12.3	1.15
10	9.44	0.86
25	8.16	0.53
40	6.99	0.33
	Concn. = 3 m	
0	18.6	3.37
10	16.0	2.45
25	13.5	−0.88
40	10.2	1.07

(3) J. H. Stern and A. A. Passchier, *J. Phys. Chem.*, **67**, 2420 (1963).

(4) J. H. Stern and C. W. Anderson, *ibid.*, **68**, 2528 (1964).

(5) G. N. Lewis and M. Randall, "Thermodynamics," revised by K. S. Pitzer and L. Brewer, McGraw-Hill Book Co., Inc., New York, N. Y., 1961, p. 571.

(6) J. H. Stern and A. A. Passchier, *J. Phys. Chem.*, **66**, 752 (1962).

(7) T. F. Young, Y. C. Wu, and A. A. Krawetz, *Discussions Faraday Soc.*, **24**, 37 (1957).

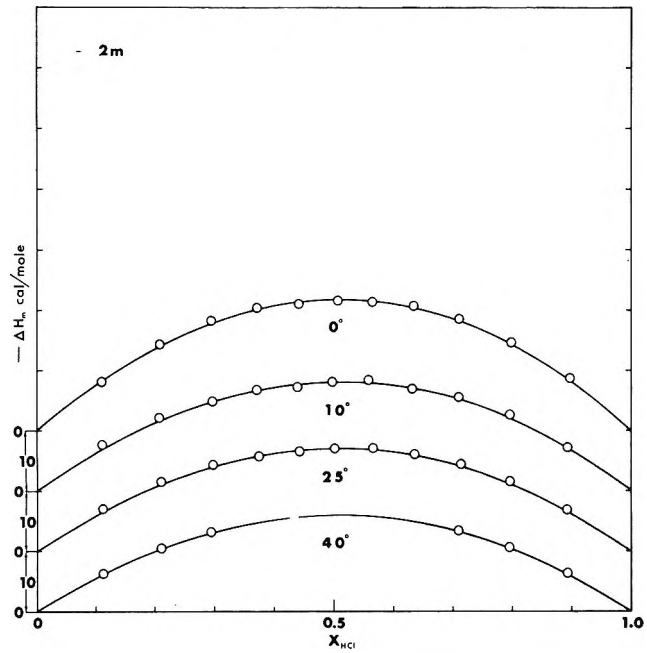

Figure 1. Heats of mixing, ΔH_m, as a function of the solute mole fraction of HCl, X_{HCl}, 2 m.

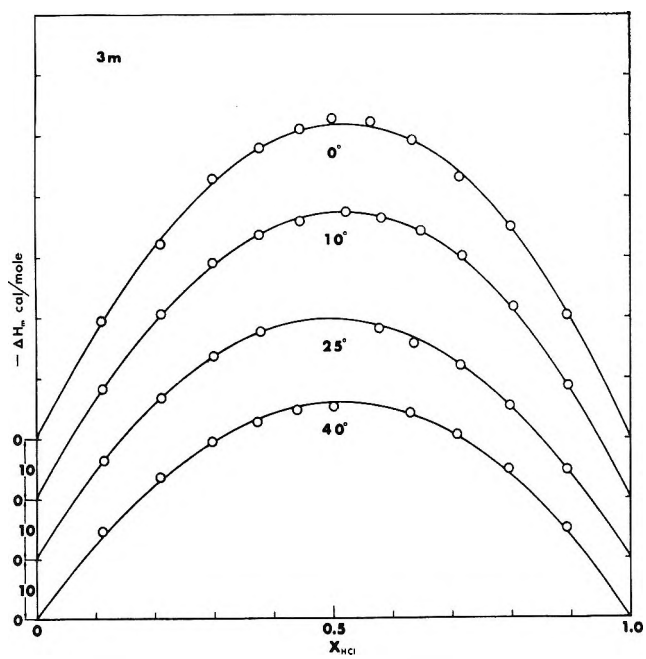

Figure 2. Heats of mixing, ΔH_m, as a function of the solute mole fraction of HCl, X_{HCl}, 3 m.

curves are nearly parabolic and are thus consistent with the quadratic dependence of ΔH_m on X. The observed symmetry for the HCl–KCl system indicates that the temperature derivatives of both β-terms are equal or very close to zero.

From e.m.f. results as a function of temperature, estimated values of ΔH_m *via* eq. 5 may be obtained. These estimates are in disagreement with direct heats with respect to both their magnitude and sign. E.m.f. data predict inversions in sign with positive heats below approximately 25° and negative heats above this temperature at all molalities. On the basis of direct heats for all systems measured at this laboratory, it is very unlikely that inversions in sign occur either as a function of concentration or temperature.

ΔF_m^E values calculated from e.m.f. data are subject to a relatively high error (±1 cal./mole) due to the uncertainty of calculated Harned coefficients. Since the magnitudes of ΔF_m^E are generally much lower than those of the heats, calculated excess entropies ΔS_m^E are based mainly on the more accurate values of ΔH_m.

Table II gives values of all three thermodynamic properties ΔF_m^E, ΔH_m, and ΔS_m^E at $X = 0.50$. It may be observed that, in general, all three excess properties show the same algebraic trends as a function of concentration for all systems studied at this laboratory. As with HCl–NaCl, ΔH_m and ΔS_m^E approach zero with increasing temperature and decreasing concentration. It thus appears that systems of this nature tend to obey the Brønsted–Guggenheim theory and approach ideal solution behavior with increasing temperature and decreasing concentration. It may be noted that thermal effects for HCl–KCl are much smaller below 2 m than in other systems studied here. ΔH_m at 25° was found by Young and co-workers[7] to be −3.5 cal./mole for 1 m mixtures at $X = 0.50$. Measurements at this laboratory show that ΔH_m for 0.5 m mixtures is approximately −0.25 cal./mole at the same temperature and solute mole fraction.

Since ΔH_m is known over a range of temperatures, it is possible to obtain the change in heat capacity,

Table II: Summary of ΔF_m^E, ΔH_m, and ΔS_m^E at $X = 0.5$

t, °C.	ΔF_m^E, cal./mole	$-\Delta H_m$, cal./mole	$-\Delta S_m^E$, e.u.
	Concn. = 2 m		
0	3	24.6	0.09
10	3	21.3	0.08
25	4	21.1	0.07
40	5	20.7	0.07
	Concn. = 3 m		
0	1	51.9	0.19
10	1	47.4	0.17
25	1	39.8	0.14
40	(1)	36.6	(0.12)

ΔC_p, per mole of solute per degree, resulting from the mixing process. The apparent molal heat capacity of the mixture $\Phi C_{p(2,3)}$ as a function of solute mole fraction at a given total molality is of interest. No data of this type appear to have been published. It can be shown that $\Phi C_{p(2,3)}$ is related to ΔC_p and the apparent molal heat capacities of each pure binary electrolyte $\Phi C_{p(2)}$ and $\Phi C_{p(3)}$, respectively, by the equation

$$\Phi C_{p(2,3)} = \Delta C_p + X_2 \Phi C_{p(2)} + (1 - X_2)\Phi C_{p(3)} \quad (9)$$

Table III shows ΔC_p data and calculated values of $\Phi C_{p(2,3)}$ for HCl–NaCl and HCl–KCl at 25° and $X = 0.50$, based on ΦC_p data of the pure binary electrolytes HCl,[8] NaCl,[9] and KCl.[10]

ΔC_p for both systems is quite small in comparison to $\Phi C_{p(2,3)}$. Thus $\Phi C_{p(2,3)}$ at $X = 0.50$ is approximately equal to the average of the apparent molal heat capacities of the pure binary electrolytes at the same total molality. One may therefore obtain reasonable estimates of the heat capacities of similar systems in the absence of ΔC_p data.

Table III: Apparent Molal Heat Capacities, $\Phi C_{p(2,3)}$, of HCl–KCl and HCl–NaCl at Mole Fraction $X = 0.5$ at 25°

System	m	$-\Phi C_{p(2,3)}$, cal./mole deg.	ΔC_p, cal./mole deg.
HCl–KCl	1	(21.6)	
	2	17.8	0.02
	3	14.9	0.3
HCl–NaCl	1	17.6	−0.2
	2	13.2	−0.4
	3	10.3	−0.6

Acknowledgment. The authors are grateful to the United States Army Research Office (Durham) for financial support.

(8) F. T. Gucker, Jr., and K. H. Schminke, *J. Am. Chem. Soc.*, **54**, 1358 (1932); values at 3 m were determined by extrapolation.

(9) See ref. 5, p. 376; values at 3 m were determined by extrapolation.

(10) See ref. 5, p. 643.

Infrared and Gravimetric Study of the Surface Hydration of γ-Alumina

by J. B. Peri

Research and Development Department, American Oil Company, Whiting, Indiana *(Received July 20, 1964)*

Infrared and gravimetric studies have yielded new information on the surface hydration of γ-alumina. Dry γ-alumina was found to "chemisorb" one molecule of water per 11–16 Å.^{2} of surface at 100°, depending on rehydration procedure. Desorption of chemisorbed water on subsequent heating under vacuum was studied at temperatures between 100 and 900°. Characteristic dehydration isotherms showed that a rapid initial weight loss was followed by a slow continuing loss. Because of these characteristics, the extent of surface hydration is governed primarily by the drying temperature. In addition to the three major isolated hydroxyl bands previously noted in infrared spectra of dry alumina (3800, 3744, and 3700 cm.$^{-1}$), two additional bands are often observed at 3733 and 3780 cm.$^{-1}$. Changes in the bands were studied as a function of temperature. Rehydration of the surface between 400 and 800° was also studied by direct spectroscopic observation of the hot alumina. Results show that hydroxyl groups, although apparently mobile, persist as such on the surface at high temperatures on distinct types of sites rather than in a completely random state. Readsorption of water cannot alone explain the difficulty in removing residual hydroxyl groups at high temperatures. Free energy of activation for desorption of water apparently increases continuously as the surface concentration of hydroxyl groups decreases. Although "strain" sites are undoubtedly created by dehydration, characterization of such sites as strained Al–O–Al linkages seems inadequate.

Introduction

Strongly dried aluminas chemisorb at least a monolayer of water when exposed to moisture at room temperature. Although several crystallographic forms of high-area alumina exist, available information suggests that their surface hydration is similar. The forms most often investigated are usually characterized as either γ- or η-alumina, but mixtures of these two rather similar forms are probably common.

The hydrated surface of γ-alumina retains 13 molecules of water per 100 Å.^{2} of surface after evacuation at 25° for 100 hr.,[1] and even after drying at 120°, it may still retain 8.25 molecules per 100 Å.^{2}.[2] Although much of this water is held as hydroxyl groups on the surface, infrared studies show that some of the water strongly adsorbed at 25° remains molecular.[3]

When wet γ-alumina is heated above 100°, some of the adsorbed water is desorbed while some reacts to form hydroxyl groups. At higher temperatures these, as well as pre-existing hydroxyl groups, gradually condense to eliminate water. Surface hydroxyl groups are not completely eliminated, however, even by drying under vacuum at 800–1000°.[3]

Important catalytic properties of γ-alumina are associated with "acid" sites created on the surface during removal of hydroxyl groups at temperatures above 400°. Hydroxyl groups of at least three chemically distinct types remain on the surface after the alumina has been dried under vacuum above 650°,[3] but none of these types appears catalytically active, *per se*, for the isomerization of 1-butene.[4] Instead, the active sites appear to involve abnormal exposure of aluminum ions[4] or creation of strained Al–O–Al linkages[5] on the surface

(1) J. J. Kipling and D. B. Peakall, *J. Chem. Soc.*, 834 (1957).

(2) J. H. de Boer, J. M. H. Fortuin, B. C. Lippens, and W. H. Meijs, *J. Catalysis*, **2**, 1 (1963).

(3) J. B. Peri and R. B. Hannan, *J. Phys. Chem.*, **64**, 1526 (1960).

(4) J. B. Peri, *Actes Congr. Intern. de Catalyse, 2e, Paris, 1960*, **1**, 1333 (1961).

(5) E. B. Cornelius, T. H. Milliken, G. A. Mills, and A. G. Oblad, *J. Phys. Chem.*, 59, 809 (1955).

when hydroxyl groups are removed. Some degree of strain is known to characterize crystal surfaces.[6]

Although much progress has been made toward explaining the surface hydration of aluminas, present knowledge remains meager. Because the crucial importance of surface hydration has often been overlooked, much of the literature on catalytic properties of aluminas is of questionable significance. Further understanding of the details of surface hydration is clearly needed.

The present work was undertaken to obtain additional information on the surface hydration of γ-alumina by infrared and gravimetric techniques. Alumina aerogel plates were studied.

Experimental

Materials. Because minor differences in procedure may lead to unsatisfactory plates or may otherwise influence the properties of the alumina, the preparative procedure is described in detail. Unless otherwise noted, reagent grade chemicals were used.

Alumina sol was typically prepared from 80 g. of aluminum metal pellets (0.3 to 0.6 cm., 99.99 +% pure), 60 ml. of glacial acetic acid, 3 l. of distilled water, and 0.1 g. of red mercuric oxide. These materials were combined in a three-necked Pyrex flask equipped with a reflux condenser, a stirrer, and a thermocouple. The flask was warmed with a heating mantle to initiate the reaction. Then the mantle was dropped, and the reaction was allowed to proceed at 65–70° for 24 to 48 hr. The sol was decanted from any unreacted aluminum or coarse precipitate and, if it showed more than a slight milky opalescence, was centrifuged for 15 min. at 30,000 *g* in an angle-head centrifuge.

The clear sol (~5% Al_2O_3) was floated as a 0.3- to 0.6-cm. layer on clean mercury or carbon tetrachloride in a 20.3-cm. crystallization dish. Open weighing bottles of 10% aqueous ammonia solution were suspended inside the dish, which was covered with a large watch glass. Gelation normally required about 2 hr., but the time varied with the thickness of the sol layer and the amount and concentration of the ammonia solution. (Excessive exposure to ammonia gave opaque plates, whereas correct exposure gave clear, firm plates.)

The plates were broken into suitable pieces and carefully transferred to a crystallization dish containing methanol. (The plates never occupied more than 20% of the volume of methanol in the dish.) The dish was gently swirled once or twice a day, and the methanol was replaced at 2- to 4-day intervals; it was changed at least four times over a 2-week period.

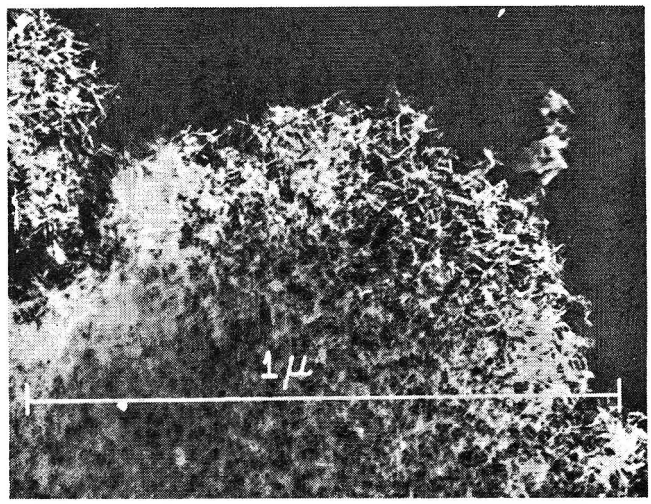

Figure 1. Electron micrograph of calcined alumina aerogel.

After alcohol exchange, the plates were packed loosely in a glass autoclave liner (3.2 cm. i.d. and 26.7 cm. in length) filled with pure methanol. The liner was placed in a stainless steel autoclave, and methanol was added to fill the autoclave completely, which was then sealed and heated slowly to 260° while the methanol was bled off slowly, as necessary, to keep the pressure below 1500 p.s.i. Between 260 and 280° bleeding was continued for about 2 hr. to maintain the pressure as long as possible in the range from 1200 to 1500 p.s.i. Ultimately, the pressure was slowly lowered, and the autoclave was evacuated for about 0.5 hr. while still hot (~300°). The clear aerogel was removed from the autoclave and calcined in air or oxygen at 600° before use.

X-Ray analysis showed that the original sol, which had been dried in air at 130°, was mainly amorphous with some microcrystalline Boehmite; the calcined aerogel was γ-alumina.

For electron micrographs, the calcined aerogel was ground in ethanol, and a thin film of the suspension was dried onto a carbon supporting film. Figure 1 illustrates the typical rod- or lath-like appearance of the alumina particles. Some samples also contained sheet-like structures.

Spectroscopic analysis of a typical plate showed <0.035% impurities, mostly silicon (0.019%).

Because small amounts of carbon dioxide are strongly held by γ-alumina, the water used in this work was distilled into the vacuum system from a solution containing a few per cent of barium hydroxide and was further

(6) W. A. Weyl, *Trans. N. Y. Acad. Sci.*, 12, 245 (1950); "A New Approach to Surface Chemistry and Heterogeneous Catalysis," Mineral Industries Experiment Station Bulletin 57, State College, Pa., 1951; "Structure and Properties of Solid Surfaces," R. Gomer and C. S. Smith, Ed., University of Chicago Press, Chicago, Ill., 1953, p. 147.

degassed by vacuum distillation before admission to the cell.

Equipment and Techniques. Most of the equipment and techniques used in this work have been described.[3,4] However, in some of the infrared work, a Beckman IR-9, double-beam, grating spectrometer was used to re-examine hydroxyl stretching bands at a higher resolution than was possible in previous studies. Desorbed gases were, in some instances, analyzed by mass spectrometry.

Gravimetric Study

Rehydration at 100°. Three aerogel plates were used in the gravimetric study. All had surface areas, as measured by nitrogen adsorption, in the range of 310–350 m.^{3}/g. Infrared spectra were recorded at intervals during the gravimetric studies.

Plate I (dry weight, 0.210 g.) was evacuated in the cell for 2 hr. at 800°, and its nitrogen adsorption at −195.6° was measured. Then it was held at 100° for 9 days while water vapor was admitted in small doses. The weight changes showed that the initial doses were rapidly and irreversibly adsorbed. However, above a total adsorption approximating 53% of a filled monolayer (6.25 molecules of water/100 Å.^{2} assumed as 100%), a significant fraction of the water held after 0.5- to 1-hr. equilibration could be desorbed by evacuation for 30 min. through a trap cooled with liquid nitrogen. Further additions of water were incompletely adsorbed, but adsorption increased slowly with time—due mainly to an increase in the irreversible adsorption. The results are summarized in Figure 2.

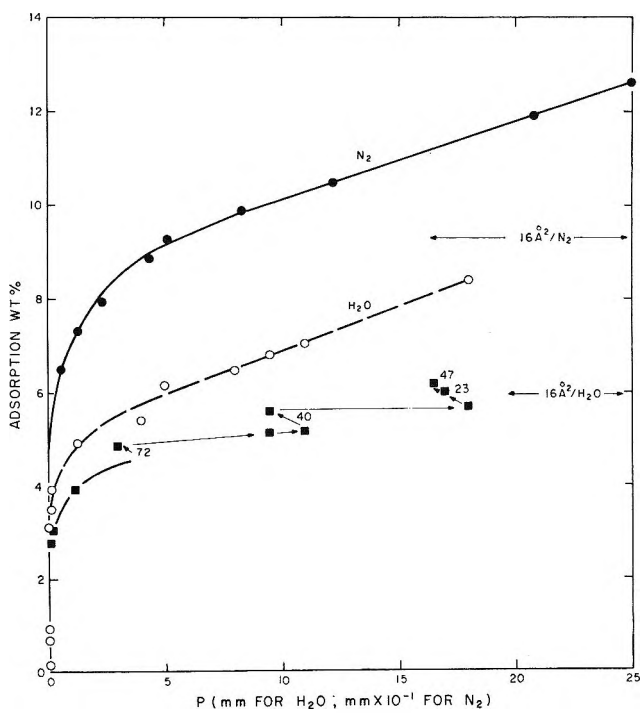

Figure 2. Adsorption of water (100°) and nitrogen (−195.6°) on alumina aerogel.

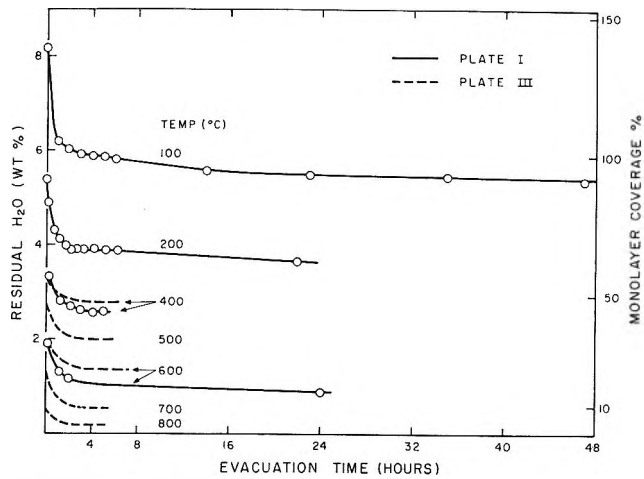

Figure 3. Dehydration of alumina aerogel.

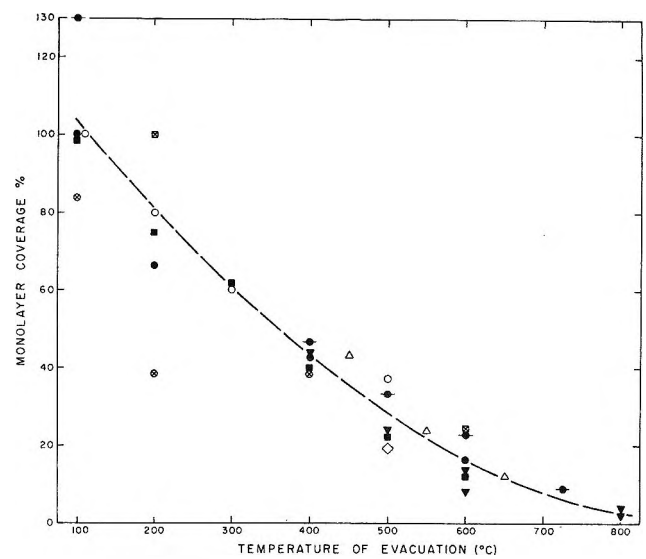

Figure 4. Dehydration of alumina (drying times normally 1–25 hr.): ○, Haldeman and Emmett[8]; △, Hindin and Weller[9]; ⊗, Whalley and Winter[10]; △, Kloosterziel[11]; ⊠, Boreskov, *et al.*, 100 hr.[12]; ●, plate I; ■, plate II; -●-, plate III; ▼, deuterium exchange.

Open points on the water isotherm represent measurements made 0.5 to 1 hr. after each addition of water. The set of solid points below this isotherm represents irreversible adsorption measured after evacuation through the cold trap for 0.5 hr. from an initial pressure represented by the ordinate. Numbers on arrows between points represent the elapsed time (in hours) between measurements. Following each evacuation the cell was closed off, and the water in the cold trap

was allowed to revaporize. All other time intervals represented by arrows between points are between 0.5 and 1 hr.

Maximum total adsorption at the highest pressure studied (18 mm.) was approximately 9.3 molecules/100 Å.^{2}. Subsequent evacuation at 100° reduced this to 6.4/100 Å.^{2} after 2 hr. and to 5.7/100 Å.^{2} after 71 hr.

Rehydration of plate II under similar conditions produced similar results. The isotherm obtained after 0.5- to 1-hr. equilibration again gave a B point corresponding to approximately 6.25 molecules/100 Å.^{2}. Slowly increasing irreversible adsorption in a closed cell (at an initial pressure of 5 mm.) gave 8.7 molecules/100 Å.^{2} (final pressure, 1.5 mm.) after 2 days' equilibration. This was reduced to approximately 6.2/100 Å.^{2} after 1-hr. evacuation.

Plate III was rehydrated by exposure to water vapor at saturation pressure ($\sim$ 200 mm.) and at room temperature for 16 hr. and then was held at 100° for 2 hr. at the same pressure. Despite the much shorter equilibration time at 100°, maximum adsorption was appreciably greater than that obtained with plates I and II. Increasing the period of heating at 100° to 16 hr. did not increase the adsorption. Total adsorption at 100° and 20 mm. never exceeded 12.5 molecules/100 Å.^{2}. After evacuation for 2 hr. at 100°, 8.3 molecules/100 Å.^{2} (or one hydroxyl group/6 Å.^{2}) remained.

The rehydration experiments indicate that the area per water molecule retained after evacuation for 1 hr. at 100° may range from 11 to 16 Å.^{2}, depending on the method and extent of rehydration. Clearly, equilibrium was not reached either during readsorption of water vapor at 100° or during the period of evacuation arbitrarily used to define irreversible adsorption. Although rehydration at room temperature (under conditions where physically adsorbed water is held to a considerable extent by the alumina) yields higher values for the chemisorbed water retained after evacuation at 100°, it is not obvious that such chemisorption represents only water or hydroxyl ions held on the same surface measured by nitrogen adsorption.

Dehydration of the Hydrated Surface. After rehydration as described, the plates were dried by evacuation at progressively higher temperatures. Figure 3 shows the data obtained for plates I and III. Correction was made for a small difference in specific surface areas. Plate II, which was dried by evacuation for about 2 hr. at several temperatures from 100 to 600°, showed a similar behavior.

The existence of the sloping plateaus in the dehydration curves suggests that, despite variations in drying procedures, some uniformity should exist in literature data on surface hydration of alumina. Abundant data are available, but they are usually complicated by variations in drying conditions and, in the case of older data, by unknown surface area. Data reported by Gregg and Wheatley,[7] for example, indicate that drying in air above 600° caused loss of surface area at almost the same rate as loss of water, the surface remaining about 33% covered with hydroxyl groups. Figure 4 presents data, recalculated to show surface coverage with hydroxyl groups, from published studies of high-area alumina[8-12] in which samples were dehydrated under reasonably good vacuum and surface areas were given. Points representing work by Haldeman and Emmett[8] were calculated from a curve representing maximum hydration. Points obtained from study of the aerogel plates discussed above and from equilibrium deuterium exchange on other similar plates in this laboratory are also included. For data of the present study, surface coverage after 5-hr. evacuation is plotted for plates I and II. Considering the wide variations in alumina preparation, rehydration, and drying procedures, agreement is fairly remarkable. The only data located which appear to be in major disagreement[13] have been acknowledged as irreproducible.[14] Thus, a reasonable estimate for surface hydroxyl coverage can probably be made if the temperature of dehydration under vacuum is known.

Infrared Study

Spectra of Hydroxyl Groups on Dry Alumina. The major characteristics of spectra obtained during vacuum dehydration of γ-alumina at elevated temperatures have been described.[3] Further information on detailed changes in the isolated hydroxyl bands on "dry" alumina has been obtained. In addition to the three major bands due to isolated, chemically distinct, hydroxyl groups, two other bands are sometimes evident in the region from 3700 to 3800 cm.$^{-1}$: one lies near 3780 cm.$^{-1}$ and is normally most apparent after the alumina has been dried under vacuum at 600–650°; the other occurs near 3733 cm.$^{-1}$ and is typically observed as a shoulder on a stronger band at 3744 cm.$^{-1}$.

(7) S. J. Gregg and K. H. Wheatley, *J. Chem. Soc.*, 3804 (1955).

(8) R. G. Haldeman and P. H. Emmett, *J. Am. Chem. Soc.*, **78**, 2917 (1956).

(9) S. G. Hindin and S. W. Weller, *Advan. Catalysis*, **9**, 70 (1957).

(10) E. Whalley and E. R. S. Winter, *J. Chem. Soc.*, 1175 (1950).

(11) H. Kloosterziel, "Chemisorption," W. E. Garner, Ed., Butterworth and Co., Ltd., London, 1957, p. 76.

(12) G. K. Boreskov, V. B. Dzisko, and M. S. Borisova, *Zh. Fiz. Khim.*, **27**, 1176 (1953).

(13) J. H. de Boer and G. M. M. Houben, *Proc. Intern. Symp. Reactivity Solids, Gothenburg, 1952*, **1**, 237 (1954).

(14) J. H. de Boer, "Chemisorption," W. E. Garner, Ed., Butterworth and Co., Ltd., London, 1957, p. 85.

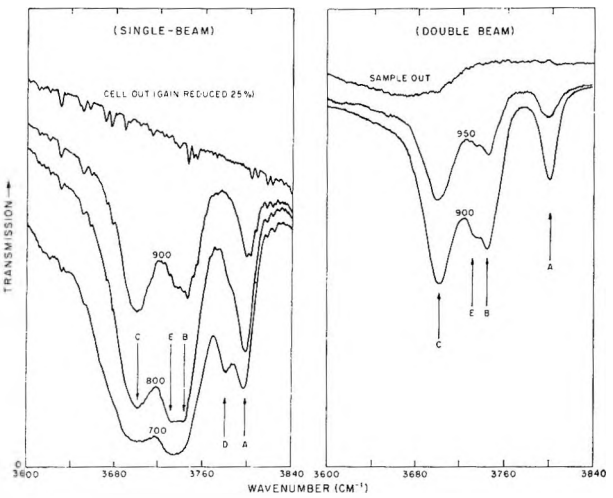

Figure 5. Spectra of alumina dried at indicated temperatures, °C.

Except on very dry alumina these bands are typically difficult or impossible to locate because of overlapping.

Figure 5 illustrates spectra obtained during dehydration of an aerogel plate by evacuation for 0.5 hr. at progressively higher temperatures. The frequencies (at 40°) of the five bands found are given in Table I.

Table I

Band	Wave number, cm.⁻¹ Current	Previous[a]
A	3800	3795
B	3744	3737
C	3700	3698
D	3780	..
E	3733	..

Corresponding deuteroxyl bands fall between 2730 and 2805 cm.$^{-1}$. Bands A, B, and C are the most prominent after the usual (1–2 hr.) dehydration under vacuum above 650°, but the other two bands persist to some extent. Three isolated hydroxyl bands, corresponding approximately to the A, B, and C bands described above, have been reported for other aluminas.[15,16]

The frequencies depend on temperature as well as extent of surface hydration. In view of the difficulty of resolving these overlapping bands, some difference in the frequencies reported should be expected, even had the aluminas studied all been identical. Additional bands are found on alumina dried below 600°, apparently reflecting hydrogen-bonded hydroxyl, but little further information was obtained from studies of "wetter" alumina. Some isolated hydroxyl groups

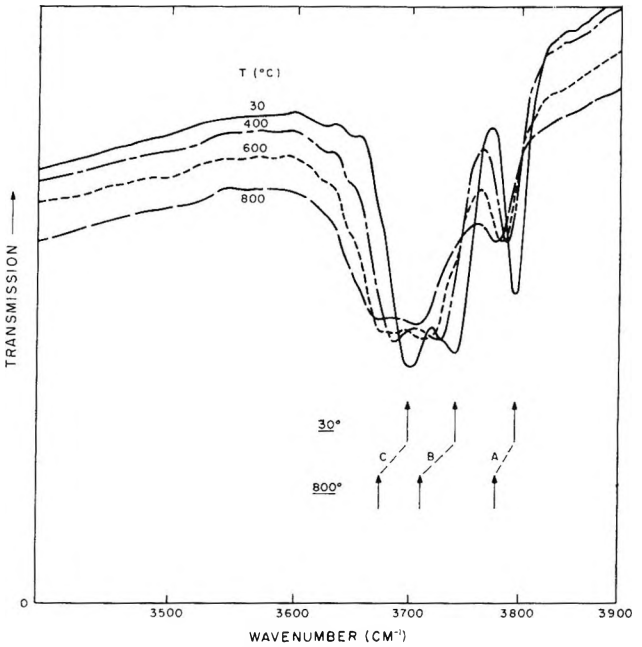

Figure 6. Spectra of alumina showing changes in hydroxyl bands with temperature.

appear to exist, however, even on extensively hydrated alumina.[17]

Additional evidence was obtained by direct infrared study of alumina at elevated temperatures. The aerogel plates were dried by evacuation at 800–1000°, and spectra were recorded at the drying temperature and at various lower temperatures, the number of surface hydroxyl groups remaining constant (Perkin-Elmer 12C spectrometer, LiF prism). Figure 6 illustrates typical changes in frequency and configuration as the temperature was decreased after initial drying at 800°. All changes were reversible on reheating. The major hydroxyl bands shift to lower frequencies and broaden with increasing temperature. Frequency shifts appear to differ for the individual bands, ranging from ~20 cm.$^{-1}$ for the A band to ~35 cm.$^{-1}$ for the B band, as the temperature is changed between 30 and 800°. Nevertheless, the bands appear to persist as distinct entities, indicating that even at 800° hydroxyl groups exist on distinct surface sites and are not in completely random motion.

The possibility that the hydroxyl groups observed at lower temperatures do not actually exist on alumina at high temperatures but are formed by readsorption of water only on cooling is excluded by these experi-

(15) R. H. Lindquist and D. G. Rea, presented at 136th National Meeting, American Chemical Society, Atlantic City, N. J., Sept. 1959.

(16) D. J. C. Yates and P. J. Lucchesi, *J. Chem. Phys.*, **35**, 243 (1961).

(17) A. V. Uvarov, *Zh. Fiz. Khim.*, **36**, 1346 (1962).

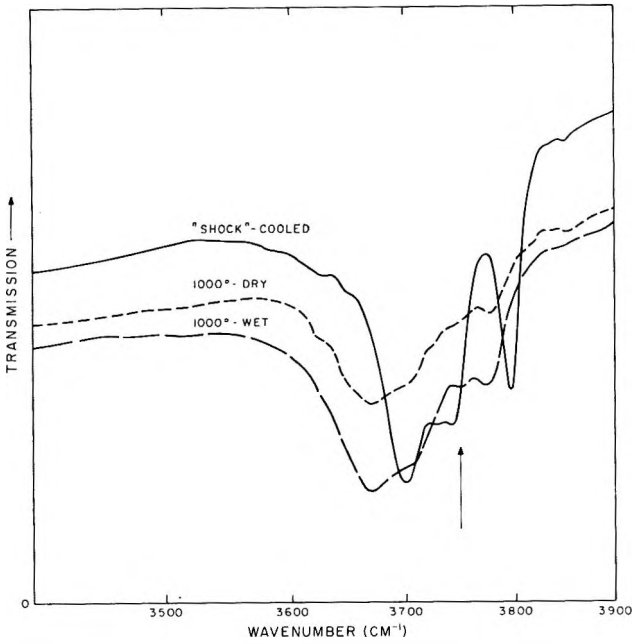

Figure 7. Spectra of alumina showing hydroxyl-stretching bands after readdition of water at 1000°.

ments. The observed frequency shifts probably reflect changes due to increased vibration of the hydroxyl groups perpendicular to the surface, as well as possible increased lateral interaction with neighboring oxide ions.

Experiments were also made to determine approximately how the number and types of hydroxyl groups on the surface at high temperatures depended on the partial pressure of water vapor in the cell. First, an alumina aerogel plate was alternately exposed to flowing dry nitrogen (P_2O_5-dried) and flowing wet nitrogen (saturated at room temperature) between 500 and 1000° while spectra of the hot alumina were recorded. Typical spectra at 1000° are shown in Figure 7, which also includes a spectrum recorded at room temperature after the quartz cell had been plunged abruptly into an ice bath after brief drying at 1000°. This spectrum does not differ appreciably from spectra obtained for the slowly cooled alumina.

Equilibrium chemisorption of water apparently occurred rapidly under the conditions of the experiments. Spectra recorded after 1 hr. contact with wet nitrogen showed little or no change from those recorded after 5-min. contact. Redrying in flowing dry nitrogen for 1 hr. restored the spectrum obtained after originally drying for 1 hr. The results showed that chemisorption of water increased markedly in the presence of moisture, although certainly not in direct proportion to the increase in water pressure.

At temperatures between 700 and 1000° the additional chemisorbed water appeared to exist mostly as isolated hydroxyl groups, but these were not all identical with pre-existing groups. At least one new band was produced near 3750 cm.$^{-1}$ (indicated by the arrow in Figure 7) by chemisorption of water at 800 to 1000°.

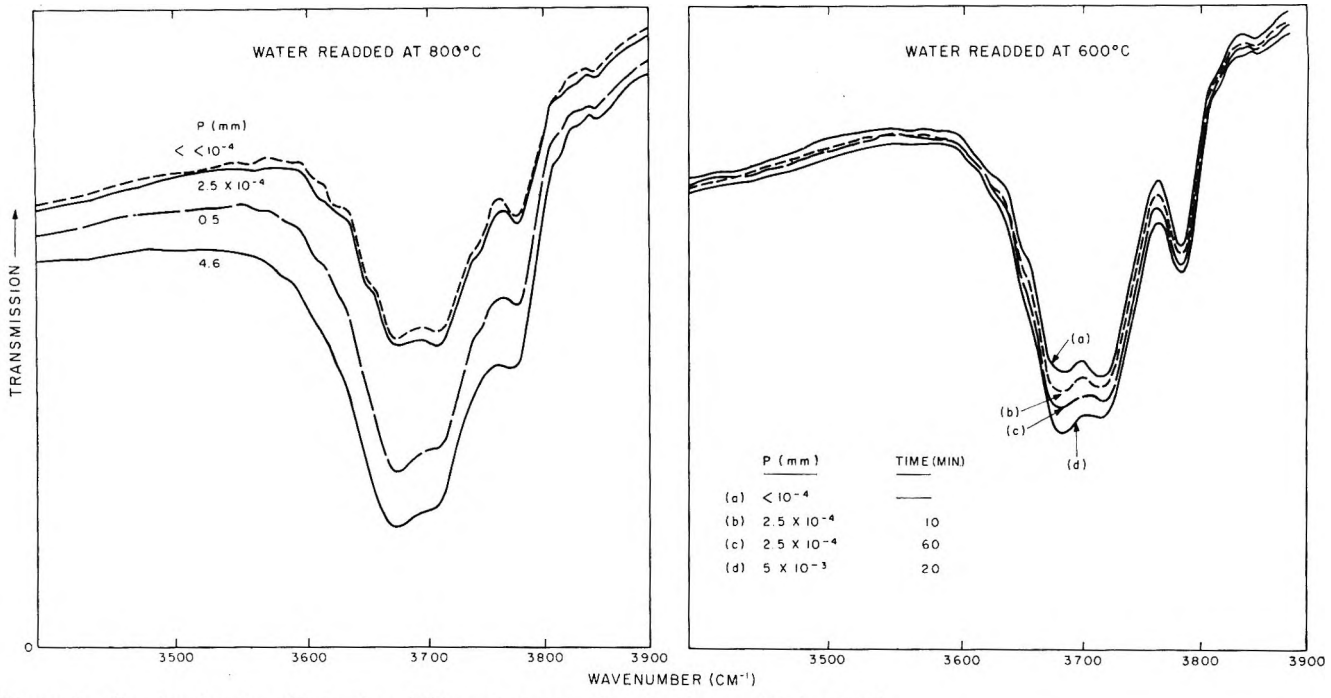

Figure 8. Spectra showing effects of readdition of water to hot alumina predried at 800°.

This band (allowing for the frequency shift due to temperature) apparently corresponds to the D band found at room temperature near 3780 cm.$^{-1}$.

Alumina dried at 500° gained fewer isolated hydroxyl groups when subsequently exposed to flowing wet nitrogen at 500° than did alumina dried at higher temperatures when exposed to wet nitrogen (at the drying temperatures) but showed a greater increase in absorbance due to hydrogen-bonded hydroxyl groups (broad band below 3680 cm.$^{-1}$).

After the alumina had been dried at 1000° and cooled to produce the spectrum shown in Figure 7, rehydration of the surface was attempted by exposure for 1 hr. to wet nitrogen at 100°. Then the alumina was redried at 500°. A subsequent spectrum indicated that the B and D bands had been only partially restored to their normal relative intensities after 500° drying. All isolated hydroxyl bands had previously been found to be fully restored in the spectrum after more thorough rehydration and redrying, but the B and D bands were typically less easily restored than the A and C bands.

In additional experiments, an aerogel plate was dried at 800° by evacuation for 0.5 hr. through a trap cooled with liquid nitrogen, and then was exposed to water vapor at various low pressures at 600 and 800°. Vapor pressure was controlled by means of suitable cooling mixtures applied to a trap holding ice or water. Typical results are shown in Figure 8. Equilibrium adsorption was not reached in these experiments. Although water at 0.5 mm. or above is chemisorbed fairly rapidly at 800° to form isolated hydroxyl groups, chemisorption occurs only very slowly below 5×10^{-3} mm.

Bands above 4000 cm.$^{-1}$. Bands due to a combination of an OH stretching vibration with other vibrations would be expected to lie above 4000 cm.$^{-1}$ and could ultimately provide further information on the characteristics of the hydroxyl groups. In an attempt to locate such bands a very thick (~250 mg./cm.^{2}) sample predried under vacuum at 750° was used. Weak bands were located near 4585 and 4350 cm.$^{-1}$, and possibly at 4107 cm.$^{-1}$. These are evidently combination bands involving the hydroxyl groups. They appear to be relatively much weaker than a corresponding band on microporous glass (4540 cm.$^{-1}$) and were not identified as corresponding to particular OH stretching bands.

Retention of Carbon Oxides. When the aerogel plates (which had been calcined in oxygen and evacuated at 600°) were initially heated from 600 to 800°, the desorbed gases contained small amounts of carbon monoxide, carbon dioxide, and hydrogen, in addition to the principal product, water. Both carbon dioxide and hydrogen could have been produced from carbon monoxide and water. The amount of carbon monoxide or carbon dioxide could have covered, at most, about 1% of the surface.

Careful study of concurrent spectral changes showed slight decreases in absorption between 1200 and 1700 cm.$^{-1}$, probably reflecting loss of $-COO^-$, CO_3^{-2}, HCO_3^-, or similar groups. On one plate, definite bands near 1380 and 1500–1600 cm.$^{-1}$ persisted after repeated evacuation at 700° and were accompanied by a band near 2350 cm.$^{-1}$, apparently caused by molecular carbon dioxide. Although both carbon dioxide and carbon monoxide are chemisorbed by dry alumina, neither is usually held strongly enough to account for the observations. The presence of a few closed pores in the aerogel plates might explain these findings.

In most subsequent work, plates were calcined at 600° in oxygen, dried at 800°, and then rehydrated to minimize possible complications from chemisorbed carbon oxides. Although possibly a troublesome complication, chemisorbed carbon oxides apparently are not normally involved in the development of active sites and do not significantly affect the characteristics of the isolated hydroxyl bands.

Discussion

The surface chemistry of γ-alumina is complex. Many different crystal planes, edges, or corners may be exposed. Moreover, transition aluminas are commonly believed to possess defect spinel structures wherein various arrangements of the aluminum ions are possible. There is reason to think, however, that γ-alumina may preferentially expose one crystal face. Strong pseudo-morphic relations are known to exist between Boehmite and γ-alumina, and electron and X-ray diffraction evidence suggests that dehydration of gelatinous Boehmite yields γ-alumina in which a considerable part of the surface is formed by the 100 plane of a spinel lattice.[18] Arguments for the preferred exposure of the 111 face[19] based on the greater density of packing of oxide ions on this face of dry alumina are unconvincing because actual exposure may still reflect the relative stabilities of hydrated faces (hydroxyl packing) rather than those of dehydrated faces.

It is reasonable to suppose, as have past workers,[1,2] that chemisorption of water should be closely related to the spacing of oxide ions on exposed faces of a cubic,

(18) B. C. Lippens, "Structure and Texture of Aluminas," Thesis, Technische Hogeschool of Delft, The Netherlands, 1961.

(19) J. H. de Boer, G. M. M. Houben, B. C. Lippens, W. H. Meijs, and W. K. A. Walrave, *J. Catalysis*, 1, 1 (1962).

close-packed, oxide lattice. Each oxide ion in a 111 plane occupies 6.74 Å.^{2}, whereas on a 100 face the area per oxide is 7.9 Å.^{2}. The B points observed in 100° adsorption isotherms suggest exposure of the 100 face. The other evidence indicates, however, that maximum retention of water at 100° (or even at 120°) is somewhat greater than expected, even for the 111 face. Some excess hydration beyond that expected from complete filling of either crystal face with one water molecule for every two oxide ions is apparently possible. How much (and why) is not presently clear.

In light of the ability of alumina to retain strongly 13 molecules of water/100 Å.^{2} at room temperature, some excess hydration at 100° should not be surprising. An alumina trihydrate surface may form,[1] at least to some extent, at low temperatures, and it might be only slowly decomposed at 100°. Rehydration might also extend to underlying layers. Slow penetration of water by diffusion of protons through the solid oxide lattice could lead to the hydration of a surface which is inaccessible to the nitrogen used for surface area measurements (for example, at contact points between primary particles or in closed pores). Thus, quite aside from the uncertainties involved in determining absolute surface areas by nitrogen adsorption, evidence on the maximum extent of hydration cannot easily establish which faces (if any) are preferentially exposed.

The very slow chemisorption of water at 100°, beyond 50% monolayer coverage, apparently reflects some type of reorganization of the surface. This process appears to be facilitated greatly by exposure to water at lower temperatures, suggesting that mobility of surface ions is considerably enhanced by physically absorbed water.

As suggested by Weyl[6] and others,[5] strain exists at a crystal surface. To minimize surface energy, metal oxide crystals characteristically chemisorb water, whenever possible, usually to form hydroxyl ions, because two hydroxyl ions can more readily minimize the field irregularities arising at a free surface than can a single oxide ion. Oxide ions, being more polarizable than metal cations, are preferentially exposed after removal of chemisorbed water. Dehydration thus exposes a strained oxide surface which is abnormally reactive. At least, on γ-alumina, however, the strain is not uniformly distributed over the surface but appears to be exceptionally concentrated at relatively few sites. Exactly how such localization of strain occurs is not clear. Some of the surface hydroxyl groups are very difficult to remove, and it is apparently the removal of such groups which creates the high-energy strain sites.

Readsorption of water must seriously limit the extent to which surface hydroxyl groups can be removed from alumina by heating in a humid atmosphere. When a typical powder sample of alumina is dried by calcination in air, slow diffusion of water out of the sample undoubtedly results in "self-steaming" which leaves a fairly high concentration of hydroxyl groups on the surface. Drying by evacuation through a trap cooled with liquid nitrogen is far more efficient for removal of surface hydroxyl groups. Eventually, equilibrium readsorption of water must become important in limiting removal of surface hydroxyl groups, even on vacuum drying. The spectroscopic and gravimetric evidence indicates, however, that the principal cause of the plateaus observed on vacuum dehydration lies not in readsorption of water but in a steady increase of the free energy of activation for desorption as the surface coverage with hydroxyl groups decreases.

The heat of adsorption of water increases with the temperature at which the alumina is predried and may exceed 100 kcal./mole for very low surface coverages on alumina predried at 538°.[5] Some decrease was noted on alumina predried at 649°.[20] Calorimetric data[21] show heats of adsorption of water vapor at 20–25° on alumina predried under vacuum at various temperatures up to 450° which fall between 15 and 22 kcal./mole for complete surface coverage. The very high heats of adsorption observed on partial surface hydration of very dry alumina must reflect relief of a localized surface strain.[5] Some other type of strain-relieving mechanism apparently becomes operative on the surface of dry alumina above 500–600°.[20]

Cornelius, *et al.*,[5] have proposed that the high-energy sites on alumina are strained Al–O–Al linkages, formed at high temperatures by condensation of residual hydroxyl groups which are increasingly separated as a result of progressive dehydration of the surface. Although this proposal accounts well for some aspects of the observed behavior, weaknesses are evident. On a regular lattice, hydroxyl ion spacings would fall into distinct groups, only a few of which could apparently permit condensation without disruption of the lattice. Creation of such strained linkages would require virtual immobility of the hydroxyl groups on the surface at high temperatures. The infrared evidence suggests that, although isolated hydroxyl groups are relatively immobile on dry alumina at 250°, migration (possibly through proton transfer) occurs

(20) A. G. Oblad, S. W. Weller, and G. A. Mills, "Second International Congress on Surface Activity," Vol. 2, Academic Press, New York, N. Y., 1957, p. 309.

(21) W. H. Wade and N. Hackerman, *J. Phys. Chem.*, **64**, 1195 (1960).

fairly readily at 400–600°. This, however, is the temperature range wherein highly strained oxide linkages are presumed to be created.

The energy of the sites created during dehydration apparently does not increase indefinitely but passes through a maximum. Results of the present study indicate, however, that the free energy of activation for desorption continues to increase with increasing degree of dehydration up to at least 800°. This suggests that reorganization of the surface involving migration of hydroxyl ions together, rather than the condensation step, may become rate-determining. The increase in free energy of activation for desorption could be largely entropic in origin at very high temperatures.

An explanation for the various types of isolated hydroxyl groups on the surface of dry γ-alumina is presently lacking. Virtually all groups must be on the surface. Although such groups could, for example, be located on different exposed crystal faces, edges, or corners, the detailed changes in relative band intensities and frequencies on dehydration and in other experiments are difficult to understand on such a basis. The changes are more easily explained in terms of changes in local environment on one crystal face brought about by migration of ions or chemisorption of other molecules.

Conclusion

Much remains to be learned about the details of surface hydration, the creation of high-energy sites, and the significance of the various types of isolated hydroxyl groups on the surface of γ-alumina. Accumulating evidence, however, virtually requires some improvement in present concepts of the alumina surface. With further development, the simple model proposed previously[4] appears capable of explaining the observations to date. The characteristics of a revised and extended version of this model are discussed in the following paper.

Acknowledgment. The assistance of Mr. J. Kekich in the experimental work is gratefully acknowledged.

A Model for the Surface of γ-Alumina[1]

by J. B. Peri

Research and Development Department, American Oil Company, Whiting, Indiana *(Received July 20, 1964)*

To account for the surface hydration and catalytic properties of γ-alumina, a statistical model is proposed on the assumption of preferred exposure of a single crystal face. The behavior of the model was investigated by a Monte Carlo method using an IBM 705 computer. Given a square lattice initially filled with hydroxyl ions, adjacent ions are assumed to combine randomly, provided only that local order is preserved in the residual oxide lattice, to form water, which is desorbed. This restriction permits removal of only 67% of the original hydroxyl layer and creates a two-domain surface lattice of residual oxide ions. Further dehydration, made possible by removal of the local order restriction, creates defects of various types in the domain boundaries, and leaves five types of isolated hydroxyl ions, differing in nearest neighbor configuration and covering about 10% of the surface. Mobility of surface ions, required to remove the final 10% of the hydroxyl ions, tends to minimize defects and leads to predominance of three types of hydroxyl ions. Five previously reported infrared bands between 3700 and 3800 cm.$^{-1}$ are tentatively assigned to the isolated hydroxyl ions. Defects produced in the domain boundaries can account for the catalytically active "strain" sites generated on γ-alumina by surface dehydration.

Introduction

Various crystallographically distinct forms of alumina exist. Among these, two high-area transition forms, η- and γ-alumina, are of greatest catalytic interest. They are widely thought to have rather similar defect spinel lattices. Which crystal planes are preferentially exposed and how aluminum ions are distributed at the surface are not known. Electron and X-ray diffraction studies indicate, however, that γ-alumina may preferentially expose the 100 plane of spinel.[2]

The surface hydration and catalytic activity of γ-alumina have been discussed in previous papers.[3-5] Ionic surfaces normally terminate in anions.[6,7] Oxide surfaces, unless highly dried, are usually covered with hydroxyl groups formed by chemisorption of water. Removal of such groups from alumina leaves a strained surface on which strained oxide linkages have been postulated as active sites.[8] Active sites on γ-alumina have also been identified with cation defects arising from its presumed defect spinel structure,[9] with such defects which have captured protons,[10] or with aluminum ions abnormally exposed as a result of surface dehydration.[4] Various chemically distinct types of hydroxyl groups also persist on the surface of alumina even after drying at 800–1000°.[5]

Accumulating evidence on the relationship between surface hydration and the nature of active sites of γ-alumina justifies the development of a model to aid interpretation and correlation of observations. A preliminary version has been briefly outlined.[4] The proposed model has already proved useful, and it embodies certain concepts which may be applicable to other surfaces.

The work of Langmuir,[11] Roberts,[12] and others on

(1) Presented in part at Combined Southeast-Southwest Regional Meeting, American Chemical Society, New Orleans, La., Dec. 1961.

(2) B. C. Lippens, "Structure and Texture of Aluminas," Thesis, Technische Hogeschool of Delft, The Netherlands, 1961.

(3) J. B. Peri and R. B. Hannan, *J. Phys. Chem.*, **64**, 1526 (1960).

(4) J. B. Peri, *Actes Congr. Intern. Catalyse, 2e, Paris*, **1**, 1333 (1961).

(5) J. B. Peri, *J. Phys. Chem.*, **69**, 211 (1965).

(6) W. A. Weyl, *Ann. N. Y. Acad. Sci.*, **12**, 245 (1950); "Structure and Properties of Solid Surfaces," R. Gomer and C. S. Simth, Ed., University of Chicago Press, Chicago, Ill., 1953, p. 147.

(7) K. Moliere, W. Rathje, and I. N. Stranski, *Discussions Faraday Soc.*, **5**, 21 (1949).

(8) E. B. Cornelius, T. H. Milliken, G. A. Mills, and A. G. Oblad, *J. Phys. Chem.*, **59**, 809 (1955).

(9) A. Eucken, *Discussions Faraday Soc.*, **8**, 128 (1950).

(10) D. A. Dowden, *J. Chem. Soc.*, 242 (1950).

(11) I. Langmuir, *ibid.*, 511 (1940).

(12) J. K. Roberts, *Proc. Roy. Soc.* (London), **A152**, 445 (1935).

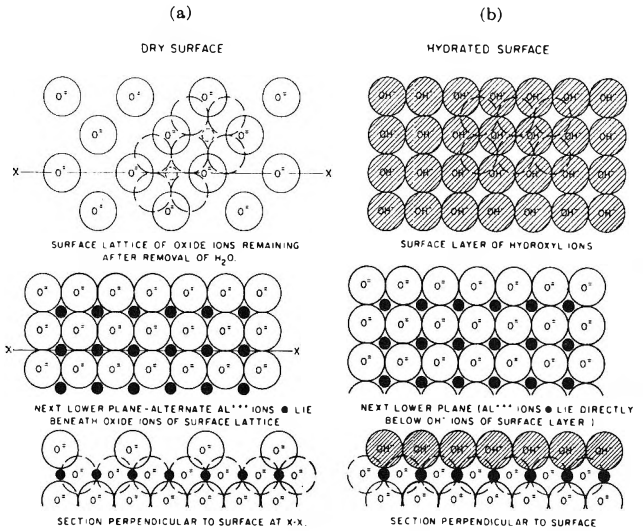

Figure 1. Ideal surfaces of γ-alumina.

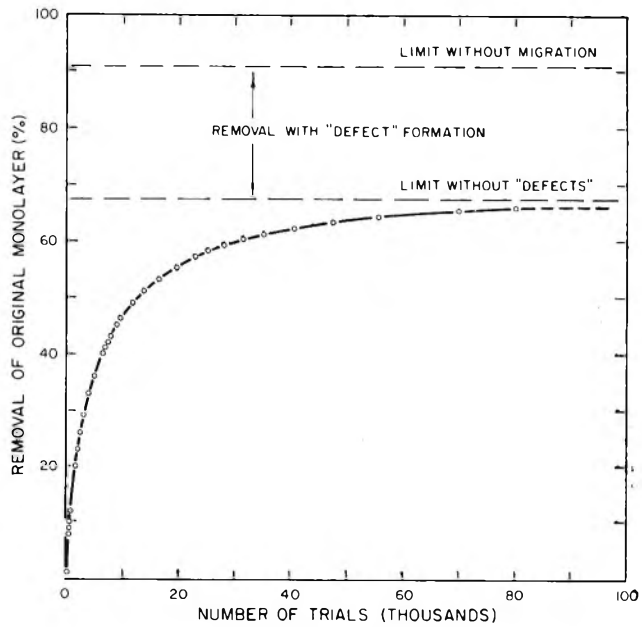

Figure 2. Removal of hydroxyl pairs from square lattice (IBM 705 computer).

statistical effects in adsorption of vapors on metals is relevant to the present subject although the processes involved differ considerably.

Characteristics of the Model

For simplicity, the assumptions are initially more restrictive than necessary and are in most cases indefensible in detail. Modifications will be discussed after the basic concepts have been established.

Ideal Surface Structures. The proposed "surface" includes two outer layers of an ionic crystal. Only one face is assumed to be exposed. On "ideal" dry alumina the top layer contains only oxide ions, regularly arranged, as shown in Figure 1a, over aluminum ions in octahedral sites in the next lower layer. Only half as many oxide ions are present in the top layer as in the next lower layer, which represents the 100 plane of a cubic, close-packed, oxide lattice where each oxide ion occupies an area of about 8 Å.^{2}, and aluminum ions are located in all interstices between oxide ions. The stoichiometry of the two upper layers combined corresponds to Al_2O_3. At 100° or somewhat higher, depending on the method of rehydration, sufficient chemisorbed water is held to convert the top layer to a filled, square lattice of hydroxyl ions, as represented in Figure 1b. Each hydroxyl ion is assumed to be directly over an aluminum ion in the next lower layer. When the top layer is thus filled, the two upper layers combined correspond stoichiometrically to $Al_2O_3 \cdot H_2O$. Removal of water from this surface must expose oxide ions.

Dehydration without Migration of Hydroxyl Ions. During dehydration of the surface, adjacent hydroxyl ions combine to form water molecules, which are then desorbed. For each molecule of water formed, one oxide ion is left in the top layer, and one aluminum ion is left in an incomplete octahedral site in the next lower layer. Complete regular removal of the surface hydroxyl ions would ultimately produce the surface lattice of oxide ions shown in Figure 1a. Random combination of adjacent hydroxyl ions leaving an oxide ion on either of two sites with equal probability would yield a completely disordered surface oxide lattice. About 8% of the original hydroxyl monolayer would be left as isolated hydroxyl ions (having no adjacent hydroxyl ion neighbor) on several types of sites differing in nearest neighbor configuration.

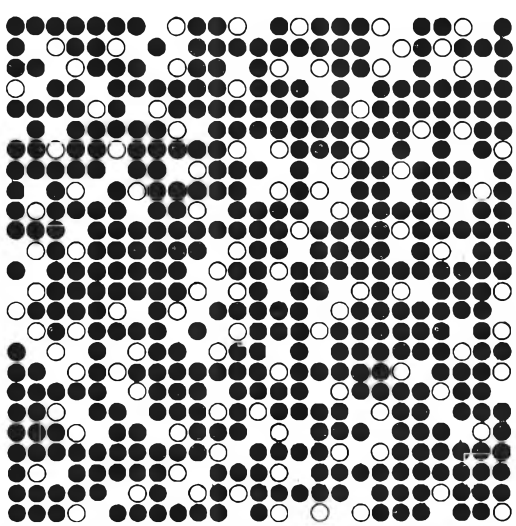

Figure 3. Surface showing 30% removal: ●, OH^-; ○, O^{-2}.

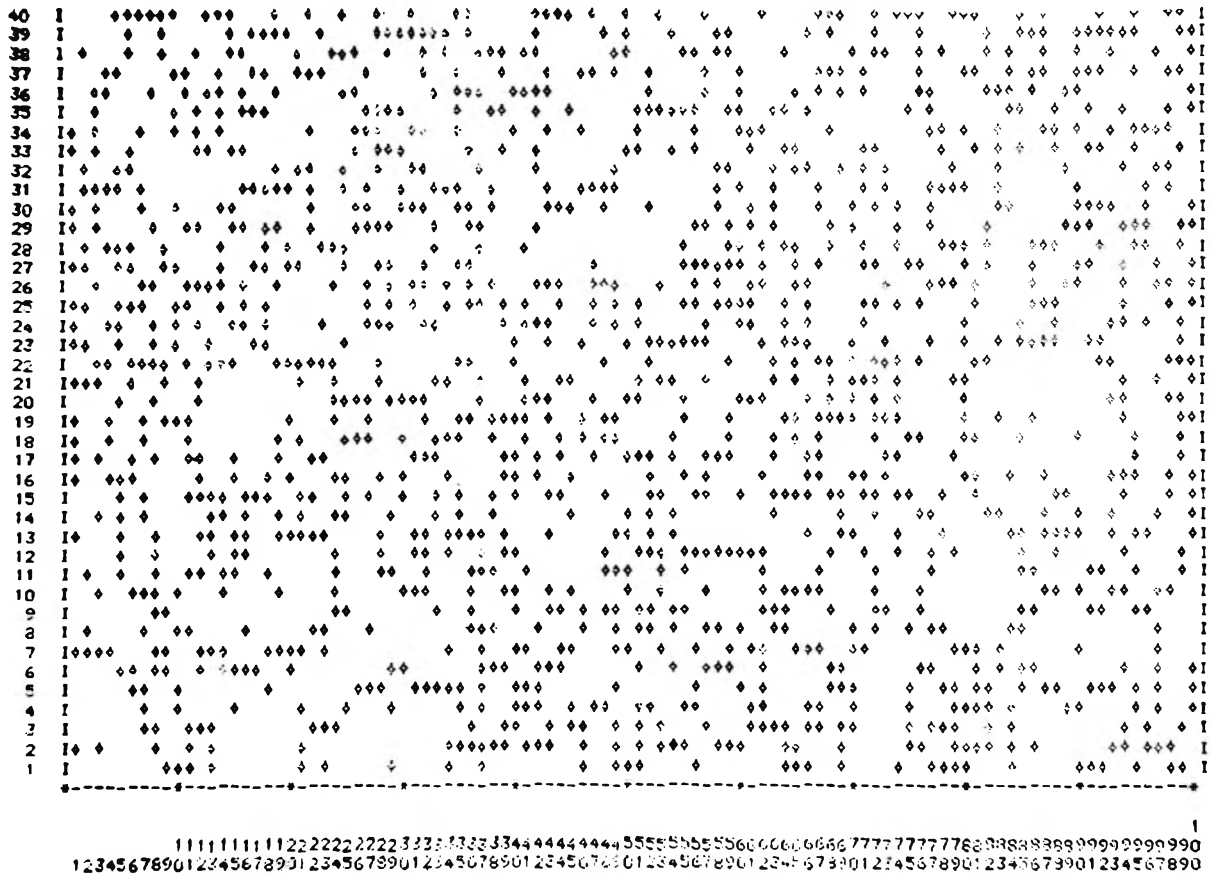

Figure 4. Distribution of hydroxyl groups after 65.4% removal (computer printout).

To reduce the disorder that would result from a purely random process, the assumption is made that water must initially be removed in such a way that two (or more) oxide ions are not left on immediately adjacent sites, and two (or more) immediately adjacent sites are not left vacant (*i.e.*, local order must be preserved in the residual oxide lattice). So long as this requirement is maintained, a large fraction of the original hydroxyl monolayer cannot be removed.

The removal of water from a hydroxyl monolayer in accordance with this limitation was studied with an IBM 705 computer. "Pseudo-random" numbers[13] generated by the computer were used to select a pair of adjacent hydroxyl ions on a square lattice containing 10,000 sites. The edges of the lattice were joined, right to left and top to bottom, to avoid edge effects. If the selected pair could be removed without leaving the residual oxide ion adjacent to another oxide ion or leaving a vacant site adjacent to another vacant site, it was removed. If this could not be done, the computer randomly selected another pair and again tested for possible removal. "Printouts" of the entire lattice at periodic intervals showed the location of all surface ions and tallied the total number of trials and the extent of hydroxyl removal. As shown in Figure 2 the rate of hydroxyl removal decreased rapidly with decreasing surface coverage, approaching zero at approximately 67% removal.

The appearance of the surface (top layer) during this stage of removal is illustrated by Figures 3, 4, and 5. Figures 3 and 5 represent only $^1/_{16}$ of the total area of the computer printout. Figure 4 shows 40% of the actual computer printout of hydroxyl sites. (A separate printout gave oxide and vacant site locations.) The last three or four possible pairs were removed by visual inspection of Figure 4 (lower left section) to yield Figure 5.

The oxide surface lattice develops in two domains, designated as odd or even. Oxide ions in an odd domain, if in an odd-numbered horizontal row, are in an even vertical row (and *vice versa*). Oxide ions in an even domain have coordinates which are both even or both odd. Within each domain, oxide ions are

(13) G. E. Forsythe, "Monte Carlo Method," National Bureau of Standards, Applied Mathematics Series, Vol. 12, U. S. Department of Commerce, Washington, D. C., 1951, p. 34.

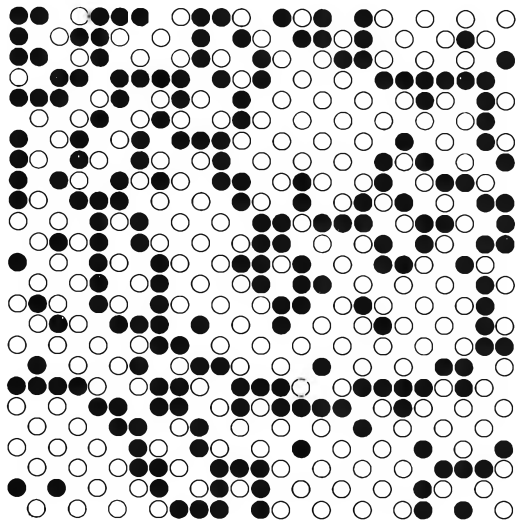

Figure 5. Surface showing 67.8% removal (maximum without defects).

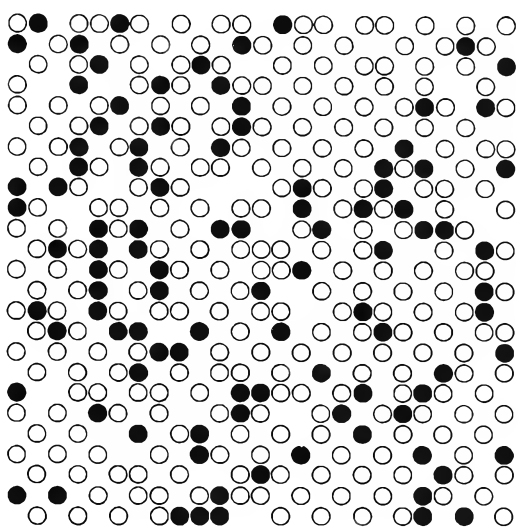

Figure 6. Surface showing 82.8% removal (random defects).

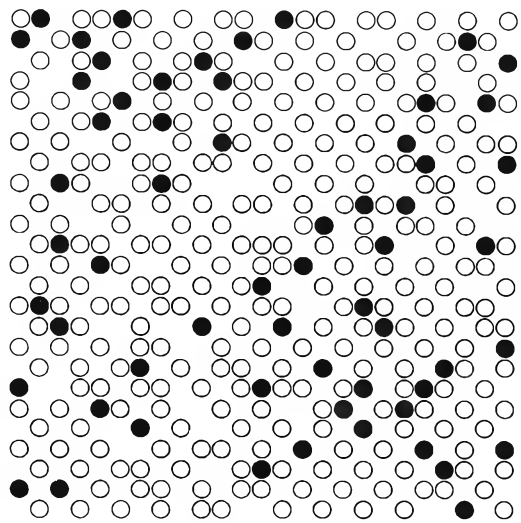

Figure 7. Surface showing 90.4% removal (no pairs remaining).

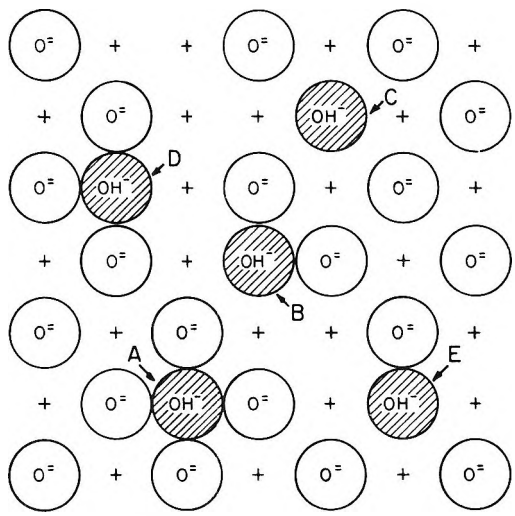

Figure 8. Types of isolated hydroxyl ions (+ denotes Al^{+3} in lower layer).

regularly arranged, and the two domains are energetically equivalent. As can be seen in Figure 5, the remaining hydroxyl ions tend to concentrate in the boundaries between the two domains although many isolated hydroxyl ions are left in otherwise regular oxide domains.

Further dehydration of the surface illustrated in Figure 5 requires the creation of oxide and/or vacancy defects (*i.e.*, two or more oxide ions, or two or more vacancies on immediately adjoining sites). When the restriction for preservation of local order was removed, and hydroxyl removal by the computer was continued randomly to 82.8% removal, the surface represented by Figure 6 was obtained. Many isolated, as well as rowed and paired, hydroxyl ions remain. Various types of defects are evident.

Random removal of all possible remaining hydroxyl pairs from Figure 6 by inspection left the surface shown in Figure 7. It has many defects, which are found on close inspection to lie in the boundaries between oxide domains. The remaining hydroxyl ions, covering 9.6% of the lattice, are found on five types of sites on which they have from zero to four nearest oxide neighbors, as illustrated and identified by letter in Figure 8. The occurrence of a sixth type, in which two oxide ions are symmetrically located on opposite sides of the hydroxyl ion, was negligible.

Dehydration with Migration of Hydroxyl Ions. No

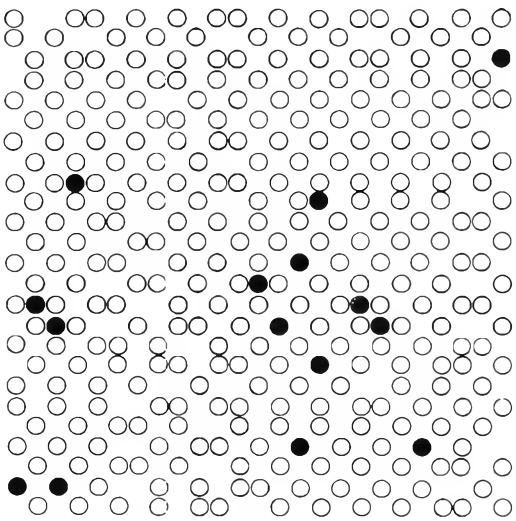

Figure 9. Surface showing 97.6% removal (rules 1–4).

further dehydration is possible without migration of surface ions. Infrared and other evidence[3–5] indicates that, at 600°, protons, at least, migrate readily on the surface. In the range from 400 to 600° some mobility exists. Migration of oxide (and aluminum) ions is shown by gradual loss of surface area at 800° and by slow formation of α-alumina at still higher temperatures. Therefore, at the drying temperatures needed to reduce the surface hydroxyl coverage below 9.6% monolayer ($\geq$650°), surface ions must be mobile. Implications as to the degree of such mobility are not clear, however. Even at 1000°, as indicated by infrared spectra, surface hydroxyl ions on alumina apparently do not possess the mobility of a two-dimensional gas but are normally attached to characteristic sites of different types.[5] Loss of surface area does not necessarily indicate high mobility of the ions in plane surfaces. Oxide and aluminum ions at crystal edges and corners undoubtedly migrate more easily than those in plane surfaces, and such migration could explain loss of area without requiring mobility of most surface ions, nor does the exchange of oxygen atoms between the surface of alumina and oxygen or water require much mobility of oxide ions. Although protons on "dry" alumina appear to be mobile only above 400°, protons can transfer between hydroxyl ions to form water and an oxide ion (or *vice versa*) at 200° or lower. Explanation of this apparent anomaly must lie in the transfer processes involved.

To permit further consideration of the migration of hydroxyl ions on the surface, the following assumptions were made. (1) Migration occurs through single-space moves of an ion to an *adjacent* vacant site or through proton transfer from a hydroxyl ion to an adjacent ion in the top layer. (2) Defect minimization is favored, and moves which reduce defects occur very readily. (3) Proton transfer usually occurs more readily than migration of a hydroxyl ion, *per se*, and the transfer occurs more readily to an adjacent hydroxyl than to an adjacent oxide. (4) Hydroxyl ions migrate more readily than oxide ions. (5) The relative ease of any move depends additionally on the nature of the resultant surface defect.

Restriction of proton transfer to moves between ions in the top layer may be justified by the "electrical double-layer" characteristic of the dry surface or, in any case, by the factors which cause residual hydroxyl ions to remain with high preference on the surface rather than in the interior of alumina crystals.

On the basis of the above assumptions, a set of rules was established to govern removal of the final 9.6% monolayer of hydroxyl ions. In order of decreasing priority, these rules are as follows. (1) Water is removed from any adjacent hydroxyl pair in a way which leaves the least possible defect. (The degree of defect is taken as the maximum number of oxide contacts per oxide ion in an oxide defect or as the maximum number of vacant site contacts per vacancy in a vacancy defect. Where a choice exists, oxide defects are avoided rather than vacancy defects. When no choice is involved, removal is random.) (2) Wherever possible, defects are reduced or eliminated by single-space moves of protons from hydroxyl ions to adjacent oxide ions or of hydroxyl or oxide ions to adjacent vacant sites. (3) Migration of a proton to an adjacent oxide ion is permitted as an intermediate step if no defect more serious than a "triplet" oxide defect (two oxide ions immediately adjoining another) results. (4) Migration of a hydroxyl ion to an adjacent vacant site is permitted if no increase in defect character results.

The move having the highest priority was always chosen, and on this basis hydroxyl ions were removed from the surface depicted in Figure 7 by inspection. Edge effects were avoided by examining the surface beyond the area shown to assess possible moves near the edges. Rules were invoked, in order, as necessary to permit continued removal of hydroxyl ions. Less than 200 single-space moves were needed to reduce the coverage to 2.4% monolayer, but the complexity of the necessary move sequences increased very greatly as the number of hydroxyl ions decreased.

The surface obtained after such removal is illustrated in Figure 9. The remaining hydroxyl ions can be removed only by moves not permitted under the four existing rules. A three-dimensional model of a portion of the surface represented by Figure 9 is shown in

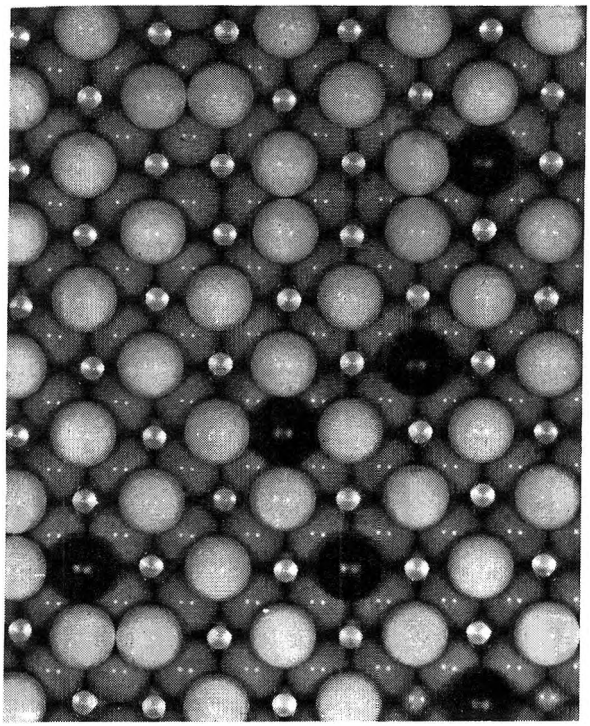

Figure 10. Dry γ-alumina. Black, OH^-; gray and white, O^{-2}; small, Al^{+3}.

Figure 10. The defects remaining in Figure 9 are either oxide or vacancy defects of special types. These will be discussed later.

The various types of hydroxyl ions were removed at different rates during the process. Those in the regular domain regions (A- and C-sites) were removed most slowly because under the rules they could not migrate, either through proton or hydroxyl ion moves. Of the three remaining types, two (D and E) were readily converted, through defect minimization, into the third (B), which was eliminated fairly readily through further moves. Changes in the relative numbers of the five types at various stages of the removal process are shown in Figure 11.

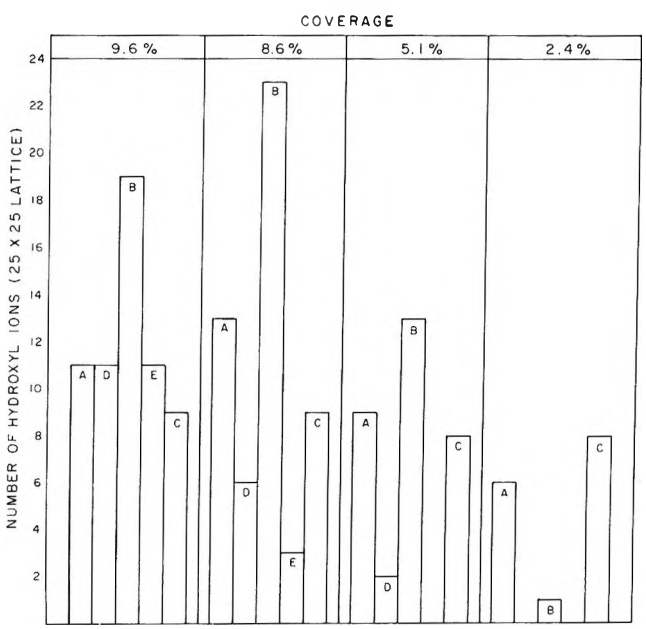

Figure 11. Changes in distribution of hydroxyl types during progressive removal.

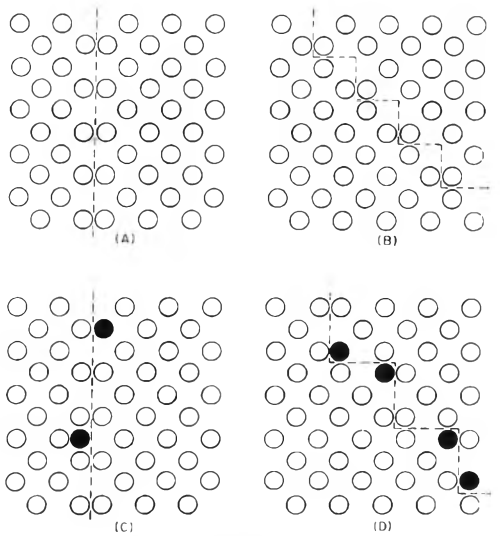

Figure 12. Defects and hydroxyl ions in domain boundaries.

The details of surface rearrangement are very speculative. In reality, the moves governed by the rules would probably occur concurrently and possibly in different order. The rules obviously do not cover all possible moves but only those assumed to occur most easily. Mobility of ions on the surface is probably less restricted at high temperatures than suggested. If oxide ions may migrate where no defect more serious than a triplet would result, many new moves become possible, and the domain regions in the oxide lattice may change appreciably in size and shape. All such factors would cause some change in the hydroxyl removal process. So long as the principles of preservation of local order and defect minimization are upheld, however, generally similar results would be obtained.

The surface lattice is probably indistinct at very high temperatures, with ions vibrating strongly about regular sites of attachment and frequently moving to adjacent vacant sites. Vacancies and "interstitial" oxide ions must exist, to some extent, in regular domain areas of the surface oxide lattice, and domain boundaries constantly shift in position. Hydroxyl ions and oxide ions are probably freely interconvertible as protons transfer from hydroxyl to oxide on close approach of the ions. Protons may even migrate through lower

oxide layers or be desorbed as water and readsorbed to form hydroxyl ions again. As the alumina cools, however, all protons are again captured by oxide ions to form hydroxyl ions on characteristic lattice sites, preferentially, in such a way as to minimize surface defects.

A close relation exists between the types of hydroxyl ions and the defects pictured by the model. Triplet defects (*i.e.*, an oxide ion with two oxide nearest neighbors or a vacant site adjoining two vacant sites) capture protons or hydroxyl ions to form B-site hydroxyl ions. Pair defects (two oxide ions or two vacancies on immediately adjoining sites) similarly form E- or D-site hydroxyl ions. Attachment of protons at interstitial oxide ions or of hydroxyl ions at vacant oxide sites in regular domain areas produces A- or C-site hydroxyl ions.

Pair and triplet defects are found only in the boundaries between the two domains of the surface-oxide lattice and must exist in such boundaries as long as the two domains remain, unless sufficient water is chemisorbed to eliminate them. In general, odd and even domains can adjoin at regular boundaries of two types, as illustrated in Figure 12 (A and B). Boundaries of both types must coexist because either type occurs at corners of a domain region bounded principally by boundaries of the other type. (Boundaries of both types can easily be found in Figure 9.) One of these can be characterized as a "pair-defect"; the other, as a "triplet-defect" boundary. A pair-defect boundary is static, and no transfer of oxide ions can occur across it without creation of triplet defects. Rearrangement of the surface oxide lattice, thus, requires formation of triplet-oxide defects, even though a pair-defect boundary may represent a less defective configuration.

Defects in either boundary could theoretically be eliminated by retention of sufficient chemisorbed water, held as hydroxyl ions, but the boundaries cannot retain hydroxyl ions to this extent at high temperatures. Chemisorption of water as isolated B-site hydroxyl ions eliminates triplet defects which are higher energy configurations than the pair defects which would be eliminated by D- or E- site hydroxyl ions. This is illustrated in Figure 12 (C and D). Retention of B-site in preference to D- or E-site hydroxyls is thus understandable.

Refinement of Assumptions. Most of the assumptions for the development of the simple model are oversimplified. Experimentally, a surface *completely* filled with hydroxyl ions appears to be unrealizable. Whenever sufficient water is chemisorbed to produce a filled hydroxyl monolayer, some of the water seems to be held molecularly. Because hydroxyl ions are characteristically somewhat larger than oxide ions, a complete hydroxyl monolayer possibly could not be superimposed on a close-packed oxide layer. To the maximum possible extent, however, hydroxyl ions would probably occupy normal lattice positions. When "crowding" became too great, water could be held, as such, to minimize surface energy. (A surface equilibrium $2OH^- \rightleftarrows H_2O + O^{-2}$ could be involved.)

The assumption of random removal of pairs (subject to the restriction that local order is preserved) is probably inconsistent with differences expected in the ease of removal of various hydroxyl pairs as a result of differences in near-neighbor configuration. Rather than occur randomly, removal of hydroxyl pairs might spread from a relatively few (randomly chosen) initial points, or occur through systematic removal of pairs in other ways. Nevertheless, if the requirement for preservation of local order is retained, it matters relatively little whether removal proceeds regularly from comparatively few or from many points selected at random.

The sites on which the various types of isolated hydroxyl ions have been pictured require at least minor modification. Owing to electrostatic repulsion between ions of like charge, we should expect some distortion of the regular lattice spacings in the vicinity of these ions. Thus, for example, the oxide nearest neighbors of A- and B-site hydroxyl ions would probably be slightly further, and the oxide ions closest to C-site hydroxyl ions would be slightly closer, than pictured.

Interpretation of Experimental Observations

Assignment of Infrared Bands to Hydroxyl Ions of Various Types. The five types of hydroxyl ion sites shown in Figure 8 differ in local charge density because of their nearest neighbor configurations. The most negative (A-site) has four oxide ion nearest neighbors; the most positive (C-site), four immediately adjacent vacant sites. If sites in the regular oxide lattice are regarded as neutral, an "interstitial" hydroxyl ion (A-site) would be associated with an extra electron, while a hydroxyl ion replacing an oxide ion on a regular site would represent a local deficiency of one electron. The other sites would fall between these limits, B-sites being approximately neutral. Other factors being equal, the frequencies of the corresponding stretching bands would probably decrease with decreasing electron density (A > D > B > E > C). The chemical properties of the hydroxyl ions should vary similarly with type of site, the A-site ions being the most basic and the C-site ions the most acidic. The five isolated hydroxyl bands observed in infrared spectra of dry alumina are,

Table I

Band	Wave number, cm.$^{-1}$	Site	No. of oxide nearest neighbors
A	3800	A	4
B	3744	B	2
C	3700	C	0
D	3780	D	3
E	3733	E	1

therefore, tentatively assigned to hydroxyl ions on the five types of sites as given in Table I.

At surface coverages above 9.6% monolayer, some hydroxyl ions have one or more hydroxyl ion nearest neighbors, and hydroxyl bonding is assumed to occur between them. Since both protons in a pair of adjoining hydroxyl ions cannot simultaneously form bonds to the other hydroxyl ion, one of them should give rise to an "isolated" hydroxyl infrared band. Each hydroxyl ion in a pair of adjacent hydroxyl ions may have four significant nearest neighbor configurations, the number of oxide ion nearest neighbors ranging from 0 to 3. Paired hydroxyl ions may thus contribute four isolated hydroxyl bands, as well as bands corresponding to vibrations in which the proton is directly involved in hydrogen-bond formation. The frequencies

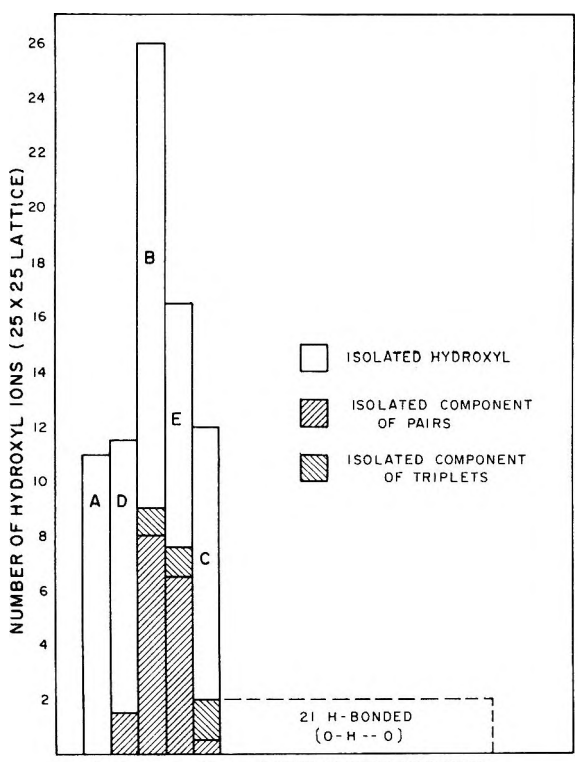

Figure 13. Distribution of hydroxyl types in Figure 6.

of the bands should, as for hydroxyl ions having no hydroxyl nearest neighbors, increase with the number of adjacent oxide ions.

The influence of the adjacent (hydrogen-bonding) hydroxyl cannot be exactly assessed. On the basis of formal charge, an adjacent hydroxyl should be equivalent to half an oxide ion, but, because the bond from this hydroxyl tends to remove an electron from the free hydroxyl ion, the net effect would probably be roughly equivalent to that of an adjacent oxide vacancy. The hydroxyl ions of all types (single, pair, triple) on the final computer printout section shown in Figure 6 have been counted and plotted in Figure 13. An adjacent hydroxyl ion has been assumed equivalent to an adjacent vacant site. Half of the paired hydroxyls and one-third of the hydroxyl ions with two nearest hydroxyl ion neighbors have been considered as isolated, in addition to those having no hydroxyl ion nearest neighbors. The remainder are assumed to be directly bonded through their protons. Hydrogen-bonded hydroxyl groups produce broad bands at frequencies below those of isolated hydroxyl groups. They have been indicated in Figure 13 as a block at the low-frequency side of the isolated hydroxyl ions. At high coverages with hydroxyl groups, hydrogen bonding would be expected to be extensive on the model surface although an isolated band or bands would be expected to persist.

Spectral changes observed as alumina is dried can be explained by the model. The assumption is made that relative band intensities are roughly proportional to the number of corresponding hydroxyl ion types. Comparison of Figures 11 and 13 with published spectra[3-5] and with data on surface hydroxyl coverage as a function of drying temperature[5] shows that, in addition to accounting fairly well for general changes in band intensities and in the number and relative frequencies of types of isolated bands on dry alumina, the model can explain the following points: (1) disappearance of hydrogen-bonded hydroxyl bands at a surface coverage of ~10% monolayer (no paired hydroxyl groups left at 9.6% coverage); (2) marked reduction in D and E bands as surface coverage changes from 10 to 8% monolayer; (3) faster disappearance of the B band as compared to the A and C bands below 8% monolayer.

At 2.4% monolayer coverage the B band persists in infrared spectra although, according to the removal scheme, no B-site hydroxyl ions should remain. Permitting additional surface migration of oxide ions or less restricted proton migration would avoid this result. Such moves must, in any case, be permitted to remove the final 2.4% monolayer. Agreement between the

model and the changes in the infrared bands can evidently be made as good as the experimental observations permit. This, although purely a curve-fitting process, demonstrates that the model can explain the spectral data.

Defects on Dry Alumina; Catalytically Active Sites. Of the types of defects created during dehydration, those presently imagined to have the greatest catalytic importance are the triplet vacancies, found in the boundaries between regular oxide domain regions. These vacancy defects characteristically adjoin pair or triplet oxide defects or B-site hydroxyl ions. They provide unusual exposure of the aluminum ions in the underlying layer and should constitute strong "acid" sites for adsorption of unsaturated hydrocarbons, ammonia, and other "electron-rich" molecules. Larger vacancy defects, such as oxide ions missing from regular surface oxide domain sites, may coexist to a slight extent, and these should be very strongly acidic.

In a broad sense, any irregularity in charge distribution in the surface layer constitutes a defect of some sort. When every aluminum ion in the underlying layer is covered with a hydroxyl ion in the top layer, the surface presumably represents a low-energy configuration wherein the electrostatic repulsion between adjacent hydroxyl ions is minimized by hydrogen bonding. Such a configuration is defect-free. On an idealized, completely regular, dry surface, however, the oxide ions in the top layer cover only half of the aluminum ions in the next lower layer, resulting in adjoining sites of charge excess and charge deficiency. Description of the oxide ions in the top layer as O^{-2} is, of course, an approximation. Some degree of electron sharing with the aluminum ions lying below the adjoining vacant sites undoubtedly occurs. The oxide ions in the top layer are not regarded, however, as being located midway between two aluminum ions in the next lower layer with equal sharing of electrons with both aluminum ions. Single vacant sites are, thus, weak Lewis acids, and oxide ions in the surface lattice are weak Lewis bases. Both are "defects" which can be minimized by chemisorption of water or various other molecules. The character of such defects is, moreover, affected by neighboring sites, and a broad spectrum of defect energies should result from the many possible nearest neighbor (and next nearest neighbor) configurations (as can be seen in Figure 3). Isolated vacant sites differ significantly from other vacancy defects, however, because the aluminum ions in the next lower plane are more completely coordinated and less accessible to adsorbed molecules.

The number of defects of all types could be obtained from the computer printouts, but, in view of the arbitrary assumptions employed, little present purpose would be served by such tabulation. During the final stages of hydroxyl ion removal the pair and triplet defects, which seem of greatest interest, were present to approximately the extent shown in Table II.

Table II

OH coverage, %[a]	Defects/1000 Å.² Vacancy Pair	Vacancy Triplet	Oxide Pair	Oxide Triplet
8.6	4.8	3.4	7.1	1.1
5.6	5.1	3.1	6.9	2.5
2.4	7.1	2.5	5.9	4.8

[a] 100% = 8 Å.²/OH.

Defects are apparently considerably more numerous than the sites reponsible for strong adsorption of butene[4,14] or ethylene[15] on alumina. Previous work has indicated that roughly 0.6 site/1000 Å.² holds olefins strongly. If such sites can only be triplet vacancies, the model still provides 4 to 5 times as many sites as needed. Several explanations are possible. Reorganization of the surface with higher retention of hydroxyl ions in shortened domain boundaries could markedly reduce the number of defects. Possibly, only certain of the triplet vacancies can strongly adsorb olefins. Differences exist in the configurations of adjoining oxide or hydroxyl ions. These differences may, for example, restrict strong adsorption to those triplet vacancies which suitably adjoin triplet oxides. Finally, experimental data on olefin adsorption may not correctly indicate the maximum number of possible sites for strong adsorption. Additional evidence is clearly needed.

Rehydration of a Dry Surface. Results achieved in rehydration of dry γ-alumina depend on the experimental conditions.[5] Above 600°, isolated hydroxyl ions are created by chemisorption of water at low pressures. This requires either sufficient mobility to permit hydroxyl ions (or protons) originally on adjacent sites to separate, or simultaneous chemisorption of two water molecules on neighboring sites in such a way that proton transfer between hydroxyl ions can desorb water and leave two isolated hydroxyl ions. Either mechanism can produce isolated ions of all five types to an extent limited by the rate of recombination of the hydroxyl ions. Such behavior is easily explained by the model.

At much lower temperatures, adsorbed water tends

(14) Y. Amenomiya and R. J. Cvetanović, *J. Phys. Chem.*, 67, 2046 (1963).

(15) Y. Amemomiya and R. J. Cvetanović, *ibid.*, 67, 144 (1963).

to be held either as such or as hydrogen-bonded hydroxyl ions. Chemisorption of water vapor at 100° rapidly covers the surface with the equivalent of about 50% hydroxyl monolayer (32 Å.²/water molecule), but further chemisorption is much slower. This suggests that a "packing" effect may be involved. This could arise if, for example, a given hydroxyl ion cannot easily immediately adjoin more than two other hydroxyl ions. Random chemisorption to form pairs of hydroxyl ions would give ~50% hydroxyl monolayer. Slow reorganization (not difficult with high surface hydroxyl coverage and appreciable water vapor pressure) would permit additional adsorption up to 66–67% monolayer with no more than two hydroxyl nearest neighbors, and up to 75% monolayer with no more than three neighbors. Complete coverage (probably impossible) with hydroxyl would require four neighbors. Molecular water would also be strongly held on a surface less than 100% filled with hydroxyl ions.

A similar argument might explain the increased hydration at 100° if alumina is first exposed to water vapor at room temperature. At room temperature enough water is strongly held to permit attachment of one *molecule* at each oxide and vacant site on the model surface (8 Å.²/water molecule). Desorption might require a "condensation" reaction between two adjacent water molecules to desorb one water molecule and leave two hydroxyl ions in the surface. Adjoining water molecules could combine easily until removal of additional water would require more than two hydroxyl ion nearest neighbors per hydroxyl ion. At this point (~50% of the surface covered with water molecules and 50% with hydroxyl ions) surface reorganization would be required to permit removal of additional water. The total coverage would correspond to 125% monolayer (12.8 Å.²/water molecule). However, some explanation is needed for the failure of molecular water to readily adsorb strongly at 100° to produce this coverage.

Near 300°, adsorbed water readily forms hydroxyl ions, but these are mostly paired (hydrogen-bonded). Because surface coverage is only partial, hydroxyl ions would tend to desorb on subsequent dehydration through recombination with their original partners. Fewer isolated hydroxyl ions (and fewer new defects) should therefore be formed on subsequent drying than if the surface had first been completely rehydrated at 100° or below.

Dehydration Isotherms. The simple, random removal process employed to illustrate the model might, at first glance, be expected to yield a dehydration isotherm somewhat resembling Figure 2, *i.e.*, exhibiting some type of break near 33% surface coverage. This has not been observed. Closer appraisal of the partially dehydrated surface shows that a very large number of different site configurations, undoubtedly differing in energy, are created during dehydration. Dehydration behavior would thus probably reflect the progressively increasing severity of defects of all types created by removal of hydroxyl ions. This should reduce or eliminate discontinuities otherwise expected in the dehydration curves. Dehydration can also be regarded as analogous to charging an electrical condenser, since the dry surface is assumed to have a much more pronounced "double-layer" character than the hydroxyl-filled surface. The concentration dependence of the dehydration rate would, thus, appear to be of higher order than otherwise expected. As ionic migration becomes possible in the course of hydroxyl removal, the entropic factor should become increasingly important. Ultimately, the rate of dehydration is probably governed by a large entropy factor, second-order kinetics, and possible readsorption of water. Although quantitative interpretation is not possible at present, the model, with moderate refinement, can be reconciled with observed dehydration isotherms.

Exchange Reactions of Hydroxyl Ions. The three principal types of isolated hydroxyl ions on dry alumina (A-, B-, and C-site hydroxyl ions according to the model) exchange hydrogen with deuterium, deuterium oxide, butene, etc., at different rates.[3,4] Such "exchange" does not, however, require substitution of deuterium on the same site from which the hydrogen was removed. A proton (or hydroxyl ion) may be removed from one site while a deuteron (or deuteroxyl ion) is added at a similar neighboring site. Because hydrogen exchange occurs readily between surface hydroxyl ions and adsorbed molecular water (or deuterium oxide), traces of water may play an intermediate role in exchange between hydroxyl groups and other molecules (*e.g.*, deuterium and butene) which exchange more slowly.

The exchange behavior of the various types of hydroxyl ions with deuterium oxide can be plausibly explained by the model. Deuterium oxide adsorbs on "dry" alumina with transient formation of two deuteroxyl ions through random addition of a deuteron to an oxide ion, the second deuteroxyl ion being attached at an adjacent vacant site. If one of the deuteroxyl ions adjoins a pre-existing hydroxyl ion, transfer of a proton from the hydroxyl ion to the deuteroxyl ion can form HDO. Desorption of HDO leaves a deuteroxyl ion on the surface, usually on a site similar to that holding the original hydroxyl group. This process should occur readily at A- or C-site hydroxyl ions (and desorption of HDO should normally leave

either an A- or C-site deuteroxyl ion), but less often with B-site hydroxyl ions.

Usually, however, formation of only one new deuteroxyl ion is possible in an exchange reaction. Thus, presumably, $D_2 + O^{-2} \rightleftarrows OD^- + D^-$. Exchange can occur in the manner described above only if D^- can easily recapture a proton from a hydroxyl ion on a site corresponding to that on which the deuteroxyl ion was formed. The most common oxide ions in the surface are the regular domain oxide ions. If a deuteroxyl can be transiently formed under exchange conditions at any surface oxide ion, it would be formed mostly from regular domain oxide ions. Exchange could result, however, only if the D^- ion immediately adjoined a hydroxyl ion. This is possible near C-site (or B-site) hydroxyl ions. No A-site hydroxyl should be exchangeable through such a mechanism because initial attachment of D^+ to an interstitial oxide ion (presumably very rare) would be needed, and the D^- ion cannot, in any case, adjoin an A-site hydroxyl ion. Exchange with B-site hydroxyl ions should be much less frequent than with C-site hydroxyl ions.

Experimentally, the C-band (3700 cm.$^{-1}$) is, as expected, usually most easily replaced by the corresponding OD-band in exchange reactions (*e.g.*, deuterium or butene) but in some cases the A-band (3800 cm.$^{-1}$) also shows rapid change. This can be readily understood if traces of water can play an intermediate role, as suggested by recent evidence.[16] Other mechanisms for exchange are possible, however. Observation of "exchange" of surface hydroxyl ions is seldom unambiguous because resolution of the bands often leaves much to be desired, new types of hydroxyl ions may be formed by chemisorption of hydrogen-containing molecules, and traces of water may be involved. Very careful study of exchange reactions is needed before results are used to evaluate the model.

Conclusion

Observations to date are plausibly explained by a simple model for the surface of γ-alumina. Although inherent defects, sites on crystal edges or corners, and various exposed crystal faces may exist, they are not needed to explain either the various types of hydroxyl groups or the generation of active sites on dry alumina.

Rather than strained oxide linkages,[8] high energy "strain" sites on dry alumina can be defects which persist in boundaries between odd and even surface oxide domains.

The present model is, of course, speculative. The surface may be very different from that depicted and possibly much more complex. Faces other than the 100 face may be exposed to a major extent. The model should prove applicable to other faces which can be approximated by a square lattice, but could not be readily applied, for example, to a 111 face.

Serious efforts should be made to determine whether the 100 face is actually preferentially exposed on γ-alumina and whether known faces of other crystalline forms of alumina exhibit similar characteristics. Further evidence, obtained from infrared and related studies of the adsorption of ammonia on γ-alumina, is discussed in the following paper.

Acknowledgment. Special acknowledgment is due to Mr. W. B. Traver, who programmed the model for the IBM 705 computer.

(16) W. K. Hall, H. P. Leftin, F. J. Cheselske, and D. E. O'Reilly, *J. Catalysis*, 2, 506 (1963).

Infrared Study of Adsorption of Ammonia on Dry γ-Alumina[1]

by J. B. Peri

Research and Development Department, American Oil Company, Whiting, Indiana *(Received July 20, 1964)*

Because chemisorption of ammonia on γ-alumina has been thought to measure "acid" sites related to catalytic activity, the mechanism of adsorption was studied by infrared techniques, supplemented by deuterium exchange, gravimetry, and mass spectrometry. At 50° roughly 30% monolayer of ammonia chemisorbs immobily on alumina predried at 800°. Pre-existing hydroxyl groups are all strongly affected, and new hydroxyl groups are formed. The new groups are all affected by further (physical) adsorption at about 70% monolayer coverage. Adsorbed ammonia produces major infrared bands at 3400, 3355, 3100, and 1620 cm.$^{-1}$, and other bands at 3540, 3485, 3260, 3210, 1560, and 1510 cm.$^{-1}$. Partial desorption of ammonia by heating increases hydroxyl bands and changes N–H bands. Most ammonia held at 50° is undissociated; some forms NH_2^- + OH^-; little, if any, forms NH_4^+. That held at 400° exists as NH_2^- + OH^-. No NH_2^- is held at 400° on alumina predried at 400°. The NH_2^- is held at 800° following reaction of ammonia with chlorided alumina. Adsorption of ammonia appears analogous to adsorption of water and is explained by a model for the surface. Sites which chemisorb ammonia to form NH_2^- + OH^- appear to include those which strongly hold and isomerize olefins. These sites are ion-pair or "acid–base" sites.

Introduction

γ-Alumina is widely used as a catalyst and catalyst support. Its catalytic activity is closely related to certain "acid" sites developed when chemisorbed water is removed from the surface.[2-5] These sites are believed to be aluminum ions (Lewis acids) exposed in the surface in small numbers as a result of condensation of surface hydroxyl groups.[5] A recent model explains how such sites may be created.[6] Hydroxyl ions of several types which persist on the alumina surface in small numbers even after evacuation at high temperatures constitute (weak) Brønsted acids.[5]

Adsorption of ammonia poisons the acid sites on alumina and is generally regarded as a measure of surface acidity. Originally, chemisorption of NH_3 was thought to require formation of NH_4^+.[7] Then evidence from infrared studies indicated that on dry alumina it normally occurs through coordination of ammonia with Lewis acid sites.[8,9] More recent infrared evidence suggests, however, that ammonia may be held at 400° as NH_2^- and OH^- ions.[10] If such chemisorption occurs on catalytically important sites, the concept of acid sites on alumina should be modified to include the important role of oxide ions (base sites) in adsorption and catalysis. Consequently, the nature of ammonia adsorption was studied in greater detail through the use of infrared techniques, isotopic exchange, and gravimetry. Study was confined to alumina predried at 400° or higher.

Experimental

Preparation of the γ-alumina aerogel plates has been described.[11] These plates had specific surface areas of

(1) Presented at 142nd National Meeting, American Chemical Society, Atlantic City, N. J., Sept. 1962.

(2) V. C. F. Holm and R. W. Blue, *Ind. Eng. Chem.*, **43**, 501 (1951).

(3) S. G. Hindin and S. W. Weller, *Advan. Catalysis*, **9**, 70 (1957).

(4) Y. Trambouze, L. de Mourges, and M. Perrin, *J. chim. phys.*, **51**, 723 (1954).

(5) J. B. Peri, *Actes Congr. Intern. Catalyse, 2e, Paris, 1960*, **1**, 1333 (1961).

(6) J. B. Peri, *J. Phys. Chem.*, **69**, 220 (1965).

(7) G. W. A. Rijndners and G. C. A. Schuit, *Rec. trav. chim.*, **69**, 668 (1950).

(8) A. N. Webb, *Ind. Eng. Chem.*, **49**, 261 (1957).

(9) R. P. Eischens and W. A. Pliskin, *Advan. Catalysis*, **10**, 1 (1958).

(10) J. B. Peri and R. B. Hannan, *J. Phys. Chem.*, **64**, 1526 (1960).

(11) J. B. Peri, *ibid.*, **69**, 211 (1965).

approximately 300 m.²/g., as measured by nitrogen adsorption.

Ammonia (Matheson anhydrous) was dried by passage over freshly ignited calcium oxide and freed of permanent gases by freezing and evacuation. Deuterium oxide (Stewart Oxygen Co.) was used without further purification. 1-Butene was as previously described.[5]

The infrared cells, spectrometers, and vacuum systems have also been described.[5,10] The cells permitted *in situ* treatment of the alumina plates and study in the lithium fluoride or calcium fluoride spectral range depending on the cell and optics used. Cell C included a quartz helix balance so that weight and spectral changes could be followed simultaneously.[5]

In a typical experiment, an aerogel plate was calcined in oxygen at 600° to remove organic contaminants and evacuated at 800° for 1 to 2 hr. It was then rehydrated by exposure to water vapor at about 1 cm. pressure at 100° and subsequent heating in water vapor at 400°. Finally the plate was dried by evacuation at a specified temperature, usually for 1 to 2 hr. After evacuation at 800°, the surface usually held 2 to 5% monolayer of hydroxyl ions.

After the plate had been cooled to room temperature, or to 50°, ammonia was admitted in small, measured doses. Weight, pressure, and spectral changes were followed concurrently in some of the experiments. Initial small additions of ammonia were completely adsorbed within a few minutes, but with higher surface coverages at higher pressures, spectra and weight changed slowly, even after long equilibration.

Desorbed gas was, in some experiments, analyzed by mass spectrometry.

Gravimetric Study

The nature and extent of adsorption of ammonia depend on the pretreatment of the alumina, the temperature of adsorption, and on other variables.

Figure 1 illustrates weight changes of an aerogel plate, previously dried at 800°, following addition of small doses of ammonia at 50°. The plate had a specific surface area of 293 m.²/g. and a dry weight of 0.21 g. Initial additions of ammonia were rapidly and almost completely adsorbed until the surface was 20–30% covered (100% coverage assumed as 6.25 molecules of ammonia/100 Å.², corresponding to one molecule for every two hydroxyl ions on a hydroxyl-covered surface or for each oxide ion in the outer layer on a fully dehydrated surface[6]). Further additions gave increased total adsorption at higher equilibrium pressures until 50–60% of the surface was covered.

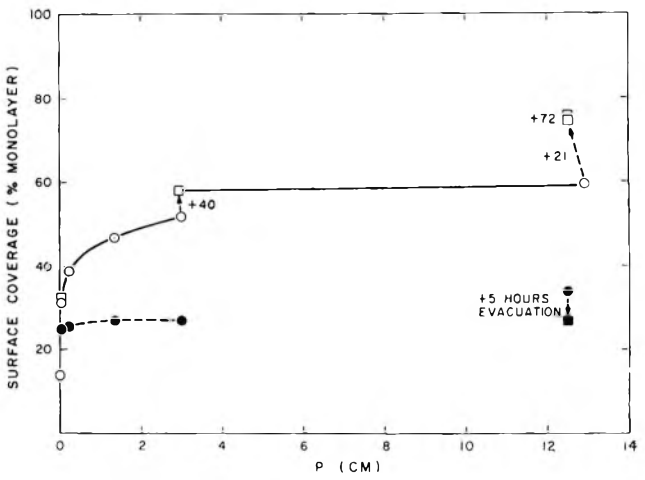

Figure 1. Adsorption of NH_3 (50°).

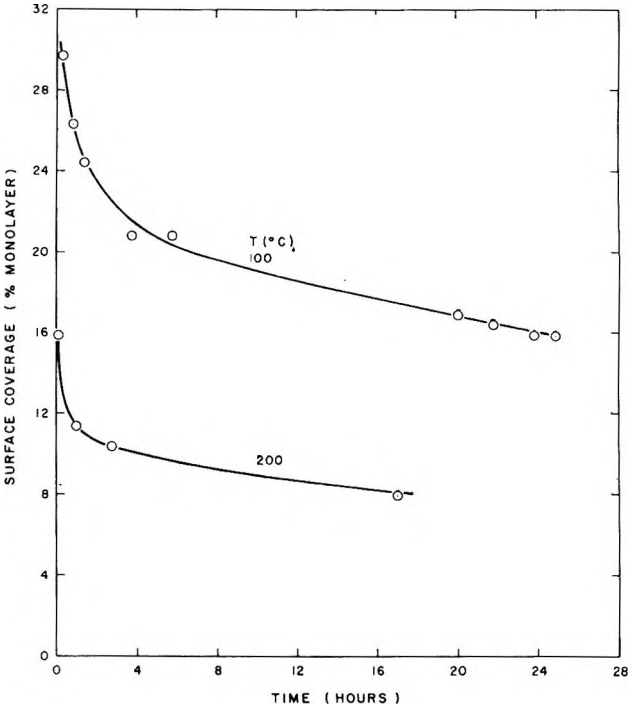

Figure 2. Desorption of NH_3.

Adsorption was usually recorded after 0.5 to 1 hr. equilibration. Results are represented by open points in Figure 1. The numbers shown between points give elapsed equilibration times in hours, where greater than 1 hr. Ammonia in excess of 25–30% monolayer was, at least initially, held much less tightly than that first adsorbed. The solid points in Figure 1 represent retention of ammonia after evacuation for 0.5 hr. from the initial pressures shown. Slow adsorption at pressures above 2 cm. markedly increased total adsorption on standing, but most of the gain was due to weakly

held ammonia. At 12.5 cm., the adsorption corresponded to 75% coverage after 48 hr., but this was reduced to 34% after 0.5-hr. evacuation and to 27% after 5 hr. Of the total increase in adsorption at higher pressures (nearly 5 days after adsorption was measured at 1 mm.), less than 25% was held strongly enough to be retained after 0.5-hr. evacuation. Adsorption appeared similar on alumina predried at 600°, but extended gravimetric study was made only on alumina dried at 800°.

Figure 2 illustrates desorption of ammonia after the adsorption described above. Much of the ammonia was not readily removed at 200° or at even higher temperatures. Gravimetric data were, in this instance, unreliable after evacuation at 400°, but infrared spectra showed that some ammonia was retained. Desorption of ammonia appears similar to desorption of water,[11] but ammonia is held less strongly. In both cases the free energy of activation for desorption appears to increase steadily with decreasing surface coverage.

Infrared Study

During the gravimetric experiments infrared study of the aerogel plate was made in cell C; other plates were studied in cell A or cell C. In some experiments, the plates were pretreated with deuterium or deuterium oxide to give a surface holding deuteroxyl instead of hydroxyl ions before adsorption of ammonia.

Certain features of the spectral changes have been reported previously.[10] Detailed examination shows adsorption of ammonia to be fairly complex.

Bands Produced by Ammonia Adsorption. When ammonia was adsorbed at 50° on alumina predried at 800°, two relatively sharp bands appeared at 3355

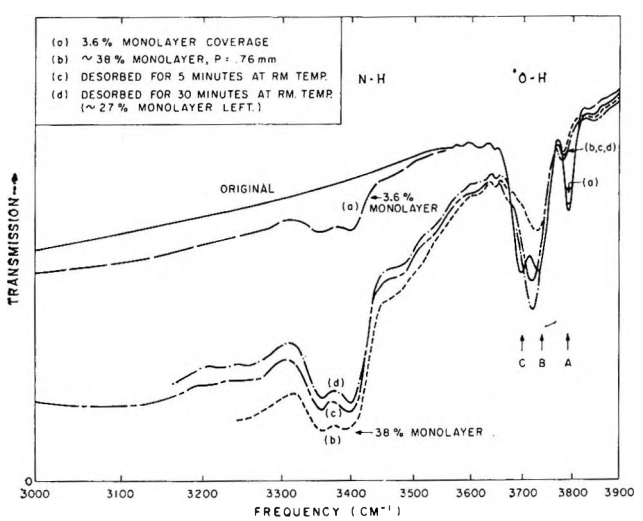

Figure 3. Spectra showing adsorption of NH_3 on (800°-predried) alumina.

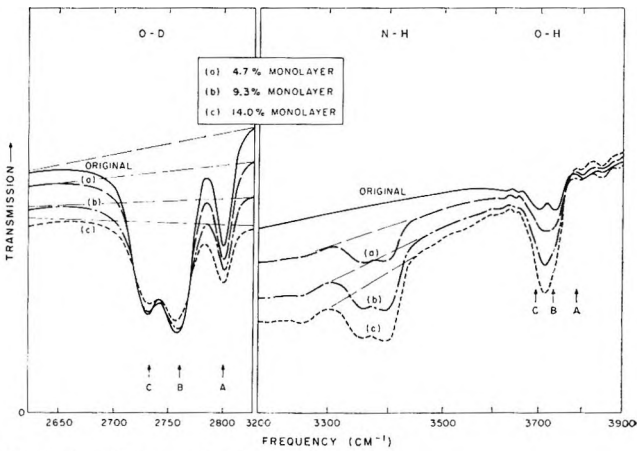

Figure 4. Spectra showing adsorption of NH_3 on deuterated alumina.

and at 3400 cm.$^{-1}$, as shown in Figure 3. Weaker bands were found near 3485 and 3540 cm.$^{-1}$, and again near 3210 and 3260 cm.$^{-1}$. A strong, broad band having a maximum near 3100 cm.$^{-1}$ also appeared. With the possible exception of the two above 3400 cm.$^{-1}$, all these bands appear to be caused principally by N–H stretching vibrations. Any major contribution from hydrogen-bonded hydroxyl stretching is excluded by results, to be described later, on fully deuterated alumina.

Several bands assignable to $-NH_2$ or NH_3 deformation modes were also produced at lower frequencies. A strong band appeared near 1620 cm.$^{-1}$, and others near 1560 and 1510 cm.$^{-1}$.

No other bands directly attributable to adsorbed ammonia were found (1260–3900 cm.$^{-1}$). In particular, none was observed near 1400 cm.$^{-1}$, as should have resulted from formation of NH_4^+. If such a band exists, it must be very weak and broad.

Effects of Ammonia Adsorption on Hydroxyl and Deuteroxyl Bands. Figure 3 shows how adsorption of ammonia affects the hydroxyl stretching bands originally present in the spectrum. Three major bands (A, B, and C) were originally present, representing three chemically distinct types of hydroxyl ions.[10] The central band (B) appeared to be much less reduced in intensity than the other two. When gaseous and physically adsorbed ammonia was removed by a trap cooled with liquid nitrogen, this band was restored to at least its original intensity, or a similar one was produced at a slightly lower frequency.

This phenomenon was investigated in closer detail on a deuterated aerogel plate. After deuterium exchange at 600°, the plate was dried by evacuation for 30 min. at 800°, leaving the surface about 3.2% covered with deuteroxyl ions (a total of 5.0×10^{19} ions calcu-

lated from deuteroxyl band absorbance). Ammonia added at room temperature in three successive doses, each containing 3.6×10^{19} molecules, was almost completely adsorbed. Resulting spectral changes are shown in Figure 4. The maximum surface coverage was 14%. The intensities of the three deuteroxyl bands were reduced to nearly equal extents. At the same time, a new hydroxyl band was formed at ~3725 cm.$^{-1}$ between the normal frequencies of the B and C hydroxyl bands. It could not have originated from simple exchange with deuteroxyl, because it differed in frequency from any of the original hydroxyl bands. The apparent slight effect of ammonia adsorption on the B band (*e.g.*, Figure 3) was, thus, misleading; it had resulted from formation of a new hydroxyl band.

Strong N–H stretching bands at 3355 and 3400 cm.$^{-1}$, plus weaker bands at 3260 and 3210 cm.$^{-1}$, were also produced, together with the deformation band at 1620 cm.$^{-1}$. No other bands were detected.

The reduction of deuteroxyl band intensities and the increase of the new hydroxyl band were closely proportional to the amount of ammonia adsorbed, but calculations showed that a one-to-one relation did not exist. To determine the true relation, changes in the numbers of deuteroxyl and hydroxyl groups were obtained from the absorbance changes for the bands and the average apparent (peak intensity) absorptivities previously determined in deuterium-exchange experiments (deuteroxyl = 8.6×10^5 cm.^{2}/mole; hydroxyl = 7.8×10^5 cm.^{2}/mole). Base lines were drawn for the deuteroxyl bands (as indicated by dashed lines in Figure 4) to eliminate the effect of the underlying broad band. From the known adsorption of ammonia and the changes in the numbers of deuteroxyl and hydroxyl groups, calculation showed that only 25% of the adsorbed ammonia molecules eliminated preexisting isolated deuteroxyl groups, while only 10% formed new hydroxyl groups.

Evidently chemisorbed ammonia is essentially immobile at a surface coverage of 14%. Certainly it did not completely exchange with the original deuteroxyl groups, even after several days. The over-all H:D ratio after chemisorption of 14% monolayer of ammonia was such that complete exchange would have reduced deuteroxyl band intensities to ~13.4% of their original values compared with the observed 44%. Free mobility plus exchange would, moreover, have yielded corresponding hydroxyl bands instead of the unusual, new hydroxyl band.

As additional ammonia was adsorbed, the deuteroxyl bands continued to shrink; when the surface was 30–40% covered, they finally disappeared. Spectra

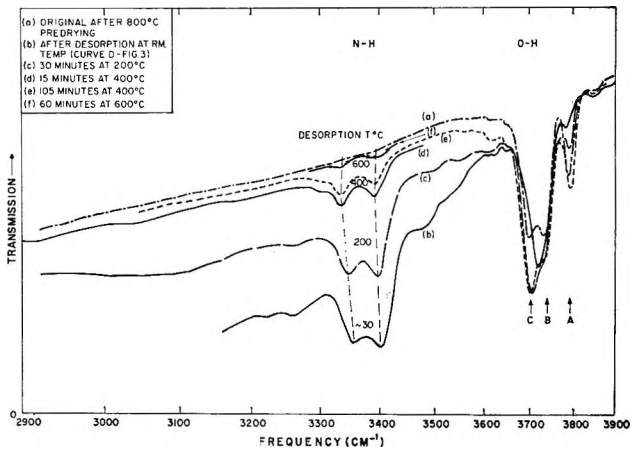

Figure 5. Spectra showing desorption of NH_3 from (800°-predried) alumina.

recorded during the gravimetric experiments showed that the A and C hydroxyl bands vanished at 30% coverage, and the remaining hydroxyl band ultimately disappeared at 60–70% coverage.

Desorption of Ammonia. Removal of weakly held ammonia (above roughly 30% coverage) by evacuation for 0.5 hr. at room temperature caused appearance of a hydroxyl band lying between the normal B and C band positions, as shown in Figure 3 (c and d). Little or no restoration of the original A or C bands occurred. The weak bands above and below the main N–H stretching bands were more evident after evacuation.

Desorption at higher temperatures was studied after the spectra shown in Figure 3 had been recorded. Ammonia desorbed from the heated alumina was collected in a trap cooled with liquid nitrogen. Typical spectra recorded in the N–H and O–H stretching region are shown in Figure 5.

After the plate had been heated at 200° for 30 min., the C band had reappeared and increased to well beyond its original intensity. The other hydroxyl bands increased only slightly. All N–H stretching bands decreased in intensity. The bands at 3400 and 3355 cm.$^{-1}$ shifted to slightly lower frequencies, and the weak bands near 3485 and 3540 cm.$^{-1}$ shifted to slightly higher frequencies. The broad band at 3100 cm.$^{-1}$ remained, but was much weaker. The bands at 1620 cm.$^{-1}$ and 1560 cm.$^{-1}$ also decreased markedly, but the deformation band at 1510 cm.$^{-1}$ seemed unaffected.

Heating at 400° for 2 hr. gave further changes. The A band increased markedly; the other hydroxyl bands changed very little. The two major N–H stretching bands decreased in intensity and again shifted to lower frequencies (3386 and 3335 cm.$^{-1}$),

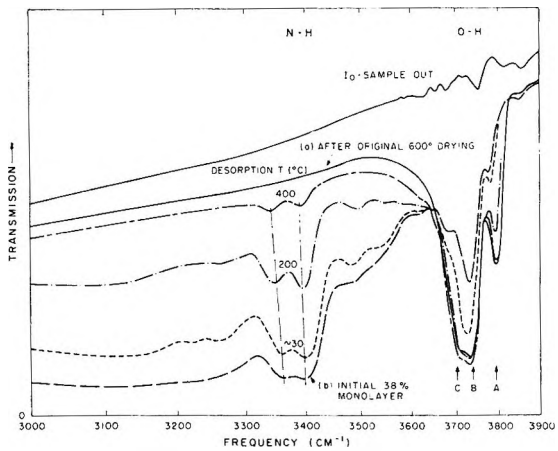

Figure 6. Spectra showing desorption of NH_3 from (600°-predried) alumina.

with a shoulder appearing at 3300 cm.$^{-1}$. The other bands in the N–H stretching region disappeared. The deformation bands at 1620 cm.$^{-1}$ and 1560 cm.$^{-1}$ lso disappeared, but the band at 1510 cm.$^{-1}$ retained over 50% of its original intensity. Based on the intensity of the N–H stretching bands, the surface coverage with chemisorbed ammonia decreased from about 3.5%, after 15 min. heating, to roughly 2.5% after 2 hr.

After the plate had been heated at 600° for 1 hr., only a trace remained of the N–H bands at 3386 and 3335 cm.$^{-1}$ and 1510 cm.$^{-1}$. The hydroxyl bands were still slightly more intense than on the original dry alumina, but the relative intensities of the three bands now more closely resembled those originally observed.

Heating at 800° removed all N–H bands and left the hydroxyl bands in apparently the same condition as after original evacuation at 800°.

As the temperature of evacuation was increased, the ratio between absorbance of the N–H stretching bands and the absorbance *increase* in the hydroxyl bands decreased steadily. After heating at 400° it corresponded to 0.54–1.0 new hydroxyl group produced for each remaining chemisorbed molecule of ammonia. The calculations assumed equal absorptivities for initially adsorbed ammonia and for the chemisorbed ammonia finally retained. The range depends on whether the intensity of the N–H bands was measured from the I_0 curve (giving a ratio of 1.0) or from base lines such as those in Figure 4.

Effects of Predrying below 800°. When alumina was predried below 800° certain differences were noted in the adsorption of ammonia. Figure 6 illustrates the adsorption and desorption of ammonia on the aerogel plate represented by Figure 3 after it had been rehydrated and subsequently dried at 600°. Because the isolated hydroxyl bands were more intense and less well resolved than on the drier alumina, changes in individual bands are not as easily seen, but they appear generally similar to those noted earlier. The stretching and deformation bands assignable to adsorbed ammonia changed after heating in much the same way as on the drier alumina. The weak bands at 3485 and 3540 cm.$^{-1}$ were slightly more intense than before. Less ammonia was retained after evacuation at 400°, however, and none after evacuation at 600°.

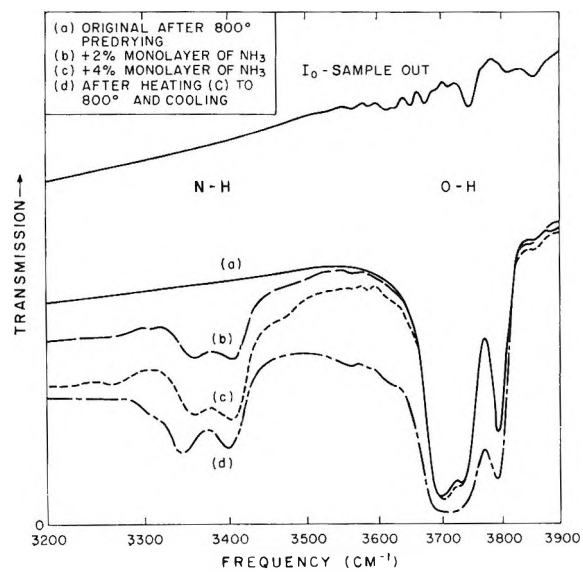

Figure 7. Spectra obtained during reaction of NH_3 with alumina.

The same aerogel plate was then rehydrated and dried at 400°. Adsorption of ammonia now gave still less information about changes in isolated hydroxyl bands. Bands due to adsorbed ammonia were generally similar to those on drier alumina, but the band at 1560 cm.$^{-1}$ was much weaker than before, and there was no band at 1510 cm.$^{-1}$. Some N–H stretching bands were still detectable after desorption of ammonia at 300°, but were absent after evacuation at 400°. During desorption, the weak bands at 3485 and 3540 cm.$^{-1}$ were relatively more intense than in previous experiments, being nearly as intense as the bands at 3400 and 3355 cm.$^{-1}$ after desorption at 200°.

Throughout the experiments on alumina predried at different temperatures, the broad band at 3100 cm.$^{-1}$ did not change markedly in relative intensity at a given surface coverage with ammonia, despite large variations in the number of hydroxyl groups originally present. This band appeared to be proportional to the intensity of the sharper N–H stretching bands. It clearly was not caused by hydrogen bonding from hydroxyl groups to adsorbed ammonia.

Reactions of Ammonia at Low Coverage on Alumina. Decomposition of ammonia and its reaction with the surface at low coverages were studied on a thick sample of alumina aerogel (1.16 g. total, ~220 mg./cm.^{2}). After being dried at 800° for 1.5 hr., the alumina was exposed to sufficient ammonia (in two additions) to cover 4% of the surface. Spectra before and after these additions are shown in Figure 7. Evacuation at room temperature for over 3 hr. desorbed little or no ammonia. The cell was then closed off, heated at 400° for over 3 hr., and cooled to room temperature. The cell pressure rose on heating but fell again on cooling as ammonia was readsorbed. A low residual pressure was noted, which, if caused entirely by ammonia decomposition to nitrogen and hydrogen, represented about 4% of the adsorbed ammonia.

Heating the closed cell at 600° for 1 hr. gave little additional pressure increase, but heating at 800° for 2.3 hr. gave a permanent pressure increase after cooling, which indicated that about 20% of the adsorbed ammonia had decomposed to nitrogen and hydrogen. Mass spectrometric analysis of the gas phase showed hydrogen (77.6 mole %), nitrogen (16.1 mole %), and carbon monoxide (3.8 mole %). The H:N ratio was higher than theoretical. When the remaining ammonia was desorbed at 800°, the major components were hydrogen (38.8 mole %), ammonia (28.2 mole %), and nitrogen (17.5 mole %). Minor amounts of carbon dioxide, carbon monoxide, water, and other gases were also reported. The H:N ratio was, in this case, lower than theoretical. (The total nitrogen and hydrogen recovered represented well over 70% of the theoretical value from decomposition of unrecovered ammonia.) The over-all H:N ratio in the recovered material was very close to 3. Evidently the "ammonia" held by the alumina before final desorption at 800° contained somewhat less hydrogen than represented by NH_3. As much as 25% may have had a composition corresponding to NH_2, the other 75% corresponding to NH_3 (or $NH_2^- + OH^-$). A spectrum recorded at this point is also shown in Figure 7. The increase in the isolated-hydroxyl stretching bands and the typical shift in the N–H stretching bands are quite apparent. A broad increase in absorption below 3700 cm.$^{-1}$ apparently shows formation of some hydrogen-bonded hydroxyl.

Retention of Ammonia on Chlorided Alumina. A chlorided alumina plate was prepared by treating the aerogel plate used in the gravimetric work with HCl at 600° and evacuating at 800°. This treatment removed virtually all hydroxyl groups.

Ammonia was added to the chlorided alumina at 400° (3 cm. pressure in cell). After heating at 400 and 600° the cell was evacuated at 600° and again at 800°. Sample weight and spectral changes were followed throughout this process. Addition of ammonia at 400° caused an initial increase in weight, but subsequent heating and evacuation gradually decreased the weight. After final evacuation for 1 hr. at 800° the aerogel plate had lost about 0.75 of the weight gained after original chloriding (and 800° evacuation), showing extensive removal of chloride ions from the surface. Appreciable amounts of white sublimate (presumably NH_4Cl) were deposited on the cell walls above the furnace section during heating.

Spectra showed that only traces of hydroxyl were formed during these experiments, but NH_4^+ was apparently formed and held fairly strongly on the surface. After evacuation at 800° chemisorbed ammonia was held on a surface that was virtually free of hydroxyl groups. The N–H bands remaining resembled those previously found for chemisorbed ammonia on alumina (800° predried) after evacuation at 400°, but were more intense. Comparison of the intensities of the N–H stretching bands with those of the hydroxyl bands remaining after the original aerogel plate had been dried at 800° showed that roughly as much NH_2^- was retained as necessary to replace the hydroxyl groups originally held at 800°. Reaction of ammonia with chlorided alumina at high temperatures must replace chloride ions on the surface with NH_2^- ions. Such NH_2^- ions apparently play the same role as hydroxyl ions in minimizing surface defects and cannot be readily removed by heating even at 800°. The similarity of the N–H bands found in these experiments to bands discussed previously provides evidence that NH_2^- is formed to some extent on unchlorided alumina.

Ammonia Poisoning of Active Sites for Isomerization of 1-Butene. When predried above 400°, alumina readily catalyzes isomerization (double-bond shift) of butene at room temperature.[5] Because chemisorbed ammonia is known to poison the active sites on alumina, experiments were made to determine the relation between retention of ammonia and the isomerization activity of dry alumina.

A fairly thick aerogel plate was predried by evacuation at 800° for 2 hr. and, after cooling to room temperature, was exposed to 1-butene at 4.1 mm. The rate of isomerization was estimated from changes in the relative intensities of bands at 3017 and 2964 cm.$^{-1}$ in C–H stretching spectra recorded at short intervals. The cell was then evacuated at 400° to remove the adsorbed butene, and the alumina plate was exposed (at 400°) to 5 cm. of ammonia for 5 min. Following this, the cell was evacuated for 10 min. and cooled to room temperature. After a spectrum had

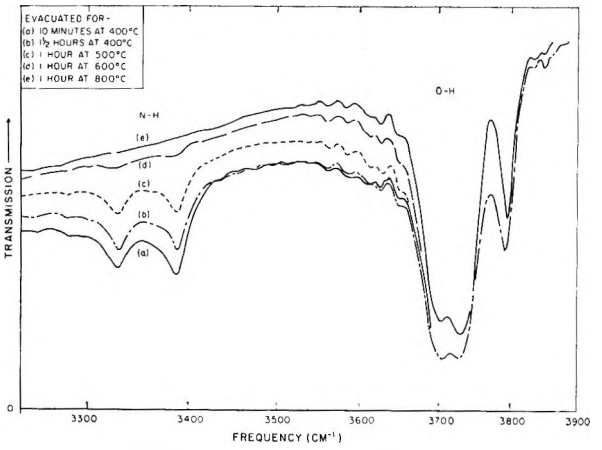

Figure 8. Spectra showing retention of NH_3 at 400° and higher (poisoning butene isomerization).

been recorded, butene was admitted as before, and the rate of isomerization was again determined. This process was repeated several times, with progressive removal of chemisorbed ammonia by evacuation for longer times and at higher temperatures.

The spectra in the O–H and N–H stretching regions are shown in Figure 8. Maximum retention of chemisorbed ammonia, estimated from absorbance and weight changes, was about 5% monolayer. The N–H bands after evacuation at 400° were similar to those previously described. The frequencies of these bands did not appear to shift during progressive removal of the chemisorbed ammonia.

The relative rate of isomerization was estimated as before on the alumina represented by each of the spectra shown in Figure 8. Isomerization rates varied with ammonia retention roughly as shown in Table I.

Table I

Ammonia retained, % monolayer	5	3.8	2.3	0.5	0
Relative rate of isomerization	8	17	45	~100	100

Over 90% of the sites active for isomerization were, therefore, blocked by chemisorption of about 5% monolayer of ammonia.

Discussion

The fundamental frequencies of ammonia (gas) are found near 3337 (ν_1), 3414 (ν_3), 1628 (ν_4), and 950 cm.$^{-1}$ (ν_2).[12] Both ν_1 and ν_2 are split by inversion doubling, but splitting for ν_1 is too small to be detectable, and ν_2 falls below the frequency range studied. Thus no information was obtainable on possible inversion transitions. In the N–H stretching region, primary amines and (organic) amides show two N–H stretching bands, while secondary amines and amides show only a single band. For primary amines the two stretching bands fall in the 3300–3500-cm.$^{-1}$ range, while, for amides, they are generally in the 3400–3500-cm.$^{-1}$ range.[13] An $-NH_2$ deformation band is found around 1600 cm.$^{-1}$ for both primary amines and amides. Published infrared data on metal amides are scarce, but $-NH_2$ in $Hg(NH_2)Br$ shows a bending band at 1505 cm.$^{-1}$.[14] Bands due to NH_3^+ deformation vibrations (amino acids) also occur in this region[13]; agreement is fairly general that a strong band exists in the range 1485–1550 cm.$^{-1}$. The NH_3^+ stretching frequencies are represented by a single band in the 3030–3130-cm.$^{-1}$ region[13]; NH_4^+ stretches normally fall near 3200 cm.$^{-1}$ with a deformation band in the range 1390–1430 cm.$^{-1}$.

Three of the major bands observed when ammonia is initially adsorbed on dry alumina (3400, 3355, and 1620 cm.$^{-1}$) show either adsorption of molecular ammonia or formation of amino groups ($-NH_2$) or amide ions (NH_2^-). The formation of $-NH_2$ or NH_2^- presumably requires simultaneous formation of hydroxyl groups ($NH_3 + O^{-2} \rightarrow NH_2^- + OH^-$). The evidence shows, however, that only about one ammonia molecule in ten reacts in this way. The spectra also eliminate NH_4^+ as a major product of adsorption although small amounts may exist. Most of the ammonia is, thus, initially adsorbed molecularly.

The fourth major band (3100 cm.$^{-1}$) observed on initial adsorption appears to be caused by hydrogen bonding of adsorbed ammonia to surface oxide ions. Such bonding alone, however, can hardly provide sufficient energy to hold molecular ammonia as strongly as observed. Coordination of the nitrogen atom with aluminum ions or hydroxyl groups must play the major role. Strong coordination of ammonia with aluminum ions might also produce stretching bands near 3100 cm.$^{-1}$. NH_3^+, for example, could occur as a limiting result of electron donation to an aluminum ion and contribute to absorption in this region of the spectrum.

When alumina is heated to 400°, molecular ammonia either desorbs or reacts with surface oxide ions to form hydroxyl and amide ions. The evidence for NH_2^-

(12) G. Herzberg, "Molecular Spectra and Molecular Structure," Vol. II, D. Van Nostrand Co., Inc., New York, N. Y., 1945, p. 295.

(13) L. J. Bellamy, "The Infrared Spectra of Complex Molecules," Methuen and Co., Ltd., London, 1954, pp. 175–222.

(14) I. Nakagawa, R. B. Penland, S. Mizushima, T. J. Lane, and J. V. Quagliano, *Spectrochim. Acta*, 9, 199 (1957).

(rather than NH^{-2}) rests principally on the presence of two N–H stretching bands (3386 and 3335 cm.$^{-1}$) and on results of the experiments on chlorided alumina. Results of the material balance study generally support this assignment but suggest that a small fraction of the chemisorbed NH_3 may exist as NH^{-2} (as might result from $NH_3 + O^{-2} \rightarrow NH^{-2} + H_2O\uparrow$). The band at 1510 cm.$^{-1}$ is also evidently caused by NH_2^-.

The weak bands at 3485 and 3540 cm.$^{-1}$ apparently reflect some interaction between adsorbed ammonia and pre-existing hydroxyl ions, but the nature of this is unknown. The weak N–H stretching bands at 3210 and 3260 cm.$^{-1}$ may reflect coordination of ammonia at special surface sites or traces of NH_4^+. The band at 1560 cm.$^{-1}$ corresponds to some form of chemisorbed ammonia held less strongly than the NH_2^- responsible for the band at 1510 cm.$^{-1}$.

The behavior of ammonia on dry alumina resembles that of water. Both are strongly adsorbed at low temperatures but are largely held molecularly. Reaction of water with oxide ions forms hydroxyl ions, while ammonia gives hydroxyl and NH_2^- ions. Retention of ammonia after evacuation is determined by prior drying of the alumina. Some chemisorbed ammonia can be retained after evacuation below the temperature at which the alumina was originally dried, but normally not at this temperature.

On heating, proton transfer from ammonia to oxide ions must occur fairly readily and reversibly at many points on the surface. Ammonia is, however, normally desorbed in preference to water. After evacuation at 400°, only NH_2^- ions which do not immediately adjoin hydroxyl ions probably remain on the surface and are ultimately eliminated through encounters with migrating protons (coming from hydroxyl ions). If NH_2^- ions can be substituted for the hydroxyl ions normally remaining on alumina that has been dried at high temperatures, they can be held very tenaciously.

The general features of ammonia chemisorption seem reasonably clear, but important details require further explanation. Although no unique interpretation is presently possible, some speculation can be offered, based on a model[6] for the alumina surface.

Figures 9 and 10 in ref. 6 represent a surface believed similar to that obtained after drying alumina at 800°. Ammonia could be held in various ways. Hydrogen bonding from ammonia to a single oxide ion is not likely to produce strong adsorption. Several other possible methods of attachment could, however, hold ammonia immobily at 50°. Certain sites might be preferred during adsorption, but in the absence of further information, all sites involving defects or hydroxyl ions (where two-point attachment or NH_4^+ formation is possible) are assumed to be equally favored for initial strong adsorption.

Table II

	Sites/1000 Å.^{2}
Hydroxyl ions	4
Triplet vacancies	3
Triplet oxides	4
Pair vacancies	6
Pair oxides	6
Total	23

The number of isolated hydroxyl ions and defects expected on a surface 3.2% covered with hydroxyl ions can be estimated from previous information[6] as shown in Table II. If one ammonia molecule can be tightly held at each hydroxyl and at each defect, a total of 23 molecules can be held per 1000 Å.^{2} of surface, corresponding to ~37% surface coverage (100% = 62.5/1000 Å.^{2}), in fair agreement with observation. At this point all pre-existing hydroxyl ions should be affected. Chemisorption of ammonia to form hydroxyl ions and NH_2^- should occur most easily at triplet defects. If such chemisorption occurs only at triplet *vacancies*, 3 molecules per 1000 Å.^{2} (4.8% monolayer) could thus be chemisorbed.

We might expect, from the relative numbers of various sites, that 13% of the ammonia initially adsorbed would form new hydroxyls (*vs.* ~10% observed) and that 17.5% would affect existing hydroxyls (*vs.* ~25% observed). The remaining ammonia would be strongly held by coordination with aluminum ions at pair-vacancy defects or by strong hydrogen bonding at oxide defects. The slow increase in adsorption of ammonia can be explained by slow rearrangement of ammonia on the surface.

Most of the detailed spectral changes observed during adsorption and desorption of ammonia might be qualitatively explained in terms of changes in type of binding and nearest neighbor configuration on the model surface, but because of the extreme complexity of such changes and the many uncertain assumptions required, such interpretation does not appear warranted at present.

Conclusion

Adsorption of ammonia on dry γ-alumina occurs in several ways. Most ammonia is strongly adsorbed as such, but certain sites that chemisorb ammonia as NH_2^- and hydroxyl ions appear essential for butene isomerization. They should be described as "acid–base" or "ion-pair" sites although the role of the

aluminum ion is often more evident than that of the oxide ion (*e.g.*, in adsorption of butene). Adsorption on an aluminum ion should cause partial electron withdrawal from an adsorbed molecule. Proton transfer may then occur from the adsorbed molecule to an adjoining oxide ion, provided that the resulting anion and hydroxyl ion can be suitably held by the surface. Present results suggest that butene isomerization may occur through transient formation of a carbanion.

Attempts to relate total ammonia retention on alumina to catalytic activity appear destined to very limited success. Ammonia adsorption on chlorided alumina provides, at best, ambiguous evidence on acidity because NH_2^- can readily replace chloride ions.

Acknowledgments. The cooperation of Dr. R. B. Hannan, who performed the experiments involving decomposition of ammonia over alumina, and of Mr. J. Kekich, who assisted in most of the experimental work, is gratefully acknowledged.

The Crystal Structure of Sodium Tetrachloroferrate(III)

by R. Ronald Richards and N. W. Gregory

Department of Chemistry, University of Washington, Seattle, Washington *(Received July 20, 1964)*

The crystal structure of $NaFeCl_4$ is found to be orthorhombic, $P2_12_12_1$, with unit cell dimensions $a_0 = 10.304$, $b_0 = 9.880$, $c_0 = 6.235$ Å. The crystal contains slightly distorted tetrahedral $FeCl_4$ groups; sodium atoms are surrounded by six chlorine atoms at distances between 2.78 and 3.09 Å. Bond distances, angles, and packing characteristics are discussed.

In conjunction with a thermodynamic study[1] we have determined the crystal structure of sodium tetrachloroferrate(III). Crystallographic data for compounds of the type $MFeCl_4$ have not been found in the literature. However Friedman and Taube,[2] and Friedman,[3] on the basis of visible and ultraviolet spectra and melting point data, suggest that the iron in such substances is in the form of an $FeCl_4^-$ ion. Friedman also concluded, from magnetic susceptibility measurements, that the $FeCl_4^-$ ion is tetrahedral and noted that the visible spectra of $FeCl_4^-$ in ether and of $KFeCl_4$ solid are similar. A tetrahedral arrangement in solution is also indicated by Raman spectra.[4] Magnetic susceptibility measurements and optical and Mossbauer spectra indicate that the iron in $(pyH)_3Fe_2Cl_9$ (py = pyridine) is present in the form of tetrahedral $FeCl_4^-$ ions.[5] The crystal structure of $NaAlCl_4$, which appears to be isomorphous with $NaFeCl_4$, has been reported by Baenziger.[6]

Experimental

$NaFeCl_4$ was formed by subliming $FeCl_3$, prepared by reaction of Mallinckrodt A.R. iron wire (99.95%) with commercial tank chlorine at 425° in a vacuum system, onto an equimolar amount of B and A reagent grade NaCl, which had been dried under high vacuum at 500°. The mixture was melted (m.p. 163°)[7] in an ampoule, sealed off from the vacuum line, and cooled slowly. Large crystals (1–2-mm. cubes or plates) were observed to grow at the surface of the melt as the mass

(1) R. R. Richards and N. W. Gregory, *J. Phys. Chem.*, **68**, 3089 (1964).

(2) H. L. Friedman and H. Taube, *J. Am. Chem. Soc.*, **72**, 2236 (1950).

(3) H. L. Friedman, *ibid.*, **74**, 5 (1952).

(4) J. A. Woodward and M. J. Taylor, *J. Chem. Soc.*, 4473 (1960).

(5) A. P. Ginsberg and M. B. Robin, *Inorg. Chem.*, **2**, 817 (1963).

(6) N. C. Baenziger, *Acta Cryst.*, **4**, 216 (1951).

(7) C. M. Cook and W. E. Dunn, *J. Phys. Chem.*, **65**, 1505 (1961).

Table I: Structure Factors and Phase Angles for Sodium Tetrachloroferrate(III)

	$10\|F_o\|$	$10\|F_c\|$	Phase angle, mcycles
	H, 0, 0		
2	1063	936	000
4	636	616	500
6	656	635	000
10	483	468	500
12	214	211	500
	H, 1, 0		
2	315	320	500
3	963	923	750
5	1000	971	750
7	475	500	750
9	394	411	750
11	245	236	750
	H, 2, 0		
0	1073	1000	000
2	1185	1119	000
3	78	74	750
4	1057	1045	000
5	305	306	750
6	283	242	000
8	343	367	500
9	150	209	250
10	264	236	500
	H, 3, 0		
1	678	688	250
2	375	373	000
3	404	381	750
4	269	281	500
5	1454	1422	750
6	299	284	500
7	449	458	750
11	245	248	750
	H, 4, 0		
0	1443	1479	000
1	533	538	750
2	803	784	000
4	305	316	000
5	140	147	250
6	244	270	000
8	171	150	500
10	200	251	500
	H, 5, 0		
1	240	244	750
2	184	184	500
3	522	534	750
4	337	329	500
5	455	474	750
7	365	395	750
9	331	354	750
10	163	165	500
	H, 6, 0		
0	1332	1332	000
1	308	323	750
2	418	459	000
5	177	213	750
6	345	313	000
9	184	188	250
10	276	266	500
	H, 7, 0		
3	381	384	750
4	180	188	500
5	446	472	750
6	296	261	500
7	225	184	750
8	163	122	500
9	171	165	750
11	178	154	750
	H, 8, 0		
1	262	280	750
2	381	388	000
4	438	397	000
8	212	157	500
	H, 9, 0		
1	137	152	250
4	289	278	500
5	388	417	750
6	203	198	500
7	221	224	750
	H, 10, 0		
0	429	388	000
1	234	250	750
2	144	178	000
	H, 11, 0		
2	148	102	500
3	174	180	750
	H, 0, 1		
2	211	222	250
5	263	268	250
6	327	346	750
7	153	183	250
9	279	268	750
11	228	198	750
	H, 1, 1		
2	446	408	944
3	1011	923	038
4	558	538	041
5	143	125	924
6	364	348	075
7	329	327	608
8	267	256	912
10	198	190	933
	H, 2, 1		
0	321	346	000
1	719	707	276
2	925	892	752
3	398	370	307
4	247	262	295
5	132	111	172
6	181	158	144
8	325	329	737
	H, 3, 1		
1	529	540	989
2	517	495	508
3	205	203	698
4	630	597	979
5	235	208	600
6	640	629	999
7	162	178	030
	H, 4, 1		
1	420	456	311
2	491	502	802
3	284	307	229
4	214	205	062
5	284	268	172
7	178	165	528
8	200	184	717
9	184	187	735
	H, 5, 1		
0	213	231	250
1	264	282	468
2	498	495	982
3	606	628	978
4	315	332	910
5	187	218	841
7	293	261	528
8	222	203	050
	H, 6, 1		
0	454	478	000
1	501	543	253
2	209	177	161
6	250	242	816
	H, 7, 1		
4	221	243	984
6	284	275	080
	H, 8, 1		
1	214	238	399
2	280	337	799
3	258	243	318
4	176	158	901
5	182	168	078
	H, 0, 2		
2	504	469	500
3	824	761	500
4	413	371	500
6	201	190	000
9	338	343	500
	H, 1, 2		
2	570	558	886
3	294	278	100
5	225	226	294
6	381	382	669
7	327	336	296
9	162	153	113
10	252	244	193
	H, 2, 2		
0	106	117	500
1	614	629	022
2	383	372	544
4	253	271	518
5	953	886	506
6	176	156	186
7	251	247	488
11	190	158	544
	H, 3, 2		
0	280	302	750
1	523	537	253
2	480	477	738
3	487	474	297
4	496	476	750
5	123	108	607
7	143	153	212
8	194	218	189
9	239	209	228
	H, 4, 2		
0	278	301	500
1	114	114	082
2	292	316	507
3	281	275	405
4	272	291	299
5	461	468	490
7	158	184	562
	H, 5, 2		
0	845	884	750
1	280	271	506
2	210	196	807
5	204	218	223
6	321	317	806
7	274	255	296
10	227	210	266

Table I (*Continued*)

	$10\|F_o\|$	$10\|F_c\|$	Phase angle, mcycles
	H, 6, 2		
1	194	193	490
2	193	224	505
3	350	358	407
4	281	288	462
9	210	189	505
	H, 7, 2		
0	358	389	750
1	204	220	391
2	275	290	872
3	137	157	193
	H, 8, 2		
0	173	155	500
1	233	254	098
4	161	147	272
5	362	367	519
	H, 9, 2		
2	165	150	829
4	172	181	770
	H, 10, 2		
3	179	166	335
	H, 11, 2		
0	235	237	750
1	186	154	505
	H, 0, 3		
3	1430	1327	750
4	234	217	750
5	335	358	750
6	377	366	750
7	427	423	250
8	314	314	750
	H, 1, 3		
2	423	390	487
3	352	341	028
4	360	356	498
5	172	144	074
6	523	515	531
8	408	387	499
	H, 2, 3		
1	867	870	713
2	365	346	677
3	446	455	698
4	374	364	766
5	113	97	947
6	242	264	814
8	227	186	670
	H, 3, 3		
0	142	128	750
1	365	373	095
2	900	919	519
3	490	482	046
4	140	136	515
5	148	147	942
6	201	132	451
7	161	134	367
8	501	505	502
10	203	179	507
	H, 4, 3		
1	483	496	805
2	163	182	647
3	523	559	767
4	326	319	627
5	240	239	575
6	256	265	720
8	206	220	831
	H, 5, 3		
1	423	426	018
2	159	174	616
4	314	341	571
6	419	402	493
7	202	208	221
8	282	216	465
	H, 6, 3		
1	197	208	618
2	280	284	609
3	622	636	714
4	200	208	623
5	135	177	761
6	206	203	846
7	211	219	293
	H, 7, 3		
0	194	205	750
1	168	201	120
2	198	226	557
3	271	286	097
4	152	162	487
6	212	225	533
8	232	235	506
	H, 8, 3		
1	355	350	741
2	148	167	551
	H, 9, 3		
1	212	214	123
2	249	296	557
	H, 0, 4		
2	353	347	000
4	315	356	000
6	189	153	500
7	222	186	000
	H, 1, 4		
2	210	235	187
3	158	174	633
4	327	320	305
5	277	269	648
6	174	166	714
7	177	189	809
	H, 2, 4		
0	309	357	000
1	241	268	021
2	251	247	905
3	188	198	872
7	174	167	067
	H, 3, 4		
0	274	277	250
1	332	319	721
2	169	181	333
3	277	277	824
7	192	173	707
9	200	171	736
	H, 4, 4		
0	165	190	000
1	291	285	923
2	235	212	967
3	197	189	056
	H, 5, 4		
0	272	263	750
2	152	166	334
3	164	172	956
4	277	279	252
5	234	235	778
7	193	143	644
	H, 6, 4		
2	196	186	956
3	168	168	718
4	185	196	004
	H, 8, 4		
0	195	201	000
2	199	202	802

solidified. A crystal suitable for X-ray analysis was obtained by crushing the solid (in a drybox) and selecting fragments. Fragments were placed in separate Lindeman glass capillary tubes (0.4 mm. o.d., wall thickness 0.015 mm.) and, after evacuation and subsequent addition of *ca.* 0.7 atm. of argon, anchored in a small piece of Apiezon W wax (by melting and then cooling the wax). In spite of all the precautions, evidence of slight surface reaction, presumably with traces of moisture, could be seen on the hygroscopic crystal. There was no indication that this had any observable effect on the X-ray data.

The external form of the crystal, *ca.* 0.6 mm. long and 0.09 by 0.15 mm. wide, approximated that of a parallelepiped split diagonally along two mutually perpendicular faces and resembled the end of a blunt knife.

The capillary was oriented so the crystal could be rotated along its *c*-axis. Unit cell dimensions (a_0 = 10.304, b_0 = 9.880, c_0 = 6.235 (±0.01 Å.)) were determined from rotation and Weissenberg photographs on which were superimposed rotation patterns of NaCl (a_0 = 5.640 Å.). Copper Kα radiation (1.54178 Å.) was used for determination of cell dimensions. To minimize film shrinkage errors, the distances between sodium chloride lines were used to calibrate the camera

radius for the rotation photograph; points along the zero-layer line were used for the Weissenberg.

The lattice was found to be orthorhombic, with $h00$ and $0k0$ reflections extinct for odd values of h and k, respectively. $00l$ reflections were not observed for rotation about c, but the space group was assumed to be $P2_12_12_1$, with four equivalent positions (x, y, z; $^1/_2 - x$, $-y$, $^1/_2 + z$; $^1/_2 + x$, $^1/_2 - y$, $-z$; $-x$, $^1/_2 + y$, $^1/_2 - z$) by analogy with the structure reported for $NaAlCl_4$ which has very similar cell dimensions.[6] The density, experimentally determined as 2.25 g. cm.$^{-3}$ by weighing a calibrated tube filled with solidified melt, compared favorably with the value 2.31 g. cm.$^{-3}$, calculated on the basis of four molecules in the unit cell.

Using zirconium-filtered molybdenum radiation (Kα 0.7107 Å.), integrated photographic intensity data were collected for the first five levels ($hk0$ to $hk4$) with a Nonius-integrating, equi-inclination Weissenberg camera. Multiple films (except for the fourth level) and timed exposures were used. A uniform 1-mil sheet of brass was inserted between the films. The relative intensities of the same reflections indicated a film–brass–film ratio of 3.59. The small variation of absorption due to different beam angles for the first, second, and third levels, as compared with the zero levels, was ignored. Camera integration was in one direction only, and each spot was scanned in the perpendicular direction with a Moll-type densitometer which was used in conjunction with a Leeds and Northrup amplifier and recorder with logarithmic slide wire. The area under each curve was assumed proportional to the intensity.

Forty of the weaker reflections of the zero, first, and third levels were estimated by eye; weak reflections on the second film were used as standards, and intensity values were assigned to these by dividing the first film-photometered intensity by the film ratio. In the final calculations 286 reflections were used. No correction was applied for absorption. To obtain statistically better data and to average out absorption effects, the entire film for the zero and first levels and for both lower half-quadrants of the second through fourth levels were photometered.

The $NaAlCl_4$ atomic coordinates of Baenziger were used for the initial trial structure.[6] Calculations were performed on an IBM 709 computer using the "X-ray 63" program of the crystallographic group at the University of Washington. The level-to-level scaling was initially taken as proportional to the exposure time but was finally used as a parameter in the refinement program. Scattering factors and dispersion corrections were based on data taken from the "International Tables for X-Ray Crystallography."[8,9] The structure was refined using a full matrix least-squares program by Busing, Martin, and Levy,[10] modified for the "X-ray 63" system by Professor J. M. Stewart. The residual minimized was $\Sigma w_{hkl}(|F_o| - |F_c|)^2$ where w_{hkl} is the weight of a particular reflection. A Hughes weighting scheme was used[11] although the same atomic positions, but with slightly higher standard deviations, were obtained with unitary weighting factors. Twenty-nine parameters were varied: eighteen atomic positions, six isotropic temperature factors, and five scale factors. The final value of $R = \Sigma(|F_o| - |F_c|)/\Sigma|F_o|$ was 0.058. A detailed list of calculated and observed structure factors may be found in Table I. Of *ca.* 160 unobserved reflections in the observable range, none of the F_c values were significantly above the observed threshold value.

Results and Discussion

The atomic and thermal parameters are listed in Table II. The thermal parameters are not indicative of the actual thermal motion since temperature factors are not independent of the level-to-level scaling.

Table II: Atomic and Thermal Parameters for $NaFeCl_4$(s)

Atom		x/a_0	y/b_0	z/c_0	B
Fe	Position	0.03816	0.4886	0.2127	2.87
	Std. dev. × 10^3	0.29	0.44	0.62	90
Na	Position	0.1187	0.2138	0.6970	6.04
	Std. dev. × 10^3	1.26	1.27	2.64	310
Cl_I	Position	0.03392	0.4924	0.5622	4.04
	Std. dev. × 10^3	0.61	0.88	1.42	150
Cl_{II}	Position	0.1504	0.3118	0.1131	3.79
	Std. dev. × 10^3	0.67	0.65	1.49	170
Cl_{III}	Position	0.3413	0.01793	0.9238	3.84
	Std. dev. × 10^3	0.56	0.74	1.15	140
Cl_{IV}	Position	0.3718	0.3274	0.5732	3.61
	Std. dev. × 10^3	0.67	0.66	1.56	160

The crystal contains discrete, slightly distorted, tetrahedral $FeCl_4$ groups, with the sodium atoms located in some of the empty spaces between tetrahedra. The atomic positions are not displaced greatly from those reported for $NaAlCl_4$.[6] A projection of the unit

(8) "International Tables for X-Ray Crystallography," Vol. II, Kynoch Press, Birmingham, England, 1959, p. 236.

(9) See ref. 8, Vol. III, 1962, p. 215.

(10) W. R. Busing, K. O. Martin, and H. A. Levy, ORNL-TM-305, August 1962.

(11) E. Q. Hughes, *J. Am. Chem. Soc.*, **63**, 1737 (1941).

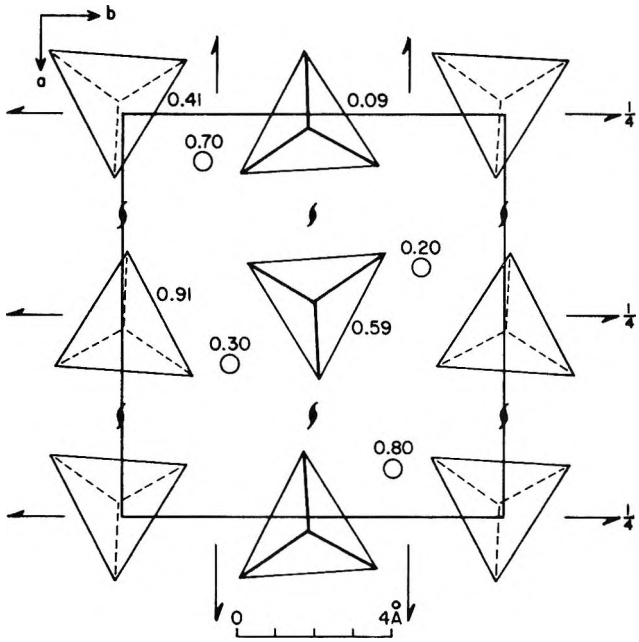

Figure 1. Projection of $FeCl_4^-$ tetrahedra on (001).

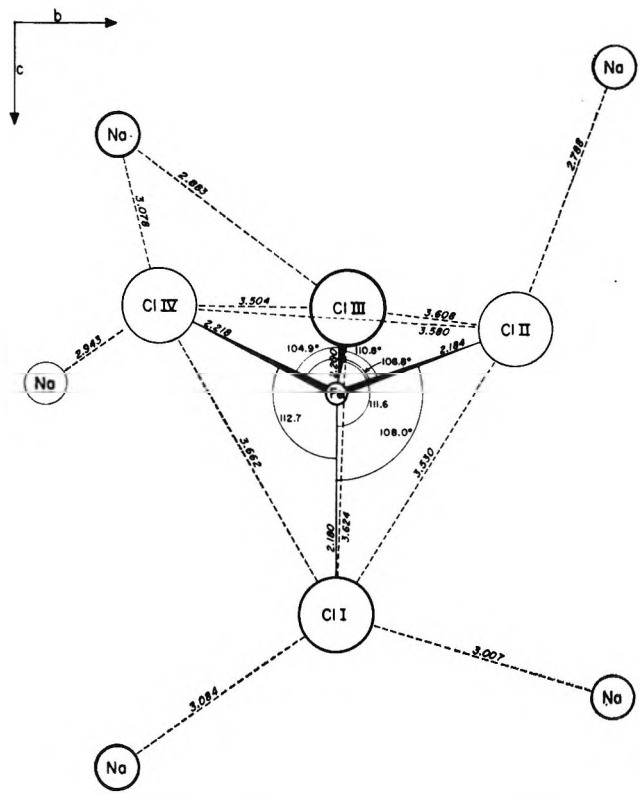

Figure 2. Bond distances and angles in $NaFeCl_4$ crystal.

Table III: Interatomic Distances (Å.) and Angles within the $FeCl_4^-$ Tetrahedron

	Distance, Å.	Std. dev., Å.
$Fe–Cl_I$	2.180	0.010
$Fe–Cl_{II}$	2.184	0.008
$Fe–Cl_{III}$	2.200	0.008
$Fe–Cl_{IV}$	2.218	0.008
Cl_ICl_{II}	3.530	0.013
Cl_ICl_{III}	3.624	0.013
Cl_ICl_{IV}	3.662	0.012
$Cl_{II}Cl_{III}$	3.608	0.010
$Cl_{II}Cl_{IV}$	3.580	0.010
$Cl_{III}Cl_{IV}$	3.504	0.010
	Other distances	
$Na–Cl_I$	3.007	
$Na–Cl_I$	3.084	
$Na–Cl_{II}$	2.788	
$Na–Cl_{II}$	3.781	
$Na–Cl_{III}$	2.883	
$Na–Cl_{III}$	3.318	
$Na–Cl_{IV}$	2.943	
$Na–Cl_{IV}$	3.078	
	Interatomic angle, deg.	Std. dev., deg.
Cl_IFeCl_{II}	107.98	0.44
Cl_IFeCl_{III}	111.64	0.47
Cl_IFeCl_{IV}	112.70	0.48
$Cl_{II}FeCl_{III}$	110.77	0.42
$Cl_{II}FeCl_{IV}$	108.81	0.39
$Cl_{III}FeCl_{IV}$	104.93	0.38

cell on (001) is shown in Figure 1. The four tetrahedra in the unit cell are arranged so that each has a face nearly parallel to the (001) plane. The elevation of this face and the elevation of the sodium atoms (represented as circles) are indicated on the figure. All of the tetrahedra along the a-axis ($b = 0$) point below the plane of the paper and those at $b = 0.5$ point above the plane.

Some interatomic distances and angles are listed in Table III. The standard deviations represent the combined uncertainty of the atomic positions and cell dimensions.

The average Fe–Cl distance is 2.196 Å. This value is considerably shorter than the Fe–Cl distance (2.48 Å.) in ferric chloride.[12] However, in the latter case, the iron atom is octahedrally coordinated to six chlorine atoms.

Only one sodium–chlorine distance (2.788 Å.) is shorter than the sodium–chlorine distance in sodium chloride (2.82 Å.). Each sodium atom has six chlorine neighbors 2.788–3.084 Å. distant and one slightly farther away at 3.318 Å.

The distances and angles within the $FeCl_4$ group are also shown in Figure 2. The $Cl_{III}FeCl_{IV}$ angle of 104.9°

(12) N. Wooster, *Z. Krist.*, **83**, 35 (1932); N. W. Gregory, *J. Am. Chem. Soc.*, **73**, 472 (1951).

differs from the tetrahedral angle of 109.47° by twelve times the standard deviation. The Cl_IFeCl_{IV} angle is nearly seven standard deviations larger than 109.47°. The remaining ClFeCl angles lie between the two extremes. The irregularities appear to be associated with electrostatic interactions as a Jahn–Teller distortion would not be expected for tetrahedral d^5 Fe(III). The sodium atom approximately midway between Cl_{III} and Cl_{IV} may be largely responsible for the small 104.9° angle (see Figure 2; Cl_{III} is above the plane of the other three chlorines). A void between adjacent tetrahedra exists in a location such that movement of Cl_I towards the void would cause the Cl_IFeCl_{IV} angle and the Cl_ICl_{IV} distance to be larger than normal. The attraction of the two sodium atoms near Cl_I and the repulsion of the neighboring chlorine atoms would be expected to contribute to this shift. The drawing together of Cl_{III} and Cl_{IV} may also contribute to the large value of the Cl_IFeCl_{IV} angle. The values of the remaining angles follow qualitatively from these considerations.

Acknowledgments. We wish to express our thanks and appreciation to Professor Lingafelter's group for use of and for assistance with the computer programs, and in particular to Dr. C. H. L. Kennard. Financial support was received from the U. S. Army Research Office (Durham) which we acknowledge with thanks.

Electron Magnetic Resonance and Electronic Spectra of Tetrachloroferrate(III) Ion in Nonaqueous Solution[1]

by Terry B. Swanson and Victor W. Laurie[2]

Department of Chemistry, Stanford University, Stanford, California *(Received July 20, 1964)*

Solutions of $FeCl_3$ in various organic solvents including pyridine, N,N-dimethylformamide, acetonitrile, acetone, and dimethyl sulfoxide have been shown to contain the tetrachloroferrate ($FeCl_4^-$) ion by studies of the electron magnetic resonance (e.m.r.) and electronic spectra. It is found that the amount of $FeCl_4^-$ formed is solvent dependent. E.m.r. line widths are also found to be strongly solvent dependent. Addition of LiCl or raising the temperature increases the $FeCl_4^-$ concentration. Studies of the temperature dependence of the e.m.r. intensity have been used to determine thermodynamic quantities for the reaction $2FeCl_3 \rightleftharpoons FeCl_2^+ + FeCl_4^-$ in pyridine. Equilibrium constants for this reaction in a number of solvents are given. E.m.r. g-values and electronic oscillator strengths have been measured for some solutions.

Introduction

Spectroscopic techniques have long been recognized and used as one of the most valuable methods available for the study of ions and their complexes in solution. Ultraviolet and visible spectroscopy in particular, and also infrared spectroscopy, have been utilized extensively in the study of solutions. More recently, nuclear magnetic resonance has been employed to gain information about solutions and solution processes. However, very little use has been made of electron magnetic resonance (e.m.r.) in the study of solutions although

(1) Presented in part at the 144th National Meeting of the American Chemical Society, Los Angeles, Calif., March 1963.

(2) Alfred P. Sloan Fellow.

this technique has been widely used in the study of solids. Some work, mostly in aqueous solution, has been carried out, but the amount of information has been rather limited.[3-7] Very little work has been done in nonaqueous solvents.

This work reports some exploratory investigations of iron(III)–chloro complexes in a number of organic solvents by e.m.r. and ultraviolet spectroscopy. Fe(III) in aqueous solution exhibits a very broad e.m.r. absorption, presumably because of complex hydrated species. In organic solvents however, a large range of line widths is observed and e.m.r. promises to provide a technique for the study of complex formation and solvent effects.

Experimental

Materials. The $FeCl_3$ used was anhydrous reagent powder, sublimed, obtained from Matheson Coleman and Bell. All other materials were of reagent grade quality.

Apparatus. An e.m.r. spectrometer utilizing mainly Varian components and operating in the X-band region near 9.5 kMc. was used. The resonances from samples placed in a rectangular cavity operating in the TE_{012} mode were detected by using a microwave bridge arrangement. An automatic frequency control circuit was used to lock the klystron to the sample cavity. Audio field modulation of 400 c.p.s. was employed. The linear magnetic field sweep was calibrated by using a sample of 0.05 *F* $VO(ClO_4)_2$ in H_2O.

The apparatus used for varying the sample temperature was similar to that described by Varian.[8] A copper–constantan thermocouple was inserted in the quartz dewar just outside the cavity to measure the sample temperature to $\pm 0.5°$. While passing through a spectrum the temperature could be held constant to within this limit.

All ultraviolet and visible spectra were obtained at room temperature using a Bausch and Lomb Spectronic 505. A path length of 0.010 or 0.005 cm. was normally used. The region from 200 to 800 mμ could be scanned.

E.m.r. Lines. When an e.m.r. signal was observed, it consisted of a single, essentially symmetrical line. Experimentally, the first derivative of the absorption line was recorded. The line width (w) was taken to be the horizontal distance, and the height (h), the vertical distance between the maximum and minimum amplitudes of the derivative. Intensities of e.m.r. lines were assumed proportional to hw^2.

Experimental Procedure. Solutions were prepared by weighing out the proper quantities of solutes into a volumetric flask. After addition of the solvent, a small quantity of the solution was withdrawn with a syringe, placed in a stock, 1-mm. i.d. Pyrex tube, and sealed. This, then, served as the sample for e.m.r. measurement. g-Values were measured by using 2,2-diphenyl-1-picrylhydrazyl as a reference.

Results

Tetrachloroferrate ($FeCl_4^-$) Ion. The $FeCl_4^-$ ion is known to exist in many organic solvents[7,9-14] as well as in aqueous solution.[15] Investigations have shown this species to be a tetrahedral complex.[16] Observations of the ultraviolet and visible spectrum of solutions containing the $FeCl_4^-$ ion show an intense absorption characteristic of this ion. The spectrum consists of three distinct absorptions at approximately 240, 312, and 360 mμ (Figure 1). There is also a broad absorption peak centered at about 750 mμ, but this peak is not unique to $FeCl_4^-$.

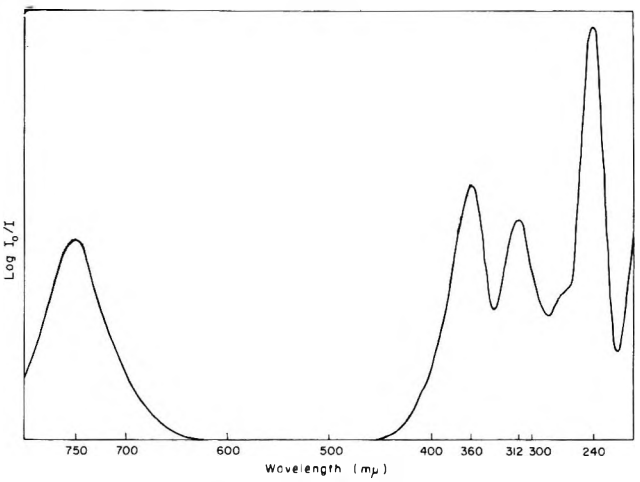

Figure 1. Spectrum of the $FeCl_4^-$ ion.

Comparison of E.m.r. and Ultraviolet Spectra. A comparison of the e.m.r. intensity and ultraviolet intensity for various concentrations of $FeCl_3$ in acetonitrile is

(3) N. S. Garif'yanov, *Dokl. Akad. Nauk SSSR*, **103**, 41 (1955).
(4) B. N. Kozyrev, *Izv. Akad. Nauk SSSR, Ser. Fiz.*, **21**, 828 (1957).
(5) B. R. McGarvey, *J. Phys. Chem.*, **61**, 1232 (1957).
(6) N. S. Garif'yanov, *Soviet Phys. JETP*, **10**, 1101 (1960).
(7) G. R. Hertel and H. M. Clark, *J. Phys. Chem.*, **65**, 1930 (1961).
(8) Varian Associates Technical Information Bulletin, Vol. 2, No. 4.
(9) P. A. McCusker and S. M. S. Kennard, *J. Am. Chem. Soc.*, **81**, 2976 (1959).
(10) R. J. Myers and D. E. Metzler, *ibid.*, **72**, 3772, 3776 (1950).
(11) G. J. Brealey and N. Uri, *J. Chem. Phys.*, **20**, 257 (1952).
(12) H. Friedman, *J. Am. Chem. Soc.*, **74**, 5 (1952).
(13) D. W. Meek, Ph.D. Thesis, University of Illinois, 1962.
(14) R. L. Carlson, Ph.D. Thesis, University of Illinois, 1962.
(15) G. A. Gamlen and D. O. Jordan, *J. Chem. Soc.*, 1435 (1953).
(16) L. A. Woodward and M. J. Taylor, *ibid.*, 4473 (1960).

shown in Figure 2. It is clearly shown that the e.m.r. intensities correspond closely to the ultraviolet intensities at 240, 312, and 360 mμ. This leads to the conclusion that the e.m.r. absorption arises from the $FeCl_4^-$ species, rather than other ferric species which may be present. This may be attributed to the fact that less symmetrical ferric species might be expected to have much broader resonances and, therefore, would not be detected.[5] Figure 2 also demonstrates that the absorption near 750 mμ is not characteristic of the $FeCl_4^-$ ion. This absorption is observed whenever ferric species of any kind are present in solution.

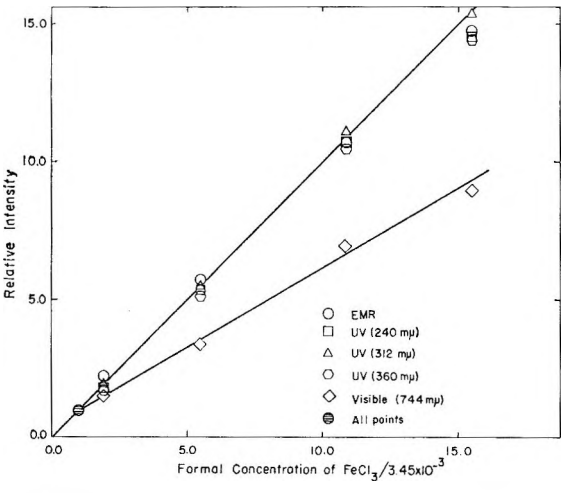

Figure 2. Comparison of the e.m.r. and ultraviolet intensities for various concentrations of $FeCl_3$ in acetonitrile.

Plots of intensity *vs.* $FeCl_3$ concentration in other solvents used in this study have also been obtained. They are qualitatively similar to Figure 2 and show that the e.m.r. absorption can be assigned to the $FeCl_4^-$ ion in the solvents studied. Further evidence for the assignment of the e.m.r. absorption to the $FeCl_4^-$ species is the large increase in intensity which occurs upon addition of chloride ion.

Comparison of the e.m.r. intensities with a standard solution of 2,2-diphenyl-1-picrylhydrazyl shows that all five electrons of the ferric participate within ±15%.

$FeCl_3$ in N,N-Dimethylformamide, N-Methylformamide, and Formamide. Anhydrous $FeCl_3$ when dissolved in N,N-dimethylformamide gives a clear, amber-colored solution. E.m.r. line widths for various solutions are 85, 82, 75, and 71 gauss for 0.083, 0.065, 0.013, and 0.0092 *F* $FeCl_3$, respectively.

The e.m.r. intensity increases only slightly over the range 25–111° for $FeCl_3$ in N,N-dimethylformamide. However, there is some decrease in line width with increasing temperature. Also, saturation of the solution

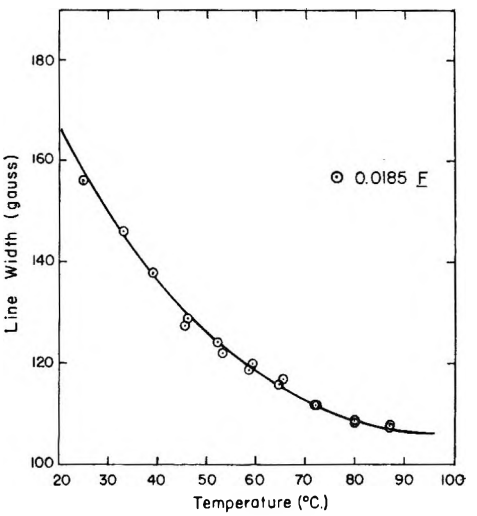

Figure 3. E.m.r. line width *vs.* temperature for 0.0185 *F* $FeCl_3$ in dimethyl sulfoxide.

with LiCl increases the integrated e.m.r. intensity by 2.2.

Ultraviolet spectra of solutions of $FeCl_3$ in N,N-dimethylformamide show the absorption characteristic of $FeCl_4^-$.

No e.m.r. signal can be observed at room temperature from solutions of $FeCl_3$ in N-methylformamide or formamide. Furthermore, no signal is observed even when LiCl or HCl is added to the solution. The ultraviolet spectrum does not show the presence of $FeCl_4^-$.

$FeCl_3$ in Acetonitrile. Solutions of anhydrous $FeCl_3$ in acetonitrile are yellow or orange, depending on the concentration, but become very faint yellow upon addition of LiCl.

The e.m.r. resonance has a comparatively narrow breadth, being 62 gauss for an 8×10^{-4} *F* solution, and neither the line width nor intensity is affected, within experimental error, by a temperature increase. However, the integrated intensity of the absorption line increases by about a factor of 2 upon saturation of a dilute solution of $FeCl_3$ with LiCl.

Acetonitrile is an ideal solvent in which to study the $FeCl_4^-$ ion since there is no solvent absorption in the 200–800 mμ region. The molar extinction coefficients of the three strong ultraviolet peaks at 240, 312, and 360 mμ are 12,500, 7150, and 7550 l. $mole^{-1}$ $cm.^{-1}$, respectively. These values are for dilute solutions of $FeCl_3$ saturated with LiCl.

$FeCl_3$ in Nitromethane. The ultraviolet spectrum shows the presence of $FeCl_4^-$. The e.m.r. line width is approximately 100 gauss for a 0.05 *F* $FeCl_3$ solution. An integrated intensity increase of about 2 is noted upon saturation of the solution with LiCl.

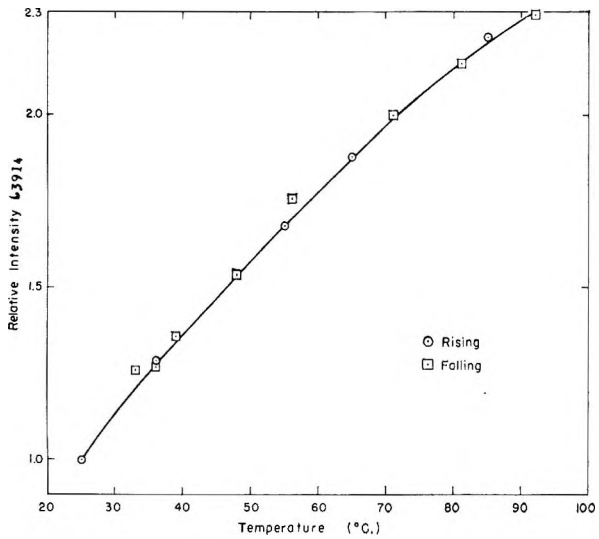

Figure 4. E.m.r. intensity *vs.* temperature for 0.20 *F* $FeCl_3$ in pyridine.

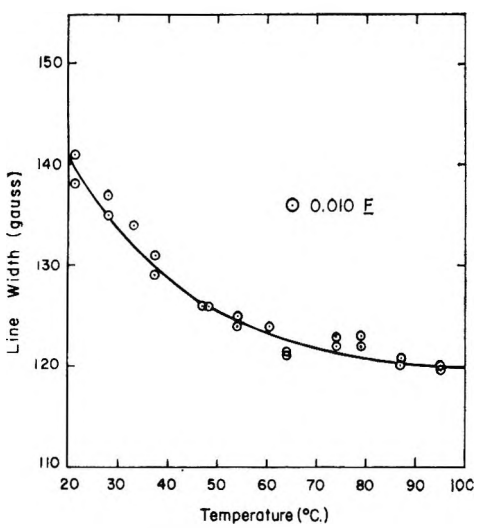

Figure 5. E.m.r. line width *vs.* temperature for 0.01 *F* $FeCl_3$ in pyridine.

$FeCl_3$ in Dimethyl Sulfoxide. Carlson[14] has reported that the predominant Fe(III) ion in dimethyl sulfoxide is $FeCl^{+2}$. However, the e.m.r. spectrum of $FeCl_3$ in dimethyl sulfoxide shows that a small amount of $FeCl_4^-$ is present. With increasing temperature as well as with addition of chloride ion a rapid increase in e.m.r. intensity occurs. Figure 3 shows the line width *vs.* temperature curve for a solution of 0.0185 *F* $FeCl_3$ in dimethyl sulfoxide.

$FeCl_3$ in Ethanol. The ultraviolet spectra of solutions of $FeCl_3$ plus LiCl in absolute ethanol show very pronounced $FeCl_4^-$ characteristics. It has previously been shown[11] that $FeCl_4^-$ is formed quantitatively by addition of LiCl to dilute solutions of $FeCl_3$ in ethanol.

Table I: E.m.r. Line Widths in Various Solvents[a]

Solvent	Line width, gauss
Acetone	54
Acetyl chloride	135
Acetonitrile	65
Propionitrile	76
Acrylonitrile	72
n-Butyronitrile	103
n-Valeronitrile	133
Benzonitrile	183
Nitromethane	96
Nitroethane	107
2-Nitropropane	124

[a] All concentrations were 0.01 *F*.

In this study, the e.m.r. spectrum shows a very broad absorption with a width of about 555 gauss at room temperature. The integrated intensity also indicates essentially all ferric species are in the form of $FeCl_4^-$.

$FeCl_3$ in Other Solvents. The e.m.r. spectrum of solutions of $FeCl_3$ in a number of other solvents has been observed. Table I gives the $FeCl_3$ concentration and the line width. All solutions exhibit a strong $FeCl_4^-$ pattern in the ultraviolet.

$FeCl_3$ in Pyridine. Anhydrous $FeCl_3$ is quite soluble in pyridine giving a clear, reddish brown solution. The e.m.r. spectrum of a number of solutions of different concentrations has been observed. Line widths are 220, 175, and 140 gauss for 0.47, 0.20, and 0.042 *F* solutions, respectively.

It was found that the e.m.r. absorption intensity is a strong function of temperature. A typical example is shown in Figure 4 where the e.m.r. intensity is plotted *vs.* temperature for 0.20 *F* $FeCl_3$ in pyridine. The circles represent intensities measured as the temperature was raised while the squares are those intensities measured as the temperature was being lowered to the room temperature value. The results show that the intensity change with temperature is a reversible process.

We have also studied the effect of additional chloride ion (in the form of LiCl) on the e.m.r. intensity. Various quantities of LiCl were added to solutions of $FeCl_3$ in pyridine, and a large increase in intensity was noted. The ratio of e.m.r. intensity for the solution saturated with LiCl to the intensity with no added LiCl was measured for three different formalities of $FeCl_3$, covering a range in concentration from 0.01 to 0.19 *F* $FeCl_3$. In all three cases the ratio of intensities was found to be 8.0 at a temperature of 25°.

Although the over-all e.m.r. intensity of solutions of $FeCl_3$ in pyridine increases with temperature, the line

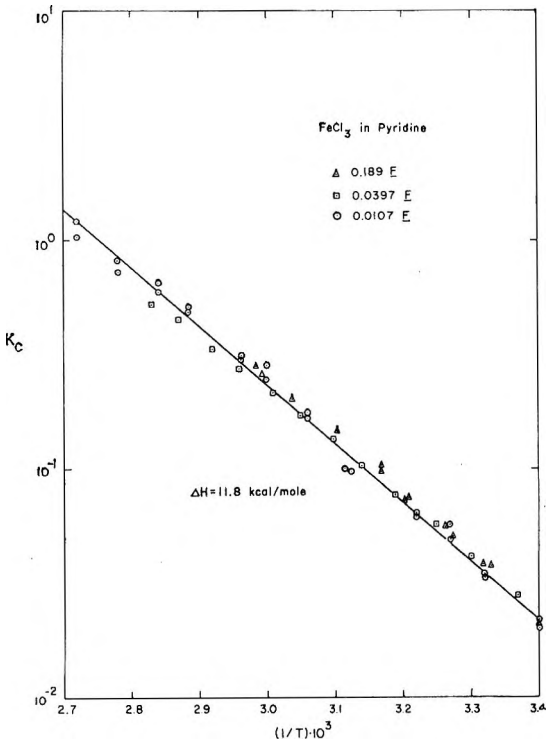

Figure 6. K_c *vs.* $1/T$ for the reaction $2FeCl_3 \rightleftharpoons FeCl_2^+ + FeCl_4^-$ in pyridine.

width decreases. This is shown in Figure 5 for 0.01 *F* $FeCl_3$. The line width is seen to decrease rather rapidly at first but appears to have reached a nearly constant value near 100°. This is qualitatively similar to the results on dimethyl sulfoxide solutions (see Figure 3).

The ultraviolet spectrum of $FeCl_3$ in pyridine does not show a strong $FeCl_4^-$ spectrum when no LiCl has been added to the solution. However, addition of LiCl changes the spectrum to one that is qualitatively similar to that observed for $FeCl_4^-$. The ultraviolet spectra corroborate the e.m.r. observation that a large increase in $FeCl_4^-$ concentration occurs upon addition of LiCl.

Thermodynamic Data for $FeCl_3$–Pyridine Solutions. The following reaction is postulated for $FeCl_3$ in pyridine.

$$2FeCl_3 \rightleftharpoons FeCl_2^+ + FeCl_4^- \qquad (1)$$

(The $FeCl_3$ and $FeCl_2^+$ probably contain solvent molecules as well as Cl^- in the first coordination sphere.)

Since the e.m.r. absorption is due to the $FeCl_4^-$ species and the e.m.r. intensity when a solution is saturated with LiCl represents a $FeCl_4^-$ concentration equal to the total iron concentration, we can follow the $FeCl_4^-$ concentration as a function of temperature by following the e.m.r. absorption as a function of temperature. The equilibrium constant for the proposed reaction is given by

$$K_c = \frac{[FeCl_2^+][FeCl_4^-]}{[FeCl_3]^2} \frac{\gamma_{FeCl_2^+}\gamma_{FeCl_4^-}}{\gamma_{FeCl_3}^2} \approx \left(\frac{[FeCl_4^-]}{[FeCl_3]}\right)^2 \qquad (2)$$

where the term, $\gamma_{FeCl_2^+}\gamma_{FeCl_4^-}/\gamma_{FeCl_3}^2$, containing the activity coefficients has been assumed to be close to unity. Using the fact that $[FeCl_3] = F_{FeCl_3} - 2[FeCl_4^-]$ (F_{FeCl_3} is the concentration of ferric chloride based on no reaction taking place) an equilibrium constant can be calculated for (1). Furthermore ΔH for the reaction can be obtained from the temperature dependence of the equilibrium constant, eq. 2, which can be determined by following the temperature dependence of the e.m.r. spectrum of $FeCl_4^-$. This has been done for three formalities of ferric chloride in pyridine, 0.0107, 0.0397, and 0.189 *F*. Figure 6 shows K_c, calculated using eq. 2, plotted *vs.* $1/T$. A straight line fit is obtained for all three concentrations. The observed ΔH value is 11.8 ± 0.6 kcal. mole^{-1}. Other thermodynamic values at 25° are $K_c = 0.028 \pm 0.01$, $\Delta F = 2.2$ kcal. mole^{-1}, and $\Delta S = 32$ cal. mole^{-1} deg.$^{-1}$.

Equilibrium Constants for $2FeCl_3 \rightleftharpoons FeCl_2^+ + FeCl_4^-$ in Various Solvents. By comparison of the e.m.r. intensities of 0.01 *F* $FeCl_3$ in various solvents, we have determined the amount of $FeCl_4^-$ existing in each solvent. This enables the calculation of K_c for reaction 1 in each solvent. Table II shows the $FeCl_4^-$ concentrations and equilibrium constants obtained. Also included in the table are the dielectric constants (see Conclusion) of the solvents and the e.m.r. line widths.

E.m.r. Line Widths at 35 kMc. Solutions of ~0.01 *F* $FeCl_3$ in acetonitrile, N,N-dimethylformamide, nitromethane, and pyridine were observed in an e.m.r. spectrometer operating at 35 instead of 9.5 kMc., as was usually the case. Within the experimental error of ±5 gauss the line widths at 35 kMc. were identical with those observed at 9.5 kMc., indicating a nearly isotropic *g*-value.

Table II: Equilibrium Constants and Line Widths

Solvent	$[FeCl_4^-]$ at 25°, *M*	K_c at 25°	ϵ at 20°	Line width, gauss
Acetonitrile	~0.005	$\geq 10^3$	37.5	62
Nitromethane	~0.005	$\geq 10^3$	39.4	96
N,N-Dimethylformamide	0.00455	~26	37.7	72
Pyridine	0.00125	0.028	12.5	136
Dimethyl sulfoxide	0.00071	...[a]	48.9	176

[a] Results from this system do not fit the equilibrium given by (1).

Oscillator Strengths. Careful observation of the ultraviolet spectrum of 0.0061 *F* $FeCl_3$ in acetonitrile saturated with LiCl points to an unresolved peak occurring between 260 and 280 mμ. As shown in Figure 7, the spectrum can be considered as arising from four rather than three peaks. Four overlapping gaussian curves reproduce the experimental curve satisfactorily. The oscillator strengths of the four individual peaks have been calculated using the expression $f \approx 4.6 \times 10^{-9} \epsilon_{max} \Delta\nu$, where f is the oscillator strength, ϵ_{max} is

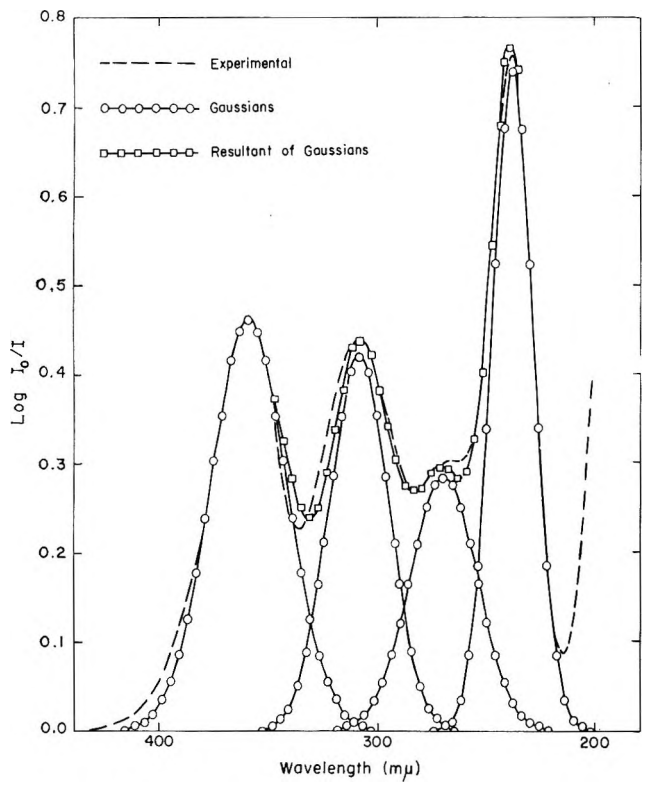

Figure 7. Ultraviolet spectrum of 0.0061 *F* $FeCl_3$, saturated LiCl in acetonitrile. Gaussian curves used to reproduce experimental curve.

the maximum value of the molar extinction coefficient for the absorption, and $\Delta\nu$ is the width (in $cm.^{-1}$) of the absorption peak at one-half its maximum value. Oscillator strengths are 0.23, 0.096, 0.11, and 0.11 for the 238, 270, 309, and 359 mμ absorptions, respectively.

The four absorptions mentioned in the previous paragraph arise from intramolecular charge-transfer processes. Such a transfer takes place by the transfer of a charge from an orbital predominantly associated with a Cl^- to an orbital predominantly associated with the Fe^{+3}. This conclusion is arrived at by observation of the ultraviolet and visible spectrum of $FeBr_3$ plus LiBr in acetonitrile. In this case the absorption pattern is similar to that for the $FeCl_4^-$ species, except that it is spread out and shifted to the red. The four peaks in this case occur at 278, 316, 390, and 470 mμ and have the same intensity relationship to each other as do the peaks in the $FeCl_4^-$ pattern. In the bromide case, $FeBr_4^-$ is the absorbing species, and the absorptions appear at lower energies relative to $FeCl_4^-$ because of the lower electronegativity of bromine as compared to chlorine.

g-Values. E.m.r. *g*-values for $FeCl_3$ in pyridine, N,N-dimethylformamide, and acetonitrile were all determined to be 2.021 ± 0.005 by comparison with a 2,2-diphenyl-1-picrylhydrazyl standard. The free-electron *g*-value is 2.0023.

Conclusion

In the solvents, acetonitrile, nitromethane, N,N-dimethylformamide, and pyridine, the effect of temperature and Cl^- are accounted for by the equilibrium, $2FeCl_3 \rightleftharpoons FeCl_2^+ + FeCl_4^-$. An increase in temperature shifts the equilibrium to the right and sufficient additional Cl^- converts all ferric species to $FeCl_4^-$. It has been noticed (see Table II) that the solvent dielectric constant plays some role in determining the position of the equilibrium. The solvents with high dielectric constants support equilibria lying far to the right. Pyridine with a considerably lower dielectric constant gives rise to an equilibrium lying farther to the left.

Although results in dimethyl sulfoxide do not fit the equilibrium, addition of Cl^- does favor formation of $FeCl_4^-$ as does an increase in temperature.

$FeCl_4^-$ is formed in appreciable quantities in many other solvents, including acetone, acetyl chloride, benzonitrile as well as aliphatic nitriles, and nitro compounds. However, $FeCl_4^-$ does not form in appreciable quantities in N-methylformamide or formamide, even upon addition of large amounts of Cl^-. Both of these solvents have very high dielectric constants (NMF, 190; formamide, 109) which may cause the breakup of the $FeCl_4^-$. Similar effects have been noted for N-methylacetamide.[14]

E.m.r. line widths are strongly solvent dependent but are not frequency dependent. Within a homologous series of solvents there seems to be a nearly linear dependence of line width on viscosity. However, the gross variations in line width among different kinds of solvents depend on other, as yet undetermined, factors.

The ultraviolet spectrum of the $FeCl_4^-$ ion has been shown to arise from charge-transfer processes from a chloride to the iron. That such is the case is confirmed by comparison with the ultraviolet spectrum of the $FeBr_4^-$ ion.

g-Values lie near the free-electron value as expected for S-state ions.

Acknowledgment. The authors wish to thank Professor R. L. White, Department of Electrical Engineering, Stanford University, for obtaining the 35-kMc. spectra. Financial assistance from the Advanced Research Projects Agency of the Department of Defense through the Center for Materials Research at Stanford University is gratefully acknowledged.

Reactions of Aqueous Salts with High Area Aluminas

by Kenneth C. Williams, John L. Daniel, Walter J. Thomson, Roy I. Kaplan,

Department of Chemistry, University of Mississippi, University, Mississippi

and Russell W. Maatman[1]

Department of Chemistry, Dordt College, Sioux Center, Iowa *(Received July 24, 1964)*

The coupled or equivalent exchange of the cations and anions of 11 salts, chiefly alkali metal and alkaline earth chlorides, with surface H^+ and OH^- of a commercial α-basic aluminum oxide was studied. Adsorption equilibrium constants and reaction site densities are reported. These site densities and those for two salts with other aluminas are low, so that the area per site is of the order of $1\text{–}10 \times 10^2$ Å.^{2}, suggesting the reaction is very specific. Site density depends upon both anion and cation. In three other systems which are at least partially irreversible (where the salts are LiCl, $NiCl_2$, or $Cu(NO_3)_2$) the total amount of reaction with the surface is much greater. Here, there are probably both exchange reactions, which are partially irreversible, and equivalent exchange reactions.

Introduction

Aqueous electrolytes react with the surface of alumina by ion exchange with surface Al^{+3}, surface OH^-, H^+ of surface OH^-, or impurity, such as Na^+.[2-13] Some transition metal salts subsequently precipitate[3,14]; *e.g.*, $CuCl_2$ reacts to form $Cu_2(OH)_3Cl$.[6] Unless there is ion exchange with Al^{+3} or an impurity, there can be exchange of equivalent amounts of cation and anion with H^+ and OH^-, giving the appearance of "molecular" adsorption.[4,10,11]

The purpose of the present work is to obtain site densities from the "molecular" adsorption isotherms of several metal salts on porous, high surface area, commercial aluminas. In the systems chosen, the other reactions are negligible. To obtain the isotherms it was necessary to use the principles of (but not all the analytical procedures of) a method developed for systems in

(1) Correspondence to be sent to this author.

(2) G. Venturello, *Atti reale accad. sci. Torino*, **79**, 288 (1943–1944).
(3) E. N. Gapon and T. B. Gapon, *Dokl. Akad. Nauk SSSR*, **60**, 817 (1948).
(4) W. Fischer and A. Kulling, *Naturwissenschaften*, **35**, 283 (1948).
(5) R. Fricke and W. Neugebauer, *ibid.*, **37**, 427 (1950).
(6) H. Schafer and W. Neugebauer, *ibid.*, **38**, 561 (1951).
(7) F. Umland and W. Fischer, *ibid.*, **40**, 439 (1953).
(8) J. D'Ans and D. Jänchen, *Chemiker Ztg.*, **79**, 605 (1955).
(9) W. Fischer and A. Kulling, *Z. Elektrochem.*, **60**, 680 (1956).
(10) F. Umland, *ibid.*, **60**, 689 (1956).
(11) F. Umland, *ibid.*, **60**, 701 (1956).
(12) F. Umland, *ibid.*, **60**, 711 (1956).

Table I: Sources and Descriptions of Aluminas[a]

	Aluminas				
Code	200S	Al 1404	Al 1602	Al 1706	Al 1906
Source	Houdry	Harshaw	Harshaw	Harshaw	Harshaw
% Na_2O	0.1–0.2	0.04	...	0.03	0.02
% SiO_2	...	<0.10	5.9	...	0.50
% C	...	1.3	2.5	...	...
% CaO	...	0.9	...	1.27	...
% MgO	...	...	...	0.47	...
Crystalline form	*b*	γ	γ	γ	η[c]
Surface area, $m.^2/g.$	159	180–200	210–240	217	181
Pore volume, ml./g.	0.32[c]	0.45[c]	0.50[c]	0.82[c]	0.64[c]

[a] In the form of 0.32-cm. cylindrical pellets. Except where indicated, data are supplied by manufacturer. [b] α-Basic aluminum oxide, AlO(OH), determined by us. [c] Determined by us.

which the surface area–solution volume ratio is very high.[15] In every system the site density is surprisingly small. In addition, there are reported results for the more complicated Cu^{+2} and Ni^{+2} systems, where the other reactions cannot be neglected.

Experimental

Materials. Sources and descriptions of the aluminas used are in Table I. Before use, all aluminas were heated for 2 hr. at 450° in air.

General Procedure. Equilibration of alumina with solutions was carried out according to the method used in silica gel studies.[16] The amount of an ion within the pores of 1 g. of alumina after the desired time of solution–solid contact, y, is $[c_iV - c_f(V - PW)]/W$, where V ml. of solution of concentration c_i mole/ml. is mixed with W g. of alumina of pore volume P ml./g., and where c_f is the concentration of the solution outside the porous particles after contact. Usually, V/W was 1.5 ml./g., with W = 20 g. A typical plot of y *vs.* c_f is curve 1 of Figure 1.

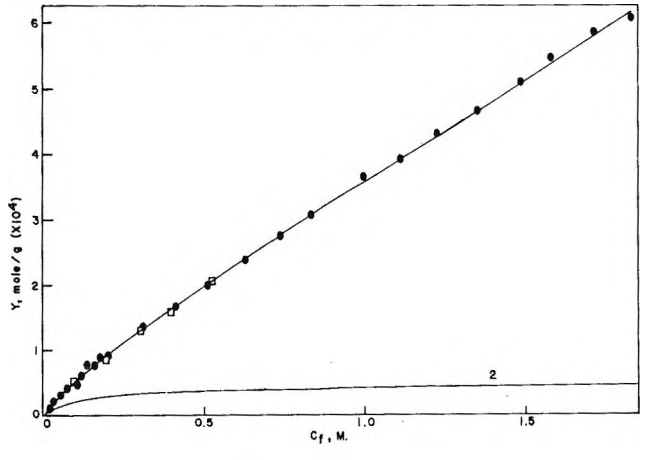

Figure 1. Uptake of KCl by 200S alumina at 20°: curve 1, y *vs.* c_f; curve 2, y_a *vs.* c_f. ●, 2–4-days equilibration; □, 16-days equilibration.

Analytical. Chloride and metal ion analyses were made by silver dichlorofluorescein and EDTA titrations, respectively. Qualitative tests for Al^{+3} were made with aluminon. A Beckman GS pH meter was used for pH measurements.

Results and Discussion

Nature of the Reaction. Equivalent anion–cation or "molecular" adsorption is shown to be the principal reaction by a negative aluminon test for Al^{+3} in the final solution, a negligible pH change-accompanying reaction, or equivalent differences between initial and final cation and anion concentrations. Equivalent adsorption in the similar systems listed in Tables II and III is indicated by the results for representative cases. With the $La(NO_3)_3$–Al_2O_3 (200S) system there was the largest pH change; c_i (molar), pH (initial), and pH (final) were, respectively, 0.1, 5.12, 5.75; 0.3, 5.00, 5.40; 0.5, 4.80, 5.23; 0.7, 4.57, 5.09; 0.8, 4.48, 4.99. For the $BaCl_2$–Al_2O_3 (200S) system are given typical data indicating equivalent cation and anion adsorption, where (in molarities) c_i, c_f, based on Ba^{+2} analysis, and c_f, based on Cl^- analysis, were, respectively, 0.0901, 0.0662, 0.0662; 0.181, 0.131, 0.128; 0.181, 0.130, 0.128; 0.248, 0.190, 0.190; 0.311, 0.249, 0.250; 0.499, 0.433, 0.433; 0.626, 0.556, 0.555. The lack of a time effect (Figure 1 is typical) also suggests equivalent adsorption since with alumina the salt reactions other than equivalent adsorption are characteristically slow.[5] The existence of the shoulder in the adsorption isotherm (see below for derivation of the typical adsorption isotherm, curve 2 of Figure 1) proves reversibility. To show reversibility is thus proved, consider what would happen were the reaction irreversible. In an irreversible reaction enough KCl in solution below $c_f \sim 0.6$ M would add to the surface to occupy all adsorption sites, and the isotherm in the observable region would be flat. Since it is not flat in that concentration range, the reaction is not irreversible.

Method of Calculation. A y-value of curve 1 of Figure 1 is the sum of y_a, adsorbed KCl, and y_d, KCl

(13) G. I. Kobyshev, *Izv. Akad. Nauk SSSR, Ser. Fiz.*, **24**, 752 (1960).

(14) L. Liepina, A. Veiss, and V. Breicis, *Latvijas PSR Zinatnu Akad. Vestis*, **4**, 49 (1959).

(15) (a) R. W. Maatman and C. D. Prater, *Ind. Eng. Chem.*, **49**, 253 (1957); (b) B. L. McConnell, K. C. Williams, J. L. Daniel, J. H. Stanton, B. N. Irby, D. L. Dugger, and R. W. Maatman, *J. Phys. Chem.*, **68**, 2941 (1964).

(16) For our recent silica gel studies see J. Stanton and R. W. Maatman, *J. Colloid Sci.*, **18**, 132 (1963); **18**, 878 (1963); D. L. Dugger, J. H. Stanton, B. N. Irby, B. L. McConnell, W. W. Cummings, and R. W. Maatman, *J. Phys. Chem.*, **68**, 757 (1964).

Table II: Summary of Results in 200S Alumina Systems[a]

Salt	−5° c_f, M[b]	−5° B, mole/g. × 10^4	−5° K, M^{-1}	20° c_f, M[b]	20° B, mole/g. × 10^4	20° K, M^{-1}	−50° c_f, M[b]	−50° B, mole/g. × 10^4	−50° K, M^{-1}
NaCl	...	..	..	0.02–2.0(16)	0.39	8	0.02–2.0(16)	0.43	..
KCl	0.2–1.8(24)	0.62	9	0.02–1.8(29)	0.47	8	0.1–1.5(14)	0.21	..
$MgCl_2$	...	..	..	0.01–1.4(23)	0.95	27	0.01–1.4(22)	1.17	24
$MgBr_2$	...	..	..	0.03–1.6(10)	0.76	33	...	..	..
$Ca(NO_3)_2$	...	..	..	0.05–1.3(17)	0.99	46	...	..	..
$CaCl_2$	0.1–1.0(6)	0.94	..	0.01–2.0(21)	0.94	34	0.1–1.0(5)	0.94	..
$CaBr_2$	0.04–0.2(5)	0.80	..	0.01–1.8(16)	0.80	40	...	..	..
CaI_2	...	..	..	0.03–0.8(16)	0.62	41	...	..	..
$SrCl_2$	...	..	..	0.04–1.8(22)	0.87	33	...	..	..
$BaCl_2$[c]	0.02–0.7(11)	0.97	30	0.02–1.2(23)	0.97	27	0.02–0.7(11)	0.97	32
$La(NO_3)_3$	...	..	..	0.01–0.8(18)	1.07	265	0.03–0.8(8)	1.07	..

[a] R.m.s. error in B is less than 5%; K value omitted where r.m.s. error is greater than 15% or where there is an insufficient number of points. [b] Range of final concentration of salt; number of experimental points is in parentheses. [c] At 35°, c_f range, number of experimental points, B, and K are, respectively, 0.02–0.7 M, 11, 0.97 × 10^4 mole/g., and 29 M^{-1}.

dissolved in the pore volume liquid. To obtain y_a for the adsorption isotherm, y_d is determined from the slope of y *vs.* c_f by means of a method reported earlier.[15] This method takes into account a possible KCl concentration difference between the pore volume solution and the solution outside the pore volume in systems in which the pore area–pore volume ratio is high. (The reason for the possible concentration difference and the means of treating this phenomenon in a necessarily complex solution–solid model are given in some detail in ref. 15b.) The adsorption isotherm, y_a ($=y - y_d$) *vs.* c_f, is curve 2 of Figure 2. The adsorption plateau, B, is 4.7×10^{-5} mole site/g. of alumina.

Since solute addition to fixed sites is postulated, a Langmuir-type plot, *i.e.*, c_f/y_a *vs.* c_f, should be linear with the intercept = $1/BK$ and the slope = $1/B$, where K is the adsorption equilibrium constant. The addition reaction and its equilibrium constant are more complex than is here assumed if cation and anion exchanges for surface H^+ and OH^- are not coupled. Thus, within the limits allowed by the accuracy of the data, it is sufficient to assume for MX_2 salts that one MX_2 "molecule" reacts with one $(>AlOH)_1$ surface complex. This is in contrast with the independent reaction of one M^{+2} ion and two X^- ions with one $(>AlOH)_2$ and two (>AlOH) surface complexes. In the adsorption equilib-

Table III: Salt Adsorption by Five Aluminas at 20°

Alumina	Salt	c_f range, M	No. of points	B, mole/g. × 10^4	Area/ "molecule,"[a] Å.^{2}
200S	$CaCl_2$	0.01–2.0	21	0.94	282
Al 1906	$CaCl_2$	0.03–0.9	7	0.67	448
Al 1404	$CaCl_2$	0.37–1.0	5	0.73	432
Al 1706	$CaCl_2$[b]	0.03–0.9	7	0.95	379
Al 1602	$CaCl_2$	0.38–1.0	5	0.37	1010
200S	$SrCl_2$	0.04–1.8	22	0.87	304
Al 1906	$SrCl_2$	0.1–0.9	8	0.62	484
Al 1706	$SrCl_2$	0.03–1.0	9	0.70	514

[a] Calculated by using average surface area given in Table I. [b] Slightly more cation than anion taken up at low concentrations.

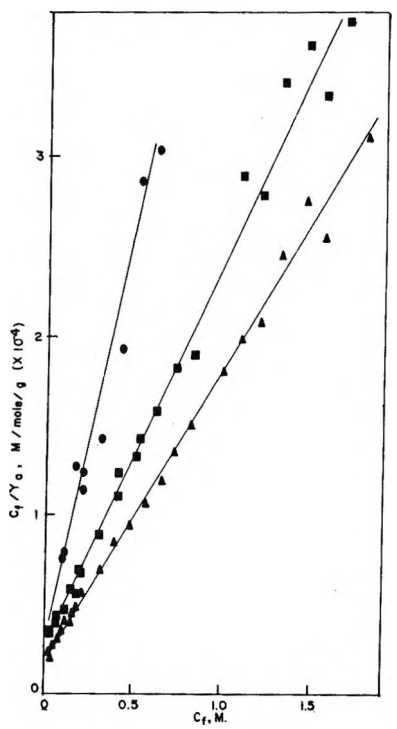

Figure 2. c_f/y_a *vs.* c_f for KCl–200S alumina systems: ▲, 5°; ■, 20°; ●, 50°. Four 50° points of Table II not in range of figure.

rium constant calculation the concentration of the water eliminated is considered constant.

Figure 2 shows Langmuir plots for the $KCl-Al_2O_3$ (200S) system at three temperatures. Values of B and K for 11 salts with 200S alumina are summarized in Table II. In Table III a comparison of B values for a few salts with five different aluminas is given. In addition, in Table III, B values and surface areas (Table I) are combined to give the area containing the adsorption site for one salt "molecule," assuming sites are uniformly distributed over the surface.

Conclusions for Equivalent Adsorption Systems. The magnitude of K and its temperature insensitivity might be thought to indicate there is physical adsorption, a term which has been suggested for this reaction.[6] This seems to be a poor term to use for this reaction. "Adding" ions probably exchange with both surface water and ions, and there is a low site density with all aluminas. These facts suggest the reaction is very specific.

Consistent with the coupled exchange concept is the dependence of B upon both cation and anion. Thus, with 200S alumina, B values have the order indicated: $MgCl_2 > MgBr_2$; $Ca(NO_3)_2 > CaCl_2 > CaBr_2 > CaI_2$; alkaline earth chlorides > alkali metal chlorides, especially if compared on an equivalent basis. Both cation and anion effects have been reported for several substances which compete with H_2PtCl_6 for alumina adsorption sites, permitting a uniform deposition of platinum, even in large alumina particles.[17]

An interesting point is the unique, unmistakable temperature dependence of B in the $KCl-Al_2O_3$ (200S) system.

Comparing K values is difficult because B varies (and since B must be determined before K, the error in K is large), but there is no doubt the order is $MX_3 > MX_2 > MX$.

Irreversible Systems. Plots (not shown) of the type shown in Figure 1 for $NiCl_2$ and $Cu(NO_3)_2$ with 200S alumina exhibited no definite shoulder even as low as $c_f = 0.05\ M$, indicating practical irreversibility. In neither case would extensive water-washing remove the characteristic color from the previously impregnated particles packed in a column. Slow reaction was observed with $NiCl_2$; thus, B at 20° was found to be 1.5×10^{-4} mole/g. (six points, $c_f = 0.1$–$0.9\ M$) and 2.2×10^{-4} mole/g. (seven points, $c_f = 0.05$–$0.9\ M$) in 2- and 21-day experiments, respectively. For $Cu(NO_3)_2$ a B value of 2.0×10^{-4} mole/g. was obtained in both 2-day (ten points, $c_f = 0.05$–$0.9\ M$) and 10-day (four points, $c_f = 0.1$–$0.8\ M$) experiments. With $LiCl-Al_2O_3$ (200S) (seventeen points, $c_f = 0.01$–$0.08\ M$) B was found to be well above 2.5×10^{-4} mole/g.; the curve shows no evidence of reversibility. In all these irreversible cases the B values are large. This agrees with the idea that the addition reaction occurs with all salts but that only in some cases is there further reaction.

Acknowledgments. Part of this work was supported by A.E.C. Contracts AT-(40-1)-2759 and AT-(11-1)-1354. W. T. and R. K. were participants in the N.S.F. Undergraduate Research Participation Program at the University of Mississippi in the summer of 1963. We thank Dr. Anthony Cariani for the X-ray determinations.

(17) R. W. Maatman, *Ind. Eng. Chem.*, 51, 913 (1959).

Kinetics of Fluorination. II. The Addition of Fluorine to *cis*- and *trans*-Perfluorobutene-2[1]

by Alan S. Rodgers

Contract Research Laboratory, Minnesota Mining and Manufacturing Company, St. Paul, Minnesota 55119
(Received July 24, 1964)

The kinetics of the reaction $CF_3CF{=}CFCF_3 + F_2 \rightarrow CF_3CF_2CF_2CF_3$ have been investigated in the gas phase between 220 and 250°K. with reactant concentrations varied between 2 and 10×10^{-4} M. The rate of reaction was found to be given by $d[C_4F_{10}]/dt = 2.6 \times 10^8 \exp(-8200/RT)[C_4F_8]^{1/2}[F_2]^{3/2}$, and neither the surface-to-volume ratio of the reaction vessel nor the total gas concentration had an appreciable effect upon this rate. The *cis* and *trans* isomers of perfluorobutene-2 were kinetically indistinguishable. These results are interpreted in terms of a free-radical chain mechanism in which the initiating reaction is: $CF_3CF{=}CFCF_3 + F_2 \longrightarrow CF_3CF_2\dot{C}FCF_3 + \dot{F}$.

Introduction

An investigation of the reaction of fluorine with several halogen-substituted olefins led Miller and Dittman[2] to suggest that the initiation step in fluorination was the reaction of fluorine with an olefin.

$$>C{=}C< + F_2 \longrightarrow >\dot{C}{-}C<F + \dot{F} \qquad (1)$$

This suggestion received both favorable[3] and unfavorable[4] comment. However, recent independent work from two laboratories[5,6] has indicated that the kinetics of the addition of fluorine to the carbon–carbon double bond conforms to the mechanism 1 to 4, thus providing quantitative evidence in support of the proposed initiation reaction.

$$>C{=}C< + \dot{F} \longrightarrow >\dot{C}{-}C<F \qquad (2)$$

$$F>C{-}\dot{C}< + F_2 \longrightarrow F>C{-}C<F + \dot{F} \qquad (3)$$

$$2F>C{-}\dot{C}< \longrightarrow \text{termination} \qquad (4)$$

Neither reaction, however, was an example of simple fluorine addition. In the study of 2,3-dichloroperfluorobutene-2, side reactions resulted in the formation of 2-chloroperfluorobutane, and, as a result, only the initial rates could be studied.[6] Fluorine-substitution reactions were also present in the reaction of ethylene with fluorine.[5] Such side reactions should not, however, occur in the fluorination of perfluorobutene-2. Consequently, this reaction should provide a simple test of the proposed mechanism.

Experimental

The apparatus and experimental procedure have been described in detail previously.[6] Briefly, the reactants were brought to the experimental temperature separately, and the reaction was started by mixing through pressure expansion. Pressure equilibration was attained in approximately 5 sec. with no measurable effect upon the gas temperature. The progress of the reaction was monitored by continuously recording the pressure in the reaction vessel. There were three reaction vessels used in this work: (a) a 140-cc. glass flask, coated with Teflon and packed with 10 g. of Teflon turnings, resulting in a surface-to-volume ratio (S/V) of 2.9 cm.$^{-1}$; (b) a 148-cc. glass flask packed with 10 g. of Teflon turnings, S/V = 2.9 cm.$^{-1}$, 33%

(1) This research was supported by the Advanced Research Projects Agency and was monitored by the Bureau of Naval Weapons.

(2) W. T. Miller and A. L. Dittman, *J. Am. Chem. Soc.*, **78**, 2793 (1956).

(3) N. N. Semenov, "Chemical Kinetics and Reactivity," Vol. 1, Pergamon Press, New York, N. Y., 1958, pp. 260–271.

(4) J. M. Tedder, "Advances in Fluorine Chemistry," Vol. 2, M. Stacey, J. C. Tatlow, and A. G. Sharpe, Ed., Butterworth and Co., Ltd., London, 1961, pp. 107–109.

(5) G. A. Kapralova, L. Yu. Rusin, A. M. Chaikin, and A. E. Shilov, *Dokl. Akad. Nauk SSSR*, **150**, 1281 (1963).

(6) A. S. Rodgers, *J. Phys. Chem.*, **67**, 2799 (1963).

of the total surface area being glass; (c) a 316-cc. glass flask packed with Teflon turnings, $S/V = 1.6$ cm.$^{-1}$, 45% of the total surface area being glass. The surface of each reaction vessel was conditioned by exposure to 100 to 200 mm. of fluorine for 24 hr. prior to its use initially and was reconditioned only if exposed to the atmosphere or other sources of contamination.

Perfluorobutene-2 was obtained from Matheson Co., Inc., and was found to be a mixture of the *cis* and *trans* isomers in a 1:4 mole ratio. The isomers were separated by preparative g.l.c. using a 1.27 cm. o.d. × 4.87 m. column packed with 33% (by weight) KEL-F tetramer oil (Minnesota Mining and Manufacturing Co.) on Celite. Analyses of reaction products were made on a 0.636 cm. o.d. × 7.31 m. column with the same stationary and support phases. The separated isomers were found to be 99% *trans* and 97% *cis* (determined by peak height measurements), respectively, and were identified by infrared spectroscopy. The fluorine gas was obtained from Matheson Co., Inc., and was passed through a sodium fluoride scrubber and stored in a monel flask. It was analyzed by reaction with mercury, 99.5% of the gas reacting. Hexafluoroethane (E. I. du Pont de Nemours and Co.) was used as the diluent gas in the reactions; g.l.c. analysis indicated less than 0.1% C_2F_4 by volume. Prior to each experiment, all condensable materials were thoroughly degassed at the temperature of liquid nitrogen and at a pressure of less than 1×10^{-3} mm.

Results

Products. Gas–liquid chromatographic analysis of the products of the reaction of F_2 with *cis*- and *trans*-perfluorobutene-2 could detect only perfluorobutane, identified by infrared spectroscopy. The stoichiometry of the reaction is

$$CF_3CF{=}CFCF_3 + F_2 \longrightarrow CF_3CF_2CF_2CF_3 \qquad (5)$$

When given sufficient time, reactions characteristically attained more than 90% of the expected pressure decrease according to eq. 5, corresponding to discrepancies of about 0.5 mm. or less.

Analyses for the *cis–trans* ratio of the residual olefin were made for those reactions with excess olefin. The results presented in Table I show that no change in the ratio of the isomers occurred as a result of fluorination, for either *cis*- or *trans*-perfluorobutene-2.

Kinetics. One would anticipate that the rate of the reaction between fluorine and perfluorobutene-2 would follow

$$\frac{d[C_4F_{10}]}{dt} = K[C_4F_8]^{1/2}[F_2]^{3/2} \qquad (6)$$

Table I: Effect of Fluorination upon the Isomer Ratio in Perfluorobutene-2

Run	% reaction (theor.)	% *trans*	% *cis*
	trans-$CF_3CF{=}CFCF_3$		
	0		1
1	66		0.8
6	69		1.1
9	69		1.2
	cis-$CF_3CF{=}CFCF_3$		
	0	3.1	
12	54	2.7	
13	50	2.7	
15	67	2.3	

which was found for 2,3-dichloroperfluorobutene-2.[6] The integrated form of eq. 6 is

$$K(t - t_0) = \frac{2}{[C_4F_8]_0 - [F_2]_0} \times \left[\left(\frac{[C_4F_8]_t}{[F_2]_t}\right)^{1/2} - \left(\frac{[C_4F_8]_0}{[F_2]_0}\right)^{1/2}\right] \qquad (7)$$

The subscripts 0 and t indicate the values of the given quantities at times t_0 and t. Table II shows the agreement obtained by applying both equations to the data from one run.

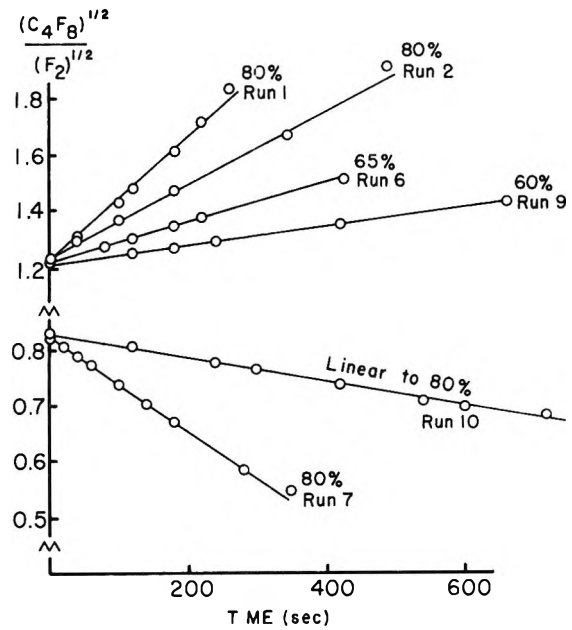

Figure 1. Plots based on integrated rate equation for reaction of *trans*-perfluorobutene-2 with fluorine. Per cent reaction of last data point is indicated. Experimental conditions are given in Table III.

Table II: Specific Rate Constant for the Reaction of F_2 with *trans*-$CF_3CF{=}CFCF_3$[a]

Time, sec.	ΔP, mm.	Rate $\times 10^2$ mm.$^{-1}$ sec.	$K \times 10^5$ mm. sec.$^{-1}$ Eq. 6	Eq. 7 ($t_0 = 0$)
30	0.5	1.73	15.0	13.2
90	1.4	1.40	12.3	14.2
150	2.2	1.15	14.4	14.9
240	3.2	0.944	15.0	12.9
480	4.9	0.515	13.4	14.5
600	5.5	0.486	15.5	14.6
			Av. 14.3	14.1

[a] Temp. = 222°K.; $P^0_{C_4F_8}$ = 14.9 mm.; $P^0_{F_2}$ = 10.2 mm.; $P^0_{C_2F_6}$ = 76 mm.

The specific rate constants for the fluorination reactions were routinely determined by eq. 7 through plots of $([C_4F_8]/[F_2])^{1/2}$ *vs.* time. The slopes were calculated by least-squares procedure. Such graphs were generally linear to 80% reaction, and typical examples are shown in Figure 1. The results for both *cis*- and *trans*-perfluorobutene-2 are summarized in Table III.

Table III: Summary of the Kinetic Data for Reaction of Fluorine with Perfluorobutene-2

Run no.	T, °K.	Initial pressure, mm. C_4F_8	F_2	Total[a]	K, l. mole^{-1} sec.$^{-1}$
			trans		
1	248	11.8	7.8	197.5	15.9
2	248	7.7	5.0	99.0	14.6
				Av.	15.2 ± 0.6
3[b]	247	10.15	9.6	95.1	14.6
4[b]	247	6.2	7.4	95.6	12.8
5[b]	247	6.5	10.9	96.6	12.8
				Av.	13.4 ± 0.6
6	233	15.2	10.4	98.1	4.6
7	233	10.0	14.7	93.7	5.11
8[b]	233	10.1	14.1	95.6	5.1
				Av.	4.9 ± 0.3
9	222	14.9	10.2	101.0	2.02
10	222	7.2	10.4	294.7	2.08
				Av.	2.05 ± 0.03
11[b]	220	19.6	8.0	87.0	1.85
			cis		
12	247	10.4	5.6	101	14.4
13	236	15.1	7.0	100.5	6.03
14	228	7.1	11.0	99.1	3.62
15	218	10.2	16.0	200.5	1.43
16	218	15.2	10.2	101.0	1.51
				Av.	1.47 ± 0.04

[a] C_2F_6 was added as diluent. [b] Reaction flask coated with Teflon.

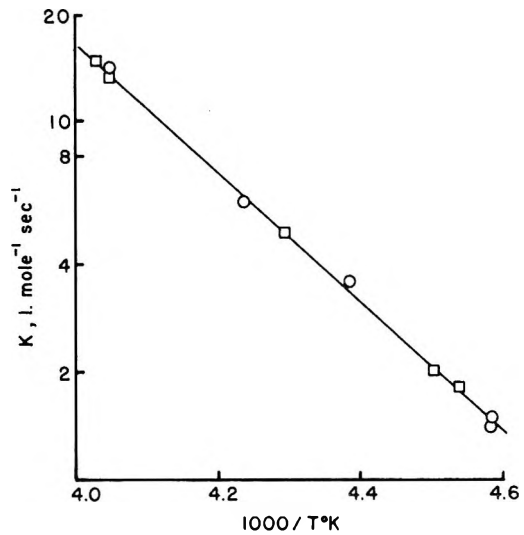

Figure 2. Temperature dependence and comparison of the rate constants for the reaction of *cis*- and *trans*-perfluorobutene-2 with fluorine: ———, least squares, *trans* isomer only; □, average values for *trans* isomer; O, data points for *cis* isomer.

These results are compared in Figure 2. The curve represents a least-squares treatment of log K as a function of $1/T$ for the *trans* isomer, and the circular points represent the data obtained for the *cis* isomer. It is evident that the rates of fluorination of the two isomers are experimentally indistinguishable. A least-

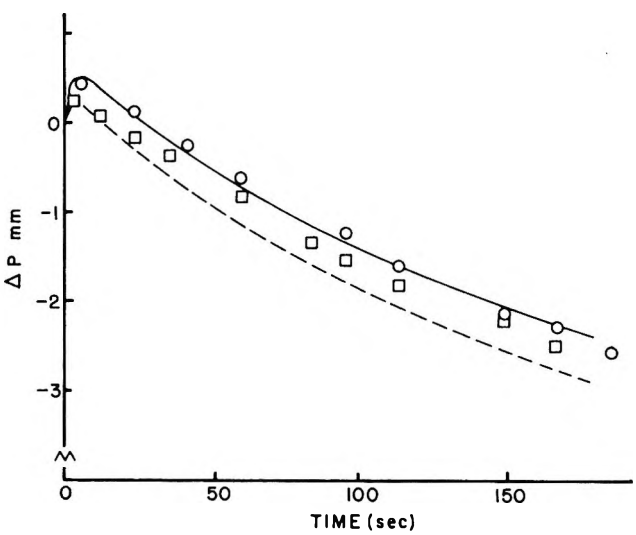

Figure 3. Pressure *vs.* time for reaction of *trans*-perfluorobutene-2 with fluorine at 232°K. Surface-to-volume ratio is 1.6 cm.$^{-1}$: O, $P_{C=C}$ = 12.1 mm., P_{F_2} = 7.8 mm., P_T = 200 mm.; ———, calculated by eq. 10 and 11; □, $p_{C=C}$ = 12.0 mm., P_{F_2} = 7.1 mm., P_T = 107 mm.; - - - -, calculated by eq. 10 and 11.

squares treatment of all the data of Table III resulted in

$$\log K \text{ (l. mole}^{-1} \text{ sec.}^{-1}) = 8.413 \pm 0.1 - \frac{1797 \pm 30}{T} \quad (8)$$

or

$$K = (2.59 \pm 0.6) \times 10^8 \exp\left(\frac{-8194 \pm 140}{RT}\right) \quad (9)$$

The reactor used in the above experiments has a surface-to-volume (S/V) ratio of 2.9 cm.$^{-1}$. To investigate the effect of surface, the 316-cc. reaction vessel was used and packed with 10 g. of Teflon turnings, reducing the S/V to 1.6 cm.$^{-1}$. The packing was added with the hope that an isothermal reaction would still be obtained. This hope was not realized; thus, it was necessary to take into account self-heating of the reaction gases using a convective heat-transfer model. The necessary equations[7,8] are

$$\frac{dX}{dt} = K(A - X)^{1/2}(B - X)^{3/2} \quad (10)$$

$$NC_v \frac{dU}{dt} = Q\frac{dX}{dt} - \frac{\alpha S}{V}(U - U_0) \quad (11)$$

In eq. 10 and 11, the symbols X, A, B, and N represent the concentrations of product, olefin, fluorine, and total gas, respectively; Q denotes the heat of reaction; α, the heat transfer coefficient, and U and U_0, the temperature of gas and walls of the reaction vessel, respectively. The heat capacity of C_2F_6[9] was used for C_v, and Q was estimated at 120 kcal./mole. $\alpha S/VC_v$ was adjusted so that the maximum observed and calculated pressures corresponded; a value of 12×10^{-3} mole l.$^{-1}$ sec.$^{-1}$ was thus obtained. The results of the calculations for two experiments are shown in Figure 3. The good agreement between the observed and calculated pressures indicates a negligible effect of surface upon this reaction.

An inhibition period of 8 to 30 sec. was observed for this reaction. Since this was only a few times greater than the mixing time of the reactants (~5 sec.), it was not considered quantitatively. It was presumably due to oxygen present in the fluorine, as was the case for 2,3-dichloroperfluorobutene-2.[6]

Discussion

The experimental results presented above have shown that the rate of addition of fluorine to both *cis*- and *trans*-perfluorobutene-2 is one-half order with respect to the olefin concentration, and three-halves order with respect to fluorine; it is independent of the total gas concentration and unaffected by a change in the surface-to-volume ratio (aside from effects due to self-heating). All these factors satisfactorily conform to the mechanism represented by reactions 1 to 4. By making the usual steady-state assumptions, one obtains

$$d[C_4F_{10}]/dt = k_3\left(\frac{k_1}{k_4}\right)^{1/2}[C_4F_8]^{1/2}[F_2]^{3/2} \quad (12)$$

Thus, from eq. 6, 9, and 12

$$E_3 - {}^1/_2E_4 + {}^1/_2E_1 = 8.2 \text{ kcal./mole}$$

Both E_3 and E_4 should be small so that the activation energy for initiation is approximately 16.5 kcal./mole.

The heat of isomerization of butene-2 is 1 kcal./mole,[10] the *trans* isomer being more stable than the *cis*. If the same difference in heat of formation is assumed for *cis*- and *trans*-perfluorobutene-2, then the identity of their rates of fluorination (and therefore the rate of reaction 1) indicates that the transition states for each isomer in reaction 1 are different; each more closely resembling their respective reactants, rather than products.

The absence of any significant change in the isomeric ratio of the residual olefin (Table I) indicates that reaction 2 is essentially irreversible and that concurrent geometric isomerization, such as observed by Ayscough, *et al.*,[11] in the photochlorination of *cis*- and *trans*-dichloroethylene, does not occur to an appreciable extent in fluorination under these experimental conditions.

In conclusion, we have shown that the reaction of fluorine with perfluorobutene-2 represents a simple, homogeneous, gas-phase addition of fluorine to the carbon–carbon double bond, that the kinetics of this addition are given by eq. 6 or 7 for at least 80% of the reaction, and, finally, that this rate equation can be interpreted in terms of the proposed mechanism, reactions 1 to 4.

Acknowledgment. The author wishes to express his appreciation to Mr. Kenneth Garton for assistance in the experimental work.

(7) N. N. Semenov, "Some Problems in Chemical Kinetics and Reactivity," Vol. 2, Pergamon Press, New York, N. Y., 1959, pp. 1–10.

(8) A more detailed explanation of the procedure may be found in ref. 6.

(9) J. S. Wicklund, H. F. Flieger, and J. F. Masi, *J. Res. Natl. Bur. Std.*, **51**, 91 (1953).

(10) A.P.I. Research Project 43, Carnegie Press, Pittsburgh, Pa., 1953, p. 715.

(11) P. B. Ayscough, A. J. Cocker, and F. S. Dainton, *Trans. Faraday Soc.*, **58**, 284 (1962).

Calculation of Diffusion Coefficients from Diaphragm Cell Diffusion Data

by R. L. Robinson, Jr., W. C. Edmister, and F. A. L. Dullien

Oklahoma State University, Stillwater, Oklahoma *(Received July 25, 1964)*

A new set of equations is presented which facilitates calculation of differential diffusion coefficients from diaphragm cell experimental results irrespective of volume changes during diffusion. These equations are free of the assumptions employed in previous relations of this type. Use of these new equations permits experiments to be designed using large initial concentration differences and long diffusion times with subsequent increase in the accuracy of the resulting diffusivities.

I. Introduction

The diaphragm cell technique has gained wide acceptance as an accurate and convenient experimental method for measurement of diffusion coefficients. A main drawback to this technique has been the difficulties met in the calculation of the "true" or differential diffusion coefficient, D, from the experimental data.

The usual procedure has been to utilize the "simple logarithmic formula"

$$\bar{D} = \ln \frac{(\Delta\rho_A)_0}{(\Delta\rho_A)_f} / \beta\theta \qquad (1)$$

where $\bar{D}$ is the "integral" diffusion coefficient, $(\Delta\rho_A)_0$ and $(\Delta\rho_A)_f$ are the initial and final concentration differences between the cell compartments, β is the "cell constant," and θ is the diffusion time. $\bar{D}$ is either assumed to equal D when plotted at the average concentration of the experiment or is related to D *via* the relation

$$\bar{D} = \frac{1}{(\Delta\rho_A)_M} \int_{\rho_M'}^{\rho_M''} D \, d\rho_A \qquad (2)$$

where $\rho_M = {}^1/_2[(\rho_A)_0 + (\rho_A)_f]$, the $'$ and $''$ refer to the closed and open compartments, and $(\Delta\rho_A)_M = \rho_M'' - \rho_M'$. Both eq. 1 and 2 are approximations[1] and have been discussed elsewhere.[2]

In order to avoid errors incurred through the use of eq. 2 and/or 1, experimenters have often used (a) small concentration differences which minimize volume changes and/or (b) short diffusion times which minimize effects of deviation from linearity in the D–ρ_A relation.[3] Dullien and Shemilt[4] presented a general solution to the diffusion equation to avoid the restrictions on eq. 1 and 2.[5] However, their work employed a tacit assumption, and Olander[6] attributed to this assumption the small effect of volume changes on D predicted by these authors. Olander presented an approximate method for finding D which predicted substantial effects of volume changes on the calculated value of D. In the present work rigorous equations are developed which show that the volume effects are much less than predicted by Olander's method.

II. Theory

A. The Experimental Error. To the present authors' notion, the chief value of any general method for calculating D is that it releases the experimenter from the restrictions imposed by approximate solutions and allows the use of large concentration differences irrespective of the magnitude of any volume changes. The effect of the initial concentration difference on the experimental precision may be seen from the following relation for the fractional standard deviation in D due to analytical errors.[7]

$$\frac{S_D}{D} = \frac{\sqrt{2}S}{(\Delta\rho_A)_0 \ln R} \sqrt{R^2 + \delta} \qquad (3)$$

(1) Equations 1 and 2 are rigorous if (a) no volume changes occur during diffusion and (b) D is linear in ρ_A.

(2) A. R. Gordon, *Ann. N. Y. Acad. Sci.*, **46**, 285 (1945).

(3) R. H. Stokes, *J. Am. Chem. Soc.*, **72**, 763 (1950).

(4) F. A. L. Dullien and L. W. Shemilt, *Trans. Faraday Soc.*, **58**, 244 (1961).

(5) Gordon (ref. 2) has presented equations which are rigorous for systems where no volume changes occur.

(6) D. R. Olander, *J. Phys. Chem.*, **67**, 1011 (1963).

(7) R. L. Robinson, Ph.D. Thesis, Oklahoma State University, 1964.

where S_D is the standard deviation of the diffusion coefficient, S is the standard deviation in the measured concentration (assumed independent of the level of concentration), R is the ratio of concentration differences as in eq. 1, and $\delta = 2$ if all four concentrations are measured, or $\delta = 3$ if the fourth concentration is found by material balance. Note that the error in D is directly proportional to $(\Delta\rho_A)_0^{-1}$, so doubling this initial concentration difference reduces the error twofold. In addition, the optimum time, θ_{opt}, for diffusion has been shown to be[7]

$$\theta_{opt} = 1.2/\beta D \qquad (4)$$

This optimum value[8] is a substantially longer time than has generally been used by experimenters. Thus, eq. 3 and 4 graphically illustrate the value of a technique for finding D which would be suitable for use with larger concentration differences and longer diffusion times.

The approximate solution of Olander[6] does not fulfill these requirements because of the assumptions he employed. His assumptions, possibly applicable for small concentration differences or in systems where volume changes are small, are certainly in error if maximum concentration differences are employed and significant volume changes occur.[9]

B. The New Set of Equations. The following development evolves a set of relations which are generally valid for diaphragm cell experiments, and these relations fulfill the requirements set forth above. Explanation of the steps is scant since the procedure parallels that from previous works[2,4,6] while avoiding their assumptions.

In general, the flux past a stationary point, accounting for both diffusive and bulk transport, may be written

$$N_A = -D\nabla\rho_A + \rho_A[N_A V_A + N_B V_B] \qquad (5)$$

where N_A is the mass flux of component A relative to a fixed reference point, and V_A is the partial specific volume of component A. (Mass or molal units may be used if consistent units are applied to all quantities.) Equation 5 may also be written for unidirectional flow as

$$N_A = \frac{-D}{1 - \rho_A V_B[V_A/V_B + N_B/N_A]} \frac{d\rho_A}{dy} \qquad (6)$$

where y is distance measured in the direction of flow. At the face of the diaphragm adjacent to the closed compartment, a material balance yields

$$\frac{N_B}{N_A} = -\frac{V_A'}{V_B'} \qquad (7)$$

Employing the "quasi-steady-state" assumption,[2] the flux ratio is invariant with distance through the diaphragm (although it varies with time), so the flux ratio in eq. 6 may be replaced *via* eq. 7, and

$$N_A = \frac{-D}{1 - \rho_A V_B[(V_A/V_B) - (V_A/V_B)']} \frac{d\rho_A}{dy} \qquad (8)$$

Since the flux N_A is assumed to be independent of position in the diaphragm, the right-hand side of eq. 8 may be represented by an equally position-independent function

$$\frac{D_*(\rho_A'' - \rho_A')}{L} \equiv \frac{D}{1 - \rho_A V_B[(V_A/V_B) - (V_A/V_B)']} \frac{d\rho_A}{dy} \qquad (9)$$

where D_* is defined by the above equation, and L is the diaphragm thickness. The following simplifications in notation may also be made

$$D/D_0 \equiv 1 + f(\rho_A),\ D_0 = D \text{ at } \rho_A = 0$$
$$G(\rho_A, \rho_A') \equiv \rho_A V_B[(V_A/V_B) - (V_A/V_B)'] \qquad (10)'$$

Combining eq. 9 and 10, and integrating from $y = 0$ to $y = L$

$$\frac{D_*}{D_0} = \frac{1}{\Delta\rho_A}\int_{\rho_A'}^{\rho_A''} \frac{1 + f(\rho_A)}{1 - G(\rho_A, \rho_A')} d\rho_A \qquad (11)$$

Writing material balances around the open and closed compartments, respectively

$$d(V''\rho_A'') = N_A A dt = -\frac{AD_*\Delta\rho_A}{L} dt$$
$$V' d\rho_A' = -N_A A dt = \frac{AD_*\Delta\rho_A}{L} dt \qquad (12)$$

where V is the total volume of solution in a compartment, A is the cross-sectional area for diffusion, and t is time. (Volume changes on mixing are reflected by changes in V''.) Rearranging and combining eq. 12

$$d\rho_A'' - d\rho_A' \equiv d\Delta\rho_A = -D_*\Delta\rho_A \frac{A}{L}\left[\frac{1}{V'} + \frac{1}{V''}\right] dt - \frac{\rho_A''}{V''} dV'' \qquad (13)$$

(8) Similar results were derived independently by A. L. van Geet and L. W. Adamson, *J. Phys. Chem.*, 68, 238 (1964).

(9) For example, to simplify the denominator of his eq. 3 (eq. 6 of this paper), Olander assumes $1/(1 - x) = 1 + x$ since the group represented by x is small. However, if pure ethanol diffuses into water, the group represented by x in eq. 6 is not so small, and the above approximation is in error by over 10%.

Defining

$$\frac{D_0}{D_*} \equiv 1 + F(\rho_A', \rho_A'') \tag{14}$$

Equation 13 may be written

$$\frac{1 + F(\rho_A', \rho_A'')}{\beta} \mathrm{d} \ln \Delta\rho_A = -D_0 \mathrm{d}t - \frac{[1 + F(\rho_A', \rho_A'')]\rho_A''}{\beta \Delta\rho_A V''} \mathrm{d}V'' \tag{15}$$

where

$$\beta \equiv \frac{A}{L}\left[\frac{1}{V'} + \frac{1}{V''}\right] \tag{16}$$

is the "cell constant." Integrating eq. 15

$$-\frac{1}{\bar{\beta}} \ln \frac{(\Delta\rho_A)_0}{(\Delta\rho_A)_f} + \int_{(\Delta\rho_A)_0}^{(\Delta\rho_A)_f} \frac{F(\rho_A', \rho_A'')}{\beta \Delta\rho_A} \mathrm{d}\Delta\rho_A = -D_0\theta - \int_{V_0''}^{V_f''} \frac{[1 + F(\rho_A', \rho_A'')]\rho_A''}{\beta \Delta\rho_A V''} \mathrm{d}V'' \tag{17}$$

where

$$\bar{\beta} = -\ln \frac{(\Delta\rho_A)_0}{(\Delta\rho_A)_f} \int_{(\Delta\rho_A)_0}^{(\Delta\rho_A)_f} \frac{\mathrm{d}\Delta\rho_A}{\beta \Delta\rho_A} \tag{18}$$

Define

$$\bar{D}\beta_0\theta \equiv \ln \frac{(\Delta\rho_A)_0}{(\Delta\rho_A)_f}, \quad \beta_0 = \beta \text{ at } t = 0 \tag{19}$$

Using eq. 19, eq. 17 may be written

$$\frac{\bar{D}}{D_0} = \frac{\bar{\beta}}{\beta_0}\left[1 + \frac{1}{D_0\theta} \int_{(\Delta\rho_A)_0}^{(\Delta\rho_A)_f} \frac{F(\rho_A', \rho_A'')}{\beta \Delta\rho_A} \mathrm{d}\Delta\rho_A + \frac{1}{D_0\theta} \int_{V_0''}^{V_f''} \frac{[1 + F(\rho_A', \rho_A'')]\rho_A''}{\beta \Delta\rho_A V''} \mathrm{d}V''\right] \tag{20}$$

The above set of equations contains no assumptions other than that of quasi-steady state. Calculation of the D *vs.* ρ_A relation from experimental results may be done *via* the following iterative process: (1) assume a D *vs.* ρ_A relation; $\bar{D}$ *vs.* $(\rho_A)_{av}$ is a logical first approximation; (2) determine $f(\rho_A)$ from eq. 10; (3) determine $F(\rho_A', \rho_A'')$ from eq. 11 and 14; (4) evaluate eq. 20; (5) define ρ_A^* as the concentration at which $\bar{D}$ is equal to D; by comparison of eq. 10 and 20, it follows that ρ_A^* may be found by equating $1 + f(\rho_A)$ to the right-hand side of eq. 20 and solving for ρ_A^*; (6) for a second iteration, assume the D *vs.* ρ_A relation equals the $\bar{D}$ *vs.* ρ_A^* relation; repeat steps 2–6 until ρ_A^* values from two successive iterations vary insignificantly.

The preceding iterative calculation technique is too tedious to be routinely applied by hand. However, the computations are quite suitable for the digital computer if the diffusion coefficient and volumetric properties can be adequately represented as analytical functions of the concentration.

For the case of no volume changes on mixing, $\bar{\beta} = \beta = \beta_0$ and $\mathrm{d}V'' = 0$. Equation 20 then reduces to the equation derived by Gordon[2] for the case of constant volumes (Gordon's eq. 17).

III. Application of the Equations

No data are currently available which would present a suitable means for illustrating the value of the preceding equations, *i.e.*, data taken using maximum possible concentration differences in a system displaying appreciable volume changes. The lack of such data is, in fact, caused by the lack of suitable relations to calculate D from the data. The above equations provide these needed relations.

Table I: Comparison of Differential Diffusivities for the Ethanol–Water System

Ethanol concn., g./cc.	Differential diffusivity, cm.²/sec. × 10⁵ — Gordon's equations[2]	Differential diffusivity, cm.²/sec. × 10⁵ — New equations
0.0	1.22	1.22
0.1	0.94	0.945
0.2	0.685	0.68
0.3	0.485	0.48
0.4	0.37	0.37
0.5	0.375	0.37
0.6	0.48	0.48
0.65	0.58	0.585
0.7	0.74	0.75
0.75	0.98	0.99
0.78507	1.245	1.235

The technique described above was applied to the data of Dullien[10] on the ethanol–water system at 25°. The resulting D–ρ_A relation was in excellent agreement with results obtained using Gordon's method assuming no volume changes (see Table I). This agreement is no doubt due in part to the very small concentration differences employed in these experiments. It should be noted that Olander applied his approximate technique to similar ethanol–water data by Hammond and Stokes.[11] He reported differences of 6% from

(10) F. A. L. Dullien and L. W. Shemilt, *Can. J. Chem. Eng.*, **39**, 242 (1961).

(11) B. R. Hammond and R. H. Stokes, *Trans. Faraday Soc.*, **49**, 890 (1953).

results of calculations assuming no volume changes. Hammond and Stokes used small concentration differences in their experiments, so application to their data of the equations from this work would probably be at odds with Olander's results. Actual calculations on Hammond and Stokes' data were not performed since these authors did not present complete data.[11] As a consequence, Olander was forced to make certain assumptions regarding initial conditions in these experiments in order to make his calculations.

IV. Conclusions

A new set of relations is presented for calculation of differential diffusion coefficients from diaphragm cell experimental data. The equations are applicable for any set of initial and final conditions in the experiment, and they account for possible volume changes during diffusion. Use of these relations makes feasible experiments using maximum initial concentration differences and optimum diffusion times for any system, with resulting reductions in errors in the measured diffusion coefficients. The relations presented herein are consistent with the equations of Gordon for the case where no volume changes occur.

Application of the new equations to the ethanol–water system gave results in agreement with those predicted by Dullien and Shemilt but differed from those of Olander.

Phase Equilibria in Solutions of Liquid Sulfur. I. Theory

by Robert L. Scott

Contribution No. 1717 from the Department of Chemistry, University of California, Los Angeles, California
(Received July 25, 1964)

The Flory–Huggins equations for high polymer solutions have been used to extend the Gee–Tobolsky–Eisenberg treatment of liquid sulfur to binary solutions. A "critical polymerization line" is deduced, below which the amount of open-chain sulfur (S_μ) is negligibly small, but above which increasing amounts of very long sulfur chains are formed. Above the critical polymerization temperature of pure sulfur (159°) the heat of mixing, positive at lower temperatures, can become negative. With a single adjustable parameter, an interchange energy w, the theory accounts for the upper and lower critical solution temperatures observed in solvent–sulfur systems; the lower critical solution temperature is a consequence of the ring–chain transition. A second upper critical solution temperature (in most systems above the normal boiling point of sulfur) is predicted. Calculated phase diagrams are in qualitative agreement with experimental measurements.

Introduction

The solubility of elemental sulfur in nonelectrolyte solvents has been a subject of interest for nearly a hundred years. The solubility of rhombic sulfur, which is entirely S_8 rings, and of liquid sulfur below 159°, which consists almost entirely of the same rings, is reasonably well understood in terms of regular solution-solubility parameter theory.[1] In particular, the lower the solubility parameter δ (lower solvent power) of the solvent, the higher the upper critical solution temperature for the sulfur–solvent mixture, as illustrated by the group of aromatic compounds in Table I.

(1) J. H. Hildebrand and R. L. Scott, "Solubility of Nonelectrolytes," 3rd Ed., Reinhold Publishing Corp., New York, N. Y., 1950, pp. 258, 259.

Table I: Solubilities of Liquid Sulfur in Aromatic Solvents[a-d]

Solvent	δ/cal.$^{1/2}$ cm.$^{-3/2}$	Critical solution temperature/°C. Upper (mixing)	Lower (unmixing)
Naphthalene	(10.2)	<82	
Biphenyl	(10.0)	<98	
Chlorobenzene	9.5	116	
Triphenylmethane	(9.4)	147	199
Benzene	9.2	163	226
Toluene	8.9	180	222
p-Xylene	8.8	None	
m-Xylene	8.8	None	

[a] A. W. Francis, Advances in Chemistry Series, No. 31, American Chemical Society, Washington, D. C., 1961. [b] A. Smith, W. B. Holmes, and E. S. Hall, *Z. physik. Chem.*, **52**, 602 (1905); *J. Am. Chem. Soc.*, **27**, 797 (1905). [c] H. R. Kruyt, *Z. physik. Chem.*, **65**, 486 (1909). [d] D. L. Hammick and W. E. Holt, *J. Chem. Soc.*, 1995 (1926).

In addition, however, three of these solvents show, above a range of temperature in which they are completely miscible with liquid sulfur, unmixing phenomena and a lower critical solution temperature. This unusual behavior has long been attributed qualitatively to an involvement with the transition between λ-sulfur and μ-sulfur, but heretofore no quantitative interpretation has been attempted.

As is well known, below 159° liquid sulfur consists almost entirely of S_8 rings (S_λ), but at this temperature it undergoes what is essentially a second-order transition above which there are increasing amounts of open-chain diradicals (S_μ) of very high molecular weight. There now exists a simple and reasonably satisfactory theory of this phenomenon due to Gee[2] and to Tobolsky and Eisenberg.[3] A more detailed examination of the thermodynamics of liquid sulfur has been carried out by Guthrie[4] in unpublished work.

In this paper this theoretical treatment is extended to binary solutions of sulfur with nonelectrolytes and accounts well for their observed properties.

Theoretical Model

Following Tobolsky and Eisenberg,[3] we assume that liquid sulfur consists of two species: S_λ, an eight-membered ring S_8, and S_μ, linear chains of n S_8 units, *i.e.*, S_{8n}. In doing so, we ignore a third species, the S_π of Aten,[5] presumably ring molecules, S_6, S_{10}, etc., present to the extent of a few per cent in liquid sulfur below and above the λ–μ transition. This will surely cause quantitative errors in the predictions but probably of no greater magnitude than those caused by the approximate character of the equations.

We may now use the familiar Flory–Huggins equations[6-8] for solutions of linear polymers to express the activities of the various components in the solution: a_λ, that of the S_8 rings (S_λ); a_n that of a chain molecule (S_μ) of n S_8 units; and a_0, that of the solvent.

$$\ln a_\lambda = \ln \phi_\lambda + 1 - (\phi_\mu/\bar{n} + \phi_0/r + \phi_\lambda) + \chi_{0\lambda}\phi_0^2 + \chi_{\lambda\mu}\phi_\mu^2 + (\chi_{0\lambda} + \chi_{\lambda\mu} - \chi_{0\mu})\phi_0\phi_\mu \quad (1)$$

$$\ln a_n = \ln \phi_n + 1 - n(\phi_\mu/\bar{n} + \phi_0/r + \phi_\lambda) + n[\chi_{0\mu}\phi_0^2 + \chi_{\lambda\mu}\phi_\lambda^2 + (\chi_{0\mu} + \chi_{\lambda\mu} - \chi_{0\lambda})\phi_0\phi_\lambda] \quad (2)$$

$$\ln a_0 = \ln \phi_0 + 1 - r(\phi_\mu/\bar{n} + \phi_0/r + \phi_\lambda) + r[\chi_{0\lambda}\phi_\lambda^2 + \chi_{0\mu}\phi_\mu^2 + (\chi_{0\mu} + \chi_{0\lambda} - \chi_{\lambda\mu})\phi_\lambda\phi_\mu] \quad (3)$$

Here $r = \bar{V}_0/\bar{V}_\lambda$, the ratio of the molar volume of solvent to that of λ-sulfur, and similarly $n = \bar{V}_n/\bar{V}_\lambda$. The volume fractions ϕ_0, ϕ_λ, and ϕ_n are the appropriate composition variables, and the volume fraction of total μ-sulfur $\phi_\mu = \sum_{n=1}^{\infty} \phi_n$. The number-average chain length $\bar{n} = (\Sigma\phi_n)/(\Sigma\phi_n/n)$. The χ-parameters are the familiar Flory coefficients for the local free energy of interaction (normalized to the unit volume of S_λ) between solvent and λ-sulfur ($\chi_{0\lambda}$), between solvent and a segment of chain sulfur ($\chi_{0\mu}$), and between λ-sulfur and chain sulfur ($\chi_{\lambda\mu}$).

These equations involve the following assumptions or approximations: (a) the Flory–Huggins theory which is only approximate for high-polymer solutions and of really uncertain validity when applied to the system solvent–λ-sulfur whose difference in size (represented by the parameter r) is not a difference in chain length; (b) the restriction (for mathematical simplicity) to chains which are integral multiples of S_8 (the error due to this approximation is surely trivial when $\bar{n} > 10^5$); (c) the assumption that the interaction constants between chain and solvent ($\chi_{0\mu}$) and chain and ring ($\chi_{\lambda\mu}$) are the same for all chain lengths (surely not true for short chains, but reasonable when nearly all chains are very long); (d) volume changes with temperature and the volume change in the S_λ–S_μ transformation can be neglected.

We shall make the further assumption that the χ

(2) G. Gee, *Trans. Faraday Soc.*, **48**, 515 (1952); *Sci. Progr.*, **170**, 193 (1955).

(3) A. V. Tobolsky and A. Eisenberg, *J. Am. Chem. Soc.*, **81**, 780 (1959).

(4) G. B. Guthrie, private communication, 1954.

(5) A. H. W. Aten, *Z. physik. Chem.*, **81**, 257 (1912); **83**, 442 (1913); **86**, 1 (1914); **88**, 321 (1914).

(6) P. J. Flory, *J. Chem. Phys.*, **10**, 51 (1942); **12**, 425 (1944).

(7) M. L. Huggins, *Ann. N. Y. Acad. Sci.*, **43**, 1 (1942).

(8) R. L. Scott and M. Magat, *J. Chem. Phys.*, **13**, 172 (1945).

values can be separated into configuration ("entropy") and interaction ("energy") terms such that (a) S_λ and a segment of S_μ are interchangeable as far as their energies of interaction with each other and with the solvent are concerned and (b) the solvent and S_λ have the same configurational effects with the chain polymer and none with each other. Thus, $\chi_{0\lambda} = w/RT$, $\chi_{0\mu} = \alpha + w/RT$, and $\chi_{\lambda\mu} = \alpha$, where α is the configurational contribution (sometimes written as χ_S) and w is the solvent–solute interchange energy. Equations 1–3 then reduce to

$$\ln a_\lambda = \ln \phi_\lambda + 1 - (\phi_\mu/\bar{n} + \phi_0/r + \phi_\lambda) + \alpha\phi_\mu^2 + (w/RT)\phi_0^2 \quad (4)$$

$$\ln a_n = \ln \phi_n + 1 - n(\phi_\mu/\bar{n} + \phi_0/r + \phi_\lambda) + n[\alpha(\phi_0 + \phi_\lambda)^2 + (w/RT)\phi_0^2] \quad (5)$$

$$\ln a_0 = \ln \phi_0 + 1 - r(\phi_\mu/\bar{n} + \phi_0/r + \phi_\lambda) + r[\alpha\phi_\mu^2 + (w/RT)(\phi_\lambda + \phi_\mu)^2] \quad (6)$$

However all the features of the sulfur–solvent systems can be accounted for qualitatively or even semiquantitatively with the equations further simplified. If we assume that the configuration parameter $\alpha = 0$ and that the molar volume of the solvent is equal to that of S_8 (*i.e.*, $r = 1$), eq. 4–6 reduce further to

$$\ln a_\lambda = \ln \phi_\lambda + (1 - 1/\bar{n})\phi_\mu + (w/RT)\phi_0^2 \quad (7)$$

$$\ln a_n = \ln \phi_n + (1 - n/\bar{n})\phi_\mu + (1 - n)(\phi_\lambda + \phi_0) + n(w/RT)\phi_0^2 \quad (8)$$

$$\ln a_0 = \ln \phi_0 + (1 - 1/\bar{n})\phi_\mu + (w/RT)(\phi_\lambda + \phi_\mu)^2 \quad (9)$$

The use of eq. 7–9 greatly simplifies the calculation of phase diagrams, and they will be used exclusively in the latter half of the paper.

Equilibrium Polymerization and the λ–μ Transition

The chemical equilibria in the sulfur–solvent systems can be represented by two reactions, one in which the eight-membered ring is opened to a chain of eight sulfur atoms and the other in which a ring is opened and added to a chain to lengthen it.

$$S_8(\lambda) \rightleftharpoons S_8(\mu) \qquad K_1'$$

$$S_8(\lambda) + S_{8n}(\mu) \rightleftharpoons S_{8(n+1)}(\mu) \qquad K_{pn}'$$

Using eq. 4–6 for the activities, we obtain the equilibrium equations

$$\ln K_1' = \ln a_1 - \ln a_\lambda = \ln \phi_1 - \ln \phi_\lambda + \alpha(1 - 2\phi_\mu) \quad (10)$$

$$\ln K_{pn}' = \ln a_{n+1} - \ln a_n - \ln a_\lambda = \ln \phi_{n+1} - \ln \phi_n - \ln \phi_\lambda + \alpha(1 - 2\phi_\mu) \quad (11)$$

We now need to examine the variation of the constant K_{pn}' with n. If we write $RT \ln K_{pn}' = -\Delta H^\circ + T\Delta S^\circ$, it seems plausible to assume that ΔH°, which involves breaking an S–S bond in $S_8(\lambda)$ and making an S–S bond in the chain, would be independent of n, at least for large n. For the standard entropy ΔS°, we can write

$$\Delta S^\circ = \bar{S}_{n+1}^\circ - \bar{S}_n^\circ - \bar{S}_\lambda^\circ \quad (12)$$

where, since the standard state is the pure liquid in each case, we can use for $\bar{S}_n^\circ$ and $\bar{S}_{n+1}^\circ$ the Flory–Huggins "entropy of disorientation"

$$\bar{S}_n^\circ = R[\ln (z/\sigma) + (n - 2) \ln (z - 1) + \ln n - n - 1] \quad (13)$$

where z is the coordination number of the quasi-lattice and σ is a symmetry number (here 2). This leads to

$$\Delta S^\circ = R[\ln (z - 1) + \ln (n + 1) - \ln n - 1] \quad (14)$$

From this we may write that $\ln K_{pn}' = \ln K_p' + \ln (n + 1) - \ln n$ where K_p' is a constant independent of n. If we further write $K_1 = K_1' e^{-\alpha}$ and $K_p = K_p' e^{-\alpha}$, we obtain

$$\phi_1/\phi_\lambda = K_1 \exp(2\alpha\phi_\mu) \quad (15)$$

$$n\phi_{n+1}/(n + 1)\phi_n\phi_\lambda = K_p \exp(2\alpha\phi_\mu) \quad (16)$$

It should be noted that ϕ_n/n and $\phi_{n+1}/(n + 1)$ are proportional to the molar concentrations (moles/unit volume), so the equilibrium constant K_p is independent of n when molar concentrations are used (the phenomenological assumption of Tobolsky and Eisenberg[3]).

It should also be noted that no explicit dependence upon the solvent appears in eq. 15 and 16. The equations are independent of the values of r and w. Only if α varies from one solvent to another can the nature of the solvent make any difference. We conclude, therefore, that the role of the solvent (as far as the λ–μ equilibrium is concerned) is almost exclusively that of a nonspecific diluent, and one would expect the λ–μ transition, the chain length distribution, etc., to be the same in all solvents at the same volume fraction ϕ_0.

From eq. 16, and the corresponding ones for n, $(n - 1)$, $(n - 2)$, etc., one obtains ϕ_n as a function of ϕ_1, ϕ_λ, and ϕ_μ

$$\phi_n = n\phi_1(K_p\phi_\lambda e^{2\alpha\phi_\mu})^{n-1} = n\phi_1\beta^{n-1} \quad (17)$$

The total volume fraction of all the chains ϕ_μ is then

$$\phi_\mu = \sum_{n=1}^{\infty} \phi_n = \phi_1 \Sigma n\beta^{n-1}$$

$$= \phi_1(1 + 2\beta + 3\beta^2 + \ldots) = \frac{\phi_1}{(1-\beta)^2}$$

$$\phi_\mu = \frac{\phi_1}{(1 - K_p\phi_\lambda e^{2\alpha\phi_\mu})^2} = \frac{K_1 e^{2\alpha\phi_\mu}\phi_\lambda}{(1 - K_p\phi_\lambda e^{2\alpha\phi_\mu})^2} \quad (18)$$

For the number-average chain length $\bar{n}$ we obtain

$$\bar{n} = \Sigma\phi_n/\Sigma(\phi_n/n) = \phi_1\Sigma n\beta^{n-1}/\phi_1\Sigma\beta^{n-1}$$

$$= (1 + 2\beta + 3\beta^2 + \ldots)/(1 + \beta + \beta^2 + \ldots)$$

$$\bar{n} = \frac{1}{1-\beta} = \frac{1}{1 - K_p\phi_\lambda e^{2\alpha\phi_\mu}} \quad (19)$$

Given K_1 and K_p as functions of temperature, together with the entropy parameter α and the total volume fraction of sulfur $\phi_S = \phi_\lambda + \phi_\mu = 1 - \phi_0$, one can calculate ϕ_μ from eq. 18. Since K_1 is very small at all temperatures of interest (about 10^{-12} at 159°), it follows from eq. 18 that ϕ_μ is very small (of the order of K_1) unless the denominator is very small. Since $\phi_\lambda \leq \phi_S$, it is clear that the line (on a T–ϕ_S diagram) along which $K_p\phi_S e^{2\alpha\phi_\mu} = 1$ plays an important role, that of a "critical polymerization line." Since along this line ϕ_μ is very small (and exactly zero if $K_1 = 0$), we shall define this critical polymerization line by

$$K_p\phi_S = K_p(1 - \phi_0) = 1 \quad (20)$$

and we shall designate the value of ϕ_S at this line by the symbol ϕ_p.

We now distinguish two approximations to the solutions of eq. 18 and 19 depending upon whether $K_p\phi_S$ is greater or less than unity. When $K_p\phi_S < 1$

$$\phi_\lambda \approx \phi_S \quad (21a)$$

$$\phi_\mu = \frac{K_1\phi_S}{(1 - K_p\phi_S)^2} \approx 0 \quad (22a)$$

$$\bar{n} = \frac{1}{1 - K_p\phi_S} \quad (23a)$$

In this region, below the critical polymerization line, there is very little chain sulfur (of the order of K_1), and what little there is has a very low molecular weight. When $K_p\phi_S > 1$

$$\phi_\lambda = \frac{1}{K_p e^{2\alpha\phi_\mu}} \quad (21b)$$

$$\phi_\mu = \phi_S - \phi_\lambda = \frac{K_p\phi_S e^{2\alpha\phi_\mu} - 1}{K_p e^{2\alpha\phi_\mu}} \quad (22b)$$

$$\bar{n} = \left[\frac{K_p\phi_S e^{2\alpha\phi_\mu} - 1}{K_1 e^{2\alpha\phi_\mu}}\right]^{1/2} \quad (23b)$$

In this region, above the critical solution line, there is a significant amount of chain sulfur, and the average number $\bar{n}$ of S_8 units in the chain is very large (of the order $K_1^{-1/2}$). It is this high molecular weight which produces the high viscosity of the solutions. For the case $\alpha = 0$, the equations further simplify

$$\phi_\lambda = \frac{1}{K_p^0} \quad (21b')$$

$$\phi_\mu = \frac{K_p^0\phi_S - 1}{K_p^0} \quad (22b')$$

$$\bar{n} = \left[\frac{K_p^0\phi_S}{K_1^0}\right]^{1/2} \quad (23b')$$

(Since the evaluation of K_1 and K_p depends upon the choice of α, as we shall see, those corresponding to $\alpha = 0$ are designated K_1^0 and K_p^0.)

All the calculations and comparisons with experiment in the remainder of the paper are based upon the following assumed equations for K_1^0 and K_p^0

$$K_1^0 = 1.1 \times 10^{-5} \exp(-16.5 \times 10^3 \text{ deg.}/T) \quad (24)$$

$$K_p^0 = 40.7 \exp(-1.60 \times 10^3 \text{ deg.}/T) \quad (25)$$

Except for the pre-exponential factor in eq. 25 (which differs because of a difference in choice of standard states), these are identical with the numbers evaluated by Tobolsky and Eisenberg[3] from Gee's analysis[2] of the experimental data for pure liquid sulfur ($\phi_S = 1$).

Figure 1 shows the critical polymerization line in sulfur solutions for three values of the configuration parameter $\alpha = 0.00$, 0.25, and 0.50. The latter two curves were obtained from the first by the following procedure. For a particular temperature above the critical polymerization temperature ($t_p = 159$°C., $T_p = 432$°K.) of pure liquid sulfur the "experimental" value of ϕ_μ at $\phi_S = 1$ (which we will call ϕ_μ^*) is given (eq. 22b') by $(K_p^0 - 1)/K_p^0$. This was substituted into eq. 21b to give a value of K_p for a nonzero α, and the new K_p was substituted into eq. 20 to yield the critical polymerization composition ϕ_p. Thus

$$\phi_p = (1 - \phi_\mu^*)e^{2\alpha\phi_\mu^*} \quad (26)$$

Also shown in Figure 1 are the experimental points for the critical polymerization line for sulfur in CS_2 determined by Katz and Larkin[9] in this laboratory. When the true volume fraction of sulfur is used, the results seem in good agreement with $\alpha = 0.25$, which is a reasonable value for high polymers in good solvents. This is strongly dependent, however, upon the assump-

(9) J. Katz and J. A. Larkin, to be published.

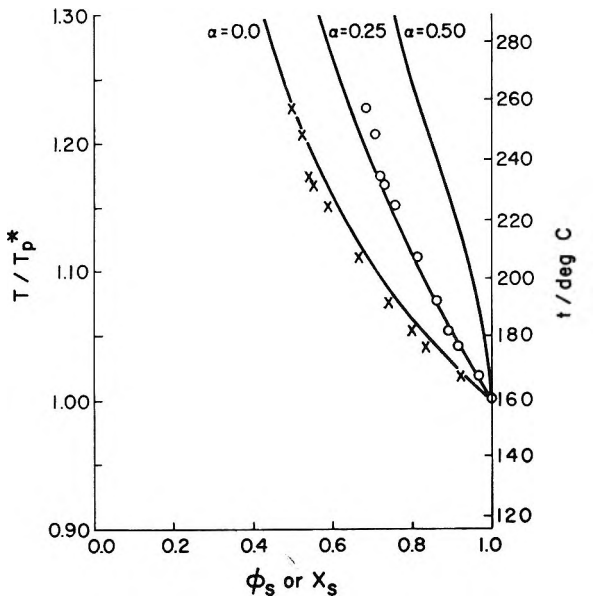

Figure 1. The critical polymerization line for solvent–sulfur systems for three values of the entropy parameter α = 0.00, 0.25, and 0.50. Experimental points of Katz and Larkin: O, abscissa is volume fraction ϕ_S of sulfur; ×, abscissa is (formal) mole fraction of sulfur, calculated assuming all sulfur is S_8.

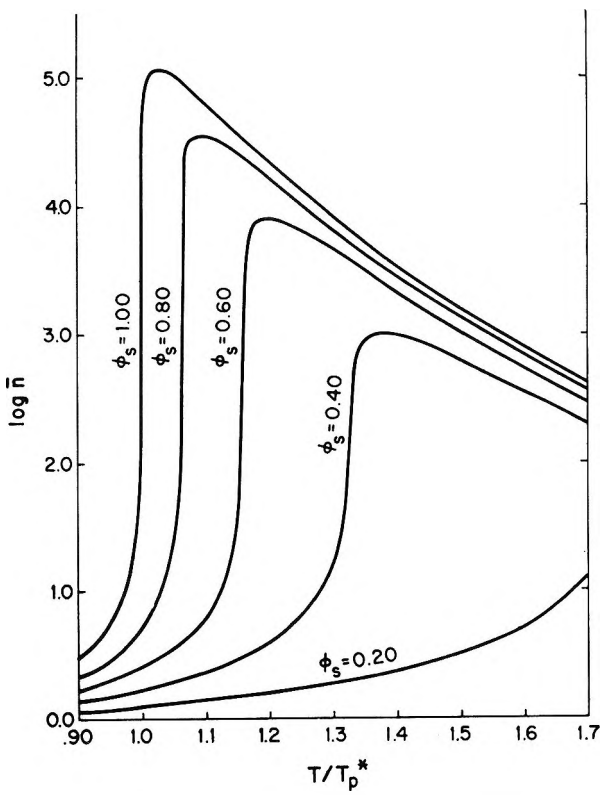

Figure 2. The average chain length $\bar{n}$ of S_μ in solvent–sulfur systems as a function of the reduced temperature T/T_p^* for various values of the total volume fraction ϕ_S of sulfur.

tion that the Flory–Huggins equation, which makes much of a large difference in molar volumes, is valid for the mixture of CS_2 with the λ-sulfur S_8 rings. If, instead, the mixture of the small molecules is a regular solution, their difference in molar volumes is irrelevant, and one should use a formal mole fraction of sulfur (based on S_8). As one sees in Figure 1, this gives good agreement for $\alpha = 0$. This uncertainty could probably be resolved by careful measurements of the thermodynamic properties (especially the excess free energy) of CS_2 + S at temperatures below the critical polymerization, but no such data presently exist.

In view of this uncertainty about a reasonable choice for α, the remainder of this paper presents results only for the simplest case $\alpha = 0, r = 1$.

Figure 2 presents the average chain length $\bar{n}$, calculated (for $\alpha = 0$) from eq. 23, 23b′, and 19 for various values of ϕ_S and T/T_p^* where T_p^* is the critical polymerization temperature for pure sulfur, 432°K. (159°C.). We see that, even with large amounts of solvent, the chain lengths are very large above the critical solution line. Only above the normal boiling point of sulfur (718°K., $T/T_p^* = 1.66$) does the average chain length get so small that the approximations of eq. 21b′, 22b′, and 23b′ begin to fail. Consequently, it is convenient in what follows to assume the limit $K_1 \to 0, \bar{n} \to \infty$.

The Heat of Mixing

In general an upper critical solution temperature is associated with a positive heat of mixing at that point, while a lower critical solution temperature is similarly associated with a negative heat of mixing. (Strictly speaking, the thermodynamic requirement[10] concerns the sign of $(\partial^2 H/\partial x^2)_{T,P}$ at the critical point, rather than the sign of ΔH^M.) Since sulfur solutions show both upper and lower critical solution temperatures with the same solvent, it is interesting to derive the heat of mixing from the simple model presented in this paper. Below the critical polymerization temperature for pure sulfur, T_p^*, the heat of mixing is simply that for solvent–λ-sulfur (for $\alpha = 0$, $r = 1$). When $T < T_p^*$

$$\Delta H^M = w\phi_S\phi_0 = w\phi_S(1 - \phi_S) \qquad (27)$$

Above T_p^* one still has the same solvent–sulfur interaction. However, because the amount of chain sulfur ϕ_μ is different in the solution and in the pure liquid sulfur, there is an additional contribution from the heat of depolymerization of some sulfur chains when the

(10) J. S. Rowlinson, "Liquids and Liquid Mixtures," Academic Press, New York, N. Y., 1959, p. 164.

sulfur and the solvent are mixed. The heat of depolymerization of sulfur chains of n units to n S_8 rings is

$$\Delta H_{depol} = -(n-1)\Delta H_p - \Delta H_\lambda \approx -n\Delta H_p \quad (28)$$

where $\Delta H_\lambda = 32.8$ kcal. and $\Delta H_p = 3.17$ kcal. are the heats of reaction associated with the ring opening and polymerization reactions. Since $\bar{n}$ is so very large, the contribution of ΔH_λ can be neglected, and one can write for the heat of mixing per mole of mixture (referred to S_8) when $T > T_p^*$

$$\Delta\tilde{H}^M = w\phi_S(1-\phi_S) + (\phi_S\phi_\mu^* - \phi_\mu)(-\Delta\tilde{H}_p) \quad (29)$$

where ϕ_μ is the volume fraction of chain sulfur in the solution and ϕ_μ^* is the volume fraction of chain sulfur in pure sulfur ($\phi_S = 1$). Since $\phi_\lambda^* = 1 - \phi_\mu^*$ is always equal (for $\alpha = 0$) to the critical polymerization volume fraction $\phi_p = 1/K_p^0$, $\phi_\mu^* = 1 - \phi_p$. We now distinguish two cases depending on whether, for the final solution at ϕ_S, $\phi_S < \phi_p$ (in which case $\phi_\mu = 0$) or $\phi_S > \phi_p$ (in which case $\phi_\mu = \phi_S - \phi_p$). When $T > T_p^*$ and $\phi_S < \phi_p$

$$\Delta\tilde{H}^M = w\phi_S(1-\phi_S) - \Delta\tilde{H}_p\phi_S(1-\phi_p) \quad (30)$$

and when $T > T_p^*$ and $\phi_S > \phi_p$

$$\Delta\tilde{H}^M = w\phi_S(1-\phi_S) - \Delta\tilde{H}_p\phi_p(1-\phi_S) \quad (31)$$

Figure 3 shows the heat of mixing as a function of ϕ_S for various temperatures while Figure 4 shows the heat of mixing as a function of temperature for various compositions. We see that, above the critical polymerization temperature T_p^* for pure sulfur, the heat of mixing decreases and will always become negative (at least for certain compositions ϕ_S). After the solution crosses the critical polymerization line, however, the heat of mixing (for positive w) will become positive again at still higher temperatures. We shall see later that the lower critical solution temperatures occur in a region where ΔH^M is definitely negative. The reversion to positive heats of mixing at still higher temperatures implies a second upper critical solution temperature; we shall find this confirmed by the theory, but at temperatures above the normal boiling point of sulfur.

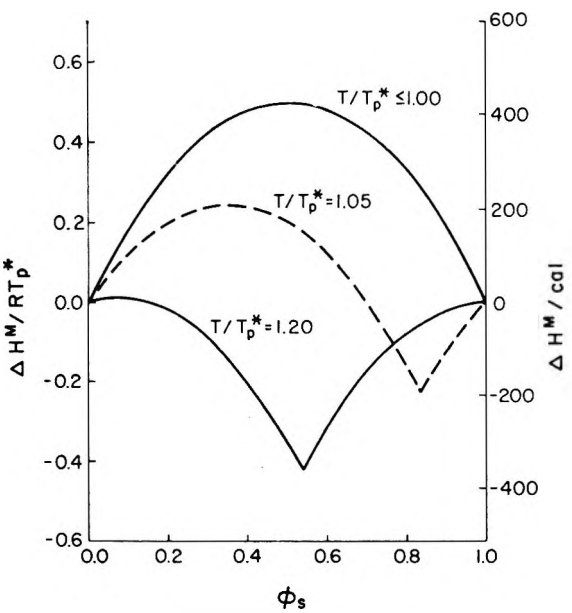

Figure 3. The heat of mixing for a solvent–sulfur system for which the interchange energy $w = 2RT_p^*$, shown as a function of total volume fraction ϕ_S of sulfur for several temperatures. (At $T = 1.20T_p^*$ part of the curve actually lies within a two-phase region; the heat of mixing is for the hypothetical homogeneous mixture.)

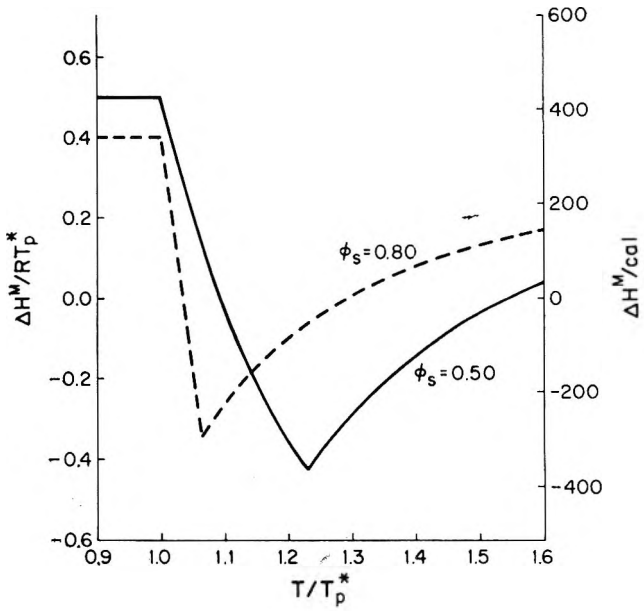

Figure 4. The heat of mixing for a solvent–sulfur system for which the interchange energy $w = 2RT_p^*$, shown as a function of temperature for two values of the total volume fraction ϕ_S of sulfur. (Parts of both curves actually lie within a two-phase region.)

Liquid–Liquid Phase Equilibria

When the interchange energy w for two liquids is sufficiently large in comparison with RT, they are not miscible in all proportions. Below the critical polymerization line, in the approximation $r = 1$, $K_1 = 0$, the two liquids, solvent and λ-sulfur, form what Guggenheim[11] has called a "simple mixture." For such mixtures the phase diagram is completely symmetric, the critical mole fraction $x_c = 0.5$, and the critical solution temperature $T_c = w/2R$. If w is tempera-

(11) E. A. Guggenheim, "Thermodynamics," 3rd Ed., North-Holland Publishing Co., Amsterdam, 1957, p. 250.

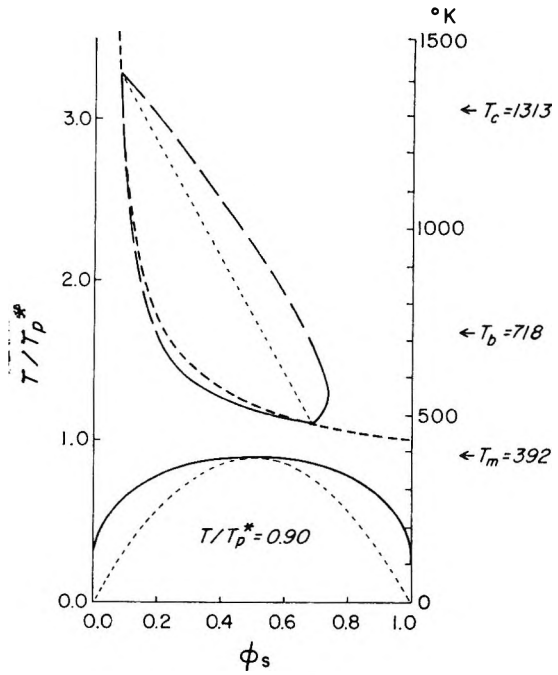

Figure 5. Phase diagram for a solvent–sulfur system for which $w/2R = T_1 = 0.90T_p^*$, showing a lower critical solution temperature and two upper critical solution temperatures. The dashed line is the critical polymerization line; the dotted lines are "spinodal" lines. (Above $T = 1.7T_p^*$ the phase boundary is shown as a broken line because the approximation $K_1^0 = 0$ ($\bar{n} = \infty$) used for the calculation is, in fact, no longer valid above this temperature.)

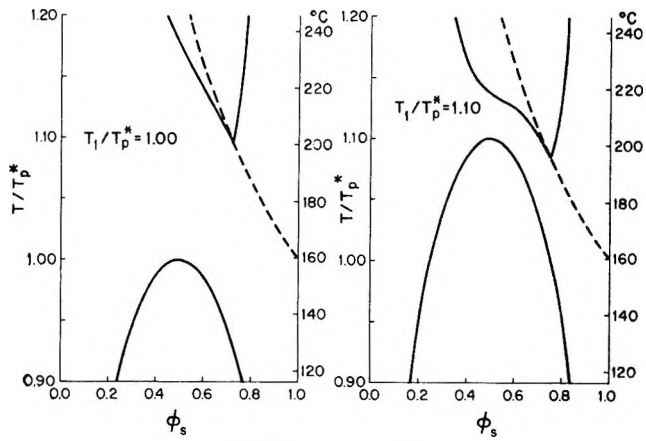

Figure 6. Phase diagrams for solvent–sulfur systems for which (a) $w/2R = T_1 = 1.000T_p^*$ and (b) $w/2R = T_1 = 1.100T_p^*$.

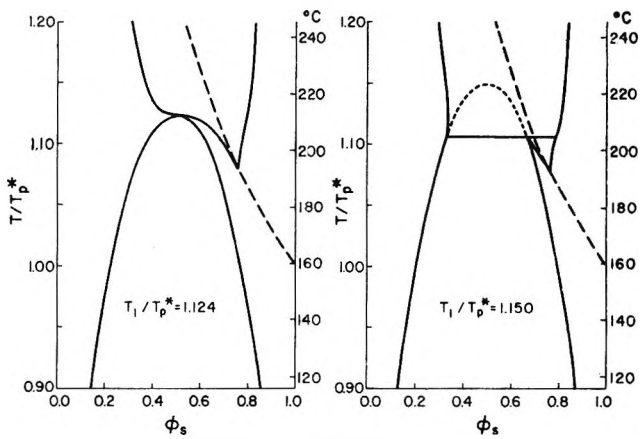

Figure 7. Phase diagrams for solvent–sulfur systems for which (a) $w/2R = T_1 = 1.124T_p^*$ and (b) $w/2R = T_1 = 1.150T_p^*$. The continuation of the low-temperature phase boundary into the two-phase region (to a hypothetical critical solution temperature at $T = T_1$) is shown by short dashes in Figure 7b.

ture independent, as we assume here, this critical solution temperature is an "upper" critical solution temperature,[12] above which the two liquids are miscible in all proportions ($w/RT < 2$).

Above the critical polymerization line, however, a significant fraction of the sulfur is in the form of high-polymer chains. For a binary mixture of solvent plus a polymer of infinite molecular weight, the Flory–Huggins equations give the critical condition as $\chi = \alpha + w/RT_c = 0.5$. Thus, even for $\alpha = 0$, the two liquids are miscible in all proportions only when $w/RT < 0.5$. As is well known, the range of "good" solvents for a high molecular weight polymer can be extremely narrow. Consequently, it is not surprising that there are solvents for sulfur which show an upper critical solution temperature T_1 and at still higher temperatures a lower critical solution temperature T_2 above which the two liquids are again only partially miscible.

Even above the critical polymerization line only part of the liquid sulfur is a high polymer, so a more quantitative treatment of the problem of phase equilibria in these systems requires an analysis of the thermodynamic equations outlined earlier in this paper. It is convenient to derive first equations for the "spinodal" line, the boundary of the region (or regions) within which the one-phase system is absolutely unstable with respect to separation into two or more phases. Since these systems are, thermodynamically speaking, *binary* systems, the spinodal line is defined by the equation

$$\left(\frac{\partial^2 \tilde{G}}{\partial \phi_S^2}\right)_{T,P} = 0 \qquad (32)$$

(12) The reader should be warned about a possible misunderstanding of the terms "upper critical solution temperature" and "lower critical solution temperature" in this paper. In conformity with accepted usage, an "upper critical solution temperature" is the temperature above which two liquids, incompletely miscible at lower temperatures, become miscible in all proportions. Conversely, there is complete miscibility below a "lower critical solution temperature" and only partial miscibility above it. In solvent–sulfur systems confusion may easily result from the fact that the lower critical solution temperature is a higher temperature than the upper critical solution temperature.

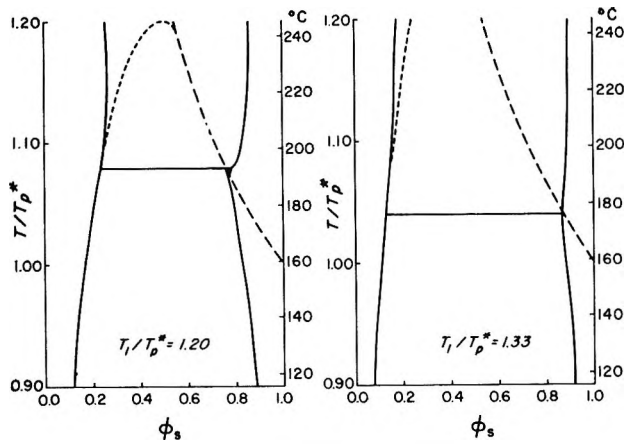

Figure 8. Phase diagrams for solvent–sulfur systems for which (a) $w/2R = T_1 = 1.200T_p^*$ and (b) $w/2R = T_1 = 1.330T_p^*$. The continuation of the low-temperature phase boundary into the two-phase region is shown with short dashes.

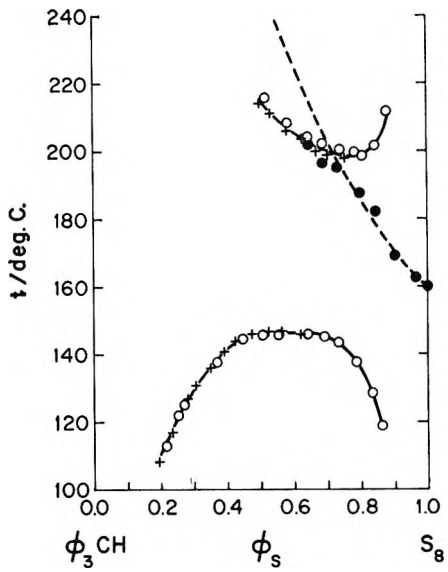

Figure 9. Experimental phase diagram for triphenylmethane–sulfur: +, data of Smith, Holmes, and Hall; O, data of Kruyt; ●, critical polymerization points from viscosity data of Mondain-Monval and Schneider.

where $\bar{G}$ is the molar Gibbs free energy, or by the completely equivalent condition

$$\left(\frac{\partial \ln a_0}{\partial \phi_S}\right)_{T,P} = 0 \tag{33}$$

For our simplified model with $\alpha = 0$, $r = 1$, $K_1^0 = 0$, we may differentiate eq. 9 with the aid of eq. 22a and 22b′, obtaining three separate spinodal lines. When $K_p^0\phi_S < 1$

$$2w\phi_S(1 - \phi_S) = RT \tag{34}$$

$$K_p^0\phi_S = 1 \tag{35}$$

when $K_p^0\phi_S > 1$

$$2w(1 - \phi_S) = RT \tag{36}$$

Equation 34 defines a parabola which is just the spinodal line for the simple mixture and is appropriate below the critical polymerization line. The maximum occurs at $\phi_S = 0.5$, and if this lies below the critical polymerization line, there may be an upper critical solution temperature $T_1 = w/2R$.

Equation 35 defines the critical polymerization line itself, the curve shown in Figure 1 and (as a dashed line) in Figures 5–8. Equation 36, appropriate only above the critical polymerization line, defines a straight line which has two intersections with that line. These intersections represent two more critical solution temperatures, a lower critical solution temperature T_2 and, at a much higher temperature, a second upper critical solution temperature T_3.

These intersections form sharp cusps in the full spinodal curve only because we have assumed the limit $K_1^0 = 0$ ($\bar{n} = \infty$). For the nonzero K_1^0 (finite chain length) the spinodal line will be a smooth curve at T_2 and T_3, although with very sharp curvature for small K_1^0.

The actual two-phase region is larger than the area within the spinodal curves, and the phase boundary (the "binodal" or "conodal" line) coincides with the spinodal line only at the critical points. Calculation of the complete phase diagram is a tedious procedure, requiring the solution of the simultaneous equations

$$a_0^\alpha = a_0^\beta \tag{37a}$$

$$a_S^\alpha = a_S^\beta \tag{37b}$$

where α and β are the two conjugate phases with volume fractions, ϕ_S^α and ϕ_S^β, and the activity of the total sulfur a_S is the same as that of λ-sulfur, a_λ. The phase diagrams shown in Figures 5–8 were calculated from eq. 7 and 9, partly by hand and partly with the aid of an IBM 7090 computer.

Figure 5 shows a calculated phase diagram for a solvent–sulfur system for which $w = 1.80RT_p^*$. This has an upper critical solution temperature $T_1 = 0.90T_p^*$, that is, at 116°C., just below the melting point of monoclinic sulfur. For illustrative purposes, the computed liquid–liquid phase diagram is shown over the entire temperature range from $T = 0$ to $T = T_3$ although the lower region is inaccessible because crystalline phases are more stable ($T < T_m$), and the high temperature region is above the normal boiling point of sulfur. Morever, above $T = 1.7T_p^*$, the average chain length $\bar{n}$ is sufficiently small (see Figure

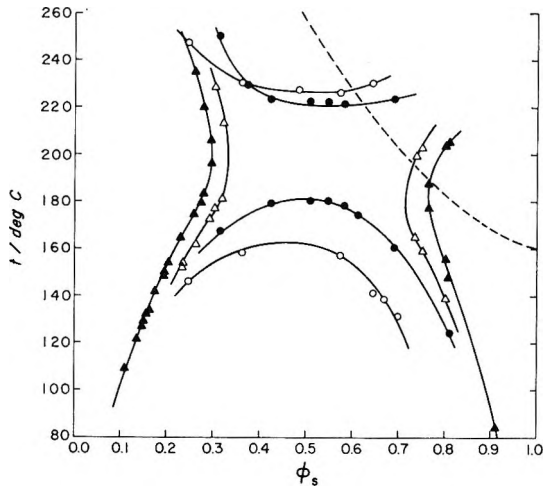

Figure 10. Experimental phase diagrams: O, benzene–sulfur (Kruyt); ●, toluene–sulfur (Kruyt); Δ, *m*-xylene–sulfur (Kruyt); ▲, *p*-xylene–sulfur (Hammick and Holt).

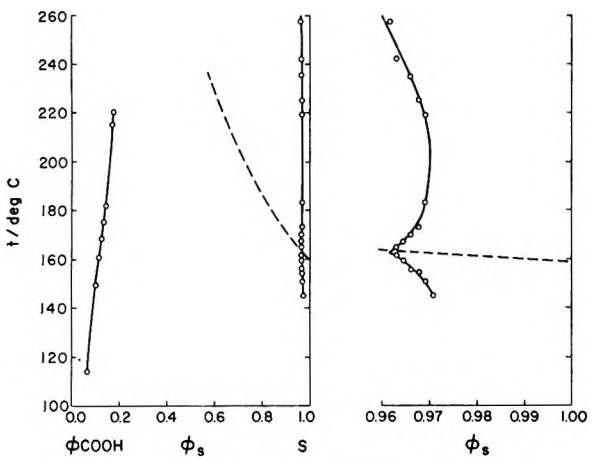

Figure 11. Experimental phase diagram for benzoic acid–sulfur (Hammick and Holt) with expanded graph of the sulfur-rich region.

2) that the approximation $K_1^0 = 0$ is no longer appropriate; consequently, the upper part of the phase diagram is shown as a dashed line. With proper allowance for the finite and changing $\bar{n}$, the upper critical solution temperature T_3 would be much lower. The spinodal lines defined by eq. 34 and 36 are shown as dotted lines.

The remaining phase diagrams (Figures 6–8) are restricted to the temperature region of practical interest, $T = 0.90T_p^*$ to $T = 1.20T_p^*$ (116 to 245°C.). Calculated diagrams are shown for six different values of $w/2RT_p^* = T_1/T_p^*$: 1.000, 1.100, 1.124, 1.150, 1.200, and 1.330. As the interchange energy w increases, the upper critical solution temperature rises, and the lower critical solution temperature falls. The region of complete miscibility narrows until the two separate two-phase regions touch at $T_1 = 1.124T_p^*$ (see Figure 7a).

For larger values of the interchange energy ($w/2R = T_1 > 1.124T_p^*$) the two-phase region is continuous, and the upper critical solution point at T_1 has disappeared. (If one prefers, it exists as a metastable point inside the two-phase region.) It is a curious feature of this model (not yet confirmed experimentally) that the lower critical solution point at T_2 (which occurs in the sulfur-rich region $\phi_S > 0.5$) persists for values of w greater than 1.124, coalescing with the lower part of the phase diagram at $T = 1.073T_p^*$, $\phi_S = 0.888$ when $w/2R = T_1 = 1.208T_p^*$.

As one goes in the other direction, that of decreasing w, the two critical solution temperatures, T_2 and T_3, associated with the presence of high molecular weight chain sulfur approach each other until the upper two-phase region disappears at $T_2 = T_3 = 1.51T_p^*$, $\phi_S = 0.29$ when $w/2R = T_1 = 0.529T_p^*$. Systems with a short interval between T_2 and T_3 are potentially observable with a carefully chosen solvent.

Figures 9–11 show some of the experimental data on sulfur solutions. Most of the measurements are quite old and were made before there was any adequate explanation of the nature and behavior of liquid sulfur at and above the λ–μ transition temperature. Moreover, the potential reactivity of the solvents with μ-sulfur (now known to be a diradical) was inadequately examined. Most of the measurements need to be repeated with care and the solutions studied by modern methods for the presence of reaction products.

Figure 9 reproduces the data of Smith, Holmes, and Hall[13] and of Kruyt[14] for triphenylmethane–sulfur. Also shown are points on the critical polymerization line derived from the viscosity measurements of Mondain-Monval and Schneider.[15] The results agree qualitatively with what one would expect from a theoretical phase diagram when $w/2R = T_1$ is about 0.97 (reasonable values of T_1 and T_2, asymmetry of the upper phase boundary with respect to the lower).

Figure 10 shows the data for benzene,[14] toluene,[14] *p*-xylene,[16] and *m*-xylene[14] with sulfur. The decreasing solubility parameter (increasing w) is clearly associated with an increase in the upper critical solution temperature T_1 and a decrease in the lower critical solution temperature T_2. In the two systems *p*-xylene–sulfur and *m*-xylene–sulfur, where there is no complete misci-

(13) See ref. *b*, Table I.

(14) See ref. *c*, Table I.

(15) P. Mondain-Monval and P. Schneider, *Bull. soc. chim. France*, [4] **43**, 1302 (1928).

(16) See ref. *d*, Table I.

bility at any temperature,[17] the asymmetry predicted by the theory is found; the temperature of maximum solubility of sulfur in solvent is about 20° higher than the temperature of maximum solubility of solvent in liquid sulfur. However, for the systems benzene–sulfur and toluene–sulfur the shape of the upper solubility curve around T_2 is much flatter than predicted from theory.

Finally Figure 11 shows the data for the system benzoic acid–sulfur.[18] This diagram is similar to what might be expected from theory when $w/2R = T_1$ is about $1.7T_p^*$; the sharp indentation in the phase boundary on the sulfur-rich side (where it crosses the critical polymerization line) is in contrast to the smoothness of the phase boundary on the solvent-rich side.

The principal problem is, thus, the detailed shape of the phase boundary in the vicinity of the lower critical solution temperature T_2. The experimental data suggest that it is not nearly so sharp as the theoretical phase diagrams (Figures 5–8) suggest. Until this problem is resolved, the existence of phase diagrams such as those shown in Figures 6b and 7 is in doubt. Additional studies, experimental and theoretical, are under way in this laboratory. Within the framework of the theory presented in this paper, the effects of nonzero K_1^0 and of nonzero α need further investigation, but preliminary calculations suggest that the inclusion of the finite $\bar{n}$ (nonzero K_1^0) has no significant effect on the phase boundary in the vicinity of T_2. A third effect to be investigated is the contribution of other sulfur species to the equilibria, *e.g.*, S_6 and S_{10} rings (S_π).

Recently, Katz,[19] working in this laboratory, has found upper and lower critical solution phenomena in the system *o*-xylene–sulfur ($t_1 = 164°$, $t_2 = 221°$), results consistent with the higher solubility parameter ($\delta = 9.0$) of this solvent compared with its isomers. This result suggests the possibility of studying pseudobinary systems: *o*-xylene–*p*-xylene–sulfur; these should cover the intermediate values of the interchange energy w. The experiments, however, are complicated by the slow reaction of *o*-xylene with μ-sulfur.

Acknowledgments. This research has been supported by a grant from the National Science Foundation. The author wishes to thank his colleagues, Professor A. E. Eisenberg and Dr. J. A. Larkin, for many helpful discussions.

(17) Hammick and Holt[16] report for the system *p*-xylene–sulfur an upper critical solution temperature of 191° for freshly melted sulfur which is initially entirely in the form of S_8 rings (S_λ). As equilibration proceeds, not to S_μ as they suggested, but rather to other rings (S_π), the equilibrium curve shown in Figure 10 results. No lower critical solution temperature T_2 will be found because the diradical S_μ will surely catalyze the λ–μ interconversion.

(18) D. L. Hammick and W. E. Holt, *J. Chem. Soc.*, 493 (1927).

(19) J. Katz and R. L. Scott, to be published.

The Reaction of Haloaliphatic Compounds with Hydrated Electrons[1]

by M. Anbar[2] and Edwin J. Hart

Argonne National Laboratory, Argonne, Illinois *(Received July 27, 1964)*

The reaction of hydrated electrons, e_{aq}^-, with haloaliphatic compounds has been investigated, using pulse radiolysis. The rate of reaction increases in the order $F \ll Cl < Br < I$ and is enhanced by neighboring electron-withdrawing groups. A satisfactory correlation is obtained between rate and the effect of electron-withdrawing groups as defined by Taft's σ^*-function. The mechanism suggested is an attack of e_{aq}^- on the halogen atom resulting in the intermediate formation of a RX^- ion, which subsequently decomposes to $R + X^-$.

Introduction

An exploratory study of the reactivities of various organic compounds toward e_{aq}^- [3,4] followed the recent discovery of the hydrated electron, e_{aq}^-, which had been identified through its absorption spectrum.[5] Aromatic compounds as well as haloaliphatic derivatives were found among the most reactive organic species. The hydrated electron interacts with aromatic compounds by a mechanism analogous to nucleophilic substitution.[6] This reaction results in the incorporation of the electron into the orbitals of the aromatic ring and in some cases to the formation of aromatic carbanions of finite stability. Aromatic bromo and iodo derivatives are more reactive than expected from their influence on the electron density of the ring and this effect was attributed to the additional reactive center in these molecules. The dechlorination of chloroacetic acid was the first haloaliphatic reaction of e_{aq}^- to be demonstrated.[7-9] Iodo- and bromoacetic acids were also found to undergo dehalogenation[9] and the formation of halide ions as products of reaction may be considered as a rule for all the $RX + e_{aq}^-$ reactions. In this study, we report the rate of reaction of e_{aq}^- with different haloaliphatic compounds and suggest a mechanism for this process.

Experimental

The rates of reaction of e_{aq}^- with haloaliphatic compounds were determined by pulse radiolysis.[4] The experimental technique has been described previously, including instrumentation[3] and estimation of errors.[6] All measurements were carried out in the pH range 9.5–10.5 in the presence of 0.001 *M* methanol in order to minimize the reaction of e_{aq}^- with H^+ and OH radicals.

Materials. Chloroacetic acid, α- and β-bromopropionic acids, α-chloropropionic acid, and trichloroacetic acid were Fluka Puriss grade; sodium fluoroacetate, β-chloropropionic acid, and benzotrichloride were Fluka purum grade; β-chloro- and β-bromoethanol were Matheson C.P. reagents; and sodium iodoacetate was an Eastman White Label chemical. All reagents were used without further purification.

Results and Discussion

The bimolecular rate constants of a number of alkyl halides and their derivatives are summarized in Table I. Their reactivity toward e_{aq}^- increases in the series $F \ll Cl < Br < I$ and the relative rates of the four monohaloacetates, F:Cl:Br:I, are 2×10^{-3}:1:5:10.

(1) Based on work performed under the auspices of the U. S. Atomic Energy Commission.

(2) On sabbatical leave from the Weizmann Institute of Science, Rehovoth, Israel.

(3) E. J. Hart, S. Gordon, and J. K. Thomas, *J. Phys. Chem.*, 68, 1271 (1964).

(4) A. Szutka, J. K. Thomas, S. Gordon, and E. J. Hart, to be published.

(5) J. W. Boag and E. J. Hart, *Nature*, 197, 45 (1963); J. P. Keene, *ibid.*, 197, 47 (1963); E. J. Hart and J. W. Boag, *J. Am. Chem. Soc.*, 84, 4090 (1962).

(6) M. Anbar and E. J. Hart, *ibid.*, 86, 5633 (1964).

(7) E. Hayon and J. Weiss, *Proc. 2nd Intern. Conf. Peaceful Uses At. Energy, Geneva, 1958*, 29, 80 (1959).

(8) E. Hayon and A. O. Allen, *J. Phys. Chem.*, 65, 2181 (1961).

(9) M. Anbar, unpublished results.

Table I: The Rate of Reaction of e_{aq}^- with Haloaliphatic Compounds

Compound	Concn., $M \times 10^3$	k, M^{-1} sec.$^{-1}$	Relative rate, $k_{RX}/k_{ClCH_2CH_2CH_2CH_3}$
CH_3COO^-	100	$2.0 + 0.5^a \times 10^{6b}$	...
FCH_2COO^-	40	$2.0 + 0.5^a \times 10^6$	0.007
F_3CCOO^-	100	$2.6 + 0.6^a \times 10^6$	...
$ClCH_2CH_2CH_2CH_3$	0.50	$3.2 \pm 0.4 \times 10^{8c}$	1.00
$CH_3CHClCH_2CH_3$	0.50	$5.1 \pm 0.8 \times 10^{8c}$	1.60
$ClCH_2CH_2OH$	0.50	$4.1 \pm 0.6 \times 10^8$	1.28
$ClCH_2CH_2COO^-$	0.50	$4.0 \pm 0.4 \times 10^8$	1.25
$CH_3CHClCOO^-$	0.50	$1.4 \pm 0.2 \times 10^9$	4.38
$ClCH_2COO^-$	0.50	$1.2 \pm 0.15 \times 10^9$	3.75
$ClCH_2C_6H_5$	0.20	$5.5 \pm 0.5 \times 10^9$	17.2
Cl_3CCOO^-	0.10	$8.5 \pm 1.0 \times 10^9$	26.6
$Cl_3CC_6H_5$	0.10	$8.3 \pm 0.9 \times 10^9$	26.0
Cl_3CH	0.02	$3.0 \pm 0.5 \times 10^{10d}$	94
Cl_3CCl	0.01	$3.0 \pm 0.5 \times 10^{10d}$	94
$BrCH_2CH_2OH$	0.50	$1.6 \pm 0.2 \times 10^9$	5.0 (1.0)[e]
$BrCH_2CH_2COO^-$	0.30	$2.7 \pm 0.3 \times 10^9$	1.68[e]
$CH_3CHBrCOO^-$	0.30	$5.3 \pm 0.8 \times 10^9$	3.4[e]
$BrCH_2COO^-$	0.167	$6.2 \pm 0.7 \times 10^9$	3.9[e]
$ICH_2CH_2COO^-$	0.067	$6.6 \pm 0.9 \times 10^9$	20.6 (1.0)[f]
ICH_2COO^-	0.10	$1.15 \pm 0.10 \times 10^{10}$	1.75[f]

[a] Upper limit of rate constant (see ref. 6). [b] Value given for comparison. [c] Value taken from ref. 5. [d] Value taken from ref. 4. [e] Relative rate toward $BrCH_2CH_2OH$. [f] Relative rate toward $ICH_2CH_2COO^-$.

This relation suggests an analogy between the $e_{aq}^- + RX$ and SN2 substitution reactions

$$Y^- + RX \longrightarrow RY + X^- \qquad (1)$$

since a relative reactivity of 5×10^{-3}:1:50:150 holds for a large number of systems.[10] This analogy does not hold, however, when the effect of substituents on the halogen carrying carbon atom is examined. In SN2 substitution, the secondary chloride reacts slower by a factor of 30–50 than the corresponding primary isomer[10,11a] in contrast with an enhancement by a factor of 1.6 in the e_{aq}^- reactions. The rate of nucleophilic substitution of chlorine on $ClCH_2CH_2OH$ is 0.1–0.2 of that on *n*-BuCl[1c] as compared with an enhancement by a factor of 1.3 for the e_{aq}^- reaction. The addition of a chlorine atom to the α-carbon has a retarding effect on the SN2 substitution,[10,11b] whereas it enhances the e_{aq}^- reaction by two orders of magnitude. Therefore, the similarity between the e_{aq}^- reactions and bimolecular nucleophilic substitutions is superficial.

The over-all reaction

$$e_{aq}^- + RX \longrightarrow R + X^- \qquad (2)$$

which formally resembles reaction 1, is expected to exhibit a solvent effect, provided reaction 2 is the rate-determining step of the e_{aq}^- interaction. As the free energy of hydration of e_{aq}^- is -40 kcal.[12] and more positive than the -70.7 kcal./mole for chloride,[13] an enhancement of the rate of reaction 2 is expected when the polarity of the solvent is increased.[14] The rate of reaction of benzyl chloride with e_{aq}^- has been measured in water, methanol,[15] and ethanol,[15] and the rate constants are 5.5, 5.0, and 5.1×10^9 M^{-1} sec.$^{-1}$, respectively. The solvation energy of the electron in water and ethanol is comparable, a result deduced from their similar absorption spectra.[15] This lack of dependence of rate on dielectric constant of the solvent indicates that the activated complexes are equally solvated. This is not surprising, assuming the formation of a large poorly solvated carbanion as the intermediate product of the e_{aq}^- reaction. In the case of naphthalene, the formation of the naphthalide ion has been demonstrated[16] and the rate of its formation was found equal in ethanol and in water.[6,16] The formation of a chloride ion from benzyl chloride as the rate-determining step would imply a solvent effect owing to the difference in ΔH of solvation of Cl^- in the different solvents.[14] If a carbanion would be formed in a fast pre-equilibrium

$$e_{aq}^- + C_6H_5CH_2Cl \rightleftharpoons C_6H_5CH_2Cl^-$$

followed by the decomposition of the latter in the rate-determining step

$$C_6H_5CH_2Cl^- \longrightarrow C_6H_5CH_2\cdot + Cl^- \quad (SN1 \text{ mechanism})$$

one would expect a *substantial* increase in the rate for solvents of greater polarity.[10] On the other hand, if $C_6H_5CH_2Cl^-$ is formed as an intermediate in the rate-determining step, only a negligible solvent effect is expected.

The formation of RX^- as an intermediate is, in fact, an oxidation–reduction reaction by which RX is reduced to $R + X^-$. Considering it still as a nucleophilic interaction, it remains to be determined whether the reactive center is the carbon atom, as in classical nucleophilic substitution, or the halogen atom. The former mechanism would imply an enhancement of the

(10) A. Streitwieser, *Chem. Rev.*, **56**, 571 (1956).

(11) (a) J. Hine, "Physical Organic Chemistry," McGraw-Hill Book Co., Inc., New York, N. Y., 1956, p. 158; (b) *ibid.*, pp. 131–133.

(12) J. H. Baxendale, *Radiation Res. Suppl.*, **4**, 139 (1964).

(13) G. E. B. Randles, *Trans. Faraday Soc.*, **52**, 1573 (1956).

(14) C. K. Ingold, "Structure and Mechanism in Organic Chemistry," Cornell University Press, Ithaca, N. Y., 1953, p. 345.

(15) I. A. Taub, D. A. Harter, M. C. Sauer, and L. M. Dorfman, *J. Chem. Phys.*, **41**, 979 (1964).

(16) S. Arai and L. M. Dorfman, *ibid.*, **41**, 2190 (1964).

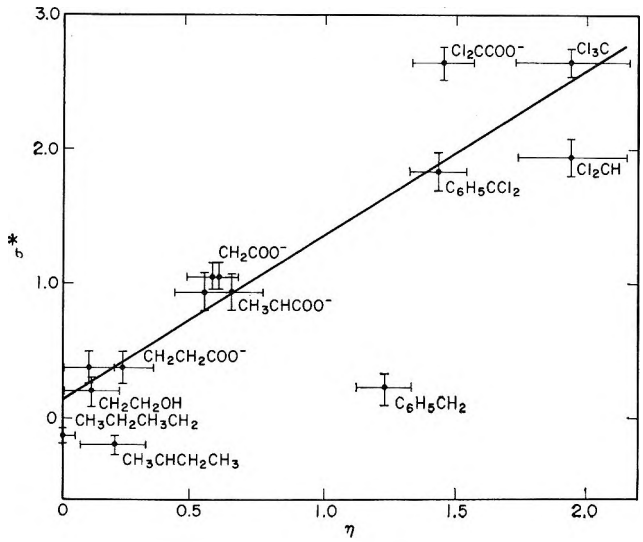

Figure 1. Plot of η as a function of σ^*.[20]
$\eta = \log [k_{RX + e_{aq}^-}/k_{Cl(CH_2)_3CH_3 + e_{aq}^-}]$

rate with increasing polarization of the C^+–X^- bond. In other words, the order of reactivity should be RF > RCl > RBr > RI, owing to the increase in electronegativity of the halogens.[17] Since the reverse order is found, an interaction of e_{aq}^- with the halogen atom as the reactive center is likely. It is also plausible that the extra electron in RX^- resides mainly on the halogen as the saturated carbon will show no tendency to accommodate an additional electron.

Because the electron affinities of the halogens are comparable (3.63, 3.78, 3.54, and 3.24 v. for F, Cl, Br, and I, respectively[17,18]), the rate of e_{aq}^- reactions does not depend on this factor. A parameter which is more likely to affect the rate of reaction of e_{aq}^- with a given halogen atom is the polarizability of the atom, which substantially increases in the halogen series from fluorine to iodine. Taking the monohaloacetates, the rates of the e_{aq}^- reactions are 2×10^6, 1.2×10^9, 6.2×10^9, and 1.15×10^{10} M^{-1} sec. $^{-1}$, compared with the values of 0.38, 2.28, 3.34, and 5.11×10^{-24} cm.^{3} for the atomic polarizabilities of F, Cl, Br, and I, respectively.[19a] In other words, the probability of an electron to be incorporated in a given halogen atom increases with its size and number of atomic orbitals. As the polarity of the C–X bond decreases in the series F to I,[17,19b] there is also a tendency toward greater electrophilic nature of the halogens.

Following this line of reasoning, one expects an increase in electrophilic character of the halogen atom induced by neighboring electron-withdrawing groups. The electron withdrawal capacity of a given group may be expressed in terms of Taft's σ^*-function.[20] Bimolecular rate constants of the e_{aq}^- + RCl reaction have been related to that of e_{aq}^- + *n*-BuCl yielding η-values, where $\eta = \log [k_{RX}/k_{n\text{-BuCl}}]$. Likewise, rate constants of the RBr reactions were related to that of $OHCH_2CH_2Br$. The η-values were then compared with σ^*-values taken or calculated from Taft's data (Table II). Plotting η against σ^* (Figure 1), a satisfactory correlation is obtained with the exception of $C_6H_5CH_2Cl$ which reacts faster than expected. The higher reaction rate of benzyl chloride may be explained by an additional interaction of e_{aq}^- with the aromatic ring.[6] The relation between η- and σ^*-values is satisfactory but it is far from perfect, which suggests that additional parameters may contribute to the rate of e_{aq}^- interaction with the aliphatic halogen. Yet the changes in electron density that are induced on the halogen atom by neighboring groups are probably the major factor in these e_{aq}^- reactions.

In a previous paper,[6] we pointed out that the reaction of e_{aq}^- with aromatic compounds is characterized by a nucleophilic attack on an available or induced electrophilic center on the organic molecule. An anion may then form as a primary product. The same mechanism applies to the reactions of e_{aq}^- with haloali-

Table II: A Correlation of Relative Rates of the RX + e_{aq}^- Reaction with the σ^* Function

R	$\eta = \log \frac{k_{RX}}{k_{n\text{-BuCl}}}$	σ^*
$CH_3CH_2CH_2CH_2\cdot$	0.00	−0.13
$CH_3\dot{C}HCH_2CH_3$	0.20 ± 0.12	−0.19
$\cdot CH_2CH_2OH$	0.11 ± 0.10	+0.20[a]
$\cdot CH_2CH_2COO^-$	0.10 ± 0.10	0.38[a]
$CH_3\dot{C}HCOO^-$	0.64 ± 0.12	0.95[b]
$\cdot CH_2COO^-$	0.57 ± 0.10	1.05
$C_6H_5\dot{C}H_2$	1.23 ± 0.10	0.215
$C_6H_5\dot{C}Cl_2$	1.43 ± 0.12	1.82[c]
$Cl_2\dot{C}COO^-$	1.45 ± 0.12	2.65[d]
$H\dot{C}Cl_2$	1.97 ± 0.22	1.94
$Cl_3C\cdot$	1.97 ± 0.22	2.65
$\cdot CH_2CH_2OH$	0.00[e]	+0.20
$\cdot CH_2CH_2COO^-$	0.23 ± 0.12[e]	0.38[a]
$CH_3\dot{C}HCOO^-$	0.53 ± 0.13[d]	0.95[b]
$\cdot CH_2COO^-$	0.59 ± 0.12[d]	1.05

[a] $\sigma^*_{RCH_2}$ calculated from $\sigma^*_R/2.8$.[16] [b] Calculated from $\sigma^*_{CH_2COOH} - \sigma^*_{C_2H}$. [c] Calculated from $\sigma^*_{CCl_3} - \sigma^*_{CH_2Cl} + \sigma^*_{C_6H_5CH_2}$. [d] Calculated from $\sigma^*_{CCl_3} - \sigma^*_{CH_2Cl} + \sigma^*_{CH_2COOH}$. [e] Related to $BrCH_2CH_2OH$.

(17) H. O. Pritchard and H. H. Skinner, *Chem. Rev.*, **55**, 745 (1955).

(18) H. O. Pritchard, *ibid.*, 52, 529 (1953).

(19) (a) L. M. Ferguson, "The Modern Structural Theory of Organic Chemistry," Prentice-Hall, Inc., Englewood Cliffs, N. J., 1963, p. 199; (b) *ibid.*, p. 200.

(20) R. W. Taft, "Steric Effects in Organic Chemistry," M. S. Newman, Ed., John Wiley and Sons, Inc., New York, N. Y., 1956, Chapter 13.

phatic compounds, but in this system the halogen atom becomes the reactive center toward e_{aq}^-. A similar behavior of haloaliphatic compounds is found in the oxidation of chromous ions which involves the halogen atom as the reactive center.[21] The electrophilic nature of organically bound halogen atoms is a latent property which may be exhibited only in the presence of an extremely reactive reducing agent. Thus in the case of haloaliphatic compounds, e_{aq}^- is not only the simplest and most reactive nucleophile but also the most elementary reducing agent in aqueous solutions. As far as reduction reactions are concerned, e_{aq}^-, with its oxidation–reduction potential of <2.7 v.[12] is capable of reducing the halogen atom while being nonreactive toward the saturated carbon atom.

It is believed that the rate of reaction of the hydrated electron with a given molecule is directly correlated with the free energy change of the system. Consequently, in a homologous series, the rate data of the e_{aq}^- reaction provide a relative measure of the oxidation potential of the reactants as long as the rates do not become diffusion controlled. This conclusion cannot be easily verified as the given reactions are not reversible and no thermodynamic data on the primary products are available.

One may look at the e_{aq}^- reactions as a process by which a negative charge, which is highly dispersed in solution,[12] is localized on a molecule which traverses its sphere of action. The probability of localization of the negative charge on the given molecule depends on the availability of an electrophilic center or of a vacant orbital on the acceptor. The rate of reaction of e_{aq}^- which is proportional to this probability is determined by the electron distribution in the substrate molecule as well as by its polarizability in the presence of the external negative charge of e_{aq}^-. The fate of the negatively charged species formed in this reaction, whether it possesses a finite stability or undergoes immediate dissociation, is of secondary importance as far as the e_{aq}^- reactivity is concerned. An understanding of the mechanism of reaction of e_{aq}^- with chemical compounds may throw light on their chemical properties as oxidizing agents and reveal their electrophilically reactive centers.

Acknowledgment. We appreciate the technical assistance of Miss P. Walsh and the cooperation of Messers B. E. Clifft and E. R. Backstrom of the Linac group.

(21) M. Anbar and E. J. Hart, to be published.

Studies on the Triplet–Triplet Energy Transfer to Rare Earth Chelates[1a]

by M. L. Bhaumik

Electro-Optical Systems, Incorporated, Pasadena, California

and M. A. El-Sayed[1b]

University of California, Los Angeles, California[1c] (*Received July 31, 1964*)

Intermolecular triplet–triplet energy transfer between aromatic carbonyls and aromatic hydrocarbons as donors and rare earth chelates as acceptors is demonstrated. This is accomplished by observing the phosphorescence from the triplet level of gadolinium chelate, as well as the intramolecularly sensitized emission of the Eu^{3+} ion in europium hexafluoroacetylacetonate. The transfer is shown to be diffusion controlled. The possibility of the transfer taking place *via* actual chemical reaction is discussed, but evidence indicates it to be highly improbable for the chelate–benzophenone system. The transfer from the benzophenone triplet level to the chelate triplet level is not found to be more efficient than that between benzophenone and naphthalene. This indicates that the heavy ion has little effect on the transfer probability. At concentrations of $\sim 10^{-3}$ mole/l. the transfer between the ketone and the europium chelate triplet levels is found to be more efficient than the transfer between ketone and the bare Eu^{+3} ion. At higher concentrations, however, a rather efficient transfer of energy from the ketone to the ion is observed. Application of the last class of material for laser purposes is discussed.

1. Introduction

Energy transfer between excited and unexcited molecules has been observed spectroscopically as well as chemically. Two types are generally distinguishable,[2] depending upon the multiplicity of the excited state of the donor, which should be the same as that of the acceptor in order to conserve spin selection rules in the transfer process. The first type is the singlet–singlet energy transfer, and the second one is the triplet–triplet energy transfer. Both the coulombic and the exchange terms are involved in the mechanism of the first type of transfer, whereas only an exchange type mechanism can account for the triplet–triplet transfer. The coulombic term can be expanded to give rise to a dipole–dipole type of interaction between the transition moments of the donor and the acceptor. This term usually dominates the exchange term for allowed transitions and gives rise to the observed fact that singlet–singlet transfer probability is orders of magnitude larger than triplet–triplet transfer. The actual efficiency of the triplet–triplet transfer can, however, be quite high because of the long lifetime of the triplet state.

The main interest of this work was triplet–triplet energy transfer. This was first observed[3] in glasses at concentrations of $\sim 10^{-2}$ M between aromatic ketones as donors and aromatic hydrocarbons as acceptors. Recently, the geometry of the donor–acceptor pair in these systems, which possess the maximum transfer probability, has been established using polarization measurements.[4] Triplet–triplet energy transfer in fluid media was detected using flash techniques[5] by observing the triplet–triplet absorption of the acceptor when sensitized by transfer from the donor.

In rare earth chelates, the phenomena of intramolecular energy transfer, $S_{ligand} \rightsquigarrow T_{ligand} \rightsquigarrow$ rare earth ion levels, has been illustrated by observing the red lines

(1) (a) Work supported in part by Rome Air Development Center, Rome, N. Y., under Contract AF 30(602)-3440; (b) consultant to Electro-Optical Systems, Inc.; (c) contribution No. 1738.

(2) D. L. Dexter, *J. Chem. Phys.*, **21**, 836 (1951).

(3) A. N. Terenin and V. Ermolaev, *Trans. Faraday Soc.*, **52**, 1042 (1956).

(4) J. K. Roy and M. A. El-Sayed, *J. Chem. Phys.*, **40**, 3462 (1964).

(5) G. Porter and M. R. Wright, *J. chim. phys.*, **55**, 705 (1958).

of Eu^{3+} when the ligand was excited.[6-12] The intramolecular energy transfer is shown to proceed *via* the triplet state. This is shown[6,8] by chemically perturbing the relative positions of the lowest triplet level and the rare earth levels. Only those chelates having a triplet level above the rare earth levels are found to transfer the energy by an intramolecular process.[12a]

By adding a donor, which possesses a triplet level above the triplet state of the chelate, the rare earth ion emission is expected to appear following the process $T_{donor} \rightsquigarrow T_{chelate} \rightsquigarrow$ rare earth ion levels $\rightarrow$ red emission. This has been recently demonstrated[13] in the system having benzophenone as donor and europium hexafluoroacetylacetonate as acceptor.

In this paper a general discussion in terms of new, extended data is given. General conclusions concerning the effect of temperature, viscosity, and the heavy ion on the transfer probability are given. Because of their unique properties, laser applications of some of these materials are examined.

2. Experimental Arrangement

The measurement of absorption spectra was done in a Carey 14 spectrophotometer. The luminescence measurements were carried out in an Aminco–Kiers spectrophosphorimeter modified for front surface excitation and viewing.[14] The excitation spectra are not corrected for either the source intensity distribution or the photomultiplier sensitivity. The temperature-dependence results were obtained in a specially designed cold cell in which the geometry could be kept constant during changes of either the temperature or the sample. A detailed description of the apparatus is given elsewhere.[15] The temperature was changed by first cooling the cell with liquid nitrogen and then gradually heating with hot, dry nitrogen gas. The excitation in this experiment was done with a Bausch and Lomb monochromator and a stabilized mercury arc. The quantum yields were measured by comparison with an EPA solution of europium thenoyltrifluoroacetonate whose efficiency was measured earlier and found[16] to be 22% at 300°K. The europium and gadolinium hexafluoroacetylacetonates were prepared by an aqueous method. A solution of hexafluoroacetylacetone and an equivalent amount of ammonium hydroxide dissolved in water was mixed with an aqueous solution of either europium or gadolinium chloride. The precipitated products were filtered, washed with water to remove ammonium chloride, and recrystallized from a mixture of ether and hexane to yield either europium hexafluoroacetylacetonate (EuHFA) with melting point of 181–182° or gadolinium hexafluoroacetylacetonate (GdHFA) with melting point of 202–203°.

The chemical analysis of the EuHFA gave C, H, and Eu_2O_3 to be 22.2, 1.4, and 22.8%, respectively, and, therefore, is characterized as europium trishexafluoroacetonate dihydrate. The percentage of C, H, and Gd_2O_3 in GdHFA was found to be 22.17, 1.37, and 22.29, respectively, and, therefore, this compound is also characterized as gadolinium trishexafluoroacetylacetonate dihydrate.

Benzophenone, acetophenone, and naphthalene were Eastman White Label chemicals and were used without any further purification. Triphenylene was obtained from K and K Laboratories. EPA (ether–isopentane–ethanol, 5:5:2) was obtained from American Instrument Co.

3. Results and Discussion

3.1 Intermolecular Energy Transfer to the Chelate Triplet State. The sensitization of the triplet level of a certain molecule can be directly observed by detecting the phosphorescence of the molecule following the sensitization process. To observe the sensitization of a chelate in this way, a rare earth ion should be used whose resonance level is higher than the lowest triplet level of the chelate; otherwise, the long-lived phosphorescence will be quenched by a fast intramolecular energy-transfer process. Gadolinium chelates satisfy this condition. Also, a rigid medium should be used in order to eliminate the diffusion-controlled quenching processes, but this also decreases the diffusion radius of the donor and acceptor. Because of this fact, and the small transition probability of triplet–triplet energy transfer, a high concentration ($\sim 10^{-2}$ to 10^{-1} M) of the donor and acceptor is used. In the present experiment, gadolinium HFA has been used as an acceptor and benzophenone as a donor in EPA glass at 77°K.

(6) R. E. Whan and G. A. Crosby, *J. Mol. Spectry.*, **8**, 315 (1962).

(7) S. I. Weissman, *J. Chem. Phys.*, **10**, 214 (1942).

(8) G. A. Crosby, R. E. Whan, and R. M. Alire, *ibid.*, **34**, 743 (1961).

(9) A. N. Sevchenko and A. Trofimov, *Zh. Eksperim. i Teoret. Fiz.*, **21**, 220 (1951).

(10) A. N. Sevchenko and A. G. Morachevsky, *Izv. Akad. Nauk SSSR, Ser. Fiz.*, **15**, 628 (1951).

(11) G. A. Crosby and M. Kasha, *Spectrochim. Acta*, **10**, 10 (1958).

(12) G. A. Crosby and R. E. Whan, *J. Chem. Phys.*, **36**, 36 (1962).

(12a) Note Added in Proof. As was pointed out recently [M. Kleinerman, *Bull. Am. Phys. Soc.*, 9, 265 (1964)], these results alone could not prove the above mechanism. In some chelates, however the above mechanism was supported using intermolecular quenching experiments (M. Bhaumik and M. A. El-Sayed, *J. Chem. Phys.*, in press).

(13) M. A. El-Sayed and M. L. Bhaumik, *ibid.*, **39**, 2391 (1963).

(14) W. H. Melhuish, *J. Opt. Soc. Am.*, **52**, 1256 (1962).

(15) M. L. Bhaumik, *J. Chem. Phys.*, to be published.

(16) M. L. Bhaumik and C. L. Telk, *J. Opt. Soc. Am.*, to be published.

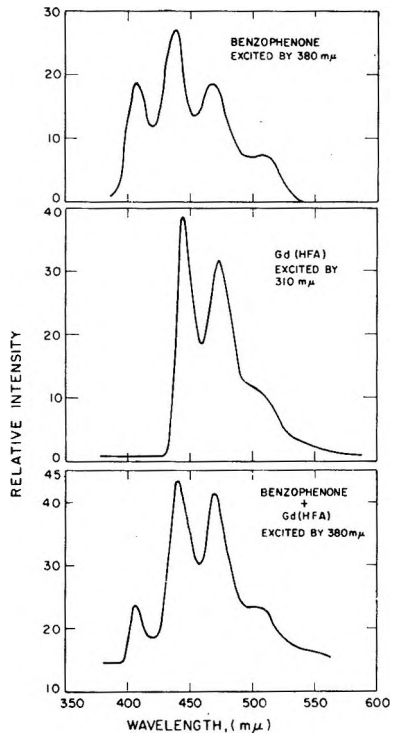

Figure 1. Phosphorescence spectra in EPA glass at 77°K. showing triplet–triplet energy transfer.

Figure 1 illustrates the phenomena of the triplet–triplet energy transfer. The upper curve is the phosphorescence of benzophenone alone. The middle curve shows the phosphorescence spectrum of Gd(HFA) excited alone in its own absorption band (3100 Å.). The lower curve is the observed emission when a mixture of benzophenone and Gd(HFA) is excited in the benzophenone absorption band at 3800 Å. It is obvious that the latter emission is composed of a mixture of benzophenone phosphorescence and the sensitized phosphorescence of Gd(HFA). It is further observed that, by adding Gd(HFA), the intensity of the benzophenone emission, as measured from its nonoverlapping, shortest wave length band, is reduced in intensity as a result of the sensitization process. Excitation of Gd(HFA) alone with wave lengths used to obtain the latter sensitized emission gave no observed phosphorescence. The last two facts exclude the possibility of the observed Gd(HFA) emission being from direct absorption.

Examination of the Heavy-Atom Effect on the Transfer Probability. The presence of Gd in the chelate complex has reduced the phosphorescence decay time of the ligand from several seconds to $\sim 10^{-3}$ sec. It was necessary to determine whether this change in the mixing of the triplet level with the singlet character was large enough to modify the transfer mechanism from exchange to a dipolar mechanism. To determine this, a comparison experiment was carried out in which the intensities of the phosphorescence from Gd(HFA) and naphthalene (both used as acceptors) were compared when the compounds were sensitized by the same concentration of benzophenone. Naphthalene and Gd(HFA) both have equal triplet–singlet energy separation. The intensities of the sensitized phosphorescence of the naphthalene and Gd(HFA) are found to be comparable. It can be shown that the intensity ratio of the sensitized emissions of the two compounds is given by the ratio of the rate constants of the transfer process from benzophenone, only if the ratio of the observed to the radiative lifetimes is the same for naphthalene and the chelate. It is very probable that the latter requirement is not satisfied and that the observed lifetime is mostly radiative for the chelate but not for naphthalene. If this is the case, the results then indicate that the transfer to naphthalene is more efficient than that to the gadolinium chelate. This observation strongly suggests that the heavy gadolinium ion *does not enhance the intermolecular triplet–triplet energy-transfer process.*

3.2 Inter–Intramolecular Transfer to the Rare Earth Ion in the Chelates. Aromatic Carbonyls as Donors. If the triplet state of the chelate is situated above the resonance level of the rare earth ion, a fast intramolecular energy-transfer process between the two levels takes place. As a result, emission from the rare earth ion replaces the chelate phosphorescence. Since the emission is due to transition in the inner 4f-shells, it can be observed even in fluid media at room temperature. In a previous communication,[13] the intermolecular energy transfer from benzophenone to Eu(HFA) was indicated. In this paper, this and other related systems were studied in greater detail.

Figure 2 shows the activation curves of different donors mixed individually with Eu(HFA). These curves are obtained when the analyzing monochromator is adjusted on the wave length of the red lines of Eu^{3+}. The Eu(HFA) has a symmetric absorption curve in the near-ultraviolet. In all the cases where a donor is present with Eu(HFA), a shoulder appears on the long wave length side of the strong Eu(HFA) absorption peak, which is due to the donor n,π^* absorption. Benzophenone, acetophenone, and benzaldehyde (not shown in Figure 2) all have their triplet levels above the triplet level of the chelate, and they all transfer their triplet excitation to the chelate levels. Cases where the triplet level of the chelate was above that of the donor were also studied, and no transfer was observed. This is discussed in the subsection on the nature of the sensitization of the Eu red lines.

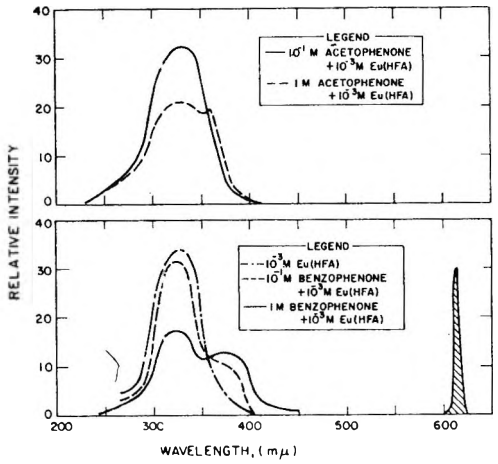

Figure 2. Activation curves of the red europium emission with two donors at various concentrations showing inter–intramolecular energy transfer; shaded line shows the europium emission.

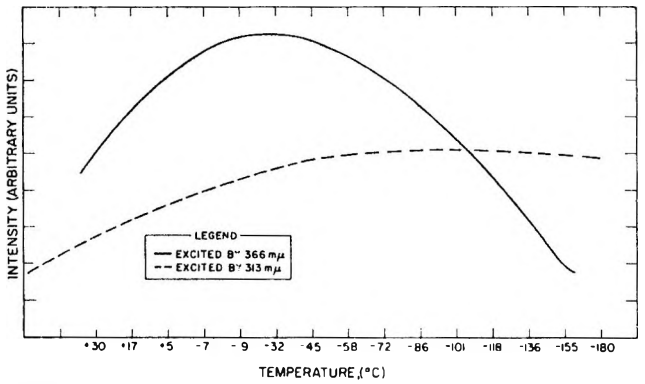

Figure 3. Intensity of europium emission at 613 mμ from EPA solutions as a function of temperature. The solid curve gives the emission from a mixture of 10^{-1} *M* benzophenone and 10^{-4} *M* Eu(HFA); the dotted curve gives the emission from 10^{-4} *M* Eu(HFA). Relative intensities of the two curves should not be compared.

Diffusion-Controlled Transfer. It is found that the inter–intra transfer, being observed in fluid media, takes place at lower concentrations than those used in glasses at 77°K. This indicates that the transfer is diffusion controlled. This conclusion has been substantiated further by studying the effect of temperature, concentration, and degassing on the transfer efficiency.

Figure 3 shows the dependence of the intensity of the Eu^{3+} red light from a mixture of Eu(HFA) (10^{-3} *M*) and benzophenone (10^{-1} *M*) on temperature. The broken line shows the behavior of the intensity of Eu^{3+} lines when the mixture is excited at 3140 Å., where the chelate absorbs. As the temperature decreases, the intensity increases because of a decrease in the intermolecular, diffusion-controlled quenching by oxygen. At low enough temperatures (depending upon the concentration of the quencher, as well as Eu(HFA)) the intensity remains constant. At this temperature, the diffusion radius of the quencher is reduced enough so that its probability of meeting an excited ion before it emits is greatly reduced.

The solid curve in Figure 3 shows the behavior of the intensity of the red Eu^{3+} light of the chelate when it is sensitized by benzophenone excitation at 3600 Å. *via* an inter–intramolecular energy-transfer process. The appearance of a maximum in the curve points out the fact that the diffusion-controlled, intermolecular energy-transfer process competes with another opposing diffusion-controlled process. The latter is the quenching at the donor triplet state. As the temperature decreases, the donor lifetime increases (because of decrease in the probability of the quenching process). This has the effect of increasing the transfer rate. On the other hand, decreasing the temperature increases the viscosity and decreases the diffusion radius of the donor and acceptor. This decreases the transfer rate. As a result of these two opposing processes, a maximum is obtained in the curve showing the transfer probability as a function of temperature. This also proves the diffusion-controlled nature of the intermolecular energy-transfer process.

Another observed fact that supports the preceding arguments is the effect of degassing on the intensity of the red lines. It is found that, whereas degassing of a solution of Eu(HFA) alone does not change the intensity of the red Eu^{3+} lines, degassing of a solution containing a mixture of benzophenone (10^{-1} *M*) and Eu(HFA) (10^{-3} *M*) is found to increase the intensity of the intermolecularly sensitized Eu^{3+} lines at room temperature. This indicates that, at the concentration of O_2 dissolved at room temperature in EPA, the rate of quenching is much slower than the rate of the intramolecular energy-transfer process ($T_{chelate} \rightsquigarrow$ rare earth ion levels) while it competes with the diffusion-controlled intermolecular energy-transfer process ($T_{benzophenone} \rightsquigarrow$ chelate).

The dependence of the transfer efficiency, as measured from the intensity of the sensitized red lines, on the concentration of both the donor and the acceptor was also studied. According to expectation of the bimolecular nature of the transfer, as the concentration of the donor or that of the acceptor increases, the rate of the transfer increases. Figure 4 shows the combined effects of both the temperature and the concentration of the acceptor, keeping the concentration of the benzophenone constant at 10^{-1} *M*.

Possibility of a Chemical Reaction. All the donors used have carbonyl groups that might chemically re-

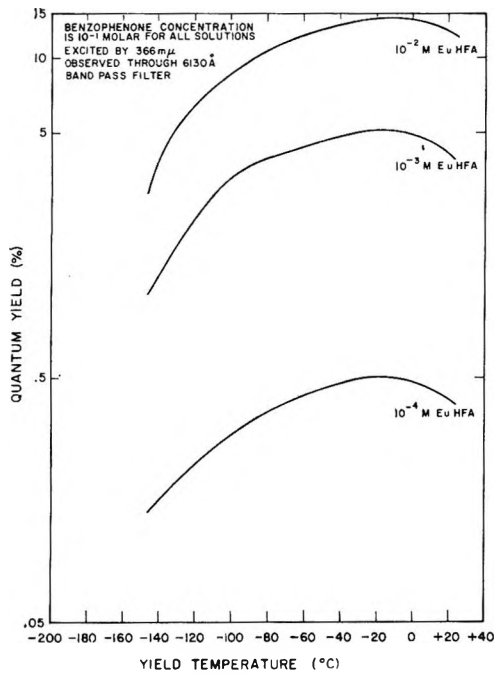

Figure 4. Quantum yield of europium emission from mixtures of benzophenone and Eu(HFA) in EPA at various temperatures and acceptor concentrations after excitation in the benzophenone absorption band at 377 mμ.

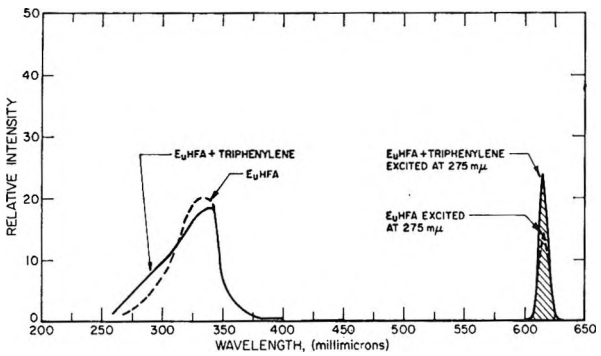

Figure 5. Activation curve of the red europium emission from an EPA solution of Eu(HFA) and triphenylene at 300°K.; shaded curves show europium emission.

act with the rare earth ion of the chelate. The transfer would then be due to the formation of actual stable chemical bonds rather than a small temporary overlap of charges during the transfer process. The following several observations, however, might rule out the possibility of a chemical reaction. (1) Solutions of 10^{-1} M benzophenone and 10^{-3} M $EuCl_3$ show lower efficiency of transfer. This has also been repeated in a solvent in which Eu^{3+} has higher quantum yield. (2) The activation curve of mixtures of benzophenone and Eu(HFA) is a simple superposition of the absorption of benzophenone and Eu(HFA). (3) The absorption curve of a mixture of the donor and acceptor is simply the superposition of the absorption spectra of the two compounds separately. (4) The intermolecular energy-transfer process is observed with aromatic hydrocarbons as donors (see the following subsection).

Aromatic Hydrocarbons as Donors. To support further the hypothesis that the transfer was not due to actual chemical binding, compounds with low complexing tendencies were used as donors. Of course, the energy condition of the transfer must be satisfied; *i.e.*, the donors must have a triplet level above the triplet level of the chelate. Also, the absorption curves of the donor and acceptor must be separated in a certain wave length range. Triphenylene was found to be a suitable donor for Eu(HFA). Figure 5 shows the activation curves obtained when the analyzing monochromator is set at the maximum of the red emission at 613 mμ. The activation curve of HFA alone is compared with that of the mixture. It is clear that, in the lower wave length region, the mixture has higher intensity, and the difference between the intensity of the two curves is due to the sensitization of the red lines with triphenylene. The maximum difference in the intensity of the two activation curves occurs at ~2700 Å.

An examination of the intensity of the red lines, as shown in Figure 5, shows that a strong europium emission is obtained when a mixture of Eu(HFA) and triphenylene is excited at 275 mμ (where triphenylene absorbs strongly and Eu(HFA) absorbs weakly). The intensity of the red light emitted from Eu(HFA) alone when excited at 275 mμ is almost one-half that resulting from intermolecular sensitization.

However, the question may arise whether this sensitization is due to singlet–singlet transfer between triphenylene and Eu(HFA) since there is an overlap (although quite small) between the donor fluorescence and acceptor absorption. Examination of the temperature dependence of the sensitization in this system shows that the transfer is mostly diffusion controlled. Also the triplet–triplet transfer efficiency in triphenylene and other aromatic systems has been observed[17] to be more efficient compared to the singlet–singlet energy transfer both in crystals[17] and in EPA glass.[18] This is undoubtedly true for triphenylene since the efficiency of singlet–triplet crossover in this case is very high. All this evidence favors a triplet–triplet transfer mechanism for the sensitization of the chelate by triphenylene.

(17) R. M. Hochstrasser, *Rev. Mod. Phys.*, **34**, 531 (1962); M. A. El-Sayed, M. T. Wauk, and G. W. Robinson, *Mol. Phys.*, **5**, 205 (1962).

(18) N. K. Chaudhuri and M. A. El-Sayed, *J. Chem. Phys.*, in press.

It is rather hard to visualize the complex formation between triphenylene and Eu(HFA). The observation of the sensitization of europium by triphenylene thus adds further support for the energy-transfer process between the donor and the acceptor being due to an intermolecular process.

Nature of the Sensitization of the Eu Red Lines. We have previously shown that adding a donor to Eu(HFA) resulted in the appearance of the sensitized red light due to an intermolecular energy-transfer process. The question, of course, arises whether this sensitization proceeds according to mechanism I or II below.

$$T^*_{donor} \rightsquigarrow T^*_{chelate} \rightsquigarrow (Eu^{3+})^* \rightarrow \text{emission} \quad \text{(I)}$$

or

$$T^*_{donor} \rightsquigarrow (Eu^{3+})^* \rightarrow \text{emission} \quad \text{(II)}$$

The following observations might indicate that the sensitization is mainly due to mechanism I.

(1) Experiments are carried out where the chelate acceptor has not satisfied the energy conditions for the transfer with respect to the triplet levels but has satisfied it with respect to the central ion levels. Benzophenone has its triplet level close to the triplet level of terbium acetylacetonate (TbAA) but still higher than the rare earth ion. Sensitization of the terbium emission is not observed in this case. On the other hand, terbium hexafluoroacetylacetonate, having a triplet level lower than that of benzophenone, is sensitized by the latter. This shows that it is the triplet state of the chelate which should satisfy the energy consideration, and, therefore, the intermolecular energy transfer must proceed to the triplet state of the chelate.

(2) As indicated previously, mixtures of $EuCl_3$ (10^{-3} M) and benzophenone (10^{-1} M) do not show efficient red emission when excited at 3660 Å. under the same experimental conditions as those used to observe the sensitization of europium lines in the chelates. This experiment was repeated using deuterated methanol (CD_3OD) as solvent where the europium ion has a quantum yield comparable to that of the chelate. This is important since no emission will be observed from an ion with low quantum yield, even if the transfer has taken place to it.

Recently it was reported[19] that when $EuCl_3$ is dissolved in acetophenone or molten benzophenone the red europium emission can be detected after exposure of several hours. We have carried out experiments in which $Eu(NO_3)_3$ and Eu(HFA) are separately dissolved in acetophenone and excited by light absorbed by acetophenone. The dependence of the sensitized emission upon the concentration of the acceptors has been examined. The sensitized emission from Eu(HFA) is observed at a concentration less than that at which emission is observed from the Eu^{3+} ion.

Comparison of the efficiency of transfer between benzophenone and the europium ion and between benzophenone and the chelate were also done by dissolving them in CD_3OD. Since the quantum yields of the europium emission from the ion and the chelate dissolved in the preceding solvent are comparable, the emission intensity can roughly be taken as a measure of the transfer efficiency. The results indicate that the efficiency of the ketone-to-Eu(HFA) transfer is about 5–10 times higher than that from ketone to Eu^{3+} ion. A possible explanation can be found if one assumes that such transfer is proportional to the cross-sectional area of the acceptor. The ratio of the square of the radius of Eu(HFA) to that of Eu^{3+} is 5–10 (depending on the value of the rare earth radius used), which is in agreement with the observed ratio for the transfer probability.

An interesting phenomenon is observed[20] if the concentration of the europium ion is increased. At a concentration of $\sim 10^{-1}$ M benzophenone and $\sim 10^{-1}$ M $EuCl_3$, an efficient diffusion-controlled sensitization of the ion by benzophenone is observed. The fluorescence decay time and the quantum yield of this type of material are comparable to those of chelate solutions and, therefore, should be considered as liquid laser materials for operations near room temperatures. Using pure biacetylbenzene as sensitizer,[21] the quantum yield of Eu^{3+} emission in CD_3OD is measured to be 25% at 300°K. The decay time of the europium emission from this solution is 1.4 msec. The molar optical density at 375 mμ is 200.

The above material, therefore, has all the advantages of the chelate system without the problems of high absorption coefficient and the chemical decomposition. The problem of decomposition in the chelate arises mainly from the low energy of the metal–oxygen bond, of the order of a few kilocalories. This can be avoided by using the diffusion-controlled sensitized fluorescence. This new type of material, therefore, possesses superior characteristics as a laser material.

Acknowledgment. The authors wish to thank Mr. Leon Ferder for help in measurements.

(19) E. Matovitch and C. K. Suzuki, *J. Chem. Phys.*, 39, 1442 (1963).

(20) While this paper was in preparation, similar observations were reported by A. Heller and E. Wasserman and by S. P. Sinha, private communication.

(21) Note Added in Proof. There is the problem of photoreaction between the (n,π^*) triplet state of the donor and the hydroxylic solvent used. If a donor that has its lowest triplet state of the (π,π^*) type or a nonhydroxylic solvent (e.g., CD_3CN) is used, the photoreaction can be minimized.

Aqueous Solutions of Nonpolar Gases[1]

by Robert A. Pierotti

School of Chemistry, Georgia Institute of Technology, Atlanta, Georgia 30332 *(Received August 3, 1964)*

A theory of gas solubility in water has been developed using the scaled-particle theory to calculate the reversible work required to introduce a solute molecule into a fluid. It yields very good agreement with experiment for the heats, entropies, and molar heat capacities of solution and for the partial molar volumes of the solutes. The "abnormal" thermodynamic properties of aqueous solutions are discussed in light of the enthalpy and entropy of cavity formation. The theory shows promise as a method for investigating the thermodynamic properties of aqueous solutions of ions and the properties of gas solubility in molten salts and molten metals. The theory has been used to determine the Lennard-Jones (6–12) pair potential parameters for water and for benzene. The values for water are $\sigma = 2.76$ Å. and $\epsilon/k = 85.3$°K. The values for benzene are $\sigma = 5.24$ Å. and $\epsilon/k = 498$°K. These parameters are discussed in relation to values reported elsewhere.

1. Introduction

The solubility of nonpolar gases in water has been a subject of considerable experimental and theoretical interest for many years. The most recent interest stems from the importance of hydrophobic bonding in proteins and from the process of the denaturation of proteins, both of which are related to the interaction of nonpolar groups in aqueous solutions.[2a,b] Recently, a number of papers have appeared in which new and more precise data have been reported on the aqueous solutions of various nonpolar gases.[3-9] Except for the work of Némethy and Scheraga,[10] few theoretical papers have appeared since the work of Eley[11,12] and Frank and Evans.[13] These papers emphasized that a fundamental difference exists between the solubility of gases in water and in unassociated organic solvents. This difference is manifest in the large negative heats, negative entropies, and positive molar heat capacities of solution always observed for aqueous solutions. Frank and Evans[13] ascribed this difference to the formation of an ordered, hydrogen-bonded structure around the solute molecule. This model of water solvation is called the iceberg theory or the frozen-layer theory, but Frank and Evans were careful to point out that the ordered structure might not be ice-like. Némethy and Scheraga[10] have approached the problem by developing a statistical thermodynamic theory of water based upon the existence of five species of water molecules differing in their number of hydrogen bonds and then considering the perturbation of the energy levels of these species by the presence of a solute molecule. They conclude that the completely hydrogen-bonded specie is energetically favored in the first solvation layer and hence partial hydrogen-bonded cages develop around each solute molecule. It is interesting that nuclear magnetic resonance studies[14] have been unable to substantiate the existence of an ice-like structure about nonionic solutes and do not indicate any significant increase or decrease in the

(1) This work was supported in part by the National Science Foundation.

(2) (a) I. M. Klotz, *Science*, **128**, 815 (1958); (b) W. Kauzmann, *Advan. Protein Chem.*, **14**, 1 (1959).

(3) T. J. Morrison and N. B. Johnstone, *J. Chem. Soc.*, 3441 (1954).

(4) D. M. Himmelblau, *J. Phys. Chem.*, **63**, 1803 (1959).

(5) C. E. Klots and B. B. Benson, *J. Marine Res.*, **21**, 48 (1963).

(6) V. H. Konig, *Z. Naturforsch.*, **18**, 363 (1963).

(7) C. E. Klots and B. B. Benson, *J. Phys. Chem.*, **67**, 933 (1963).

(8) E. Douglas, *ibid.*, **68**, 169 (1964).

(9) D. N. Glew, *ibid.*, **66**, 605 (1962).

(10) (a) G. Némethy and H. A. Scheraga, *J. Chem. Phys.*, **36**, 3382 (1962); (b) *ibid.*, **36**, 3401 (1962).

(11) (a) D. D. Eley, *Trans. Faraday Soc.*, **35**, 1281 (1939); (b) *ibid.*, **35**, 1242 (1939).

(12) D. D. Eley, *ibid.*, **40**, 184 (1944).

(13) H. S. Frank and M. W. Evans, *J. Chem. Phys.*, **13**, 507 (1945).

(14) (a) E. A. Balazs, A. A. Bothner-By, and J. Gergely, *J. Mol. Biol.*, **1**, 147 (1959); (b) F. A. Bovey, *Nature*, **192**, 324 (1961).

degree of hydrogen bonding in water as a result of the solution process.

The solubility of gases in unassociated solvents was treated with very good success by an application of the scaled-particle theory of fluids.[15] It seemed desirable to attempt to treat aqueous solutions in essentially the same manner and without explicitly introducing any assumptions about the structure of liquid water. The scaled-particle theory makes it possible to calculate the reversible work required to introduce a hard sphere into a dense fluid and has been shown to be applicable not only to nonpolar fluids, but also to molten salts, liquid metals, and polar fluids including water.[16] One would expect the major difference between aqueous and nonaqueous solutions to be in the process of creating a position in the solvent suitable to accommodate the solute molecule. It is therefore the purpose of this paper to investigate whether or not the observed difference between the thermodynamic properties of gases dissolved in the two classes of solvents can be accounted for by means of a single theory and without recourse to models dependent upon the unique structures of solvents.

2. Theory

Thermodynamic Equations. The solution process is considered for convenience to consist of two steps[15]: (1) the creation of a cavity in the solvent of suitable size to accommodate the solute molecule and (2) the introduction into the cavity of a solute molecule which interacts with the solvent.

Associated with each step is a set of thermodynamic functions in terms of which the solution process can be described. It can be shown (see ref. 15) that for extremely dilute solutions

$$\ln K = \bar{G}_c/RT + \bar{G}_i/RT + \ln (RT/V) \qquad (1)$$

where K is the Henry's law constant, $\bar{G}_c$ and $\bar{G}_i$ are the partial molar Gibbs free energy for cavity formation and interaction, respectively, V is the molar volume of the solvent, T is the absolute temperature, and R is the gas constant. Henry's law is defined here as

$$p_2 = Kx_2 \qquad (2)$$

where p_2 is the equilibrium pressure of the solute over the solution and x_2 is the mole fraction of the solute in the solution.

The molar heat of solution is given by

$$\Delta H = \left(\frac{\partial \ln K}{\partial\, 1/RT}\right)_P = \bar{H}_c + \bar{H}_i - RT + \alpha_P RT^2 \qquad (3)$$

where $\bar{H}_c$ and $\bar{H}_i$ are the partial molar enthalpies associated with cavity formation and interaction, respectively, and α_P is the coefficient of thermal expansion of the solvent.

The molar heat capacity change for the solution process is given by

$$\Delta C_P = \left(\frac{\partial \Delta H}{\partial T}\right)_P = \bar{C}_c + \bar{C}_i - R + 2\alpha_P RT + RT^2\left(\frac{\partial \alpha_P}{\partial T}\right)_P \qquad (4)$$

where $\bar{C}_c$ and $\bar{C}_i$ are the partial molar heat capacities for cavity formation and interaction, respectively.

The partial molar volume of the solute is given by

$$\bar{V}_2 = \bar{V}_c + \bar{V}_i + \beta RT \qquad (5)$$

where β is the isothermal compressibility of the solvent.

The Expression for $\bar{G}_c$. The partial molar Gibbs free energy of creating a cavity in a fluid of hard spheres was derived by Reiss, *et al.*[16a] They obtained the expression

$$\bar{G}_c = K_0 + K_1 a_{12} + K_2 a_{12}^2 + K_3 a_{12}^3 \qquad (6)$$

where the K's are functions of the density, temperature, pressure, and hard sphere diameter of the fluid and a_{12} is the radius of a sphere which excludes the centers of the solvent molecules. The K's were evaluated to be

$$K_0 = RT\{-\ln (1 - y) + (^9/_2)[y/(1 - y)]^2\} - (\pi P a_1^3)/6$$

$$K_1 = -(RT/a_1)\{[6y/(1 - y)] + 18[y/(1 - y)]^2\} + \pi P a_1^2$$

$$K_2 = (RT/a_1^2)\{[12y/(1 - y)] + 18[y/(1 - y)]^2\} - 2\pi P a_1$$

$$K_3 = (^4/_3)\pi P \qquad (7)$$

where $y = (\pi a_1^3 \rho)/6$, ρ is the number density of fluid molecules, a_1 is the hard sphere diameter of the fluid molecules, P is the pressure, R is Avogadro's number times the Boltzmann constant, and T is the absolute temperature. The radius of the sphere (a_{12}) which excludes the centers of solvent molecules is equal to $(a_1 + a_2)/2$, where a_2 is the diameter of the cavity to be created.

(15) R. A. Pierotti, *J. Phys. Chem.*, **67**, 1840 (1963). Note: a typographical error exists in eq. 22 of this paper. It should read $\Delta H_v = RT + \alpha_P RT^2[(1 + 2y)^2/(1 - y)^3]$. This equation is not applicable to water.

(16) (a) H. Reiss, H. L. Frisch, and J. L. Lebowitz, *J. Chem. Phys.*, **31**, 369 (1959); (b) H. Reiss, H. L. Frisch, E. Helfand, and J. L. Lebowitz, *ibid.*, **32**, 119 (1960); (c) H. Reiss and S. W. Mayer, *ibid.*, **35**, 1513 (1961); (d) S. W. Mayer, *ibid.*, **38**, 1803 (1963).

The Expression for $\bar{G}_i$. The partial molar Gibbs free energy for the interaction term is taken to be equal to the molar interaction energy. This approximation amounts to neglecting $P\bar{V}_i$ and $T\bar{S}_i$ in the interaction process and should be valid for the systems considered here (see ref. 15).

The interaction energy of a nonpolar solute molecule with a polar solvent can be described in terms of dispersion, inductive, and replusive interactions. The dispersion and repulsive interactions can be adequately approximated by a Lennard-Jones (6–12) pairwise additive potential while the inductive interaction energy is given by an inverse sixth power law. The total interaction energy per solute molecule is then given by

$$\epsilon_i = -C_{dis}\left\{\sum_P (r_P^{-6} - \sigma_{12}^6 r_P^{-12})\right\} - C_{ind}\sum_P r_P^{-6} \quad (8)$$

where r_P is the distance from the center of the solute molecule to the center of the Pth solvent molecule, C_{dis} is the dispersion energy constant, C_{ind} is the inductive energy constant, and σ_{12} is the distance at which the dispersion and repulsive energies are equal in magnitude.

In order to calculate ϵ_i, it is assumed that the solute molecule is immersed in the solvent. The solvent is assumed to be infinite in extent and uniformly distributed according to its number density ρ around the solute molecule.[17] The number of molecules contained in a spherical shell a distance r from the center of the solute molecule is then equal to $4\pi\rho r^2\,dr$ where dr is the thickness of the shell. Combining this with eq. 8, dividing by kT, and replacing the summation by an integration gives

$$\epsilon_i(R)/kT = -(4\pi\rho/kT)\int_R^\infty \{(C_{dis} + C_{ind})r^{-4} - C_{dis}\sigma_{12}^6 r^{-10}\}\,dr \quad (9)$$

where R is the distance from the center of the solute molecule to the center of the nearest solvent molecule. The integration yields

$$\epsilon_i(R')/kT = (\epsilon^*_{dis} + \epsilon^*_{ind})(2/R')^3/kT - (^8/_3)(\epsilon^*_{dis}/kT)(1/R')^9 \quad (10)$$

where

$$\epsilon_i^*/kT = \pi\rho C_i/6kT\sigma_{12}^3 \quad (11)$$

and R' is equal to R/σ_{12}.

The minimum in $\epsilon_i(R')/kT$ is determined by differentiation of eq. 10. At the minimum R' is equal to the sixth root of $\epsilon^*_{dis}/(\epsilon^*_{dis} + \epsilon^*_{ind})$. Since ϵ^*_{ind} is always a small fraction of ϵ^*_{dis}, R' is very nearly unity and hence

$$\bar{\epsilon}_i/kT = \bar{E}_i/RT = \epsilon_i/kT = -5.33\epsilon^*_{dis}/kT - 8.00\epsilon^*_{ind}/kT \quad (12)$$

The value of C_{dis} may be estimated by means of the Kirkwood–Muller formula[18]

$$C_{KM} = 6mc^2\left\{\frac{\alpha_1\alpha_2}{(\alpha_1/\chi_2) + (\alpha_2/\chi_2)}\right\} \quad (13)$$

where m is the mass of an electron, c is the velocity of light, α_1 and α_2 are the molecular polarizabilities of the solvent and solute, respectively, and χ_1 and χ_2 are the molecular susceptibilities of the solvent and solute.

Alternately, C_{dis} may be evaluated in terms of the empirically determined Lennard-Jones (6–12) energy parameters using[19]

$$C_{LJ} = 4\epsilon_{12}\sigma_{12}^6 = 4(\epsilon_1\epsilon_2)^{1/2}[(\sigma_1 + \sigma_2)/2]^6 \quad (14)$$

where ϵ_1 and ϵ_2 are the energy parameters for the solvent and solute, respectively, and σ_1 and σ_2 are the distance parameters of the solvent and solute. Since the potential energy is rising very rapidly with decreasing distance at σ, the values of σ_1 and σ_2 are also effectively the values of a_1 and a_2.

The value of C_{ind} is given by[19]

$$C_{ind} = \mu_1^2\alpha_2 \quad (15)$$

where μ_1 is the dipole moment of the solvent and α_2 is the polarizability of the solute.

3. Results

The Determination of σ_{H_2O}. The substitution of eq. 12 into eq. 1 yields

$$\ln K = -5.33\epsilon^*_{dis}/kT - 8.00\epsilon^*_{ind}/kT + \bar{G}_c/RT + \ln(RT/V) \quad (16)$$

Since both ϵ^*_{dis} and ϵ^*_{ind} are related to the polarizability of the solute through eq. 13 and 15, a plot of ln K *vs.* α_2 for spherical solutes (the rare gases) should be a smooth curve. It was shown in ref. 15 that the extrapolation of such a curve to zero α_2 was equivalent to obtaining the solubility of a hard sphere of diameter 2.58 Å. This was expressed as

$$\lim_{\substack{\alpha_2 \to 0 \\ \alpha_2 \to 2.58\ \text{Å}}} (\ln K) = \ln K^c = \bar{G}_c/RT + \ln(RT/V) \quad (17)$$

(17) X-Ray diffraction studies indicate that this is a good approximation for water; see M. D. Danford and H. A. Levy, *J. Am. Chem. Soc.*, **84**, 3965 (1962). It is interesting to note that the number of nearest neighbors calculated in this manner for Ar is 20 as in the argon clathrate, whereas for He and Ne it is between 7 and 8. No clathrates of He or Ne have been found.

(18) A. Muller, *Proc. Roy. Soc.* (London), **A154**, 664 (1936).

(19) J. O. Hirshfelder, C. F. Curtiss, and R. B. Bird, "Molecular Theory of Gases and Liquids," John Wiley and Sons, Inc., New York, N. Y., 1945.

where K^0 is the Henry's law constant for hard spheres of diameter 2.58 Å. Figure 1 shows such a plot for the solubility of the rare gases in water at various temperatures.

Since the hard sphere diameter of water is not known with certainty from other sources, it seemed theoretically consistent in the present context to determine it from the value of K^0 obtained from Figure 1. Table I contains the necessary physical properties of water, while Table II contains the physical properties and parameters for a number of solute gases. The dipole moment of water was taken to be 1.84 D.

Table I: Physical Properties and Parameters of Water

	Temperature, °C.		
	4°	25°	50°
$\bar{V}$, cc./mole[a]	18.02	18.08	18.25
$\alpha_P \times 10^5$, deg.$^{-1}$[a]	0	25.5	45.9
$\beta \times 10^5$, atm.$^{-1}$[b]	...	45.5	...
σ, Å.[c]	2.75	2.75	2.75
ϵ/k, °K.[c]	85.3	85.3	85.3

[a] N. A. Lange, "Handbook of Chemistry," 9th Ed., Handbook Publishers, Inc., Sandusky, Ohio, 1956. [b] E. A. Moelwyn-Hughes, "Physical Chemistry," Pergamon Press, New York, N. Y., 1957. [c] Determined as described in the text.

Table II: Properties and Parameters for the Solutes

Solute	σ_2, Å.	ϵ_2/k, °K.	$\alpha_2 \times 10^{24}$, cc./molecule
Hard sphere	2.58[a]	0	0
He	2.63[b]	6.03	0.204[a]
Ne	2.78[b]	34.9	0.393[a]
Ar	3.40[b]	122	1.63[a]
Kr	3.60[b]	171	2.46[a]
Xe	4.10[b]	221	4.00[a]
Rn	4.36[c]	290	5.86[c]
H_2	2.87[b]	29.2	0.802[a]
N_2	3.70[b]	95	1.74[d]
O_2	3.46[b]	118	1.57[d]
CO	3.76[b]	100	1.93[d]
NO	3.17[b]	131	1.70[d]
CH_4	3.82[b]	137	2.70[d]
CF_4	4.70[b]	153	2.53[e]
CCl_4	5.88[f]	327	10.10[d]
C_2H_2	4.22[f]	185	3.19[d]
C_2H_4	4.23[f]	205	3.70[d]
C_2H_6	4.42[f]	230	4.33[d]
C_6H_6	5.27[f]	440	9.89[d]

[a] See ref. 15. [b] From second virial coefficients, ref. 19. [c] From G. A. Miller, *J. Phys. Chem.*, **64**, 163 (1960). [d] E. A. Moelwyn-Hughes, "Physical Chemistry," Pergamon Press, New York, N. Y., 1957, p. 373. [e] S. Glasstone, "Textbook of Physical Chemistry," 2nd Ed., D. Van Nostrand Co., New York, N. Y., 1951. [f] From viscosity data, ref. 19.

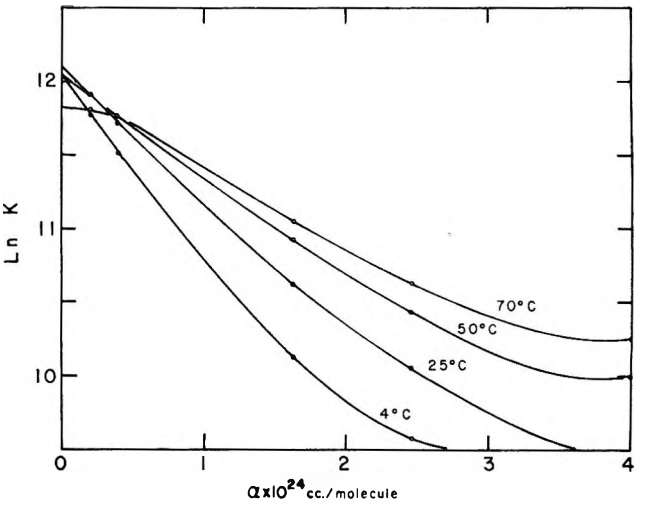

Figure 1. Experimental ln K values plotted *vs.* the polarizability of the rare gas solutes dissolved in water at various temperatures.

The values of a_{H_2O} determined in this manner were 2.75 Å. at 4, 25, and 50° and 2.74 Å. at 70°.[20,21] These values are in good agreement with values of a_{H_2O} obtained by means of an application of the scaled particle theory to compressibility data of water.[21] In that case, the values found were 2.71 Å. at 10°, 2.72 Å. at 30°, 2.71 Å. at 50°, and 2.69 Å. at 80°. Values of σ_{H_2O} from gas phase studies are 2.71 Å.[22] and 2.65 Å.[23] The oxygen–oxygen distance in ice is 2.76 Å.[24] Other values ranging from 2.50 Å.[25] up to 2.93 Å.[21] have been used or reported, but the bulk of the values center around 2.7 Å. In all subsequent calculations in this paper the value $\sigma_{H_2O} = a_{H_2O} =$ 2.75 Å. was used.

The Determination of ϵ_{H_2O}/k. As in the case of σ_{H_2O}, no single best value for ϵ_{H_2O}/k can be found in the literature. Values ranging from 167°K.[25,26] up to 775°K.[22] have been reported, but none of these seems consistent with the present treatment. The values obtained from gas phase studies using a Stockmayer potential[22] are invariably very high because they

(20) A small temperature dependence for a should be expected and the value of a should decrease with increasing temperature: H. Reiss, to be published.

(21) S. W. Mayer, *J. Phys. Chem.*, **67**, 2160 (1963).

(22) From transport properties: L. Monchick and E. A. Mason, *J. Chem. Phys.*, **35**, 1676 (1961).

(23) From the second virial coefficient: J. S. Rowlinson, *Trans. Faraday Soc.*, **45**, 974 (1949).

(24) L. Pauling, "The Nature of the Chemical Bond," 3rd. Ed., Cornell University Press, Ithaca, N. Y., 1960.

(25) J. H. van der Waals and J. C. Platteuw, *Advan. Chem. Phys.*, **2**, 1 (1959).

(26) V. McKoy and O. Sinanoğlu, *J. Chem. Phys.*, **38**, 2946 (1963).

contain contributions from more than simply dispersion forces. In addition, gas phase pair potentials are expected to be too high for use in calculations dealing with condensed phases.[27] The value 167°K. was obtained by van der Waals and Platteuw[25] by fitting the equilibrium properties of the argon clathrate to a statistical thermodynamic theory of clathrates using $\sigma_{H_2O} = 2.50$ Å. In order to compensate for the very small σ_{H_2O}, a high value of ϵ_{H_2O}/k is required. Thus we should expect a value of ϵ_{H_2O}/k smaller than 167°K. An estimate of the gas phase value of the potential parameter for water can be obtained from the polarizability and ionization energy of water using the London equation.[19] This turns out to yield $\epsilon_{H_2O}/k = 130$°K. Kestner and Sinanoğlu using third-order perturbation theory have derived formulas for estimating the correction to be applied to the gas phase parameter to obtain the corresponding value in a condensed phase. Using their equations,[28] the effective dispersion energy pair potential parameter for water in liquid water should be between 66 and 75% of the gas phase value. Therefore, a crude approximation yields that ϵ_{H_2O}/k should be between 86 and 98°K.

It is possible, using the present theory of dilute solutions, to extract the value of ϵ_{H_2O}/k from solubility data and at the same time test further the validity of eq. 7 for water. Equation 16 can be rewritten and rearranged using eq. 11, 12, and 14 to give

$$\ln K + 8.00\epsilon^*_{ind}/kT - \bar{G}_c/RT - \ln (RT/V) = -(11.17\rho/T)(\epsilon_{H_2O}/k)^{1/2}(\epsilon_2/k)^{1/2}\sigma_{12}^3 \quad (18)$$

where ϵ_2 is the Lennard-Jones energy parameter for a given solute and ρ is the number density of the solvent. The left-hand side of eq. 18 which we will designate as Δ can be calculated from experimental solubilities at a given temperature along with the known physical properties of the solutes and the solvent including σ_{H_2O} equal to 2.75 Å. A plot of $-\Delta$ *vs.* $(\epsilon_2/k)^{1/2}\sigma_{12}^3$ should be a straight line with a slope given by $(11.17\rho/T)(\epsilon_{H_2O}/k)^{1/2}$. Figure 2 shows such a graph for a large number of solutes dissolved in water at 25° and indeed a good straight line is obtained. The only gas that does not fall on or very near the line is acetylene and perhaps this is not too surprising. The value of ϵ_{H_2O}/k obtained from the slope of the line is 85.3°K. This is lower than the estimate made earlier, but considering the crudity of the theory and of the estimate, the agreement must be considered good.

In order to substantiate the present method of using gas solubility measurements for estimating the Lennard-Jones parameters for a solvent, the solubility of a number of gases in benzene was used to determine $\sigma_{\phi H}$ and

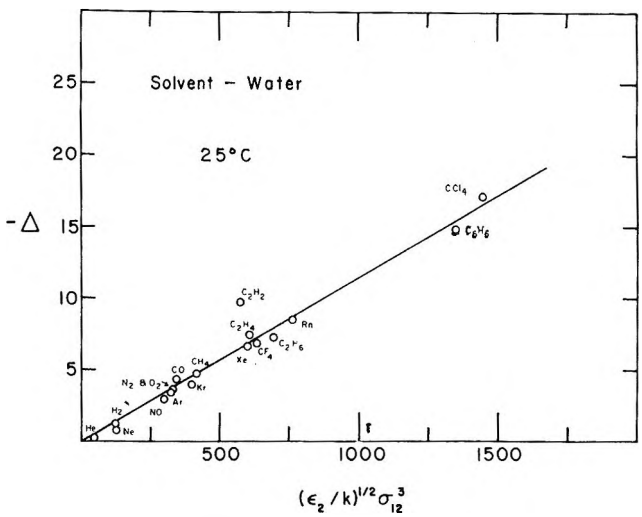

Figure 2. The function $-\Delta$ *vs.* a Lennard-Jones (6–12) solute parameter (see text).

$\epsilon_{\phi H}/k$. The data presented in ref. 15 were used for this purpose. The value of $\sigma_{\phi H}$ calculated from the intercept of the ln K *vs.* σ_2 curve was found to be 5.24 Å., while the value of $\epsilon_{\phi H}/k$ calculated from the slope of the curve $-\Delta$ *vs.* $(\epsilon_2/k)^{1/2}\sigma_{12}^3$ was 498°K. Table III compared the values of the above parameters with those determined in various other ways. The agreement is excellent with those methods which utilize the properties of the liquid state.

Table III: Comparison of Pair Potentials for Benzene Obtained from Various Sources

σ, Å.	5.24[a]	5.22[b]	5.22[c]	5.27[d]	5.26[e]
ϵ/k, °K.	498[a]	501[b]	504[c]	440[d]	494[e]

[a] Obtained from gas solubilities in the manner described in the text. [b] Obtained from the liquid state using the equation of state and the vapor pressure. [c] Obtained from the liquid state using the equation of state and the entropy. [d] Obtained from gas viscosity measurements. [e] Obtained from the cell theory of liquids of Salsburg and Kirkwood. This table except for the first column was taken from Y. Kobatake and B. J. Alder, *J. Phys. Chem.*, **66**, 645 (1962).

The Thermodynamics of the Solution Process. Calculated and experimental values of a number of thermodynamic properties are compared in Tables IV, V, and VI. Table IV compares values for the Henry's law constants at 25° obtained from eq. 1. In all cases ex-

(27) N. R. Kestner and O. Sinanoğlu, *J. Chem. Phys.*, **38**, 1730 (1963).

(28) The continuum approximation (eq. 18) was used in these calculations.

Table IV: Henry Law Constants and Gibbs Free Energies of Solution at 298°K.

Solute	Theoret. $K \times 10^4$, atm.	Exptl. $K \times 10^4$, atm.	Theoret. ΔG_{298}, cal./mole	Exptl. ΔG_{298}, cal./mole
He	10.40	14.71[a]	6820	7040
Ne	6.18	12.36[a]	6530	6930
Ar	3.10	4.10[a]	6110	6270
Kr	1.23	2.35[a]	5700	5930
Xe	1.00	1.30[a]	5450	5600
Rn	0.453	0.605[b]	5000	5130
H_2	6.58	7.10[c]	6550	6600
N_2	8.35	8.63[d]	6590	6610
O_2	4.10	4.39[d]	6270	6310
CO	9.05	5.82[c]	6750	6480
NO	1.60	2.89[c]	5730	6060
CH_4	3.94	3.92[e]	6250	6250
CF_4	16.8	27.6[a]	7110	7400
CCl_4	0.276	0.157[b]	4700	4350
C_2H_2	3.10	0.134[c]	6110	4260
C_2H_4	1.75	1.14[c]	5810	5520
C_2H_6	1.38	2.90[e]	5650	6050
C_6H_6	0.020	0.036	3130	3490

[a] See ref. 3. [b] "International Critical Tables," Vol. III, McGraw-Hill Book Co., Inc., New York, N. Y., 1928. [c] N. A. Lange, "Handbook of Chemistry," 9th Ed., Handbook Publishers, Inc., Sandusky, Ohio, 1956. [d] See ref. 8. [e] W. F. Claussen and M. F. Polglase, *J. Am. Chem. Soc.*, **74**, 4817 (1952).

cept CCl_4, C_2H_2, and C_2H_6 the predicted value is somewhat lower than the observed value. Only in the case of C_2H_4 and C_2H_6 does the predicted value of K differ from the experimental value by more than a factor of 2. In all fairness to the theory, it should be pointed out that it does much better in predicting the Gibbs free energy change associated with the solution process.

The heat of solution is given by eq. 3 in which $\bar{H}_i$ is given by eq. 12 and $\bar{H}_c$ (see ref. 15) by

$$\bar{H}_c = \alpha_P RT^2[y/(1-y)]\{[6/(1-y)][2(a_{12}/a_1)^2 - (a_{12}/a_1)] + [36y/(1-y)^2][(a_{12}/a_1)^2 - (a_{12}/a_1) + 1/4] + 1\} \quad (19)$$

Table V compares heat of solutions calculated from the present theory with observed heats at 25° wherever such heats were available. Fairly good agreement is obtained for all solutes. It should be pointed out that many of the heats are not known to better than several hundred calories per mole. Included in Table V are calculated and experimental entropies of solution at 25°. Again good agreement is achieved for most of the solutes.

The heat capacity of solution is given by eq. 4. As an approximation we take $\bar{C}_i$ to be zero. This is certainly not quite true, but the contribution to ΔC_P will

Table V: Heats and Entropies of Solutions for Aqueous Solutions at 298°K.

Solute	Theoret. $-\Delta H_{298}$, cal./mole	Exptl. $-\Delta H_{298}$, cal./mole: H[a]	F and E[c]	G and M[d]	Others	Theoret. $-\Delta S_{298}$, cal./mole-deg.	Exptl. $-\Delta S_{298}$ cal./mole-deg.: E[c]	G and M[d]	Others
He	500	390 (400)[b]	840	200	530[e]	24.6	26.5	23.8	25.0[a]
Ne	1020	1080	1880	1910	850[e]	26.3	28.8	29.2	26.9[a]
Ar	2445	3100[b]	2730	2820	2840[f]	28.7	30.2	31.1	30.5[f]
Kr	3125	3440[b]	3550	3710	...	29.6	32.3	32.9	31.5[a]
Xe	4395	4710 (4360)[b]	4490	4390	...	33.0	33.6	35.8	34.7[a]
Rn	5563	...	5500	5120	...	35.4	34.3	36.8	...
H_2	1008	905 (962)[b]	1280	1000	...	25.3	26.0	26.0	25.3[a]
N_2	2351	2500 (2640)[b]	2140	2650	2520[f]	30.0	29.8	32.1	31.0[f]
O_2	2423	2850 (2950)[b]	2990	2960	2890[f]	28.5	31.3	31.8	30.9[f]
CO	2410	...	3910	2690	...	30.7	29.8	31.0	...
NO	2432	...	2680	2900	...	27.4	29.4	30.2	...
CH_4	3095	3170 (3210)[b]	3180	3350	3052[g]	31.4	31.8	33.3	31.9[a]
CF_4	4046	...	..	..	...	37.4	..	..	...
CCl_4	9465	...	..	6665	~9000[h]	47.5	..	41.8	...
C_2H_2	3985	...	3360	3590	...	33.9	25.6	26.8	...
C_2H_4	4310	...	3790	3920	...	34.0	31.3	32.8	...
C_2H_6	4873	...	4430	4830	3983[g]	35.3	35.4	38.6	33.6[g]
C_6H_6	9355	...	..	..	...	41.8	..	..	...

[a] Himmelblau, ref. 4. [b] Calcd. by Himmelblau using data from ref. 3. [c] Frank and Evans, ref. 13. [d] D. N. Glew and E. A. Moelwyn-Hughes, *Discussions Faraday Soc.*, **15**, 150 (1953). [e] J. A. V. Butler, *Trans. Faraday Soc.*, **33**, 229 (1937). [f] Klots and Benson, ref. 7. [g] W. F. Claussen and M. F. Polglase, *J. Am. Chem. Soc.*, **74**, 4817 (1952). [h] P. M. Gross and J. H. Saylor, *ibid.*, **53**, 1744 (1931).

Table VI: Heat Capacities and Partial Molar Volumes for Aqueous Solutions at 298°K.

Solute	Theoret. ΔC_P, cal./mole-deg. 277° K.	298° K.	Exptl. ΔC_P,[a] cal./mole-deg. G and M[b]	Others	Theoret. $\bar{V}_2$, cc./mole	Exptl. $\bar{V}_2$, cc./mole
He	21.9	20.5	24.2	40.7[c]	17.9	15.5[e]
Ne	24.7	23.3	24.0	40.7[c]	20.4	...
Ar	33.4	31.4	37.8	33[d] (40.7)[c]	30.5	...
Kr	34.9	32.8	54.2	40.7[c]	33.5	...
Xe	46.0	43.3	65.6	40.7[c]	46.2	...
Rn	51.0	48.0	79.3	...	54.1	...
H_2	25.1	23.6	25.7	25.2[c]	21.1	18.9[e] (26)[f]
N_2	38.4	36.2	40.9	33[d]	36.5	32.5[e] (40)[f]
O_2	34.3	32.2	40.3	33[d]	31.5	25.8[e] (31)[f]
CO	42.8	40.3	41.3	...	39.6	28.5[e] (36)[f]
NO	29.7	28.0	41.0	...	26.2	...
CH_4	40.7	38.2	49.2	55	39.3	37.3[h] (36)[f]
CF_4	58.5	54.9	...	...	63.5	...
CCl_4	84.5	81.6	...	...	110.8	...
C_2H_2	48.4	45.5	35.5	...	49.3	...
C_2H_4	48.5	45.7	64.5	42.2[c]	49.7	...
C_2H_6	52.4	49.1	65.5	59.2[c]	55.0	51.2[h]
C_6H_6	71.6	67.0	...	...	78.8	83[g]

[a] Usually assumed independent of temperature. [b] D. N. Glew and E. A. Moelwyn-Hughes, *Discussions Faraday Soc.*, **15**, 150 (1953). [c] Morrison and Johnstone, ref. 3. [d] Klots and Benson, ref. 7. [e] Eley, ref. 12. [f] J. H. Hildebrand and R. L. Scott, "Solutions of Non-Electrolytes," 3rd Ed., Reinhold Publishing Corp., New York, N. Y., 1950. [g] Glew, ref. 9. [h] W. L. Masterson, *J. Chem. Phys.*, **22**, 1830 (1954).

be small. The effect of this approximation is to cause the calculated ΔC_P values to be too small and for the error to become greater as ϵ_2/k becomes greater. The heat capacity associated with cavity formation is given by

$$\bar{C}_c = 2\bar{H}_c/T + (\bar{H}_c/\alpha_P)\left(\frac{\partial \alpha_P}{\partial T}\right)_P - \alpha_P\bar{H}_c - \alpha_P^2RT^2[y^2/(1-y)^2]\{[12/(1-y)][2(a_{12}/a_1)^2 - (a_{12}/a_1)] + [36(1-2y)/(1-y)^2][(a_{12}/a_1)^2 - (a_{12}/a_1) + {}^1/_4] + 1\} \quad (20)$$

where only the second term is nonzero for water at 4°. Values of ΔC_P calculated at 4 and 25° are shown in Table VI along with experimental values from a number of sources. The difficulties in obtaining heat capacities from the temperature dependence of gas solubilities account for the discrepancies in the experimental quantities. The agreement between the calculated and observed values must be considered good, and, indeed, the calculated values may well be better than many of the reported values.

The partial molar volume of the solute, $\bar{V}_2$, is given by eq. 5. Although $\bar{V}_1$ cannot be evaluated, it is clear qualitatively for the systems considered here that it should be a small negative number for weakly interacting solutes and should become a larger negative number as the interaction energy increases. The partial molar volume of cavity formation can be evaluated from eq. 6 and is given by[15]

$$\bar{V}_c = 82.05(\beta/\alpha_P)(\bar{H}_c/RT) + (\pi/6)a_2^3N \quad (21)$$

where $\bar{H}_c$ is the partial molar heat of cavity formation from eq. 19, α_P and β are the coefficient of thermal expansion and the isothermal compressibility, respectively, and N is Avogadro's number. The factor 82.05 is the molar gas constant in units of cc.-atm./deg. The results of calculations of $\bar{V}_2$ are given in Table VI and they are seen to be in good agreement with experiment in the limited number of cases where data are available.

4. Discussion

The solubility of gases in water is adequately described by the same theory which successfully described the solubility of gases in organic solvents. Table VII compares theoretical and experimental data for the solubility of argon and nitrogen in benzene and water at 25°. The agreement between theory and experiment for both gases in both solvents is very good even though the magnitudes of the thermodynamic properties vary widely from benzene to water. It is clear that the scaled-particle theory gives a good approximation for the reversible work of cavity formation in both aqueous and nonaqueous solvents.

A few comments deserve to be made concerning the present theory and that of Eley.[11] Eley, by applying thermodynamic relations for the bulk properties of a homogeneous system to the process of cavity formation, concludes that the enthalpy and entropy of cavity formation for water at 4° are zero. Thus in Eley's treatment the free energy of cavity formation is zero, which is clearly impossible.[29] The present theory uses the scaled-particle theory to determine the free energy of cavity formation and then splits this up into its appropriate enthalpy and entropy terms. At 4° for water it is found that the enthalpy of cavity formation is indeed zero as determined by Eley, but that the entropy of cavity formation is a large negative value. Some typical thermodynamic values for cavity formation associated with argon in water at 25° are $\bar{G}_c$ = 4430 cal./mole, $\bar{H}_c$ = 690 cal./mole, and $\bar{S}_c$ = −12.5 e.u. The corresponding values for argon in benzene at 25° are $\bar{G}_c$ = 3610 cal./mole, H = 3520 cal./mole, and S = −0.30 e.u. It is the entropy of cavity formation that

(29) H. H. Uhlig, *J. Phys. Chem.*, **41**, 1215 (1937). Uhlig attempted to calculate the work required to create a cavity by using bulk surface tensions and the surface area created by the cavity.

Table VII: A Comparison of the Solubilities of Ar and N_2 in Benzene and Water at 298°K.

		K, atm.	ΔG, cal./mole	ΔH, cal./mole	ΔS, cal./deg.-mole	ΔC_P, cal./deg.-mole	$\bar{V}_2$, cc./mole
Ar in C_6H_6	Theoret.	940	4060	+278	−12.8	16.9	52
	Exptl.	1140	4170	+420	−16.6	. .	43
Ar in H_2O	Theoret.	31000	6110	−2445	−28.7	31.4	30.5
	Exptl.	41000	6270	−2820	−30.5	33	. .
N_2 in C_6H_6	Theoret.	2200	4560	+812	−12.6	18.8	61
	Exptl.	2260	4570	+980	−12.1	. .	53
N_2 in H_2O	Theoret.	83500	6590	−2351	−30.0	36	36
	Exptl.	86300	6610	−2520	−30.7	33	32

gives rise to the large negative entropies associated with aqueous solutions. In aqueous solutions in the vicinity of room temperature or below, the free energy of cavity formation is almost entirely manifest in the entropy term, whereas in the common organic solvents it is manifest almost entirely in the enthalpy term. This implies that the cavity formation process for water is dominated by a structural change in the solvent accompanied by only small changes in the internal energy of the solvent, while for organic solvents very minor structural changes take place and the process is dominated by changes in the internal energy of the solvents. Since the present theory is thermodynamic in origin, no direct information can be obtained concerning the structural changes involved. While one could make many speculations as to the nature of the changes taking place, let it suffice to say that with some minor alterations the pictorial models of Frank and Evans[13] and of Némethy and Scheraga[10] seem adequate. The most important point to be made along these lines is that if the degree of hydrogen bonding in the solvation layer is increased, then the degree of hydrogen bonding outside of the solvation layer must be decreased since there is too small an enthalpy change to account for any significant change in the extent of hydrogen bonding.[30]

Since the scaled-particle theory is concerned with the packing of molecular hard cores[16,20] in fluids, its success in the present context raises some interesting points. (1) Liquid water behaves as though it were made up of molecular cores of diameter 2.75 Å. confined to a volume determined by its density. Although the intermolecular interactions including hydrogen bonding determine the volume available to those cores, their packing is in accord with the scaled-particle theory at least insofar as the introduction of an additional hard sphere is concerned. (2) The thermodynamic properties of gas solubility in water and organic solvents are explainable in terms of one theory and this theory involves no assumptions concerning the structure of the solvent. (3) Since the scaled-particle theory has been shown to be applicable to molten salts and liquid metals,[16] the solubility of gases in these fluids should lend itself to the same treatment as developed here except for the necessity of modifying the interaction energy term. (4) The thermodynamic properties of infinitely dilute solutions of ions in water or other solvents should be amenable to study by including terms involving ion–dipole interactions and the reversible work of charging a particle in a dielectric medium.[31] Along these lines, it should be possible to predict the free energy change associated with the transfer of a solute molecule from one solvent to another solvent, a term related to the medium effect of Bates, *et al.*,[32] in their discussion of a generalized pH scale for aqueous and nonaqueous solutions.

5. Appendix

The thermodynamic properties associated with cavity formation in water at 25° are given by the simple formulas

$$\bar{G}_c = 1000\sigma_{12}^2 - 2008\sigma_{12} + 1141 \quad \text{(cal. mole)}$$

$$\bar{H}_c = 16.42Z \quad \text{(cal. mole)}$$

$$\bar{S}_c = (\bar{H}_c - \bar{G}_c)/T$$

where $Z = 10.68\sigma_{12}^2 - 23.91\sigma_{12} + 14.30$ and $\sigma_{12} = (2.75 + \sigma_2)/2$ Å. The value of $\bar{C}_c$ at 25° is complex, but at 4° it is given by $0.791Z$ cal./deg.-mole.

(30) Frank and Evans[13] took account of this possibility in their discussion of the solvation of ions in water. They consider a number of concentric solvation spheres in which ordering and disordering can take place.

(31) R. H. Fowler and E. A. Guggenheim, "Statistical Thermodynamics," Cambridge University Press, London, 1939, Chapter IX.

(32) (a) R. G. Bates, M. Paabo, and R. A. Robinson, *J. Phys. Chem.*, 67, 1833 (1963); (b) R. G. Bates, "Electrometric pH Determinations," John Wiley and Sons, Inc., New York, N. Y., 1954.

Rate Constants of Hydrated Electron Reactions with Some Aromatic Acids, Alkyl Halides, Heterocyclic Compounds, and Werner Complexes[1]

by A. Szutka,[2] J. K. Thomas, Sheffield Gordon, and Edwin J. Hart

Chemistry Division, Argonne National Laboratory, Argonne, Illinois *(Received August 13, 1964)*

Hydrated electron rate constants for a number of aromatic acids, aliphatic halides, heterocyclic compounds, and Werner complexes of cobalt and chromium have been measured using the pulse radiolysis technique. In the series benzoic, phthalic, and trimesic acids, the second-order rate constants of the ions are $3.0 \pm 1.0 \times 10^9$ M^{-1} sec.$^{-1}$; those of the undissociated acids are somewhat higher. Unconjugated acids such as phenylacetic and hydrocinnamic have rate constants that are lower than the above group by a factor of 300. Furan, thiophene, pyrrole, and pyrrolidine are unreactive, whereas thiazole and succinimide are reactive. In the alkyl iodides, methyl to butyl, the rate constants are $1.45 \pm 0.22 \times 10^{10}$ M^{-1} sec.$^{-1}$. The reactivity increases in the series: chloride, bromide, and iodide. The rate constants of the Werner complexes of chromium and cobalt are all above 10^{10} M^{-1} sec.$^{-1}$ and the complexes containing the metal in the cationic part of the molecule react, on the average, three times faster than the anionic part.

Introduction

The hydrated electron, e_{aq}^-, has been shown to react with bimolecular rate constants in the range of 10^9 to 3×10^{10} M^{-1} sec.$^{-1}$ with unhydrated aldehydes, ketones, conjugated double bond systems containing C=C, C=O, C≡N groups, disulfides, peroxides, and certain heterocyclic derivatives.[3] In the present work, a more detailed study is reported on the reactivity of e_{aq}^- with some aromatic acids, alkyl halides, heterocyclic ring compounds, and Werner complexes by following the decay of its optical absorption at 5780 Å.[4]

Experimental

The irradiation, solution preparation, and dilution techniques are identical with those previously described.[3,5] Briefly, the rate constants are calculated from the pseudo-first-order decay of the hydrated electron absorption in electron-irradiated aqueous solutions. The 15-Mev. electron pulse introduces about 10^{-6} M e_{aq}^- in 0.2 or 0.4 μsec. Solute concentrations range from 3×10^{-5} M for the reactive compounds to 0.1 M for unreactive ones.

Analytical grade alkyl halides were purified by washing with triply distilled water and drying over anhydrous sodium sulfate. Aromatic acids were purified by recrystallization and subsequent drying in an analytical oven. The solvents used in these purifications were triply distilled water for potassium hydrogen phthalate, trimesic acid, and hydrocinnamic acid; a solution of methanol and water for benzoic acid; methyl alcohol for cinnamic acid; petroleum ether for phenylacetic acid; and a solution of ethanol and benzene for phthalic anhydride.

Heterocyclic compounds were distilled using a Podbielniak column and collecting the middle fraction of a distillate in the case of furan, pyrrole, pyrrolidine, thiophene, and thiazole. Succinimide was recrystallized from methyl alcohol and dried at 100°. For recrystallization of imidazole, the solvent was benzene and the drying temperature was 80°. 2-Pyrrolidone was purified by repeated freezing of the compound and decanting of the liquid portion.

(1) Based on work performed under the auspices of the U. S. Atomic Energy Commission.

(2) Research Associate from University of Detroit, Detroit, Mich.

(3) E. J. Hart, S. Gordon, and J. K. Thomas, *J. Phys. Chem.*, **68**, 1271 (1964).

(4) E. J. Hart and J. W. Boag, *J. Am. Chem. Soc.*, **84**, 4090 (1962).

(5) S. Gordon, E. J. Hart, M. S. Matheson, J. Rabani, and J. K. Thomas, *ibid.*, **85**, 1375 (1963).

Table I: Werner Complexes

No.	Name	Mol. wt.	Formula
1	Potassium trisoxalatochromate(III) 3-hydrate	487.41	$K_3[Cr(C_2O_4)_3]\cdot 3H_2O$
2	Trisethylenediaminechromium(III) chloride hydrate	401.72	$[Cr(en)_3]Cl_3\cdot 3.5H_2O$
3	Potassium bisoxalatodiaquochromate(III) 2-hydrate	339.18	*cis*-$K[Cr(C_2O_4)_2(H_2O)_2]\cdot 2H_2O$
4	Potassium bisoxalatodiaquochromate(III) 3-hydrate	357.19	*trans*-$K[Cr(C_2O_4)_2(H_2O)_2]\cdot 3H_2O$
5	Hydrogen ethylenediaminetetraacetatochromate(III)	341.23	H[Cr(EDTA)]
6	Trisethylenediaminecobalt(III) chloride	345.61	$[Co(en)_3]Cl_3$
7	*trans*-Dichlorobisethylenediaminecobalt(III) nitrate	312.06	*trans*-$[Co(en)_2Cl_2]NO_3$
8	*cis*-Dichlorobisethylenediaminechromium(III) chloride hydrate[a]	296.58	*cis*-$[Cr(en)_2Cl_2]Cl\cdot H_2O$
9	*cis*-Bisthiocyanatobisethylenediaminechromium(III) thiocyanate	346.46	*cis*-$[Cr(en)_2(NCS)_2]NCS$
10	*trans*-Bisthiocyanatobisethylenediaminecobalt(III) chloride hydrate[b]	348.77	*trans*-$[Co(en)_2(NCS)_2]Cl\cdot H_2O$
11	*cis*-Bisthiocyanatobisethylenediaminecobalt(III) thiocyanate[c]	353.39	*cis*-$[Co(en)_2(NCS)_2]NCS$

[a] *Anal.* Calcd.: C, 16.20; H, 6.11; N, 18.89. Found: C, 17.19; H, 6.33; N, 19.18. [b] *Anal.* Calcd.: C, 20.69; H, 5.20; N, 24.10. Found: C, 20.69; H, 5.43; N, 24.02. [c] *Anal.* Calcd.: C, 23.78; H, 4.56; N, 27.75. Found: C, 23.46; H, 4.50; N, 28.90.

Werner complexes were prepared by Dr. J. A. McLean and his group at the University of Detroit. The list of Werner complexes with their names, molecular weights, and chemical formulas is shown in Table I.

Discussion of Results

Our rate constants for reaction of e_{aq}^- with some aromatic acids appear in Table II. In the series benzoic acid, phthalic acid, and trimesic acid, the rate constants of the ions are $3.0 \pm 1.1 \times 10^9\ M^{-1}$ sec.$^{-1}$. The rate constants of the undissociated acids are somewhat greater. Consequently, an increase in the number of carboxyl ions on the aromatic nucleus does not increase the rate constant. Of major importance is the maintenance of conjugation to the ring as is shown by a comparison of benzoic acid (3.6×10^9) and cinnamic acid (6.8×10^9). Destruction of conjugation is illustrated by phenylacetate (1.4×10^7) and hydrocinnamate (1.1×10^7) ions. Of interest too is the fact that cinnamate ion has nearly the same rate constant as the fumarate ion, 7.5×10^9. From this result we conclude that the aromatic nucleus functions by providing the conjugation required for high rate constants.

In these aromatic anions the initial point of e_{aq}^- attack is in question. Diphenyl forms the diphenylide ion in irradiated ethanol followed by rapid protonation.[6] This reaction shows primary attachment to the ring, but in irradiated benzyl chloride, formation of the transient benzyl radical is evidence that initial attack may be on the side chain.[6-8]

$$C_6H_5CH_2Cl + e_{aq}^- \longrightarrow C_6H_5CH_2\cdot + Cl^-$$

Since the isomeric phthalate ions form strongly absorbing transients directly from e_{aq}^-,[9] it is likely in this case

Table II: Rate Constants for Reaction of e_{aq}^- with Aromatic Acids and Their Ions

Compounds	Concn., m*M*	MeOH, m*M*	pH	Slope × 10^{-5}	Individual	k, M^{-1} sec.$^{-1}$, av.
Benzoic acid	1.0	1.0	5.35	25.0	5.8×10^9	5.4×10^9
	0.030	1.0	5.45	6.6	5.1×10^9	
	0.10	1.0	7.19	13.0	2.9×10^9	
	0.03	1.0	7.19	4.5	3.4×10^9	
	0.50	1.0	7.74	6.5	3.0×10^9	3.1×10^9
	0.50	1.0	7.74	7.0	3.2×10^9	
	0.10	1.0	12.30	16.5	3.8×10^9	
	0.030	1.0	12.30	4.45	3.4×10^9	3.6×10^9
Phthalic acid	0.10	1.0	5.65	2.5	5.8×10^9	
	0.10	1.0	5.65	2.7	6.2×10^9	
	0.10	1.0	5.60	2.9	6.6×10^9	6.2×10^9
	0.50	1.0	6.78	2.3	1.1×10^9	
	0.50	1.0	6.78	2.8	1.3×10^8	1.2×10^9
	1.0	1.0	12.57	7.8	1.8×10^9	
	0.5	1.0	12.80	4.0	1.8×10^9	
	0.5	1.0	12.80	4.3	2.0×10^9	1.9×10^9
Trimesic acid	0.25	1.0	5.74	3.8	3.5×10^9	3.5×10^9
	0.25	1.0	6.96	2.7	2.5×10^9	2.5×10^9
	0.125	1.0	8.84	1.45	2.8×10^9	
	0.125	1.0	8.84	1.6	3.1×10^9	3.0×10^9
	0.125	1.0	12.39	2.3	4.2×10^9	
	0.125	1.0	12.39	2.3	4.2×10^9	4.2×10^9
Phenylacetic acid	15.0	1.0	5.43	2.9	4.5×10^7	
	15.0	1.0	5.43	3.7	5.7×10^7	5.1×10^7
	37.5	1.0	12.38	2.2	1.4×10^7	
	75.0	1.0	12.28	4.5	1.4×10^7	1.4×10^7
Hydrocinnamic acid	30.0	1.0	5.43	6.3	4.9×10^7	4.9×10^7
	30.0	1.0	12.14	1.5	1.1×10^7	1.1×10^7
Cinnamic acid	0.10	1.0	7.22	3.0	6.8×10^9	6.8×10^9
	0.10	1.0	12.45	4.2	9.7×10^9	9.7×10^9

(6) I. A. Taub, D. A. Harter, M. C. Sauer, and L. M. Dorfman, *J. Chem. Phys.*, **41**, 979 (1964).

(7) M. S. Matheson and L. M. Dorfman, *ibid.*, **32**, 1870 (1960).

(8) M. Anbar and E. J. Hart, *J. Am. Chem. Soc.*, **86**, 5633 (1964).

that initial reaction is with the electron-deficient aromatic ring.

In a previous paper we reported that certain groups could increase the reactivity of benzene toward the hydrated electron.[3] The nitro group in nitrobenzene ($k = 3 \times 10^{10}\ M^{-1}$ sec.$^{-1}$) and picric acid ($k = 3.5 \times 10^{10}\ M^{-1}$ sec.$^{-1}$), the carbonyl group in phthalate ion ($k = 2 \times 10^{9}\ M^{-1}$ sec.$^{-1}$), and the ethylenic double bond in styrene ($k = 1.3 \times 10^{10}\ M^{-1}$ sec.$^{-1}$) are such groups. Other groups either had no effect or decreased the reactivity, *e.g.*, Cl in chlorobenzene, CH_3 in toluene, OH in phenol and hydroquinone, and NH_2 in aniline.

The first series of "activating" groups are normally *meta*-directing groups apart from styrene, while the second series are normally *ortho–para*-directing groups. In general, a *meta*-directing group tends to withdraw electrons from the aromatic nucleus while *ortho–para*-directing groups tend to liberate electrons to the nucleus. The e_{aq}^- may react with the positively charged aromatic nucleus giving a negative ion which protonates and effectively gives a product identical with that obtained from H atom addition to the ring. It is noteworthy in Table II that the partially ionized benzoic and phthalic acids are more reactive than the fully ionized acids, presumably because the negative benzoate and phthalate ions tend to promote electron migration to the ring, hence decreasing the attraction of the e_{aq}^- for this reactive center.

A similar explanation can be put forward to explain the reactivity of the *ortho–para*-directing C=C in styrene. Here the positive end of the system is the C=C group and the e_{aq}^- would tend to react here. A similar effect has been noted in the activation of the C=C bond by COOH, *e.g.*, methacrylic acid, fumaric acid, and maleic acid, and by another C=C as in butadiene.

This interpretation of the e_{aq}^- reactions in terms of a charge separation of the molecules may also explain the reactivity of the halogen compounds in Table IV. However, the differences in reactivity are not large enough to eliminate the effect of diffusion on these rate constants.

Heterocyclic compounds, such as furan, thiophene, pyrrole, and pyrrolidine, are unreactive with hydrated electrons. However, certain modifications of the compounds increase their reactivity drastically. This is illustrated by the pyrrole derivatives in Table III. Pyrrole has been found unreactive, while the rate constant for 2-pyrrolidone is 1.3×10^7 and for succinimide, $7.2 \times 10^9\ M^{-1}$ sec.$^{-1}$. Consequently, introduction of a carbonyl group into a compound increases the rate constant. This is in accord with the previous finding that acetone has a rate constant of $6 \times 10^9\ M^{-1}$ sec.$^{-1}$. In spite of the inertness of pyrrole and of thiophene, the presence of nitrogen and sulfur atoms in the same ring provides thiazole with a rate constant of $2.5 \times 10^9\ M^{-1}$ sec.$^{-1}$. Also, the presence of two nitrogen atoms in the same ring slightly enhances the reactivity of imidazole to $3.7 \times 10^7\ M^{-1}$ sec.$^{-1}$.

Table III: Rate Constants for Reaction of e_{aq}^- with Heterocyclic Compounds

Compound	Concn., mM	MeOH, mM	pH	Slope $\times 10^{-6}$	k, M^{-1} sec.$^{-1}$
Furan	13.88	1.0	7.94	0.18	3.0×10^6
Thiophene	2.59	25	6.73	0.73	6.5×10^7
Pyrrole	100.0	1.0	10.29	0.26	6.0×10^5
Pyrrolidine	100.0	1.0	12.08	1.8	4.2×10^6
2-Pyrrolidone	100.0	1.0	7.82	5.7	1.3×10^7
Succinimide	0.10	10.0	8.04	3.1	7.2×10^9
Imidazole	5.0	50	9.16	0.81	3.7×10^7
Thiazole	0.281	25	6.59	3.0	2.5×10^9
	0.562	50	6.59	6.1	2.5×10^9

Table IV: Rate Constants for Reaction of e_{aq}^- with Alkyl Halides[a]

Compound	Concn., mM	MeOH, mM	pH	Slope $\times 10^{-6}$	Individual	k, M^{-1} sec.$^{-1}$, av.
Methyl iodide	0.040	6.25	6.85	3.3	1.9×10^{10}	
	0.080	12.50	6.85	5.3	1.5×10^{10}	1.7×10^{10}
Ethyl bromide	0.131	3.0	7.12	6.9	1.2×10^{10}	1.2×10^{10}
Ethyl iodide	0.062	6.25	6.75	4.1	1.5×10^{10}	
	0.124	12.50	6.04	7.34	1.4×10^{10}	1.5×10^{10}
Propyl chloride	0.110	12.50	6.27	0.33	3.8×10^9	6.9×10^8
Propyl bromide	0.057	6.25	6.15	2.0	8.2×10^9	
	0.114	12.50	6.15	4.4	8.8×10^9	8.5×10^9
Propyl iodide	0.051	6.25	6.21	3.5	1.6×10^{10}	
	0.102	12.50	6.21	4.9	1.1×10^{10}	1.3×10^{10}
n-Butyl chloride	0.478	14.0	7.28	0.9	4.4×10^8	
	0.478	14.0	7.28	0.9	4.7×10^8	4.5×10^8
n-Butyl bromide	0.095	3.0	6.57	4.2	1.0×10^{10}	1.0×10^{10}
n-Butyl iodide	0.055	6.25	7.60	3.0	1.3×10^{10}	
	0.110	12.50	7.60	5.6	1.2×10^{10}	1.2×10^{10}
sec-Butyl chloride	0.471	14.0	6.64	1.1	5.1×10^8	5.1×10^8
Isobutyl chloride	0.478	14.0	5.82	1.3	6.5×10^8	5.1×10^8

The rate constants for alkyl halides are higher than those of the other compounds studied. From Table IV, it is evident that the length of branching of the aliphatic chain has no effect on the rate constant. The rate constant for all of the iodides (methyl to butyl) is

(9) S. Gordon, J. K. Thomas, and E. J. Hart, *J. Phys. Chem.*, 68, 1262 (1964).

Table V: Rate Constants for Reaction of e_{aq}^- with Cobalt and Chromium Complexes

Compound and metal ion	Concn., m*M*	MeOH, m*M*	pH	Slope $\times 10^{-5}$	Individual	Average
No. 2 + $[Cr^{III}(en)_3]^{3+}$	0.023	1.0	6.83	5.5	5.6×10^{10}	
	0.023	1.0	6.83	4.9	5.0×10^{10}	
	0.023	1.0	6.83	5.0	5.1×10^{10}	5.3×10^{10}
No. 8 + $[Cr^{III}(en)_2Cl_2]^+$	0.020	1.0	5.55	6.4	7.3×10^{10}	
	0.020	1.0	5.55	6.1	7.1×10^{10}	
	0.010	1.0	5.55	3.3	7.7×10^{10}	7.1×10^{10}
	0.010	1.0	5.55	2.9	6.6×10^{10}	
No. 9 + $[Cr^{III}(en)_2(NCS)_2]^+$	0.020	1.0	5.65	3.7	4.2×10^{10}	
	0.020	1.0	5.65	3.7	4.2×10^{10}	4.2×10^{10}
No. 6 + $[Co^{III}(en)_3]^{3+}$	0.023	1.0	6.55	7.5	7.5×10^{10}	
	0.023	1.0	6.55	6.3	6.3×10^{10}	
	0.012	1.0	6.55	4.0	8.1×10^{10}	7.3×10^{10}
	0.012	1.0	6.55	3.5	7.1×10^{10}	
No. 7 + $[Co^{III}(en)_2Cl_2]^+$	0.020	1.0	5.55	6.6	7.6×10^{10}	Corrected for (NO_3)
	0.010	1.0	5.55	4.0	9.1×10^{10}	
	0.010	1.0	5.55	3.7	8.4×10^{10}	7.1×10^{10}
No. 11 + *cis*-$[Co^{III}(en)_2(NCS)_2]^+$	0.020	1.0	6.00	6.5	8.0×10^{10}	
	0.020	1.0	6.00	4.8	5.9×10^{10}	6.9×10^{10}
No. 10 + *trans*-$[Co^{III}(en)_2(NCS)_2]^+$	0.020	1.0	6.50	4.4	5.0×10^{10}	
	0.020	1.0	6.50	4.9	5.6×10^{10}	
	0.010	1.0	6.50	2.5	5.8×10^{10}	5.4×10^{10}
	0.010	1.0	6.50	2.3	5.3×10^{10}	
No. 1 + $[Cr^{III}(C_2O_4)]^{3-}$	0.050	1.0	4.76	3.4	1.6×10^{10}	
	0.050	1.0	4.76	3.5	1.6×10^{10}	
	0.050	1.0	6.13	4.5	2.0×10^{10}	1.8×10^{10}
	0.020	1.0	5.00	1.6	1.8×10^{10}	
No. 3 + *cis*-$[Cr^{III}(C_2O_4)_2(H_2O)_2]^-$	0.097	1.0	6.40	4.9	1.2×10^{10}	
	0.097	1.0	6.40	5.5	1.3×10^{10}	
	0.048	1.0	6.40	2.5	1.2×10^{10}	1.3×10^{10}
	0.048	1.0	6.40	3.1	1.5×10^{10}	
No. 4 + *trans*-$[Cr^{III}(C_2O_4)_2(H_2O)_2]^-$	0.097	1.0	6.18	5.3	1.3×10^{10}	
	0.097	1.0	6.18	5.8	1.4×10^{10}	
	0.048	1.0	6.18	3.7	1.7×10^{10}	1.5×10^{10}
	0.048	1.0	6.18	3.8	1.8×10^{10}	
No. 5 + $[Cr^{III}(EDTA)]^-$	0.025	1.0	4.90	4.0	3.5×10^{10}	Corrected for acid
	0.025	1.0	4.90	3.8	3.5×10^{10}	content
	0.020	1.0	5.00	2.7	3.1×10^{10}	2.6×10^{10}
	0.020	1.0	5.00	3.9	4.5×10^{10}	

$1.45 \pm 0.22 \times 10^{10}$ M^{-1} sec.$^{-1}$. The reactivity increases in the series: chloride, bromide, and iodide.

The rate constants for the Werner complexes of cobalt and chromium are above 10^{10} M^{-1} sec.$^{-1}$ and fall into two distinct groups. See Table V. Complexes containing metals in the cationic part of the molecule react, on the average, three times faster than molecules containing metal in the anionic part. If the metal ion is the reactive site of the molecule, the difference in the rate constants can be attributed to the electrostatic attraction or repulsion of the hydrated electron toward the cationic or anionic portion of the molecule. No distinction is observed between complexes containing chromium and cobalt metals in the series of compounds studied although $Cr(CN)_6^{3-}$ reacts fourfold faster than $Co(CN)_6^{3-}$.[10]

Acknowledgment. The technical assistance of Mr. Edward Hagen and Miss P. D. Walsh and the cooperation of Messrs. B. E. Clifft and E. R. Backstrom during Linac operations are appreciated.

(10) M. Anbar and E. J. Hart, unpublished work.

Studies of Gaseous Atom–Molecule Reactions by Electron Paramagnetic Resonance Spectroscopy

by C. C. McDonald and R. J. Goll

Contribution No. 996 from the Central Research Department, Experimental Station, E. I. du Pont de Nemours and Company, Wilmington 98, Delaware *(Received August 17, 1964)*

Gaseous atom–molecule reactions have been investigated by a technique that combines magnetic-dipole and electric-dipole e.p.r. spectroscopy. This technique has been used to study some elementary reactions that produce OH, to detect e.p.r. spectra of SH, SD, and SO, and to examine transient species in a number of other atom–molecule reactions.

Introduction

The ability of electron paramagnetic resonance (e.p.r.) spectroscopy to detect and measure low concentrations of free radicals in dynamic systems and to identify and elucidate molecular structure provides a potentially important tool for investigations of mechanisms and kinetics of gaseous, free-radical reactions. Such studies of gaseous reactions by e.p.r. techniques become more feasible as the number of gaseous species with well-characterized e.p.r. spectra increases. Spectra of several gaseous atomic species[1-9] and of a few stable molecular species[10-15] have been detected by conventional e.p.r. techniques. Achievement of detectable concentrations of transient molecular paramagnetic species has proved difficult, not only because of the short lifetimes of such species in most gaseous environments, but because of excessive pressure-broadening of resonance lines, except at very low pressures, and also because of the distribution of free radical populations among several rotational states that exhibit individual e.p.r. spectra. Magnetic-dipole transitions between adjacent Zeeman levels are studied in conventional e.p.r. spectroscopy, but certain paramagnetic diatomic molecules[16] can also exhibit electric-dipole transitions between Zeeman levels. If these molecules have large electric-dipole moments, they are detectable by electric-dipole e.p.r. spectroscopy at much smaller concentrations than are required for magnetic-dipole spectroscopy since the intensity ratio of electric to magnetic transitions is μ_e^2/μ_0^2 (where μ_e and μ_0 represent the permanent electric dipole moment and magnetic dipole moment of the molecule). Electric-dipole e.p.r. spectroscopy was first used[13] to study NO and has recently been utilized by Radford[17a,b] to detect OH in the effluent gas stream from a discharge in H_2O vapor. We present here a technique that combines electric-dipole and magnetic-dipole e.p.r. spectroscopy for studying gaseous atom–molecule reactions

(1) R. Beringer and M. A. Heald, *Phys. Rev.*, **95**, 1474 (1954).

(2) E. B. Rawson and R. Beringer, *ibid.*, **88**, 677 (1952).

(3) V. W. Hughes and J. S. Geiger, *ibid.*, **99**, 1842 (1955).

(4) M. A. Heald and R. Beringer, *ibid.*, **96**, 645 (1954).

(5) H. G. Dehmelt, *ibid.*, **99**, 527 (1955).

(6) H. E. Radford, V. W. Hughes, and V. Beltran-Lopez, *ibid.*, **123**, 153 (1961).

(7) V. Beltran-Lopez and H. G. Robinson, *ibid.*, **123**, 161 (1961).

(8) J. S. M. Harvey, R. A. Kamper, and K. R. Lea, *Proc. Phys. Soc.* (London), **76**, 979 (1960).

(9) K. D. Bowers, R. A. Kamper, and C. D. Lustig, *ibid.*, **B70**, 1176 (1957).

(10) R. Beringer and J. G. Castle, *Phys. Rev.*, **81**, 82 (1951).

(11) M. Tinkham and M. W. P. Strandberg, *ibid.*, **97**, 951 (1955).

(12) R. Beringer and J. G. Castle, *ibid.*, **78**, 581 (1950).

(13) R. Beringer, E. B. Rawson, and A. F. Henry, *ibid.*, **94**, 343 (1954).

(14) J. G. Castle and R. Beringer, *ibid.*, **80**, 114 (1950).

(15) L. H. Piette, F. A. Johnson, K. A. Booman, and C. B Colburn, *J. Chem. Phys.*, **35**, 1481 (1961).

(16) Diatomic molecules that are not in Σ-electronic states have doubly degenerate Zeeman levels, designated $\pm\lambda$-states, that become nondegenerate in a magnetic field. Electric-dipole transitions are allowed between $+\lambda$- and $-\lambda$-states of different Zeeman levels, whereas magnetic-dipole transitions are allowed between λ-states of the same sign. For a further discussion of λ-doubling, see G. Herzberg, "Spectra of Diatomic Molecules," D. Van Nostrand Co., Inc., Princeton, N. J., 1950.

(17) (a) H. E. Radford, *Phys. Rev.*, **122**, 114 (1961); (b) *ibid.*, **126**, 1035 (1962).

and demonstrate this technique by some qualitative observations on several elementary gaseous reactions.

Experimental

A Varian V-4500 e.p.r. spectrometer and 12-in. magnet were used for this investigation. The spectrometer cavity was replaced by a cavity designed to operate in the TE-011 mode with components of both the electric and magnetic fields of the microwave radiation normal to the steady magnetic field—a necessary condition for detection of both electric-dipole and magnetic-dipole Zeeman transitions. The TE-011 cavity consisted of a hollow cylinder (7-cm. o.d., 3.8 cm. high) that was positioned in the spectrometer magnet with the flat cylinder ends facing the pole pieces. The cylinder wall was fabricated from copper, 1 cm. thick, while the top and bottom of the cavity were closed with glass plates, 0.6 cm. thick and silvered on the inside. The silver layer was sufficiently thin to admit a magnetic field, alternating at 100 kc.p.s., to the cavity but was thick enough to act as a reflecting surface for X-band microwave radiation supplied to the cavity *via* a tuning iris in the cavity wall. Copper tubes (1.2 cm. square, 3 cm. long) projected from either side of the cylinder to provide ingress and egress for quartz tubing used to conduct gas through the cavity without substantial losses of microwave radiation. Gas was contained in the cavity by a quartz vessel of 35-cc. volume, fitted snugly to the inner cavity surface. Quartz tubes (12-mm. o.d.) projected from either side of the cavity liner through the copper ports to provide for gas flow through the cavity. The cavity separated along a median plane between the end plates to permit removal of the quartz liner and was also provided with an insulated slot across the cavity wall to reduce impedance to the 100-kc.p.s. modulating field. Field modulation coils on both cavity faces were driven by a 50-w. amplifier supplied in turn by the Varian 100-kc.p.s. power supply. From observation of "modulation broadening" of resonances of atomic hydrogen, we estimate that a modulation field amplitude of 3.5 gauss could be attained in the cavity. Cavity Q was about 8000 without the quartz liner and 1600 with the liner in place.

The frequency of the microwave radiation supplied to the cavity was monitored with a Hewlett–Packard wavemeter (Model X 350 A). The steady magnetic field was measured with a proton n.m.r.-type gaussmeter (Nuclear Magnetics Corp. precision gaussmeter Model M-2) at a position adjacent to the cavity in the magnet gap. Relative intensities of e.p.r. absorption lines were estimated by comparison of the first derivative absorption curves recorded at constant, low-microwave power levels, taking the intensity of a resonance line as proportional to the product of the square of the separation of the points of maximum slope of the absorption and the maximum amplitude of the derivative curve. Absolute concentrations of paramagnetic species cannot be inferred from intensities of their electric-dipole e.p.r. spectra without a knowledge of their electric-dipole moments.

Gas flow through the cavity was controlled and measured by conventional high-vacuum techniques. Gas entered the cavity through 12-mm. o.d. quartz tubing (inlet A) at low pressure and high velocity ($\approx 10^3$ cm./sec.). A few centimeters upstream from the cavity, the gas passed through an electrodeless discharge induced by 2450-Mc.p.s. radiation from a 125-w. Raytheon diathermy power supply. The discharge-dissociated gas was made to traverse two sharp turns before entering the cavity to prevent strong cyclotron resonance from free electrons produced through photoionization of gas in the cavity by radiation from the discharge.[18] Provision was made to admix a second gas (inlet B) to the discharge-dissociated gas stream at the entrance to the cavity. The two gas streams were mixed in the cavity and pumped out through the outlet tube on the opposite side of the cavity. Gas pressure was measured in the outlet tube a few centimeters downstream from the cavity.

Results and Discussion

The sensitivity of our apparatus for detecting electric-dipole Zeeman transitions was tested by observation of the spectrum[13] of NO flowing through the cavity. A spectrum for NO($^2\pi_{3/2}$, $J = {}^3/_2$) at 0.15 mm. is shown in Figure 1. Since the nine Zeeman lines show λ-doubling, the resonances arise primarily from electric-dipole transitions. In this experiment

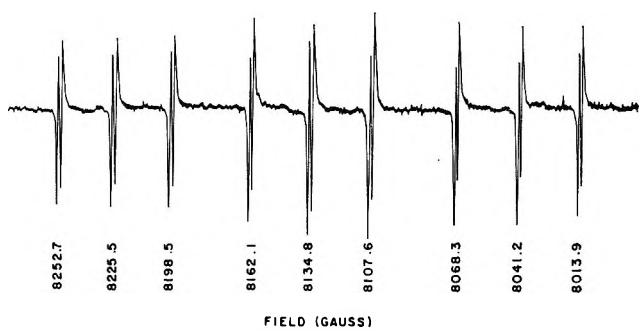

Figure 1. Electric-dipole e.p.r. spectrum of NO($^2\pi_{3/2}$, $J = {}^3/_2$) at 8.842×10^9 c.p.s.

(18) R. L. Collins, *J. Chem. Phys.*, **34**, 1425 (1961).

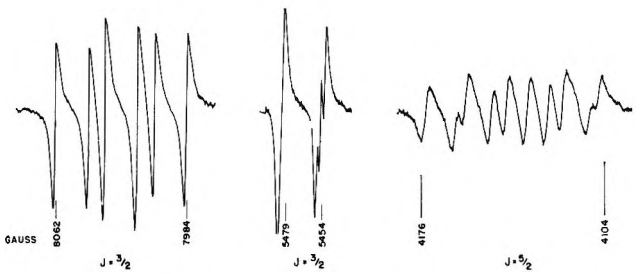

Figure 2. Electric-dipole e.p.r. spectrum of $OH(^2\pi_{3/2}, J = {}^3/_2,{}^5/_2)$ at 8.842×10^9 c.p.s.

the partial pressure of NO in the $^2\pi_{3/2}$, $J = {}^3/_2$ state was 1.5×10^{-3} mm., and it is estimated that a partial pressure of 1×10^{-4} mm. would have been detectable. The sensitivity of the instrument for detecting electric-dipole transitions of other species is modified, of course, by the values of the respective electric dipole moments relative to the dipole moment of NO.

When the effluent gas stream from a discharge in H_2O vapor in inlet A was permitted to flow through the cavity at a pressure of 0.50 mm., magnetic-dipole spectra of $H(^2S_{1/2})$[1] and $O(^3P_2,{}^3P_1)$[2] were detected, as well as electric-dipole spectra of $OH(^2\pi_{3/2}, J = {}^3/_2$ and $J = {}^5/_2)$.[17a] Representative spectra of OH are shown in Figure 2. Effluent gas streams from discharges in other gases (*e.g.*, CH_4, CF_4, CCl_4, NH_3, H_2S, and H_2S–H_2O) were examined in a similar way. Although strong magnetic-dipole spectra of atomic species (H, O, N, F, and Cl) were detected, no transient molecular species, other than OH, were observed. We conclude that the lifetimes of most transient molecular radicals are so short that the concentrations of such species obtained in a discharge outside of the e.p.r. cavity decrease to undetectable levels before the dissociated gas reaches the cavity. Indeed, although Radford[17a] inferred that the OH that he detected by e.p.r. originated in a discharge some distance upstream from the spectrometer cavity, other work[19] indicates that the lifetime of OH is too short to permit detectable concentrations of OH to survive more than a few millimeters from the discharge and suggests that OH detected by e.p.r. results from reactions in the cavity of other relatively long-lived reactive species from the discharge. Thus, we were led to attempt to produce transient molecular radicals in the cavity by admixing a gas stream containing high concentrations of atoms (such as H from dissociated H_2O or H_2) from inlet A with a molecular gas from inlet B at the entrance to the cavity. This technique was used, in experiments described below, to show that OH is formed in detectable quantities by atom–molecule reactions of species in discharge-dissociated water vapor, to detect some new e.p.r. spectra, and to make some qualitative observations on elementary atom–molecule reactions.

(*1*) *Production of OH by Reactions of H and O with H_2, O_2, and H_2O.* When partially dissociated H_2 flowed through the cavity at 0.30 mm. pressure, a strong magnetic-dipole spectrum of H was detected. When sufficient O_2 was added to the gas stream at the cavity entrance to raise the pressure to 0.40 mm., OH was detected. Further addition of O_2 caused the intensity of the OH spectrum to increase until the pressure was 0.54 mm. and to decrease at higher pressures. The intensity of the H spectrum also increased as O_2 was added as pressure increased from 0.30 to 0.40 mm. but decreased at higher O_2 flow rates. Atomic oxygen was not detected. These observations can be explained in terms of the following reactions

$$H + O_2 \longrightarrow OH + O \quad (1)$$

$$O + H_2 \longrightarrow OH + H \quad (2)$$

$$2OH \longrightarrow H_2O + H \quad (3)$$

Hydroxyl radicals are produced from O_2 and H_2 by reactions 1 and 2 without diminishing the H concentration. Reaction 3 causes an increase in the H concentration. Other reactions among these species are possible and undoubtedly occur. When the O_2 flow becomes large, back diffusion of O_2 into inlet A occurs, and the transient paramagnetic species react before they reach the cavity.

When H_2O was added to discharge-dissociated H_2 at 0.30 mm. pressure, no OH was detected until the total pressure reached 0.60 mm. The intensity of OH increased as the H_2O flow was increased while the intensity of H remained constant, and O was not detected. It is suggested that the following equilibrium is established in the gas stream through the cavity.

$$H + H_2O \rightleftharpoons H_2 + OH \quad (4)$$

The bond energies of these species require that the equilibrium be strongly displaced in favor of H and H_2O. Consequently, the addition of H_2O can cause large increases in the OH concentration while only producing a very small decrease in the H concentration.

Partially dissociated O_2 flowing through the cavity at 0.45 mm. pressure gave rise to a detectable spectrum of $O(^3P_2)$. When H_2 (25% H_2 in argon) was added to this gas stream at the cavity entrance, the intensity of O decreased, but neither OH nor H was detected. However, addition of H_2O to discharge-dissociated O_2 at 0.50 mm. caused the O spectrum to disappear and the spectrum of OH to appear when the total pressure

(19) K. Kaufman and F. P. Del Greco, *J. Chem. Phys.*, 35, 1895 (1961).

had increased to only 0.55 mm. The hydroxyl radicals detected in this experiment may arise from the endothermic reaction

$$O + H_2O \longrightarrow 2OH \quad (5)$$

or from reaction of H_2O with O_3 in the oxygen stream.

E.p.r. spectra of H, O, and OH were detected in the gas stream from a discharge in H_2O. When O_2 was added to this gas stream at the cavity entrance, the intensity of the OH spectrum increased.

It is concluded from these experiments that OH is indeed produced in detectable quantities *in situ* in the gas stream by reactions among the species (H, O, H_2, O_2, and H_2O) in the effluent stream from a discharge in H_2O.

(2) *Production of* $SH(^2\pi_{3/2})$, $SD(^2\pi_{3/2})$, *and* $SO(^3\Sigma)$. When H_2S was added at the cavity entrance to a stream of partially dissociated H_2O, a 12-line spectrum attributed to electric-dipole transitions of $SH(^2\pi_{3/2}, J = {}^3/_2)$ was detected. The spectrum of SH, shown in Figure 3, was most intense when the H_2O pressure was 0.5 to 0.6 mm. and sufficient H_2S was added to just quench the spectrum of H (a pressure increment of about 30%). The production of SH is attributed to the reaction

$$H + H_2S \longrightarrow H_2 + SH \quad (6)$$

When H_2S was added to dissociated D_2O in a similar manner, spectra of both SH and SD were detected, presumably as a consequence of the reactions

$$D + H_2S \longrightarrow HD + SH \quad (7)$$

$$D + SH \longrightarrow H + SD \quad (8)$$

Four other e.p.r. lines were detected when H_2S was added to dissociated H_2O or D_2O. These lines are believed to arise from electric-dipole transitions between Zeeman levels of *different* rotational states of $SO(^3\Sigma)$ which is produced by elementary reactions such as

$$SH + OH \longrightarrow SO + H_2 \quad (9)$$

$$SH + H \longrightarrow S + H_2 \quad (10)$$

$$SH + O \longrightarrow S + OH \quad (11)$$

$$SH + OH \longrightarrow S + H_2O \quad (12)$$

$$S + O \longrightarrow SO \quad (13)$$

Details of the e.p.r. spectra of SH, SD, and SO have been presented elsewhere.[20] The assignment of the spectrum of $SO(^3\Sigma)$ has been confirmed and extended by Daniels and Dorain[21] through observations of SO from discharge-dissociated SO_2.

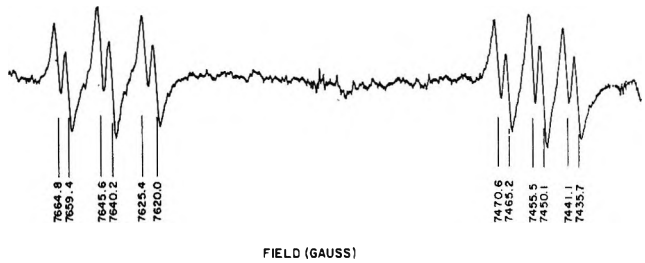

Figure 3. Electric-dipole e.p.r. spectrum of $SH(^2\pi_{3/2}, J = {}^3/_2)$ at 8.850×10^9 c.p.s.

(3) *Other Atom–Molecule Reactions.* The fast, stoichiometric reaction[22]

$$H + NO_2 \longrightarrow NO + OH \quad (14)$$

was chosen for a further test of the technique that has been presented here for the study of atom–molecule reactions. Nitrogen dioxide was added at the cavity inlet to a stream of partially dissociated H_2 at 0.40 mm. The spectrum of OH was detected and increased in intensity as NO_2 was added until the total pressure of the flowing gas reached 0.50 mm. The intensity of the spectrum of H decreased uniformly as the NO_2 flow rate was increased. No attempt was made to follow the concentrations of NO or NO_2 by e.p.r. although this should be quite feasible.[13,14] When NO_2 was added in a similar manner to dissociated H_2O, the intensity of the OH spectrum increased, and the intensity of H decreased as expected.

In other experiments, various gases were added at the cavity entrance to a stream of partially dissociated nitrogen at 0.60 mm. Addition of H_2O to the nitrogen stream caused a decrease in the intensity of the e.p.r. spectrum[4] of N, but spectra of H, O, or OH were not detected. Small amounts of CS_2 or *n*-propane quenched the spectrum of N, but again no other species were detected. When NO was added to the nitrogen stream, the intensity of N decreased, and O was detected in accordance with the known reaction[23]

$$N + NO \longrightarrow N_2 + O \quad (15)$$

The spectrum of O reached maximum intensity when sufficient NO was added to just quench the spectrum of N.

When *n*-propane was added to a stream of partially dissociated H_2 at 0.60 mm., the intensity of the H spectrum decreased, but no new species were detected.

(20) C. C. McDonald, *J. Chem. Phys.*, **39**, 2587 (1963).

(21) J. M. Daniels and P. B. Dorain, *ibid.*, **40**, 1160 (1964).

(22) W. A. Rosser and H. Wise, *J. Phys. Chem.*, **65**, 532 (1961).

(23) P. Harteck, R. R. Reeves, and G. Mannella, *J. Chem. Phys.*, **29**, 608 (1958).

However, when *n*-propane was added to a stream of dissociated D_2O, the intensity of D decreased, and a spectrum of H appeared and then was quenched at higher propane flow rates. These observations can be accounted for by the reactions

$$D + C_3H_8 \longrightarrow HD + C_3H_7 \quad (16)$$

$$D + HD \longrightarrow D_2 + H \quad (17)$$

Addition of *n*-propane to dissociated O_2 resulted in the disappearance of O and the appearance of a weak spectrum of OH, presumably as a consequence of the reaction

$$O + C_3H_8 \longrightarrow OH + C_3H_7 \quad (18)$$

In summary, it appears that the technique that has been presented here, combining magnetic-dipole and electric-dipole e.p.r. spectroscopy to examine atom–molecule reactions taking place in the gas within the spectrometer cavity, can be used for quantitative studies of species for which e.p.r. spectra have been established. It also offers an approach for detecting new e.p.r. spectra of other species. For example, molecules such as CF, CCl, CH, NS, PO, SiH, and TiO should exhibit electric-dipole transitions between Zeeman levels within rotational states of these species. This list can be expanded considerably if one considers molecules such as SO in which electric-dipole transitions between Zeeman levels of different rotational states are possible.

The Effect of Aqueous Alcohol Solutions on the Thermal Transition of Ribonuclease[1a,b]

by Eugene E. Schrier,

Department of Chemistry, Harpur College, State University of New York, Binghamton, New York

Richard T. Ingwall, and Harold A. Scheraga

Department of Chemistry, Cornell University, Ithaca, New York *(Received August 20, 1964)*

The thermal transition of ribonuclease was studied by ultraviolet difference spectrophotometry using aqueous solutions of the enzyme, containing various concentrations of alcohol. Each of the C_1–C_4 straight-chain and branched alcohols and benzyl alcohol were employed. It was found that the molar transition temperature lowerings for the straight-chain alcohols followed a smooth curve with chain length of the added alcohol. The branched alcohols gave molar lowerings which fell on a straight line above the curve for the straight-chain alcohols. A spectrophotometric titration of the phenolic groups of ribonuclease in 30 wt. % methanol solutions at 25° indicated that three tyrosines titrated abnormally and three titrated normally although a change in slope appeared in the curve at approximately 1.5 groups titrated. These results were interpreted by considering the denatured protein to be favored because of hydrophobic interactions between its nonpolar groups and the bound alcohol molecules. A model which utilizes the theory of Peller, together with binding constants for the alcohols calculated with the aid of the theory of Némethy and Scheraga, yields numerical values in close agreement with the observed transition temperature lowerings.

Introduction

In a recent communication, it was shown[2] that the thermal denaturation of ribonuclease was enhanced by the presence of alcohols in the otherwise aqueous solvent. The lowering of the transition temperature for a given concentration of added alcohol was found to increase with increasing chain length of alcohol for the straight-chain alcohols. The branched-chain alcohols gave smaller lowerings than the corresponding straight-chain alcohols. These results suggested that the transition temperature lowerings were not caused by changes in dielectric constant or effective pH on the addition of the alcohol; even though there were considerable differences in the magnitudes of the transition temperature lowerings, there were only insignificant changes in dielectric constant of the alcohol–water solutions for different members of the homologous series. The suggestion was made that hydrophobic bonding of the alcohols to the denatured protein was responsible for the effects observed.

In this paper, the previous study has been extended to include more alcohols and to determine the dependence of the transition temperature lowering on alcohol concentration. In addition, data are presented for the spectrophotometric titration of ribonuclease in aqueous methanol. A theoretical model is developed which accounts quantitatively for the denaturation data in terms of the proposal made previously.[2]

(1) (a) This work was supported by a research grant (AI-01473) from the National Institute of Allergy and Infectious Diseases of the National Institutes of Health, U. S. Public Health Service, and by a research grant (GB-2238) from the National Science Foundation; (b) presented before the Division of Biological Chemistry at the 148th National Meeting of the American Chemical Society, Chicago, Ill., Sept. 1964.

(2) E. E. Schrier and H. A. Scheraga, *Biochim. Biophys. Acta*, **64**, 406 (1962).

Experimental

Materials. Ribonuclease (Sigma 5× recrystallized) was purified further by chromatography on IRC-50 at pH 6.47 using 0.2 *M* sodium phosphate buffer. The alcohols employed were methanol, ethanol, the isomeric propanols and butanols, and benzyl alcohol. They were the best grades commercially available and were used without further purification.

Procedures. Difference spectra were run on a Cary 14 recording spectrophotometer equipped with independently controllable thermostated blocks. The reference solution was the same as the sample, and its temperature was kept at 6° in most of the runs. The optical density difference ΔD was observed at the maximum wave length (287 mμ) as the temperature of the sample cell was raised in varying intervals from 1 to 5°, depending on the expected magnitude of the ΔD. A concentration of 1.5 mg./ml. of ribonuclease was used for the samples which were also 0.005 *M* in KH_2PO_4, 0.005 *M* in Na_2HPO_4, and 0.12 *M* in KCl. Solutions of the alcohols were made up by weight, and measured aliquots of these solutions were used to dilute the previously weighed-out salts and protein. The apparent pH values of these alcoholic solutions of ribonuclease were measured with a Beckman Model G pH meter (glass and calomel electrodes) and were found to be in the range 6.9–7.5.

The procedure of Tanford, *et al.*,[3] for the spectrophotometric titration at 25° was followed. The pH scale in the methanol–water solutions was established using the methanol–water buffer solutions of de Ligny, *et al.*[4] The methanol concentration of the titration solution was 30 wt. % and KCl was added to make 0.2 *M* solutions. Optical densities of the titration solutions (0.2 mg./ml. of protein) were measured at 295 mμ on a Beckman DU spectrophotometer. The pH values of the solutions were measured to 0.001 pH unit on a specially constructed pH meter.

Results

Figures 1, 2, 3a, and 3b show the results of the difference spectral measurements. In these figures the observed transition temperatures, the temperatures corresponding to the midpoint of the over-all difference spectra produced during denaturation, are plotted against the molarity of alcohol in the solution. The conversion of weight per cent to molarity was carried out with densities estimated from the data in the "International Critical Tables." While the plots for the lower alcohols are nearly straight over the concentration range employed, those for the propanols and *t*-butyl alcohol are curved. In any case, it can be seen that the transition temperature decreases regularly with

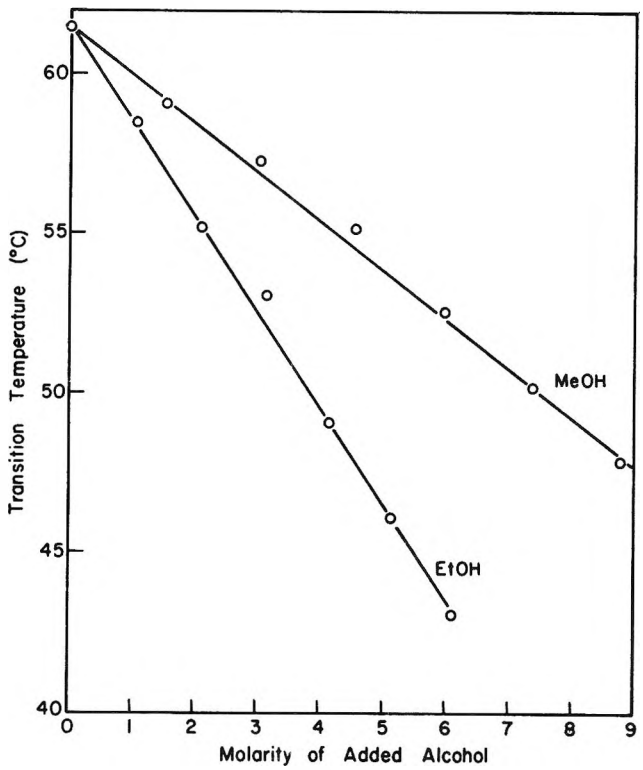

Figure 1. The effect of aqueous methanol and ethanol solutions on the transition temperature of ribonuclease.

alcohol concentration for any particular alcohol. Figure 4 shows the transition temperature lowering as a function of chain length of alcohol for 1 *M* alcohol solutions. The value for *n*-butyl alcohol is extrapolated from the data at lower concentrations (see Figure 3a). The lowerings for the straight-chain alcohols lie on a smooth curve (Figure 4a) while those for the branched alcohols lie on a straight line (Figure 4b). Benzyl alcohol, which is not represented in Figure 4, is the best denaturant giving the largest lowering (extrapolated) for a 1 *M* solution (see Figure 3a). It also should be noted that the lowering given for isobutyl alcohol in ref. 2 is incorrect. The correct value is given here.

The shapes of the curves of ΔD *vs.* temperature (not shown here) appear to be similar in the cases of the purely aqueous and alcoholic solutions. Furthermore, values of ΔH_{obsd} could be obtained from the temperature dependence of the equilibrium constants calculated from a two-state model; see, *e.g.*, ref. 5. The van't Hoff plots were curved, and, hence, high and low values

(3) C. Tanford, J. D. Hauenstein, and D. G. Rands, *J. Am. Chem. Soc.*, **77**, 6409 (1955).

(4) C. L. de Ligny, P. G. M. Luykx, M. Rehbach, and A. A. Wieneke, *Rec. trav. chim.*, **79**, 713 (1960).

(5) J. G. Foss and J. A. Schellman, *J. Phys. Chem.*, **63**, 2007 (1959).

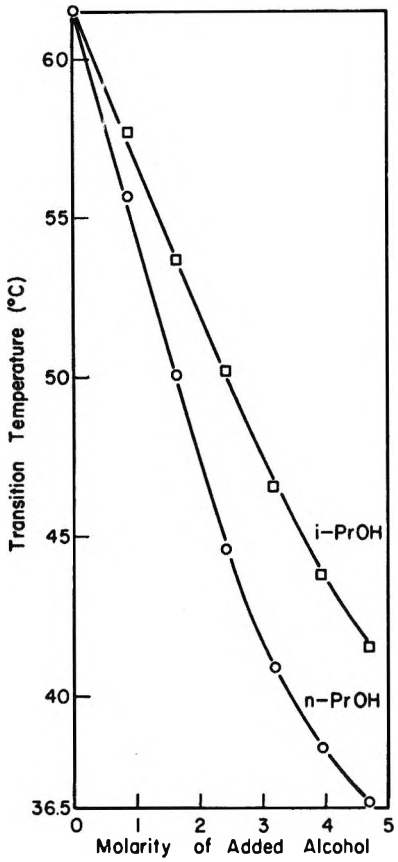

Figure 2. The effect of aqueous *n*-propyl and isopropyl alcohol solutions on the transition temperature of ribonuclease.

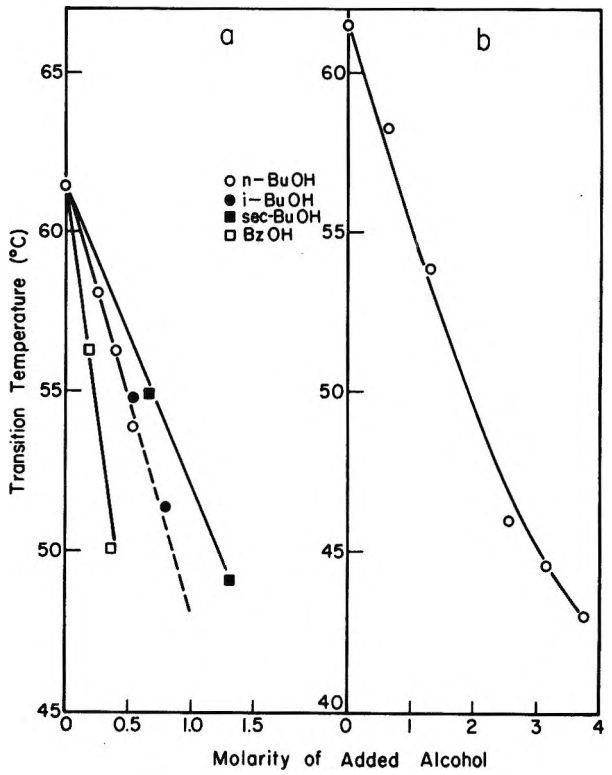

Figure 3. (a) The effect of aqueous *n*-butyl, isobutyl, *sec*-butyl, and benzyl alcohols on the transition temperature of ribonuclease. (b) The effect of aqueous *t*-butyl alcohol on the transition temperature of ribonuclease.

of ΔH_{obsd} were obtained from the respective branches of the van't Hoff plots. While these values are not useful in themselves at present, they are diagnostic of variations between runs under different solvent conditions. It was found that these values of ΔH_{obsd} showed no trend with alcohol concentration, with the nature of the alcohol employed, and, on the average, did not differ from the values of the quantities observed for the thermal transition of ribonuclease in water alone. The average, from all transitions, for ΔH_{obsd} from the high branch is 137 kcal./mole while for the low branch it is 16 kcal./mole. The reversibility of these transition curves was discussed previously.[2]

Figure 5 shows the results of the spectrophotometric titration of ribonuclease in 30 wt. % methanol solutions. The pH scale refers to aqueous methanol buffers. The values of the "number of tyrosines titrated" were obtained by dividing the molar extinction coefficient at 295 mμ by 2630.[3] In addition to the well-known change in slope and attendant irreversible titration behavior which occurs after approximately three tyrosines have been titrated, a heretofore unobserved break appeared at about 1.5 tyrosines titrated. The position of the break was shown to be independent of the direction of titration but was not readily observable in titrations at 10 and 40° in 30 wt. % methanol solution. We do not understand the origin of this break at about 1.5 tyrosines titrated.

Discussion

We wish to account for the enhancement of the thermal denaturation of ribonuclease in the presence of alcohol solution in terms of a simple model. First of all, the spectrophotometric titration data suggest that no major changes have occurred in the structure of the native protein upon the addition of 30 wt. % methanol at 25° since three buried tyrosines are still present. Secondly, the fact that the transition enthalpies are the same for all transitions suggests that the lowering of the transition temperature by the addition of alcohols is largely entropy dependent.

These two suggestions are compatible with the proposal that the lowering of the transition temperature is the result of the binding of the nonpolar portion of the alcohol molecule to the denatured protein. This binding is assumed to come about through the forma-

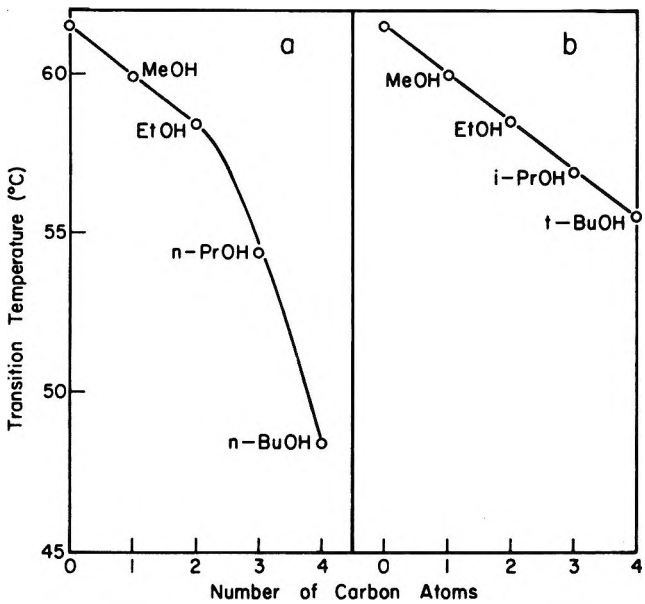

Figure 4. (a) The transition temperature of ribonuclease in 1 *M* alcohol solutions (straight-chain). (b) The transition temperature of ribonuclease in 1 *M* alcohol solutions (branched-chain), together with data for MeOH and EtOH.

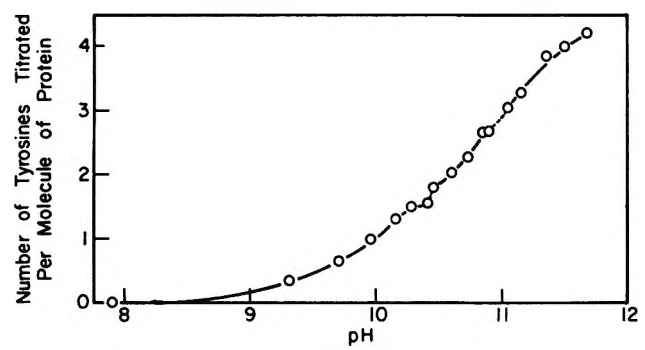

Figure 5. The spectrophotometric titration of ribonuclease at 25° in 30 wt. % methanol, at a KCl concentration of 0.20 *M*.

tion of hydrophobic bonds between the hydrocarbon portion of the alcohols and nonpolar binding sites on the protein. It is known from theory[6] that the heat of aliphatic hydrophobic bond formation is zero at a temperature of around 55° which is the region about which all the transitions center. Hence, the lack of any difference between ΔH_{obsd} for ribonuclease, with and without added alcohol, is in agreement with the concept of the participation of hydrophobic bonds in the transition temperature lowerings. A quantitative development of the foregoing is obtained by using the theory of Peller[7] which was derived to account for the influence of a denaturant, such as a urea, on the thermal helix-to-coil transition of a polypeptide. In Peller's theory, the denaturant is assumed to bind to the exposed amide linkage of the polypeptide, and it is proposed that there are two binding sites per residue. If it is assumed, as has been suggested,[6] that the burying of nonpolar residues and the formation of hydrophobic bonds in a native protein is part of the origin of the lowering of the free energy in helix formation, then the formation of the random coil from the helix by the exposure of nonpolar groups to a solvent environment more favorable than that of pure water should be analogous to the enhancement of the helix–coil transition by the binding of urea to exposed amide groups. In other words, it would appear that the form of Peller's equations can be preserved even though the binding of denaturants is not directly to the helix-forming portion of the polypeptide but is instead to nonpolar groups which help in stabilizing the helix. The transition temperature in aqueous alcohol solution is, thus, given by the formula

$$T_t = \frac{T_t^\circ}{1 + \frac{RT_t^\circ}{\Delta h} \ln (1 + K_B a_t)} \qquad (1)$$

where T_t° is the transition temperature in the absence of denaturant, Δh is the heat of rupture of a peptide hydrogen bond, K_B is the association constant for the binding of alcohol to the protein, and a_t is the activity of the denaturant. This formula is eq. 10a in Peller's paper,[7] except for a factor of 2 multiplying the logarithmic term. This factor was a consequence of assuming two binding sites per residue. One binding site per residue is assumed here. Equation 1 may be simplified, if $(RT_t/\Delta h) \ln (1 + K_B a_t) \ll 1$ and $K_B a_t \ll 1$, to

$$T_t^\circ - T_t \cong \frac{R(T_t^\circ)^2}{\Delta h} K_B a_t \qquad (2)$$

Therefore, if it is assumed that $a_t \approx C$, the lowering of the transition temperature should vary linearly with the concentration of free alcohol. It has been shown previously in Figures 1–3 that there is a linear dependence of transition temperature on molarity at low alcohol concentration. This correlation of theory and experiment encouraged us to calculate the extent of the transition temperature lowering for the different alcohols by estimating the K_B values. The value 1500 cal./residue has been suggested[8] for Δh and can be used here. The estimation of K_B values has been carried out only for the straight-chain alcohols, C_1 through C_4. The following assumptions have been made in the estimation.

(6) G. Némethy and H. A. Scheraga, *J. Phys. Chem.*, **66**, 1773 (1962).
(7) L. Peller, *ibid.*, **63**, 1199 (1959).
(8) J. A. Schellman, *Compt. rend. trav. lab. Carlsberg*, **29**, 223 (1955).

(a) The entropy loss on binding, per mole of alcohol bound, ΔS_B, is given to a good approximation by the entropy of dimerization of small model compounds in aqueous solutions. This is based on the premise that both processes, dimerization and binding, correspond to the loss of translational entropy of one molecule, since a monomer has been lost in the case of dimerization in solution; similarly, through binding, a molecule has been removed from solution. The effect on the entropy of the changes in mass in the first process is insignificant in this approximation. Data are available for three association processes for model compounds. Schellman[8] reported $\Delta S_D = -13.7$ e.u. for dimerization of urea. Klotz and Franzen[9] give $\Delta S_D = -10$ e.u. for the dimerization of N-methylacetamide in water, while Cartwright and Monk's data[10,11] lead to a value of -9 e.u. for formic acid dimerization. Using these values, the average, -11 e.u., is assigned as ΔS_B.

(b) Before hydrophobic bond energies can be estimated, something must be assumed about the nature of the alcohol binding site. Such a site will be a nonpolar group or possibly several nonpolar groups arranged in a favorable orientation for multiple hydrophobic bonds. The possibility of multiple hydrophobic bonds or a hydrophobic region allows us to make the following assumption. The binding site for a particular nonpolar group of an alcohol is the mirror image, *on the average*, of the binding group itself. For example, the butyl group may bind to a leucyl group and form a hydrophobic bond of less strength than it might form if it were bound instead to another butyl group. But it is possible that the butyl group may fit into a slot between two leucyl groups and, thus, form a multiple hydrophobic bond which is much stronger than the butyl–butyl bond.

The equilibrium constants for association can then be calculated by combining the entropy lost on binding, $\Delta S_B = -11$ e.u., from the estimate made above, with the free energy of hydrophobic bond formation calculated from the theory of Némethy and Scheraga[6] for methyl–methyl, ethyl–ethyl, propyl–propyl, and butyl–butyl hydrophobic bonds. The polar end of the alcohol is considered to retain its hydrogen bonding to water so that there is no contribution to the free energy of binding due to enthalpy changes associated with the polar group. The calculation is carried out at 335°K., which is the transition temperature of ribonuclease in a purely aqueous medium. The standard free energy of binding, ΔF_B°, is then given by

$$\Delta F_B^\circ = \Delta F_{H\phi}^\circ - T\Delta S_B^\circ \qquad (3)$$

where $\Delta F_{H\phi}^\circ$ is the free energy contribution due to the formation of hydrophobic bonds between the alcohols and the denatured protein. The equilibrium constants are given by

$$\Delta F_B^\circ = -2.3RT \log K_B \qquad (4)$$

Table I gives the relevant data and the resulting equilibrium constants. The hydrophobic bond free energies have been calculated without the correction for the loss of rotational free energy on hydrophobic bond formation, *i.e.*, the $\Sigma\Delta F_{rot}$ term in eq. 5 of ref. 6 which is included in the theory of Némethy and Scheraga.[6] This correction, amounting, at most, to a few tenths of a kilocalorie per bond, was not part of the original statistical mechanical development of the theory and has yet to be verified experimentally.

Table I: Hydrophobic Bond Free Energies and Equilibrium Constants for the Binding of Alcohol Molecules to the Denatured Form of Ribonuclease at 335°K.

Side chain	$\Delta F_{H\phi}^\circ$, kcal./mole	$K_B \times 10^2$
CH_3-	−0.80	1.31
CH_3CH_2-	−1.15	2.22
$CH_3CH_2CH_2-$	−1.55	4.06
$CH_3CH_2CH_2CH_2-$	−1.95	7.40

The K_B values may be used in eq. 2, together with $\Delta h = 1500$ cal./residue, to calculate the lowering of the transition temperature of ribonuclease produced by the presence of 1 *M* alcohol. The calculated values are given in Table II, together with the experimental data for the same quantities which are also shown in Figure 4a. The agreement between the calculated and experimental values is very good, lending support to the

Table II: Calculated and Experimental Values for the Lowering of the Transition Temperature of Ribonuclease by 1 *M* Alcohol Solutions

Alcohol	Calcd. lowering, T, °K.	Exptl. lowering (Figure 4a) T, °K.
CH_3OH	1.9	1.6
CH_3CH_2OH	3.3	3.1
$CH_3CH_2CH_2OH$	6.0	7.1
$CH_3CH_2CH_2CH_2OH$	11.0	13.1

(9) I. M. Klotz and J. D. Franzen, *J. Am. Chem. Soc.*, **84**, 3461 (1962).

(10) D. R. Cartwright and C. B. Monk, *J. Chem. Soc.*, 2500 (1955).

(11) E. E. Schrier, M. A. Pottle, and H. A. Scheraga, *J. Am. Chem. Soc.*, **86**, 3444 (1964).

proposed model. The sharp increase in transition temperature lowering with chain length, indicated in Figure 4a, appears, therefore, to be the result of increasingly strong hydrophobic bonding to the denatured protein. A similar model pertains to the branched-chain alcohols, but here the concept of effective chain length introduced in ref. 2 must be included in the calculation of hydrophobic bond free energies. It may be supposed, from the fact that the branched alcohols do not give as large molar lowerings as their straight-chain counterparts, that only some fraction of the carbons are capable of interacting with the nonpolar residues of the protein to form hydrophobic bonds. A quantitative theory for interaction of the branched chains could be developed in the manner described above by estimating these fractions.

While denaturation of proteins by various agents is still not completely understood, much of the general picture has emerged within the past few years. The study reported here lends weight to the supposition that the exposure of the nonpolar groups of the native structure to the solvent is one important feature of the denaturation process.

Acknowledgment. The excellent technical assistance of Mrs. Mary Thomas, Mrs. Marcia Pottle, and Mrs. Barbara Toupin is gratefully acknowledged, as is the help in the purification of ribonuclease given us by Dr. Tatsuo Ooi.

Diffusion Studies. I. Diffusion Coefficients in Liquids by a Radiometric Porous-Frit Method[1]

by Arthur E. Marcinkowsky, Frederick Nelson, and Kurt A. Kraus

Chemistry Division, Oak Ridge National Laboratory, Oak Ridge, Tennessee *(Received August 24, 1964)*

A porous-frit method for measuring self-diffusion coefficients and tracer diffusion coefficients of solutes in liquid systems has been investigated. A thin slab of porous material (*e.g.*, porcelain) is saturated with a solution containing a radioisotope of the element of interest. A solution of the same composition, but not containing tracer, is rapidly pumped past the frit. From the counting rate of the frit as a function of time, the diffusion coefficient ($\mathfrak{D}$) is obtained after calibrating the frit with a solute of known $\mathfrak{D}$. Through use of γ-energy discrimination techniques and appropriate recording equipment, the method may be applied to simultaneous measurement of diffusion coefficients of several radioisotopes. The method is rapid and yields values of $\mathfrak{D}$ accurate to a few per cent. Typical examples of diffusion coefficient measurements in aqueous solutions are presented.

The porous-frit method,[2-4] particularly when combined with radiometric techniques,[4] is a simple, rapid, method capable of yielding diffusion coefficients with reasonable precision. The present paper describes further tests and applications of the method to measurements of self-diffusion and tracer diffusion coefficients in aqueous electrolyte solutions.

Experimental

Frits approximately 0.3 × 0.7 × 1.5 cm. were cut from bulk material (unglazed porcelain plate) with a

(1) Research sponsored by the Office of Saline Water, U. S. Department of the Interior, under Union Carbide Corporation's contract with the U. S. Atomic Energy Commission.

glass saw and ground by hand to various uniform thicknesses on a glass plate with a mixture of coarse carborundum (No. 320) and glycerol. Final polishing was carried out with fine carborundum (No. 600) in glycerol. The edges and corners of the frits were rounded to minimize danger of chipping. The frits were washed with water to remove glycerol, and then with hot 6 *M* HCl–1 *M* NaCl to remove other impurities and with distilled water.

Thicknesses of the frits, as measured with a micrometer, ranged from 0.033 to 0.174 ± 0.002 cm. Several measurements were taken over the surface of each frit and an average value was calculated. The pore size of the frits was measured microscopically and ranged from 0.025 to 4 μ; the average pore size was less than 1 μ.

For diffusion measurements, a frit was equilibrated with a solution containing an appropriate tracer. Excess solution was removed by wiping. The frit was supported vertically in a tapered glass tube in front of a counter and, after establishing the initial counting rate, was rapidly "eluted" by pumping solution not containing tracer past it while measuring the counting rate as a function of time. In most experiments, about 200–300 ml. of eluting solution was circulated past the frit in a loop arrangement described earlier.[4a] The pump, a variable speed type, permitted a large range of linear flow rates past the frit. Temperature of the solutions was maintained at 25.0 ± 0.1°.

The counting equipment consisted of a flat, 3.8-cm. Tl-activated sodium iodide crystal detector, associated amplifiers, a multichannel analyzer (modified Packard, Model 15), and a time-base generator (Radiation Instruments Development Laboratories, Model 54–6). The analyzer was used in the multiscaler mode to collect counts over preset time intervals. Counts accumulated in each time interval were stored in successive channels; the time-base generator was used to set the period of the counting intervals and, at the end of each interval, to advance to the next channel. For single tracer measurements, 400 channels were available. At the end of a run, data were printed out with an IBM typewriter.

The equipment also permits simultaneous measurement of counting rates of two tracers provided they have significantly different γ-spectra. A schematic diagram of the equipment is given in Figure 1. Pulses from the detector are routed to two single-channel analyzers which are set to span characteristic γ-energy regions for each tracer; pulses from both single-channel analyzers are mixed and fed into the analog-digital converter. These pulses, through 4-μsec. delay lines, are used to route the counting data to the appropriate

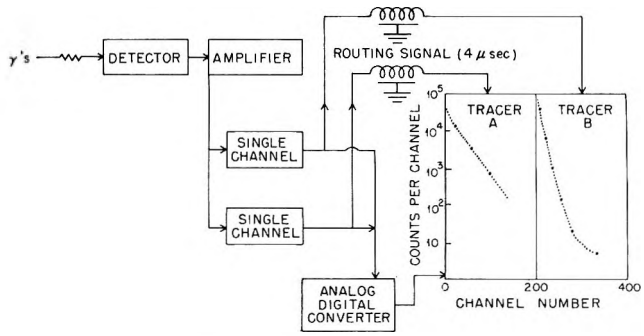

Figure 1. Simultaneous counting of two tracers with a multichannel analyzer.

memory unit of the analyzer. Counts of the individual tracers are stored in separate halves of the memory of the multichannel analyzer. With two crystals, counting rates of four different tracers may be measured simultaneously and, in these cases, the data are stored in separate quarters of the memory unit.

The radioisotopes ^{42}K ($T_{1/2}$ = 12.4 hr.), ^{82}Br ($T_{1/2}$ = 35.5 hr.), ^{65}Zn ($T_{1/2}$ = 246 days), and ^{131}I ($T_{1/2}$ = 8 days) were obtained from the Radioisotopes Division of ORNL. The ^{22}Na ($T_{1/2}$ = 2.6 years) was obtained from Nuclear Science and Engineering Corp. Tracer solutions for diffusion measurements were prepared by evaporating aliquots of "stock" tracer solutions to dryness and taking up the residue with appropriate electrolyte solutions. Reagent grade chemicals were used throughout. For solutions for which viscosity data were not available, viscosities were measured relative to water with a Cannon–Ubbelohde viscometer at 25 ± 0.02°.[5]

Results and Discussion

1. Method. The porous-frit method apparently was first used by Wall, Grieger, and Childers[2a] for determining diffusion rates of slowly diffusing polymers. They suspended a porcelain disk, saturated with the solution of interest, in a bath from the arm of an analytical balance and determined the weight change of the frit as a function of time. The bath liquid was vigorously stirred except when weighings were made. From the weight–time data, relative diffusion rates

(2) (a) F. T. Wall, P. F. Grieger, and C. W. Childers, *J. Am. Chem. Soc.*, **74**, 3562 (1952); (b) F. T. Wall and R. C. Wendt, *J. Phys. Chem.*, **62**, 1581 (1958).

(3) F. Grün and C. Blatter, *J. Am. Chem. Soc.*, **80**, 3838 (1958).

(4) (a) F. Nelson and K. A. Kraus in "Production and Use of Short-Lived Isotopes from Reactors," Vol. I, IAEA, Vienna, 1962–1963, p. 191; (b) F. Nelson, *J. Polymer Sci.*, **40**, 563 (1959).

(5) We are indebted to Dr. R. J. Raridon and Mr. C. G. Westmoreland of the ORNL Chemistry Division for carrying out these viscosity measurements.

were determined from which diffusion coefficients were obtained by calibrating the frits with material of known diffusion coefficients.

In the radiometric porous frit method,[4] which is similar to the method of Wall, *et al.*, a porous frit is saturated with a solution containing a radioisotope and a solution of the same composition but not containing tracer is pumped past the frit; the counting rate, C, of the frit is determined as a function of time. These measurements are made continuously, in contrast with the weighing method where stirring must be interrupted or the frit removed from the bath during the time a measurement is made. Diffusion coefficients may be evaluated from the counting rate–time data if the flow rate past the frit is sufficiently rapid so that the tracer concentration at the frit–solution interface can be set substantially equal to zero.

With these boundary conditions and the additional restriction that $\mathfrak{D}$ does not vary with concentration of tracer, the diffusion equation has a simple solution[6]: after an initial transient, the counting rate of the frit decreases as $e^{-\lambda_s t}$ where $\lambda_s = A\mathfrak{D}$ and A is a constant which is characteristic for each frit. This asymptotic exponential relation has been shown to hold even for irregularly shaped frits.[3]

When $\mathfrak{D}$ varies with concentration of the diffusing substance, interpretation of concentration–time functions is difficult. As pointed out by Wall and Wendt,[2b] the functional relationship between concentration and diffusion must be available (or assumed) in order to evaluate $\mathfrak{D}$ from the data. The present study is restricted to tracer and self-diffusion systems in which $\mathfrak{D}$ can reasonably be assumed independent of concentration of tracer.

The (diffusional) "decay constant" λ_s is readily evaluated from the linear portion of a plot of ln C (or log C) *vs.* time. The frit constant A is determined by a calibration experiment with a standard, *i.e.*, a material for which $\mathfrak{D}$ is known; $\mathfrak{D}$ for a tracer of interest may then be obtained from the relationship, $\mathfrak{D} = \mathfrak{D}_{std}\lambda_s/\lambda_{s(std)} = \lambda_s/A$, where $\mathfrak{D}_{std}$ and $\lambda_{s(std)}$ are the diffusion coefficient and observed slope for the standard.

As in Wall's method, the assumption is made throughout that there are no significant or specific interactions between the frit material and the solute whose $\mathfrak{D}$ is to be determined. With pores as large as those of unglazed porcelain and solutes of size small compared with the size of the pores (as is the case here) there should be no serious problems at reasonable concentrations of the solute of interest. However, at high dilution and in carrier-free tracer experiments, adsorptive properties of the frit material may cause errors, if the frit material has significant adsorptive capacity or reasonable selectivity for the tracer. In this case, reliability of the method may be tested by determining the distribution coefficient D of the tracer between frit and solution; D should be unity if expressed in terms of amount of tracer in the frit per gram of imbibed solution and amount of tracer per gram of contacting solution. It is also desirable to check separately for the absence of radioactive impurities in the tracer which might be selectively adsorbed by the frit material.

When short-lived tracers are used, significant radioactive decay of the tracer may occur during the experiment. The (asymptotic) diffusional decay constant may then be obtained from the observed slope, $\lambda_{obsd} = -\mathrm{d}\ \ln C/dt$ through the relation $\lambda_s = \lambda_{obsd} - \lambda$, where λ is the radioactive decay constant.

2. Calibration. For calibration of the frits, diffusion of Na^+ in 1 M NaCl solution was chosen as standard. Not only has self-diffusion of Na^+ in NaCl solutions been extensively studied by diaphragm cell and capillary tube methods but convenient γ-emitting tracers of Na (^{22}Na and ^{24}Na) are also available. While for 1 M NaCl values of $\mathfrak{D}_{Na}$ ranging from 1.20 to 1.30×10^{-5} cm.^{2} sec.$^{-1}$ have been reported,[7-11] it appears from the most recent study by Mills[11] that precise values for the self-diffusion coefficients of Na^+ have now been established for a fairly wide range of NaCl concentrations. Mills carefully corrected for, or avoided, sources of error in the capillary tube and diaphragm methods he used and was able to obtain agreement (within 1%) between the two methods; for 1 M NaCl, $\mathfrak{D}_{Na} = 1.234 \times 10^{-5}$ cm.^{2} sec.$^{-1}$ was found and we have used this value for calibrations.

To obtain meaningful calibration results and measurements of $\mathfrak{D}$, $-\mathrm{d}\ \ln C/\mathrm{d}t = \lambda_{obsd}$ should be independent of flow rate. In a series of tests with the 0.33- and 0.53-mm. frits in 1 and 5 M NaCl solutions, λ_s was measured as a function of flow rate in the range *ca.* 0.1–115 cm./sec. A broad plateau was observed in the region 1 to 50 cm./sec. where λ_s remained constant within limits of experimental error. At lower flow rates, λ_s was lower than the plateau value, while at flow rates above 50 cm./sec., λ_s was significantly greater than the plateau value, particularly

(6) W. Yost, "Diffusion in Solids, Liquids, Gases," Academic Press, Inc., New York, N. Y., 1952, Chapter 8, p. 37.

(7) J. M. Neilson, A. W. Adamson, and J. W. Cobble, *J. Am. Chem. Soc.*, **74**, 446 (1952).

(8) J. H. Wang and S. Miller, *ibid.*, **74**, 1611 (1952).

(9) R. Mills and J. W. Kennedy, *ibid.*, **75**, 5696 (1953).

(10) R. Mills and A. W. Adamson, *ibid.*, **77**, 3454 (1955).

(11) R. Mills, *ibid.*, **77**, 6116 (1955).

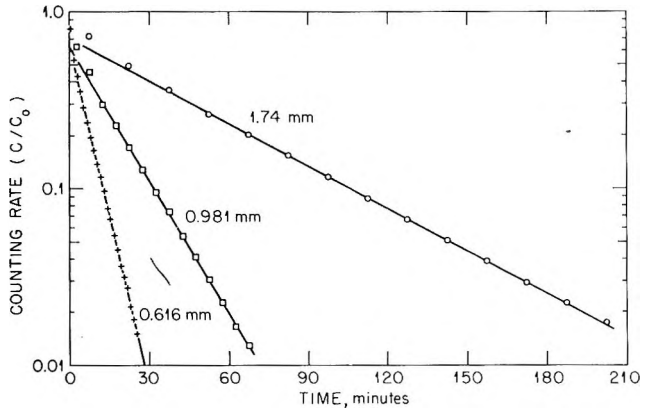

Figure 2. Calibration of porous frits of various thicknesses (^{22}Na + 1 *M* NaCl, 25°).

if the frits were placed in the supporting holder at a slight angle to the direction of flow. On the basis of these experiments, all calibration and diffusion measurements were carried out at flow rates of *ca.* 10–20 cm./sec. and precautions were taken to align the frits parallel with the direction of flow.

Typical calibration experiments are shown in Figure 2. For these experiments, 0.616-, 0.981-, and 1.74-mm. frits were saturated with 1 *M* NaCl containing ^{22}Na and then eluted with 1 *M* NaCl. The initial counting rates of the frits were about 5×10^4 counts/min. Counting intervals were 25, 50, and 100 sec., respectively. The data plotted represent summations over several counting intervals. After an initial transient, log C/C_0 decreases linearly with time, with λ_s ranging from 2.38×10^{-3} to 3.01×10^{-4} sec.$^{-1}$, which corresponds to diffusion "half-times" of 4.84 to 38.3 min.

Calibration data for frits of various thickness and from two different samples of porcelain are summarized in Table I; values of λ_s represent an average of at least two determinations. To illustrate reproducibility, five individual values are listed for the 0.981-mm. frit along with the average value. Reproducibility seems better than ±2%.

The constant, $A = \lambda_{s(Na)}/\mathfrak{D}_{Na}$, which should be independent of the electrolyte used to calibrate the frit, was computed for each frit. Considering the frit as an "infinite slab," A should be[6] inversely proportional to the square of the thickness d and as shown in Table I, the product, Ad^2, is essentially constant for a given frit material as expected. However, for two different porcelain samples, Ad^2 shows significant differences presumably because of differences in structure and porosity of the materials.

3. Diffusion of K^+ and I^- in KI Solutions. Diffusion coefficients of K^+ and I^- in 0.5 and 1 *M* KI solutions were determined and the results are compared in Table II with measurements of Mills and Kennedy[9] obtained by the capillary tube method. Agreement between the two methods seems satisfactory; the frit method yields diffusion coefficients which are lower but within experimental error (2–3%) of corresponding measurements by the capillary tube method.

Table I: Calibration of Porous Frits with NaCl Solution[a]

Material	d, mm.		$\lambda_s \times 10^3$, sec.$^{-1}$	$A \times 10^{-2}$, cm.$^{-2}$	Ad^2
Porcelain I	0.616		2.38	1.93	0.732
	.752		1.51	1.22	0.690
	.981		0.933		
			0.942		
			0.938		
			0.944		
			0.933		
		Av.	0.938	0.760	0.731
	1.28		0.549	0.445	0.729
	1.74		0.301	0.244	0.739
Porcelain II	0.33		12.0	9.72	1.058
	0.53		4.66	3.78	1.062

[a] 1 *M* NaCl + ^{22}Na, 25°, $\mathfrak{D}_{Na} = 1.234 \times 10^{-5}$ cm.^{2} sec.$^{-1}$.

Table II: Self-Diffusion Coefficients of K^+ and I^- in KI Solutions at 25°

		$\mathfrak{D} \times 10^5$, cm.^{2} sec.$^{-1}$		
M KI	Ion	Frit method	Capillary tube method[a]	Difference, %
0.5	K^+	1.96	2.03	3.6
1.0		1.99	2.03	3.0
0.5	I^-	1.91	1.96	2.0
1.0		1.88	1.94	2.6

[a] Data of Mills and Kennedy, ref. 9.

4. Zn(II) in KCl Solutions. In preliminary experiments, tracer Zn(II) (*ca.* 10^{-7} *M*) in neutral KCl solutions was found to adsorb appreciably on porcelain; no adsorption occurred, however, if a small amount of acid (*ca.* 10^{-3} to 10^{-2} *M* HCl) was present. Hence, to avoid adsorption difficulties, diffusion measurements were carried out with KCl solutions containing 10^{-2} *M* HCl.

Diffusion coefficients of tracer Zn(II) in 0.25–4.0 *M* KCl (10^{-2} *M* HCl) are compared in Table III with data of Wang[12] obtained by the capillary tube method. For the latter, KCl solutions containing 5×10^{-4}

(12) J. H. Wang, *J. Am. Chem. Soc.*, **76**, 1528 (1954).

M HCl were used; in addition, possible adsorption of ^{65}Zn tracer on the walls of the capillary was avoided through use of 5×10^{-3} M Zn(II) solutions. While diffusion coefficients of Zn(II) obtained by the frit method are generally slightly lower than those obtained by the capillary tube method, agreement between the two methods is within experimental error.

Table III: Diffusion Coefficients of Tracer Zn(II) in KCl Solutions (10^{-2} M HCl) at 25°

	$\mathfrak{D} \times 10^5$, cm.² sec.⁻¹		
M KCl	Frit method	Capillary tube method[a]	Difference, %
0.25	0.71	0.73	2.8
1.00	0.81	0.82	1.2
2.00	0.93	0.94	1.1
3.00	0.97	0.97	0.0
4.00	0.94	0.95	1.1

[a] Data of Wang, ref. 12.

5. Diffusion of K^+ in KCl Solutions. Diffusion coefficients of K^+ in 0.25–4.0 M KCl solutions (containing 5×10^{-4} M HCl) were determined and the product $\mathfrak{D}^* = \mathfrak{D}\eta/\eta_0$, where η/η_0 is the viscosity of the medium relative to water, was computed. As seen in Table IV, while $\mathfrak{D}_K$ decreases significantly with increasing KCl concentration, $\mathfrak{D}^*_K$ shows only minor variations with increasing ionic strength.

Table IV: Self-Diffusion Coefficients of K^+ in KCl Solutions at 25°

M KCl	$\mathfrak{D}_K \times 10^5$, cm.² sec.⁻¹	$\mathfrak{D}^*_K \times 10^5$, cm.² sec.⁻¹
0.00	1.96[a]	1.96
0.25	1.91	1.92
1.00	1.85	1.86
2.00	1.84	1.86
3.00	1.84	1.91
4.00	1.75	1.90

[a] Nernst limiting value ($\mathfrak{D}^0$) computed from conductivity data.

6. Diffusion of Br^- in HBr, NaBr, and KBr Solutions. Diffusion coefficients $\mathfrak{D}$ and $\mathfrak{D}^*$ of Br^- in 0.1–8.8 M HBr, 0.05–2.5 M NaBr, and 0.1–4.0 M KBr were determined and are given in Table V. For all three electrolytes, $\mathfrak{D}_{Br}$ decreases appreciably with increasing ionic strength while $\mathfrak{D}^*_{Br}$ varies only slightly. A similar invariance of $\mathfrak{D}^*_{Br}$ with ionic strength was observed earlier[4] with tracer Br^- in HCl, LiCl, and benzyltrimethylammonium chloride solutions. Although for the latter electrolyte the influence of viscosity on diffusion is particularly large at high concentrations, $\mathfrak{D}^*_{Br}$ is remarkably constant over a wide range of ionic strength.

Table V: Self-Diffusion Coefficients of Br^- in HBr, NaBr, and KBr Solutions at 25°[a]

Electrolyte	M	$\mathfrak{D}_{Br} \times 10^5$, cm.² sec.⁻¹	$\mathfrak{D}^*_{Br} \times 10^5$, cm.² sec.⁻¹
HBr	0.174	2.00	2.02
	0.702	1.90	1.95
	1.36	1.81	1.88
	2.46	1.73	1.87
	4.91	1.53	1.87
	8.78	1.13	1.86
NaBr	0.050	1.94	1.95
	0.50	1.90	1.96
	1.00	1.78	1.90
	1.50	1.75	1.93
	2.00	1.67	1.93
	2.50	1.58	1.91
KBr	0.100	1.95	1.95
	0.500	1.96	1.93
	1.00	1.93	1.87
	2.00	1.92	1.84
	3.00	1.86	1.81
	4.00	1.77	1.78

[a] $\mathfrak{D}^0_{Br} = 2.079 \times 10^{-5}$ cm.² sec.⁻¹.

7. Diffusion of Zn(II) in HCl and $HClO_4$ Solutions. As pointed out by Wang,[12] the rapid increase of D_{Zn} with increasing KCl concentration implies that Zn(II) diffuses considerably more rapidly in the form of chloride complexes than in uncomplexed forms. Since solutions of higher chloride concentration can be prepared with HCl than with KCl, it appeared of interest to measure diffusion coefficients of Zn(II) over a wider range of chloride concentration through use of HCl solutions. The results are shown in Table VI for 0.1 to 10 M HCl solutions along with corresponding data for the diffusion of Zn(II) in essentially noncomplexing media, 0.2 to 10 M $HClO_4$.

The observed values for $\mathfrak{D}_{Zn}$ may be compared with the diffusion coefficient of Zn^{+2} at infinite dilution ($\mathfrak{D}^0_{Zn}$) computed from conductivity data and the Nernst equation, $\mathfrak{D}^0_i = RT\lambda^0_i/z_iF^2$, where R is the gas constant, F is the Faraday, T is absolute temperature, λ^0_i is the equivalent conductance of diffusing species i, and z_i is its valence. Using $\lambda^0_{Zn} = 52.8$[13] and $z_i = 2$, $\mathfrak{D}^0_{Zn} = 0.71 \times 10^{-5}$ cm.² sec.⁻¹ was computed. At low acid concentrations (0.1 M HCl or $HClO_4$)

(13) B. B. Owen and R. W. Gurry, *J. Am. Chem. Soc.*, **60**, 3074 (1938).

Table VI: Tracer Diffusion of Zn(II) in $HClO_4$ and HCl Solutions at 25°

Electrolyte	M	$\mathfrak{D}_{Zn} \times 10^6$, cm.² sec.⁻¹	$\mathfrak{D}^*_{Zn} \times 10^6$, cm.² sec.⁻¹
$HClO_4$	0.100	0.72	0.72
	1.00	0.72	0.73
	5.97	0.56	0.88
	9.04	0.37	1.01
HCl	0.100	0.71	0.71
	1.00	0.76	0.81
	1.50	0.80	0.87
	2.02	0.85	0.95
	4.00	0.82	1.02
	6.04	0.75	1.06
	10.0	0.59	1.09

the observed values for $\mathfrak{D}_{Zn}$ are the same, within experimental error, as the computed value for $\mathfrak{D}^0_{Zn}$. In $HClO_4$, $\mathfrak{D}_{Zn}$ decreases with increasing $HClO_4$ concentration, particularly at high $HClO_4$ concentrations where viscosity effects are large. In HCl, however, $\mathfrak{D}_{Zn}$ increases with increasing M HCl to a slight maximum, $\mathfrak{D}_{Zn} = 0.85 \times 10^{-5}$ cm.² sec.⁻¹, near 2 M HCl and then decreases with further increase of HCl concentration.

More revealing of differences in diffusion of the Zn(II) species in HCl and $HClO_4$ solutions are the variations of $\mathfrak{D}^*_{Zn}$ (Figure 3). For $HClO_4$ solutions, $\mathfrak{D}^*_{Zn}$ rises gradually with increasing acid concentration; in HCl, $\mathfrak{D}^*_{Zn}$ rises very rapidly with increasing HCl concentration and levels out near 4 M HCl. The rapid increase of $\mathfrak{D}^*_{Zn}$ between 0.1 and 2 M HCl may be attributed to chloride complexing reactions which occur particularly in this region of chloride concentration.[14] In the region 4 to 10 M HCl, where Zn(II) presumably exists principally as negatively charged chloride complexes, $\mathfrak{D}^*_{Zn}$ increases only slightly with increasing M HCl.

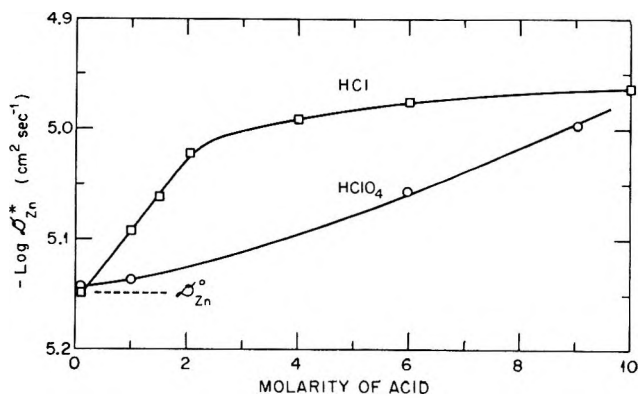

Figure 3. Diffusion of tracer Zn(II) in HCl and $HClO_4$ solutions.

8. Discrimination Techniques; Diffusion of Tracer Zn(II) and K^+ in KCl Solutions. To test the method for simultaneously measuring diffusion rates of two radioisotopes, diffusion coefficients of ^{65}Zn and ^{42}K in KCl solutions were determined. This system appeared particularly suitable for testing purposes since the results could be compared with the diffusion coefficients of Zn(II) and K^+ in KCl solutions established by integral counting techniques (Tables III and IV). In addition, the principal γ-energies of ^{65}Zn and ^{42}K, 1.12 and 1.52 Mev., respectively, are easily discriminated.

The experiments were carried out with the 0.98-mm. frit; the frit was equilibrated with slightly acidified 0.25–4.0 M KCl solutions containing ^{42}K and ^{65}Zn and then eluted. Diffusion rates were measured by counting pulses in the regions 1.0–1.2 and 1.4–1.6 Mev.; these energy regions conveniently span the principal γ-energy peaks of ^{42}K and ^{65}Zn, respectively.

The results of a typical experiment are shown in Figure 4, a semilog plot of counting rate, corrected for "background," *vs.* time. After an initial transient, the counting rates of the two tracers decrease with time in the expected exponential manner.

The "background" corrections for the ^{65}Zn counting data include room background and also a correction for scattered radiation from the higher energy ^{42}K. For the latter, the counting rate of ^{42}K in the ^{65}Zn

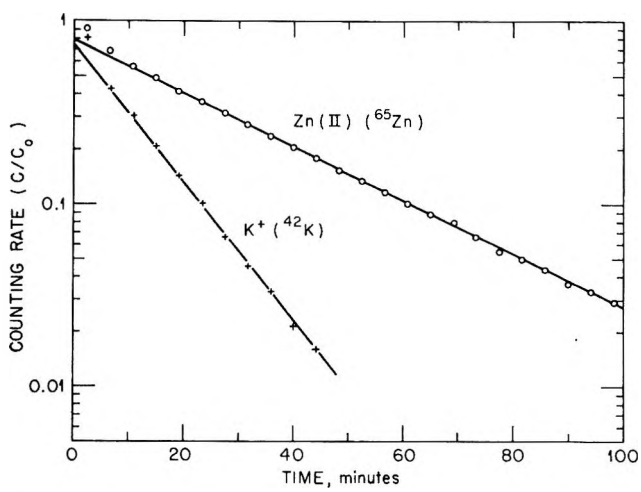

Figure 4. Simultaneous measurement of diffusion rates, K^+ and Zn(II) in 1 M KCl (0.981-mm. frit, 25°).

(14) K. A. Kraus and F. Nelson, "Symposium on the Structure of Electrolytes," Electrochemical Society Meeting, Spring, 1957, Walter J. Hamer, Ed., John Wiley and Sons, Inc., New York, N. Y., 1959.

region (1.0–1.2 Mev.) was established relative to its "normal" counting rate at 1.4–1.6 Mev., and from these data appropriate "background" corrections were computed.

Diffusion coefficients of K^+ and Zn(II) obtained by the γ-discrimination method were in excellent agreement with corresponding values from Tables III and IV determined by integral counting. The extent to which the methods agree is illustrated in Table VII, where the ratio, R, of diffusion coefficients obtained by γ-discrimination methods to those obtained by integral counting are given for K^+ and Zn(II) in 0.25–4.0 M KCl. Within experimental error, the same value of $\mathfrak{D}$ was obtained by the two methods and hence R is seen to be essentially unity for the various experiments.

Table VII: Ratio of Diffusion Coefficients Measured by γ-Discrimination and Integral Counting Methods: K^+ and Zn(II) in KCl Solutions at 25°

	Ratio of diffusion coefficients, R	
M KCl	K^+	Zn(II)
0.25	1.01	1.00
1.00	1.02	0.99
3.00	1.01	0.99
4.00	1.03	1.01

9. Summary. We have endeavored in these studies to illustrate the general applicability of the radiometric porous-frit method. The speed and simplicity of the technique are especially advantageous. The method also has broad applicability since convenient tracers for most elements are now available and hence systematic and comparative diffusion studies may be carried out in a reasonably short time.

With the thin frits we have used, usually 0.3 to 1.0 mm. in thickness, a diffusion experiment can usually be completed in less than 1 hr. In systems where diffusion rates are slow, more time is required; however, in principle at least, time requirements may be minimized by use of even thinner frits.

Acknowledgment. The authors are indebted to Mr. J. W. Woody, Jr., and Mr. J. A. Keathley of the ORNL Instrument Division for assembling the counting equipment and for helpful advice concerning its use.

The Thermodynamic Properties of Soluble Monolayers Produced by the Normal Alcohols (C_8 to C_{12}) at the Water–Octane Interface

by Joseph J. Jasper and Barton L. Houseman

Department of Chemistry, Wayne State University, Detroit, Michigan *(Received August 27, 1964)*

The interfacial surface pressures produced by soluble monolayers of five normal alcohols (C_8 to C_{12}) at the water–octane interface were measured and their values were used to calculate the entropies, latent heats, and enthalpies of adsorption over a temperature and concentration range. These values are presented in tables as functions of the temperature and concentration. The interfacial surface excess concentrations and effective molecular areas of the oriented dipoles were also calculated and their respective values are given in a table. Plots (not shown) of the molecular areas as functions of the interfacial surface pressures show a discontinuity similar to a gaseous to liquid-expanded transition at 30 and 50°.

In an earlier report[1] a differential method, furnished by a vertical-pull filmometer, was described for measuring the interfacial surface pressures produced by a series of monolayers consisting of five long-chain normal alcohols C_8 to C_{12}. Since it was desired to measure the interfacial surface pressures under conditions uncomplicated by such factors as reciprocal solubility, the immiscible liquid components selected for the different systems were water and *n*-octane. These remained virtually mutually immiscible over the temperature range of the measurements. The monolayers formed spontaneously at the interface between the immiscible liquids as a result of positive adsorption from the octane phase. The interfacial surface pressures were varied by changing the temperature and the concentrations of the alcohols in the octane phase.

Experimental

Purification of the Compounds. The alcohols selected for the monolayer component of the systems were 1-octanol, 1-nonanol, 1-decanol, 1-undecanol, and 1-dodecanol. This series of alcohols meets the requirement of insolubility in the aqueous phase while remaining in the liquid state at ambient temperatures. The exact procedure for the purification and test of purity of these compounds, and also for that of the water and *n*-octane used, was described in a previous paper.[1]

Description of Apparatus. Since a complete description of the instrumentation, operation, and chief sources of error was previously given,[1] these will not be repeated herein. It is worthwhile, however, to reemphasize the importance of preparing the pendant slide for operation since it is very probably the most critical part of the apparatus. For the present investigation it was necessary that the pendant slide consist of a substance chemically inert, insoluble in *n*-octane and water, but readily wetted by the former of these and not by the latter. DuPont Teflon met these prerequisites quite satisfactorily. Numerous tests proved that the surface of the slide must be very clean, mirror-smooth, and nonporous, to obtain a very small contact angle with *n*-octane. Any appreciable departure from a practically zero contact angle was readily detected. It was found that a contact angle appreciably greater than zero is labile and shows appreciable hysteresis in the vertical motion of the pendant slide. This effect is readily detected in the behavior of the balance pointer. Thus, a sudden decrease in the sensitivity of the balance and a shortening of the period and average arc of the pointer indicated hysteresis, and the experimental results were rejected.

(1) J. J. Jasper and B. L. Houseman, *J. Phys. Chem.*, **67**, 1548 (1963).

Table I: Free Energy of Formation of the Monolayers (ergs cm.$^{-2}$) as a Function of the Temperature and Concentration (m)

	1-Octanol			1-Nonanol			1-Decanol			1-Undecanol			1-Dodecanol		
m	25°	35°	45°	25°	35°	45°	25°	35°	45°	25°	35°	45°	25°	35°	45°
0.01	41.1	42.6	43.1	41.0	42.3	42.8	41.1	42.4	43.1	40.9	42.5	43.4	41.0	42.2	42.8
0.02	36.4	38.0	38.9	36.2	37.9	39.1	36.4	38.0	40.2	36.5	38.3	39.5	36.6	38.2	39.2
0.03	33.3	35.1	36.1	33.2	35.0	36.3	33.7	35.4	36.6	33.8	35.6	36.9	33.7	35.4	36.7
0.04	31.2	32.9	34.1	31.2	32.9	34.3	31.5	33.2	34.5	31.6	33.5	34.8	31.9	33.4	34.8
0.05	29.6	31.4	32.7	29.8	31.3	32.7	30.2	31.8	33.1	30.3	31.9	33.2	30.4	31.7	32.7
0.07	27.5	28.9	29.9	27.7	29.1	30.1	28.2	29.6	30.7	28.5	29.9	31.0	28.6	29.9	30.9
0.10	25.8	26.8	27.4	26.0	27.0	27.7	26.4	27.5	28.3	26.8	27.9	28.8	27.0	28.0	28.8
0.15	24.2	24.8	25.1	24.6	25.2	25.5	25.0	25.7	26.1	25.2	26.1	26.7	25.5	26.3	26.8
0.20	23.1	23.6	23.7	23.6	24.1	24.3	24.1	24.6	24.9	24.3	25.0	25.4	24.6	25.3	25.7
0.30	21.9	22.1	22.0	22.3	22.6	22.7	22.9	23.3	23.5	23.3	23.8	24.1	23.6	24.1	24.4

Results

If it is assumed that the surface pressure equation[2] can be applied to monolayers at the interface between mutually immiscible liquids, it may be written as

$$P_i^s = \gamma_i - \gamma_f \tag{1}$$

in which P_i^s represents the lateral pressure exerted by the interfacial monolayer, γ_i the interfacial free surface energy of the pure interface, and γ_f the interfacial free surface energy with the monolayer present. It is to be noted that P_i^s is the difference in the magnitude of two interfacial free energies. The larger of these, γ_i, involves the interface between the pure liquid components, and the smaller, γ_f, the same interface occupied by the oriented dipoles which constitute the interfacial monolayer. It is pertinent, therefore, to note that the quantity $(\gamma_i - \gamma_f)$ represents the decrease in the interfacial free surface energy as a consequence of the positive adsorption of the alcohols from the octane phase and will always be negative for a positively adsorbed solute. Equation 1, therefore, can be written as

$$P_i^s = -\Delta\gamma_i = -\Delta F_{ad} \tag{2}$$

Equation 1 can be rearranged to read

$$P_i^s - \gamma_i = -\gamma_f \tag{3}$$

which enables the calculation of the free energy decrease attending the formation of unit area of film-covered interfaces. Values of $-\gamma_f$ are readily calculated by subtracting the interfacial tensions of the pure interface from P_i^s, which is measured directly. The interfacial tensions of the water–octane system are given as functions of the temperature by the equation

$$\gamma_i = 50.904 + 0.0241t - 0.00143t^2 \tag{4}$$

which was derived from the data of Harkins and Cheng.[3] The γ_f values for the five alcohols at ten concentrations for the temperature range 25 to 45° are shown in Table I.

The thermodynamic equation of Clapeyron was modified by Lord Kelvin for application to two-dimensional liquid surfaces. This equation can be applied to the interfacial region between mutually immiscible liquids and, accordingly, takes the form

$$-(d\gamma_i/dT) = L_i^s/T \tag{5}$$

in which L_i^s represents the latent heat of formation of unit area of interface. With the aid of this equation various thermodynamic quantities involving the interfacial region can be calculated. Substitution of P_i^s in eq. 5 gives

$$(dP_i^s/dT) = L_i^s/T = \Delta S_i^s \tag{6}$$

This equation is general for the interfacial region and, accordingly, can be applied to both the pure and the film-covered interface. Thus, from the temperature differential of P_i^s, the latent heat, L_{ad}^s, and the entropy, ΔS_{ad}^s, attending the formation of unit area of monolayer-covered interface can be determined. Values of (dP_i^s/dT) for the various concentrations of alcohols were obtained from large-scale plots of interfacial surface pressure *vs.* temperature isopleths. Slopes were measured with a tangentimeter[4] for the different temperatures. From these values, the entropies and latent heats of adsorption attending the monolayer formation were calculated. These are shown in Tables II and III, respectively.

(2) W. D. Harkins, "The Physical Chemistry of Surface Films," Reinhold Publishing Corp., New York, N. Y., 1952, p. 121.

(3) W. D. Harkins and Y. C. Cheng, *J. Am. Chem. Soc.*, **43**, 35 (1921).

(4) A similar instrument was used and described by V. R. Damerell, K. H. Gayer, and H. Laudenslager, *J. Phys. Chem.*, **49**, 436 (1945).

Table II: Entropies of Adsorption (ergs cm.$^{-2}$ deg.$^{-1}$) as Functions of the Temperature and Volume-Molal Concentration

	1-Octanol					1-Nonanol			1-Decanol					1-Undecanol			1-Dodecanol		
m	25°	35°	45°	55°	65°	25°	35°	45°	25°	35°	45°	55°	65°	25°	35°	45°	25°	35°	45°
0.01	0.25	0.16	0.12	0.09	0.07	0.23	0.16	0.14	0.23	0.17	0.13	0.11	0.10	0.24	0.19	0.16	0.22	0.16	0.14
0.02	0.25	0.19	0.16	0.15	0.15	0.25	0.21	0.20	0.25	0.21	0.20	0.17	0.16	0.26	0.22	0.20	0.25	0.20	0.19
0.03	0.25	0.21	0.19	0.18	0.18	0.26	0.22	0.22	0.25	0.21	0.20	0.17	0.16	0.27	0.22	0.21	0.25	0.22	0.21
0.04	0.25	0.22	0.20	0.19	0.19	0.24	0.23	0.23	0.23	0.22	0.23	0.22	0.22	0.25	0.23	0.22	0.24	0.22	0.21
0.05	0.24	0.23	0.20	0.19	0.19	0.23	0.21	0.22	0.22	0.22	0.22	0.22	0.22	0.22	0.22	0.22	0.21	0.19	0.19
0.07	0.19	0.20	0.20	0.20	0.20	0.19	0.19	0.20	0.20	0.20	0.20	0.23	0.26	0.19	0.20	0.20	0.19	0.18	0.19
0.10	0.16	0.16	0.16	0.19	0.21	0.16	0.16	0.16	0.17	0.17	0.17	0.20	0.29	0.17	0.18	0.17	0.17	0.16	0.16
0.15	0.12	0.12	0.12	0.16	0.20	0.13	0.12	0.12	0.14	0.13	0.13	0.17	0.26	0.15	0.15	0.15	0.15	0.14	0.14
0.20	0.11	0.10	0.10	0.14	0.19	0.12	0.11	0.11	0.11	0.12	0.12	0.16	0.24	0.13	0.13	0.13	0.13	0.13	0.12
0.30	0.08	0.08	0.08	0.11	0.15	0.09	0.09	0.09	0.10	0.10	0.10	0.13	0.17	0.11	0.11	0.11	0.11	0.11	0.11

Table III: Latent Heats of Adsorption (ergs cm.$^{-2}$) as Functions of the Temperat ure and Volume-Molal Concentration

	1-Octanol					1-Nonanol			1-Decanol					1-Undecanol			1-Dodecanol		
m	25°	35°	45°	55°	65°	25°	35°	45°	25°	35°	45°	55°	65°	25°	35°	45°	25°	35°	45°
0.01	75	49	38	30	24	69	49	45	69	52	41	36	34	72	59	52	66	49	45
0.02	75	59	51	49	51	75	65	64	75	65	64	56	54	78	68	64	75	62	60
0.03	75	65	60	59	61	78	68	70	75	65	70	66	64	81	68	67	75	68	67
0.04	75	68	64	62	64	72	71	73	69	68	73	72	74	75	71	70	72	68	67
0.05	72	71	64	62	64	69	65	70	66	68	70	72	74	66	68	70	63	59	60
0.07	57	62	64	65	68	57	59	64	60	62	64	75	88	57	62	64	57	55	60
0.10	48	49	51	62	71	48	49	51	51	52	54	66	98	51	52	54	51	49	51
0.15	36	37	38	52	68	38	37	48	42	40	41	56	88	45	46	48	45	43	45
0.20	33	31	32	46	64	35	34	35	33	37	38	52	81	39	40	41	39	40	38
0.30	24	25	26	36	51	27	28	29	30	31	32	43	57	33	34	35	33	34	35

Table IV: Enthalpy of Adsorption (ergs cm.$^{-2}$) as Functions of the Temperature and Volume-Molal Concentration

	1-Octanol					1-Nonanol			1-Decanol					1-Undecanol			1-Dodecanol		
m	25°	35°	45°	55°	65°	25°	35°	45°	25°	35°	45°	55°	65°	25°	35°	45°	25°	35°	45°
0.01	85	56	44	35	28	79	57	51	79	60	47	41	38	82	67	57	76	57	51
0.02	89	71	61	58	58	89	77	74	89	77	73	64	60	92	80	74	89	74	70
0.03	92	80	73	70	70	95	83	83	92	80	82	76	72	97	82	79	92	83	79
0.04	94	85	79	75	75	91	88	88	88	85	88	84	84	94	87	84	91	85	81
0.05	93	90	80	77	77	90	84	86	86	86	86	86	86	86	86	86	83	77	76
0.07	80	83	83	82	83	80	80	83	82	82	82	91	102	79	82	82	79	75	78
0.10	73	72	73	82	89	73	72	72	75	74	75	85	114	74	74	74	75	71	71
0.15	62	62	62	74	89	64	62	71	68	64	64	78	107	70	70	70	70	67	67
0.20	61	57	57	70	87	62	60	69	60	62	62	75	102	65	65	65	65	65	62
0.30	53	53	53	62	76	..	..	..	58	58	58	67	80	60	60	60	60	60	60

The two-dimensional analog of the well-known free energy equation can be written as

$$\Delta H_{ad}^{s} = P_i^{s} + T\left(\frac{dP^{s}}{dT}\right) \qquad (7)$$

and this provides a method for calculating the enthalpy of adsorption. These are tabulated in Table IV.

The following form of the Gibbs equation was employed in the calculation of the surface-excess concentration, Γ, per unit area

$$\Gamma = \frac{1}{RT}\frac{dP_i^{s}}{d \ln C} \qquad (8)$$

To accomplish this purpose, a series of isotherms was

constructed by plotting the interfacial surface pressures as functions of the logarithm of the volume molality. The maximum slope at the various temperatures over the total concentration range (0.01 to 0.3 volume m) was selected for the calculation of the values of Γ. With this value available, the effective areas of the oriented dipoles in the monolayer were readily determined. These values are shown in Table V.

Table V: Maximum Surface Excess and Minimum Molecular Area as Functions of the Temperature

Compound	$-(\partial P_i^s/\partial \ln C)$			Surface excess, moles cm.$^{-2}$ × 10^{10}			Area per molecule, Å.^{2}		
	20°	30°	50°	20°	30°	50°	20°	30°	50°
1-Octanol	7.5	7.6	8.0	3.1	3.0	2.9	54	56	58
1-Nonanol	7.6	7.5	7.8	3.1	3.0	2.9	56	58	60
1-Decanol	7.2	7.3	7.4	3.0	2.9	2.8	56	58	60
1-Undecanol	7.3	7.5	7.4	3.0	3.0	2.8	56	56	60
1-Dodecanol	7.1	7.4	7.4	2.9	2.9	2.8	58	58	60

Discussion of Results

In an earlier report involving the five alcohols under consideration, it was shown that the values of $-\Delta F_{ad}$ increased rapidly with the concentration and appeared to be approaching a limiting value whose magnitude may possibly be determined by the structure of the monolayer. The magnitude of this quantity, however, was found to decrease with increasing temperature for all concentrations, as might be expected since adsorption phenomena are involved.

From reference to eq. 1 and 2, it is evident that the quantity P_i^s represents the decrease in the free interfacial surface energy resulting from positive adsorption during the formation of the interfacial monolayer. By application of appropriate and presently available data in eq. 3, the free energy decrease attending the formation of the monolayer-covered interface can be calculated. This will be designated as the free energy of formation of the monolayer. The magnitude of this quantity at the various concentrations and temperatures is shown in Table I.

It is to be noted that the free energies of the monolayer formations increase with the temperature and that these values decrease with increasing concentration at all temperatures. This increase appears to be the consequence of the decrease in positive adsorption from a solution with increasing temperatures. When the interfacial surface pressures of the five alcohols are plotted as functions of the concentration for the different temperatures of Table I[5] of the present report, the resulting isotherms prove that the greatest decrease in adsorption for the same increase in the temperature occurs at the smaller concentrations (0.01 to *ca.* 0.04 m). The interfacial surface pressures are a logical measure of adsorption, since they are proportional to the concentration of the adsorbed solute in the interface. Above *ca.* 0.05 m, this difference gradually decreases and becomes practically constant and nearly equal for all five alcohols at 0.2 m. The desorption resulting from the increased temperature would tend to cause the properties to approach those of the pure interface with the concomitant increase in the values of the free energies of monolayer formation. At the larger concentrations, however, an increasingly greater fraction of the total solute molecules are in the surface region as the result of diffusion pressure, and increased temperatures would have a lesser effect. These conclusions appear to be in accord with the data shown in Table I and are further supported by the data of Table II. The entropies of adsorption are very sensitive to temperature changes at low concentrations but are virtually independent of temperature at higher concentrations. This fact is evident in Table II. The P_i^s *vs.* ln C isotherms (not shown in this report) flatten out with increasing temperature at the lower concentrations, indicating that $\partial P^s/\partial \ln C$ of eq. 8, and, therefore, the surface excess, is decreasing. However, at larger concentrations (*ca.* 0.05 m and above), the value of $\partial P^s/\partial \ln C$ gradually increases at all temperatures, but this effect appears to be most pronounced at the higher temperatures.

A possible explanation of this increase in the surface excess with the temperature may involve the deviation of the octane solutions of the alcohols from ideality. Thus, at the lower temperatures, the use of concentrations rather than activities yields low values of the surface excess.[6] It is to be expected that this deviation should be smaller at the higher temperatures.

An examination of Table II shows that entropies of adsorption (ΔS_{ad}^s) decrease with increasing temperature for all of the alcohols up to *ca.* 0.05 volume m and then become virtually constant for the same temperature range (25 to 45°).

It is also to be noted that the entropy values increase with the concentration, pass through a maximum, and then decrease. These values may be the resultant of two effects, one to decrease and the other to increase the entropy. Thus, positive adsorption of solute molecules and their orderly orientation in the interface would decrease the entropy while diffusion pressure might lead to increasing disorder in the transitional phase. The

(5) See Table I of ref. 2.

(6) E. Hutchinson, *J. Colloid Sci.*, **3**, 219 (1948).

entropy change attending the latter is probably a logarithmic function of the concentration, since plots of the entropy of adsorption *vs.* volume molality give curves which closely resemble a logarithmic function. The same explanation appears to apply to the enthalpy and latent heats of adsorption, since the plots are very similar to those of the entropies.

Plots of the molecular areas of the oriented dipoles as functions of the interfacial surface pressure (not included in this report) show a well-defined point of discontinuity characteristic of a gaseous to liquid-expanded transition for all of the alcohols except 1-nonanol at 30 and 50°. With the exception of the latter, the transition pressures and areas form a fairly uniform series with increasing chain length, the pressures decreasing and the areas increasing slightly. At 20° the three shorter chain alcohols formed the condensed phase only. A similar transition was observed by Hutchinson and Randall[7] with 1-octanol, 1-decanol, and 1-dodecanol monolayers at the water–benzene interface.

The failure of the 1-nonanol to fall in line with the other alcohols leads the authors to assume that, regardless of the apparent purity of this compound as verified by vapor phase chromatographic analysis, a small amount of an isomeric alcohol was present.

The table of interfacial surface pressures of the five alcohols as functions of the temperature and concentration[1] reveals that Traube's rule does not apply to these interfacial monolayers. At low concentration, the interfacial surface pressures are independent of the chain length at low concentrations of the alcohols. At higher concentrations, the trend is in the direction opposite to that predicted.

(7) E. Hutchinson and D. Randall, *J. Colloid Sci.*, **7**, 151 (1952).

A Microcalorimetric Study of Liquid–Liquid Displacement Phenomena[1]

by Norman Hackerman and W. H. Wade

Department of Chemistry, The University of Texas, Austin, Texas *(Received August 14, 1964)*

Heat effects have been noted for the displacement of hydrocarbons from high energy metal oxide surfaces by water. The magnitude of the heats of displacement is in quantitative agreement with the heats of adsorption, thus satisfying the thermodynamic rigor. The measurements were performed in an immersion microcalorimeter.

Introduction

Fluid flow through porous media has long been a problem of considerable importance in the chemical and petroleum industries. One particular aspect, the equilibrium description of two-phase liquid systems within porous media, has remained an incompletely solved practical problem. The basic sources of difficulty are a lack of knowledge of the geometrical structures of the porous media, the chemical complexity of one or both of the liquid phases, and uncertainties in the nature of the chemical interactions between the pure phases and the surfaces of the porous media. One of the most common examples of such complex behavior is hydraulic displacement of crude oils from natural reserviors where the theoretical attractiveness of such processes is undermined by phenomena such as channeling and irreversible adsorption of impurities from the hydrocarbon phase by the substrate.

(1) This paper was presented orally at the 38th National A.I.Ch.E. Meeting.

Some years ago a thermodynamic study was undertaken here to provide some insight into the nature of the basic displacement process. Heats, free energies, and entropies of adsorption were obtained from experiments on a number of pure liquid phases in contact with high-energy metal oxide surfaces (H_2O, MeOH, and hexane on SiO_2, Al_2O_3, and TiO_2).[2-7] Focusing attention on adsorption enthalpies, calorimetrically measured heats of immersion corresponding to the immersion of a surface in a pure liquid are closely related to the more common differential gas phase heats of adsorption by

$$\Delta H_i(n_0) = \int_{n_0}^{n_{max}} \left(\frac{\partial \Delta H}{\partial n} - \Delta H_v \right) dn + \Delta H_s \cdot \Omega \quad (1)$$

and thus have an equally sound thermodynamic basis. $\Delta H_i(n_0)$ is the heat of immersion of a surface initially covered to the extent of n_0 moles of the immersant liquid, $\partial \Delta H/\partial n$ is the gas phase differential heat of adsorption, ΔH_v is the molar heat of vaporization of pure liquid, n is the number of moles adsorbed, ΔH_s is the surface enthalpy of pure liquid (obtained from surface tension measurements as a function of temperature), and Ω is the surface area of the adsorbate film on a surface equilibrated in the gas phase at a relative pressure, $P/P^0 = 1$.

Although many workers have measured heats of immersion for a variety of systems of outgassed powders in pure liquids and two-component single phase liquids, no measurements of the heats for the displacement of one preadsorbed liquid by a second have been undertaken. The systems most easily described are those where a weakly bonded adsorbate is displaced by a strongly bonded one. The experimental studies are for the displacement of hexane and decane from Al_2O_3 and SiO_2 powders by water, but other immersional pairs would be equally suitable to the following treatment.

If two identical samples of powdered substrate with a given surface state as defined by an equilibrium outgassing temperature and pressure are independently immersed in two pure liquid phases, α and β, the resulting heats of immersion are ΔH_i^{α} and ΔH_i^{β}. If the process involving phase α is reversed, the heat is $-\Delta H_i^{\alpha}$. Thus for the process where the substrate is pre-equilibrated in liquid phase α followed by subsequent immersion in phase β, the resulting heat of displacement is

$$\Delta H_D^{\alpha\beta} = \Delta H_i^{\beta} - \Delta H_i^{\alpha} \quad (2)$$

provided that the process as described is thermodynamically spontaneous and no spurious heat effects due to α–β interactions occur. The latter objection can be overcome by an appropriate selection of immersion liquid pairs, *e.g.*, hydrocarbon–water, and further by presaturation of the aqueous phase in the calorimeter with hydrocarbon. Thus from eq. 2 the measured heat of displacement of liquid phase α by phase β should be the difference of the measured heats of immersion in the pure phases if the process goes to completion. In addition, the time dependence of heat evolution should provide some insight to the kinetics of the displacement process.

Experimental

Four powdered substrate samples of various particle sizes were investigated. Three of the samples were Al_2O_3 with specific surface areas, Σ, of 2.72, 104, and 221 m.²/g. and the remaining sample was SiO_2 with a surface area of 188 m.²/g. The heats of immersion of these samples in hexane and water have been previously reported along with other pertinent data.[2b-4] The 221 m.²/g. Al_2O_3 sample is a condensed gel with a grain size of ~0.2 mm., whereas the other samples were loosely packed powders composed of unconsolidated particles.

Approximately 20-m.² samples were placed in thin-walled Pyrex ampoules, attached to a high vacuum system, and outgassed at selected temperatures from 100 to 450° at an ultimate pressure of 10^{-6} torr for 48 hr. After cooling to room temperature, Phillips research grade *n*-hexane (in some few experiments *n*-decane was substituted for *n*-hexane) previously dehydrated over Linde 4A Molecular Sieve was distilled onto the adsorbent samples so that the samples were immersed under bulk liquid. The ampoules were sealed off for subsequent loading in the calorimeter.

The microcalorimeter used in these studies has been described previously.[2a] It is of the thermistor temperature-sensing, twin differential, adiabatic type. Temperature excursions on sample breakage were $>10^{-3}$° and calibrations were performed electrically. Heat output was detected by a Leeds and Northrup Mueller G-2 bridge, the output coupled to a Liston–Becker d.c. amplifier, and then traced on a Moseley recorder. An R-C filter on the recorder input with a

(2) (a) A. C. Makrides and N. Hackerman, *J. Phys. Chem.*, **63**, 594 (1959); (b) W. H. Wade, R. L. Every, and N. Hackerman, *ibid.*, **64**, 355 (1960).

(3) W. H. Wade and N. Hackerman, *ibid.*, **64**, 1196 (1960).

(4) W. H. Wade and N. Hackerman, *ibid.*, **66**, 1823 (1962).

(5) R. L. Every, W. H. Wade, and N. Hackerman, *ibid.*, **65**, 25 (1961).

(6) R. L. Every, W. H. Wade, and N. Hackerman, *ibid.*, **65**, 937 (1961).

(7) W. H. Wade and N. Hackerman, Advances in Chemistry Series, No. 43, American Chemical Society, Washington, D. C., 1964, p. 222.

time constant of 10 sec. was used to smooth the heat–time curve.

The calorimeter fluid was 250 ml. of distilled water and ~1 ml. of hexane. The hexane was introduced for two reasons: (1) to presaturate the water, eliminating any heat of solution effects, and (2) to establish hexane–air and hexane–water interfaces (with their resultant enthalpies of formation) of constant area which would not change when displaced hexane coalesced at the top of the aqueous phase.

Experimentally measured heats of displacement, $\Delta H_D^{\alpha\beta}$, for the four samples are displayed in Figure 1. The solid lines in the immediate vicinity of the experimental points correspond to the displacement heats calculated by eq. 2 from previously published appropriate values of ΔH_i^{α} and ΔH_i^{β}.[2b-4]

It was meaningless to attempt to follow the displacement processes by noting heat evolution as a function of time. Equilibrium was reached in 1–2 min., roughly consistent with the 10-sec. time constant of the filter on the input of the recorder. Within this limitation, the displacement process is as rapid as the immersion processes for the outgassed surfaces in pure hexane or pure water. This same behavior was noted for all samples.

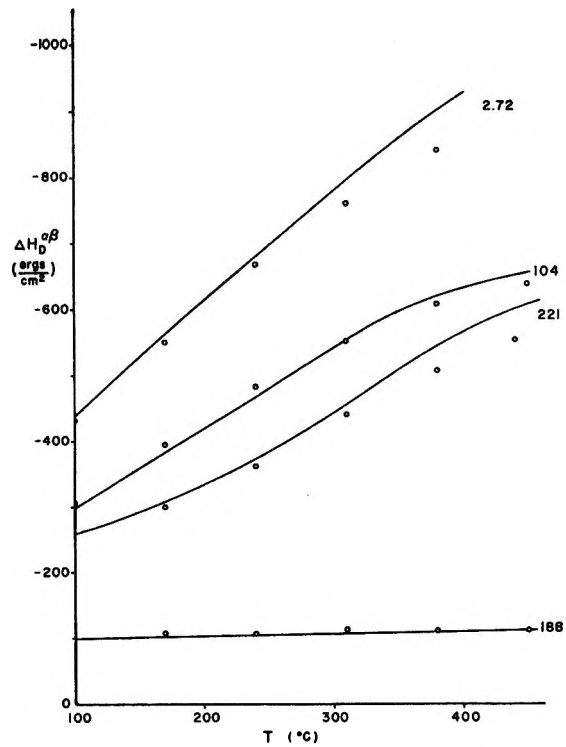

Figure 1. Heats of displacement, $\Delta H_D^{\alpha\beta}$: calculated values, solid line; with accompanying experimental points, open circles.

Discussion

The data of Figure 1 clearly establish the validity of eq. 2, but, more importantly, justify the underlying assumptions, namely that a weakly interacting phase should be quantitatively displaced by a strongly interacting one. The reproducibilities of the experimental heats for pure phases or for two-phase displacements are ±2–3%, which is the extent of agreement noted in Figure 1 at lower outgassing temperatures. In general, at higher outgassing temperatures the disagreement increases to ±6–8%, and, more significantly, the experimental values of $\Delta H_D^{\alpha\beta}$ are uniformly lower than the calculated ones. This slight disagreement for exhaustively outgassed samples is probably due to the slow removal of minute traces of residual water in the hexane in the sample bulbs not removed by the molecular sieve. Such an effect was at times noted for the immersion of outgassed samples in pure hexane in that a rapid heat evolution due to hexane adsorption was followed by a slight but gradual heat effect best ascribed to the displacement of small amounts of hexane adsorbate by residual water in the sealed-off microcalorimeter bulbs. That this effect becomes significant only at higher outgassing temperatures is understandable in terms of the heat of adsorption of water as a function of coverage. Alumina samples outgassed at high temperatures (~450°) show a dramatic decrease of the differential heats of adsorption for very small surface population by water. This is consistent with the usual interpretation that alumina surfaces are anything but monoenergetic, that this distribution of site energies extends to high energies, and that depopulation of these sites occurs at outgassing temperatures up to 450° and probably to temperatures of 1000°.

A consideration of the observed rapid kinetics permits some interesting speculation of the 221 m.²/g. alumina gel. The other three samples rapidly disperse in the stirred calorimeter fluid so that the entire surface area of the powder is available for the displacement process. On the other hand, dispersion of the gel grains exposes <1% of the gel surface[8] contained primarily in the interior of the grains. The pore openings in the grains are <50Å.[2] This indicates that water probably penetrates the gel interior by a diffusion process and hexane exits by the same mechanism. The straight diffusion process is of course aided by any imbalance in the hydrostatic equilibrium at the microscopic level arising from a distribution of pore sizes (assuming that different sized pore openings are interconnected)

(8) W. H. Wade, *J. Phys. Chem.*, 68, 1029 (1964).

where invasion through the smallest pore is thermodynamically preferred. Without more intimate knowledge of the pore structure, the relative importance of this latter mechanism cannot be assessed; however, a bulk diffusion mechanism would require excessively large diffusion coefficients. An alternate process of surface diffusion into the interior of the grains and into dead-ended pores would be attractive since the bulk rates would not need to be as large. The pores could be left highly populated by hexane as long as the surface is covered by two to three molecular layers of water. This emphasizes that the calorimetric measurements here performed are not necessarily sensitive to the equilibrium microscopic liquid structure of the pore but only the adsorptive state of the pore surfaces.

In conclusion, the heats of displacement indicate that the exchange process is rapid and quantitative but in the case of gels with internal pore structure it is impossible to tell if there is complete exchange of bulk pore liquid.

Acknowledgment. The authors wish to thank the American Petroleum Institute and the Robert A. Welch Foundation for continued support of these studies. Appreciation is expressed to Mr. James E. Gardner for performing the microcalorimetric measurements.

Heats of Immersion. VIII. Differential Heats of Adsorption as a Function of Particle Size for the Alumina–Water System

by Raymond L. Venable, William H. Wade, and Norman Hackerman

Department of Chemistry, The University of Texas, Austin, Texas 78712 *(Received August 27, 1964)*

Differential heats of adsorption have been determined from measurement of the heats of immersion of alumina powders pre-equilibrated with various amounts of water vapor. The data are interpreted to show that there is a wide distribution of adsorption energies and that both localized and mobile adsorption occur during formation of the first monolayer. The energy of adsorption in the second layer is not zero and differs significantly for the three samples. Entropy calculations show the inert adsorbent model to be invalid.

Introduction

It has been shown in previous communications from this laboratory[1-3] that there is a significant decrease in the heat of immersion/cm.^{2} (ΔH_i) with increased specific surface area of silica and alumina samples on immersion in water. The present work investigates this phenomenon in more detail. The objective was to locate the regions of the differential heat–coverage curves wherein the specific differences among the samples give rise to the differences in the integral heats of immersion.

Experimental

The alumina samples used have been described previously[3] and only essential information is given in Table I.

The samples were outgassed at 10^{-6} mm. for 48 hr. at 160 ± 3° before admitting water vapor to them.

(1) A. C. Makrides and N. Hackerman, *J. Phys. Chem.*, **63**, 594 (1959).

(2) W. H. Wade, R. L. Every, and N. Hackerman, *ibid.*, **64**, 355 (1960).

(3) W. H. Wade and N. Hackerman, *ibid.*, **64**, 1196 (1960).

Table I

Sample	Area, m.²/g.	Crystal
A	2.72	α-Al_2O_3
B	104[a]	γ-Al_2O_3
C	221	Amorphous

[a] Sample B was previously reported to have a specific surface area of 109 m.²/g.

The pressure of the water vapor in equilibrium with the adsorbent was measured with a manometer containing Apiezon C oil. The samples were allowed to equilibrate with water vapor until no measurable pressure change could be observed over a period of 1 hr. Water vapor was added in repeated small doses allowing only minor pressure fluctuations. This was done to minimize any effects due to adsorption irreversibility. For all samples the heat of immersion curves were determined with pressure increasing. Samples B and C were also saturated with water vapor and the heat of immersion curves were determined for samples equilibrated on the desorption branch of the isotherm.

The calorimeter is of the twin adiabatic type with thermistor temperature-sensing elements and has been described previously.[1] All measurements were made at 25 ± 0.1°. For samples B and C, thin-walled spherical Pyrex bulbs which shattered completely upon breaking were used. The measured heats for these samples were corrected for the heat of bulb breaking. For sample A, thick walled cylinders with breakable tips were used. The heat of tip breakage for such bulbs has been found to be negligible.[2]

For samples A and B, the adsorption isotherms previously determined[4] were used. For sample C, the adsorption and the desorption isotherms were determined in this work using a volumetric apparatus already described.[5]

The integral entropies of adsorption were calculated from the equation[6]

$$T(S_s - S_l) = \frac{U - U_0}{n_s} + \frac{\pi}{n_s} - RT \ln P/P_0 \quad (1)$$

In this equation, S_s is the entropy per mole of the adsorbate, S_l is the entropy per mole of bulk liquid adsorbate, U is the heat of immersion of the solid with n_s moles of water preadsorbed, U_0 is the heat of immersion of the clean solid, and π is the free energy of adsorption calculated from the Gibbs equation. Equation 1 assumes that the adsorbent is inert.

The Gibbs equation was used in the form

$$\pi = RT \int_0^P \Gamma \, d \ln P$$

In this work, Γ was replaced by n_s which is expressed as moles of adsorbate/g. of adsorbent, and π was calculated in units of kcal./g. of adsorbent using plots of n_s/P *vs.* P/P_0 and integrating graphically.

Results and Discussion

Figure 1 shows the isotherms used for this work. Those for A and B were reported[4] to be reversible at all relative pressures. In ref. 4, the desorption process was not carried to very low relative pressures so that these data are not available. The isotherm for sample C as obtained in this study has an open loop which did not disappear upon measurement.

The heat of immersion curves are presented in Figure 2 as plots of ΔH_i in kcal./g. *vs.* n_s/g. Calorimeter samples were outgassed, film equilibrated, and immersed in duplicate. Each heat of immersion curve

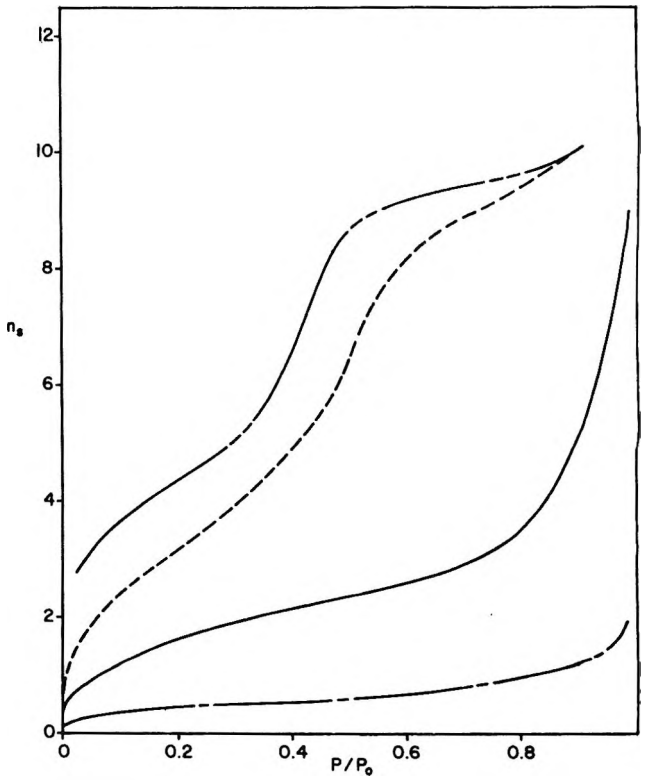

Figure 1. Adsorption isotherms for water on alumina powders with n_s in moles adsorbed/g. of adsorbent × 10^3 (× 10^4 for sample A): A, — · — ·; B, ———; C, adsorption – – – –; C, desorption — · — ·.

(4) R. L. Every, W. H. Wade, and N. Hackerman, *J. Phys. Chem.*, **65**, 937 (1961).

(5) N. Hackerman and A. C. Hall, *ibid.*, **62**, 1212 (1958).

(6) G. Jura and T. L. Hill, *J. Am. Chem. Soc.*, **74**, 1598 (1952).

consists of 50 to 75 duplicate points over the entire relative pressure spectrum. For the sake of clarity, experimental points are not shown. The majority of points were for low relative pressures where ΔH_i varies rapidly. The curves for A and B are typical for immersion in water of nonporous metal oxide powders having nonhomogeneous surfaces. Sample C is a gel and the heat curve is typical of samples possessing internal pore structure.[7] When plotted as ΔH_i *vs.* P/P^0 in the inset of Figure 2, it can be seen that the heat curve obtained for B after adsorbing to saturation pressure and then desorbing progressively reproduces the curve obtained corresponding to the adsorption branch from saturation pressure back to a relative pressure of approximately 0.1. From a relative pressure of 0.1 back to samples evacuated at 25° for 96 hr., the heats of immersion of the desorption samples are lower than those obtained from the adsorption branch at equal relative pressures. This indicates that part of the water adsorbed after outgassing B at 160° is very strongly bonded. The heat

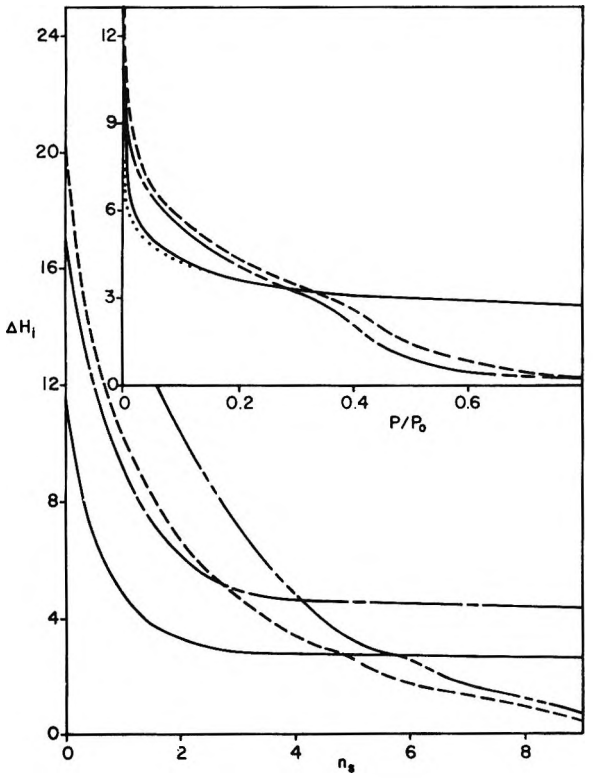

Figure 2. Heat of immersion, ΔH_i, in kcal./g. $\times 10^3$ *vs.* n_s in moles adsorbed/g. $\times 10^3$: A, — — — (ΔH_i and n_s multiplied by 5×10^4); B, ———; C, adsorption, – – – –; C, desorption, — - - —. Inset shows ΔH_i in kcal./g. $\times 10^3$ *vs.* P/P^0: B, adsorption, ———; B, desorption, ... for P/P_0 less than ~0.15 and ——— for P/P^0 greater than ~0.15; C, adsorption, — – —; C, desorption, — - - —.

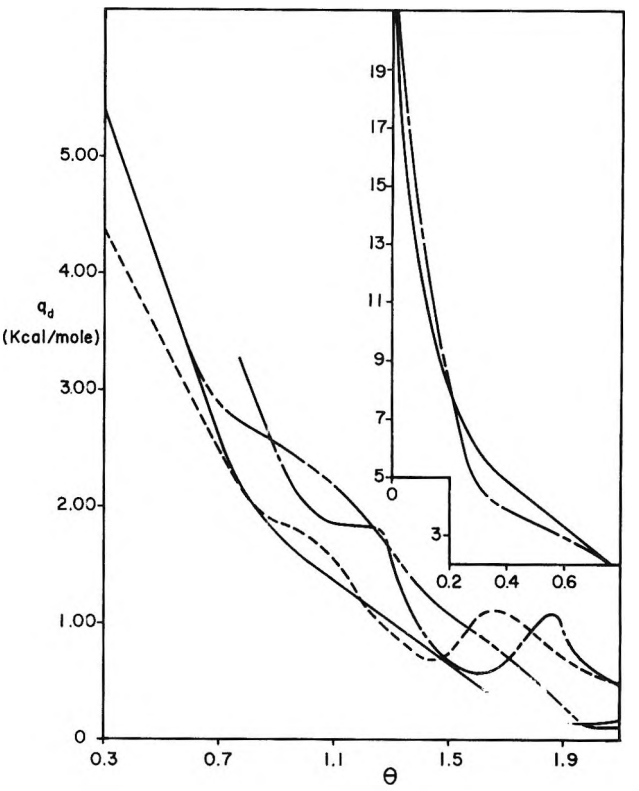

Figure 3. Differential heat of adsorption, q_{d}, *vs.* coverage, θ: A and B for θ less than 0.7, ———; A for θ greater than 0.7, — - - —; B for θ greater than 0.7; C, adsorption, – – – –; C, desorption ,— – —. In the inset: A and B, ———; C, adsorption, — – —.

of immersion curve obtained upon desorption for C is lower at all relative pressures than the heat curve obtained when following the adsorption branch of the isotherm. This reflects the irreversible adsorption which prevented closing of the hysteresis loop of the adsorption isotherm.

The differential heats obtained by graphical differentiation of the heat of immersion curves of Figure 2 are shown in Figure 3 and are relative to the liquid state. Points below a coverage of 0.3 monolayer are shown in the inset.

From the inset it can be seen that, at coverages below 0.2 monolayer, the differential heat curves are approximately linear and decrease extremely rapidly with increasing coverage. There are two possible causes for this drastic decrease in differential heat with coverage: extreme heterogeneity of the surface and repulsive interactions between adsorbate molecules. At these low coverages when the adsorbate molecules are far apart the latter possibility can be ruled out

(7) J. J. Chessick and A. C. Zettlemoyer, *Advan. Catalysis*, 11, 263 (1959).

almost completely. The most plausible explanation is that the decrease in differential heats at these low coverages is caused by adsorption onto a rather wide distribution of energy sites all having relatively high adsorption energies. It would appear that the distribution of these high energy sites is approximately the same for all samples. Adsorption in this region probably results in very strong localized bonding of the adsorbate.

In the region of 0.2–0.3 monolayer there is a change in slope and another linear portion of the differential heat curve appears where the differential heats still decrease, but much less rapidly than before. Since this linear portion begins at the rather low coverage of 0.3 monolayer, it seems unlikely that the change in slope was caused by interactions between adsorbate molecules. The explanation offered here is that these portions of the curves represent more or less mobile adsorption in the first layer. There must once again be a rather wide distribution of adsorption energies for this mobile adsorption.

There is a second transition region in the vicinity of 0.7–0.8 monolayer which probably represents the onset of adsorbate interactions. For samples A and B this is followed by a third approximately linear portion of the differential heat curve extending almost to the completion of the second layer. After completion of the second layer, the differential heat relative to the liquid state is practically zero for A and B. This clearly shows that the energy of adsorption for the second layer is quite different from that for subsequent layers, which probably resembles the unperturbed liquid state.

Sample C has a minimum and a maximum in this region and there is another such minimum and maximum at higher relative pressures which are not shown here. These minima and maxima are thought to be related to capillary condensation in pores[8-10] and will be discussed in a subsequent publication. It has been shown[11,12] that the surface areas of powders pre-equilibrated with vapors decrease with the amount of vapor adsorbed. In the case of sample C, this change of surface area was shown[13] to be as great as 40% at less than monolayer coverage. This certainly invalidates any quantitative concept of surface coverage for C. However, for comparison with samples of other specific surface areas the concept of coverage is very useful in a qualitative way.

A more detailed comparison of the differential heat curves is in order. In the very low coverage region (below 0.2 monolayer) the differential heats for all samples seem to be approximately equal at equal coverages. Any apparent differences probably are not significant because the differential heats for this coverage range were obtained from the very steeply sloping portions of the heat of immersion curves of Figure 2 and the adsorption isotherms of Figure 1. Therefore, small errors in the graphical differentiation process lead to rather large errors in the differential heats obtained. It should be pointed out, though, that when the differential heats are plotted in kilocalories per mole of water adsorbed *vs.* moles of water adsorbed, the areas under the respective curves give the experimental heats of adsorption, exclusive of the heat of liquefaction of water, within ±5%. This means that the differential heats shown are probably very nearly correct. Since the differential heats in the low coverage region are considered to be due to localized adsorption, this similarity of differential heats probably indicates that the energy distribution of these adsorption sites is quite similar for the three samples.

The differential heats in the coverage range from 0.3 to 0.75, which are thought to represent mobile adsorption during formation of the first layer, are very nearly the same for A and B. However, the differential heats during formation of the second layer are much higher for A than for B. This indicates that the long-range forces responsible for the energy of interaction of the second layer are stronger in A than in B. Therein probably lies the reason for the heat of immersion in ergs/cm.^{2} for the clean solid being higher for A than for B.[3] The energy of mobile adsorption during formation of the first layer is lower for C than for A or B. This is probably the reason that the heat of immersion of the clean solid is even lower for C than for B.

Figure 4 shows plots of the integral entropy of adsorption, ΔS_a, *vs.* coverage. It is interesting to note that during formation of the first layer, the entropy change per mole of adsorbate is very close for all three samples at equal coverages. During formation of the second layer, the entropy change per mole of adsorbate on A is greater than for B or C. This would result from a greater ordering of the adsorbate molecules in the second layer on A and can be correlated with the greater energy of interaction as seen from the differential heat curves.

The magnitude of the entropy change for adsorption cannot be overlooked. The entropy per mole of liquid

(8) A. V. Kiselev, *Proc. Intern. Congr. Surface Activity, London*, **2**, 189 (1952).

(9) G. L. Kington and P. S. Smith, *Trans. Faraday Soc.*, **60**, 705 (1964).

(10) G. L. Kington and P. S. Smith, *ibid.*, **60**, 721 (1964).

(11) W. H. Wade, *J. Phys. Chem.*, **68**, 1029 (1964).

(12) C. Pierce, *ibid.*, **62**, 655 (1958).

(13) N. Hackerman and W. H. Wade, *ibid.*, **68**, 1592 (1964).

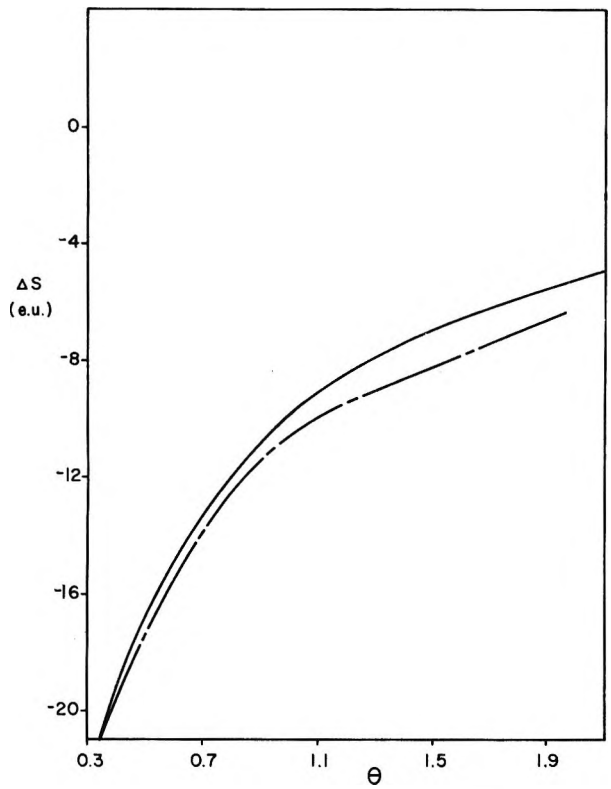

Figure 4. Entropy of adsorption ΔS in cal. deg.$^{-1}$ mole^{-1} *vs.* coverage, θ: A, — — —, B and C, ———.

water at 25° is 16.72 cal./deg. Since ΔS_a is negative and greater than 16.72 cal./deg. at low coverages, this indicates perturbation of the solid adsorbent. In fact, adsorption theory based on an inert adsorbent requires a minimum in the integral entropy curve in the neighborhood of the monolayer.[6] There is normally an increase in the entropy of the adsorbate at low coverages relative to the entropy of the liquid state followed by a decrease at high coverages. No minima are observed in the entropy curves presented here. It should be remembered that the ΔS calculated by eq. 1 contains the entropy change of the adsorbent as well as that of the adsorbate. If the entropy change of the solid is large and negative, it can override the increase in entropy of the adsorbate at low coverages. This change in the entropy of the adsorbent invalidates the concept of calculating the thermodynamics function of the adsorbate species in such systems because it is impossible to separate the contribution of the adsorbent from that of the adsorbate.

Summary and Conclusions

Heats of immersion have been measured as a function of coverage with preadsorbed water for the alumina samples with widely differing specific surface areas. From these heat of immersion curves, the differential heats of adsorption relative to the liquid state were obtained by graphic differentiation. The differential heats showed that the adsorption energies for formation of the first layer on the substrates apparently can be divided into two broad classifications: one representing localized adsorption and the other mobile adsorption.

Differences in the adsorption energies for mobile adsorption in the first layer are probably the reason that the heat of immersion of the clean solid in ergs/cm.^{2} for sample C is lower than for A or B.[3] The differences in the heats of immersion for samples A and B appear to arise because the adsorption energies for formation of the second layer are higher for A than for B. The energies of adsorption during formation of the second layer are clearly shown to be considerably greater than for subsequent layers. The differential heat curves for both the adsorption and desorption branches of the isotherm for sample C have maxima and minima which are related to capillary condensation.

These data appear to support the previous hypothesis that the major differences between different Al_2O_3 surfaces lies in differences in surface order or crystallinity. The electrostatic field strength and hence field–dipole interaction energies are greater at large distances for ordered (low-area) samples. The apparent high second layer heats of the high-area gel sample arise from extraneous factors such as capillary condensation and extreme surface area diminution.

Acknowledgments. The authors wish to thank the American Petroleum Institute and the Robert A. Welch Foundation for their support of these studies. Also, appreciation is expressed to Mr. James E. Gardner for making the calorimetric measurements and to Mr. Jerry Matlock for determining one of the adsorption isotherms.

The Coordination Number of Small Spheres

by William H. Wade

Department of Chemistry, University of Texas, Austin, Texas 78712 *(Received August 27, 1964)*

Water adsorption isotherms were obtained for uncompressed and compressed Al_2O_3 spheres of 75 Å. radius. The isotherms for the compressed samples reach a saturation value for a given porosity sample. Nitrogen surface areas were obtained for these samples both bare and with water preadsorbed. The analysis of these data ultimately yields the coordination numbers of the powder samples which were found to vary from 3 to 10.

Introduction

In a previous publication,[1] experimental data were given for the variation of the area of the exposed surface of water films on a substrate as a function of the total amount of adsorbate. V_{ads} measurements were performed on powdered samples with areas (Σ) varying from 2.72 to 220 m.^{2}/g. The high specific area samples, $65 \leqslant \Sigma \leqslant 220$, all exhibited a rapid loss of Σ for small volumes adsorbed, V_{ads}, followed by a more gradual loss of area with increasing V_{ads}. The sole low Σ sample (2.72 m.^{2}/g.) showed no rapid initial drop but only a gradual diminution.

These data were interpreted in terms of a dual adsorption model blending uniform film adsorption and capillary condensation at the contact points of the adsorbent particles. The adsorbent particles were assumed to be uniform spheres of radius R, packed to a uniform coordination number, n. The mathematical formulation of this model correlated qualitatively but only semiquantitatively with the experimental data.

In the initial study, the coordination number, n, was treated as an adjustable parameter. No attempt was made to evaluate or vary this parameter independently for a given sample. The best fit values of $3 \leqslant n \leqslant 5$ for the high Σ samples of low bulk density appeared reasonable as did the value of $n = 9$ for the 2.72 m.^{2}/g. sample.

Kiselev[2] has attempted to estimate n for silica gel samples by gas adsorption techniques but has not attempted to vary n for a given sample. From geometrical considerations, Manegold[3] has evaluated the bulk porosity of agglomerates of spheres with given coordination numbers. Porosity is defined as the percentage void volume of the total external pack volume. Melrose[4] has estimated coordination numbers as a function of liquid densities from which "porosities" can be obtained, and Smith, Foote, and Busang[5] experimentally determined n for randomly packed lead shot of different porosities.

Carman and Raal[6] and others[7] have noted that adsorption isotherms can be varied for particular samples by compression. This procedure enhances capillary condensation by increasing the coordination number. Unfortunately, individual particle geometry was not noted and no calculations of powder pack porosities were attempted for these samples.

An attempt will be made to correlate film areas, adsorption isotherms, and porosities of a single type of material to assess further the importance of capillary condensation to the total adsorption isotherm and establish the variability of the coordination number.

Experimental

A single sample of Al_2O_3 was used for all the studies reported on here. As received it has a surface area of 104.0 m.^{2}/g.[1] Samples of this material were compressed in a hardened steel die with a hydraulic press at various pressures (10^3 to 10^5 p.s.i.) for various times

(1) W. H. Wade, *J. Phys. Chem.*, **68**, 1029 (1964).

(2) A. V. Kiselev, *Dokl. Akad. Nauk SSSR*, **98**, 431 (1954).

(3) E. Manegold, *Kolloid-Z.*, **96**, 186 (1941).

(4) J. Melrose, private communication.

(5) W. O. Smith, P. D. Foote, and P. F. Busang, *Phys. Rev.*, **34**, 1271 (1929).

(6) P. C. Carman and F. A. Raal, *Proc. Roy. Soc.* (London), **A209**, 59 (1951).

(7) N. N. Avgul, G. I. Berezin, A. V. Kiselev, I. A. Lygina, and G. G. Muttik, *Zh. Fiz. Khim.*, **31**, 1111 (1957); J. H. de Boer, *Proc. Colston. Res. Soc.*, **10**, 68 (1958).

(5 min. to 8 hr.). The thickness of the pellets was measured to 10^{-3} in. with a micrometer. Water adsorption isotherms were obtained on three compressed samples using a volumetric adsorption apparatus. Pressures were read with a wide bore (~3 cm.) mercury manometer.[8] Each isotherm consisted of 25–40 experimental points covering the relative pressure range of 0.05 to 0.98. Samples were thermostated at 25 ± 0.01°.

The surface areas of the three samples were obtained by B.E.T. analysis of N_2 isotherms on a separate volumetric adsorption apparatus. Each N_2 isotherm consisted of six experimental points spanning the range $0.04 < P/P^0 < 0.25$. The assumed nitrogen molecular area was 16.3 Å.^{2}. Surface areas were obtained for samples both solely outgassed (160° for 8 hr.) and outgassed and subsequently equilibrated with water at four relative pressures as described previously.[1]

Electron microscopy had shown the particles to be ~150 Å. in diameter and spherical or at worst ellipsoidal (major:minor axis ratio $\lesssim$ 1.3). No extensive particle size analysis was attempted from the electron microscope pictures, but the spread appears relatively narrow. The density of the alumina was measured as 3.60 g./cc. using a pycnometer with water as the displaced liquid.

Results

The adsorption isotherms for the three compressed samples are given in Figure 1. For comparison, the adsorption isotherm for the uncompressed, as received material is also reproduced.[9] Many of the low relative pressure points for all isotherms have been omitted since all of the curves lie on each other in this region. All of the compressed samples exhibit limiting values of adsorbate volume at $P/P^0 = 1.0$. If the adsorbate is assumed to have the normal density of liquid water, the porosities of the compressed samples can be calculated. These values are listed in Table I along with the values obtained from the measured dimensions of the compressed pellets. For identification purposes, the uncompressed sample is labeled A. B, C, and D represent the compressed samples in the order of decreasing porosity.

The measured film areas are plotted in Figure 2 as a function of the appropriate water equilibration pressure. These pre-equilibration pressures were not extended to large values (except for the uncompressed sample) for it is obvious from Figure 1 that capillary condensation ultimately sets in, invalidating the proposed model.[1]

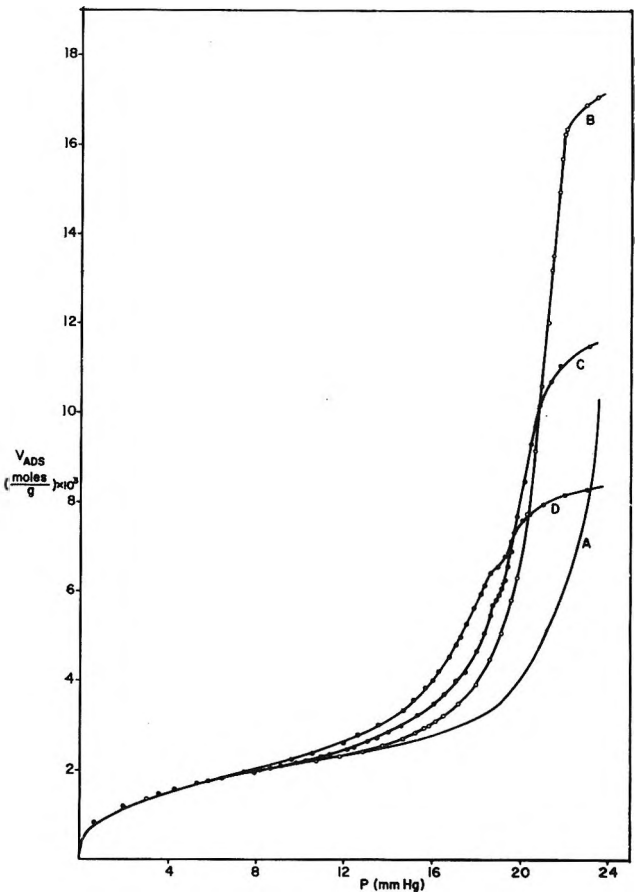

Figure 1. Adsorption isotherms for the four uncompressed and compressed samples.

Discussion

In the previously proposed model of physical adsorption,[1] two modes of adsorbate retention were considered: a uniform film of statistical thickness, t, and capillary condensate held in the contacting zones of spherical adsorbent particles. The saddle-shaped menisci are characterized by two radii of curvature, r_m and $(\sqrt{(R + t + r_m)^2 - R^2} - r_m + R + t)/2$ where R is the adsorbent particle radius and r_m is the concave radius of curvature. In terms of these parameters and δ, the density of the adsorbent particles, it was possible to write an expression for the total volume of adsorbate as well as the area on the outside of the adsorbate film[10]

(8) D. E. Meyer and W. H. Wade, *Rev. Sci. Instr.*, **33**, 1283 (1962).

(9) R. L. Every, W. H. Wade, and N. Hackerman, *J. Phys. Chem.*, **65**, 937 (1961).

(10) Note the difference in eq. 1 of ref. 1, which contained two typographical errors not detected in proof.

$$V_{ads} = \frac{3}{4R^3\delta}\left\{\frac{4}{3}[(R+t)^3 - R^3] + \frac{nRr_m}{A}[A^2 - R^2 + r_m^2] - \frac{n}{3}\frac{R^3r_m^3}{A^3} - \frac{nRr_m^2[A^2-R^2]}{A^2} - \frac{n}{3}\left[\frac{Rr_m}{A}+t\right]^2\left[3(R+t) - \frac{Rr_m}{A} - t\right] - nr_m^2\sqrt{A^2-R^2}\sin^{-1}\frac{R}{A} - nR\Omega^2 + n\Omega^2\sqrt{2R\Omega+\Omega^2}\sin^{-1}\frac{R}{R+\Omega}\right\} \text{ (cc./g.)} \quad (1)$$

where $A = R + t + r_m$, and

$$\Sigma = \frac{3\times10^4}{2R^3\delta}\left\{2(R+t)^2 + nr_m\sqrt{A^2-R^2}\sin^{-1}R/A - \frac{nr_m^2R}{A} - n(R+t)\left[\frac{Rr_m}{A}+t\right]\right\} \text{ (m.}^2\text{/g.)} \quad (2)$$

where n is the coordination number, δ is the density of the adsorbent particles, Ω is the radius of the film molecules, and the other terms are as defined above. To relate the V_{ads} to relative pressure, two connective equations are needed to express r_m and t separately as a function of P/P^0. The Kelvin equation as applied to the pendular rings of capillary condensate is given by [1,11]

$$\ln P/P^0 = 2.303\frac{\gamma\bar{V}}{R_GT}\left\{\frac{1}{r_m} - \frac{2}{\sqrt{A^2-R^2} - r_m + R + t}\right\} \quad (3)$$

where γ is the liquid–vapor interfacial tension, $\bar{V}$ is the molar volume, R_G is the gas constant, and T is the absolute temperature. In the previous study, t was neglected to simplify the calculations. In the present study it is not, because an analytical function is used to relate t to P/P^0.

It is commonly observed that the B.E.T. equation only faithfully reproduces adsorption isotherms up to $P/P^0 = 0.30$–0.35. The Frenkel–Halsey–Hill equation

$$\ln P/P^0 = -\frac{K}{V_f^3} \quad (4)$$

has been shown[12] to reproduce isotherms to relative pressures of 0.98. V_f is the volume of the uniform film and K is a constant. V_f is related to t by assuming the thickness of a statistical monolayer using the value of $t = 3.54$ Å. as discussed by Lippens.[13] Equation 4 was fitted to the experimental data of the uncompressed sample A at $P/P^0 = 0.30$ to arrive at

$$\ln P/P^0 = -\frac{65.0}{t^3} \quad (4a)$$

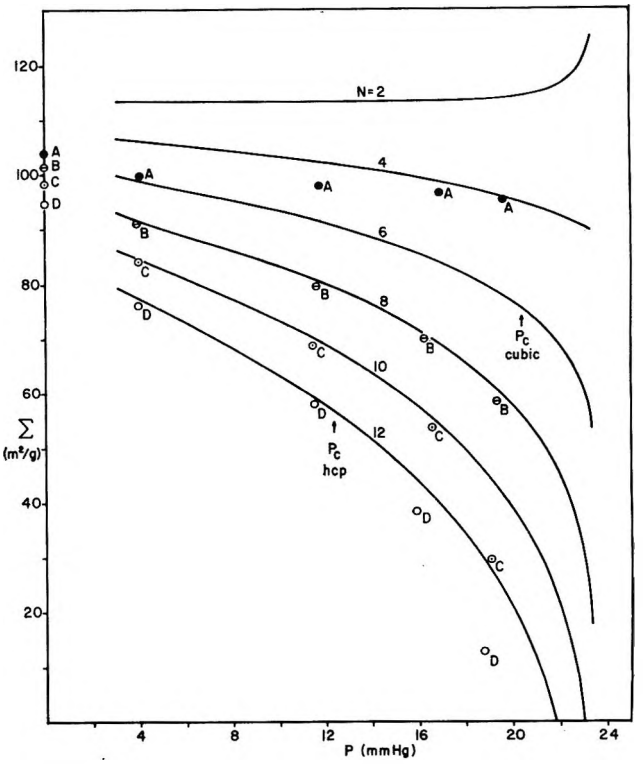

Figure 2. Experiment surface areas for bare samples (plotted on ordinate) and samples equilibrated at pressures shown. The solid lines are calculated for n = 2, 4, 6, 8, 10, and 12.

At high relative pressures the calculated values of t appear to assume too low a value, but if the capillary condensate is added assuming $n = 4$ for the uncompressed sample (previously found to yield the best fit), the calculated and experimental isotherms agree to better than 1% up to the highest relative pressures studied ($P/P^0 = 0.97$).

In eq. 2, the surface area is the geometrical area of the film and does not take into account that the area measuring probes (N_2 molecules in this study) may not find all this area accessible. Karnaukhov and Kiselev[14] have considered this problem for packed spheres and

(11) B. G. Aristov, A. P. Karnankhov, and A. V. Kiselev, *Russ. J. Phys. Chem.*, **36**, 1159 (1962).

(12) D. M. Young and A. D. Crowell, "Physical Adsorption of Gases," Butterworth and Co., Ltd., London, 1962, pp. 167–170.

(13) B. C. Lippens, Thesis, University of Delft, 1961.

(14) A. P. Karnaukhov and A. V. Kiselev, *Russ. J. Phys. Chem.*, **34**, 1019 (1960).

arrived at an approximate equation which is here normalized to unit weight of sample.

$$\Sigma = \frac{3 \times 10^4}{2R^2\delta}\{2R - nr_{N_2}\} \quad (\text{m.}^2/\text{g.}) \qquad (5)$$

where r_{N_2} is the radius of the nitrogen molecule and the other terms are as before. This equation is only valid for films with negligible capillary condensate. Nitrogen surface areas are measured at coverages of $\theta = 1 \pm 0.2$, and in this region the volume of nitrogen capillary condensate is negligible as can be shown by application of eq. 1. For spheres with no water film present, the nitrogen areas should be a linear function of n by eq. 5; however, R must be known before surface areas can be calculated from this equation (assuming δ is known). In the present study, R was calculated using $\Sigma = 104.0$ m.^{2}/g. for the uncompressed sample, assuming $n = 4$, $\delta = 3.60$, and $r_{N_2} = 2.16$. R is found to be 75.4 Å. This value of R can then be used along with the measured surface areas of the compressed samples to calculate their coordination numbers. These values of n are listed in Table I.

Table I

	Porosity, %		Coordination number		
Sample	From bulk dimensions	From adsorption isotherms	From surface areas of bare solid	From porosities	From film areas
A	93	..	4	3	4–6
B	53	53	5 6	5.6	8
C	41	43	7 7	7 2	10
D	31	35	10.0	9.3	12

When the various porosity samples have been equilibrated with water films and frozen, there will be no excluded area if $r_m > r_{N_2}$, and the surface areas as a function of pressure will be given by eq. 2 combined with eq. 4a and 3. Figure 2 illustrates this variation of Σ with P for $n = 2$ to 12 using $R = 75.4$ and $\delta = 3.60$. The points at zero pressure were calculated from eq. 5. Calculations were not extended below a pressure of 3 mm. for at this point $r_m > r_{N_2}$. At lower water pressures there is a transition region where neither eq. 2 nor 5 is valid.

These calculated curves for the Σ variation assure no particular packing geometry and for their validity assume that adjacent pendular rings do not overlap. As discussed by Kruyer[15] and others,[1,11] the pressure at which overlap occurs marks the onset of capillary condensation and the point at which eq. 1 and 2 become invalid. In ref. 1 and 15, such critical pressures are listed for simple geometric packings assuming $t = 0$. Using Kruyer's definition of ϕ as the angle between the center line of regularly packed spheres and the line from the center of a sphere to the center of the regular array forming the opening between spheres, it can easily be shown that at the instant of merging of adjacent pendular rings

$$t + r_m = R(\text{sec. } \phi - 1) \qquad (6)$$

From eq. 3 and 4a ($t + r_m$) as a function of P can be obtained assuming R is known. For cubic packing ($\phi = 45°$) of spheres with $R = 75.4$ Å., the critical pressure $P_c = 12.4$ mm., and for hexagonal close packing (h.c.p.; $\phi = 30°$), $P_c = 20.6$. These values are noted in Figure 2 and mark the limit of validity for the two curves where $n = 6$ and 12, respectively. For cubic packing, at P_c the isotherm should discontinuously rise to its maximum value and become horizontal at higher pressures, and the surface area should simultaneously drop to zero. For $n = 12$, Kiselev[11] has shown that a more complicated behavior exists and that capillary condensation for this particular sample should occur in two or three stages. The absence of such behavior in the experimental results indicates that the samples here produced are not geometrically simple but have a variety of geometrical configurations which the measurements average. In addition, there is a spectrum of R values, the 75.4 Å. being an average value. These two effects produce adsorption isotherms of finite slope during capillary condensation and wash out any fine structure due to h.c.p. regimes. Some indication of such fine structure exists for samples C and D, for at ~18 mm. small inflection points are observed.

Due to these complications, film area measurements were not extended to thick water films where capillary condensation would have invalidated the comparisons to the calculated values. In addition, Σ values of very thin water films were not obtained because of the probable invalidity of the Kelvin equation where r_m is of molecular dimensions.

The experimental film areas for samples A through D are plotted in Figure 2. As observed previously, the uncompressed sample A fits $n = 5$–6 at low pressures and $n = 4$ at high pressures. This lack of agreement over the entire range of film coverages has been discussed.[1] The compressed samples B–D closely follow the theoretical curves for $n = 8$, 10, and 12, respectively, and are so listed in Table I. For sample B, the fit is

(15) S. Kruyer, *Trans. Faraday Soc.*, **54**, 1758 (1958).

particularly good, which probably coincides with the fact that all equilibration pressures are $<P_c$. For sample C, the highest pressure point is considerably below the $n = 10$ curve, reflecting that some pore filling has occurred, and for sample D the latter two points indicate similar behavior.

Obviously, from these measurements film areas are found to be a function of the coordination number but the best fit values are greater by 2 units than obtained from the surface areas of the bare solid packs and those calculated from porosity measurements which are discussed later. It has been suggested to the author that the variation of Σ with water film coverage may be due to the filling of cracks and micropores at low relative pressure of water. This cannot explain a substantial amount of the present data, for if correct there should be little effect on Σ due to variation of the bulk porosity, *i.e.*, coordination number, but it might explain the observation that the film areas on the samples are approximately 8 m.^{2}/g. lower than the values corresponding to n values of 3, 6, 8, and 10 to give rough agreement with other measurements. It is very unlikely that one could ever prepare h.c.p. samples by compression of powders. Moreover, the $P_c = 12.4$ for h.c.p. does not correspond to the steepest rising portion of the adsorption isotherm for sample D. The P_c of 20.6 does correspond to the steepest portion of the B adsorption isotherm, further indicating that $n = 6$ for this sample. The arbitrary addition of 8 m.^{2}/g. to all of the experimental areas of films equilibrated at $\sim$4 and 11 mm. would place these points on the $n = 3$, 6, 8, and 10 curves. The independence of this increment from the extent of compression is compatible with a surface roughness explanation. Since electron microscope pictures at 50,000$\times$ show the particles to be spheroidal, the surface roughness must have characteristic dimensions <10 Å. An alternate explanation would be that a reasonable percentage of the spheres lie very close to one another but do not quite contact. A bridging water film formed at low relative pressures would thus very efficiently reduce the available surface area.

Kruyer[15] gives a graph of porosity *vs.* coordination number which is a composite of theoretical values for simple geometric systems[3] and measurements from ref. 2 and 5. Using this graph, the coordination numbers of the four samples were obtained from the porosities averaged from the two types of measurements. These coordination numbers are also listed in Table I.

If it can be assumed that the film area estimations of n are too large by two units, then the various measurements are certainly consistent within the limits of accuracy. The coordination number of the uncompressed material is 3–4 and the compressed samples have values of 5–6, 7–8, and 9–10. These coordination numbers are, of course, most probable values and it would certainly be a mistake to assign any single geometric shape to an entire sample. Rather, there are small regimes of a variety of geometries. For example, pore filling in sample D as manifested in its isotherm occurs over a wide pressure range corresponding roughly to the limits set by the triangular and square windows corresponding to h.c.p. and cubic packing. From Figure 1, pore filling appears to become more discontinuous in going from sample D to C to B. This probably does not mean that the geometry distribution is any narrower at high pressures, since r_m is increasing very rapidly.

The water desorption branches of these isotherms are being obtained at the present time from which analyses of pore size distributions will be obtained. Pore area hysteresis data on the same samples are also being obtained by direct B.E.T. measurements. These will be discussed in a later paper.

Acknowledgment. The author wishes to thank the American Petroleum Institute and the Robert A. Welch Foundation for their continued interest and support. The calculations of film areas were performed by Miss Josephine Barto and the film area measurements by Mr. A. C. Falk.

Rate of Oxidation of Iron to Wustite in Water–Hydrogen Gas Mixtures

by E. T. Turkdogan, W. M. McKewan, and L. Zwell

Edgar C. Bain Laboratory for Fundamental Research, United States Steel Corporation, Research Center, Monroeville, Pennsylvania *(Received August 28, 1964)*

Experimental results are given on the rate of oxidation to wustite of purified iron strips in water vapor–hydrogen gas mixtures in the temperature range 850–1150°. In the early stages of oxidation the rate is controlled essentially by an oxide–gas phase boundary reaction such that the initial rate is directly proportional to the product $(1 - 1/a_O'')p_{H_2O}$ where a_O'' is the oxygen activity at the surface of wustite in equilibrium with the gas phase. This is in agreement with the rate equation derived for an activated complex involving a molecule of water vapor. At later stages of oxidation, diffusion in wustite is shown to play a prominent role in controlling the rate of oxidation. The part of the rate data obeying a parabolic law is shown to be in reasonably good agreement with that calculated from the self-diffusivity of iron in wustite.

Introduction

If the oxide formed during oxidation of a metal is not volatile, but is a continuous dense solid layer adjacent to the metal, there are three major rate-controlling processes to be considered—those applicable to the formation of very thin oxide films of thicknesses less than about 10^3 Å., those involved when the thickness of the oxide layer is within about 10^3–10^6 Å., and that for the growth of the oxide scales of thicknesses greater than about 10^6 Å.

In the very early stages of oxidation, the mechanism of the formation of thin oxide film is complex, involving (i) nucleation and growth, (ii) diffuse electrical double layers with an effective thickness, comparable with that of the growing oxide layer, and (iii) strain in the oxide film, resulting from incompatibility of the atomic arrangements in the metal and metal oxide at the interface. This phase of oxidation will not be considered here; references to previous theoretical and experimental work on this subject may be found, for example, in a book by Kubaschewski and Hopkins[1] on oxidation of metals and alloys.

When the oxide layer is of sufficient thickness, *e.g.*, $>10^3$ Å., so that nucleation and electrical double layers no longer dominate the rate of oxidation, the reaction rate is controlled essentially by a gas–metal oxide interfacial reaction involving chemisorption of oxygen-bearing species and their subsequent dissociation resulting in the transfer of oxygen to the oxide phase. This has been demonstrated to be the case by a number of investigators[2–5] for the oxidation of iron to wustite in carbon dioxide–carbon monoxide atmospheres.

As the boundary reaction approaches asymptotically to the state of interfacial equilibrium, the rate of oxidation is controlled essentially by the rate of migration of metal cations and electrons (in the case of wustite formation) to the oxide–gas interface against an oxygen potential gradient. The parabolic rate of oxidation of iron to wustite at a given oxygen potential is readily calculable from the known self-diffusivity of iron in wustite,[6] using Wagner's theoretical rate equation.[7]

In this paper the results are given on the oxidation of iron to wustite in water vapor–hydrogen atmospheres at temperatures in the range 850–1150°.

Experimental

The apparatus used in these experiments were the same as those employed by one of the authors[8] pre-

(1) O. Kubaschewski and B. E. Hopkins, "Oxidation of Metals and Alloys," 2nd Ed., Butterworth and Co. Ltd., London, 1962.

(2) K. Hauffe and H. Z. Pfeiffer, *Z. Metallk.*, **44**, 27 (1953).

(3) F. S. Pettit, R. Yinger, and J. B. Wagner, *Acta Met.*, **8**, 617 (1960).

(4) W. W. Smeltzer, *Trans. AIME*, **218**, 674 (1960).

(5) F. S. Pettit and J. B. Wagner, *Acta Met.*, **12**, 35 (1964).

(6) L. Himmel, R. F. Mehl, and C. E. Birchenall, *Trans. AIME*, **197**, 827 (1953).

(7) C. Wagner, *Z. physik. Chem.*, B21, 25 (1933); "Atom Movements," American Society for Metals, Cleveland, Ohio, 1951, pp. 153–173.

viously in the study of the rates of reduction of iron oxides in hydrogen–water vapor mixtures.

Experimental Procedure. The iron (Ferrovac E) used in these experiments contained the following impurities: 0.005% C, 0.001% Mn, 0.002% P, 0.006% S, 0.006% Si, 0.025% Ni, 0.002% Cr, 0.004% V, 0.02% W, 0.01% Mo, 0.001% Cu, 0.01% Co, 0.007% O, and 0.003% N. This iron rod, 0.8 cm. in diameter, was cold-rolled to a strip about 1.5 cm. wide and 0.05 cm. thick. A strip about 6 cm. long was used in an oxidation experiment. The surface of the strip was first cleaned by rubbing with a 0000 emery paper; after degreasing with carbon tetrachloride, it was suspended in the reaction vessel by a nickel wire and annealed for about 16 hr. in a stream of pure hydrogen at a temperature the same as that for the subsequent oxidation experiment.

During the oxidation experiment at a given temperature, controlled within ±2°, and in a given water vapor–hydrogen atmosphere, weight increase due to oxidation was recorded continuously. Unless otherwise stated, in all cases oxidation was carried out until all the metal was oxidized. The total hydrogen flow into the reaction vessel was within the range 500–1000 ml./min., and the oxygen flow was adjusted in accordance with the particular water vapor–hydrogen mixture required for the oxidation experiment.

Microsections. The cross sections of some of the samples were examined under a microscope; photomicrographs given in Figure 1 are typical examples of the microsections observed. It should be noted that the iron–wustite interface is relatively smooth and free of blisters, even after 95% of oxidation. The blisters and cavities in the wustite phase were noted only at the extreme edges of the samples, where there is greater stress concentration, arising from the formation of the oxide layer.

Most of the stresses in wustite near the interface are expected to be relieved by plastic flow of the oxide, and, as a result, holes created by the precipitation of vacancies are filled; hence, a sharp metal–oxide interface is maintained during oxidation. Small cavities appearing in the iron layer after 95% oxidation are clearly seen in Figure 1b. Toward the end of oxidation, cavities also begin to appear at the metal–oxide interface, as indicated by a small, dark patch on the right-hand side of Figure 1b. The large angular holes in the wustite layer in Figure 1b may have resulted from mechanical erosion of the brittle oxide during the polishing operation. As the remainder of the iron layer becomes thinner, the cavities within the metallic layer become larger. When all the metal is oxidized,

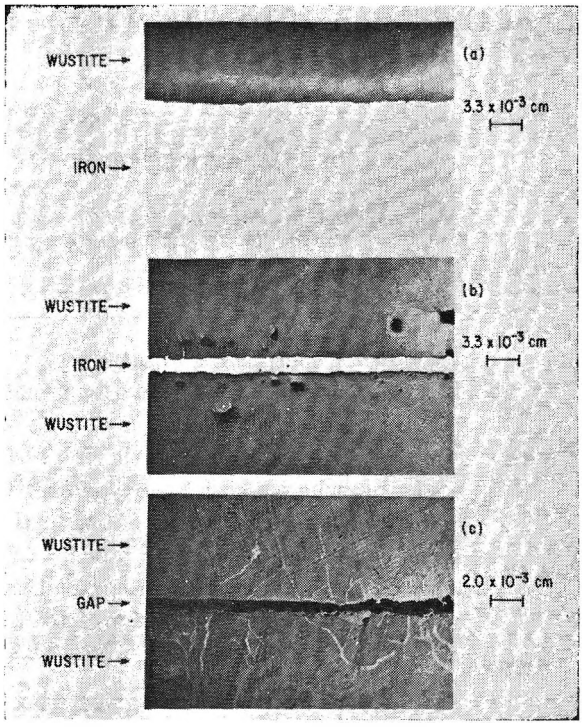

Figure 1. Microsections showing iron–wustite interfaces after oxidation of iron in H_2O–H_2 (p_{H_2O}/p_{H_2} = 4) at 950°: (a) 30% oxidized, (b) 95% oxidized, and (c) 100% oxidized. (Initial thickness of iron strip is 0.05 cm.)

a gap remains between the two oxide layers, as seen from the photomicrograph in Figure 1c.

The average thickness of the gap is about 5×10^{-4} cm. as compared with the initial thickness of the iron strip, 5×10^{-2} cm. This marked difference is indicative of the occurrence of plastic flow in the growing wustite at the temperatures employed.

The microscopic examinations also revealed that the surface of the oxide formed is rough, particularly at later stages of oxidation. The true surface area of the oxide is, therefore, somewhat larger than that given by its gross dimensions. On the other hand, because of the edge effect, the metal–oxide interfacial area decreases slightly with increasing reaction time. In reporting the rate data per unit area, the original surface area of the sample is used after making due allowance for expansion at the experimental temperature. This is considered to be a reasonable estimate of the average areas of the reaction surfaces.

X-Ray Measurements on Wustite. In a few experiments iron strip was partly oxidized, and, at the end of a required reaction time, the sample was pulled to the top of the reaction tube where it was cooled rapidly in a

(8) W. M. McKewan, "Chipman Conference on Physical Chemistry of Process Metallurgy," Massachusetts Institute of Technology, in press.

stream of pure helium. The oxide layer was manually stripped from the surface of iron; part of it was used for chemical analysis and the remainder subjected to X-ray analysis.

Experience has shown that quenched wustite does not remain unchanged for prolonged aging times in its metastable state at room temperature. To avoid the experimental uncertainties which may arise from dissociation and oxidation of quenched wustite, the samples were analyzed chemically and examined by X-ray soon after quenching.

The lattice constant of wustite was measured by the back-reflection X-ray diffractometer technique, using iron as a comparison standard. One of the interesting observations was that the oxide showed a very strong (100) texture; *i.e.*, the (100) planes are parallel to the surface. None of the samples gave powder patterns, either because of preferred growth or large grain size. In these measurements, the lattice parameters of the wustite samples on the oxide–gas surface were determined from the positions of the (400) peaks, using cobalt $K\alpha_1$ and $K\alpha_2$ radiations; the (211) and (220) peaks of α-iron served as standards. The lattice parameters measured by this technique are conservatively considered to be accurate to about 1 part in 5000.

When thin oxide films, obtained by short-time oxidation of iron, were examined by back-reflection X-ray at the iron–wustite interface, the diffraction peaks were very sharp, and lattice parameters could be measured accurately. With thicker oxide films, the (400) peaks taken from the outer surface were broader, and the lattice parameters obtained were taken as average values for the average wustite composition of the specimen near the surface.

Results

The experimental results are given in a graphical form in Figure 2, where gain in weight in g. of O/cm.^{2} is plotted against time in min., for temperatures of 850, 950, 1050, and 1150°, for $H_2O + H_2$ (= 1 atm.) gas mixtures having $p_{H_2O}/p_{H_2} = 4$, 2, and 1. In all cases, the oxygen potential is below that required for the formation of magnetite. In all the oxidation experiments, weight gain per unit area is found to decrease with increasing time of oxidation, indicating that, with increasing thickness of the oxide layer, diffusion in wustite plays an increasingly more prominent role in controlling the rate of oxidation.

In Figure 3 the gain in weight squared (g. of O/cm.^{2})^2 is plotted against time for $p_{H_2O}/p_{H_2} = 2$. The curves become essentially linear after a certain reaction time, suggesting close approach to oxide–gas surface equilibrium. When this stage is reached, the diffusion of iron

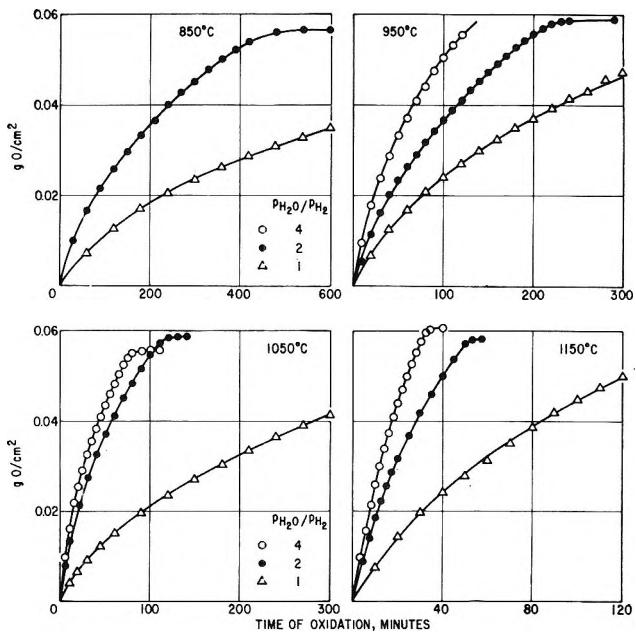

Figure 2. Experimental results on rate of oxidation of purified iron strips (~6 × 1.5 × 0.05 cm.) in H_2O–H_2 = 1 atm. at several temperatures.

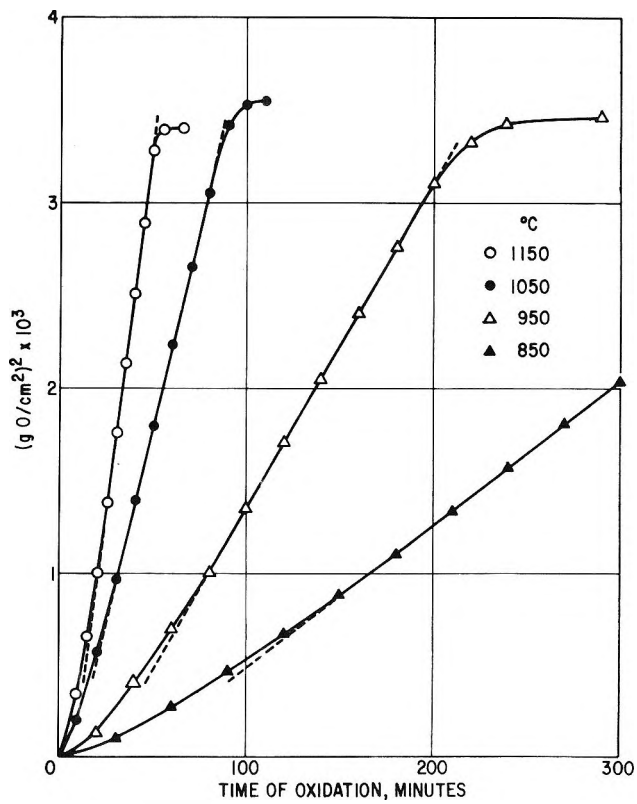

Figure 3. Rate data for $p_{H_2O}/p_{H_2} = 2$, given in Figure 2, are replotted as (g. of O/cm.^{2})^2 *vs.* time showing that a parabolic relation is obeyed during part of the oxidation time.

in wustite is expected to play a more prominent role in controlling the rate of oxidation. The reasonable validity of this argument is demonstrated later. Similar curves are obtained for other gas compositions, but for the sake of brevity they are not reproduced here. The point of departure from linearity at longer reaction times corresponds to almost complete oxidation of iron. During the subsequent oxidation time, the concentration gradient across wustite gradually disappears until the entire oxide is in equilibrium with the gas phase.

In a few experiments carried out at 950° the oxide layer, stripped from the metal, was analyzed chemically in the usual manner, and, as seen from the results given in Figure 4a, the ratio Fe^{3+}/Fe^{2+}, corresponding to the average wustite composition, increases with time of oxidation. The horizontal, broken lines are those calculated average compositions corresponding to p_{H_2O}/p_{H_2} = 4 and 1 when the oxide–gas interfacial equilibrium is reached.

The lattice parameters given in Figure 4b were obtained from the oxide–gas surface of the quenched wustite samples. A decrease in lattice parameter indicates an increase in Fe^{3+}/Fe^{2+}.

In connection with the X-ray data, it should be pointed out that, in view of the penetration of Kα radiations into the wustite sample, the measured parameters are average values for the surface layers. Furthermore, owing to the difficulties experienced in suppressing the dissociation of wustite during quenching, the X-ray measurements are subject to some errors. It is probably for this reason that there is much disparity in the lattice parameter measurements made on quenched wustite samples by a number of investigators.[9-11] In other words, although the X-ray data given in Figure 4b indicate an increase in the ratio Fe^{3+}/Fe^{2+} at the oxide surface with time, the latter cannot be evaluated from the available scattered data on lattice parameter *vs.* wustite composition.

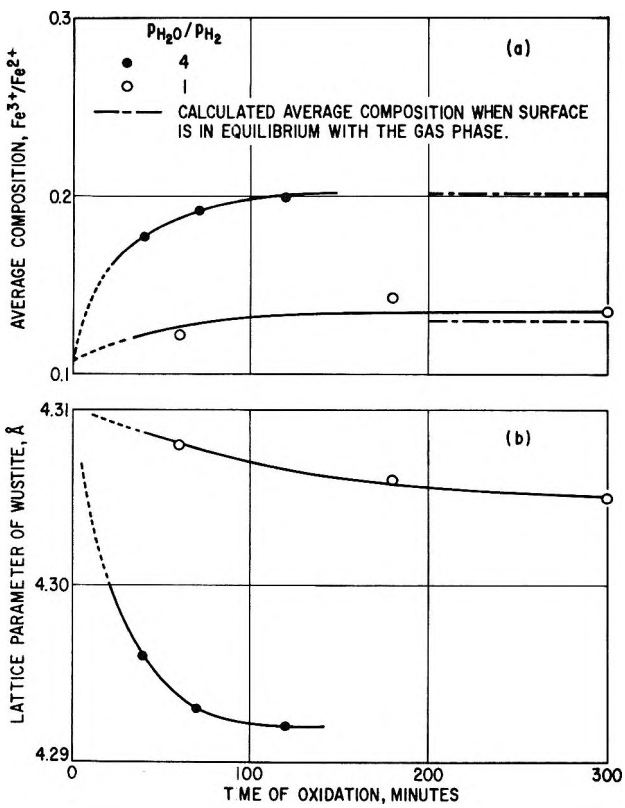

Figure 4. Variation in average (a) wustite composition and (b) lattice parameter at oxide–gas surface with time of oxidation of iron in H_2O-H_2 mixtures at 1 atm. and 950°.

Discussion

Rate of Phase Boundary Reaction. The over-all phase boundary reaction occurring at the surface of the wustite may be represented by

$$H_2O(g) + 2e \longrightarrow O^{2-} + H_2(g) \qquad (1)$$

The surface of wustite forming is considered to contain a fixed number of sites, c sites/cm.^{2}, fractions of which are assumed to be occupied by the following adsorbed species. $\theta_{H_2O} + \theta_{H_2} + \theta_O + \theta_\dagger + \theta_\square = 1$, where subscripts indicate the adsorbed species (†, activated complex; □, vacant sites).

Based on quasi-chemical considerations, the activities of the adsorbed species may be represented in terms of the fractions of sites, thus

$$a_{H_2O} = k_1 \frac{\theta_{H_2O}}{\theta_\square} \qquad (2)$$

$$a_{H_2} = k_2 \frac{\theta_{H_2}}{\theta_\square} \qquad (3)$$

$$a_O = k_3 \frac{\theta_O}{\theta_\square} \qquad (4)$$

$$a_\dagger = k_4 \frac{\theta_\dagger}{\theta_\square} \qquad (5)$$

where k_1, k_2, k_3, and k_4 are the proportionality factors for a given temperature. The choice of appropriate standard states for these activities is given later in the text.

One of the possible forms of the activated complex forming at the surface from the gas phase is that involving a molecule of water vapor. Then, in ac-

(9) E. R. Jette and F. Foote, *J. Chem. Phys.*, **1**, 29 (1933); *Trans. AIME*, **105**, 276 (1933).

(10) V. Cirilli and C. Brisi, *Ann. chim.* (Rome), **41**, 508 (1951).

(11) P. K. Foster and A. J. E. Welch, *Trans. Faraday Soc.*, **52**, 1628 (1956).

cordance with Eyring's theory of absolute reaction rates, an equilibrium may be assumed with the reactant, $H_2O(g)$, and the activated complex, $[H_2O]_\dagger$, thus

$$H_2O(g) = [H_2O]_\dagger \tag{6}$$

$$K_\dagger = \frac{a_\dagger}{a_{H_2O}} \tag{7}$$

where $K_\dagger$ is the equilibrium constant. By combining this equation with those given in (4) and (5), the following expression is obtained for the fraction of sites occupied by the activated complex

$$\theta_\dagger = K_\dagger \frac{k_3}{k_4} \frac{\theta_O}{a_O} a_{H_2O} \tag{8}$$

It should be noted that the values of θ_O and a_O for oxygen at the surface refer to the composition of wustite at the oxide–gas surface and a_{H_2O} is the water vapor activity of the gas phase.

In terms of Eyring's theory of absolute reaction rates, the rate of dissociation of the activated complex is given by

$$\text{rate of oxidation} = \frac{RT}{Nh} c\theta_\dagger \tag{9}$$

where RT/Nh is the universal specific rate constant, the symbols having the usual significance, and c is the total number of sites per unit area, in molecules/cm.^{2}. By inserting the value of $\theta_\dagger$ from eq. 8 in 9, and replacing a_{H_2O} by the partial pressure, p_{H_2O}, in atm., the rate equation becomes

$$\text{rate of oxidation} = \frac{RT}{Nh} ck_\dagger \frac{k_3}{k_4} \frac{\theta_O}{a_O} p_{H_2O} \tag{10}$$

In view of the microscopic reversibility of the reaction processes, the rate equation for the reverse reaction (reduction) is based on the dissociation of the activated complex $[H_2O]_\dagger$ to water vapor. In this case, the activated complex is taken to be in equilibrium with the reactants H_2 and O at the wustite surface. Following the procedure given above, a rate equation for the reverse reaction is obtained, thus

$$\text{rate of reduction} = \frac{RT}{Nh} cK_\dagger \frac{k_3}{k_4} \frac{\theta_O}{a_O''} p_{H_2O} \tag{11}$$

which differs from eq. 10 only in the term a_O'', being the oxygen activity at the wustite surface in equilibrium with the gas phase.

The equation for the net rate of oxidation is of course given by the difference of eq. 10 and 11. For the temperature range studied, a mean temperature may be used for the value of T in eq. 11. Furthermore, assuming that the entropy of activation for reaction 6 is independent of temperature, the temperature dependence of the reaction rate may be given in the form of the Arrhenius equation, thus

$$\frac{dn}{dt} = k'\theta_O \left(\frac{1}{a_O} - \frac{1}{a_O''}\right) p_{H_2O} e^{-E/RT} \tag{12}$$

where k' is the over-all rate constant containing the constants given in eq. 11 and the mean experimental temperature. The heat of activation, E, is an apparent heat of activation which is the sum of the heat of activation for reaction 6 and those pertaining to the constants k_3 and k_4.

As indicated by eq. 12, for a given gas composition and temperature, the rate of oxidation decreases as the oxygen activity, a_O, at the surface of wustite increases with reaction time. However, this effect may be somewhat counteracted by an increase in the value of θ_O with increasing oxygen activity.

In the initial stages of oxidation, when the oxide layer is very thin, the values of a_O and θ_O at the surface will be very close to those for the iron–wustite equilibrium. By taking the iron–wustite equilibrium as the reference state for oxygen activity, *i.e.*, $a_O = 1$ by definition, the initial isothermal rate of oxidation of iron, covered with a thin layer of wustite, may be represented by

$$\left(\frac{dn}{dt}\right)_0 = k'' \left(1 - \frac{1}{a_O''}\right) p_{H_2O} \tag{13}$$

The oxygen activity a_O'' is a function of temperature and oxygen potential of the gas. Over the range studied the value of a_O'' is within the range 1 to about 6.

By drawing tangents to the rate curves in Figure 2 at $t = 0$, the initial rates of oxidation are obtained, and in Figure 5 they are plotted against the product $(1 - 1/a_O'')p_{H_2O}$ for each temperature. Within the limits of the experimental errors, the results on initial rates are in reasonable support of rate eq. 13.

A similar rate equation is expected to hold for the initial stages of oxidation in carbon dioxide–carbon monoxide atmospheres. The rates reported by Pettit and Wagner[5] and Hauffe and Pfeiffer[2] for early stages of oxidation are plotted in Figure 6 against the product $(1 - 1/a_O'')p_{CO_2}$. These results again support the possible validity of eq. 13.

In some experiments, Pettit and Wagner introduced argon into the oxidizing atmosphere, and, as seen from the results in Figure 5, the effect of argon addition is no more than a mere dilution of the partial pressures of reacting gases.

The temperature dependence of the rate constant k'' is shown in Figure 7. The following apparent heats of

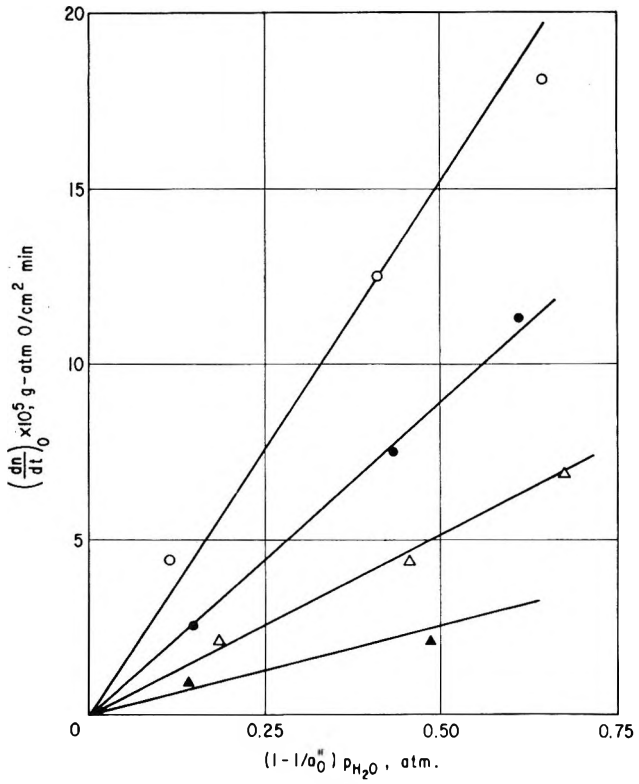

Figure 5. Linear variation of the initial rate of oxidation of iron with the product $(1 - 1/a_O'')p_{H_2O}$. Oxidizing atmosphere is $p_{H_2O} + p_{H_2} = 1$ atm.

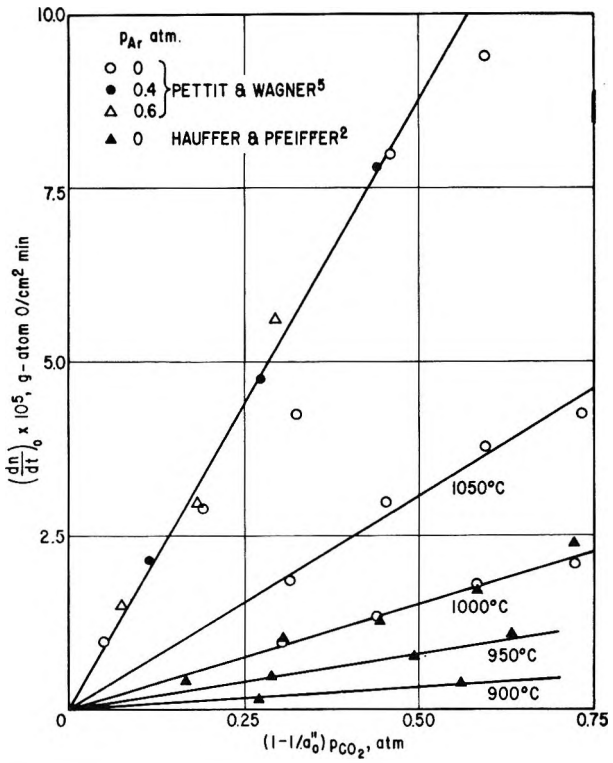

Figure 6. Linear variation of the initial rate of oxidation of iron with the product $(1 - 1/a_O'')p_{CO_2}$. Oxidizing atmosphere is $p_{CO_2} + p_{CO} + p_{Ar} = 1.0$ atm.

activation are obtained: for H_2O–H_2 atmospheres, $E = 19.2$ kcal./g.-atom of O; for CO_2–CO atmospheres, $E = 52$ kcal./g.-atom of O.

If the activated complex formed from a molecule of $H_2O(g)$ or $CO_2(g)$ is $2(OH)^-$ or $(CO_3)^{2-}$, the rate equation obtained is similar to those already discussed, *i.e.*, initial rate being directly proportional to the product $(1 - 1/a_O'')p_i$ where the subscript i represents H_2O or CO_2 as the case may be.

Parabolic Rate of Oxidation. The self-diffusivities of iron in wustite have been measured by Himmel, *et al.*,[6] over wide ranges of oxygen potential and temperature. Their values of D_{Fe}^* are plotted in Figure 8 against the atomic ratio N_O/N_{Fe}. Since iron cations migrate in wustite *via* the cation vacant sites, it is reasonable that $D_{Fe}^* \rightarrow 0$, at an idealized nonphysical composition of ferrous oxide with $N_O/N_{Fe} = 1$. It is for this reason that the lines are drawn to pass through the origin of the coordinates.

Since the oxygen potential at the iron–wustite interface is fixed for any given temperature, the rate of oxidation of iron, controlled by diffusion in wustite, is readily calculable[7] from the self-diffusivity data for any given oxygen activity at the oxide–gas interface. Thus

$$\frac{dn}{dt} = \frac{k_r}{Z\xi} \tag{14}$$

where dn/dt = instantaneous rate of oxidation at time t, g.-atom of O/cm.^{2} sec.; $Z = 2$, valency of oxygen; ξ = instantaneous thickness of wustite layer at time t, cm.; k_r = "rational rate constant," g.-equiv./cm. sec.

The value of k_r is derived from the self-diffusivity of iron in wustite using the expression[7]

$$k_r = \bar{c} \int_{a_O'}^{a_O''} \frac{N_O}{N_{Fe}} D_{Fe}^* \, d \ln a_O \tag{15}$$

where a_O = activity of oxygen in wustite, primes (′) and (″) indicate oxygen activities in wustite at iron–wustite and wustite–gas interfaces, respectively; N = atom fraction of oxygen and iron, as indicated by the subscripts; $\bar{c}$ = average concentration of iron or oxygen ion in wustite = 0.161 g.-equiv. of O/cm.^{3}.

In more practical units, the parabolic oxidation of iron may be represented by the expression

$$m^2 = k_p t + I \tag{16}$$

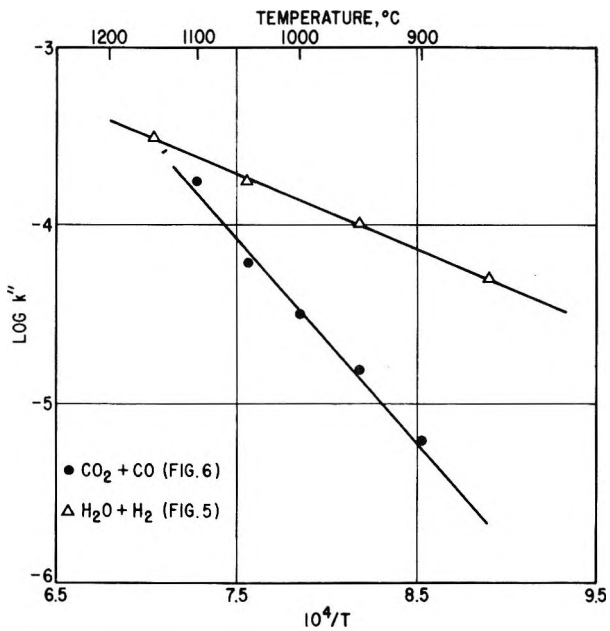

Figure 7. Temperature dependence of the rate constant for the oxide–gas phase boundary reaction for oxidation of iron to wustite in CO_2–CO or H_2O–H_2 atmospheres.

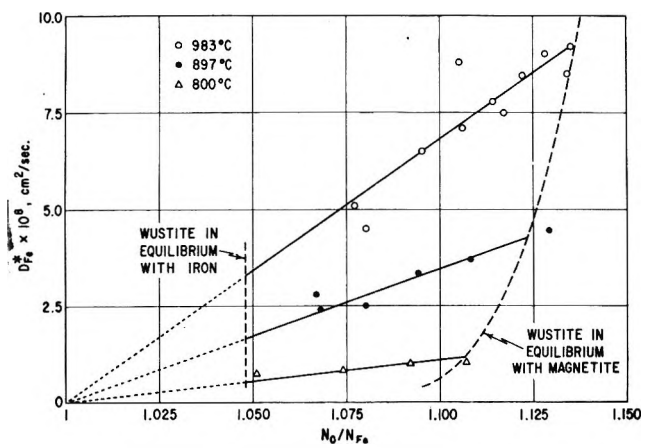

Figure 8. Variation of self-diffusivity of iron with temperature and composition of wustite (from data of Himmel, Mehl, and Birchenall[6]).

where m is the gain in weight per unit area, k_p is the rate constant, and I is a constant for a particular experiment. By appropriate change of units, the value of k_p, in (g. of O)^2/cm.^{4} sec., can be derived from the value of k_r, thus

$$k_p = \frac{2\rho(M_O)^2}{ZM_w} k_r \qquad (17)$$

where ρ is density of wustite, M_w its molecular weight, and M_O the atomic weight of oxygen. Taking M_w = 67.5 g./g.-atom of O and ρ = 5.4 g./cm.^{3} for average wustite composition, the conversion factor is given by

$$k_p = 20.58k_r \qquad (18)$$

The parabolic rate constant, k_p, thus obtained is plotted in Figure 9 against log a_O'' and compared with those derived from the slopes of the linear parts of the curves as plotted in Figure 3. In Figure 9 are also included the values of k_p obtained by Paidassi[12] for values of a_O'' corresponding to wustite–magnetite equilibrium.

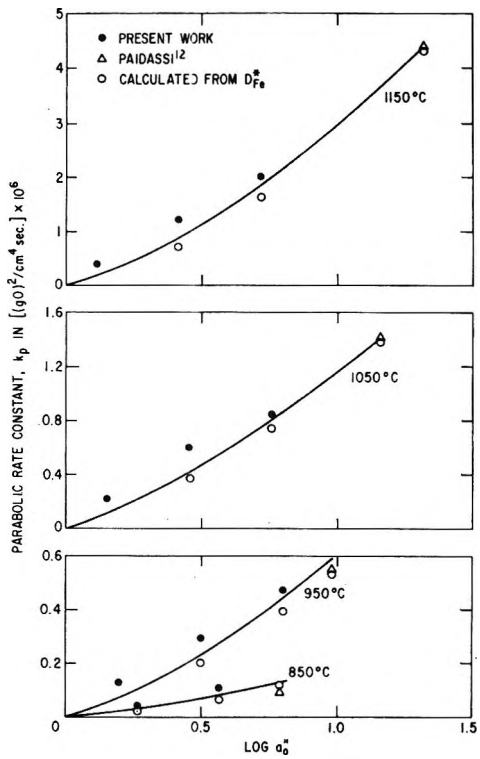

Figure 9. Variation of the parabolic rate constant, for the oxidation of iron to wustite, with oxygen activity at the surface of the oxide.

The values of k_p derived from the parabolic portions of the rate data of the present work are a little higher than those calculated from the diffusivity data.

However, allowing for the experimental uncertainties involved, it is reasonable to state that the oxide–gas equilibrium is closely approached in the present work, prior to the complete oxidation of iron; then the reaction proceeds in accordance with the diffusion process in the wustite phase.

Conclusions

It is found that the initial rate of oxide–gas phase boundary reaction in the oxidation of iron to wustite is

(12) J. Paidassi, *Acta Met.*, **6**, 184 (1958).

greater in water vapor–hydrogen gas mixtures than those obtained by other investigators using carbon dioxide–carbon monoxide gas mixtures. It is shown that, for both types of atmospheres, the initial rate is directly proportional to the product $(1 - 1/a_O'')p_i$ where p_i is either p_{H_2O} or p_{CO_2}, and a_O'' is the oxygen activity at the wustite surface in equilibrium with the gas phase. This observation is in accord with the rate equation derived on the basis of the assumption that the activated complex formed at the surface involves a molecule of H_2O or CO_2. From the temperature dependence of the rate constant, the following apparent heats of activation are obtained. For oxidation in $H_2O + H_2$, $E = 19.2$ kcal./g.-atom of O, and for oxidation in $CO_2 + CO$, $E = 52$ kcal./g.-atom of O.

Acknowledgment. The authors wish to thank the following members of this laboratory: L. S. Darken for valuable discussions in the course of this work and B. B. Rice for carrying out the experimental work.

NOTES

The Heats of Formation of Solid Tetrasulfur Tetranitride and Tetraselenium Tetranitride

by Carla K. Barker, A. Wallace Cordes, and John L. Margrave

Departments of Chemistry, University of Wisconsin, Madison, Wisconsin, University of Arkansas, Fayetteville, Arkansas, and Rice University, Houston, Texas *(Received May 4, 1964)*

Although there have been extensive investigations of the chemical reactivity of tetrasulfur tetranitride (S_4N_4) and various closely related compounds ($S_4N_4H_4$, $S_4N_4F_4$, S_2N_2, $(SN)_x$),[1] there appears to be little reliable information on the heats of formation of these materials or on the strength of N–S or N–Se bonds, in general. The data of Berthelot and Vieille have been re-evaluated[2] and favor $\Delta H_f°[S_4N_4(c)] \approx \Delta H_f°[Se_4N_4(c)] \approx 128$ kcal./mole. The questionable purity of the materials and the uncertainty about the reactions actually studied minimize the reliability of these results.

Further quantitative data come from a partial analysis of the band spectra of NS(g) and $NS^+(g)$,[3] and these have been used in the JANAF Tables to deduce the values $D°_{298}(NS) = 115 \pm 25$ kcal./mole and $\Delta H_f°[NS(g)] = 63 \pm 25$ kcal./mole.[4] There are no data on diatomic SeN(g).

The Heat of Formation of S_4N_4

In these experiments samples of S_4N_4 were prepared and purified by recrystallization from dioxane and from benzene as described by Jolly[5] and were made available to us through the courtesy of Prof. E. M. Larsen and Mr. G. McDonald of the University of Wisconsin. An electrically heated platinum wire was used to initiate the decomposition of $S_4N_4(s)$ to the elements in the presence of nitrogen as a pressurizing gas

$$S_4N_4(s) = 4S(s) + 2N_2(g)$$

Mass spectrometric examination of the residual gas showed only N_2, while X-ray studies indicated that the solid phase was mainly an amorphous form of sulfur.

The heat of decomposition, measured in five different runs, is presented in Table I and from the data the standard heat of formation is calculated to be $+110.0 \pm 2.0$ kcal./mole with the major part of this uncertainty being arbitrarily added to allow for the poorly defined final state of the sulfur since the actual experimental data are reproducible to $\pm 0.5\%$.

From this result, the standard heats of formation of S(g) = 65.6 kcal./mole and of N(g) = 113.0 kcal./mole,[4] and an estimated heat of sublimation for S_4N_4 = 15 ± 5 kcal./mole and, assuming only N–S bonds in

(1) (a) M. Goehring, *Quart. Rev.* (London), **10**, 437 *(1956)*; (b) M. Becke-Goehring, Special Publication No. 10, The Chemical Society, London, 1957, p. 146.

(2) (a) M. Berthelot and P. Vieille, *Ann. chim. phys.*, **27**, 202 (1882); (b) "Selected Values of Chemical Thermodynamic Properties," National Bureau of Standards Circular 500, U. S. Government Printing Office, Washington, D. C., 1950.

(3) (a) R. Barrow, G. Drummond, and P. Zeeman, *Proc. Phys. Soc.*, **67**, 365 (1954); (b) K. Dressler, *Helv. Phys. Acta*, **28**, 563 (1955).

(4) "JANAF Thermochemical Tables," D. R. Stull, Ed., The Dow Chemical Co., Midland, Mich., June 30, 1961.

(5) W. L. Jolly, "Synthetic Inorganic Chemistry," Prentice-Hall, Englewood Cliffs, N. J., 1960, pp. 166–168.

Table I: Heat of Decomposition of S_4N_4

Run	m (*in vacuo*), g.	ΔR, ohm	$-\Delta E_{tot}$, cal.	ΔE_{ign}, cal.	$-\Delta E_c$, cal. g.$^{-1}$	Deviation, cal. g.$^{-1}$
6	0.51725	0.0038310	310.01	2.08	595.73	−7.48
7	0.51791	0.0038669	312.92	1.62	601.44	−1.77
8	0.46528	0.0035172	284.62	1.68	608.58	5.37
9	0.48342	0.0036097	292.10	1.88	600.77	−2.44
10	0.50166	0.0038072	308.09	2.54	609.51	6.30
				Av.	603.21	±2.58

ΔE_d = −111.16 ± 0.47 kcal./mole $\Delta H_d°$ = −110.01 ±0.47 kcal./mole

$\Delta E_d°$ = −111.16 ± 0.47 kcal./mole $\Delta H_f°$ = +110.01 ± 0.47 kcal./mole

S_4N_4, one calculates the average N–S bond strength in S_4N_4 to be 73.5 ± 1 kcal./mole.

This number is consistent with the value for D(NS) = 115 ± 25 kcal./mole on the argument that the bond in NS(g) is of order 2.5, while that in S_4N_4 is of order 1.65.[6] If a direct proportionality were applicable, the average (N–S) bond in S_4N_4(g) would be estimated as 75 kcal./mole. With this model one concludes that the actual energy effects to be associated with S–S or N–N interactions in S_4N_4 are small ($\leq$20 kcal./mole). One further predicts the average N–S single-bond energy to be ~45 kcal./mole.

The Heat of Formation of Se_4N_4

Samples of crystalline Se_4N_4 were synthesized at the University of Arkansas, shipped with caution to the University of Wisconsin, and decomposed in the bomb calorimeter by the same technique as used for S_4N_4. The elements were the only decomposition products and thus, by averaging the data from Table II, one finds the heat of formation of solid Se_4N_4 to be +147.7 ± 6.0 kcal./mole. The samples were analyzed to be ~99% pure, but the properties of Se_4N_4 (it explodes on the slightest touch when dry, much like NI_3) preclude excessive handling and purification. If anything, the most exothermic decompositions are probably the most characteristic since small amounts of decomposition may have occurred in the time between the synthesis and the calorimetric run for a particular sample. By using only runs 5, 7, 8, and 9, which are most exothermic and most consistent, one calculates $\Delta H_f°$ = +163 ± 3 kcal./mole and this latter value is recommended for Se_4N_4(s).

From this latter heat of formation, the standard heats of formation of Se(g)[7] and of N(g),[4] an estimated heat of sublimation for Se_4N_4 of 20 ± 10 kcal./mole, and assuming that Se_4N_4(s) has approximately the same

Table II: Heat of Decomposition of Se_4N_4[a]

Run	m (*in vacuo*); g.	ΔR, ohm	$-\Delta E_{tot}$, cal.	ΔE_{ign}, cal.	$-\Delta E_d$, cal. g.$^{-1}$	Deviation, cal. g.$^{-1}$
1	0.05921	0.0002493	20.32	0.61	372.59	−27.71
2	0.03281	0.0001520	12.39	0.56	360.67	−39.63
4	0.06737	0.0002860	23.32	0.66	336.40	−63.90
5	0.08527	0.0004773	38.91	0.61	449.21	48.91
6	0.13822	0.0006414	52.29	0.71	373.23	−37.07
7	0.14152	0.0007422	60.50	0.56	423.60	23.30
8	0.12406	0.0006818	55.58	0.60	443.24	42.94
9	0.11430	0.0006411	52.26	1.57	443.56	43.26
					Av. 400.31	± 16.06

ΔE_d = −148.86 ± 5.97 kcal./mole $\Delta H_d°$ = −147.68 ± 5.97 kcal./mole

$\Delta E_d°$ = −148.86 ± 5.97 kcal./mole $\Delta H_f°$ = +147.68 ± 5.97 kcal./mole

[a] Runs 1 and 2 were made on the original samples received; runs 4, 5, and 6 were made on a second group of samples; runs 7, 8, and 9 were made on the last group of samples received.

structure as S_4N_4(s) with only N–Se bonds, one calculates the average N–Se bond energy in Se_4N_4(g) to be 59 ± 10 kcal./mole. If the bond order is 1.65, by analogy with S_4N_4, then one predicts that D(N–Se) = 90 ± 20 kcal./mole (bond order = 2.5); D(N–Se$^+$) = 108 ± 20 kcal./mole (bond order = 3.0); and that the average N–Se single bond energy $\approx$ 40 kcal./mole.

Acknowledgment. The authors are pleased to acknowledge the support of this work by the United States Atomic Energy Commission, by the American Chemical Society through a grant from the Petroleum Research Fund, and by the Selenium–Tellurium Development Association.

(6) D. Chapman and T. Waddington, *Trans. Faraday Soc.*, 58, 1291, 1679 (1962).

(7) G. N. Lewis, M. Randall, K. S. Pitzer, and L. Brewer, "Thermodynamics," 2nd Ed., Mc Graw-Hill Book Co., New York, N. Y., 1961.

Association of Secondary Amines with Tetrahydrofuran[1a]

by H. Hartig and W. W. Brandt[1b]

Department of Chemistry, Illinois Institute of Technology, Chicago, Illinois 60616 (*Received April 21, 1964*)

The steric effects modifying the H-bonding tendency of certain polar groups are of great interest because they may well determine certain chemical and physical

rate constants. Smith and Creitz[2] obtained infrared data showing that 3-pentanols with increasing numbers of alkyl groups close to the hydroxyl group are incapable of forming H-bonded polymers or even dimers. Similarly, Bellamy and Williams[3] studied several phenols and found the differences between the OH stretching frequencies of the H-bonded and nonbonded state to be relatively small whenever the OH group was strongly sterically hindered. Earlier studies in this laboratory[4] showed that the carbonyl group's ability to form H bonds can be markedly reduced by the presence of bulky groups on neighboring carbon atoms.

The present study is concerned with the >N–H group, which is of great interest in the study of polyamides, proteins, and polypeptides. Bellamy and Williams[3] noticed that the constants of the H-bonding equilibrium were much more sensitive to the presence of sterically hindering groups than the difference between the frequencies of the absorption bands of the nonbonded and the bonded species, respectively. These authors concluded that in the series of compounds studied, the steric effects are primarily affecting the ease of H-bond formation, and only secondarily the bond strength. Both frequency shifts and equilibrium constants of H-bond formation were determined in the present study, so as to see if the findings of Bellamy and Williams hold for secondary amines as well.

The choice of secondary amines for comparative studies is somewhat limited by difficulties in their synthesis or purification and by their limited stability and solubility in interesting solvents. Tetrahydrofuran is a convenient proton acceptor because its infrared and ultraviolet spectra do not interfere with those of the secondary amines, it is unreactive under the experimental conditions, and it is a good solvent for the amines chosen. Also, there are some literature data on diphenylamine in tetrahydrofuran[5] which may lead to important comparisons.

The problem of obtaining accurate constants for association equilibria has been discussed in some detail by other workers.[6a,b] To gain confidence in the results of this work, two spectrophotometric methods (infrared and ultraviolet) were used. N.m.r. chemical shift measurements of the amino hydrogen signal were found to be not feasible with the available equipment.

Experimental Methods and Procedures

(*A*) *Materials.* The hydrocarbon solvents used were Spectroquality reagent grade from Matheson Coleman and Bell, Inc., or from the Phillips Petroleum Co. Tetrahydrofuran (THF) was Fisher Certified grade. The solvents were redistilled over sodium and the center fraction distilling within a range of 0.3° was used. The di-*o*-tolylamine was prepared by the third procedure of Weston and Adkins[7] with copper dust prepared from zinc and copper sulfate as catalyst. The compound was recrystallized several times, the last time from 2,2,4-trimethylpentane. The m.p. was 51.5–52.5° before the last step (lit.[8] 52–53). Di-*p*-tolylamine (K and K Laboratories) was also recrystallized from the same solvent until the ultraviolet spectrum remained constant and showed no shoulder at 2850 Å. Diphenylamine (Purissimum grade of Fluka A. G., Switzerland) was recrystallized once from 2,2,4-trimethylpentane. Di-2,2-naphthylamine (Aldrich Chemical Co.) also was recrystallized from the same solvent until its ultraviolet spectrum became constant. Di-1,1-naphthylamine was prepared by the method of Hodgeon and Mersden[9] and was recrystallized until its melting point remained constant at 115–116.5°. The solutions needed were prepared by drybox techniques and the exposure to the atmosphere during the spectroscopic measurement was kept to a minimum because of the known hygroscopicity of tetrahydrofuran. To avoid systematic errors, all solutions and reference solvents in a given series of runs were treated in a similar fashion.

(*B*) *Infrared Measurements.* A Perkin-Elmer Model 21 spectrophotometer with a NaCl prism was used. The slit width was 50 mμ and it was found that the transmittance measured at half this slit width was lower by 3%. From the research of Philpotts and co-workers,[10] it appears that in the present experiments the measured peak heights are all affected to the same fractional extent because the infrared absorption bands investigated in the present work are broader and the slit widths lower than those used by these authors. It can be shown that the equilibrium constants do not carry systematic errors from this source.

(1) (a) This work was supported by a grant from the U. S. Public Health Service (GM-10288); (b) direct requests for reprints to this author.

(2) F. A. Smith and E. C. Creitz, *J. Res. Natl. Bur. Std.*, **46**, 145 (1951).

(3) L. J. Bellamy and R. L. Williams, *Proc. Roy. Soc.* (London), **A254**, 119 (1960).

(4) W. W. Brandt, *J. Am. Chem. Soc.*, **85**, 2628 (1963).

(5) A. B. Sannigrahi and A. K. Chandra, *J. Phys. Chem.*, **67**, 1106 (1963).

(6) (a) N. J. Rose and R. S. Drago, *J. Am. Chem. Soc.*, **81**, 6138 (1959); (b) P. R. Hammond, *J. Chem. Soc.*, 479 (1964).

(7) P. E. Weston and H. Adkins, *J. Am. Chem. Soc.*, **50**, 859 (1928).

(8) I. M. Heilbron, *et al.*, "Dictionary of Organic Compounds," Oxford University Press, New York, N. Y., 1934.

(9) H. Hodgeon and E. Mersden, *J. Chem. Soc.*, 1181 (1938).

(10) A. R. Philpotts, W. Thain, and P. G. Smith, *Anal. Chem.*, **23**, 268 (1951).

Table I: Infrared Measurements on Solutions of Secondary Amines in Mixtures of Tetrahydrofuran (THF) and Hydrocarbons[a]

Amine	Diphenylamine			Di-*o*-tolylamine
Concentration, mole/l.	0.02	0.2	0.2	0.2
Hydrocarbon solvent	2,2,4-Trimethylpentane		Cyclohexane	2,2,4-Trimethylpentane
Peak positions, cm.$^{-1}$				
Free >N–H	3459	3465		3442
Bonded >N–H				
in hydrocarbon	(3380)	(3380)	(3378)	(3386)
in tetrahydrofuran	3364	3362	3363	3374
Molar extinction coefficients, l./mole cm.				
Free >N–H in hydrocarbon	29	29		15
Bonded >N–H in tetrahydrofuran	113	119	118	56
K, l./mole	1.53 ± 0.15	1.45 ± 0.1	1.53 ± 0.1	0.44 ± 0.02

[a] THF concentrations range from 0.06 to 12.2 moles/l.; temperature, 22°. Values in parentheses are extrapolated to infinite THF concentration. K equilibrium constant evaluated by the method of Rose and Drago[6a] at the peak maxima of the bonded >N–H bands.

(C) Ultraviolet Measurements. A Cary Model 14 spectrophotometer of the Applied Physics Corp. was used, using a slit width of about 0.4 mm. It was shown experimentally that the peak heights are not dependent on slit widths under the experimental conditions.

(D) Data Treatment. The ultraviolet molar extinction coefficients of the amines (or diphenyl ether) in a series of solutions containing various amounts of tetrahydrofuran (THF) were used to obtain K values from the equation[11] (see Figure 1)

$$\frac{[B]_0}{\epsilon - \epsilon_0} = \frac{1}{(\epsilon_1 - \epsilon_0)K} + \frac{[B]_0}{\epsilon_1 - \epsilon_0} \cdots \qquad (1)$$

Here $[B]_0$ is the analytical concentration of the H acceptor B, while ϵ, ϵ_0, and ϵ_1 are the apparent molar extinction coefficient of the proton donor, the actual extinction coefficient of the unbonded proton donor, AH, and of the bonded proton donor, AH - - - B, respectively.

The equation is valid if [AH - - - B] << [B], if only 1:1 complexes are formed, and if the Beer–Lambert law holds.

In view of the data obtained in this work and the discussion of Scott[12] and Hayman,[13] eq. 1 is preferable to certain forms of the Benesi–Hildebrand equation recommended by Hammond,[14] because it leads to relatively precise values of K valid at infinitely low concentrations of THF.

[AH - - - B] << [B] can be shown to be well justified in all ultraviolet measurements. For example, for diphenylamine at a concentration of 0.77×10^{-3} mole/l., eq. 1 yields K = 1.43 ± 0.1 l./mole while the more elaborate method of evaluation reported by Rose and Drago[6a] which is free from the assumption [AH - - - B] << [B] yields K = 1.44 ± 0.1 l./mole. The infrared measurements, on the other hand, always required the use of the Rose and Drago method,[6a] to avoid errors of 10 to 20%. The infrared extinction coefficients were obtained from the peak heights at the absorption band maxima, thus the solvent shifts[15] of the bands were rendered harmless.

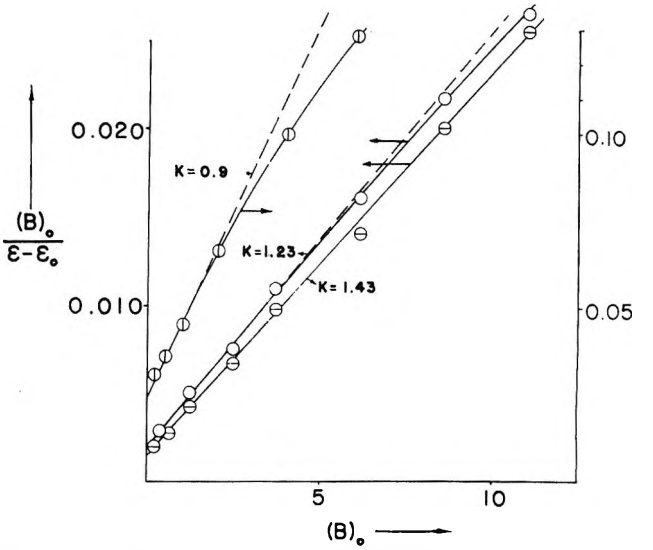

Figure 1. Plots based on eq. 1 for evaluation of K (see text). Di-*o*-tolylamine, ⊖, and diphenylamine, ⊖, in 2,2,4-trimethylpentane; diphenylamine in cyclohexane, O (ultraviolet data).

(11) J. A. A. Ketelaar, *Rec. trav. chim.*, 71, 1104 (1952).
(12) R. L. Scott, *ibid.*, 75, 787 (1956).
(13) H. J. G. Hayman, *J. Chem. Phys.*, 37, 2290 (1962).
(14) See eq. 2c and 2d of ref 6.
(15) L. J. Bellamy and H. L. Hallam, *Trans. Faraday Soc.*, 55, 220 (1959).

Table II: Ultraviolet Measurements on Solutions of Secondary Amines in Mixtures of Tetrahydrofuran (THF) and Hydrocarbons

Solute	Diphenylamine					Di-o-tolylamine	Di-p-tolylamine	Di-1,1-naphthylamine	Di-2,2-naphthylamine	N-Methyldiphenylamine	Diphenyl ether
Concentration, mole/l.	2.55×10^{-5}	3.1×10^{-5}	0.77×10^{-3}	3.4×10^{-5}	0.8×10^{-3}	1.2×10^{-3}	0.87×10^{-3}	3.5×10^{-5}	1.7×10^{-5}	1.4×10^{-3}	1.0×10^{-3}
Hydrocarbon solvent	2,2,4-Trimethylpentane			Cyclohexane				2,2,4-Trimethylpentane			
Tetrahydrofuran concentration range, moles/l.	0.06 to 11.0	0.06 to 2.5	0.06 to 11.0	0.06 to 9.2	0.06 to 11.0	0.06 to 6.1	0.06 to 6.1	0.06 to 11.6	0.06 to 6.1	0.06 to 6.1	0.06 to 6.1
Temperature, °C.	31	32	30	28	31	28	26	27	27	28	29
Peak positions, Å., in hydrocarbon	2815	2816	2820	2831	2825	2784	2842	3361	3131	2928	2444	2784
in mixture with 5 moles/l. of THF	2855	2856	2856	2863	2860	2796	2878	3378	2497	3164	2649	2933	2453	2784
Molar extinction coefficient[a] (l./mole cm.) $\times 10^{-3}$ in hydrocarbons	1.75	1.72	1.67	1.75	1.66	1.28	1.71	2.14	2.24	4.24	2.72	1.15	0.96	0.18
K, l./mole	1.38 ± 0.1	1.44 ± 0.1	1.43 ± 0.1	1.41 ± 0.1[b]	1.23 ± 0.1[b]	0.9 ± 0.3[c]	1.35 ± 0.1	0.0 ± 0.1	0.8 ± 0.3	1.1 ± 0.2	0.9[c] ± 0.2	0.17 ± 0.05	0.2 ± 0.05	0.1 ± 0.20

[a] Based on nominal path lengths of ultraviolet cells used. [b] Slight nonlinearity. [c] Strong nonlinearity in standard plot.

Results

The spectrophotometric results are summarized in Tables I and II.

The equilibrium constant obtained for the system diphenylamine–THF disagrees appreciably with that obtained earlier by Sannigrahi and Chandra[5]; we do not know the reason for this.

The variations of the absorption band intensities of di-*o*-tolylamine and of the 340-mμ band of di-1,1-naphthylamine in solutions containing differing amounts of THF were quite small and had to be smoothed before eq. 1 could be used to evaluate the K values.

The intensities of the absorption bands of di-*o*-tolylamine and the 250-mμ band of di-1,1-naphthylamine decrease with increasing concentration of THF, but eq. 1 still leads to a definite value for K.

Discussion

A comparison of the infrared and ultraviolet results shows that there is good agreement of the equilibrium constants of diphenylamine obtained by the two methods. The small differences which exist probably cannot be ascribed to a dependence of K on the amine concentration, because within each group of data (infrared and ultraviolet) there appears to be no trend with concentration.

The steric hindrance to H-bond formation by di-*o*-tolylamine is seen in the low K values obtained for this compound, relative to diphenylamine and di-*p*-tolylamine. Interestingly, di-1,1-naphthylamine also appears to have more difficulties in forming H bonds than di-2,2-naphthylamine. Contrary to Bellamy and Williams' findings,[3] one notes from the infrared frequencies given in Table I that the strength of H bonds formed by the sterically hindered di-*o*-tolylamine is lower than that of the H bonds formed by diphenylamine. The low K, therefore, does not only reflect a lowering of the probability of H-bond formation.

The ultraviolet measurements on N-methyldiphenylamine and on diphenyl ether show that associations other than H bonding probably affect the observed K values, albeit to a small extent.

The differences between the K values obtained for di-*o*-tolylamine from infrared and ultraviolet data, respectively and the discrepancy of the K values derived from the two ultraviolet absorption bands of di-1,1-naphthylamine are clearly outside the experimental errors. Ross and Labes[16] similarly found the association equilibrium constant K of 1,3,5-trinitrobenzene with N,N-dimethylaniline in chloroform to depend on the wave length at which K was obtained.

(16) S. D. Ross and M. M. Labes, *J. Am. Chem. Soc.*, **79**, 76 (1957).

They showed that one can, however, fit the data by assuming higher order (1:2) complexes to be formed in addition to the 1:1 complexes. Hayman,[13] however, cast doubt on the physical significance of the equilibrium constants derived in this fashion.

Gardner, *et al.*,[17] found K values dependent on the wave length for the association of substituted naphthylenes with picric acid. They interpreted this in terms of contact charge-transfer interactions[18] and solvent perturbations,[19] rather than by assuming the presence of higher order associates. Hayman[13] has discussed the interpretation of spectrophotometric data in some detail and has shown that complementary data from other sources are needed to distinguish between the various possibilities. In any case, it is important to note that the amines suspected to experience much steric hindrance to H bonding, that is di-*p*-tolylamine and di-1,1-naphthylamine, seem most susceptible to the above-mentioned complications, in accordance with Gardner's findings.[17]

Obviously, the present results mean that much care is necessary in the selection of model compounds for the study of structural effects on H-bonding equilibria.

Acknowledgment. The authors are indebted to Dr. E. Loeser and Mr. R. Basalay for their preparation of compounds needed in this work.

(17) P. D Gardner, R. L. Brandon, N. J. Nix, and I. Y. Chang, *J. Am. Chem. Soc.*, **81**, 3413 (1959).

(18) L. E. Orgel and R. S. Mulliken, *ibid.*, **79**, 4839 (1957).

(19) N. S. Bayliss and C. J. Breckenridge, *ibid.*, **77**, 3957 (1955).

The Effect of Water Activity on Ion-Exchange Selectivity

by H. Laudelout

Catholic University of Louvain, Heverlee, Belgium

and Henry C. Thomas

Department of Chemistry, University of North Carolina, Chapel Hill, North Carolina *(Received July 15, 1964)*

It appears that a purely thermodynamic relation between the water content of an ion exchanger and its selectivity has not been exploited in the past. This relation predicts the change in selectivity with water activity from the change in water content with composition. Since considerable interest attaches to ion-exchange behavior for concentrated solutions, with low water activity, where apparently anomalous effects appear, an investigation along the lines here suggested may be in order.

For an ion-exchange reaction between A^{+z_A} and B^{+z_B} in an exchanger containing a definite number of fixed charges which also imbibes anion, say X^{-z_X}, one may write an equilibrium constant expression for the cation exchange

$$K = \frac{N_A^{z_B} m_B^{z_A} \gamma_B^{z_A}}{N_B^{z_A} m_A^{z_B} \gamma_A^{z_B}} \frac{f_A^{z_B}}{f_B^{z_A}} \equiv K_c \frac{f_A^{z_B}}{f_B^{z_A}} \qquad (1)$$

In this expression the m's and γ's are written for molalities and activity coefficients in the solution phase. The ratio of the ion activity coefficients is thermodynamically determinate

$$\left(\frac{\gamma_B^{z_A}}{\gamma_A^{z_B}}\right)^{z_X} = \frac{(\gamma_B^{z_X}\gamma_X^{z_B})^{z_A}}{(\gamma_A^{z_X}\gamma_X^{z_A})^{z_B}} = \frac{\gamma_{BX}^{z_A}}{\gamma_{AX}^{z_B}}$$

The composition of the exchanger phase is expressed so that

$$N_A + N_B = 1 + N_X \qquad (2)$$

that is, the N's are given as fractions of the exchange capacity in equivalents; "exchange capacity" here refers to the total fixed charge, exclusive of imbibed anion. One equivalent of exchanger therefore contains $1 + N_X$ equivalents of cation.

The activity coefficients f_A and f_B refer to the neutral combinations of cation, exchanger, and imbibed anion and are thermodynamically defined quantities for the exchanger phase. When desired, numerical values of these activity coefficients may be obtained from integrations of the Gibbs–Duhem equation of the exchanger phase, provided that sufficient experimental data are available.

The Gibbs–Duhem equation for one equivalent of exchanger containing $n_A = N_A/z_A$, $n_B = N_B/z_B$, and $n_X = N_X/z_X$ moles of the various ions and n_S moles of water is

$$n_A \, d \ln f_A N_A + n_B \, d \ln f_B N_B + n_X \, d \ln f_X N_X + n_S \, d \ln a_s = 0$$

Here a_s is written for the activity of the imbibed water, which we may take to be always equal to the activity of the water in the equilibrating solution. All quantities in the equation will then refer to an exchanger in equilibrium with a given solution. The quantity f_X has the nature of an individual ion activity coefficient. Its use is forced upon us by our choice of

means for expressing the composition of the exchanger; it is not, however, susceptible of determination from exchange data and drops out of the final expressions for the determination of f_A and f_B. In the following argument we need only its existence, and our result in no way depends upon a knowledge of its value.

The Gibbs–Duhem equation may then be written

$$N_A \, d \ln (f_A N_A)^{z_B} + N_B \, d \ln (f_B N_B)^{z_A} + \frac{z_A z_B}{z_X} N_X \, d \ln f_X N_X + z_A z_B n_S \, d \ln a_s = 0 \quad (3)$$

From the expression for the true equilibrium constant K we get

$$d \ln K_c + d \ln f_A^{z_B} = d \ln f_B^{z_A} \quad (4)$$

Using this relation to eliminate f_B from (3), separating the various activity coefficients from the concentration variables, and making a series of replacements such as

$$N_B \, d \ln K_c = d(N_B \ln K_c) - \ln K_c \, dN_B$$

$$z_B(1 + N_X) \, d \ln f_A = d\{z_B(1 + N_X) \ln f_A\} - z_B \ln f_X \, dN_X$$

we arrive at the expression

$$z_B dN_A + z_A dN_B + \frac{z_A z_B}{z_X} dN_X + z_B d\{(1 + N_X) \ln f_A\} + \frac{z_A z_B}{z_X} d(N_X \ln f_X) = (z_B \ln f_A + \frac{z_A z_B}{z_X} \ln f_X) \, dN_X + \ln K_c \, dN_B - z_A z_B n_S \, d \ln a_s \quad (5)$$

The quantity on the left of (5) is a perfect differential; so, then, must be the quantity on the right. Part of the necessary and sufficient condition for this is the relation we seek

$$\left(\frac{\partial \ln K_c}{\partial \ln a_s}\right)_{N_B, N_X} = -z_A z_B \left(\frac{\partial n_S}{\partial N_B}\right)_{a_s, N_X} = +z_A z_B \left(\frac{\partial n_S}{\partial N_A}\right)_{a_s, N_X} \quad (6)$$

since, also, at constant N_X we have $dN_B = -dN_A$.

Expression 6 in essence predicts the change in the selectivity coefficient with total molality of the equilibrating solution, which determines the solvent activity, from a knowledge of the change in water content with composition. As remarked above, this result in no way depends on a knowledge of f_X. It might be suggested at once that the simplest case of application of (6) will be to an exchanger with no imbibed anion, *i.e.*, for N_X constant and equal to zero. In this case the formula can be derived directly without the necessity of introducing the anion activity coefficient at any stage.

Zeolites form a class of cation exchangers which imbibe little or no anion and so offer an opportunity for the simplest application of (6). A study of the consequences of our expression 6 might be made in the following manner.

The selectivity coefficient K_c would be obtained from a series of chromatographic experiments in the usual fashion. At the same time, the free volume of the chromatographic column would be determined by a measurement of its anion content, say by displacing chloride with nitrate, or less ambiguously by displacing chloride with an identical solution containing tagged chloride ion. Such a procedure would *define* the region of cation uptake as that region free of anion. If this definition coincides closely with that given by a free volume determined simply by weight increase, the zeolite will thus be shown not to take up anion. The water content of the zeolite would then be determined by a measurement of the volume of the column accessible to H_2O^{18}. The difference between this volume and that accessible to anion measures n_S.

In order to obtain sufficiently large effects, it would be necessary to compare values of K_c for dilute solutions with those obtained at high concentrations of electrolyte, selecting solutions for which sufficient vapor pressure data are available to make possible the calculation of a_s.

Such a study would make possible an assessment of the extent to which sorbed ions are associated with a constant amount of water. This extreme of simplicity (which is scarcely to be expected) would be represented by

$$n_S = n_S{}^A N_A + n_S{}^B N_B + n_S{}^0 \quad (7)$$

that is, a linear formula for the variable part of the water content, implying fixed ionic hydration. This would result in the following requirement for a pair of singly charged ions

$$\left(\frac{\partial \ln K_c}{\partial \ln a_s}\right)_{N_A} = N_S{}^A - n_S{}^B \quad (8)$$

Thus one would expect a linear variation of $\ln K_c$ with $\ln a_s$, provided that the water content of the pure ionic forms changes inappreciably with water activity as is undoubtedly true for the rigid zeolitic crystals. This relation implies that one could predict the change in $\ln K_c$ with $\ln a_s$ from a pair of measurements of

water content for the monoion zeolites. It would be of interest to see how closely this simple relation approximates to the facts.

Some Thermodynamic Aspects of Ion-Exchange Equilibria in Mixed Solvents

by A. R. Gupta

Atomic Energy Establishment, Trombay Chemistry Division, Bombay 28, India *(Received June 27, 1964)*

When ion-exchange equilibrium is regarded as the equilibrium state of the reversible bimolecular reaction

$$Z_B AR + Z_A B^{+Z_B} \rightleftharpoons Z_B A^{+Z_A} + Z_A BR \qquad (1)$$

where Z_A and Z_B are the valencies of ions A and B, respectively, and R refers to the univalent functional group of the ion exchanger, the equilibrium constant K is given by

$$K = \left(\frac{a_{BR}}{a_{B^{+Z_B}}}\right)^{Z_A} \left(\frac{a_{A^{+Z_A}}}{a_{AR}}\right)^{Z_B} \qquad (2)$$

Ekedahl, Hogfeld, and Sillén[1] and, independently, Argersinger, Davidson, and Bonner[2] have considered the activities of the components AR and BR as a whole, rather than the single ion activities in exchanger phase; in other words, the exchanger phase has been regarded as a solid solution of the components AR and BR. In the earlier treatments, solvent absorbed by the exchanger was completely neglected, but in later analysis of this problem this has been taken into consideration.[3-5] Gaines and Thomas[4] have given a thermodynamically rigorous treatment of this equilibrium and have defined the standard state for the exchanger phase as that of the monoionic form of the exchanger in equilibrium with an infinitely dilute solution of the corresponding salt, *i.e.*, pure water. This choice of the standard state implies that it is independent of the outside solution. The equation for the thermodynamic equilibrium of the uni-univalent exchange system in water (subsequently we will be considering only uni-univalent exchanges—an extension to other cases is obvious), derived on this basis, using the Gibbs–Duhem equation and the law of mass action, is

$$\ln K = \int_0^1 \ln K_a dN_{BR} + \int_{a_w(N_{BR}=1)}^{a_w(N_{AR}=1)} n_w \, d \ln a_w + \int_{a_w=1(N_{BR}=1)}^{a_w(N_{BR}=1)} (V_B/\tau - n_w) \, d \ln a_w - \int_{a_w=1(N_{AR}=1)}^{a_w(N_{AR}=1)} (V_A/\tau - n_w) \, d \ln a_w \qquad (3)$$

where K_a is the selectivity coefficient (K_D) for reaction 1 corrected for the solution phase activity coefficients (K_D being defined by $K_D = (N_{BR} m_{A^+})/(N_{AR} m_{B^+})$, where N's are the mole fractions of the resin components and m's are molalities of the ions in the outside solution), V_B and V_A are the equivalent volumes of pure B and A forms of the exchanger, τ is the molar volume of the water vapor, and n_w is the number of moles of water associated with one equivalent of the exchanger. The first integral takes into consideration the dependence of selectivity coefficients on resin composition. The other three integrals refer to the variations in the water sorption by the ion exchanger. The second integral implies the integration of the equivalent moisture, n_w, of the ion exchanger over the two extremes of resin composition, at a constant ionic strength, m. The second and third integral rationalize the standard state of the ion exchanger from that of the monoionic form of the exchanger in equilibrium with an m molar solution of the corresponding salt to that of the monoionic form of the exchanger in equilibrium with pure water (an infinitely dilute solution of the corresponding salt). The resin phase activity coefficients are implicitly taken care of in this equation (for a fuller discussion of this subject, see ref. 6).

When ion-exchange equilibria in mixed solvents are to be considered on this basis, many difficulties arise in obtaining a thermodynamically rigorous solution of the problem. The addition of another solvent introduces another term in the Gibbs–Duhem equation. The integration to be performed on isothermal surfaces (see ref. 4) to solve the resulting equations for the exchanger phase activity coefficients becomes quite complicated. Another difficulty lies in the choice of the standard states. For these reasons, a mathematically rigorous solution will not be attempted here, but the problem will be considered on general physicochemical principles. Equation 3, derived for the aqueous systems by Gaines and Thomas, will be taken as the model, and then the various terms will be corrected, using the appropriate activity coefficients. The final results thus will be derived on a semiempirical basis, but will be thermodynamically correct as will be pointed out at appropriate places.

(1) E. Ekedahl, E. Hogfeld, and L. G. Sillén, *Acta Chem. Scand.*, **4**, 556, 828 (1950).

(2) W. J. Argersinger, Jr., A. W. Davidson, and O. D. Bonner, *Trans. Kansas Acad. Sci.*, 53, 404 (1950).

(3) E. Hogfeld, *Arkiv Kemi*, **5**, 147 (1952).

(4) G. L. Gaines and H. C. Thomas, *J. Chem. Phys.*, **21**, 714 (1953).

(5) A. W. Davidson and W. J. Argersinger, Jr., *Ann. N. Y. Acad. Sci.*, **57**, 105 (1953).

(6) L. W. Holm, *Arkiv Kemi*, **10**, 151 (1956).

One can have the standard state of infinite dilution of the electrolyte in the mixed solvent, or one can select that of infinite dilution in either of the two solvents. Similarly, one can select any of the three possibilities for the ion-exchanger phase. If one selects the standard state of infinite dilution in the mixed solvent and makes the assumption that solvent composition inside the exchanger and the outside solution is the same, eq. 3 holds true identically for such a system, n_s replacing n_w. The work of Gregor,[7] Strobel,[8] and Bonner[9] on the swelling characteristics of PSS-type ion exchangers has shown that the ion exchangers do show a preference for one of the solvents. Furthermore, the equilibrium constants calculated on this basis cannot be correlated with those in aqueous systems because of the differences in the standard states in the two systems. As the interest in this field centers around mixed solvents involving water and in the comparison of the exchange data in the mixed solvents with that obtained in aqueous systems, we will here adopt the standard state for the electrolyte as that of infinite dilution in water. The standard state for the exchanger phase then becomes that of the monoionic form of the exchanger in equilibrium with water. The activities of water inside the exchanger and in the outside solution are taken to be equal. The standard states thus become identical with those used in aqueous systems. Thus this choice of the standard states will afford a direct comparison of the exchange data in aqueous systems and in mixed solvents involving water. This choice further implies that the effect of the added solvent is completely determined by its effect on the activities of exchanger phase, electrolytes, and water, and, as such, the added solvent can be considered as a diluent to the water present in the system.

The selectivity coefficient for a uni-univalent exchange is given by

$$K'_D = \frac{N_{BR} m_{A^+}}{N_{AR} m_{B^+}} \tag{4}$$

The prime refers to the quantities in the mixed solvents. This has to be corrected for solution phase activity coefficients to give K'_a, *i.e.*

$$K'_a = K'_D \times \frac{\gamma'^2_{\pm AX}}{\gamma'^2_{\pm BX}} \tag{5}$$

Mean molal activity coefficients in mixed solvents can be obtained with reference to the state of infinite dilution in the mixed solvent. This then is corrected for the activity coefficient of the salt at infinite dilution in mixed solvent referred to the standard state in aqueous solutions. Åkerlof[10] has determined the latter quantity for some alkali metal chlorides in methanol–water mixtures and has called it $\gamma_{\infty MCl}$. Strobel[11] has used the symbol γ^0_{MCl} in the same manner which will be adopted for use here. Thus $\gamma'^2_{\pm AX}$ can be written as the product of $\gamma^{0\,2}_{\pm AX}$ and $\gamma''^2_{\pm AX}$ where γ'' refers to the activity coefficients with the standard state of infinite dilution in mixed solvent. Referring to eq. 3, the first integral term changes to the following term for ion exchange in mixed solvents

$$\int_0^1 \ln K'_a \, dN_{BR} \tag{6}$$

The second, third, and fourth integrals in eq. 3, as discussed above, take care of the variations in the equivalent moisture content over the whole range of resin composition, finally referring them to the standard state for the ion exchanger involving pure water. The meaning of n_w terms in mixed solvents needs some clarification. As we have seen, with the standard state of infinite dilution in mixed solvents n_w corresponds to the total number of moles of solvent per equivalent of resin. When the standard state is of infinite dilution in one of the solvents, the representation of the system with reference to this standard state will not include any terms corresponding to the other solvent. Thus, n_w will represent the actual number of moles of water per equivalent of exchanger under the specified conditions. Now we can consider the processes involved in the ion exchange in mixed solvents corresponding to the second, third, and fourth integrals of eq. 3 in the following three steps. First, we integrate the variations in equivalent moisture over the water activities covering the whole range of ion-exchanger compositions at a particular ionic strength and solvent composition. Second, the correction for the effect of the ionic strength on equivalent moisture of the monoionic form of exchangers is applied, referring them to the state of infinite dilution in mixed solvent. Finally, we correct the equivalent moisture of pure exchangers at infinite dilution in the mixed solvent to that of infinite dilution in water.

The first step will involve the integral

$$\int_{a_w(N_{H_2O})(N_{BR}=1)}^{a_w(N_{H_2O})(N_{AR}=1)} n_w \, d \ln a_w \tag{7}$$

where $a_w(N_{H_2O})$ refers to the water activity in the solvent mixture having N_{H_2O} mole fraction of water.

(7) H. P. Gregor, M. H. Gottlieb, and D. Nobel, *J. Phys. Chem.*, **59**, 10 (1955).

(8) R. W. Gable and H. A. Strobel, *ibid.*, **60**, 513 (1956).

(9) O. D. Bonner and J. Moorefield, *ibid.*, **58**, 555 (1954).

(10) G. Åkerlof, *J. Am. Chem. Soc.*, **52**, 2353 (1930).

(11) R. G. Fessler and H. A. Strobel, *J. Phys. Chem.*, **67**, 2562 (1963)

The limit $a_w(N_{H_2O})(N_{BR} = 1)$ then implies water activity of an m molar solution of electrolyte BX in the mixed solvent having N_{H_2O} mole fraction of water (m is the ionic strength, which is maintained constant during the experiments of this type). Similarly, the upper limit of eq. 7 can also be defined. The second step will involve the integrals

$$+ \int_{a^0_w(N_{H_2O})(N_{BR}=1)}^{a_w(N_{H_2O})(N_{BR}=1)} (V_{B/\tau} - n_w)\, d \ln a_w - \int_{a^0_w(N_{H_2O})(N_{AR}=1)}^{a_w(N_{H_2O})(N_{AR}=1)} (V_{A/\tau} - n_w)\, d \ln a_w \quad (8)$$

The first term in expression 8 takes into consideration the variations in equivalent moisture when the outside solution changes from m molar solution of BX in mixed solvent to an infinitely dilute solution of BX in the same solvent. The lower limit $a^0_w(N_{H_2O})(N_{BR} = 1)$ then means water activity in an infinitely dilute solution of BX in a solvent having N_{H_2O} mole fraction of water. The upper limits in expression 8 have already been explained while discussing expression 7. The second term in an analogous way refers to the exchanger AR. The third step involves the integrals

$$+ \int_{a_w=1(N_{BR}=1)}^{a^0_w(N_{H_2O})(N_{BR}=1)} (V_{B/\tau} - n_w)\, d \ln a_w - \int_{(a_w=1)(N_{AR}=1)}^{a^0_w(N_{H_2O})(N_{AR}=1)} (V_{A/\tau} - n_w)\, d \ln a_w \quad (9)$$

Here the limits of the first integral are from an infinitely dilute solution of BX in the mixed solvent (having N_{H_2O} water mole fraction) to that of an infinitely dilute solution of BX in water. The second integral refers to the exchanger AR. The V/τ terms occurring in expressions 8 and 9 are comparatively small compared to n_w terms for a moderately cross-linked exchanger.[4,5] Combining expressions 6–9 and neglecting V/τ terms, $\ln K$ for a uni-univalent exchange in a mixed solvent (water = N_{H_2O}) can be written as

$$\ln K = \int_0^1 \ln K'_a\, dN_{BR} + \int_{a_w(N_{H_2O})(N_{AR}=1)}^{a_w(N_{H_2O})(N_{BR}=1)} n_w\, d \ln a_w - \int_{a^0_w(N_{H_2O})(N_{BR}=1)}^{a_w(N_{H_2O})(N_{BR}=1)} n_w\, d \ln a_w + \int_{a^0_w(N_{H_2O})(N_{AR}=1)}^{a_w(N_{H_2O})(N_{AR}=1)} n_w\, d \ln a_w - \int_{a_w=1(N_{BR}=1)}^{a^0_w(N_{H_2O})(N_{BR}=1)} n_w\, d \ln a_w + \int_{a_w=1(N_{AR}=1)}^{a^0_w(N_{H_2O})(N_{AR}=1)} n_w\, d \ln a_w \quad (10)$$

As this expression for $\ln K$ refers to the standard states of electrolytes, exchanger phase, and water to those at infinite dilution in water, it should be independent of the composition of the outside solution. For an exchange system, on a particular ion exchanger, K calculated from expression 10 for the case of mixed solvents should be the same as that obtained from expression 3 for the corresponding aqueous case, irrespective of the ionic strength and solvent composition used.

Comparative Importance of Various Terms in Expression 10. The first integral on the right-hand side of eq. 10 can be written as

$$\int_0^1 \ln K'_a\, d N_{BR} = \int_0^1 \ln\left(K'_D \times \frac{\gamma^0{}^2_{\pm AX}}{\gamma^0{}^2_{\pm BX}} \times \frac{\gamma''{}^2_{\pm AX}}{\gamma''{}^2_{\pm BX}}\right) dN_{BR} = \int_0^1 \ln K'_D\, dN_{BR} + 2 \ln \frac{\gamma^0_{\pm AX}}{\gamma^0_{\pm BX}} + 2 \ln \frac{\gamma''_{\pm AX}}{\gamma''_{\pm BX}} \quad (11)$$

The last two terms for some uni-univalent electrolytes in alcohol–water mixtures have been determined by a few workers.[10,12] The ratios $\gamma''_{\pm AX}/\gamma''_{\pm BX}$ are close to 1, whereas $\log \gamma^0_{\pm AX}/\gamma^0_{\pm BX}$ terms are quite significant. Thus as a first approximation, as has been done by Strobel,[11] the last term in eq. 11 can be dropped. The second integral in the right-hand side of eq. 10 is expected to be negligible, as the water activities generally will not vary very much, when an m molar solution of electrolyte BX gradually changes into an m molar solution of AX, keeping the ionic strength and solvent composition constant. This will be particularly so if the ionic strength is low ($m \leq 0.1$). In a recent communication[13] from these laboratories, the contribution of similar terms in aqueous systems (eq. 3; second integral on the right-hand side) at 0.1 m ionic strength has been determined to be negligible. The third and the fourth integrals again are not expected to contribute much. The influence of 0.1 m electrolyte on water activities in mixed solvents will be very small compared to the influence of the organic solvent on water activity. Thus, the major contribution to $\ln K$ will come from the last two integrals. Summing up, as a first approximation ($m \leq 0.1$), the expression for $\ln K$ reduces to

$$\ln K \simeq \int_0^1 \ln K'_D\, dN_{BR} + 2 \ln \frac{\gamma^0_{\pm AX}}{\gamma^0_{\pm BX}} - \int_{a_w=1(N_{BR}=1)}^{a^0_w(N_{H_2O})(N_{BR}=1)} n_w\, d \ln a_w + \int_{a_w=1(N_{AR}=1)}^{a^0_w(N_{H_2O})(N_{AR}=1)} n_w\, d \ln a_w \quad (12)$$

(12) I. T. Oiwa, *Sci. Rept. Tohoku Univ., First Ser.*, **41**, 129 (1957).

(13) M. R. Ghate, A. R. Gupta, and J. Shankar, private communication.

Discussion of the Available Experimental Data. The experimental data on ion-exchange equilibria in mixed solvents are not very extensive and no single study covers all of the aspects discussed here. In particular, no one has determined selectivity coefficients as a function of resin composition in mixed solvents. However, the following general features for ion-exchange equilibria in mixed solvents have been recognized.

(i) A general increase in K_D on addition of the organic solvent has been observed.[9,11,14-18] A maximum has been obtained by Sakaki[15] as well as Strobel[11] in alkali metal ion–hydrogen ion exchange on PSS-type exchangers in alcohol–water systems, when the mole fraction of alcohol is increased to 0.7 or greater.

(ii) A linear dependence of log K_D on $1/D$ (where D is the dielectric constant of the medium) in the ascending part of the log K_D *vs.* $1/D$ curve has been obtained.

The explanations of these phenomena range from the differences in the hypothetical desolvation energy involved in ion exchange[15] to the changes in solution and exchanger phase activity coefficients.[11,12] Recently, Athavale and co-workers[17] have studied alkali metal ion–NH_4^+ or H^+ exchange systems in mixed solvents on PSS-type exchangers. They have compared the equilibrium constants determined at one resin composition and seemingly this resin composition is not even the same for all the systems being compared. As such, conclusions drawn by them on the basis of this comparison are highly questionable. Sakaki's and Strobel's data on uni-univalent exchange systems in alcohol–water media have been obtained at various alcohol concentrations but unfortunately only at one resin composition. As the exchanger composition has been maintained at $0.5N_{BR}$, there is some justification in equating the equilibrium constant to the selectivity coefficient at this composition.[19] These studies also lack the solvent uptake data for the different forms of exchangers. As such, no quantitative application of eq. 10 or 12 is possible. Therefore, an explanation of the above-mentioned general features, on the basis of these equations, perforce will have to be qualitative; rather, it will be shown that these equations can lead to these observed features. The main points to be explained are a linear dependence of log K_D on $1/D$ at low alcohol concentrations and the maximum in the log K_D *vs.* $1/D$ curve.

Referring to the approximate eq. 12 and recalling that major contributions come from the γ^0 terms (the last two integrals making opposite contributions of the same order of magnitude), let us consider the situation when the organic solvent is present in low concentrations. The last two integrals of eq. 12, taken together, will make approximately a constant contribution to log K. Then the actual variations in log K'_D will be due to log γ^0 terms, which have a linear dependence on $1/D$. As alcohol concentration is increased, the last two integrals will make varying and lower contributions, and log K'_D will exhibit a maximum and then decrease. Strobel has attributed the variations in K (obtained when K_D is corrected for the γ^0 terms) to the changes in resin phase activity coefficients. (Other authors[6] have used the concept of increased ion-pair formation in resin phase to explain the increase in K_D in mixed solvents, but the resin phase activity coefficients incorporate all such effects.) These variations in K, most probably, are partly due to the approximation used in equating the equilibrium constant to the value of K_D at $0.5N_{BR}$ and partly to the neglect of solvent absorption terms. In eq. 10 or 12 above, the resin phase activity coefficients as well as the sorption terms are implicitly included. Experiments on some simple exchange systems in mixed solvents, where the solvent sorption data will also be determined, are in progress so that the above equations can be verified.

Acknowledgment. The author expresses his sincere thanks to Dr. J. Shankar for his encouragement and keen interest during the course of this investigation.

(14) G. M. Panchenkov, V. T. Gorshkov, and M. V. Kuklanova, *Zh. Fiz. Khim.*, **32**, 361, 616 (1958).

(15) T. Sakaki, *Bull. Chem. Soc. Japan*, **28**, 217, 219 (1955).

(16) E. A. Materova, Z. L. Vert, and G. P. Grinberg, *J. Gen. Chem. USSR*, **24**, 959 (1954).

(17) V. T. Athavale, C. V. Krishnan, and C. Venkateswarlu, *Inorg. Chem.*, **3**, 533 (1964).

(18) M. R. Ghate, Ph.D. Thesis, Bombay University, Oct. 1963.

(19) E. Hogfield, *Acta Chem. Scand.*, **9**, 151 (1955).

The Vapor Pressure of Copper Phthalocyanine

by James Curry and Robert W. Shaw, Jr.

Department of Chemistry, Williams College, Williamstown, Massachusetts *(Received July 24, 1964)*

There are many references in the literature to the sublimation of copper phthalocyanine in the temperature interval 400–500°. Lawton[1] investigated the remarkable thermal stability of this substance. For example, he found that the infrared spectra of copper

(1) E. A. Lawton, *J. Phys. Chem.*, **62**, 384 (1958).

phthalocyanine did not change if the compound was heated under vacuum for 1 hr. at 800°.

We have been interested in growing single crystals of copper phthalocyanine to use in studying the semiconducting properties of this substance. In order to select suitable conditions for the growth of crystals, we have found it expedient to measure the vapor pressure of solid copper phthalocyanine as a function of temperature. From such measurements, one may also calculate thermodynamic data useful in characterizing the intermolecular forces holding the molecules together in the crystal.

Experimental

The Knudsen rate-of-effusion method was used for the measurements. The cell consisted of a 1.5 × 1.5 cm. platinum crucible which was closed with a piece of aluminum foil containing a small orifice. The foil was firmly bound to the crucible by a chromel wire. The diameter of the hole was measured by means of a microscope with a calibrated eyepiece, and the thickness of the foil was measured with a micrometer. The data for the cells are given in Table I.

Table I: Dimensions of Orifice

Cell	Diameter, cm.	Length, cm.
1	0.290	0.0080
2[a]	0.242	0.0030
3	0.0792	0.0020
4	0.0440	0.0040
5	0.0400	0.0040

[a] This cell had a square hole. The diameter given is that of a round hole of equivalent area.

Copper phthalocyanine, procured from the Du Pont Co., was sublimed in a stream of nitrogen and single crystals of the β form were obtained. These were thoroughly ground in a Wig-L-Bug. The powder was mixed with some crushed Pyrex glass before it was put into the crucible. This was done to avoid caking, although there was no evidence that this precaution was necessary.

The cell was placed at the closed end of a quartz tube of 18-mm. i.d., the other end of which formed one section of a 35/25 ball-and-socket joint. This tube in turn could be connected to a movable vacuum system which reduced the pressure to 10^{-6} mm. During a run, the tube containing the cell was placed in a Temco Model 1515 electric furnace through a specially constructed door. Temperatures were measured with a calibrated chromel–alumel thermocouple. Calibration runs were made to determine the temperature at the crucible relative to the temperature of the air in the furnace.

In measuring vapor pressures by the Knudsen rate-of-effusion method, the start and the end of a run are always associated with some uncertainty. This situation was compensated for by making two runs—a short one of 1 hr. and a longer one of 3 to 6 hr.—at the same temperature. It was assumed that the conditions at the beginning and end of both runs were the same, so in order to get data for calculating the vapor pressure, the weight loss and time of the first run were subtracted from the second.

Results

Vapor pressures were measured in the range 384 to 449°. The Knudsen equation for ideal conditions is

$$P = \frac{w}{at}\left(\frac{2\pi RT}{M}\right)^{1/2} \tag{1}$$

where P is the vapor pressure, w is the loss in weight in grams, a is the area of the orifice in cm.^{2}, t is the effusing time in seconds, M is the molecular weight of the effusing species, R is the gas constant, and T is the absolute temperature. For various reasons this equation is usually not directly applicable. Clausing[2] has shown that the orifice area must be multiplied by a correction factor in order to take into account the finite length of the hole. Thus the Knudsen equation becomes

$$P_S = \frac{w}{act}\left(\frac{2\pi RT}{M}\right)^{1/2} \tag{2}$$

where P_S is the steady-state pressure in the cell and c is the Clausing correction factor. Often the pressure in the effusion cell, as calculated from eq. 2, is less than the vapor pressure because the condensation coefficient of the substance is less than unity and because of the geometry of the cell. These matters have been discussed by Whitman,[3a] Motzfeldt,[3b] and Speiser and Spretnak.[3c] Stern and Gregory[3d] as well as Hildenbrand and Hall[3e] have evaluated their data by using the Motzfeldt equation and we have done likewise. This involves using the equation

$$P_S = P - \left(\frac{1}{\alpha} + \frac{1}{W_A} - 2\right)\frac{ca}{A}P_S \tag{3}$$

(2) P. Clausing, *Ann. Phys.*, 12, 961 (1932).

(3) (a) C. I. Whitman, *J. Chem. Phys.*, **20**, 161 (1952); (b) K. Motzfeldt, *J. Phys. Chem.*, **59**, 139 (1955); (c) R. Speiser and J. W. Spretnak, Vacuum Metallurgy Electrothermics and Metallurgy Division of the Electrochemical Society, 1955, pp. 155–160, 186–187; (d) J. H. Stern and N. W. Gregory, *J. Phys. Chem.*, **61**, 1226 (1957); (e) D. L. Hildenbrand and W. F. Hall, *ibid.*, **68**, 989 (1964).

where α is the condensation coefficient, W_A is the Clausing factor for the interior of the cell, and A is the area of the surface of the effusing material. For the cell used in this work $W_A = 0.5$, so eq. 3 reduces to

$$P_S = P - \left(\frac{1}{A\alpha}\right) caP_S \qquad (4)$$

The steady-state pressures and the vapor pressures are given in Table II. The steady-state pressures were calculated using eq. 2, assuming that the copper phthalocyanine was not associated in the vapor phase. The magnitude of $1/A\alpha$ was found by plotting P_S against caP_S for the various cells at one temperature. The points fell on a reasonably good straight line, and thus it seems that α does not change appreciably in the temperature range studied. From the slope of the line the value of $1/A\alpha$ was found to be 54 cm.$^{-2}$. Using this and eq. 4, the values of P were calculated. A plot of log P against $1/T$ gave a good straight line. A least-squares treatment of the data gives the equation log $P_{mm} = 17.575 - 13900/T$ with the standard deviation of the slope being 260. Thus for copper phthalocyanine in the range 384–449°, the heat of sublimation is 63.6 ± 1.2 kcal./mole and the entropy of sublimation (to P = 1 atm.) is 67.2 cal./deg./mole.

Table II: Summary of Pressure Data[a]

T, °K.	Cell	$P_S \times 10^3$, mm.	$P \times 10^3$, mm.
687	2	0.602	2.09
687	2	0.557	1.95
685	2	0.521	1.82
681	2	0.354	1.23
717	5	14.38	15.50
722	5	16.75	17.80
711	5	9.70	10.46
702	5	4.82	5.12
661	1	0.0860	0.380
675	1	0.206	0.910
661	1	0.0940	0.416
657	1	0.0664	0.295
706	4	7.81	8.30
698	4	4.09	4.36
697	4	3.82	4.07
690	3	1.708	2.14
700	3	3.41	4.27
693	3	2.35	2.95

[a] The runs are listed in the order they were made.

From $1/A\alpha$ it is possible to calculate the condensation coefficient if the area of the solid phase of the effusing material is known, but it is difficult to estimate this when a powder is used. In this work the nominal area of the surface was 1.77 cm.^{2}. If this area is used, α comes out to be about 0.01. Since the true area is undoubtedly larger than the nominal area, the true value of α is probably less than 0.01. When the crystal structure of copper phthalocyanine is considered, it is not surprising that the condensation coefficient is so low. The molecule is large and flat, and Robertson[4] has shown that the planes in adjoining rows of molecules are almost at right angles to each other. Thus one would expect that in only a small fraction of the collisions the molecule makes with the crystal is the molecular orientation favorable for condensation.

(4) J. M. Robertson, *J. Chem. Soc.*, 1195 (1936).

Dynamic Mechanical Properties of Dilute Solutions of Poly-α-methylstyrene

by J. E. Frederick and John D. Ferry

Department of Chemistry, University of Wisconsin, Madison, Wisconsin *(Received July 25, 1964)*

An extensive study of dynamic mechanical properties of dilute polystyrene solutions has been recently reported.[1] In this work, viscous solvents were used so the viscoelastic dispersion could be observed in the low audiofrequency range, and measurements at different molecular weights and concentrations were interpreted by the theories of Zimm,[2] Rouse,[3] and Tschoegl.[4] We now report some additional measurements on poly-α-methylstyrene, undertaken to determine whether the additional steric hindrance of the methyl group would influence the behavior significantly.

Experimental

Two samples of poly-α-methylstyrene were generously given us by Dr. P. Rempp of the Centre de Recherches sur les Macromolécules, Strasbourg. They had been prepared by anionic polymerization and presumably had sharp molecular weight distributions; their weight-average molecular weights, determined at Strasbourg by light scattering, were 349,000 and 630,000. They were dried *in vacuo* at 60° for several

(1) J. E. Frederick, N. W. Tschoegl, and J. D. Ferry, *J. Phys. Chem.*, **68**, 1974 (1964).

(2) B. H. Zimm, *J. Chem. Phys.*, **24**, 269 (1956).

(3) P. E. Rouse, Jr., *ibid.*, **21**, 1272 (1953).

(4) N. W. Tschoegl, *ibid.*, **40**, 473 (1964).

days. (Attempts were made to study a third sample with molecular weight 45,000, but this was too low for satisfactory measurements in dilute solution.)

Solutions for viscoelastic measurements, in the concentration range from 1 to 3%, were prepared in Aroclor 1248 (a mixture of partially chlorinated diphenyls) as previously described for polystyrenes.[1] Similar solutions at lower concentrations were used for capillary measurements of steady-flow viscosity, from which the intrinsic viscosities in Aroclor 1248 at 25° were estimated to be 0.8 and 1.0 dl./g., respectively. The solvent viscosity was 2.67 poises at 25°.

Measurements were made as before[1] with the apparatus of Birnboim and Ferry,[5] between 0.06 and 400 c.p.s. Data at a single temperature of 25° were sufficient to encompass the important dispersion region, though for some of the solutions measurements were also made at 10° and reduced in the usual manner[1] to 25° to extend the effective frequency range.

Results and Discussion

The results for $M = 630{,}000$ at three concentrations are shown in Figure 1, calculated as the reduced contributions of the polymer to the components of the complex viscosity,[6] $\eta'_R = (\eta' - v_1\eta_s)/(\eta - v_1\eta_s)$ and $\eta''_R = \eta''/(\eta - v_1\eta_s)$. Here η' and η'' are the real and imaginary components of the complex viscosity of the solution, η_s is the solvent viscosity, and v_1 is the volume fraction of solvent. Alternative representations as the storage and loss components of the complex shear modulus are plotted in an unpublished report[7] together with tables of numerical data. The abscissa in Figure 1 is the logarithm of the circular frequency ω multiplied by a factor such that, when the data are matched to a pair of theoretical curves, the position of the origin of the latter (shown by a cross on the abscissa axis in each case) provides a determination of the molecular weight.[6] Specifically, the location of the cross corresponds to log S/M, where S is a numerical factor given by the theory.

The shapes of the frequency dependence of η'_R and η''_R, in the theory of Tschoegl, are specified by two parameters: h, a measure of the strength of the hydrodynamic interaction between different segments of the same polymer molecule, and ϵ, a measure of the departure from Gaussian chain statistics. In the present case, ϵ is taken as 0 because the intrinsic viscosities within their limited precision indicate that d log $[\eta]$/d log $M \leq 0.5$. The value of h is chosen empirically to give the best fit to the shape of the frequency dependence, between the limits of 0 and ∞ which correspond to the special cases of the original Rouse and Zimm theories, respectively. For the theoretical curves which match the data in Figure 1, $h = \infty$ at 1 and 2% concentration, and $h = 15$ at 3%; there is a shift from Zimm-like toward Rouse-like behavior with increasing concentration, as observed repeatedly for polystyrene.[1]

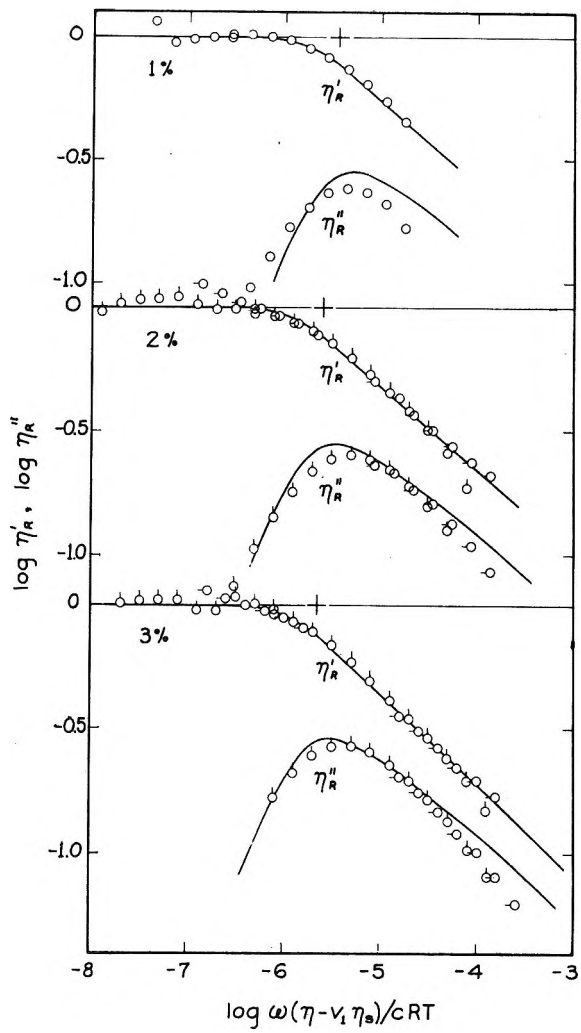

Figure 1. Logarithmic plots of η'_R and η''_R for sample with $M = 630{,}000$ at three concentrations as indicated. Pip up (or no pip), 25°; pip left, 10°. In the abscissa, c is polymer concentration in g./ml. Curves are drawn for theories of Zimm (1 and 2%) or Tschoegl (3%) with values of h given in Table I.

Values of h together with other derived data are given in Table I for the solutions of Figure 1 and also two solutions of the sample of lower molecular weight, the detailed data for which are available elsewhere.[7] The behavior is Zimm-like for all except the one with the highest M and c.

(5) M. H. Birnboim and J. D. Ferry, *J. Appl. Phys.*, **32**, 2305 (1961).
(6) N. W. Tschoegl and J. D. Ferry, *J. Phys. Chem.*, **68**, 867 (1964).
(7) J. E. Frederick, Ph.D. Thesis, University of Wisconsin, 1964.

For polystyrene[1] and polyisobutylene,[6] h has been found to decrease with increasing M and/or c, and it is of interest to compare the behavior of poly-α-methylstyrene with that of these other polymers under corresponding conditions. For this purpose, the mean square end-to-end distance $\langle r^2 \rangle$ is a more rational measure of molecular size than M, and so this has been calculated for all the solutions concerned from the relation $\langle r^2 \rangle = \alpha^2(\langle r_0^2 \rangle / M)M$. The values of $\langle r_0^2 \rangle / M$ were taken from the review of Stockmayer and Kurata[8]; the expansion factor α was taken as unity for poly-α-methylstyrene in A-1248; and for the other solutions α was calculated from intrinsic viscosity data,[1,6] using eq. 30, 34, and 38 of ref. 4. The comparison is shown in Figure 2 where values of h are located on a logarithmic map of c *vs.* $\langle r^2 \rangle$. The polystyrene and polyisobutylene data are consistent in representing a monotonic shift of h from ∞ toward 0 (Zimm-like toward Rouse-like behavior) with increasing c and $\langle r^2 \rangle$. The poly-α-methylstyrene has somewhat higher values of h than does the polystyrene under comparable conditions. Thus, it is necessary to go to slightly higher concentrations or coil sizes to achieve a given change in effective hydrodynamic interaction corresponding to a shift toward Rouse-like behavior. However, there is no striking manifestation of internal stiffness or steric hindrance of the poly-α-methylstyrene.

Table I: Parameters and Derived Calculations[a]

$M \times 10^{-3}$	Concn., wt. %	$c \times 10^2$, g./cc.	η_s, poises	h	S	log M_{ve}	log M_{ve}/M	log τ_1
349	2	2.88	20.4	∞	2.368	5.73	0.19	−2.24
	3	4.32	42.6	∞	2.368	5.82	0.28	−1.98
630	1	1.45	8.9	∞	2.368	5.82	0.02	−2.30
	2	2.88	25.0	∞	2.368	5.97	0.17	−1.90
	3	4.32	57.6	15	2.236	6.00	0.20	−1.62

[a] All at 25°.

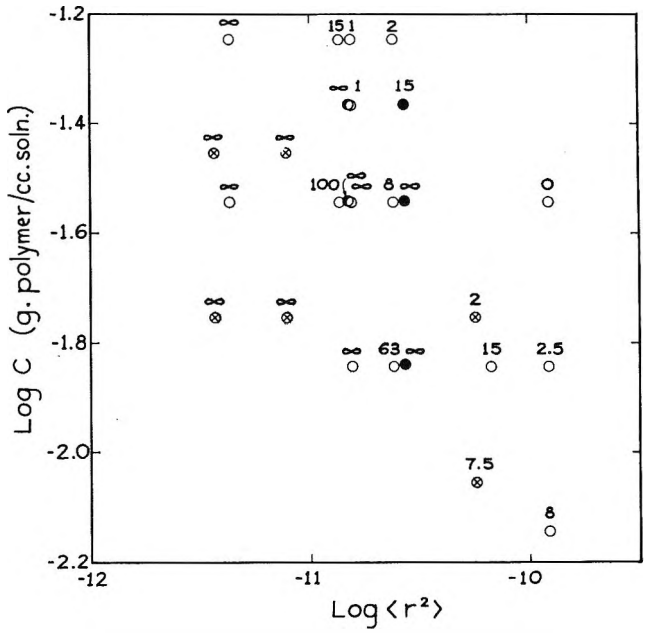

Figure 2. Map of values of parameter h as a function of concentration and mean square end-to-end distance for three polymers. Open circles, polystyrene[1] in A-1248; black circles, poly-α-methylstyrene in A-1248; crossed circles, polyisobutylene in Primol D.[3]

The logarithms of the molecular weights, M_{ve}, obtained from the cross positions in Figure 1 and similar plots for the other solutions are also given in Table I. As usual, the apparent molecular weight from the viscoelastic measurements is somewhat too large, to a degree which increases with increasing concentration. Values of log τ_1, the terminal relaxation time, calculated from the relation $\tau_1 = (\eta - v_1\eta_s)M_{ve}/cRTS$, are also given in Table I.

Recent investigations by Lamb[9] and Philippoff[10] have shown that at very high frequencies η' approaches a limiting value η_∞ which is somewhat higher than η_s, suggesting that the frequency-dependent contribution of the polymer to the viscosity should appear as $\eta - \eta_\infty$ rather than $\eta - v_1\eta_s$. For most of the solutions described here, the difference is probably relatively small. This question will be considered in a later communication.

Acknowledgment. This work was supported in part by the U. S. Public Health Service under Grant GM-10135.

(8) W. H. Stockmayer and M. Kurata, *Advan. Polymer Sci.*, **3**, 196, (1963).

(9) J. Lamb and A. J. Matheson, *Proc. Roy. Soc.* (London), **A281**, 207 (1964), and personal communication.

(10) W. Philippoff, *Trans. Soc. Rheol.*, in press.

Theoretical Refinement of the Pendant Drop Method for Measuring Surface Tensions

by David Winkel

Department of Chemistry, The University of Wyoming, Laramie, Wyoming *(Received July 27, 1964)*

At present there are relatively few static methods suitable for measuring surface tensions under orthobaric conditions. Two examples are the sessile drop method[1,2]

and the pendant drop method.[1,3-5] Unfortunately, each requires difficult measurements of high precision. For the pendant drop these are the maximum diameter of the drop, d_e, and the ratio d_s/d_e. This can best be seen by referring to Figure 1, a typical drop shape. For example, assume that d_e is overestimated, then d_s will be measured at a location too high and consequently will be underestimated. The fundamental difficulty is that d_s is dependent on d_e in such a fashion that errors cascade. A smaller source of error arises because d_s is measured on a sloping portion of the drop.

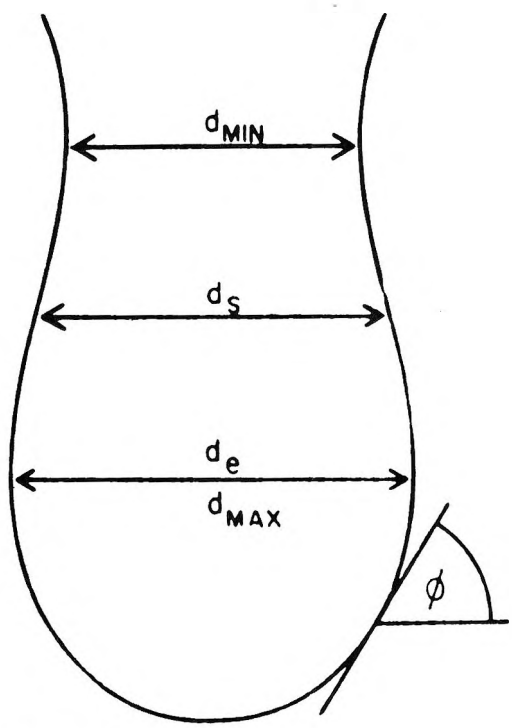

Figure 1.

There is no reason why other ratios cannot be used in the pendant drop method. The present paper describes a method using the ratio of the maximum to minimum diameter. This is the optimum method for two reasons: (1) the two diameters involved are independent, as are errors in each measurement; and (2) both diameters are measured where they are nearly independent of height.

The method can best be understood by referring to the fundamental equation for drop shape.[6]

$$\frac{1}{\left(\frac{R}{b}\right)} + \frac{\sin\phi}{\left(\frac{x}{b}\right)} = 2 + \beta\left(\frac{y}{b}\right) \qquad (1)$$

where b is the radius of curvature at the vertex, $\beta = -\rho g b^2/\gamma$, ρ is density, g is gravity, γ is the surface tension, R/b is the reduced principal radius of curvature, x/b and y/b are reduced x- and y-coordinates, and ϕ is shown in Figure 1. It is readily seen that the parameter controlling the shape of the drop is β while b controls the size of the drop. Since $\gamma = -\rho g b^2/\beta$, both b and β must be measured in order to obtain the surface tension.

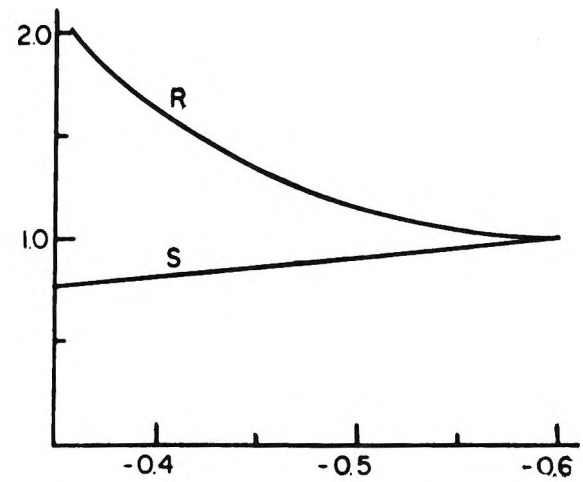

Figure 2.

Any characteristic ratio of drop dimensions will be a function of β only, and conversely. Fordham[4] has calculated d_s/d_e as a function of β, which as noted above is not the optimum ratio. The author has calculated d_{max}/d_{min} as a function of β. Their relative merits can be seen by referring to Figure 2, which shows both d_s/d_e and d_{max}/d_{min} as functions of β. As is readily seen, a given error in d_{max}/d_{min} causes a much smaller error in β than the same error in d_s/d_e.

The method for determining b is the same as that of Andreas *et al.*[3] Since Xe/b is known from the calculations and

$$2Xe = d_{max} \qquad (2)$$

$$b = \frac{d_{max}}{2\left(\frac{Xe}{b}\right)} \qquad (3)$$

(1) F. Bashforth and J. C. Adams, "An Attempt to Test the Theories of Capillary Action," University Press, Cambridge, England, 1883.

(2) A. M. Worthington, *Phil. Mag.*, 20, 51 (1885).

(3) J. M. Andreas, E. A. Hauser, and W. B. Tucker, *J. Phys. Chem.*, **42**, 1001 (1938).

(4) S. Fordham, *Proc. Roy. Soc.* (London), **A194**, 1 (1948).

(5) D. O. Niederhauser and F. E. Bartell, "Report of Progress—Fundamental Research on the Occurrence and Recovery of Petroleum," 1948-1949, p. 114.

(6) A. W. Adamson, "Physical Chemistry of Surfaces," Interscience Publishers, Inc., New York, N. Y., 1960.

therefore

$$\gamma = \frac{\rho g {d_{max}}^2}{H} \quad (4)$$

where

$$H = -4\beta\left(\frac{Xe}{b}\right)^2 \quad (5)$$

Since β does not appear explicitly, only tables of H *vs.* $d_{max}/d_{min} = R$ have been calculated.

The method of solution was in principle somewhat similar to a graphical method due to Lord Kelvin[7] except for several important modifications. Assume X_i/b and Y_i/b to be known. Trial values of X_{i+1}/b and Y_{i+1}/b (X'_{i+1} and Y'_{i+1}) can be found by

$$\Delta\left(\frac{X'}{b}\right) = \Delta\left(\frac{S}{b}\right)\cos\left(\phi_i + \frac{\Delta\phi}{2}\right) \quad (6)$$

$$\Delta\left(\frac{Y'}{b}\right) = \Delta\left(\frac{S}{b}\right)\sin\left(\phi_i + \frac{\Delta\phi}{2}\right) \quad (7)$$

where S/b is the independent variable and $\Delta\phi = \Delta S/R_i$. A trial value of R_{i+1}/b, R'_{i+1}/b, can be calculated from

$$\frac{1}{\frac{R'_{i+1}}{b}} = 2 + \beta\frac{Y'_{i+1}}{b} - \frac{\sin(\phi_i + \Delta\phi)}{\frac{X'_{i+1}}{b}} \quad (8)$$

A corrected (unprimed) value of $1/(R_i/b)$ is obtained from

$$\frac{1}{\frac{R_i}{b}} = {}^1/_2\left(\frac{1}{\frac{R_i}{b}} + \frac{1}{\frac{R_{i+1}}{b}}\right) \quad (9)$$

and from this corrected (unprimed) values of X_{i+1}/b and Y_{i+1}/b can be readily calculated by repeating the entire calculation once using the corrected value of R_i/b.

Convergence was good enough so that increments of 0.01 could be used for $\Delta S/b$. Furthermore, this method is well adapted for an electronic computer. The above procedure was programmed in machine language on a Bendix G-15 computer and solutions obtained for $-0.35 < \beta < -0.60$ in steps of 0.001. From these, tables of X_{max} and X_{min} *vs.* β were obtained by second-order interpolation using Bessel's formula. Consistency was checked by noting the constancy of higher order differences. From these tables R and H *vs.* β were in turn calculated. Again consistency was checked from higher order differences. A table of H *vs.* R was next obtained by linear interpolation and is to be published separately.

Acknowledgments. The author is grateful to the Petroleum Research Fund, which supported this work by a grant. Dr. R. S. Hansen contributed helpful discussion during the course of the work. Indiana University supplied time on their IBM 709 for an independent recalculation which confirmed the G-15 calculation.

(7) W. Thomson, *Nature*, **34**, 290 (1886).

Interaction of Alkali Metal Cations with Silica Gel[1]

by H. Ti Tien

Department of Chemistry, Northeastern University, Boston, Massachusetts *(Received September 24, 1964)*

The equilibrium selectivity order of an ion-exchanging system for the alkali metal ions is usually either that of the Hofmeister series[2] or the sequence which follows the crystal radii.[3,4] In cases in which these series are not observed, there are two theories which have been advanced recently explaining their existence.[5-7] Maatman, *et al.*, reported equilibrium exchange studies between alkali metal cations (Li, K, Na) and silica gel.[8] They found that the lithium ion is less preferred than either Na^+ or K^+, whereas no difference in selectivity coefficients was observed between Na^+ and K^+. They estimate the pK value of the silanol group of silica gel to be about 6–8. Further, Maatman, *et al.*, compare the environment of the oxygen atoms of $-OSiO^-$ and OH^- groups in aqueous solution. From their results they conclude that the reactions of these groups with the metal ions are similar. Previously, Dalton, McClanahan, and Maatman[9] measured the equilibrium

(1) The experimental work was done at Department of Basic Research, Eastern Pennsylvania Psychiatric Institute, Philadelphia, Pa., while the author was on the staff, 1957–1963.

(2) O. D. Bonner, *J. Phys. Chem.*, **59**, 719 (1955).

(3) H. P. Gregor, M. J. Hamilton, R. J. Oza, and F. Bernstein, *ibid.*, **60**, 266 (1956).

(4) C. E. Marshall and G. Garcia, *ibid.*, **63**, 1663 (1959).

(5) (a) D. O. Rudin and G. Eisenman, *Abstr. Commun. 21st Congr. Physiol., Buenos Aires*, 237 (1959); (b) G. Mattock, "pH Measurement and Titration," Macmillan Co., New York, N. Y., 1961, pp. 130–134.

(6) G. N. Ling, *J. Gen. Physiol.*, **43**, 149 (1960).

(7) H. T. Tien, *J. Phys. Chem.*, **68**, 1021 (1964).

(8) D. L. Dugger, J. H. Stanton, B. N. Irby, B. L. McConnell, W. W. Cummings, and R. W. Maatman, *ibid.*, **68**, 757 (1964).

(9) R. W. Dalton, J. L. McClanahan, and R. W. Maatman, *J. Colloid Sci.*, **17**, 207 (1962).

pH values of solutions containing silica gel and various alkali cations. The sequence of increasing pH value was found to be Li < Na < Cs < K.

Earlier, we also carried out exchange studies on silica gel. The results for the five alkali metal ions are presented here. Although Maatman, *et al.*, found no difference in selectivity coefficients between sodium and potassium ions, their reported value for lithium ion is in fair agreement with our data. Our interest in performing the exchange reactions between the alkali cations and silica gel was directed toward establishing the equilibrium selectivity sequence. The purpose of this note, in addition to presenting complete selectivity coefficient values, is to make a few observations in view of available data.

Experimental

Chemicals. Davison silica gel under the designation Code-40 (6–12 mesh) was used. The gel as received was conditioned by alternating treatment with 1 *N* NaOH and 1 *N* HCl. At the end of the third cycle, the gel was washed with distilled and deionized water, converted into the sodium form, and dried in air. The other chemicals used were of reagent grade as reported earlier.[7]

Procedure. The exchange was carried out at pH 6.7 by contacting the gel in the sodium form with 0.1 *N* chloride solutions of various alkali metals at 25°. Four sets of solutions were used with various cation (Li, K, Rb, Cs) to sodium ion ratios of 1:9, 3:7, 5:5, 7:3, and 9:1. The equilibrium selectivity values were determined with the aid of radioactive Na^{22} as the tracer. Other experimental details and the evaluation of selectivity coefficients were essentially the same as described previously.[7]

Table I: Equilibrium Selectivity Coefficients at pH 6.7

Cation	K_{Na}^{c}
Li^+	0.65
Na^{+a}	1.00
K^+	1.8
Rb^+	2.4
Cs^+	3.2

[a] Reference cation.

Results and Discussion

Table I presents equilibrium selectivity coefficients for the five alkali metal ions. The reference cation used in all cases was Na^+.

The cation exchange reaction in the present case may be represented as

$$C^+ + NaR = CR + Na^+ \quad (1)$$

where R denotes the exchange site (*i.e.*, $-OSiO^-$) of silica gel and C^+ and Na^+ are the exchanging cations. The equilibrium selectivity coefficient is defined in the usual manner and is given by

$$K_{Na}^{c} = \frac{[CR][Na^+]}{[NaR][C^+]} \quad (2)$$

The terms in brackets are equilibrium concentrations. Since the log–log plots of $[CR]/[NaR]$ *vs.* $[Na^+]/[C^+]$ give straight lines with slope equal to unity in all cases studied, the interpretation of data is greatly simplified. The linear plots imply that the equilibrium selectivity coefficients, K_{Na}^{c}, obtained in the present investigation are not affected by the composition in the gel phase. Further, the activity coefficient ratios, both in the aqueous phase and the gel phase, may be taken to be equal to unity. Therefore, as a first approximation at least, the K may be assumed to be the true thermodynamic equilibrium constant. From the results given in Table I, the order of affinity of the silica gel for alkali metal ions is Cs > Rb > K > Na > Li, which is the familiar Hofmeister series.

The fact that we were able to measure appreciable differences among the five alkali metal ions, in contrast to the study reported by Maatman, *et al.*, indicates that a higher order of resolution is possible using tracer technique. Maatman, *et al.*, report the $\Delta F°$ (in kcal.) as follows: the $\Delta F°$ for Li^+ is 10.1; the $\Delta F°$ values for Na^+ and K^+ are the same, being 9.6 in both cases. Since the free energy and the equilibrium constant are related by the familiar equation, $\Delta F° = -RT \ln K$, and the equilibrium constants are logarithmically additive, the difference between any pair therefore is easily calculated. The free energy difference between Li^+ and Na^+ (or K^+) is 0.5 kcal. as given by Maatman, *et al.* Hence, the equilibrium selectivity coefficient, K_{Na}^{Li}, is about 0.43, which is in fair agreement with the value obtained in the present study. However, the sequence Li > Na > Cs > K reported earlier by Dalton, *et al.*,[9] based on equilibrium pH measurements is in apparent contradiction with the recent work of Maatman, *et al.*,[8] and our finding reported here. If the pK value 6–8 of the silanol group of silica gel is accepted as estimated by Maatman, *et al.*, the interpretation based on the ion-exchange mechanism seems to be a dubious one. This may be seen from the following considerations. The pK value of an acid may be interpreted as a measure of electric field strength of the anion. The higher

the pK value the greater is the electric field intensity, which in turn should have a greater tendency to accept protons from neighboring water molecules (or free H^+). This phenomenon would cause the so-called "localized hydrolysis" as proposed by Robinson and Harned.[10,11] According to the Robinson–Harned theory, the intensity of the field around the cation, interacting with an anion through oriented water molecules, should increase in the order Li > Na > K > Rb > Cs. In terms of equilibrium selectivity coefficient sequence, it follows that an ion-exchange system having weak acidic groups such as carboxylic resins (*e.g.*, IRC-50) should give the same order just mentioned. This has been shown to be in accord with experimental results.[3,4,7]

To explain the apparent contradiction in the observed orders noted earlier and in the present finding, the following interpretation is offered. The silica gel used, according to the manufacturer's data, indicates that more than 50% of the surface area is associated with pores having radii between 10 and 30 Å. If we view the interaction of alkali metal cations with silica gel as a case of physical sorption, then the observed Hofmeister series may be explained on the basis of the hydrated radius of cations. Thus since the hydrated radius of lithium ion is the largest, it would have the least opportunity to interact with the gel surface. The lithium ion therefore would be the least preferred. This is essentially the interpretation given by Dalton, *et al.*[9] In regard to the exchange reaction as represented by eq. 1 and 2, the applicability to a physical sorption is not entirely surprising, since ion-exchange reactions can be treated as special cases of physical sorption, which may be represented by the empirical Freundlich adsorption isotherm, $y = ax^n$ (*i.e.*, $y = [CR]/[NaR]$, $x = [C^+]/[Na^+]$, and $a = K_{Na}^{c}$). The constant n is equal to unity in eq. 2. The exchange sites of silica gel, instead of being identified as $-SiO^-$ groups, may be described simply as the "active" sites available for physical sorption. The order Li > Na > Cs > K observed by Dalton, *et al.*,[9] at high electrolyte concentrations and pH values is also explainable from the above considerations. The silica gel is apparently capable of both exchange reaction and physical sorption depending on the experimental conditions. From eq. 1 it can be seen that at high electrolyte concentrations and pH values the ion-exchange reaction is favored, which gives the order of increasing affinity from Li^+ to Cs^+. On the other hand, the pore sizes of the gel will effectively exclude the larger ions, in which case a reversal of selectivity order is to be expected. Therefore, depending on experimental conditions, these two contrasting factors (*i.e.*, the exchange reaction and physical exclusion) may result in "unexpected" sequences of preference, such as the one noted by Dalton, *et al.*

Acknowledgment. The author wishes to express his appreciation to Dr. D. O. Rudin, Department of Basic Research, Eastern Pennsylvania Psychiatric Institute, Philadelphia, Pa., for many stimulating discussions during his stay at the Institute.

(10) R. A. Robinson and H. S. Harned, *Chem. Rev.*, **28**, 419 (1941).
(11) H. T. Tien, *J. Phys. Chem.*, **67**, 532 (1963).